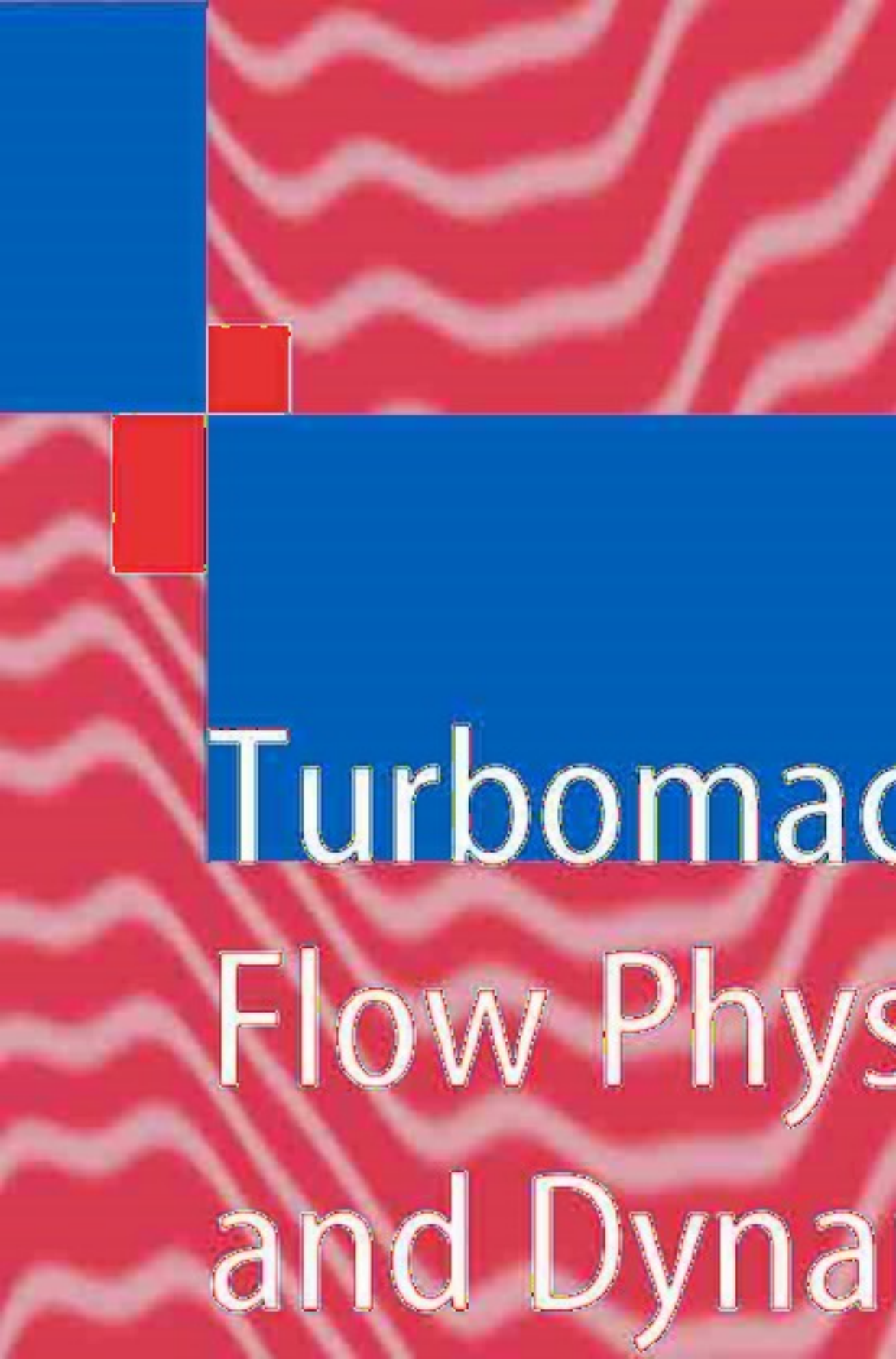
Turbomac
Flow Phys
and Dyna

Turbomachinery Flow Physics and Dynamic Performance

Meinhard Schobeiri

Turbomachinery Flow Physics and Dynamic Performance

With 317 Figures

Springer

Author

Prof. Meinhard Schobeiri
Texas A & M University
Department of Mechanical Engineering
College Station, TX 77843-3123
USA

ISBN 978-3-540-22368-9 **Springer Berlin Heidelberg New York**

Library of Congress Control Number: 2004113684

Springer is a part of Springer Science+Business Media

springeronline.com

Printed in Germany

Typesetting: Data conversion by the authors.
Final processing by PTP-Berlin Protago-TEX-Production GmbH, Germany
Cover-Design: medionet AG, Berlin
Printed on acid-free paper 62/3020Yu - 5 4 3 2 1 0

Preface

Turbomachinery performance, aerodynamics, and heat transfer have been subjects of continuous changes for the last seven decades. Stodola was the fist to make a successful effort to integrate the treatment of almost all components of steam and gas turbines in a single volume monumental work. Almost half a century later, Traupel presented the third and last edition of his work to the turbomachinery community. In his two-volume work, Traupel covered almost all relevant aspects of turbomachinery aerodynamics, performance, structure, rotordynamics, blade vibration, and heat transfer with the information available up to the mid-seventies. In the meantime, the introduction of high speed computers and sophisticated computational methods has significantly contributed to an exponential growth of information covering almost all aspects of turbomachinery design. This situation has lead to a growing tendency in technical specialization causing the number of engineers with the state-of-the-art combined knowledge of major turbomachinery aspects such as, aerodynamics, heat transfer, combustion, rotordynamics, and structure, to diminish. Another, not minor, factor in the context of specialization is the use of "black boxes" in engineering in general and in turbomachinery in particular. During my 25 years of turbomachinery R&D experience, I have been encountering engineers who can use commercial codes for calculating the complex turbomachinery flow field without knowing the underlying physics of the code they use. This circumstance constituted one of the factors in defining the framework of this book, which aims at providing the students and practicing turbomachinery design engineers with a sold background in turbomachinery flow physics and performance. As a consequence, it does not cover all aspects of turbomachinery design. It is primarily concerned with the fundamental turbomachinery flow physics and its application to different turbomachinery components and systems. I have tried to provide the turbomachinery community, including students and practicing engineers, with a lasting foundation on which they can build their specialized structures.

I started working on this book when I left Brown Boveri, Gas Turbine Division in Switzerland (1987) and joined Texas A&M University. A part of my lecture notes in graduate level turbomachinery constitutes the basics of this book, which consists of three parts. Part I encompassing Chapters 1 to 6 deals with turbomachinery flow physics. Explaining the physics of a highly three-dimensional flow through a turbine or a compressor stage requires adequate tools. Tensor analysis is a powerful tool to deal with this type of flow. Almost all graduate level fluid mechanics and computational fluid dynamics (CFD) courses at Texas A&M University, and most likely at other universities, make use of tensor analysis. For the reader, who might not be familiar with the tensor analysis, I tailored the quintessential of tensor analysis in Appendixes A and B to the need of the reader who is willing to spend a few hours on this topic.

Chapters 2 and 3 deal with the Kinematics and Differential Balances in turbomachinery in three-dimensional form. In dealing with three-dimensional turbulent flows through a turbomachinery component, I refrained from presenting a multitude of existing turbulence models for three reasons. Firstly, the models are changing continuously; the one which is thought today to be the ultimo ratio may be obsolete tomorrow. Secondly, there is a vast amount of papers and publications

devoted to turbulence modeling and numerical methods in turbomachinery. In my view, summarizing these models and methods without getting into details is not appropriate for a text. Thirdly, the emergence of the direct numerical simulation (DNS) as the ultimate solution method, though not very practical at the time being, will in the near future undoubtedly eliminate the problems that are inherently associated with Reynolds averaged Navier Stokes equations (RANS). Considering this situation, I focused my effort on briefly presenting the RANS-equations and introducing the intermittency function. The resulting equations containing the product of the intermittency and the Reynolds stress tensor clearly illustrate how the accuracy of these two models affect the numerical results. As a logical followup, Chapter 4 extensively discusses the integral balances in turbomachinery. Chapters 5 and 6 deal with a unified treatment of energy transfer, stage characteristics, and cascade and stage aerodynamics. Contrary to the traditional approach that treats turbine and compressor stages of axial or radial configuration differently, I have tried to treat these components using the same set of equations.

Part II of this book containing Chapters 7 through 11 starts with the treatment of cascade and stage efficiency and loss determination from a physically plausible point of view. I refrained from presenting recipe-type of empirical formulas that have no physical foundation. Chapters 10 and 11 deal with simple designs of compressors and turbine blades and calculation of incidence and deviation. Radial equilibrium is discussed in Chapter 11 which concludes Part II.

Part III of the book is entirely dedicated to dynamic performance of turbomachinery components and systems. Particular attention is paid to gas turbine components, their individual modeling, and integration into the gas turbine system. It includes Chapter 12 to 18. Chapter 12 introduces the non-linear dynamic simulation of turbomachinery systems and its theoretical background. Starting from a set of general four dimensional partial differential equations in temporal-spatial domain, two-dimensional equation sets are derived that constitute the basis for component modeling. The following Chapter 13 deals with generic modeling of turbomachinery components and systems followed by Chapters 14, 15, 16, and 17 in which individual components ranging from the inlet nozzle to the compressor, combustion chamber, turbine, and exhaust diffuser are modeled. In modeling compressor and turbine components, non-linear adiabatic and diabatic expansion and compression calculation methods are presented. Chapter 18 treats gas turbine engines, design and dynamic performance. Three representative case studies conclude this chapter. In preparing Part III, I tried to be as concrete as possible by providing examples for each individual component.

In typing several thousand equations, errors may occur. I tried hard to eliminate typing, spelling and other errors, but I have no doubt that some remain to be found by readers. In this case, I sincerely appreciate the reader notifying me of any mistakes found; the electronic address is given below. I also welcome any comments or suggestions regarding the improvement of future editions of the book.

My sincere thanks are due to many fine individuals and institutions. First and foremost, I would like to thank the faculty of the Technische Universität Darmstadt, from whom I received my entire engineering education. I finalized major chapters of

the manuscript during my sabbatical in Germany, where I received the Alexander von Humboldt Prize. I am indebted to the Alexander von Humboldt Foundation for this Prize and the material support for my research sabbatical in Germany. My thanks are extended to Prof. Bernd Stoffel, Prof. Ditmar Hennecke, and Dipl. Ing. Bernd Matyschok for providing me with a very congenial working environment. I truly enjoyed interacting with these fine individuals. NASA Glenn Research Center sponsored the development of the nonlinear dynamic code GETRAN, which I used to simulate cases in Part III. I wish to extend my thanks to Mr. Carl Lorenzo, Chief of Control Division, Dr. D. Paxson, and the administration of NASA Glenn Research center. I also thank Dr. Richard Hearsey for providing me with a three-dimensional compressor blade design example that he obtained from his streamline curvature program. I also would like to extend my thanks to Dr. Arthur Wennerstom for providing me with the updated theory on the streamline curvature method.

I am also indebted to TAMU administration for partially supporting my sabbatical that helped me in finalizing the book. Special thanks are due to Mrs. Mahalia Nix, who helped me in cross-referencing the equations and figures and rendered other editorial assistance.

Last but not least, my special thanks go to my family, Susan and Wilfried for their support throughout this endeavor.

September, 2003
College Station, Texas

M.T. Schobeiri
tschobeiri@mengr.tamu.edu

Contents

III Turbomachinery Dynamic Performance

Nomenclature

A	force vector
b	trailing edge thickness
c	blade chord length
c	speed of sound
c	blade chord length
C_D	cascade drag coefficient
C_f	friction coefficient
C_i,,	constants
C_L	blade lift coefficient
C_L^*	camberline lift coefficient
c_p, c_v	fpecific heat capacities
d	frailing edge thickness in cascade front d = $b/\sin\alpha_2$
D	dimensionless trailing edge thickness
D	diffusion factor
D	material or substantial differential operator
D	deformation tensor
De	equivalent diffusion factor
D_h	Hydraulic diameter
D_m	modified diffusion factor
e	specific total energy
E	total energy
E_λ	Planck's spectral emissive power
e_i	orthonormal unit vector
f	flot thickness/trailing edge thickness ratio $f = s/b$
F	auxiliary function
F	auxiliary function
F	fuel
F	force
f_C,	reheat factor for a compressor with n stages
f_T,	recovery factor for a turbine with n stages
f_∞	recovery factor for infinite number of stages
G	circulation function
g_i, g^i	co, covariant base vectors in orthogonal coordinate system
G_i	fuxiliary functions
$\mathbf{G}_i$	transformation vector
h	hot

h	specific enthalpy
h	height
h, H	specific static, specific total enthalpy
H	immersion ratio
H	shape factor
H	immersion ratio
H_{12}	form factor, $H_{12} = \delta_1/\delta_2$
H_{13}	form factor, $H_{32} = \delta_3/\delta_2$
$\dot{q}$	heat flux
i	incidence angle
i	incidence angle
i	Shaft number
I	Moment of inertia
I	Intermittency function
I_1, I_2, I_3	principle invariants of deformation tensor
J	Jacobian transformation function
k	thermal conductivity
K	specific kinetic energy
l, m	coordinates introduced for radial eqilibrium
L	stage power, Length
l_m	specific shaft power
m	mass
M	Mach number
M	vector of moment of momentum
$\mathbf{M}_a$	axial vector of moment of momentum
$\dot{m}$	mass flow
n	polytropic exponent
n	number of stations
n	normal unit vector
Nu	nusselt number
p, P	static, total pressure
P	pressure side
$P = p + \rho V^2/2$	total pressure
Pr	Prandtl number
P,S	pressure, suction surface
q	specific thermal energy
Q	thermal energy
Q	strength of sink or source
r	degree of reaction
r	position vector in conformal transformation
R	radius in conformal transformation
$R = \rho_3/\rho_2$	density ratio
R	radiation
R	radius of the mean flow path
Re	Reynolds number

r_i,	radius of stage stream surface
r_i,	radius of stage stream surface
R_w	thermal resistance
s	specific entropy
s	Shock
s	slot thickness, surface
S	spacing
S_i	cross section at station i
St	Stanton number
Str	Strouhal number
t	tangential unit vector
t	time
t	thickness
T	tangential force component
T, T^*	absolute static temperature
T	static temperature
$\mathbf{T} = e_i e_j \tau_{ij}$	atress tensor
T	tangential force component
Q	thermal energy flow
T_o	stagnation or total temperature
Tr	trace of second order tensor
u	specific internal energy
u	specific internal energy
U, V, W	rotational, absolute, relative velocity components
v	specific volume
V	volume
V_{max}	maximum velocity on suction surface
X	state vector
x_i	coordinates
Z	stage profile loss
α	*heat transfer coefficient*
α, β	absolute and relative flow angles
α_{st}	stagnation angle in conformal transformation
γ	intermittency factor
γ	specific circulation function, shock angle
Γ	circulation strength
$\mathbf{\Gamma}$	circulation vector
Γ^i_{jk}	Christoffel symbol
γ_{min}, γ_{max},	minimum, maximum intermittency
δ	boundary layer displacement thickness
δ	*deviation angle*
δ	*boundary layer displacement thickness*
δ	*Kronecker delta*
δ_1, δ_2, δ_3,	*boundary layer dissplacement, momentum, energy thickness*
Δ_1, $\Delta 2$	dimensionless boundary layer displacement thickness

Δ_1, Δ_2	dimensionless displacement, momentum thickness
ϵ	loss coefficient ratio
ϵ	convergence tolerance
ζ	loss coefficient
ζ	loss coefficient
η	velocity ratio
η	efficiency
η	velocity ratio
θ	segment angle
Θ	boundary layer momentum thickness,
Θ	shock expansion angle
Θ	temperature ratio
κ	ratio of specific heats
κ	isentropic exponent
λ	wave length
λ	stage load coefficient
Λ	load function
μ	mass flow ratio, Kinematic viscosity
μ	absolute viscosity
μ,ν,ϕ	velocity ratios
ν	kinematic viscosity
ν_m	straight cascade stagger angle
$\boldsymbol{\xi}$	position vector in material coordinate system
ξ	distance ratio $\xi = x/b$
ξ_i	components of position vector $\boldsymbol{\xi}$
π	pressure ratio
$\boldsymbol{\Pi}$	stress tensor, $\boldsymbol{\Pi} = e_i e_j \pi$
Π	stress tensor
ρ	sensity
ρ	ensity
σ	cascade solidityσ = c/s
σ	cascade solidityσ = c/s
τ	temperature tratio
τ_o	wall sear stress
τ_o	wall sear stress
ϕ	stage flow coefficient
Φ, ψ	potential, stream function
Φ	potential function
X	complex function
ψ	isentropic stage load coefficient
Ψ	stream function
ω	angular velocity
$\boldsymbol{\Omega}$	Rotation tensor

Subscripts, superscripts

a, t	axial, tangential
c	compressible
C	compressor
C	cold side
C, S, R	cascade, stator, rotor
Fi	film
F	flame
G	combustion gas
H	hot side
in	inlet
ex	exit
max	maximum
s	isentropic
s	shock
/, //	stator, rotor

1 Introduction, Turbomachinery, Applications, Types

Turbomachines are devices within which conversion of total energy of a working medium into mechanical energy and vice versa takes place. Turbomachines are generally divided into two main categories. The first category is used primarily to produce power. It includes, among others, steam turbines, gas turbines, and hydraulic turbines. The main function of the second category is to increase the total pressure of the working fluid by consuming power. It includes compressors, pumps, and fans.

1.1 Turbine

Turbines serve as power producing devices. Figure 1.1 exhibits a large steam turbine used for base load power generation. It consists of an integrated *high pressure* (HP), an *intermediate pressure* (IP), and two identical *low pressure* (LP) components.

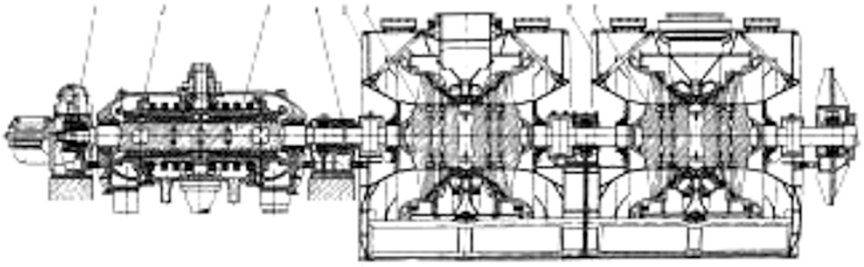

Fig 1.1: A large steam turbine for base load power generation with an integrated high pressure, an intermediate pressure part (left), and two identical double inflow low pressure turbine components (Brown Boveri & Cie design).

Each component incorporates a number of *stages* consisting of *stator-* and *rotor-blading*. Steam at a given level of total energy, enters the HP-turbine component shown in Fig. 1.2, passes through the first stator row, and undergoes a certain degree of deflection, which is necessary to provide appropriate inlet conditions for the rotor row that follows. The stator blades are attached to the inner casing, which is under higher pressure than the outer one, Fig. 1.2. During the course of deflection, the working fluid is accelerated. As a result, the potential energy of steam is partially converted into kinetic energy, which is used in the following rotor blading. Due to the rotational motion of the rotor, a part of the total energy is converted into mechanical energy, generating shaft power. This process is repeated

in the following stages until the exit conditions are reached. The HP-turbine component is characterized by a relatively small blade height compared to the LP-component. As seen in Figs. 1.1, the cross sections of the integrated HP- and IP-part, experience only a moderate change due to a moderate increase in specific volume. In contrast, the specific volume changes drastically within the LP-part, requiring an excessive opening of the cross section to accommodate large blade heights.

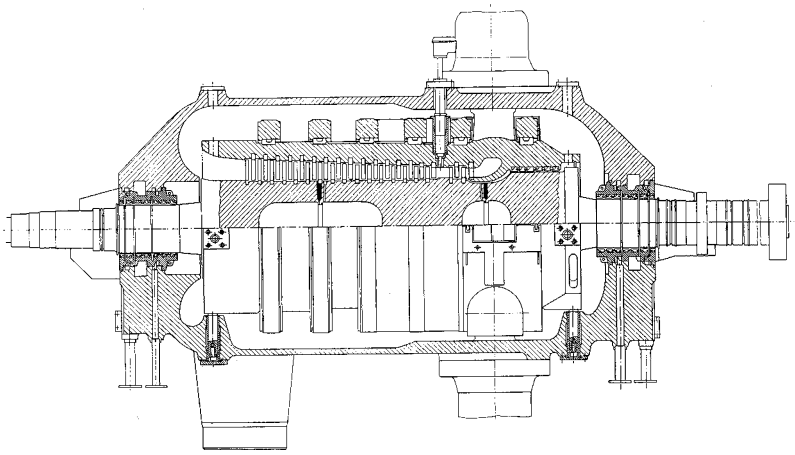

Fig. 1.2: A typical HP-steam turbine with the first control stage, inner and outer casings and labyrinth seal packets, (ABB Power Generation)

Fig. 1.3: A three stage high pressure research turbine at *TPFL.* The blades are cylindrical with tip shroud to reduce the tip leackage losses

Figure 1.2 shows an HP-turbine with a control stage and a multi-stage arrangement attached to a shaft that consists of three welded discs. It also reveals the labyrinths installed on both shaft ends to seal the high pressure steam against the atmospheric pressure. HP-turbine blades may have cylindrical (2-D) or three-dimensionally (3-D) bowed blades. Figures 1.3 and 1.4 show two different rotors with the 2-D cylindrical and 3-D bowed blade. The cylindrical blades are more cost effective and easier to manufacture than the 3-D bowed blades, however, their efficiency is below the 3-D blade efficiency.

Fig. 1.4: A three-stage high pressure research turbine with bowed blades and tip shroud to reduce secondary flow and tip clearance losses

Details of a typical LP-turbine component are shown in Fig. 1.5. Characteristic features of this component are the symmetric configuration of the shaft and the blading, as well as the steep increase in blade height. The symmetric configuration is used to cancel the axial thrust on the bearings. In contrast to the HP-components with a high back pressure, the back pressure of LP-component corresponds to the condenser pressure, which is a fraction of the environmental pressure and strongly depends on environmental temperature.

Figure 1.6 exhibits the details of a typical labyrinth seal. The kinetic energy of the jets through the labyrinth clearance is dissipated within the labyrinth chambers preventing the leakage mass flow to become excessive. While the HP-labyrinths reduce the steam leakage to the atmosphere, the LP-seals prevent the atmospheric air to penetrate into the LP-turbine, disrupting the condenser vacuum.

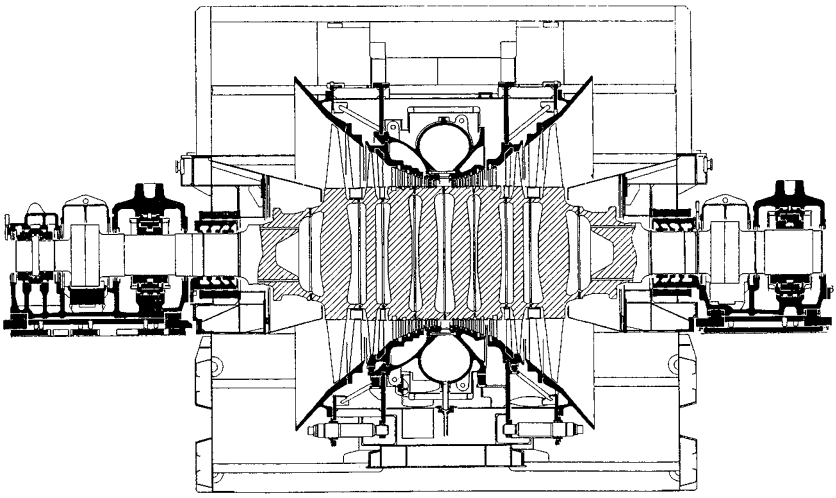

Fig. 1.5: A double inflow low pressure turbine component(ABB Power generation).

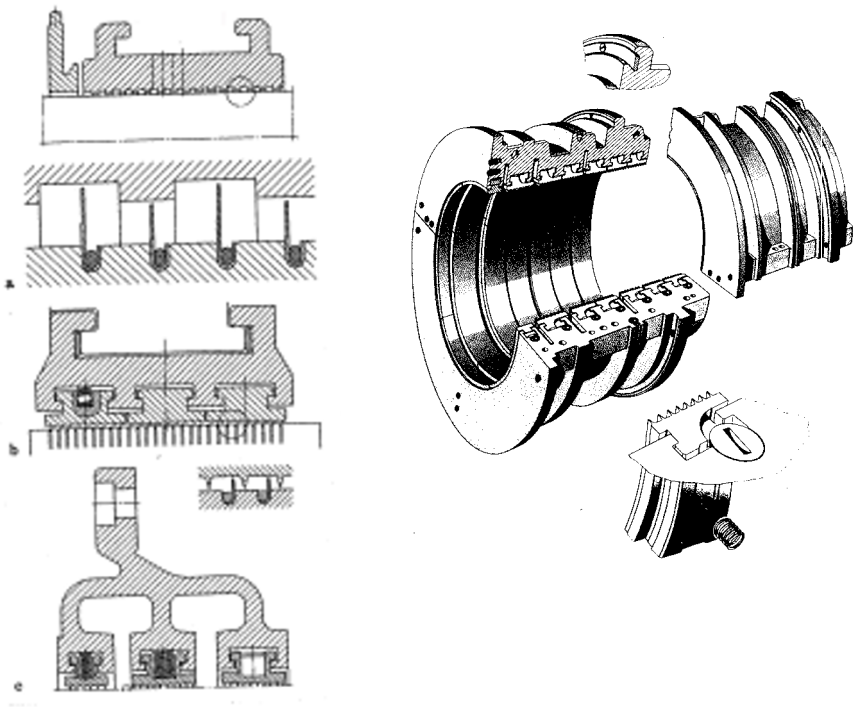

Fig. 1.6: HP-turbine labyrinth seals

1.2 Compressor

The function of a compressor is to elevate the total pressure of the working fluid. According to the conservation law of energy, this total pressure increase requires external energy input which must be added to the system in the form of mechanical energy.

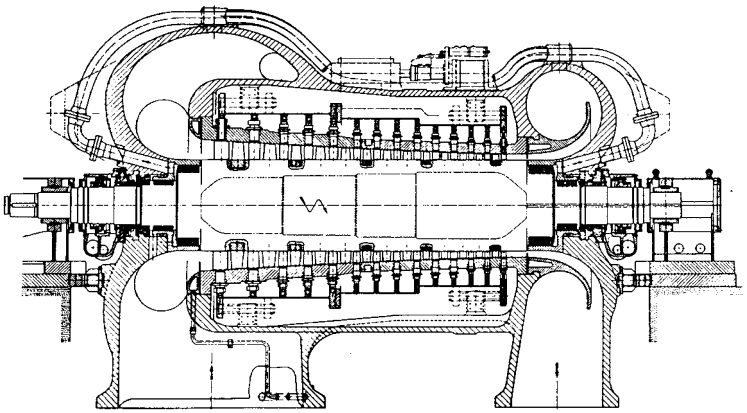

Fig. 1.7: A multi-stage high pressure compressor (Sulzer)

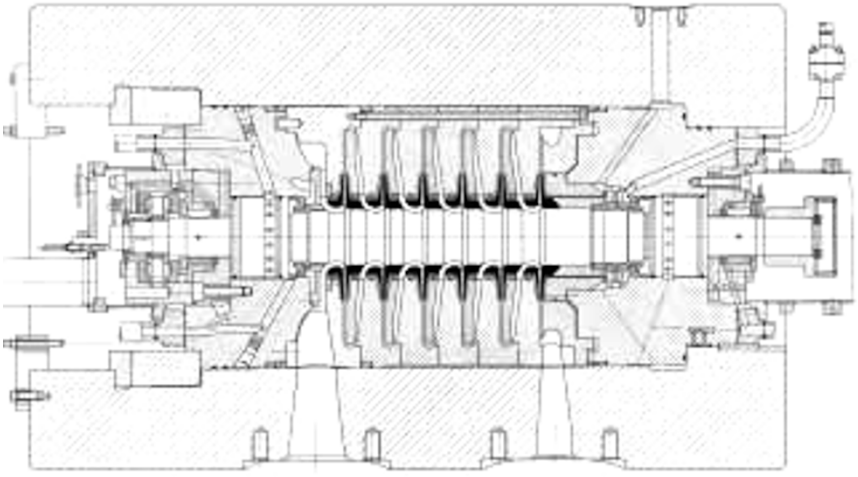

Fig. 1.8: A high pressure centrifugal compressor with an exit pressure of up to 900 bar and a volume flow rate of up to 300,000 m^3/h (MANNESMANN-DEMAG)

The compressor rotor which is driven either by an electric motor or a turbine, exerts forces on the fluid medium and therefore increases its pressure. Compressors are utilized, among others, in pipeline systems, chemical industry, steel production for blowing oxygen and oxygen enrichment of blast furnace air, biological sewage treatments, and gas liquefaction. In power generation and aircraft gas turbines the compressor component provides the pressure ratio essential for maintaining the process of power or thrust generation. Pumps are a special type of turbo compressor with liquids as working fluids. Pumps have a wide application field. In base load power generation they serve as the feed water pumps and main condenser pumps to elevate the steam pressure from condenser pressure to boiler pressure. Pumps are also major components in rocket engines.

Fig. 1.9: Rotor unit of a heavy duty gas turbine with multi-stage compressor and turbine, compressor pressure ratio 15:1, (ABB-GT13E2)

Figure 1.7 shows a high pressure axial compressor with a carefully designed inlet nozzle and exit diffuser. To balance the axial thrust originating from the pressure difference, the pressures on both sides of the shaft are balanced through a connecting pressure equalizing pipe. Figure 1.8 shows major design features of a high-pressure compressor with a wide variety of applications. The area of application for these types of compressors include chemical and petrochemical industries, amonia plants, urea and methanol synthetics, gas pipeline, and nuclear reactors. Figure 1.9 shows the integration of the compressor component onto the shaft of a heavy duty power generation gas turbine. The compressor component provides the optimum process pressure ratio of 15:1 and a design flow of 525 kg/s that are essential for generating

a power output of 161 MW. Significantly higher pressure ratios can be obtained by utilizing centrifugal compressors.

1.3 Application of Turbomachines

1.3.1 Power Generation, Steam Turbines

There is a wide range for application of turbomachines; a few of them are already mentioned above . The most important application field is electric power generation. Demand of electrical energy is covered by large (up to 1300 MW) and medium size (up to 400 MW) steam turbines, Fig. 1.1. Steam turbines of small size are used in the chemical and paper industry as well as in transportation systems. Hydraulic turbines are used primarily for electric power generation.

1.3.2 Power Generation, Gas Turbines

Another important application field of turbomachines is gas turbine technology. A gas turbine engine incorporates compressor and turbine components. As power generating units, gas turbines are used to cover the electric energy demand during peak load periods. The thermal energy of exhaust gases of a gas turbine can be used to generate steam for additional power generation. This is accomplished by a combined cycle which exhibits an efficient device for base load power generation with an overall thermal efficiency of over 55%. Figure 1.9 exhibits a conventional single-spool

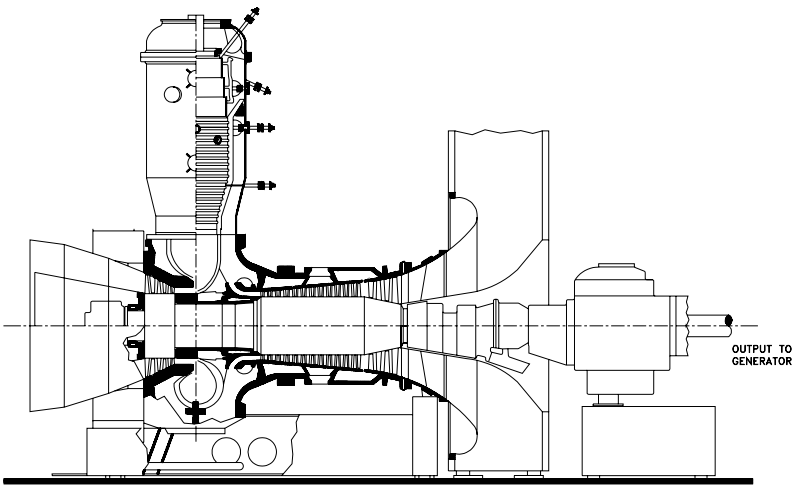

Fig. 1.10: Single-spool power generation gas turbine engine with a multi-stage compressor, a combustion chamber, and multi-stage turbine, (GT-9, ABB).

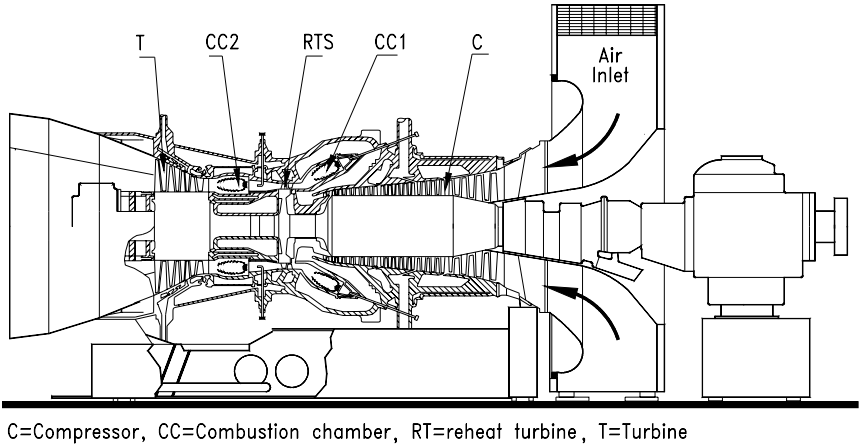

Fig. 1.11: Schematic cross- section of GT-24 gas turbine engine with a single stage reheat turbine and a second combustion chamber, ABB.

power generation gas turbine engine with a thermal efficiency close to 33%. To substantially improve the thermal efficiency without a significant increase in turbine inlet temperature, a well-known reheat principle as a classical method for thermal efficiency augmentation is applied. This standard efficiency improvement method is routinely applied in steam turbine power generation, and for the first time, in 1948, it was applied to a power generation gas turbine plant in Beznau, Switzerland, Frutschi [1]. The plant is still operational after almost half a century, has a turbine inlet temperature of 600 ^{o}C, and an efficiency of 30%, which is remarkably high for this very low turbine inlet temperature.

Despite the predicted high efficiency at the conventional turbine inlet temperature, the sequential combustion did not find its way into the aircraft and power generation gas turbine design. The reason was the inherent problem of integrating two combustion chambers into a conventionally designed gas turbine engine. This issue raised a number of unforeseeable design integrity and operational reliability concerns. ABB (former Brown Boveri & Cie) was the first to develop a gas turbine engine with a single shaft, two combustion chambers, and a reheat turbine stage followed by a multi-stage turbine, Fig. 1.11.

1.3.3 Aircraft Gas Turbines

Besides power generation, gas turbines play an important role in transportation. Aircraft gas turbines are the main propulsion systems of large, medium, and small size aircrafts. As an example, a high bypass ratio aircraft gas turbine engine is shown in Fig. 1.12.

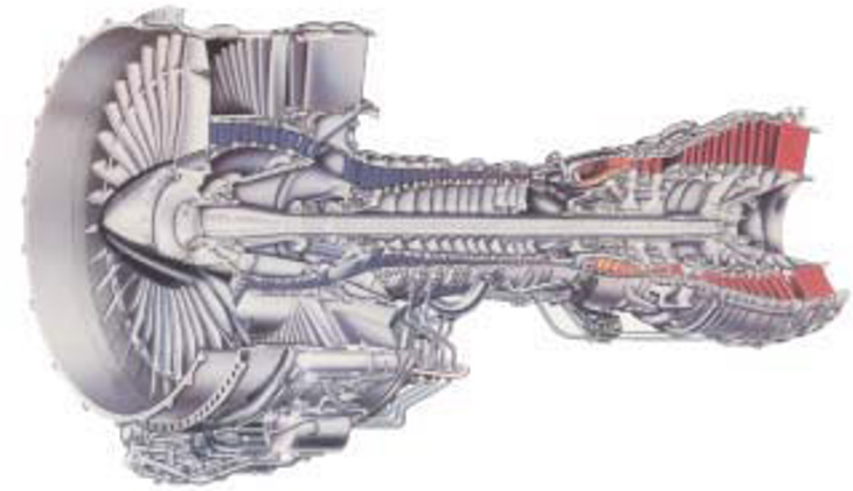

Fig. 1.12: Twin-spool, high bypass ratio aircraft engine (Pratt & Whitney)

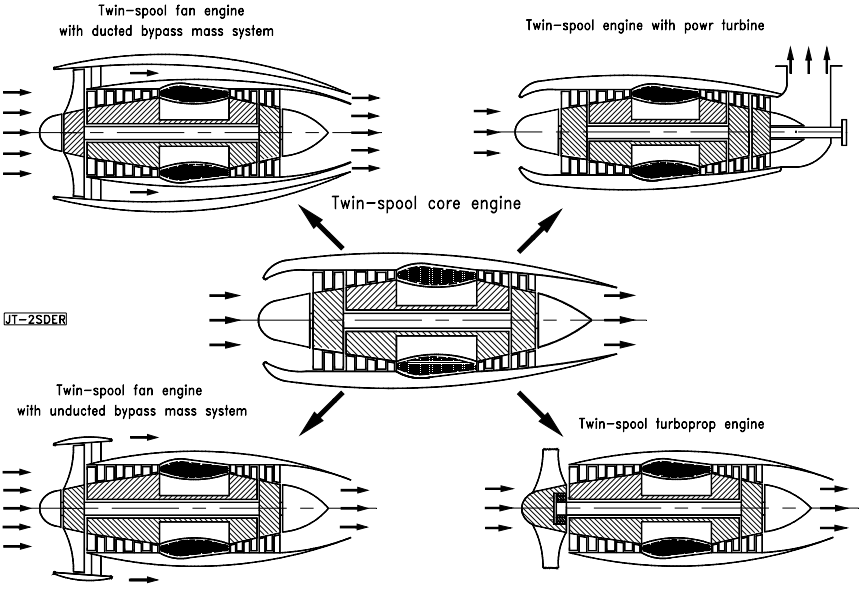

Fig. 1.13: Schematic of a twin-spool core engine with its derivatives

It consists of *a high pressure and a low pressure spool*. The low pressure spool carries the *fan stage* and the LP-turbine component. The HP- turbine drives the HP-compressor via the connecting shaft. The two spools running at two different rotational speed are connected aerodynamically with each other.

Using a single spool or a twin spool core engine, a variety of derivatives can be designed to perform different functions as Fig. 1.13 suggests.

1.3.4 Diesel Engine Application

Turbochargers, which are small gas turbines, are applied to small and large Diesel engines, to increase the effective mean piston pressure and therefore improve the thermal efficiency of Diesel engine. As an example, typical turbocharger for large Diesel engines is shown in Fig. 1.14. It consists of an air filter, inlet nozzle, a radial compressor stage, driven by a single stage axial turbine. Exhaust gas from Diesel engine enters the turbocharger turbine side and drives the turbine. The turbine drives the compressor stage that sucks air from the environment and delivers it to the piston, thereby substantially increasing the mean effective piston pressure and thermal efficiency of the engine. High efficiency of 45% are achieved by turbocharging large large engines. The compression process is accomplished by a single radial impeller.

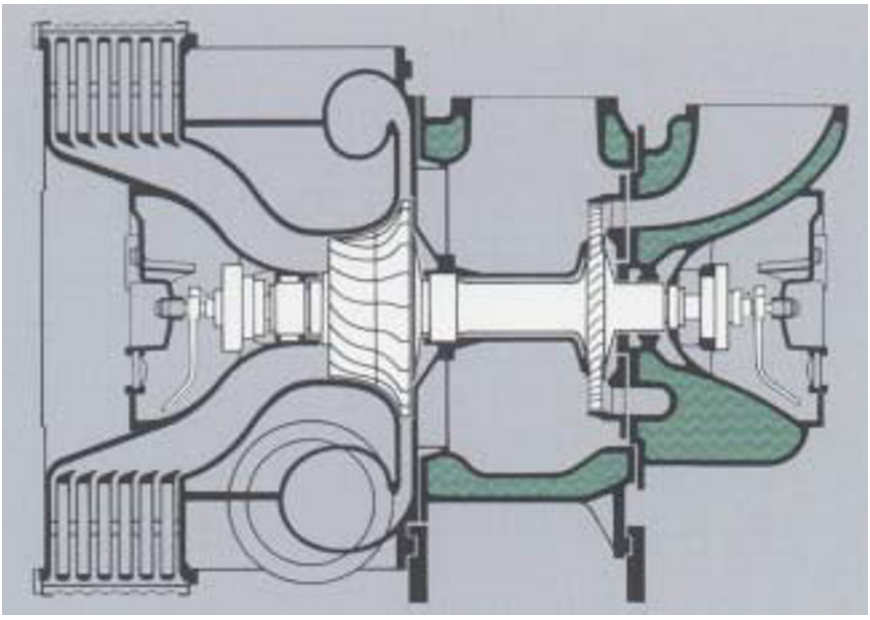

Fig. 1.14: Turbocharger for a large Diesel engine of 10 MW power, compressor pressure ratio 4.0:1 (ABB)

1.4 Classification of Turbomachines

Turbomachines are classified into different categories according to their specific applications. Following parameters determine the type of the turbomachines: (1) Working fluid, liquid or gaseous, (2) required power generation for turbines, (2) required pressure ratio and mass flow for compressors.

1.4.1 Compressor Types

Radial compressors are generally used for higher pressure ratios and small mass flow rates. For pressure ratios up to 35 and higher mass flow rates, axial compressors are used. For liquid working fluids, radial compressors (pumps) are common.

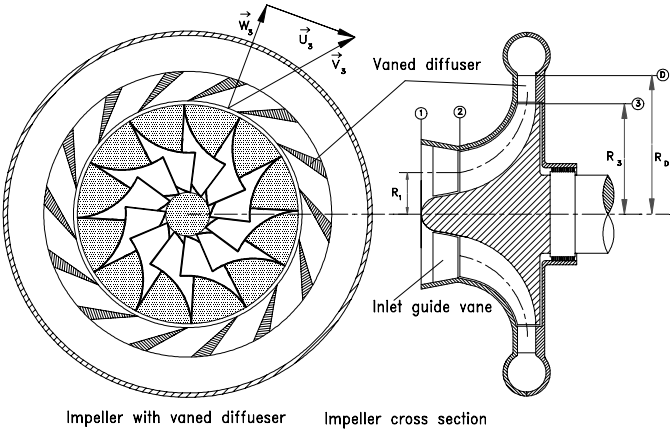

Fig. 1. 15: single stage radial compressor with an inlet guide vane and exit diffuser

Fig. 1.16: Radial compressor rotor, 3-D image, front view, cross section

Figure 1.15 exhibits the cross section of a typical radial compressor rotor with the exit diffusers to reduce the exit kinetic energy of the working medium. A 3-D image of such a rotor is shown in Fig. 1.16

1.4.2 Turbine Types

A significant criterion for selecting gas or steam turbine types is the mass flow. For small mass flow rates, both axial and radial turbines can be used. However, for higher mass flow rates the application of the axial type is the common practice. Hydraulic turbine types depends on the head and capacity of water sources. The axial type (Kaplan turbine) is especially applied to low head, high capacity; while the radial type (Francis turbine) is for medium head. For very high hydraulic head, a special water wheel (Pelton wheel) is used.

1.5 Working Principle of a Turbomachine

The conversion of total energy into shaft work or vice versa, can also be established with simple reciprocating (piston-cylinder) engines. Why should a turbomachine be applied? The answer to this question involves the limitation of power and mass flow associated with the reciprocating engines. The reciprocating engine, which works entirely on the displacement principle, is not able to transfer large amount of mass flow or mechanical energy. The largest operating Diesel engine has a power output of about 20 MW, whereas a large steam power plant may produce up to 1300 MW. Unlike the reciprocating engines the working principle of a turbomachine is based on exchange of momentum between the blading and the working fluid.

References, Chapter 1

1.1 Frutschi, H.U., 1994, “Advanced Cycle System with new GT24 and GT26 Gas Turbines, Historical Background,” ABB Review 1/94.

2 Kinematics of Turbomachinery Fluid Motion

2.1 Material and Spatial Description of the Flow Field

2.1.1 Material Description

The turbomachinery aerodynamic design process has been experiencing continuous progress using the Computational Fluid Dynamics (CFD) tools. The use of CFD-tools opens a new perspective in simulating the complex three-dimensional (3-D) turbomchinery flow field. Understanding the details of the flow motion and the interpretation of the numerical results require a thorough comprehension of fluid mechanics laws and the kinematics of fluid motion within the turbomchinery component. Kinematics is treated in many fluid mechanics texts. Aris [1] and Spurk [2] give excellent accounts of the subject. In the following sections, a compact and illustrative treatment is given to cover the basic needs of the reader.

The kinematics is the description of the fluid motion and the particles without taking into account how the motion is brought about. It disregards the forces that cause the fluid motion. As a result, in the context of kinematics, no conservation laws of motion will be dealt with. Consequently, the results of kinematic studies can be applied to all types of fluids and exhibit the ground work that is necessary for

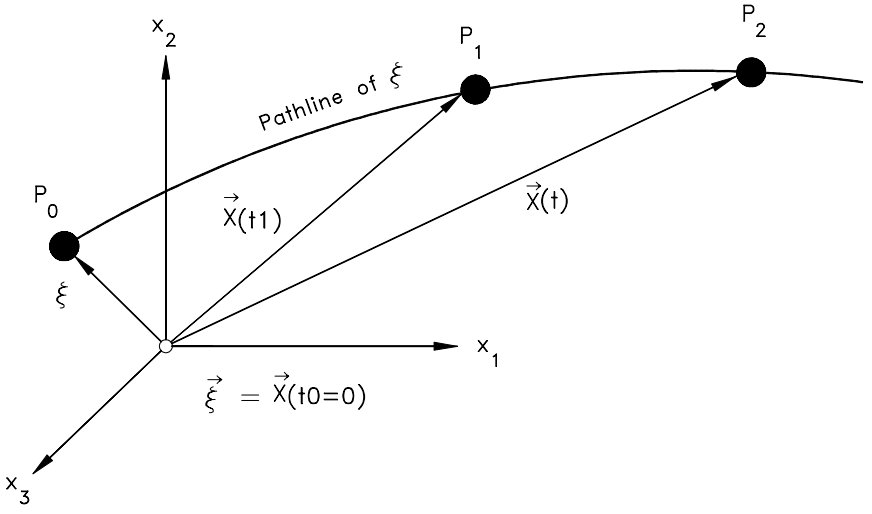

Fig. 2.1: *Material description* of a fluid particle at different instants of time.

describing the dynamics of the fluid. The motion of a fluid particle with respect to a reference coordinate system is in general given by a time dependent position vector $\boldsymbol{x}(t)$, Fig. 2.1.

To identify a particle or a *material point* at a certain instance of time $t = t_0 = 0$, we introduce the position vector $\boldsymbol{\xi} = \boldsymbol{x}(t_0)$. Thus, the motion of the fluid is described by the vector:

$$\boldsymbol{x} = \boldsymbol{x}(\boldsymbol{\xi}, t), \quad x_i = x_i(\boldsymbol{\xi}, t) \tag{2.1}$$

with x_i as the components of vector $\mathbf{x}$, as explained in A1.1. Equation (2 .1) describes the path of a material point that has an initial position vector $\boldsymbol{\xi}$ that characterizes or better labels the material point at $t = t_0$. We refer to this description as the *material description*. It should be mentioned that the term *Lagrangian description* is also used, but is lacking descriptive quality and is forgotten or confused by students. Considering another material point with different $\boldsymbol{\xi}$- coordinates their paths are similarly described by Eq. (2.1). If we assume that the motion is continuous and single valued, then the inversion of Eq. (2 .1) must give the initial position $\boldsymbol{\xi}$ or material coordinate of each fluid particle which may be at any position $\boldsymbol{x}$ and any instant of time *t;* that is,

$$\boldsymbol{\xi} = \boldsymbol{\xi}(\boldsymbol{x}, t), \quad \xi_i = \xi_i(\boldsymbol{x}, t) \tag{2.2}$$

The necessary and sufficient condition for an inverse function to exist is that the *Jacobian transformation function*

$$J = \left(\varepsilon_{kmn} \frac{\partial x_k}{\partial \xi_1} \frac{\partial x_m}{\partial \xi_2} \frac{\partial x_n}{\partial \xi_3} \right) \tag{2.3}$$

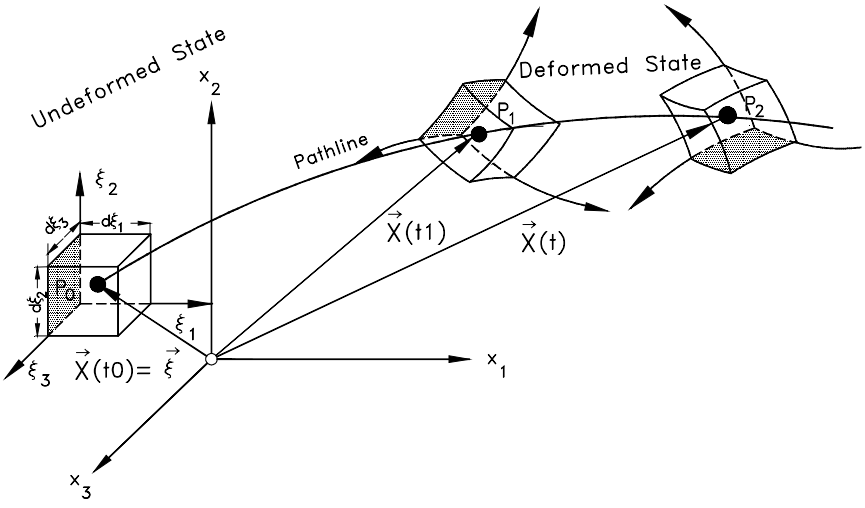

Fig. 2.2: Deformation of a differential volume at different instance of time.

does not vanish. Because of the significance of the Jacobian transformation function to fluid mechanics, we derive this function in the following section.

2.1.2 Jacobian Transformation Function and its Material Derivative

We consider a differential *material volume* at the time $t = 0$, to which we attach the reference coordinate system ξ_1, ξ_2, ξ_3, as shown in Fig. 2.2. At the time $t = 0$, the reference coordinate system is fixed so that the *undeformed* differential material volume dV_0 (Figs. 2.2 and 2.3) can be described as:

$$dV_o = (e_1 d\xi_1 \times e_2 d\xi_2) \cdot e_3 d\xi_3 = d\xi_1 d\xi_2 d\xi_3 \tag{2.4}$$

Moving through the space, the differential material volume may undergo certain deformation and rotation. As deformation takes place, the sides of the material volume initially given as $d\xi_i$ would be convected into a non-rectangular, or curvilinear form. The changes of the deformed coordinates are then:

$$dx = \frac{\partial x}{\partial \xi_1} d\xi_1 + \frac{\partial x}{\partial \xi_2} d\xi_2 + \frac{\partial x}{\partial \xi_3} d\xi_3 = \frac{\partial x}{\partial \xi_i} d\xi_i \tag{2.5}$$

Using the index notation for the position vector $x = e_k x_k$, Eq. (2 .5) may be rearranged in the following way:

$$dx = e_k \frac{\partial x_k}{\partial \xi_i} d\xi_i \equiv G_i d\xi_i \tag{2.6}$$

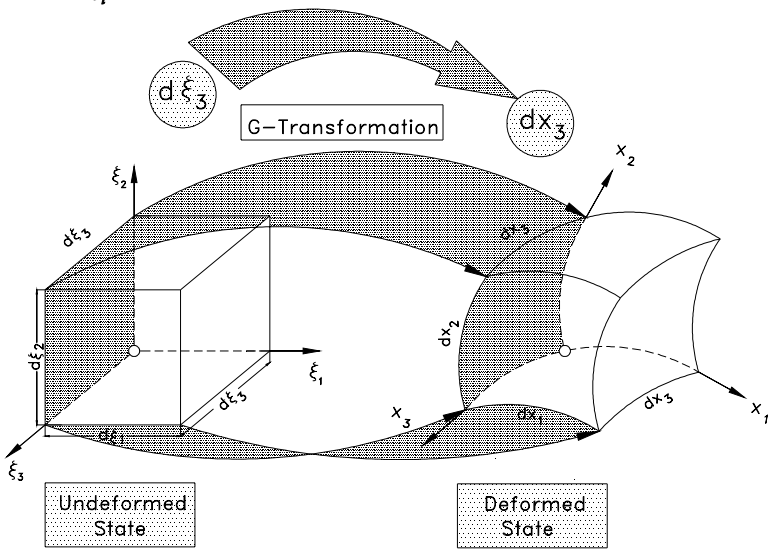

Fig. 2.3: Transformation of $d\xi_1$, $d\xi_2$, $d\xi_3$ into dx_1, dx_2, and dx_3 using G-transformation.

with the vector $\boldsymbol{G}_i$as

$$\boldsymbol{G}_i \equiv e_k \frac{\partial x_k}{\partial \xi_i} \tag{2.7}$$

where G_i is a *transformation vector function* that transforms the differential changes $d\xi_i$ into dx_i. Figure 2.3 illustrates the deformation of the material volume and the transformation mechanism. The new deformed differential volume is obtained by:

$$dV = (d\boldsymbol{x}_1 \times d\boldsymbol{x}_2) \cdot d\boldsymbol{x}_3 \tag{2.8}$$

Introducing Eq. (2 .6) into (2 .8) leads to:

$$dV = (\boldsymbol{G}_1 d\xi_1 \times \boldsymbol{G}_2 d\xi_2) \cdot \boldsymbol{G}_3 d\xi_3 \tag{2.9}$$

Inserting $\boldsymbol{G}_i$ from Eq. (2 .7) into Eq. (2 .9) and considering A2.2, we arrive at:

$$dV = \left(e_k \frac{\partial x_k}{\partial \xi_1} \times e_m \frac{\partial x_m}{\partial \xi_2} \right) \cdot e_n \frac{\partial x_n}{\partial \xi_3} d\xi_1 d\xi_2 d\xi_3 \tag{2.10}$$

Now we replace the vector product and the following scalar product of the two unit vectors in Eq. (2 .10) with the permutation symbol and the Kronecker delta:

$$dV = \varepsilon_{kml} \delta_{ln} \frac{\partial x_k}{\partial \xi_1} \frac{\partial x_m}{\partial \xi_2} \frac{\partial x_n}{\partial \xi_3} d\xi_1 d\xi_2 d\xi_3 \tag{2.11}$$

Applying the Kronecker delta to the terms with the indices *l* and *n*, we arrive at:

$$dV = \left(\varepsilon_{kmn} \frac{\partial x_k}{\partial \xi_1} \frac{\partial x_m}{\partial \xi_2} \frac{\partial x_n}{\partial \xi_3} \right) \left(d\xi_1 d\xi_2 d\xi_3 \right) \tag{2.12}$$

The expression in first parenthesis in Eq.(2 .12) represents the *Jacobian function J*.

$$J = \left(\varepsilon_{kmn} \frac{\partial x_k}{\partial \xi_1} \frac{\partial x_m}{\partial \xi_2} \frac{\partial x_n}{\partial \xi_3} \right) \tag{2.13}$$

The second parenthetesis in Eq. (2 .12) represents the initial infinitesimal material volume in the *undeformed state* at $t = 0$, described by Eq. (2 .3). Using these terms, Eq. (2 .12) is rewritten as:

$$dV = J dV_0 \tag{2.14}$$

where dV represents the differential volume in the *deformed state*, dV_0 has the same differential volume in the undeformed state at the time $t = 0$. The transformation function J is also called the *Jacobian functional determinant.* Performing the permutation in Eq. (2 .13), the determinant is given as:

$$J = \det \begin{pmatrix} \frac{\partial x_1}{\partial \xi_1} & \frac{\partial x_2}{\partial \xi_1} & \frac{\partial x_3}{\partial \xi_1} \\ \frac{\partial x_1}{\partial \xi_2} & \frac{\partial x_2}{\partial \xi_2} & \frac{\partial x_3}{\partial \xi_2} \\ \frac{\partial x_1}{\partial \xi_3} & \frac{\partial x_2}{\partial \xi_3} & \frac{\partial x_3}{\partial \xi_3} \end{pmatrix} \tag{2.15}$$

With the Jacobian functional determinant, we now have a necessary tool to directly relate any time dependent differential volume $dV = dV(t)$ to its fixed reference volume dV_0 at the reference time $t=0$ as shown in Fig. 2.4. The Jacobian transformation function and its material derivative are the fundamental tools to understand the conservation laws using the integral analysis in conjunction with control volume method. To complete this section, we briefly discuss the material derivative of the Jacobian function.

As the volume element dV follows the motion from $\boldsymbol{x} = \boldsymbol{x}(\boldsymbol{\xi}, t)$ to $\boldsymbol{x} = \boldsymbol{x}(\boldsymbol{\xi}, t + dt)$ it changes and, as a result, the Jacobian transformation function undergoes a time change. To calculate this change, we determine the material derivative of J (see A4.1); that is,

$$\frac{DJ}{Dt} = \frac{\partial J}{\partial t} + \boldsymbol{V} \cdot \nabla J \tag{2.16}$$

Inserting Eq.(2 .13) into (2 .16), we obtain:

$$\frac{DJ}{Dt} = \frac{\partial}{\partial t}\left(\varepsilon_{kmn} \frac{\partial x_k}{\partial \xi_1} \frac{\partial x_m}{\partial \xi_2} \frac{\partial x_n}{\partial \xi_3}\right) + V_j \frac{\partial}{\partial x_j}\left(\varepsilon_{kmn} \frac{\partial x_k}{\partial \xi_1} \frac{\partial x_m}{\partial \xi_2} \frac{\partial x_n}{\partial \xi_3}\right) \tag{2.17}$$

Let us consider an arbitrary element of the Jacobian determinant, for example $\partial x_1/\partial \xi_2$. Since the reference coordinate $\xi \neq f(t)$ is not a function of time and is fixed, the differentials with respect to t and ξ_2, can be interchanged resulting in:

$$\frac{\partial}{\partial t}\left(\frac{\partial x_1}{\partial \xi_2}\right) = \frac{\partial}{\partial \xi_2}\left(\frac{\partial x_1}{\partial t_1}\right) = \frac{\partial V_1}{\partial \xi_2} \tag{2.18}$$

Performing similar operations for all elements of the Jacobian determinant and noting that the second expression on the right-hand side of Eq. (2 .17) identically vanishes, we arrive at:

$$\frac{DJ}{Dt} = \left(\frac{\partial V_1}{\partial x_1} + \frac{\partial V_2}{\partial x_2} + \frac{\partial V_3}{\partial x_3} \right) J \tag{2.19}$$

The expression in the parenthesis of Eq.(2 .19) is the well known divergence of the velocity vector. Using vector notation, Eq. (2 .19) becomes:

$$\frac{DJ}{Dt} = (\nabla \cdot \boldsymbol{V})\, J \tag{2.20}$$

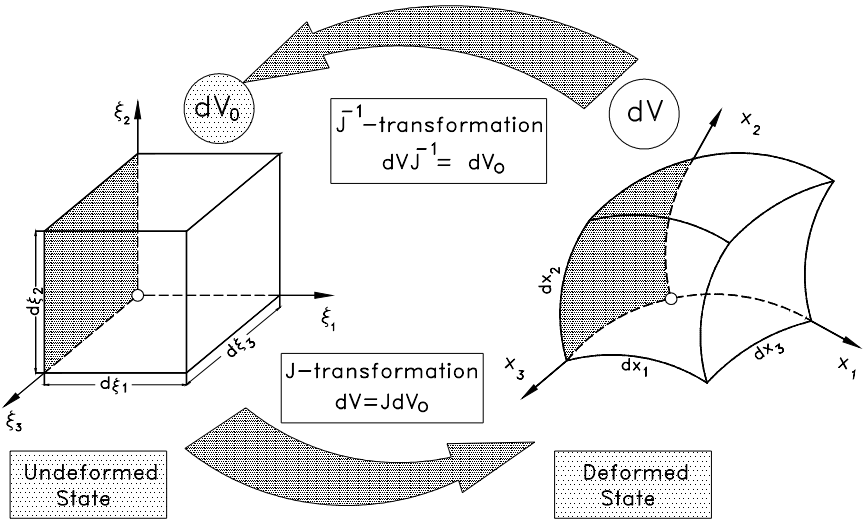

Fig. 2.4: Jacobian transformation of a material volume, change of states.

2.1.3 Spatial Description

The material description we discussed in the previous section deals with the motion of the individual particles of a continuum, and is used in *continuum mechanics*. In turbomachinery fluid dynamics, we are primarily interested in determining the flow quantities such as velocity, acceleration, density, temperature, pressure, and etc., at fixed points in space. For example, determining the three-dimensional distribution of temperature, pressure and shear stress helps engineers design turbines, compressors, combustion engines, etc. with higher efficiencies. For this purpose, we introduce the *spatial description*, which is also called the *Euler description.* The independent variables for the spatial descriptions are the space characterized by the position vector $\boldsymbol{x}$ and the time *t.* Consider the transformation of Eq. (2 .1), where $\boldsymbol{\xi}$ is solved in terms

of $\boldsymbol{x}$:

$$\boldsymbol{\xi} = \boldsymbol{\xi}(\boldsymbol{x}, t), \quad \xi_i = \xi_i(x_j, t) \tag{2.21}$$

The position vector $\boldsymbol{\xi}$ in the velocity of the material element $\boldsymbol{V}(\boldsymbol{\xi},t)$ is replaced by Eq. (2 .21):

$$\boldsymbol{V}(\boldsymbol{\xi}, t) = \boldsymbol{V}\left[\boldsymbol{\xi}(\boldsymbol{x},t), t\right] = \boldsymbol{V}(\boldsymbol{x},t) \tag{2.22}$$

For a fixed $\boldsymbol{x}$, Eq. (2 .22) exhibits the velocity at the spatially fixed position $\boldsymbol{x}$ as a function of time. On the other hand, for a fixed t, Eq. (2 .22) describes the velocity at the time t. With Eq. (2 .22), any quantity described in spatial coordinates can be transformed into material coordinates provided the Jacobian transformation function J, which we discussed in the previous section, does not vanish.

2.2 Translation, Deformation, Rotation

During a general three-dimensional motion, a fluid particle undergoes a translational and rotational motion which may be associated with deformation. The velocity of a particle at a given spatial, temporal position ($\boldsymbol{x} + \mathrm{d}\boldsymbol{x}, t$) can be related to the velocity at ($\boldsymbol{x}$, t) by using the following Taylor expansion:

$$\boldsymbol{V}(\boldsymbol{x} + d\boldsymbol{x}, t) = \boldsymbol{V}(\boldsymbol{x}, t) + d\boldsymbol{V} \tag{2.23}$$

Inserting in Eq. (2 .23) for the differential velocity change $d\boldsymbol{V} = d\boldsymbol{x}\cdot\nabla\boldsymbol{V}$, Eq. (2 .23) is re-written as:

$$\boldsymbol{V}(\boldsymbol{x} + d\boldsymbol{x}, t) = \boldsymbol{V}(\boldsymbol{x}, t) + d\boldsymbol{x}\cdot\nabla\boldsymbol{V} \tag{2.24}$$

The first term on the right-hand side of Eq. (2 .24) represents the translational motion of the fluid particle. The second expression is a scalar product of the differential displacement $d\boldsymbol{x}$ and the *velocity gradient* $\nabla\boldsymbol{V}$. We decompose the velocity gradient, which is a second order tensor, into two parts resulting in the following *identity*:

$$\nabla\boldsymbol{V} = \frac{1}{2}\left(\nabla\boldsymbol{V} + \nabla\boldsymbol{V}^{\boldsymbol{T}}\right) + \frac{1}{2}\left(\nabla\boldsymbol{V} - \nabla\boldsymbol{V}^{\boldsymbol{T}}\right) \tag{2.25}$$

The superscript T indicates that the matrix elements of the second order tensor $\nabla\boldsymbol{V}^T$ are the transpositions of the matrix elements that pertain to the second order tensor $\nabla\boldsymbol{V}$. The first term in the right-hand side represents the *deformation tensor*, which is a symmetric second order tensor:

$$\boldsymbol{D} = \frac{1}{2}\left(\nabla \boldsymbol{V} + \nabla \boldsymbol{V}^{T}\right) = e_i e_j D_{ij} = \frac{1}{2} e_i e_j \left(\frac{\partial V_i}{\partial x_j} + \frac{\partial V_j}{\partial x_i} \right) \tag{2.26}$$

with components:

$$D_{ij} = \frac{1}{2}\left(\frac{\partial V_i}{\partial x_j} + \frac{\partial V_j}{\partial x_i} \right) \tag{2.27}$$

The second term of Eq. (2 .24) is called the rotation or vorticity tensor, which is antisymmetric and is given by:

$$\boldsymbol{\Omega} = \frac{1}{2}\left(\nabla \boldsymbol{V} - \nabla \boldsymbol{V}^{T}\right) = e_i e_j \Omega_{ij} = \frac{1}{2} e_i e_j \left(\frac{\partial V_j}{\partial x_i} - \frac{\partial V_i}{\partial x_j} \right) \tag{2.28}$$

The components are:

$$\Omega_{ij} = \frac{1}{2}\left(\frac{\partial V_j}{\partial x_i} - \frac{\partial V_i}{\partial x_j} \right) \tag{2.29}$$

Inserting Eq. (2 .26) and (2 .28) into Eq. (2 .24), we arrive at:

$$\boldsymbol{V}(\boldsymbol{x} + d\boldsymbol{x},\ t) = \boldsymbol{V}(\boldsymbol{x},\ t) + d\boldsymbol{x} \cdot \boldsymbol{D} + d\boldsymbol{x} \cdot \boldsymbol{\Omega} \tag{2.30}$$

Equation (2 .30) describes the kinematics of the fluid particle, which has a combined translational and rotational motion and undergoes a deformation. Figure 2.5 illustrates the geometric representation of the rotation and deformation, [3]. Consider the fluid particle with a square-shaped cross section in the x_1-x_2 plane at the time t. The position of this particle is given by the position vector $\boldsymbol{x} = \boldsymbol{x}(t)$. By moving through the flow field, the particle experiences translational motion to a new position $\boldsymbol{x} + d\boldsymbol{x}$. This motion may be associated with a rotational motion and a deformation. The deformation is illustrated by the initial and final state of diagonal A-C, which is stretched to A'-C' and the change of the angle 2γ to $2\gamma'$. The rotational motion can be appropriately illustrated by the rotation of the diagonal by the angle $d\phi_3 = \gamma' + d\alpha - \gamma$, where γ' can be eliminated using the relation $2\gamma' + d\alpha + d\beta = 2\gamma$. As a result, we obtain the infinitesimal rotation angle:

$$d\phi_3 = \frac{1}{2}\left(d\alpha - d\beta\right) \tag{2.31}$$

where the subscript *3* denotes the direction of the rotation axis, which is parallel to x_3. Referring to Fig. 2.5, direct relationships between $d\alpha$, $d\beta$ and the velocity gradients can be established by:

$$d\alpha \approx \tan(d\alpha) = \frac{\dfrac{\partial V_2}{\partial x_1} dx_1 dt}{dx_1 + \dfrac{\partial V_1}{\partial x_1} dx_1 dt} \approx \frac{\partial V_2}{\partial x_1} dt \tag{2.32}$$

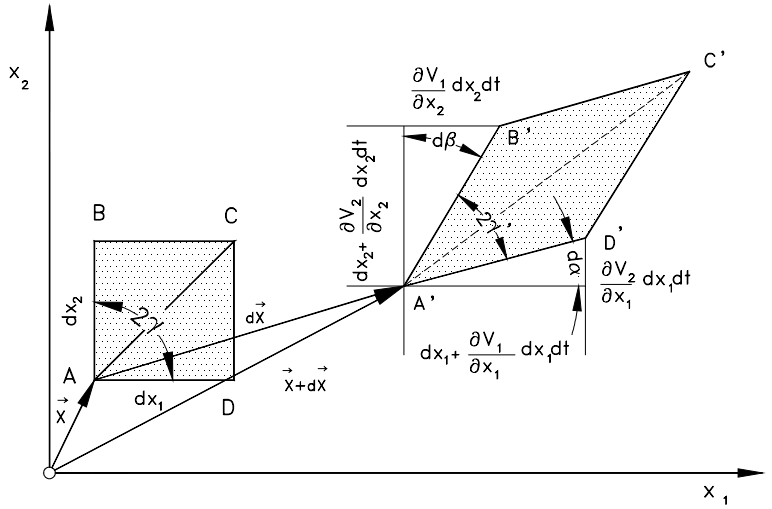

Fig. 2.5: Translation, rotation and deformation details of a fluid particle.

A similar relationship is given for:

$$d\beta \approx \tan(d\beta) = \frac{\dfrac{\partial V_1}{\partial x_2} dx_2 dt}{dx_2 + \dfrac{\partial V_2}{\partial x_2} dx_2 dt} \approx \frac{\partial V_1}{\partial x_2} dt \tag{2.33}$$

Substituting Eqs. (2 .32) and (2 .33) into Eq. (2 .31), the *rotation rate* in the x_3 - direction is found:

$$\frac{d\phi_3}{dt} = \frac{1}{2}\left(\frac{\partial V_2}{\partial x_1} - \frac{\partial V_1}{\partial x_2} \right) \tag{2.34}$$

Executing the same procedure, the other two components are:

$$\frac{d\phi_1}{dt} = \frac{1}{2}\left(\frac{\partial V_3}{\partial x_2} - \frac{\partial V_2}{\partial x_3} \right), \quad \frac{d\phi_2}{dt} = \frac{1}{2}\left(\frac{\partial V_1}{\partial x_3} - \frac{\partial V_3}{\partial x_1} \right) \tag{2.35}$$

The above three terms in Eqs. (2 .34) and (2 .35) may be recognized as one-half of the three components of the *vorticity vector* $\boldsymbol{\omega}$, which is:

$$\boldsymbol{\omega} \equiv \nabla \times \boldsymbol{V} = \varepsilon_{ijk} e_k \frac{\partial V_j}{\partial x_i}$$

$$\boldsymbol{\omega} = e_1\left(\frac{\partial V_3}{\partial x_2} - \frac{\partial V_2}{\partial x_3}\right) + e_2\left(\frac{\partial V_1}{\partial x_3} - \frac{\partial V_3}{\partial x_1}\right) + e_3\left(\frac{\partial V_2}{\partial x_1} - \frac{\partial V_1}{\partial x_2}\right) \tag{2.36}$$

Examining the elements of the rotation tensor matrix,

$$\Omega_{ij} = \begin{pmatrix} 0 & \frac{1}{2}\left(\frac{\partial V_2}{\partial x_1} - \frac{\partial V_1}{\partial x_2}\right) & \frac{1}{2}\left(\frac{\partial V_3}{\partial x_1} - \frac{\partial V_1}{\partial x_3}\right) \\ \frac{1}{2}\left(\frac{\partial V_1}{\partial x_2} - \frac{\partial V_2}{\partial x_1}\right) & 0 & \frac{1}{2}\left(\frac{\partial V_3}{\partial x_2} - \frac{\partial V_2}{\partial x_3}\right) \\ \frac{1}{2}\left(\frac{\partial V_1}{\partial x_3} - \frac{\partial V_3}{\partial x_1}\right) & \frac{1}{2}\left(\frac{\partial V_2}{\partial x_3} - \frac{\partial V_3}{\partial x_2}\right) & 0 \end{pmatrix} \tag{2.37}$$

we note that the diagonal elements of the above antisymmetric tensor are zero and only three of the six non-zero components are distinct. Except for the factor of one-half, these three distinct components are the same as those making up the vorticity vector. Comparing the components of the vorticity vector $\boldsymbol{\omega}$ given by Eq. (2 .36) and the three distinct terms of Eq. (2 .37), we conclude that the components of the vorticity vector, except for the factor of one-half, are identical with the *axial vector* of the antisymmetric tensor, Eq. (2 .37). The axial vector of the second order tensor $\boldsymbol{\Omega}$ is the double scalar product of the third order permutation tensor $\boldsymbol{\varepsilon} = e_i e_j e_k \varepsilon_{ijk}$

$$\boldsymbol{\varepsilon} : \boldsymbol{\Omega} = \varepsilon_{ijk} e_i e_j e_k : e_m e_n \Omega_{mn} = e_i \varepsilon_{ijk} \frac{1}{2}\left(\frac{\partial V_j}{\partial x_k} - \frac{\partial V_k}{\partial x_j}\right) \tag{2.38}$$

Expanding Eq. (2 .38) results in:

$$\boldsymbol{\varepsilon} : \boldsymbol{\Omega} = e_1\left(\frac{\partial V_2}{\partial x_3} - \frac{\partial V_3}{\partial x_2}\right) + e_2\left(\frac{\partial V_3}{\partial x_1} - \frac{\partial V_1}{\partial x_3}\right) + e_3\left(\frac{\partial V_1}{\partial x_2} - \frac{\partial V_2}{\partial x_1}\right) \tag{2.39}$$

Comparing Eq. (2 .39) to (2 .36) shows that the right-hand side of Eq. (2 .39) multiplied with a negative sign is exactly equal the right-hand side of Eq. (2 .36). This indicates that the axial vector of the rotation tensor is equal to the negative rotation vector and can be expressed as:

$$\nabla \times \boldsymbol{V} = -\boldsymbol{\varepsilon} : \boldsymbol{\Omega} = -e_i \varepsilon_{ijk} \frac{1}{2}\left(\frac{\partial V_j}{\partial x_k} - \frac{\partial V_k}{\partial x_j} \right) \tag{2.40}$$

The existence of the vorticity vector $\boldsymbol{\omega}$ and therefore, the rotation tensor $\boldsymbol{\Omega}$, is a characteristic of viscous flows that in general undergoes a *rotational motion.* This is particularly true for boundary layer flows, where the fluid particles moves very close to the solid boundaries. In this region, the wall shear stress forces (friction forces) cause a combined deformation and rotation of the fluid particle. In contrast, for *inviscid flows*, or the flow regions, where the viscosity effect may be neglected, the rotation vector $\boldsymbol{\omega}$ may vanish if the flow can be considered isentropic. This ideal case is called *potential flow,* where the rotation vector $\nabla \times \boldsymbol{V} = \boldsymbol{0}$ in the entire potential flow field.

2.3 Reynolds Transport Theorem

The conservation laws in integral form are, strictly speaking, valid for *closed systems*, where the *mass* does not cross the *system boundary*. In turbomachinery fluid mechanics, however, we are dealing with *open systems*, where the *mass flow* continuously crosses the system boundary. To apply the conservation laws to the turbomachinery components, we briefly provide the necessary mathematical tools. In this section, we treat the volume integral of an arbitrary field quantity $f(\boldsymbol{X},t)$ by deriving the *Reynolds transport theorem*. This is an important kinematic relation that we will use in Chapter 4.

The field quantity $f(\boldsymbol{X},t)$ may be a zeroth, first or second order tensor valued function, such as mass, velocity vector, and stress tensor. The time dependent volume under consideration with a given time dependent surface moves through the flow field and may experience dilatation, compression and deformation. It is assumed to contain the same fluid particles at any time and therefore, it is called the material volume. The volume integral of the quantity $f(\boldsymbol{X},t)$:

$$F(t) = \int_{V(t)} f(\boldsymbol{X},t)\, dv \tag{2.41}$$

is a function of time only. The integration must be carried out over the varying volume $v(t)$. The material change of the quantity $F(t)$ is expressed as:

$$\frac{DF(t)}{Dt} = \frac{D}{Dt} \int_{V(t)} f(\boldsymbol{X},t)\, dv \tag{2.42}$$

Since the shape of the volume $v(t)$ changes with time, the differentiation and integration cannot be interchanged. However, Eq. (2 .42) permits the transformation of the time dependent volume $v(t)$ into the fixed volume v_0 at time $t = 0$ by using the Jacobian transformation function:

$$\frac{DF(t)}{Dt} = \frac{D}{Dt}\int_{v_0} f(\boldsymbol{X},t)\,J dv_0 \tag{2.43}$$

With this operation in Eq. (2 .43), it is possible to interchange the sequence of differentiation and integration:

$$\frac{DF(t)}{Dt} = \int_{v_0} \frac{D}{Dt}\left(f(\boldsymbol{X},t)J\right) dv_0 \tag{2.44}$$

The chain differentiation of the expression within the parenthesis results in

$$\frac{DF(t)}{Dt} = \int_{v_0} \left(J\frac{D}{Dt}f(\boldsymbol{X},t) + f(\boldsymbol{X},t)\frac{DJ}{Dt}\right) dv_0 \tag{2.45}$$

Introducing the material derivative of the Jacobian function, Eq. (2 .19) into Eq. (2 .45) yields:

$$\frac{DF(t)}{Dt} = \int_{v_0} \left(\frac{D}{Dt}f(\boldsymbol{X},t) + f(\boldsymbol{X},t)\,\nabla\cdot\boldsymbol{V}\right) J dv_0 \tag{2.46}$$

Equation (2 .46) permits the back transformation of the fixed volume integral into the time dependent volume integral:

$$\frac{DF(t)}{Dt} = \int_{v(t)} \left(\frac{D}{Dt}f(\boldsymbol{X},t) + f(\boldsymbol{X},t)\nabla\cdot\boldsymbol{V}\right) dv \tag{2.47}$$

According to A4.1, the first term in the parenthesis can be written as:

$$\frac{Df}{Dt} = \frac{\partial f}{\partial t} + \boldsymbol{V}\cdot\nabla f \tag{2.48}$$

Introducing Eq. (2 .48) into (2 .47) results in:

$$\frac{DF(t)}{Dt} = \int_{v(t)} \left(\frac{\partial}{\partial t}f(\boldsymbol{X},\,t) + \boldsymbol{V}\cdot\nabla f(\boldsymbol{X},\,t) + f(\boldsymbol{X},\,t)\nabla\cdot\boldsymbol{V}\right) dv \tag{2.49}$$

The chain rule applied to the second and third term in Eq. (2 .49) yields:

$$\frac{DF(t)}{Dt} = \int_{v(t)} \left\{ \frac{\partial}{\partial t}f(\boldsymbol{X},\,t) + \nabla\cdot\left(f(\boldsymbol{X},\,t)\boldsymbol{V}\right)\right\} dv \tag{2.50}$$

The second volume integral in Eq. (2 .50) can be converted into a surface integral by applying the Gauss' divergence theorem:

$$\int_{v(t)} \nabla \cdot \left(f(\boldsymbol{X},\ t)\boldsymbol{V} \right) dv \ = \ \int_{S(t)} f(\boldsymbol{X},\ t)\boldsymbol{V} \cdot \boldsymbol{n}\, dS \tag{2.51}$$

where $\boldsymbol{V}$ represents the *flux velocity* and $\boldsymbol{n}$ the unit vector normal to the surface. Inserting equation (2 .51) into Eq. (2 .50) results in the following final equation, which is called the *Reynolds transport theorem*

$$\frac{DF(t)}{Dt} \ = \ \int_{v(t)} \frac{\partial}{\partial (t)} f(\boldsymbol{X},\ t) dv \ + \ \int_{S(t)} f(\boldsymbol{X},\ t)\boldsymbol{V} \cdot \boldsymbol{n} dS \tag{2.52}$$

Equation (2 .52) is valid for any system boundary with time dependent volume $V(t)$ and surface $S(t)$ at any time, including the time $t = t_0$, where the volume $V = V_C$ and the surface $S = S_C$ assume fixed values. We call V_C and S_C the *control volume* and *control surface*.

References, Chapter 2

2.1 Aris, R., 1962, “Vectors, Tensors, and the Basic Equations of Fluid Mechanics,” Dover Publication, New York.

2.2 Spurk, J, 1997, “Fluid Mechanics,” Springer-Verlag, Berlin, Heidelberg, New York.

2.3 White, F.M., 1974, “Viscous Fluid Flow,” McGraw-Hill, 1974.

3 Differential Balances in Turbomachinery

In this and the following chapter, we present the conservation laws of fluid mechanics that are necessary to understand the basics of turbomachinery flow physics from a unified point of view. The main subject of this chapter is the differential treatment of the conservation laws of fluid mechanics, namely conservation law of mass, linear momentum, angular momentum, and energy. The flow within a turbomachinery stage consisting of a *fixed stator row* followed by a rotating *rotor row*, continuously changes the frame of reference. The absolute frame of reference is rigidly connected with the stationary parts such as stators, casings, inlets, and exits, whereas the relative frame is attached to the rotating shaft, thereby turning with certain angular velocity about the machine axis. By changing the frame of reference from an absolute frame to a relative one, certain flow quantities remain unchanged, such as normal stress tensor, shear stress tensor, and deformation tensor. These quantities are indifferent with regard to a change of frame of reference. However, there are other quantities that undergo changes when moving from a stationary frame to a rotating one. Velocity, acceleration, and rotation tensor are few. Keeping in mind the particular turbomachinery flow situation, we first apply these laws to the stationary or absolute frame of reference, then to the rotating one.

The differential analysis is of primary significance to all components of a turbomachine, such as compressor, turbine, combustion chamber, inlet, and exit diffuser, where a detailed knowledge of flow quantities such as velocity, pressure, temperature, entropy, and force distributions are required. A complete set of independent conservation laws exhibits a system of partial differential equations that describes the motion of a fluid particle. Once this differential equation system is defined, its solution delivers the detailed information about the flow quantities within the computational domain with given initial and boundary conditions.

3.1 Differential Mass Flow Balance in Stationary Frame of Reference

The conservation law of mass requires that the mass contained in a material volume $v = v(t)$ must be constant:

$$m = \int_{v(t)} \rho dv \tag{3.1}$$

Consequently, Eq. (3.1) requires that the substantial changes of the above mass must disappear:

$$\frac{Dm}{Dt} = \frac{D}{Dt}\int_{v(t)} \rho\, dv = 0 \tag{3.2}$$

Using the Reynolds transport theorem (see Chapter 2), the conservation of mass, Eq. (3.2), results in:

$$\frac{D}{Dt}\int_{v(t)} \rho dv = \int_{v(t)} \left(\frac{\partial \rho}{\partial t} + \nabla.(\rho \boldsymbol{V}) \right) dv = 0 \tag{3.3}$$

Since this integral in Eq. (3.3) is zero, the integrand in the bracket must vanish identically. As a result, we may write the continuity equation for unsteady and compressible flow as:

$$\frac{\partial \rho}{\partial t} + \nabla.(\rho \boldsymbol{V}) = 0 \tag{3.4}$$

Equation (3.4) is a coordinate invariant equation. Its index notation in the Cartesian coordinate system given in Appendix A, is:

$$\frac{\partial \rho}{\partial t} + \frac{\partial (\rho V_i)}{\partial x_i} = 0 \tag{3.5}$$

Expanding Eq. (3.5), we get:

$$\frac{\partial \rho}{\partial t} + \frac{\partial (\rho V_1)}{\partial x_1} + \frac{\partial (\rho V_2)}{\partial x_2} + \frac{\partial (\rho V_3)}{\partial x_3} = 0 \tag{3.6}$$

For an orthogonal curvilinear coordinate system, the continuity equation (3.6) for an incompressible fluid is written as (see Appendix B5.1):

$$\frac{\partial \rho}{\partial t} + \nabla.(\rho \boldsymbol{V}) = \frac{\partial \rho}{\partial t} + (\rho V^i)_{,i} + (\rho V^j)\Gamma^i_{ij} = 0 \tag{3.7}$$

Applying Eq. (3.7) to a cylindrical coordinate system with the Christoffel symbols, Eq. (3.8), from Appendix B6.4

$$\left(\Gamma^1_{lm}\right) = \begin{pmatrix} 0 & 0 & 0 \\ 0 & -r & 0 \\ 0 & 0 & 0 \end{pmatrix}, \quad \left(\Gamma^2_{lm}\right) = \begin{pmatrix} 0 & 1/r & 0 \\ 1/r & 0 & 0 \\ 0 & 0 & 0 \end{pmatrix}, \quad \left(\Gamma^3_{lm}\right) = \begin{pmatrix} 0 & 0 & 0 \\ 0 & 0 & 0 \\ 0 & 0 & 0 \end{pmatrix} \tag{3.8}$$

and introducing the physical components, Eq. (3.7) becomes:

$$\frac{\partial \rho}{\partial t} + \frac{\partial(\rho r V_r)}{r \partial r} + \frac{1}{r}\frac{\partial(\rho V_\theta)}{\partial \theta} + \frac{\partial(\rho V_z)}{\partial z} = 0 \tag{3.9}$$

Equation (3.9) is valid only for cylindrical coordinate systems. To apply the continuity balance to any arbitrary orthogonal coordinate system, one has to determine first the Christoffel symbols as outlined in Appendix B and then find the continuity equation.

3.1.1 Incompressibility Condition

The condition for a working medium to be considered as incompressible is that the substantial change of its density along the flow path vanishes. This means that:

$$\frac{D\rho}{Dt} = \frac{\partial \rho}{\partial t} + \boldsymbol{V} \cdot \nabla \rho = 0 \tag{3.10}$$

Inserting Eq. (3.10) into (3.4) and performing the chain differentiation of the second term in Eq. (3.4) namely, $\nabla.(\rho \boldsymbol{V}) = \rho \nabla . \boldsymbol{V} + \boldsymbol{V} \cdot \nabla \rho$, the continuity equation for an incompressible flow reduces to:

$$\nabla . \boldsymbol{V} = 0 \tag{3.11}$$

In a Cartesian coordinate system, Eq. (3.11) can be expanded as written in (3.12):

$$\frac{\partial V_1}{\partial x_1} + \frac{\partial V_2}{\partial x_2} + \frac{\partial V_3}{\partial x_3} = 0 \tag{3.12}$$

In an orthogonal, curvilinear coordinate system, the continuity balance for an incompressible fluid is:

$$\nabla . \boldsymbol{V} = V^i{}_{,i} + V^J \Gamma^i_{ij} = 0 \tag{3.13}$$

Inserting the Christoffel symbols into Eq.(3.13) and the physical components for cylindrical coordinate systems, we obtain the continuity equation in terms of its physical components (3.14):

$$\frac{\partial(r V_r)}{r \partial r} + \frac{1}{r}\frac{\partial(V_\theta)}{\partial \theta} + \frac{\partial(V_z)}{\partial z} = 0 \tag{3.14}$$

3.2 Differential Momentum Balance in Stationary Frame of Reference

In addition to the continuity equation we treated above, the detailed calculation of the entire flow field through a turbomachinery component such as a compressor or turbine blade channel requires the equation of motion in differential form. In the following, we provide the equation of motion in differential form in a four-dimensional time-space coordinate. We start from Newton's second law of motion and apply it to an infinitesimal fluid element, Fig. 3.1, with mass *dm* for which the equilibrium condition is written as:

$$dm\boldsymbol{A} = d\boldsymbol{F} \tag{3.15}$$

The acceleration vector $\boldsymbol{A}$ in Eq. (3.15) is the well known material derivative defined in Appendix A1.

$$\boldsymbol{A} = \frac{D\boldsymbol{V}}{Dt} = \frac{\partial \boldsymbol{V}}{\partial t} + \boldsymbol{V}\cdot\nabla\boldsymbol{V} \tag{3.16}$$

In Eq. (3.16), $\boldsymbol{A}$ is the acceleration vector and $d\boldsymbol{F}$ the vector sum of all forces exerted on the fluid element. In the absence of magnetic, electric or other extraneous effects, the force $d\boldsymbol{F}$ is equal to the vector sum of the surface force $d\boldsymbol{F}_s$ acting on the particle surface and the gravity force $dm\mathbf{g}$ as shown in Fig. 3.8. Inserting Eq. (3.16) into Eq. (3.15), we arrive at:

$$dm\left(\frac{\partial \boldsymbol{V}}{\partial t} + \boldsymbol{V}\cdot\nabla\boldsymbol{V}\right) = d\boldsymbol{F}_s + dm\boldsymbol{g} \tag{3.17}$$

Consider the fluid element shown in Fig. 3.1 with sides dx_1, dx_2, dx_3 parallel to the axis of a Cartesian coordinate system. The stresses acting on the surfaces of this element are represented by the stress tensor $\boldsymbol{\Pi}$ which has the components π_{ij} that produce surface forces. The first index *i* refer to the axis, on which the fluid element surface is perpendicular, whereas the second index *j* indicates the direction of the stress component. Considering the stress situation in Fig. 3.1, the following resultant forces are acting on the surface dx_2dx_3 perpendicular to the x_1 axis:

$$e_1\frac{\partial \pi_{11}}{\partial x_1}dx_1dx_2dx_3\ ,\ e_2\frac{\partial \pi_{12}}{\partial x_1}dx_1dx_2dx_3\ ,\ e_3\frac{\partial \pi_{13}}{\partial x_1}dx_1dx_2dx_3 \tag{3.18}$$

The total resulting forces acting on the entire surface of the element are obtained by adding the nine components that result in Eq. (3.19):

$$\frac{d\boldsymbol{F}_S}{dv} = e_1\left(\frac{\partial\pi_{11}}{\partial x_1} + \frac{\partial\pi_{21}}{\partial x_2} + \frac{\partial\pi_{31}}{\partial x_3}\right) + e_2\left(\frac{\partial\pi_{12}}{\partial x_1} + \frac{\partial\pi_{22}}{\partial x_2} + \frac{\partial\pi_{32}}{\partial x_3}\right) + e_3\left(\frac{\partial\pi_{13}}{\partial x_1} + \frac{\partial\pi_{23}}{\partial x_2} + \frac{\partial\pi_{33}}{\partial x_3}\right) \tag{3.19}$$

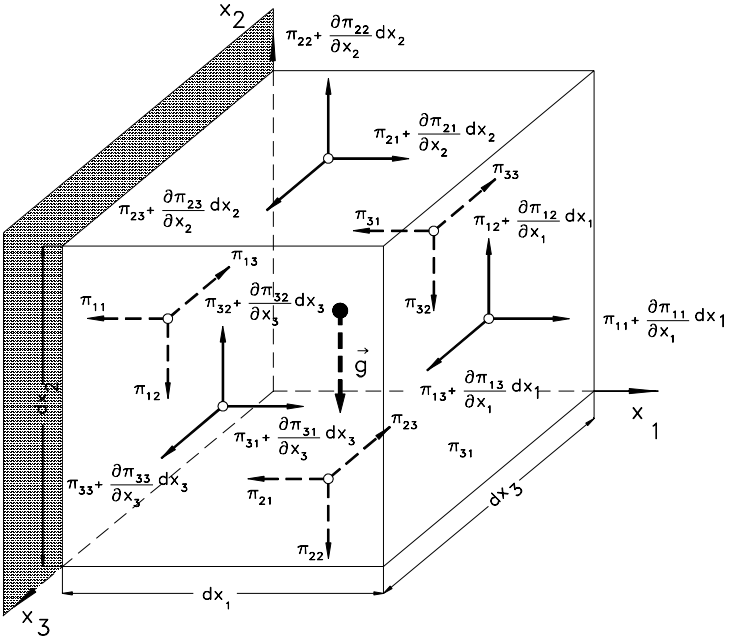

Fig. 3.1: Surface and gravitational forces acting on a volume element.

Since the stress tensor $\boldsymbol{\Pi}$ and the volume of the fluid element are written as:

$$\boldsymbol{\Pi} = e_i e_j \pi_{ij}, \quad dv = dx_1 dx_2 dx_3 \tag{3.20}$$

it can be easily shown that Eq. (3.19) is the divergence of the stress tensor expressed in Eq. (3.20)

$$\frac{d\boldsymbol{F}_S}{dv} = \nabla \cdot \boldsymbol{\Pi} \tag{3.21}$$

The expression $\nabla.\boldsymbol{\Pi}$ is the scalar differentiation of the second order tensor $\boldsymbol{\Pi}$ and is called divergence of the tensor field $\boldsymbol{\Pi}$ which is a first order tensor or a vector.

Inserting Eq. (3.21) into Eq. (3.17) and divide both sides by *dm*, results in the following **Cauchy equation of motion**:

$$\frac{\partial \boldsymbol{V}}{\partial t} + \boldsymbol{V}\cdot\nabla\boldsymbol{V} = \frac{1}{\rho}\nabla\cdot\boldsymbol{\Pi} + \boldsymbol{g} \tag{3.22}$$

The stress tensor in Eq. (3.22) can be expressed in terms of deformation tensor, as we will see in the following section.

3.2.1 Relationship Between Stress Tensor and Deformation Tensor

Since the surface forces resulting from the stress tensor cause a deformation of fluid particle, it is obvious to attempt to find a functional relationship between the stress tensor and the velocity gradient:

$$\boldsymbol{\Pi} = f(\nabla\boldsymbol{V}) \tag{3.23}$$

As we saw in Chapter 2, the velocity gradient in Eq. (3.23) can be decomposed into a symmetric part called deformation tensor and an anti-symmetric part, called rotation or vorticity tensor:

$$\nabla\boldsymbol{V} = \frac{1}{2}\left(\nabla\boldsymbol{V} + \nabla\boldsymbol{V}^{T}\right) + \frac{1}{2}\left(\nabla\boldsymbol{V} - \nabla\boldsymbol{V}^{T}\right) = \boldsymbol{D} + \boldsymbol{\Omega} \tag{3.24}$$

Consequently, the stress tensor may be set:

$$\boldsymbol{\Pi} = f(\nabla\boldsymbol{V}) = f(\boldsymbol{D}, \boldsymbol{\Omega}) \tag{3.25}$$

with the deformation tensor as:

$$\boldsymbol{D} = e_i e_j D_{ij} = \frac{1}{2} e_i e_j \left(\frac{\partial V_i}{\partial x_j} + \frac{\partial V_j}{\partial x_i}\right) \tag{3.26}$$

and the rotation tensor, which is antisymmetric, and is given by:

$$\boldsymbol{\Omega} = \frac{1}{2} e_i e_j \Omega_{ij} = \frac{1}{2} e_i e_j \left(\frac{\partial V_i}{\partial x_j} - \frac{\partial V_j}{\partial x_i}\right) \tag{3.27}$$

Since the stress tensor $\boldsymbol{\Pi}$ in Eq. (3.25) is a *frame indifferent quantity*, it remains unchanged or invariant under any changes of frame of reference. Moving from an absolute frame into a relative one exhibits such a change in frame of reference. Thus, the stress tensor $\boldsymbol{\Pi}$ satisfies the principle of *frame indifference*, also called the

principle of material objectivity. To satisfy the objectivity principle, the arguments of the functional f must also be frame indifferent quantities. This is true only for the first argument $\boldsymbol{D}$ in Eq. (3.25). The second argument $\boldsymbol{\Omega}$ in Eq. (3.25) is not a frame indifferent quantity. As a consequence, the stress tensor is a function of deformation tensor $\boldsymbol{D}$ only.

$$\boldsymbol{\Pi} = f(\boldsymbol{D}) \tag{3.28}$$

A general form of Eq. (3.28) may be a polynomial in $\boldsymbol{D}$:

$$\boldsymbol{\Pi} = f_1\boldsymbol{I} + f_2\boldsymbol{D} + f_3(\boldsymbol{D}\cdot\boldsymbol{D}) \tag{3.29}$$

with $\boldsymbol{I} = e_i e_j \delta_{ij}$ as the unit Kronecker tensor. To fulfill the frame indifference requirement, the functions f_i must be invariant. This means they depend on either the thermodynamic quantities, such as pressure, or the following three-principal invariant of the deformation tensor:

$$I_{1D} = Tr\boldsymbol{D} = \nabla\cdot\boldsymbol{V} = D_{ii} \tag{3.30}$$

$$I_{2D} = \frac{1}{2}\left(I_{1D}{}^2 - \boldsymbol{D}:\boldsymbol{D}\right) = \frac{1}{2}\left(D_{ii}D_{jj} - D_{ij}D_{ij}\right) \tag{3.31}$$

$$I_{3D} = \det D_{ij} \tag{3.32}$$

Of particular interest is the category of those fluids for which there is a linear relationship between the stress tensor and the deformation tensor. Many working fluids in turbomachinery flow application such as air, steam, and combustion gases belong to this category. They are called the **Newtonian fluids** for which Eq. (3.29) is reduced to:

$$\boldsymbol{\Pi} = f_1\boldsymbol{I} + f_2\boldsymbol{D} \tag{3.33}$$

where the functions f_1 and f_2 are given by:

$$f_1 = (-p + \lambda\nabla\cdot\boldsymbol{V}) \quad , \quad f_2 = 2\mu \ , \ \bar{\mu} = \lambda + \frac{2}{3}\mu \tag{3.34}$$

with μ as the absolute viscosity and $\bar{\mu}$ as the bulk viscosity. Introducing Eq. (3.34) into (3.29) results in the **Cauchy-Poisson law**:

$$\boldsymbol{\Pi} = (-p + \lambda\nabla\cdot\boldsymbol{V})\boldsymbol{I} + 2\mu\boldsymbol{D} \tag{3.35}$$

The first term on the right-hand side associated with the unit Kronecker tensor $p\boldsymbol{I}$, represents the contribution of the thermodynamic pressure to the normal stress. The

second term $(\lambda\nabla\cdot\boldsymbol{V})\boldsymbol{I}$, exhibits a normal stress contribution caused by a volume dilatation or compression due to the compressibility of the working medium. For an incompressible medium, this term identically vanishes. Finally, the last term expresses a direct relationship between the shear stress tensor and the deformation tensor. For an incompressible fluid, Eq. (3.35) reduces to:

$$\boldsymbol{\Pi} = -p\boldsymbol{I} + 2\mu\boldsymbol{D} \tag{3.36}$$

3.2.2 Navier-Stokes Equation of Motion

Inserting Eq. (3.35) into (3.22):

$$\rho\frac{\partial V}{\partial t} + \rho\boldsymbol{V}.(\nabla\boldsymbol{V}) = \nabla\cdot\left[(-p + \lambda\nabla\cdot\boldsymbol{V})\boldsymbol{I} + 2\mu\boldsymbol{D}\right] + \rho\boldsymbol{g} \tag{3.37}$$

This is often referred to as the **Navier-Stokes equation for compressible fluids**. For incompressible flows with constant shear viscosity and negligible gravity forces, Eq. (3.37) reduces to:

$$\rho\frac{\partial\boldsymbol{V}}{\partial t} + \rho\boldsymbol{V}\cdot(\nabla\boldsymbol{V}) = \nabla\cdot(-p\boldsymbol{I} + 2\mu\boldsymbol{D}) \tag{3.38}$$

Performing the differentiation on the right hand side and dividing by ρ leads to:

$$\frac{\partial\boldsymbol{V}}{\partial t} + \boldsymbol{V}.(\nabla\boldsymbol{V}) = -\frac{1}{\rho}\nabla p + \nu\Delta\boldsymbol{V} \tag{3.39}$$

with $\nu = \mu/\rho$ as the kinematic viscosity and the *Laplace operator* $\Delta = \nabla\cdot\nabla = \nabla^2$. Equation (3.37) or its special case Eq. (3.39) with the equation of continuity and energy, exhibits a system of partial differential equations. This system describes the flow field completely. Its solution yields the detailed distribution of flow quantities. Equation (3.39) in Cartesian index notation is written as:

$$\frac{\partial V_i}{\partial t} + V_j\frac{\partial V_i}{\partial x_j} = -\frac{1}{\rho}\frac{\partial p}{\partial x_i} + \nu\frac{\partial^2 V_i}{\partial x_j\partial x_j} \tag{3.40}$$

Using the Einstein summation convention, the three components of Eq. (3.40) are:

$$\frac{\partial V_1}{\partial t}+V_1\frac{\partial V_1}{\partial x_1}+V_2\frac{\partial V_1}{\partial x_2}+V_3\frac{\partial V_1}{\partial x_3}=-\frac{1}{\rho}\frac{\partial p}{\partial x_1}+\nu\left(\frac{\partial^2 V_1}{\partial x_1^2}+\frac{\partial^2 V_1}{\partial x_2^2}+\frac{\partial^2 V_1}{\partial x_3^2}\right)$$

$$\frac{\partial V_2}{\partial t}+V_1\frac{\partial V_2}{\partial x_1}+V_2\frac{\partial V_2}{\partial x_2}+V_3\frac{\partial V_2}{\partial x_3}=-\frac{1}{\rho}\frac{\partial p}{\partial x_2}+\nu\left(\frac{\partial^2 V_2}{\partial x_1^2}+\frac{\partial^2 V_2}{\partial x_2^2}+\frac{\partial^2 V_2}{\partial x_3^2}\right) \tag{3.41}$$

$$\frac{\partial V_3}{\partial t}+V_1\frac{\partial V_3}{\partial x_1}+V_2\frac{\partial V_3}{\partial x_2}+V_3\frac{\partial V_3}{\partial x_3}=-\frac{1}{\rho}\frac{\partial p}{\partial x_3}+\nu\left(\frac{\partial^2 V_3}{\partial x_1^2}+\frac{\partial^2 V_3}{\partial x_2^2}+\frac{\partial^2 V_3}{\partial x_3^2}\right)$$

To obtain the components of the Navier-Stokes equation in an orthogonal curvilinear coordinate system, we use the index notation outlined in Appendix B:

$$\begin{aligned}\boldsymbol{g}_i\left(\frac{\partial V^i}{\partial t}+V^jV^i_{,j}+V^jV^k\Gamma^i_{kj}\right) &= -\frac{1}{\rho}\boldsymbol{g}_i g^{ji}p_{,j}+\nu\boldsymbol{g}_m\Big[V^m_{,ik}+\\ &\quad V^n_{,i}\Gamma^m_{nk}+V^n_{,k}\Gamma^m_{ni}-V^m_{,j}\Gamma^j_{ik}+\\ &\quad V^p\left(\Gamma^n_{pi}\Gamma^m_{nk}-\Gamma^j_{ik}\Gamma^m_{pj}+\Gamma^m_{pi,k}\right)\Big]g^{ik}\end{aligned} \tag{3.42}$$

Using the Christoffel symbols and the physical components for a cylindrical coordinate system as specified in Appendix A, we arrive at the component of Navier-Stokes equation in r-direction:

$$\begin{aligned}&\frac{\partial V_r}{\partial t}+V_r\frac{\partial V_r}{\partial r}+\frac{V_\Theta}{r}\frac{\partial V_r}{\partial\theta}+V_z\frac{\partial V_r}{\partial z}-\frac{V_\Theta^2}{r}=-\frac{1}{\rho}\frac{\partial p}{\partial r}+\\ &\nu\left(\frac{\partial^2 V_r}{\partial r^2}+\frac{1}{r^2}\frac{\partial^2 V_r}{\partial\Theta^2}+\frac{\partial^2 V_r}{\partial z^2}-2\frac{\partial V_\Theta}{r^2\partial\Theta}+\frac{\partial V_r}{r\partial r}-\frac{V_r}{r^2}\right)\end{aligned} \tag{3.43}$$

in θ-direction,

$$\begin{aligned}&\frac{\partial V_\Theta}{\partial t}+V_r\frac{\partial V_\Theta}{\partial r}+\frac{V_\Theta}{r}\frac{\partial V_\Theta}{\partial\Theta}+V_z\frac{\partial V_\Theta}{\partial z}+\frac{V_rV_\Theta}{r}=-\frac{1}{\rho}\frac{\partial p}{r\partial\Theta}\\ &+\nu\left(\frac{\partial^2 V_\Theta}{\partial r^2}+\frac{1}{r^2}\frac{\partial^2 V_\Theta}{\partial\Theta^2}+\frac{\partial^2 V_\Theta}{\partial z^2}+\frac{2}{r^2}\frac{\partial V_r}{r^2\partial\Theta}+\frac{1}{r}\frac{\partial V_\Theta}{\partial r}-\frac{V_\Theta}{r^2}\right)\end{aligned} \tag{3.44}$$

and in z-direction:

$$\frac{\partial V_z}{\partial t} + V_r\frac{\partial V_z}{\partial r} + \frac{V_\Theta}{r}\frac{\partial V_z}{\partial z} + V_z\frac{\partial V_z}{\partial z} = -\frac{1}{\rho}\frac{\partial p}{\partial z} + \\ +\nu\left(\frac{\partial^2 V_z}{\partial r^2} + \frac{\partial^2 V_z}{r^2\partial\Theta^2} + \frac{\partial^2 V_z}{\partial z^2} + \frac{1}{r}\frac{\partial V_z}{\partial r}\right) \tag{3.45}$$

3.2.3 Special case: Euler Equation of Motion

For the special case of steady flow and negligible viscosity, Eq. (3.39) is reduced to:

$$\frac{\partial \boldsymbol{V}}{\partial t} + \boldsymbol{V}.(\nabla \boldsymbol{V}) = -\frac{1}{\rho}\nabla p \tag{3.46}$$

This equation is called *Euler equation of motion.*

3.3 Some Discussions on Turbomachinery Flow, Navier-Stokes Equations

The flow in a turbine or compressor component is characterized by a three-dimensional, highly unsteady motion with random fluctuations due to the interactions between the stator and rotor rows. Considering the flows within the blade boundary layer, based on the blade geometry and pressure gradient, three distinctly different flow patterns can be identified: 1) laminar flow (or non-turbulent flow) characterized by the absence of stochastic motions, 2) turbulent flow, where flow pattern is determined by a fully stochastic motion of fluid particles, and 3) transitional flow characterized by intermittently switching from laminar to turbulent at the same spatial position. Of the three patterns, the predominant one is the transitional flow pattern. The Navier-Stokes equations presented in this section generally describe the unsteady flow through a turbomachinery component. Using a direct numerical simulation (DNS) approach delivers the most accurate results [1]. However, the computational domain must be at least as large as the physical domain. As extensively discussed in [1], the application of DNS, for the time being, is restricted to simple flows at low Reynolds numbers. For calculating the complex turbomachinery flow field with a reasonable time frame, Reynolds averaged Navier-Stokes (RANS) can be used. This issue is discussed in Section 3.6.

3.4 Energy Balance in Stationary Frame of Reference

For the complete description of flow process, the total energy equation is presented. This equation includes mechanical and thermal energy balances.

3.4.1 Mechanical Energy

The mechanical energy balance is established by the scalar multiplication of the equation of motion, Eq. (3.22), with the local velocity vector:

$$\rho \boldsymbol{V} \cdot \frac{D\boldsymbol{V}}{Dt} = \boldsymbol{V} \cdot (\nabla \cdot \boldsymbol{\Pi}) + \rho \boldsymbol{g} \cdot \boldsymbol{V} \tag{3.47}$$

The expression on the right-hand side is obtained from the differentiation:

$$\boldsymbol{V} \cdot (\nabla \cdot \boldsymbol{\Pi}) = \nabla \cdot (\boldsymbol{\Pi} \cdot \boldsymbol{V}) - Tr(\boldsymbol{\Pi} \cdot \nabla \boldsymbol{V}) \tag{3.48}$$

The velocity gradient $\nabla \boldsymbol{V}$ can be decomposed into deformation $\boldsymbol{D}$ and rotation $\boldsymbol{\Omega}$ part as shown in Eq. (3.24):

$$\nabla \boldsymbol{V} = \frac{1}{2}\left(\nabla \boldsymbol{V} + \nabla \boldsymbol{V}^T\right) + \frac{1}{2}\left(\nabla \boldsymbol{V} - \nabla \boldsymbol{V}^T\right) = \boldsymbol{D} + \boldsymbol{\Omega} \tag{3.49}$$

With this operation, the trace of the second order tensor in Eq. (3.49) is calculated from:

$$Tr(\boldsymbol{\Pi} \cdot \nabla \boldsymbol{V}) = \boldsymbol{\Pi} : \boldsymbol{D} + \boldsymbol{\Pi} : \boldsymbol{\Omega} \tag{3.50}$$

Since the second term on the right-hand side of Eq. (3.50) vanishes identically, Eq. (3.48) reduces to:

$$\boldsymbol{V} \cdot (\nabla \cdot \boldsymbol{\Pi}) = \nabla \cdot (\boldsymbol{\Pi} \cdot \boldsymbol{V}) - \boldsymbol{\Pi} : \boldsymbol{D} \tag{3.51}$$

As a result, the mechanical energy balance, Eq. (3.48), becomes:

$$\rho \frac{D}{Dt}\left(\frac{V^2}{2}\right) = \nabla \cdot (\boldsymbol{V} \cdot \boldsymbol{\Pi}) - \boldsymbol{\Pi} : \boldsymbol{D} \tag{3.52}$$

Incorporating Eq. (3.35) for Newtonian fluids into (3.52) leads to:

$$\begin{aligned} \rho \frac{D}{Dt}\left(\frac{V^2}{2}\right) = \nabla \cdot & \left[\boldsymbol{V} \cdot (-p + \lambda \nabla \cdot \boldsymbol{V}) I + 2\mu \boldsymbol{V} \cdot \boldsymbol{D}\right] - \\ & - \left[(-p + \lambda \nabla \cdot \boldsymbol{V}) \nabla \cdot \boldsymbol{V} + 2\mu \boldsymbol{D} : \boldsymbol{D}\right] + \rho \boldsymbol{V} \cdot \boldsymbol{g} \end{aligned} \tag{3.53}$$

with $\boldsymbol{I} : \boldsymbol{D} = \nabla \cdot \boldsymbol{V}$. The sum of the last two terms in the second bracket is called the *dissipation function*:

$$\Phi = \lambda (\nabla \cdot \boldsymbol{V})(\nabla \cdot \boldsymbol{V}) + 2\mu \, \boldsymbol{D} : \boldsymbol{D} \tag{3.54}$$

The incompressible flow Eq. (3.54) reduces to:

$$\Phi = 2\mu \, \boldsymbol{D} : \boldsymbol{D} \tag{3.55}$$

The dissipation function indicates the amount of mechanical energy dissipated as heat, which is due to deformation caused by viscosity. Consider a viscous flow along a stator or rotor blade. Close to the wall in the *boundary layer region,* the velocity experiences a high deformation because of a no-slip condition. By moving outside the boundary layer, the rate of deformation decreases leading to lower dissipation. To analyze the individual terms in the equation of energy and to demonstrate the role of shear stress and its effect on the dissipation of mechanical energy, we introduce a second order tensor,

$$\boldsymbol{T} = \lambda(\nabla\cdot\boldsymbol{V})\boldsymbol{I} + 2\mu\,\boldsymbol{D} \tag{3.56}$$

which we call the *friction stress tensor*. The off-diagonal components of this tensor represent the shear stress components and characterize the *shear-deformative behavior* of this tensor. The diagonal components of this tensor

$$T_{ii} = \lambda\frac{\partial V_i}{\partial x_i} + 2\mu\, D_{ii} \tag{3.57}$$

exhibit additional contributions to the normal stress components. For an incompressible flow with $\nabla\cdot\boldsymbol{V} = D_{ii} = 0$, these terms identically disappear. Inserting Eq. (3.56) into (3.53)**,** we arrive at:

$$\rho\frac{D}{Dt}\left(\frac{V^2}{2}\right) = -\boldsymbol{V}\cdot\nabla p + \nabla\cdot(\boldsymbol{T}\cdot\boldsymbol{V}) - \boldsymbol{T}:\boldsymbol{D} + \rho\boldsymbol{V}\cdot\boldsymbol{g} \tag{3.58}$$

Equation (3.58) exhibits the mechanical energy balance in differential form. The first term on the right-hand side represents the rate of mechanical energy due to the change of pressure acting on the volume element. The second term is the rate of work done by viscous forces on the fluid particle. The third term represents the rate of irreversible mechanical energy due to the friction stress. It dissipates as heat and increases the internal energy of the system. This term corresponds to the dissipation function defined by Eq. (3.54). Finally, the forth term represents the mechanical energy necessary to overcome the gravity force acted on the fluid particle. Equation (3.58) exhibits the general differential form of mechanical energy balance for a viscous flow. For a steady, incompressible, inviscid flow, Eq. (3.58) is simplified as:

$$\boldsymbol{V}\cdot\nabla\left(p + \frac{1}{2}\rho V^2 + \rho gz\right) \equiv d\left(p + \frac{1}{2}\rho V^2 + \rho gz\right) = 0 \tag{3.59}$$

where the vector **g** is replaced by $\boldsymbol{g} = -g\nabla z$. Integration of the above equation leads to the Bernoulli equation of energy.

$$p + \frac{1}{2}\rho V^2 + \rho gz = Constant \tag{3.60}$$

This equation is easily derived by multiplying the Euler equation of motion with a differential displacement.

3.4.2 Thermal Energy

The thermal energy balance is described by the first law of thermodynamics, which is postulated for a closed "thermostatic system". For this system, properties such as temperature, pressure, entropy, internal energy, etc., have no spatial gradients. Since, in an open system such as a turbomachine the thremodynamic properties undergo time and spatial changes, the classical first law must be formulated under open system conditions. To do so, we start from an open system, within which a steady flow process takes place and replaces the differential operator, d, from classical thermodynamics, by the substantial differential operator D. This operation implies the requirement that the thermodynamic system under consideration be at least in a locally stable equilibrium state. Starting from the first law for an internally irreversible system:

$$du = \delta Q - pdv + |\delta w_f| \tag{3.61}$$

where u is the internal energy, and Q the thermal energy added to (or removed from) the system, p the thermodynamic pressure, v the specific volume and δw_f the part of mechanical energy dissipated as heat by the internal friction. The subscript f refers to the irreversible nature of the process caused by internal friction. Applying the differential operator D:

$$\frac{Du}{Dt} = \delta\dot{Q} - p\frac{Dv}{Dt} + \delta\dot{w}_f \tag{3.62}$$

where $\delta\dot{Q}$ is the rate of thermal energy added (or removed) to or from the open system per unit mass and time. It can be expressed as the divergence of the thermal energy flux vector $\delta\dot{Q} = -\nabla\cdot\boldsymbol{\dot{q}}/\rho$. The rate of the mechanical energy dissipated as heat $\delta\dot{w}_f$ is identical to the third term $\boldsymbol{T}:\boldsymbol{D}/\rho$ in Eq. (3.58):

$$\frac{Du}{Dt} = -\frac{\nabla\cdot\boldsymbol{\dot{q}}}{\rho} - p\frac{Dv}{Dt} + \frac{\boldsymbol{T}:\boldsymbol{D}}{\rho} \tag{3.63}$$

The negative sign of $-\nabla\cdot\boldsymbol{\dot{q}}$ is introduced to account for a positive heat transfer to the system. Furthermore, since the first term on the left-hand side is per unit mass and time, the divergence of the heat flux vector $\nabla\cdot\boldsymbol{\dot{q}}$ as well as the dissipation term $\boldsymbol{T}:\boldsymbol{D}$, had to be divided by the density to preserve the dimensional integrity. Multiplying both sides of Eq. (3.63) with ρ, we obtain

$$\rho\frac{Du}{Dt} = -\nabla\cdot\boldsymbol{\dot{q}} - \rho p\frac{Dv}{Dt} + \boldsymbol{T}:\boldsymbol{D} \tag{3.64}$$

In Eq. (3.64), first we replace the specific volume v by $1/\rho$ and consider the continuity equation

$$\frac{D\rho}{Dt} = -\rho\nabla\cdot\boldsymbol{V} \tag{3.65}$$

then we insert Eq. (3.65) into (3.64) and arrive at:

$$\rho\frac{Du}{Dt} = -\nabla\cdot\dot{\boldsymbol{q}} - p\nabla\cdot\boldsymbol{V} + \boldsymbol{T}:\boldsymbol{D} \tag{3.66}$$

In Eq. (3.66) the internal energy can be related to the temperature by the thermodynamic relation $u = c_v T$ with c_v as the specific heat at constant volume. The heat flux vector $\dot{\boldsymbol{q}}$ can also be expressed in terms of temperature using the *Fourier heat conduction law*. For an *isotropic medium* the Fourier law of heat conduction is written as:

$$\dot{q} = -k\nabla T \tag{3.67}$$

with k (kJ/m^{2}secK) as the thermal conductivity. Introducing Eq. (3.67) into (3.66), for an incompressible fluid we get:

$$\rho C_v\frac{DT}{Dt} = \nabla^2 T + 2\mu\,\boldsymbol{D}:\boldsymbol{D} \tag{3.68}$$

For a steady flow, Eq. (3.68) can be simplified as:

$$C_v\boldsymbol{V}\cdot\nabla T = \frac{k}{\rho}\nabla^2 T + 2\nu\,\boldsymbol{D}:\boldsymbol{D} \tag{3.69}$$

3.4.3 Total Energy

The combination of the mechanical and thermal energy balances Eqs. (3.58) and Eq. (3.66) results in the following *total energy equation:*

$$\rho\frac{D}{Dt}\left(u + \frac{V^2}{2}\right) = -\nabla\cdot\dot{\boldsymbol{q}} - \nabla\cdot(p\boldsymbol{V}) + \nabla\cdot(\boldsymbol{T}\cdot\boldsymbol{V}) + \rho\boldsymbol{V}\cdot\boldsymbol{g} \tag{3.70}$$

We may rearrange the second and third term on the right-hand side of Eq. (3.70)

$$\rho\frac{D}{Dt}\left(u + \frac{V^2}{2}\right) = -\nabla\cdot\dot{\boldsymbol{q}} + \nabla\cdot\left[\boldsymbol{V}\cdot(-p\boldsymbol{I} + \boldsymbol{T})\right] + \rho\boldsymbol{V}\cdot\boldsymbol{g} \tag{3.71}$$

The argument inside the parenthesis within the bracket exhibits the stress tensor.

$$\rho\frac{D}{Dt}\left(u + \frac{V^2}{2}\right) = -\nabla\cdot\dot{\boldsymbol{q}} + \nabla\cdot\left(\boldsymbol{V}\cdot\boldsymbol{\Pi}\right) + \rho\boldsymbol{V}\cdot\boldsymbol{g} \tag{3.72}$$

Thus, the second term on the right-hand side constitutes the mechanical energy necessary to overcome the surface forces. Equation (3.72) may be written in different forms using different thermodynamic properties. Since in an open system enthalpy is used, we replace the internal energy by the enthalpy $h = u - pv$ and find

$$\rho\frac{D}{Dt}\left(h + \frac{V^2}{2}\right) = \frac{\partial p}{\partial t} + -\nabla\cdot\dot{\boldsymbol{q}} + \nabla\cdot\left(\boldsymbol{T}\cdot\boldsymbol{V}\right) + \rho\boldsymbol{V}\cdot\boldsymbol{g} \tag{3.73}$$

The expression in the parenthesis is called the *total enthalpy*. For steady state, the gravitational term may be brought into the parenthesis by considering $\boldsymbol{V}\cdot\boldsymbol{g} = -\boldsymbol{V}\cdot\nabla(gz) = -d(gz)$.

3.4.4 Entropy Balance

The second law of thermodynamics expressed in terms of Gibbs entropy equation is

$$ds = \frac{\delta Q}{T} = \frac{du + pdv}{t} \tag{3.74}$$

The infinitesimal heat δQ added to or rejected from the system may include the heat generated by the irreversible dissipation process. Replacing the differential d by the material differential operators, we arrive at:

$$T\frac{Ds}{Dt} = \frac{Du}{Dt} + p\frac{Dv}{Dt} \tag{3.75}$$

The right-hand side of Eq. (3.75) is expressed by Eq. (3.66) as:

$$\frac{Du}{Dt} + p\frac{Dv}{Dt} = -\frac{1}{\rho}\nabla\cdot\dot{\boldsymbol{q}} + \frac{1}{\rho}\boldsymbol{T}:\boldsymbol{D} \tag{3.76}$$

replacing the left-hand side of Eq. (3.76) by Eq. (3.75) results in

$$\rho\frac{Ds}{Dt} = = -\frac{1}{T}\nabla\cdot\dot{\boldsymbol{q}} + \frac{1}{T}\boldsymbol{T}:\boldsymbol{D} \tag{3.77}$$

The second term on the right-hand side, which include the second order friction tensor ***T,*** is the dissipation function Eq. (3.54)

$$\rho \frac{Ds}{Dt} = -\frac{1}{T}\nabla\cdot\dot{\boldsymbol{q}} + \frac{1}{T}\Phi \tag{3.78}$$

This equation shows clearly that the total entropy change Ds/Dt generally consists of two parts. The first part is the entropy change due to a reversible heat supply to the system (addition or rejection), and may assume positive, zero, or negative values. The second term exhibits the entropy production due to the irreversible dissipation and is always positive. Thus, Eq. (3.78) may be modified as:

$$\begin{aligned} &\rho \frac{Ds}{Dt} = \rho\left(\frac{Ds}{Dt}\right)_{rev} + \rho\left(\frac{Ds}{Dt}\right)_{irr}, \\ &\text{with } \rho\left(\frac{Ds}{Dt}\right)_{rev} = -\frac{1}{T}\nabla\cdot\dot{\boldsymbol{q}}, \quad \text{and } \rho\left(\frac{Ds}{Dt}\right)_{irr} = \frac{\Phi}{T} \end{aligned} \tag{3.79}$$

The reversible part exhibits the heat added/rejected reversibly to/from the system, thus the entropy change can assume positive or negative values, whereas for the irreversible, the entropy change is always positive.

3.5 Differential Balances in Rotating Frame of Reference

3.5.1 Velocity and Acceleration in Rotating Frame

Accounting for the particular flow situation in turbomachinery stage, we consider a rotating frame of reference that is attached to the rotor, thus turns with an angular velocity $\boldsymbol{\omega}$ about the machine axis. From a stationary observer point of view, a fluid particle that travels through a rotation frame has at an arbitrary time t the position vector $\boldsymbol{r}$ and a *relative velocity* $\boldsymbol{W}$. In addition, it is subjected to the inherent rotation of the frame causing the fluid particle to rotate with the velocity $\boldsymbol{\omega}\times\boldsymbol{r}$. Thus, the observer located outside the rotating frame observes the velocity

$$\boldsymbol{V} = \boldsymbol{W} + \boldsymbol{\omega}\times\boldsymbol{r} \tag{3.80}$$

Inserting Eq. (3.80) into Eq. (3.16), the substantial acceleration is found

$$\frac{D\boldsymbol{V}}{Dt} = \frac{\partial(\boldsymbol{W} + \boldsymbol{\omega}\times\boldsymbol{r})}{\partial t} + (\boldsymbol{W} + \boldsymbol{\omega}\times\boldsymbol{r})\cdot\nabla(\boldsymbol{W} + \boldsymbol{\omega}\times\boldsymbol{r}) \tag{3.81}$$

We multiply Eq. (3.81) out and find

$$\frac{D\boldsymbol{V}}{Dt} = \frac{\partial \boldsymbol{W}}{\partial t} + \frac{\partial(\boldsymbol{\omega}\times\boldsymbol{r})}{\partial t} + \boldsymbol{W}\cdot\nabla\boldsymbol{W} + \\ + \boldsymbol{W}\cdot\nabla(\boldsymbol{\omega}\times\boldsymbol{r}) + (\boldsymbol{\omega}\times\boldsymbol{r})\cdot\nabla\boldsymbol{W} + (\boldsymbol{\omega}\times\boldsymbol{r})\cdot\nabla(\boldsymbol{\omega}\times\boldsymbol{r}) \tag{3.82}$$

Investigating the terms in Eq. (3.82), we begin with the second term on the right-hand side

$$\frac{\partial(\boldsymbol{\omega}\times\boldsymbol{r})}{\partial t} = \boldsymbol{\omega}\times\frac{\partial \boldsymbol{r}}{\partial t} + \boldsymbol{r}\times\frac{\partial \boldsymbol{\omega}}{\partial t} = \boldsymbol{r}\times\frac{\partial \boldsymbol{\omega}}{\partial t} \tag{3.83}$$

since the first term on the right-hand side of Eq. (3.82) $\partial \boldsymbol{r}/\partial t = 0$. Furthermore, the last three terms of Eq. (3.82) are:

$$(\boldsymbol{\omega}\times\boldsymbol{r})\cdot\nabla\boldsymbol{W} = \boldsymbol{\omega}\times\boldsymbol{W}, \quad \boldsymbol{W}\cdot\nabla(\boldsymbol{\omega}\times\boldsymbol{r}) = \boldsymbol{\omega}\times\boldsymbol{W}, \quad \text{and} \quad \boldsymbol{W}\cdot\nabla(\boldsymbol{\omega}\times\boldsymbol{r}) = \boldsymbol{\omega}\times\boldsymbol{r} \tag{3.84}$$

Detailed derivation of Eq.(3.84) are given in Vavra [2]. Considering Eqs. (3.83) and (3.84), Eq. (3.82) becomes

$$\frac{D\boldsymbol{V}}{Dt} = \frac{\partial \boldsymbol{W}}{\partial t} + \frac{\partial \boldsymbol{\omega}}{\partial t}\times\boldsymbol{r} + \boldsymbol{W}\cdot\nabla\boldsymbol{W} + \boldsymbol{\omega}\times(\boldsymbol{\omega}\times\boldsymbol{r}) + 2\boldsymbol{W}\times\boldsymbol{\omega} \tag{3.85}$$

The first term on the left-hand side $\nabla(\boldsymbol{\omega}\times\boldsymbol{r})$ expresses the local acceleration of the velocity field within the relative frame of reference. The second term, $\partial\omega/\partial t\times\boldsymbol{r}$, is the angular velocity acceleration. It is non-zero during any transient operation of the turbomachine where the shaft speed experiences changes. The third term, $\boldsymbol{W}\cdot\nabla\boldsymbol{W}$, constitutes the convective term within the relative frame of reference. The forth term is the centrifugal force. Finally, the last term in Eq. (3.85), $2\boldsymbol{\omega}\times\boldsymbol{W}$, is called the Coriolis acceleration. It can be equal zero only if the relative velocity vector $\boldsymbol{W}$ and the angular velocity vector $\boldsymbol{\omega}$ are parallel. As shown in Eqs. (3.84), two terms contributed to producing the Coriolis acceleration. The first term originates from the changes in circumferential velocity, $\nabla(\boldsymbol{\omega}\times\boldsymbol{r})$, in the direction of $\boldsymbol{W}$, and the second one from the spatial changes of $\boldsymbol{W}$ brought about by the rotation. The centrifugal acceleration and Coriolis accelerations are fictitious forces that are produced as a result of transformation from absolute into a relative frame of reference. Figure 3.2 shows the direction of the Coriolis force which is perpendicular to the plane described by the two vectors $\boldsymbol{\omega}$ and $\boldsymbol{W}$. The force vector, $\boldsymbol{\omega}\times(\boldsymbol{\omega}\times\boldsymbol{r})$, is perpendicular and pointing toward the axis of rotation. The direction of the radius vector $\boldsymbol{e}_r$ is expressed in terms of the radius gradient ∇R.

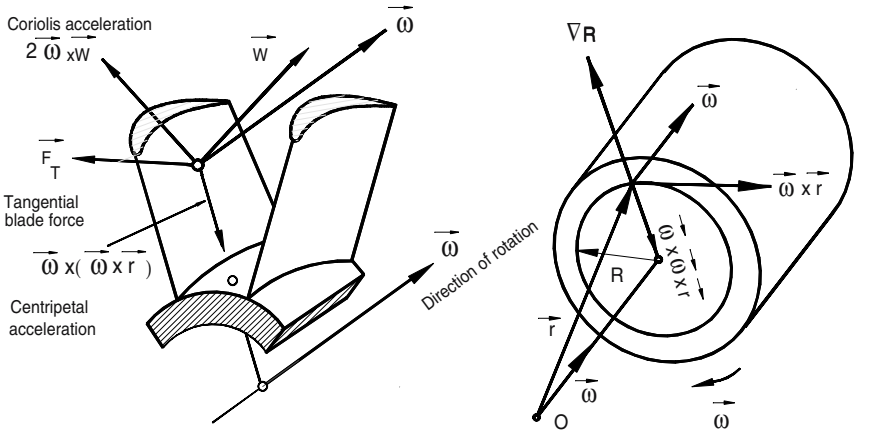

Fig. 3.2: Coriolis and centripetal forces created by the rotating frame of reference.

3.5.2 Continuity Equation in Rotating Frame of Reference

Inserting the velocity vector from Eq. (3.80) into the continuity equation for absolute frame of reference, Eq. (3.4), we obtain:

$$\frac{\partial \rho}{\partial t} + \nabla\cdot\left[\rho(\boldsymbol{W} + \boldsymbol{\omega}\times\boldsymbol{r})\right] = 0 \tag{3.86}$$

When we expand the second term in Eq. (3.86), we find:

$$\frac{\partial \rho}{\partial t} + (\boldsymbol{W} + \boldsymbol{\omega}\times\boldsymbol{r})\cdot\nabla\rho + \boldsymbol{W}\cdot\nabla\rho + \rho\nabla\cdot\boldsymbol{W} + \rho\nabla\cdot(\boldsymbol{\omega}\times\boldsymbol{r}) = 0 \tag{3.87}$$

After a simple rearrangement, Eq. (3.87) leads to:

$$\frac{\partial \rho}{\partial t} + (\boldsymbol{\omega}\times\boldsymbol{r})\cdot\nabla\rho + \boldsymbol{W}\cdot\nabla\rho + \rho\nabla\cdot\boldsymbol{W} + \rho\nabla\cdot(\boldsymbol{\omega}\times\boldsymbol{r}) = 0 \tag{3.88}$$

It is necessary to discuss the individual terms in Eq. (3.88) before rearranging them. The first term indicates the time rate of change of density at a fixed station in an absolute (stationary) frame of reference. The second term involves the spatial change of density registered by a stationary observer. Combining the first and second terms

$$\frac{\partial \rho_R}{\partial t} \equiv \frac{\partial \rho}{\partial t} + (\boldsymbol{\omega}\times\boldsymbol{r})\cdot\nabla\rho \tag{3.89}$$

expresses the time rate of change of the density within the rotating frame of reference.

From Eq. (3.89) it becomes clear that in cases where the local change of the density in an absolute frame might be zero, $\partial\rho/\partial t = 0$. In a rotating frame of reference it will become a function of time $\partial\rho_R/\partial t \neq 0$. Since the product $(\boldsymbol{\omega}\times\boldsymbol{r})\cdot\nabla\rho$ exhibits the circumferential change of the density in the rotating frame, it can vanish only if the flow within the rotating frame is considered axisymmetric. Since the last term in Eq. (3.88), $\nabla\cdot(\boldsymbol{\omega}\times\boldsymbol{r}) = 0$, identically vanishes, the equation of continuity in a rotating frame reduces to:

$$\frac{\partial_R\rho}{\partial t} + \boldsymbol{W}\cdot\nabla\rho + \rho\nabla\cdot\boldsymbol{W} = \frac{\partial_R\rho}{\partial t} + \nabla\cdot(\rho\boldsymbol{W}) = 0 \tag{3.90}$$

Equation (3.90) has the same form as Eq. (3.4), however, the spatial operator ∇ as well as the time derivative $\partial_R/\partial t = 0$ refer to the relative frame of reference. Since the flow in the rotor is understood exclusively with reference to a relative frame of reference, from now on it is unnecessary to differentiate between the operators and the time derivatives.

3.5.3 Equation of Motion in Rotating Frame of Reference

Replacing the acceleration in Eq. (3.22) by the expression obtained in (3.85):

$$\frac{\partial\boldsymbol{W}}{\partial t} + \frac{\partial\boldsymbol{\omega}}{\partial t}\times\boldsymbol{r} + \boldsymbol{W}\cdot\nabla\boldsymbol{W} + \boldsymbol{\omega}\times(\boldsymbol{\omega}\times\boldsymbol{r}) + 2\boldsymbol{\omega}\times\boldsymbol{W} = \frac{1}{\rho}\nabla\cdot\left[-p\boldsymbol{I} + \lambda(\nabla\cdot\boldsymbol{V})\boldsymbol{I} + 2\mu\boldsymbol{D}\right] + \boldsymbol{g} \tag{3.91}$$

Since the expression $\nabla\cdot(\boldsymbol{\omega}\times\boldsymbol{r}) = 0$, Eq. (3.91) is written as:

$$\frac{\partial\boldsymbol{W}}{\partial t} + \frac{\partial\boldsymbol{\omega}}{\partial t}\times\boldsymbol{r} + \boldsymbol{W}\cdot\nabla\boldsymbol{W} + \boldsymbol{\omega}\times(\boldsymbol{\omega}\times\boldsymbol{r}) + 2\boldsymbol{\omega}\times\boldsymbol{W} = \frac{1}{\rho}\nabla\cdot\left[-p\boldsymbol{I} + \lambda(\nabla\cdot\boldsymbol{V})\boldsymbol{I} + 2\mu\boldsymbol{D}\right] + \boldsymbol{g} \tag{3.92}$$

Combining the last two terms in the bracket as $\nabla\cdot\left[\lambda(\nabla\cdot\boldsymbol{V})\boldsymbol{I} + 2\mu\boldsymbol{D}\right]/\rho \equiv \boldsymbol{f}$, and setting for $\boldsymbol{g} = -\nabla(gz)$, we re-arrange Eq. (3.92) as:

$$\frac{\partial\boldsymbol{W}}{\partial t} + \frac{\partial\boldsymbol{\omega}}{\partial t}\times\boldsymbol{r} + \boldsymbol{W}\cdot\nabla\boldsymbol{W} + \boldsymbol{\omega}\times(\boldsymbol{\omega}\times\boldsymbol{r}) + 2\boldsymbol{\omega}\times\boldsymbol{W} = -\frac{1}{\rho}\nabla p + \boldsymbol{f} - \nabla(gz) \tag{3.93}$$

Using the Clausius-Gibbs relation, the pressure gradient can be expressed in terms of enthalpy and entropy gradients:

$$\delta q = Tds = dh - vdp \tag{3.94}$$

The thermodynamic properties s, h, and p are uniform continuous scalar point functions, whose changes are expressed as:

$$ds = d\boldsymbol{X}\cdot\nabla s, \quad dh = d\boldsymbol{X}\cdot\nabla h, \quad dp = d\boldsymbol{X}\cdot\nabla p, \quad ds = d\boldsymbol{X}\cdot\nabla s, \tag{3.95}$$

with $d\boldsymbol{X}$ as the differential displacement along the path of the fluid particle. We replace the quantities in Eq. (3.94) by those in Eq. (3.95) and arrive at:

$$d\boldsymbol{X}\cdot\left(T\nabla s - \nabla h + \frac{\nabla p}{\rho} \right) = 0 \tag{3.96}$$

Since the differential displacement in Eq. (3.96) , $d\boldsymbol{X} \neq 0$, the vector sum in the bracket must vanish

$$T\nabla s - \nabla h + \frac{\nabla p}{\rho} = 0 \tag{3.97}$$

Replacing the pressure gradient term in Eq. (3.93) by Eq. (3.97), we find

$$\frac{\partial \boldsymbol{W}}{\partial t} + \frac{\partial \boldsymbol{\omega}}{\partial t}\times\boldsymbol{r} + \boldsymbol{W}\cdot\nabla\boldsymbol{W} + \boldsymbol{\omega}\times(\boldsymbol{\omega}\times\boldsymbol{r}) + 2\boldsymbol{\omega}\times\boldsymbol{W} = -\nabla(h+gz) + T\nabla s - \boldsymbol{f} - \nabla(gz) \tag{3.98}$$

Further treatment of Eq. (3.98) requires a re-arrangement of few terms. As Fig. 3.8 shows, the centrifugal acceleration points in the negative direction of the gradient of the radius vector and can be written as:

$$\boldsymbol{\omega}\times(\boldsymbol{\omega}\times\boldsymbol{r}) = -\omega^2 R\nabla R = -\nabla\left(\frac{\omega^2 R^2}{2} \right) \tag{3.99}$$

With Eq. (3.99), the equation of motion in a relative frame of reference becomes:

$$\frac{\partial \boldsymbol{W}}{\partial t} + \frac{\partial \boldsymbol{\omega}}{\partial t}\times\boldsymbol{r} + \boldsymbol{W}\cdot\nabla\boldsymbol{W} + \nabla\left(h - \frac{\omega^2 R^2}{2} + gz\right) = -2\boldsymbol{\omega}\times\boldsymbol{W} + T\nabla s + \boldsymbol{f} - \nabla(gz) \tag{3.100}$$

Using the vector identity,

$$\boldsymbol{W}\cdot\nabla\boldsymbol{W} = \nabla\left(\frac{W^2}{2} \right) - \boldsymbol{W}\times(\nabla\times\boldsymbol{W}) \tag{3.101}$$

Equation (3.100) is modified as:

$$\frac{\partial \boldsymbol{W}}{\partial t} + \frac{\partial \boldsymbol{\omega}}{\partial t}\times\boldsymbol{r} + \nabla\left(h + \frac{w^2}{2} - \frac{\omega^2 R^2}{2} + gz \right) = -2\boldsymbol{\omega}\times\boldsymbol{W} + \boldsymbol{W}\times(\nabla\times\boldsymbol{W}) + + T\nabla s + \boldsymbol{f} \tag{3.102}$$

For a constant rotational speed and with $\boldsymbol{\omega}\times\boldsymbol{W} = -\boldsymbol{W}\times\boldsymbol{\omega}$, we find,

$$\frac{\partial \boldsymbol{W}}{\partial t} + \nabla\left(h + \frac{w^2}{2} - \frac{\omega^2 R^2}{2} + gz \right) = 2\boldsymbol{W}\times\boldsymbol{\omega} + \boldsymbol{W}\times(\nabla\times\boldsymbol{W}) + T\nabla s + \boldsymbol{f} \tag{3.103}$$

We introduce now the concept of the *relative total enthalpy*:

$$H_R = \nabla\left(h + \frac{w^2}{2} - \frac{\omega^2 R^2}{2} + gz \right) \tag{3.104}$$

3.5.4 Energy Equation in Rotating Frame of Reference

The energy equation for rotating frame of reference is simply obtained by multiplying the equation of motion with a differential displacement $d\boldsymbol{r}_{\boldsymbol{R}}^{*} = \boldsymbol{W}dt$ along the path of a particle that moves within a rotating frame of reference. It is given by,

$$\boldsymbol{W}dt\cdot\left[\frac{\partial \boldsymbol{W}}{\partial t} + \nabla\left(h + \frac{w^2}{2} - \frac{\omega^2 R^2}{2} + gz \right)\right] = \boldsymbol{W}dt\cdot\left[2\boldsymbol{W}\times\boldsymbol{\omega} + \boldsymbol{W}\times(\nabla\times\boldsymbol{W}) + T\nabla s + \boldsymbol{f}\right] \tag{3.105}$$

Multiplying out and re-arranging the terms, we find:

$$\frac{\partial}{\partial t}\left(\frac{W^2}{2}\right) + d_R\left(h + \frac{w^2}{2} - \frac{\omega^2 R^2}{2} + gz \right) = \boldsymbol{W}dt\cdot\left[2\boldsymbol{W}\times\boldsymbol{\omega} + \boldsymbol{W}\times(\nabla\times\boldsymbol{W}) + T\nabla s + \boldsymbol{f}\right] \tag{3.106}$$

Since the vectors $\boldsymbol{W}\times\boldsymbol{\omega}$ and $\boldsymbol{W}\times(\nabla\times\boldsymbol{W})$ are perpendicular to $\boldsymbol{W}$, their products with $\boldsymbol{W}$ are zero. As a result, Eq. (3.106) reduces to:

$$\frac{\partial}{\partial t}\left(\frac{W^2}{2}\right) + d_R\left(h + \frac{w^2}{2} - \frac{\omega^2 R^2}{2} + gz \right) = d\boldsymbol{r}_{\boldsymbol{R}}^{*}\cdot(T\nabla s - \boldsymbol{f}) \tag{3.107}$$

Multiplying out the right-hand side and considering the identity $d_R s = d\boldsymbol{r}_{\boldsymbol{R}}^{*}\cdot(\nabla s)$, Eq. (3.107) is modified as:

$$\frac{\partial}{\partial t}\left(\frac{W^2}{2}\right) + d_R\left(h + \frac{w^2}{2} - \frac{\omega^2 R^2}{2} + gz \right) = Td_R s - dt\boldsymbol{W}\cdot\boldsymbol{f} \tag{3.108}$$

The term $Td_R s \equiv \delta_R q$ identified as heat consists of two contributions. The first contribution comes from heat supplied or removed from a fluid particle that moves along its path within the relative frame of reference. We call this contribution the reversible part, $\delta_R q_{rev}$. The second contribution is the irreversible part due to the internal friction and dissipation of mechanical energy into heat, which is identical with the friction work, $\delta_R q_{irr} = dt\boldsymbol{W}\cdot\boldsymbol{f}$. We summarize the above statement in the following relation:

$$Td_R s \equiv \delta_R q = \delta_R q_{rev} + \delta_R q_{irr} = \delta_R q_{rev} + dt\boldsymbol{W}\cdot\boldsymbol{f} \tag{3.109}$$

A simple re-arrangement of Eq. (3.109) yields:

$$Td_R s - dt\mathbf{W}\cdot\mathbf{f} = \delta_R q_{rev} \tag{3.110}$$

We insert Eq. (3.110) into Eq. (3.108) and obtain:

$$\frac{\partial}{\partial t}\left(\frac{W^2}{2}\right) + d_R\left(h + \frac{w^2}{2} - \frac{\omega^2 R^2}{2} + gz\right) = \delta_R q_{rev} \tag{3.111}$$

With Eq. (3.111), the changes of relative total enthalpy in a relative frame of reference along the path of a fluid particle is expressed as:

$$d_R\left(h + \frac{w^2}{2} - \frac{\omega^2 R^2}{2} + gz\right) = \delta_R q_{rev} - \frac{\partial}{\partial t}\left(\frac{W^2}{2}\right) \tag{3.112}$$

Only for adiabatic steady flow inside the rotating frame of reference the enthalpy change is zero resulting in:

$$h + \frac{w^2}{2} - \frac{\omega^2 R^2}{2} + gz = const. \tag{3.113}$$

It should be pointed out that Eq (3.113) is strictly valid along the path of a fluid particle. If the flow within the relative frame can be approximated as steady, then Eq. (3.113) is also valid along the streamline. Its value changes however, by moving from one streamline to the next. For a turbine or a compressor rotor row under the above assumption, Eq. (3.113) is written as:

$$\left(h + \frac{w^2}{2} - \frac{\omega^2 R^2}{2} + gz\right)_2 = \left(h + \frac{w^2}{2} - \frac{\omega^2 R^2}{2} + gz\right)_3 \tag{3.114}$$

where the subscripts 2 and 3 in Eq. (3.114) refer to the inlet and exit station of the rotor row in the second term on the right-hand side.

3.6 Reynolds Averaged Navier Stokes Equations, Intermittency

As briefly discussed in Section 3.3, the transitional pattern dominates the turbomachinery flow particularly within the turbine blade boundary layer. Understanding and accurately predicting the onset and inception of the boundary layer transition under periodic unsteady inlet condition is of crucial importance for predicting the total blade pressure losses and thus the efficiency of a turbomachinery component.

The transition process under a steady inlet flow condition was first explained by Emmons [3] through the turbulent spot production theory. This theory was later promoted by Dhawan and Narasimha [4], who proposed a universal profile for

Emmon's intermittency factor for natural transition. Studies by Abu-Ghanam and Shaw [5], Gostelow and Blunden [6], Dullenkopf and Mayle [7] were conducted to determine the effect of free-stream turbulence and pressure gradient on the spot production rate and the intermittency factor. Significant contributions to unsteady boundary layer transition research were made by Pfeil and his co-researchers Pache [8] , Eifler [9], Herbst [10], and Orth [11]. Pfeil and Herbst [12], and Pfeil et al.[13], using the squirrel cage type wake generator and a flat plate, developed a wake-induced transition model that is now generally accepted as correct. They also showed that in between the induced transition regions by wakes, the boundary layer grew naturally. The original unsteady boundary layer research studies initiated by Pfeil and his co-workers at the Technical University of Darmstadt, Germany, demonstrated the significance of the unsteady transition research and its impact on the turbomachinery efficiency, resulting in a number of research papers. Studies by Mayle [14], Walker [15], and Paxson and Mayle [16] deal with the effect of unsteady wake flow on boundary layer transition. Schobeiri and his co-workers [17], [18], [19], [20] have focused their research attention on the boundary layer transition and development under the effect of unsteady wake flow and developed a new unsteady boundary layer transition model based on a universal unsteady intermittency function.

3.6.1 Physics of Intermittently Laminar-Turbulent Boundary Layer Flow

To better understand the nature of an intermittently laminar-turbulent flow, we consider first a flat plate with a smooth surface placed in a wind tunnel with a low turbulence intensity ($TI < 0.1\%$). Starting from the leading edge, the viscous flow along the plate generates two distinctively different flow regimes. Close to the wall where the viscosity effect is predominant, a thin *boundary layer* is developed, within which the velocity grows from zero at the wall (no-slip condition) to a definite magnitude at the edge of the boundary layer. Inside this thin shear layer, the flow initially constitutes a *stable laminar* flow that starts from the leading edge and extends over a certain range ①. By further passing over the plate surface, the first indications of the laminar flow instability appear in the form of infinitesimal unstable two-dimensional disturbance waves that are referred to as Tollmien-Schlichting waves ②. Further downstream, discrete turbulent spots with highly vortical cores appear *intermittently* and randomly③. Inside these wedge-like spots, the flow is predominantly turbulent with $\nabla \times \boldsymbol{V} \neq 0$. According to the experiments by Schubauer and Klebanoff [21], the leading edge of a turbulent spot moves with a velocity of $V_{le} = 0.88\,U$, whereas its trailing edge moves with a lower velocity of $V_{te} = 0.5\,U$. As a consequence, the spot continuously undergoes a deformation. Schlichting [22] summarized the transition process as follows:

① A stable laminar flow is established that starts from the leading edge and extends to the point of inception of the unstable two-dimensional Tollmien-Schlichting waves.
② Onset of the unstable two-dimensional Tollmien-Schlichting waves.
③ Development of unstable, three-dimensional waves and the formation of vortex cascades.

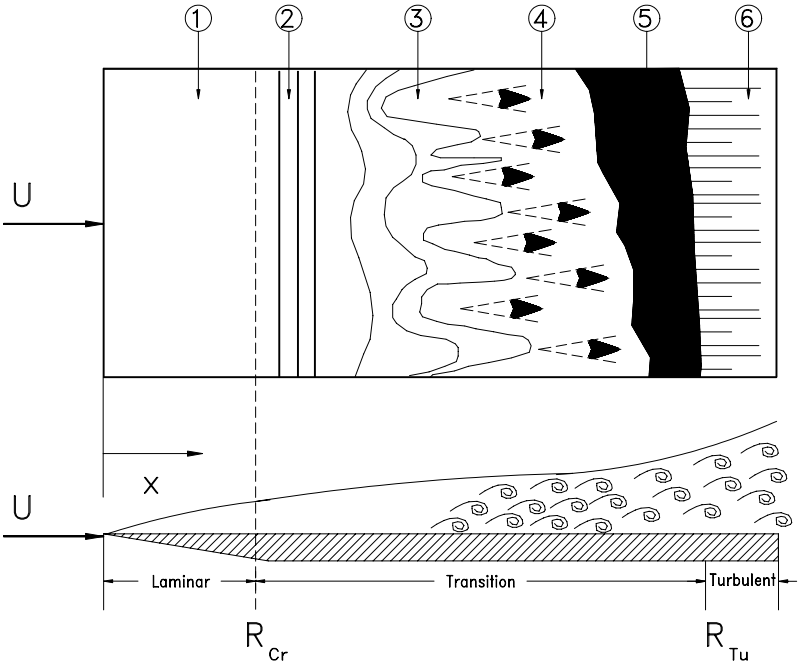

Fig. 3.3: Sketch of transition process in the boundary layer on a flat plate at zero pressure gradient by White [23].

④ Bursts of turbulence in places with high vorticity.
⑤ Intermittent formation of turbulent spots with high vortical core at intense fluctuation.
⑥ Coalescence of turbulent spots into a fully developed turbulent boundary layer.

White [23] presented a simplifying sketch, Fig. 3.3, of transition process of a *disturbance free* flow along a smooth flat plate at zero pressure gradient by assembling the essential elements of transition measured by Schubauer and Klebanoff [21].

3.6.2 Identification of Intermittent Behavior of Statistically Steady Flows

To identify the laminar and turbulent states, Kovasznay et al. [24] introduced the intermittency function $I(\boldsymbol{x},t)$. The value of I is unity for the turbulent flow regime and zero otherwise:

$$I(\boldsymbol{x},t) = \begin{cases} 1 \; for \; turbulent \; flow \\ 0 \; for \; laminar \; flow \end{cases} \tag{3.115}$$

Fig. 3.8 schematically exhibits an intermittently laminar-turbulent velocity with the corresponding intermittency function for a statistically steady flow at a given position vector $\boldsymbol{x}$. Following Kovasznay et al. [24], the time-averaged value of $I(\boldsymbol{x},t)$ is the intermittency factor γ, which gives the fraction of the time that a highly sensitive probe spends in turbulent flow in a sufficiently long period of time T:

$$\gamma(\boldsymbol{x}) \equiv \bar{I} = \frac{1}{T}\int_{t}^{t+T} I(\boldsymbol{x},t)dt \tag{3.116}$$

Experimentally, the intermittency factor γ is determined from a set of N experimental data. This requires that the integral in Eq. (3.116) be replaced by Eq. (3.117):

$$\gamma(\boldsymbol{x}) = \frac{1}{N}\sum_{i=1}^{N} I(\boldsymbol{x},t_i) \tag{3.117}$$

The hatched areas in Fig. 3.4 indicate the portion of the velocity with random fluctuations, whereas the blank areas point to signals lacking random fluctuations.

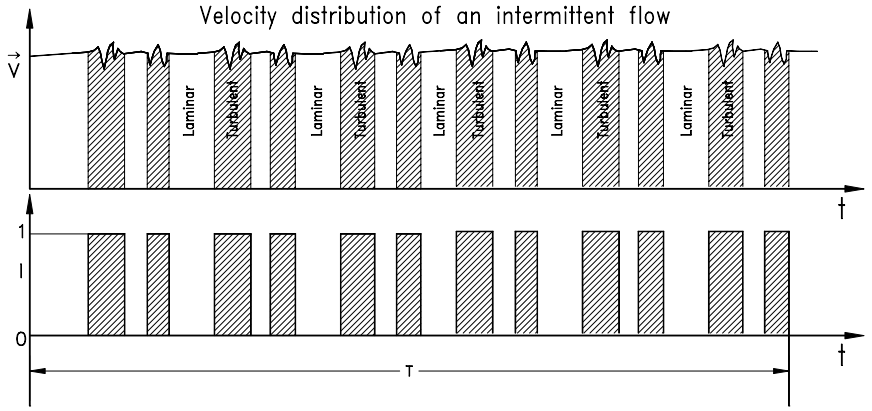

Fig. 3.4: Velocity signals an intermittent laminar-turbulent flow with corresponding intermittent function I as a function of time for a statistically steady flow.

3.6.3 Turbulent/Non-Turbulent Decisions

According to Hedley and Keffer [25], two distinct features of a turbulent flow are its rotational nature and the dissipation of mechanical energy into heat through a cascade of eddies of diminishing size. Spectral analysis is required for detecting energy cascades but it cannot be used as an instantaneous decision for the presence of turbulence. Rotational nature or vortical fluctuations could be used for instantaneous decisions but their measurement requires a complex probe. Alternatively, it is possible to use a simple probe such as a hot-wire for measuring the velocity

fluctuations and to identify the fine-scale structure in the turbulent fluid as shown in Fig. 3.8. Since the velocity fluctuation is not sufficient for making instantaneous decisions for or against the presence of turbulence, the velocity signals need to be sensitized to increase discriminatory capabilities. The commonly used method of sensitizing is to differentiate the signals. The sensitizing process generates some zeros inside the fully turbulent fluid. These zeros influence the decision process for the presence of turbulence or non-turbulence. The process of eliminating these zeros is to integrate the signal over a short period of time *T,* which produces a criterion function S(t). After short term integration, a threshold level *C* is applied to the criterion function to distinguish between the true turbulence and the signal noise. Applying the threshold level results in an indicator function consisting of zeros and 1's satisfying:

$$I(\boldsymbol{x},t) = \begin{cases} 1 \;\; when \;\; S(x,t) \geq C \\ 0 \;\; when \;\; S(x,t) < C \end{cases} \tag{3.118}$$

The resulting random square wave, $I(\boldsymbol{x},t)$, along with the original signal is used to condition the appropriate averages using the equations above. Performing the averaging process using (3.116) or (3.117) for the statistically steady flow shown in Fig. 3.5, we find an intermittency factor $0 < \gamma(\boldsymbol{x}) < 1$. This means that this particular flow is *transitional*.

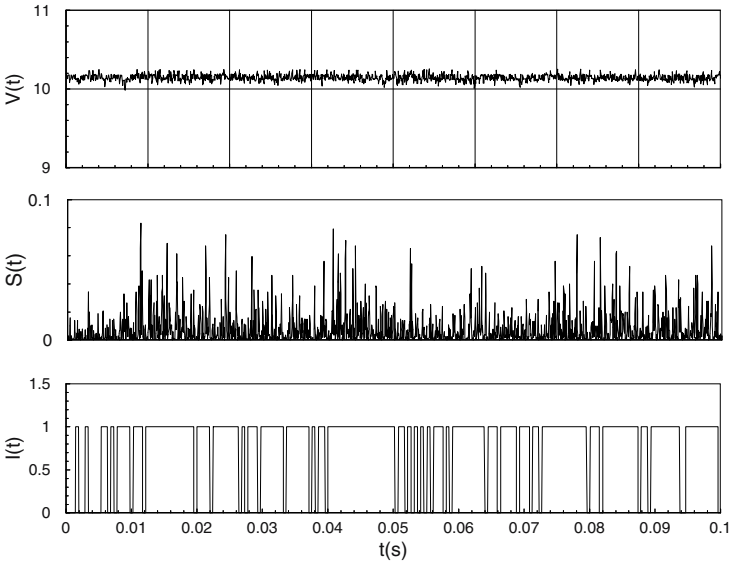

Fig. 3.5: Processing the instantaneous velocity signals for intermittency calculation for a statistically steady flow along a turbine blade. V(t)= velocity signals, S(t)= Detector function, I(t)= indicator function, for Non-turbulent I=0, for turbulent flow I=1.

Using an entire set of velocity distribution along a surface from leading edge to the trailing edge, a detailed picture about the intermittency behavior of the boundary is determined. As an example, Fig. 3.5 exhibits the intermittency distribution along a curved plate under statistically steady flow at zero pressure gradient, [26] . The velocity distribution within the boundary layer distribution is measured using a miniature hot wire probe. The measurement is performed from the leading edge to the trailing edge. From the leading edge up to a position that corresponds to $Re_{x,s}$ = $1.8x10^5$, the flow remains non-turbulent with an averaged intermittency of $\gamma = 0.0$. Figure 3.6 shows that the intermittency starts from zero at a streamwise Reynolds number $Re_{x,s}$ = $2x10^5$ and gradually approaches unity corresponding to the fully turbulent state. This is typical of natural transition and follows the intermittency function introduced by Schubauer and Klebanoff [21].

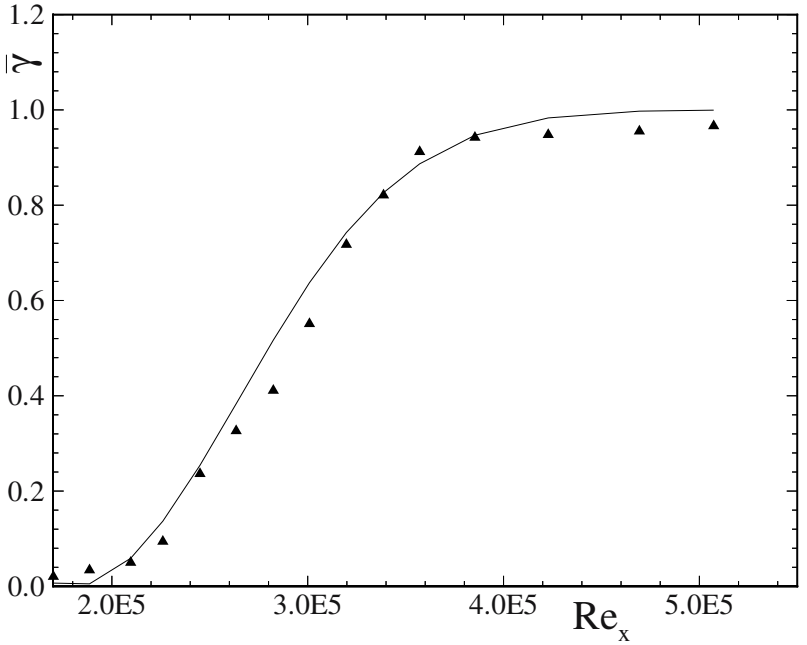

Fig. 3.6: Intermittency as a function of Re_x for no-rod or steady case on the concave surface of the curved plate at y = 0.1 mm.

3.6.4 Identification of Intermittent Behavior of a Periodic Unsteady Flow

A periodic unsteady flow is shown schematically in Fig. 3.7. This type of flow exists downstream of rotating turbine or compressor blades, where the boundary layer development along the blade surface in conjunction with the blade trailing edge thickness produce wakes that convect downstream and form a periodic flow.

Considering the velocity distribution at an arbitrary position vector $\boldsymbol{x}$ and at an *ensemble j* such as $V(t, j)$, the same procedure we applied to the statistically steady flow discussed in 3.3.1 is used to identify the nature of the periodic unsteady

boundary layer flow. The corresponding intermittency function $\boldsymbol{I}(t,j)$ at a given position vector $\boldsymbol{x}$ is shown in Fig. 3.7. For a particular instant of time identified by the subscript i for all ensembles, the ensemble average of $\boldsymbol{I}(t,j)$ over N number of ensembles results in an ensemble averaged intermittency function $<\gamma(\boldsymbol{x},t)>$. This is defined as:

$$<\gamma(\boldsymbol{x},t)> \;=\; \frac{1}{M}\sum_{j=1}^{M} I(t_i,j) \tag{3.119}$$

In Eq. (3.119), M refers to the total number of ensembles and t_i the time at which the corresponding signal was acquired.

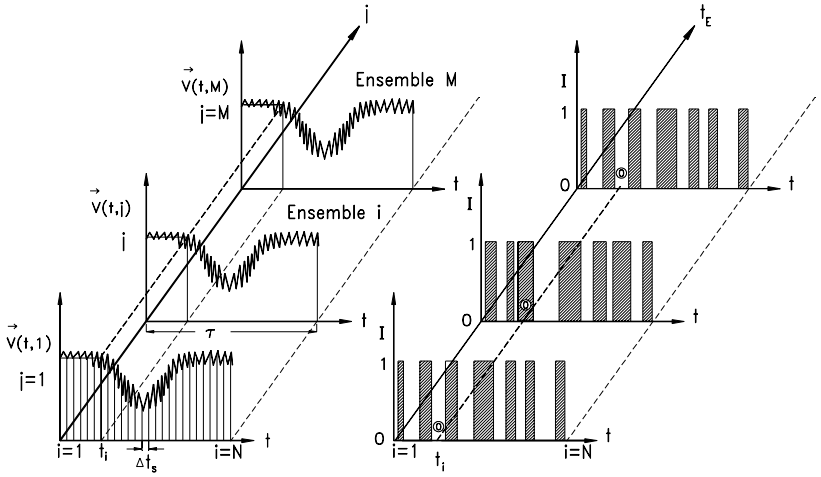

Fig. 3.7: Periodic Unsteady flow velocity with the corresponding distribution of *I(**x**,t)* at a particular position ***x***.

In contrast to the intermittency factor $\gamma(\boldsymbol{x})$, the ensemble averaged intermittency function $<\gamma(\boldsymbol{x},t)>$ is time dependent quantity. Figure 3.8 shows the processing of instantaneous velocities. For each ensemble, the velocity derivatives are obtained leading to a time dependent intermittency function $I(\boldsymbol{x},t)$. Taking the ensemble average of $I(\boldsymbol{x},t)$ as defined by Eq. (3.119) results in an ensemble averaged $<\gamma(\boldsymbol{x},t)>$**,** shown in Fig. 3.8.

3.7 Implementation of Intermittency Function into Navier Stokes Equations

3.7.1 Reynolds-Averaged Equations for Fully Turbulent Flow

In engineering, the flow quantities such as velocity, pressure, temperature, and density may generally be associated with certain time dependent fluctuations. These

fluctuations may be of deterministic or stochastic nature. Turbulent flow is characterized by random fluctuations in velocity, pressure, temperature, and density. Figure 3.9 shows the time dependent turbulent velocity vector as a function of time for steady and unsteady flow. Figure 3.9 exhibits three representative cases encountered in turbomachinery flow physics. Case (a) represents a statistically steady flow through a duct (pipe, nozzle, diffuser etc.). Case (b) reveals the statistically unsteady velocity at the exit of an air storage facility (see Chapter 20). Case (c) depicts a periodic unsteady turbulent flow with a time dependent mean. Any turbulent quantity can be decomposed in a mean and a fluctuation part, where the mean may be time dependent itself as we saw in the ensemble averaging process. For a statistically steady flow, the velocity vector is decomposed in a mean and a fluctuation term:

$$\boldsymbol{V}(\boldsymbol{x},t) = \bar{\boldsymbol{V}}(\boldsymbol{x}) + \boldsymbol{V}'(\boldsymbol{x},t) \tag{3.120}$$

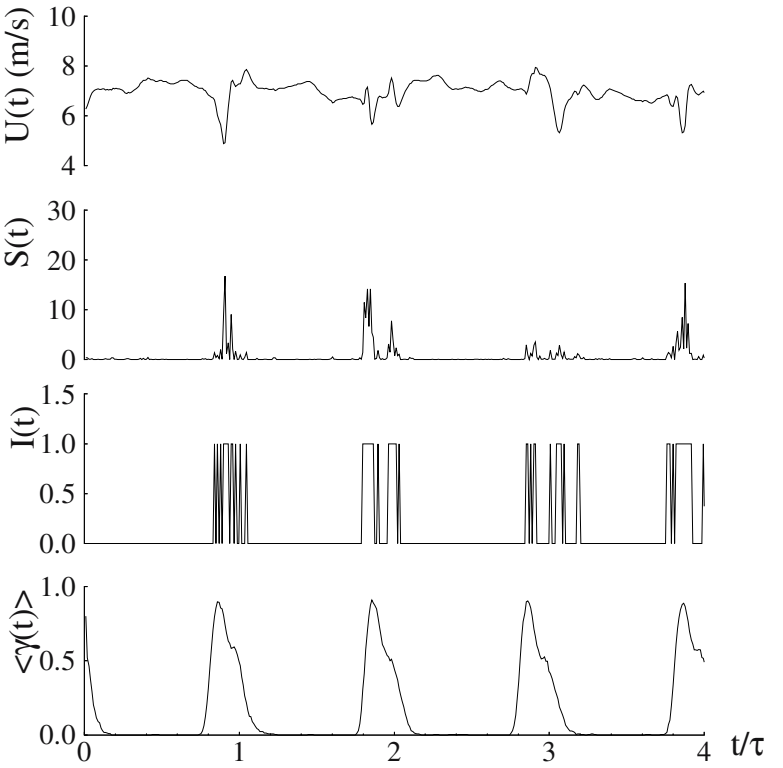

Fig. 3.8 : Calculation of ensemble averaged intermittency function from instantaneous velocities for a periodic unsteady flow along a curved plate at y = 0.1 mm

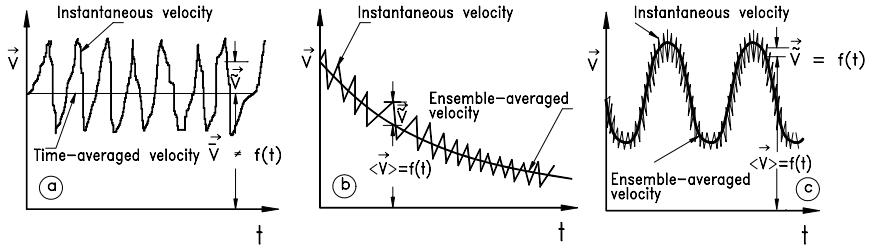

Fig. 3.9: Schematic representation of (a) statistically steady a turbulent flow, with a time independent mean, (b) statistically unsteady turbulent flow with a time dependent mean, and (c) periodic unsteady turbulent flow with a time dependent mean.

The velocity components are obtained from (3.120) as:

$$V_i(x_j,t) = \bar{V}_i(x_j) + V_i'(x_j,t) \tag{3.121}$$

For a statistically unsteady flow, the flow velocity

$$\boldsymbol{V}(\boldsymbol{x},t) = <\bar{\boldsymbol{V}}(\boldsymbol{x},t)> + \boldsymbol{V}'(\boldsymbol{x},t) \tag{3.122}$$

with $<\boldsymbol{V}(\boldsymbol{x},t)>$as the ensemble averaged velocity constructed according to Eq.(3.123) .

$$<\boldsymbol{V}(\boldsymbol{x},t)> = \frac{1}{M}\sum_{j=1}^{M} \boldsymbol{V}(t_i,j) \tag{3.123}$$

where the flow is realized *M* times and each time the velocity $\boldsymbol{V}(\boldsymbol{x},t)$ is determined at the same position $\boldsymbol{x}$ and the same instant of time *t*, Spurk [27].The velocity components are obtained from Eq. (3.122):

$$V_i(x_j,t) = <V_i(x_j,t)> + V_i'(x_j,t) \tag{3.124}$$

For a statistically steady flow, we define the time averaged quantity of a turbulent flow as:

$$\bar{Q} = \frac{1}{T}\int_0^T Q dt: \tag{3.125}$$

with *T* as a time interval, over which the quantity is averaged. For a statistically steady and highly turbulent flow, the averaged quantity $\bar{Q}$ is time independent. However, if the turbulent flow is periodically unsteady with $\tilde{T}$ as the period, the averaging duration *T* must be an order of magnitude smaller than the period of the mean

unsteady flow which means $\tilde{T} \gg T$. From Eq. (3.125), it immediately follows that:

$$\bar{\bar{Q}} = \bar{Q}, \qquad \bar{Q}' = 0, \tag{3.126}$$

The quantity Q may be a zeroth order tensor such as the temperature, pressure, density or a first order tensor such as the velocity. The spatial differentiation of the quantity is obtained from:

$$\overline{\frac{\partial Q}{\partial s}} = \frac{\partial \bar{Q}}{\partial s} \tag{3.127}$$

For a velocity measured at an arbitrary position vector $\boldsymbol{x}$ the mean is expressed as:

$$\bar{\boldsymbol{V}}(\boldsymbol{x}) = \frac{1}{T}\int_0^T \boldsymbol{V}(\boldsymbol{x}, t)dt: \tag{3.128}$$

For further consideration and for the sake of simplicity we may abandon the ensemble averaged parenthesis pair and use instead the over bar $<\boldsymbol{V}(\boldsymbol{x}, t)> \equiv \overline{\boldsymbol{V}}(\boldsymbol{x}, t) \equiv \overline{\boldsymbol{V}}$. However, we will resort to the parenthesis, whenever there is a reason for confusion. We start from the Navier-Stokes equation for incompressible flow in an absolute frame of reference:

$$\frac{\partial \boldsymbol{V}}{\partial t} + \boldsymbol{V}\cdot(\nabla \boldsymbol{V}) = -\frac{1}{\rho}\nabla p + \nu\Delta \boldsymbol{V} \tag{3.129}$$

and assume that the flow quantities are associated with certain fluctuations. We replace the velocity vector $\boldsymbol{V}$ by $\boldsymbol{V} = \bar{\boldsymbol{V}} + \boldsymbol{V}'$, the pressure $p = \bar{p} + p'$ with $\bar{\boldsymbol{V}}$, $\bar{p}$ as the ensemble averaged velocity vector, ensemble averaged pressure and $\boldsymbol{V}'$, p' the fluctuation velocity vector and pressure which are inherently time dependent.

$$\overline{\frac{\partial(\bar{\boldsymbol{V}} + \boldsymbol{V}')}{\partial t}} + \overline{(\bar{\boldsymbol{V}} + \boldsymbol{V}')\cdot\nabla(\bar{\boldsymbol{V}} + \boldsymbol{V}')} = -\overline{\frac{1}{\rho}\nabla(\bar{p} + p')} + \overline{\nu\Delta(\bar{\boldsymbol{V}} + \boldsymbol{V}')} \tag{3.130}$$

Further treatment of Eq. (3.130) in conjunction with the averaging rules Eqs. (3.125) and (3.126) mentioned above results in

$$\frac{\partial \bar{\boldsymbol{V}}}{\partial t} + \bar{\boldsymbol{V}}\cdot\nabla\bar{\boldsymbol{V}} + \nabla\cdot(\overline{\boldsymbol{V}'\boldsymbol{V}'}) = -\frac{1}{\rho}\nabla\bar{p} + \nu\Delta\bar{\boldsymbol{V}} \tag{3.131}$$

This equation is referred to as the Reynolds averaged Navier-Stokes equation of motion for incompressible flow with constant viscosity. For the statistically steady

state $\frac{\partial \bar{\boldsymbol{V}}}{\partial t} = 0$, accordingly for statistically unsteady flow we have, because $\bar{\boldsymbol{V}} = <\boldsymbol{V}>$, the time derivative $\frac{\partial \bar{\boldsymbol{V}}}{\partial t} = \frac{\partial <\bar{\boldsymbol{V}}>}{\partial t} \neq 0$. The term $(\overline{\boldsymbol{V}'\boldsymbol{V}'})$ is the *Reynolds stress tensor* and its divergence $\nabla\cdot(\overline{\boldsymbol{V}'\boldsymbol{V}'})$ is the "eddy force" acting of the fluid particle due to the turbulent fluctuations. It should be pointed out that the decomposition steps performed above were in order to find approximate solution for the Navier-Stokes equation, whose direct numerical solution until very recently appeared to be out of reach. Since the Reynolds stress tensor can not be expressed uniquely in terms of mean flow quantities, it most be modeled. This, however, is the subject of turbulence modeling. Before starting with implementation of intermittency function into the Reynolds equations, we re-arrange Eq. (3.131) as follows:

$$\frac{\partial \bar{\boldsymbol{V}}}{\partial t} + \bar{\boldsymbol{V}}\cdot\nabla\bar{\boldsymbol{V}} = -\frac{1}{\rho}\nabla\bar{p} + \nabla\cdot\left(\nu\nabla\bar{\boldsymbol{V}} - \overline{\boldsymbol{V}'\boldsymbol{V}'}\right) \tag{3.132}$$

In Eq. (3.132) we assumed that the kinematic viscosity is constant throughout the flow field. In Cartesian coordinate systems the index notation of Eq. (3.132) is :

$$\frac{\partial \bar{V}_i}{\partial t} + \bar{V}_j\frac{\partial \bar{V}_i}{\partial x_j} = -\frac{1}{\rho}\frac{\partial \bar{p}}{\partial x_i} + \frac{\partial}{\partial x_j}\left(\nu\frac{\partial \bar{V}_i}{\partial x_j} - \overline{V_i'V_j'}\right) \tag{3.133}$$

and is decomposed in its three components:

$$\frac{\partial \bar{V}_1}{\partial t}+\bar{V}_1\frac{\partial \bar{V}_1}{\partial x_1}+\bar{V}_2\frac{\partial \bar{V}_1}{\partial x_2}+\bar{V}_3\frac{\partial \bar{V}_1}{\partial x_3}=-\frac{1}{\rho}\frac{\partial p}{\partial x_1}+\nu\left(\frac{\partial^2 \bar{V}_1}{\partial x_1^2}+\frac{\partial^2 \bar{V}_1}{\partial x_2^2}+\frac{\partial^2 \bar{V}_1}{\partial x_3^2}\right) -$$

$$\left(\frac{\partial}{\partial x_1}(\overline{V'_1V'_1})+\frac{\partial}{\partial x_2}(\overline{V'_2V'_1})+\frac{\partial}{\partial x_3}(\overline{V'_3V'_1})\right)$$

$$\frac{\partial \bar{V}_2}{\partial t}+\bar{V}_1\frac{\partial \bar{V}_2}{\partial x_1}+\bar{V}_2\frac{\partial V_2}{\partial x_2}+\bar{V}_3\frac{\partial \bar{V}_2}{\partial x_3}=-\frac{1}{\rho}\frac{\partial p}{\partial x_2}+\nu\left(\frac{\partial^2 \bar{V}_2}{\partial x_2^2}+\frac{\partial^2 \bar{V}_2}{\partial x_2^2}+\frac{\partial^2 \bar{V}_2}{\partial x_3^2}\right) -$$

$$\left(\frac{\partial}{\partial x_1}(\overline{V'_1V'_2})+\frac{\partial}{\partial x_2}(\overline{V'_2V'_2})+\frac{\partial}{\partial x_3}(\overline{V'_3V'_2})\right)$$

$$\frac{\partial \bar{V}_3}{\partial t}+\bar{V}_1\frac{\partial \bar{V}_3}{\partial x_1}+\bar{V}_2\frac{\partial \bar{V}_3}{\partial x_2}+\bar{V}_3\frac{\partial \bar{V}_3}{\partial x_3}=-\frac{1}{\rho}\frac{\partial p}{\partial x_3}+\nu\left(\frac{\partial^2 \bar{V}_3}{\partial x_3^2}+\frac{\partial^2 \bar{V}_3}{\partial x_2^2}+\frac{\partial^2 \bar{V}_3}{\partial x_3^2}\right) -$$

$$\left(\frac{\partial}{\partial x_1}(\overline{V'_1V'_3})+\frac{\partial}{\partial x_2}(\overline{V'_2V'_3})+\frac{\partial}{\partial x_3}(\overline{V'_3V'_3})\right) \tag{3.134}$$

The Reynolds averaged Navier-Stokes (RANS) equation (3.132), its index notation (3.133), and the component decomposition (3.134) are derived for a fully turbulent flow which inherently includes the Reynolds stress tensor that has 9 components whose divergence is shown in Eq. (3.134). This equation cannot be applied to a transitional flow which is intermittently laminar and turbulent as is common in turbomachinery aerodynamics. To account for the intermittent nature of a transitional flow, RANS-equations require a conditioning detailed below.

3.7.2 Conditioning the RANS-Equations for Intermittency Implementation

Following Eq.(3.124), we first re-arrange the velocity vector

$$\boldsymbol{V}'(\boldsymbol{x},t) = \boldsymbol{V}(\boldsymbol{x},t) - \bar{\boldsymbol{V}}(\boldsymbol{x},t) \tag{3.135}$$

From the experiments, we know that for a non-turbulent flow, the left-hand side of Eq. (3.135) becomes zero:

$$\boldsymbol{V}(\boldsymbol{x},t) - \bar{\boldsymbol{V}}(\boldsymbol{x},t) = 0 \tag{3.136}$$

and for a fully turbulent flow, we have

$$\boldsymbol{V}(\boldsymbol{x},t) - \bar{\boldsymbol{V}}(\boldsymbol{x},t) = \boldsymbol{V}'(\boldsymbol{x},t) \neq 0 \tag{3.137}$$

Thus Eqs. (3.136) and (3.137) can be summarized as:

$$\boldsymbol{V}(\boldsymbol{x},t) - \bar{\boldsymbol{V}}(\boldsymbol{x},t) = I\boldsymbol{V}'(\boldsymbol{x},t) \tag{3.138}$$

with $I = 1$ for fully turbulent flow and $I = 0$ otherwise. To arrive at a conditioned Navier-Stokes equation for implementation of intermittency function, it is easier to modify first the Navier- Stokes equations by adding the continuity equation for incompressible flow. This results in

$$\frac{\partial \boldsymbol{V}}{\partial t} + \nabla\cdot(\boldsymbol{V}\boldsymbol{V}) = -\frac{1}{\rho}\nabla p + \nu\Delta\boldsymbol{V} \tag{3.139}$$

Inserting the velocity $\boldsymbol{V}(\boldsymbol{x},t) = \bar{\boldsymbol{V}}(\boldsymbol{x},t) + I\boldsymbol{V}'(\boldsymbol{x},t)$ from Eq.(3.138) into the Eq. (3.129), we receive:

$$\frac{\partial(\bar{\boldsymbol{V}} + I\boldsymbol{V}')}{\partial t} + \nabla\cdot\left[(\bar{\boldsymbol{V}} + I\boldsymbol{V}')(\bar{\boldsymbol{V}} + I\boldsymbol{V}')\right] = -\frac{1}{\rho}\nabla(p + p') + \nu\Delta(\bar{\boldsymbol{V}} + I\boldsymbol{V}') \tag{3.140}$$

Performing the multiplication, Eq. (3.140) is prepared for ensemble averaging:

$$\overline{\frac{\partial \bar{\boldsymbol{V}}}{\partial t} + \frac{\partial(I\boldsymbol{V}')}{\partial t} + \nabla\cdot\left[(\bar{\boldsymbol{V}}\bar{\boldsymbol{V}} + 2I\bar{\boldsymbol{V}}\boldsymbol{V}' + I^2\boldsymbol{V}'\boldsymbol{V}')\right]} = \overline{-\frac{1}{\rho}\nabla(p + p') + \nu\Delta\bar{\boldsymbol{V}} + \nu\Delta(I\boldsymbol{V}')} \tag{3.141}$$

carrying out the procedure of ensemble averaging, the following terms identically disappear:

$$\overline{I\boldsymbol{V}'} \equiv o, \quad \overline{2I\bar{\boldsymbol{V}}\boldsymbol{V}'} = 0, \tag{3.142}$$

Utilizing the $I^2 \equiv I$, we arrive at the Reynolds stress tensor:

$$\overline{I\boldsymbol{V}'\boldsymbol{V}'} = \gamma\overline{\boldsymbol{V}'\boldsymbol{V}'} = \frac{1}{T}\int_{t}^{t+T} I\,\boldsymbol{V}'\boldsymbol{V}'\,dt \tag{3.143}$$

With Eq. (3.142) and (3.143), we obtain the conditioned Reynolds equations for incompressible flow that describe non-turbulent, transitional and fully turbulent flows:

$$\frac{\partial\bar{\boldsymbol{V}}}{\partial t} + \nabla\cdot\left(\bar{\boldsymbol{V}}\bar{\boldsymbol{V}} + \gamma\overline{\boldsymbol{V}'\boldsymbol{V}'}\right) = -\frac{1}{\rho}\nabla\bar{p} + \nu\Delta\bar{\boldsymbol{V}} \tag{3.144}$$

Rearranging Eq. (3.144) leads to

$$\frac{\partial\bar{\boldsymbol{V}}}{\partial t} + \bar{\boldsymbol{V}}\cdot\nabla\,\bar{\boldsymbol{V}} = -\frac{1}{\rho}\nabla\bar{p} + \nu\Delta\bar{\boldsymbol{V}} - \gamma\overline{\boldsymbol{V}'\boldsymbol{V}'} \tag{3.145}$$

The turbulent shear strees associated with the intermittency function, $\gamma\overline{\boldsymbol{V}'\boldsymbol{V}'}$, plays a crucial role in affecting the solution of the Navier-Stokes equations. This is particularly significant for calculating the wall friction and the heat transfer coefficient distribution. Two quantities have to be accurately modeled. One is the intermittency function and the other is the Reynolds shear stress. Inaccurate modeling leads to major errors, particularly when calculating the total pressure losses, efficiencies, and heat transfer coefficients. Equation (3.145) is coordinate invariant and can be transformed to any curvilinear coordinate system within an absolute frame of reference. Its decomposition into Cartesian components yields:

$$\frac{\partial\bar{V}_1}{\partial t}+\bar{V}_1\frac{\partial\bar{V}_1}{\partial x_1}+\bar{V}_2\frac{\partial\bar{V}_1}{\partial x_2}+\bar{V}_3\frac{\partial\bar{V}_1}{\partial x_3}=-\frac{1}{\rho}\frac{\partial p}{\partial x_1}+\nu\left(\frac{\partial^2\bar{V}_1}{\partial x_1^2}+\frac{\partial^2\bar{V}_1}{\partial x_2^2}+\frac{\partial^2\bar{V}_1}{\partial x_3^2}\right)-$$

$$\left(\frac{\partial}{\partial x_1}(\gamma\overline{V'_1V'_1})+\frac{\partial}{\partial x_2}(\gamma\overline{V'_2V'_1})+\frac{\partial}{\partial x_3}(\gamma\overline{V'_3V'_1})\right)$$

$$\frac{\partial\bar{V}_2}{\partial t}+\bar{V}_1\frac{\partial\bar{V}_2}{\partial x_1}+\bar{V}_2\frac{\partial V_2}{\partial x_2}+\bar{V}_3\frac{\partial\bar{V}_2}{\partial x_3}=-\frac{1}{\rho}\frac{\partial p}{\partial x_2}+\nu\left(\frac{\partial^2\bar{V}_2}{\partial x_2^2}+\frac{\partial^2\bar{V}_2}{\partial x_2^2}+\frac{\partial^2\bar{V}_2}{\partial x_3^2}\right)-$$

$$\left(\frac{\partial}{\partial x_1}(\gamma\overline{V'_1V'_2})+\frac{\partial}{\partial x_2}(\gamma\overline{V'_2V'_2})+\frac{\partial}{\partial x_3}(\gamma\overline{V'_3V'_2})\right)$$

$$\frac{\partial\bar{V}_3}{\partial t}+\bar{V}_1\frac{\partial\bar{V}_3}{\partial x_1}+\bar{V}_2\frac{\partial\bar{V}_3}{\partial x_2}+\bar{V}_3\frac{\partial\bar{V}_3}{\partial x_3}=-\frac{1}{\rho}\frac{\partial p}{\partial x_3}+\nu\left(\frac{\partial^2\bar{V}_3}{\partial x_3^2}+\frac{\partial^2\bar{V}_3}{\partial x_2^2}+\frac{\partial^2\bar{V}_3}{\partial x_3^2}\right)-$$

$$\left(\frac{\partial}{\partial x_1}(\gamma\overline{V'_1V'_3})+\frac{\partial}{\partial x_2}(\gamma\overline{V'_2V'_3})+\frac{\partial}{\partial x_3}(\gamma\overline{V'_3V'_3})\right) \tag{3.146}$$

3.8 Modeling the Unsteady Intermittency for Turbomachinery Applications

The intermittency model developed by Emmons [3] and promoted by Dhawan and Narasimha [4] accurately predicts the intermittent behavior of the boundary layer along a flat plate or a turbine blade under steady inlet flow condition. In a turbomachinery flow environment, however, the blades are subjected to a periodic unsteady wake flow due to the stator-rotor interaction that substantially affects the inception and onset of boundary layer transitions. To establish an unsteady intermittency function for implementing into boundary layer codes and RANS-equations, Schobeiri and his co-workers [28], [29] implemented an inductive approach which is based on results of experimental and theoretical studies of unsteady wake flow and unsteady boundary layer flow.

The experiments were performed on a curved plate at zero-streamwise pressure gradient under periodic unsteady wake flow, where the frequency of the periodic unsteady flow was varied. Further boundary layer experimental studies were performed on the suction and pressure surfaces of turbine blades. The turbine cascade was integrated into a high-subsonic cascade test facility, which was designed for unsteady boundary layer transition investigations, Fig. 3.10.

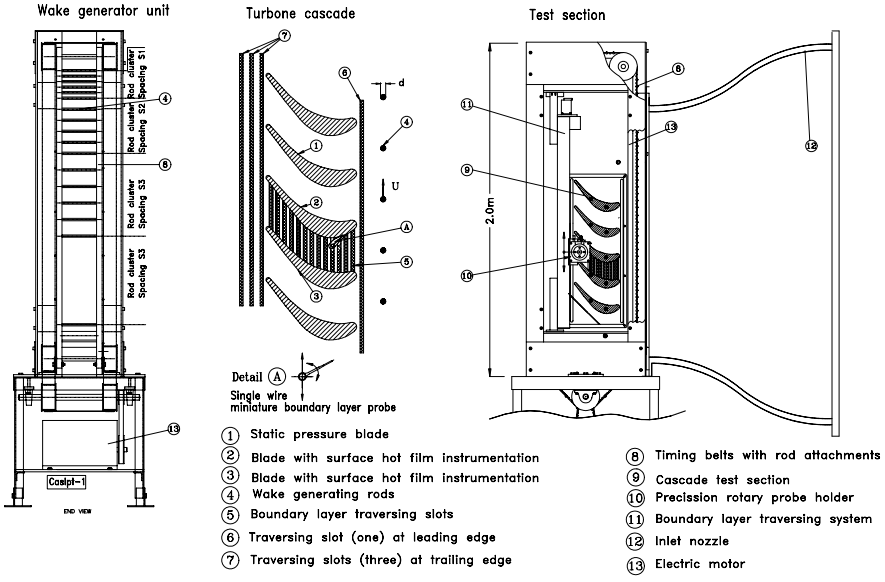

Fig. 3.10: Unsteady turbine cascade research facility at Turbomachinery Performance and Flow Research Laboratory, *TPFL*, test section, boundary layer traversing system and different rod clusters.

The facility simulates two-dimensional periodic unsteady flow by the translational motion of a wake generator with a series of cylindrical rods attached to two parallel operating timing belts driven by an electric motor. The special design of the facility

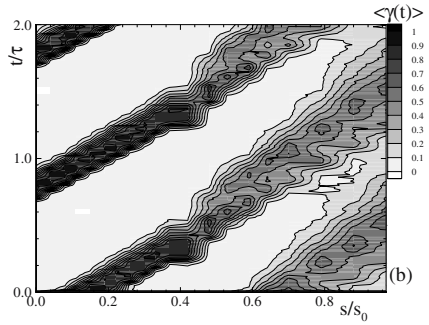

Fig. 3.11 Ensemble-averaged intermittency distribution as a function of axial distance on the concave side of the curved plate for reduced frequency Ω=1.725 at y = 10.0 mm from the surface from [26]

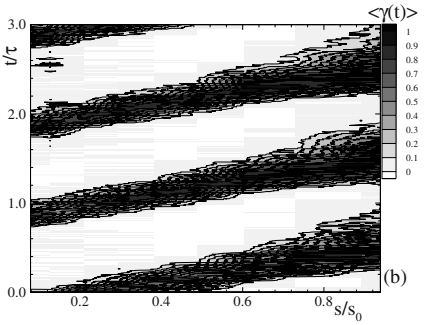

Fig. 3.12: Ensemble-averaged intermittency distribution as a function of axial distance on the pressure surface of the turbine blade for reduced frequency Ω = 0.755 at y = 2.0 mm from the surface from [26]

and the length of the belts enable a considerable reduction in the measurement time when performing the boundary layer experiments. The research facility allows measurements of up to four frequency ranges in one revolution. This is done by attaching up to four clusters of rods with different spacings to the two parallel timing belts moving with translational motion. One of the four clusters has no rods, thus simulating the steady case. The data acquisition and analysis system separates and regroups the data before applying the unsteady ensemble averaging technique. For curved plate as well as turbine blade boundary layer measurements, single-hot-wire probes with a 4 μm tungsten filament were utilized. In both cases, the probes were mounted on computer controlled linear traversing systems. The systems are capable of traversing in increments of 2.5 μm, which is essential in measuring the laminar-sublayer. To capture the transition onset, the curved plate as well as the turbine blades were traversed in streamwise and normal directions.

The intermittency distribution as a function of non-dimensional time and a reduced frequency Ω = 1.725, is shown in Figs. 3.11 for a curved plate described in [26] and in Fig. 3.12 for turbine cascade with an unsteady inlet flow reduced frequency Ω = 0.755 detailed in [26]. Similar plots are seen for other reduced frequencies. Only the first two wakes are plotted for better comparison of the effects of impinging wake frequency on the transition process. Intermittency is approximately equal to zero outside the wake region near the leading edge showing the non-turbulent behavior of the flow. Wake is represented by a thin strip with intermittency values near one, typical of a turbulent flow. As these wakes pass through the channel, the boundary layer periodically switches from non-turbulent to turbulent depending on their presence. The natural transition of the boundary layer is affected by periodic passing of wakes resulting in wake induced transition. The intermittency distributions in Figs. 3.11 and 3.12 clearly show the unsteady nature of the boundary layer transition. In this form, however, they cannot be used to quantitatively describe the

complex unsteady transition process. To establish the basic relations essential for a quantitative description of the unsteady boundary layer transition, the study by Schobeiri and his co-workers [30] is used that deal with the physics of steady and unsteady wake development in a curved environment. These studies show clearly that the turbulence structure of the steady and unsteady wake flow is determined by the wake defect, which is a Gaussian function. Following the above studies, we define a dimensionless parameter:

$$\zeta = \frac{U_w t}{b} = \frac{y}{b} \text{ with } b = \frac{1}{\sqrt{\pi}} \int_{-\infty}^{+\infty} \Gamma \, d\xi_2 \tag{3.147}$$

that relates the passing time t of a wake impinging on the plate surface with the wake passing velocity in lateral direction U_w and the intermittency width b. The latter is directly related to the wake width introduced by Schobeiri and his co-workers [30]. In an analogous way to find the defect function, we define the relative intermittency function Γ as:

$$\Gamma = \frac{<\gamma_i(t_i)> - <\gamma_i(t_i)>_{\min}}{<\gamma_i(t_i)>_{\max} - <\gamma_i(t_i)>_{\min}} \tag{3.148}$$

In Eq. (3.148), $<\gamma_i(t_i)>$ is the time dependent ensemble-averaged intermittency function, which determines the transitional nature of an unsteady boundary layer. The maximum intermittency $<\gamma_i(t_i)>_{\max}$ exhibits the time dependent ensemble averaged intermittency value inside the wake vortical core. Finally, the minimum intermittency $<\gamma_i(t_i)>_{\min}$ represents the ensemble averaged intermittency values outside the wake vortical core. Experimental results from [26] and [31] presented in Figs. 3.13 and 3.14 show that the relative intermittency function Γ closely follows a Gaussian distribution, which is given by:

$$\Gamma = e^{-\zeta^2} \tag{3.149}$$

Here ζ is the non-dimensionalized lateral length scale. Using this function as a universally valid relationship for relative intermittency, the intermittency function $<\gamma_i(t_i)>$ is completely determined if additional information about the minimum and maximum intermittency functions $<\gamma_i(t_i)>_{\min}$ and $<\gamma_i(t_i)>_{\max}$ are available. The distribution of $<\gamma_i(t_i)>_{\min}$ and $<\gamma_i(t_i)>_{\max}$ in the streamwise direction are plotted in Fig. 3.15 and 3.16 for $\Omega = 0$, and 1.033. The steady case shown in Fig. 3.15 serves as the basis for comparison of the maximum and minimum values. In the steady case, the intermittency starts to rise from zero at a streamwise Reynolds number of $Re_{x,s} = 2x10^5$ and gradually approaches the unity corresponding to the fully turbulent state. This is typical of natural transition and follows the intermittency function introduced by Dhawan and Narasimha [4]. The distributions of maximum and minimum turbulence intermittencies $<\gamma_i(t_i)>_{\min}$ and $<\gamma_i(t_i)>_{\max}$ in the streamwise direction are shown in Fig. 3.16. For each particular streamwise location on the plate surface with a streamwise Reynolds number, for example $Re_{x,s} = 1x10^5$, two corresponding,

distinctively different intermittency states are periodically present. At this location, $<\gamma_i(t_i)>_{max}$ corresponds to the condition when the wake with the high turbulence intensity core impinges on the plate surface at a particular instant of time. Once the wake has passed over the surface, the same streamwise location is exposed to a low turbulence intensity flow regime with an intermittency state of $<\gamma_i(t_i)>_{min}$, where no wake is present. As seen, $<\gamma_i(t_i)>_{min}$ has the tendency to follow the course of the steady (no-wake) intermittency distribution exhibited in Fig.3.15, with a gradual increase from an initial *non-turbulent* state with a value of zero approaching a final state of 0.8. This was expected as $<\gamma_i(t_i)>_{min}$ is calculated outside the wake region where the turbulence

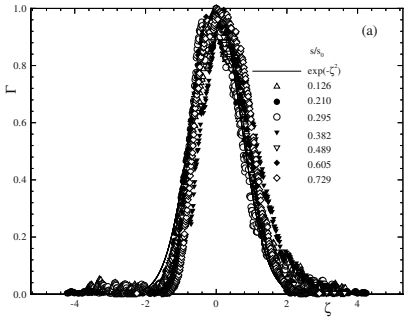

Fig. 3.13: Relative intermittency as a function of non-dimensionalized lateral coordinate for $\Omega = 0.755$ at y = 0.1 mm on the pressure surface of the turbine blade.

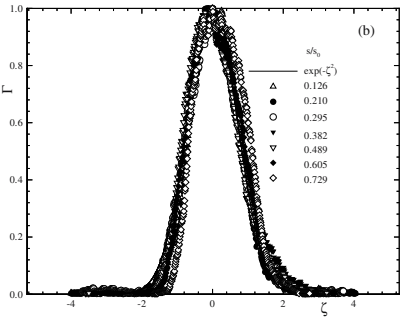

Fig. 3.14: Relative intermittency as a function of non-dimensionalized lateral coordinate for $\Omega = 1.51$ at y = 0.1 mm on the pressure surface of the turbine blade.

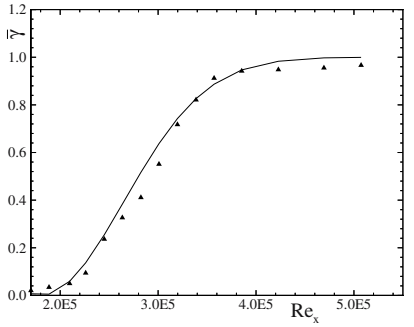

Fig. 3.15: Intermittency as a function of Re_x for $\Omega = 0$ or steady case on the concave surface of the curved plate

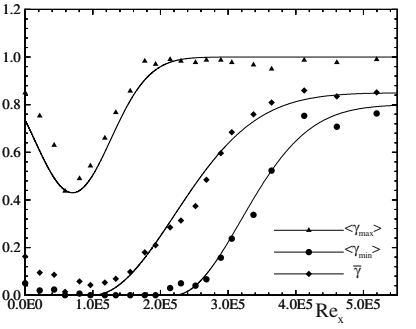

Fig. 3.16: Maximum, minimum and time-averaged intermittency as a function of axial Reynolds number for $\Omega = 1.033$.

intensity is relatively small. On the other hand, $<\gamma_i(t_i)>_{max}$ reveals a fundamentally different behavior that needs to be discussed further. As Fig. 3.3 shows, the wake flow with an intermittency close to 1 impinges on the blade surface. By convecting downstream, its turbulent fluctuations undergo a strong damping by the wall shear stress forces. The process of damping continues until $<\gamma_i(t_i)>_{max}$ reaches a minimum. At this point, the wall shear forces are not able to further suppress the turbulent fluctuations. As a consequence, the intermittency again increases to approach the unity, showing the combined effect of *wake induced* and *natural transition* due to an increased turbulence intensity level. The damping process of the high turbulence intensity wake flow discussed above explains the phenomena of *the becalming* effect of a wake induced transition observed by several researchers including Pfeil and Herbst [12]. Figure 3.15 also shows the average intermittency which is a result of the integral effect of periodic wakes with respect to time.

References, Chapter 3

3.1. Frziger, H.J., Peric,: Computational Methods for Fluid Dynamics, 3rd Edition, Springer-Verlag , Berlin heidelberg New York.

3.2. Vavra, M.H., 1960, Aerothermodynamics and Flow in Turbomachines, John Wiley &Sons, New York

3.3. Emmons, H. W., 1951, "The Laminar-Turbulent Transition in Boundary Layer-Part I," J. Aero. Sci., Vol. 18, pp. 490-498.

3.4. Dhawan, S., and Narasimha, R., 1958, "Some Properties of Boundary Layer Flow During The Transition From Laminar to Turbulent Motion," *Journal of Fluid Mechanics*, Vol. 3, pp. 418-436.

3.5. Abu-Ghannam, B. J., and Shaw, R., 1980, "Natural Transition of Boundary Layers-The Effects of Turbulence, Pressure Gradient and Flow History," *J. Mech. Eng. Sci.*, Vol. 22, pp. 213-228.

3.6. Gostelow, J. P., and Blunden, A. R., 1989, "Investigations of Boundary Layer Transition in an Adverse Pressure Gradient," ASME *Journal of Turbomachinery*, Vol. 111, pp. 366-375.

3.7. Dullenkopf, K., Mayle, R. E., 1994, ASME Paper No. 94-GT-174.

3.8. Pache, W., 1976, "Zur Frage der Entwicklung von Strömungsgrenz-schichten bei instationärer Zuströmung in Turbomachinen," Dissertation D-17, Technische Hochschule Darmstadt Germany.

3.9. Eifler, J., 1975, "Zur Frage der freien turbulenten Strömungen, insbesondere hinter ruhenden und bewegten Zylindern," Dissertation D-17, Technische Hochschule Darmstadt, Germany.

3.10. Herbst, R., 1980, "Entwicklung von Strömung-grenzsschichten bei instationärer Zuströmung in Turbomaschinen," Dissertation D-17, Technische Hochschule Darmstadt, Germany.

3.11. Orth, U., 1992, "Unsteady Boundary-Layer Transition in Flow Periodically Disturbed by Wakes," ASME Paper No. 92-GT-283.

3.12. Pfeil, H., and Herbst, R., 1979, "Transition Procedure of Instationary Boundary Layers," ASME Paper No. 79-GT-128.

3.13. Pfeil, H., Herbst, R., and Schröder, T., 1983, “Investigation of the Laminar-Turbulent Transition of Boundary Layers Disturbed by Wakes,” ASME *Journal of Engineering for Power*, Vol. 105, pp. 130-137.

3.14. Mayle, R. E., 1991, “The Role of Laminar-Turbulent Transition in Gas Turbine Engines,” *Journal of Turbomachinery*, Vol. 113, pp. 509-537.

3.15. Walker, G.J., 1989, “Modeling of Transitional Flow in Laminar Separation Bubbles,” *9th Int. Symp. Air Breathing Engines*, pp. 539-548.

3.16. Paxson, D.E., Mayle, R.E., 1991, “Laminar Boundary Layer Interaction With an Unsteady Passing Wake,” *Journal of Turbomachinery*, Vol. 113, pp. 419-427.

3.17. Schobeiri, M. T., and Radke, R., 1993, "Effects of Periodic Unsteady Wake Flow and Pressure Gradient on Boundary Layer Transition Along The Concave Surface of A Curved Plate," ASME Paper No. 94-GT-327.

3.18. Schobeiri, M. T., Read, K., and Lewalle, J., 1995, “Effect of Unsteady Wake Passing Frequency on Boundary Layer Transition: Experimental Investigation and Wavelet Analysis,” ASME Paper No. 95-GT-437.

3.19. Chakka, P., Schobeiri, M.T. , 1999, “Modeling of Unsteady Boundary Layer Transition on a Curved Plate under Periodic Unsteady Flow Condition: Aerodynamic and Heat Transfer Investigations,” ASME Transactions, *Journal of Turbo machinery,* January 1999, Vol. 121, pp. 88-97.

3.20. Wright, L., Schobeiri, M. T., 1999, “The Effect of Periodic Unsteady Flow on Boundary Layer and Heat Transfer on a Curved Surface,”ASME Transactions, *Journal of Heat Transfer,* November 1998, Vol. 120, pp. 22-33.

3.21. Schubauer, G. B., and Klebanof, P.S., “Contributions on the Mechanics of Boundary Layer Transition, NACA TN 3489 (1955) and NACA Rep. 1289 (1956).

3.22. Schlichting, H., 1979, “Boundary Layer Theory, McGraw-Hill Company, Seventh Edition.

3.23. White, F. M. 1974, “Viscose Fluid Flow,” McGraw-Hill, New York.

3.24. Kovasznay, L.S.G., Kibens, V. and Blackwelder, R.F., 1970, *J. Fluid Mech.*, Vol. 41, pp. 283.

3.25. Hedley, B. T., and Keffer F. J., 1974, “Turbulent/Non-Turbulent Decisions in an Intermittent Flow,” *Journal of Fluid Mechanics*, Vol. 64, pp. 625-644.

3.26. Chakka, P., Schobeiri, M.T. , 1999, “Modeling of Unsteady Boundary Layer Transition on a Curved Plate under Periodic Unsteady Flow Condition: Aerodynamic and Heat Transfer Investigations,” ASME Transactions, *Journal of Turbomachinery,* January 1999, Vol. 121, pp. 88-97.

3.27. Spurk, J. H., 1997, “Fluid Mechanics,” Springer, ISBN 3-540-61651-9 Springer-Verlag Berlin Heidelberg New York.

3.28. Schobeiri, M. T., Pappu, K., Wright, L., 1995, “Experimental Sturdy of the Unsteady Boundary Layer Behavior on a Turbine Cascade,” ASME 95-GT-435, presented at the International Gas Turbine and Aero-Engine Congress and Exposition, Houston, Texas, June 5-8, 1995.

3.29. Schobeiri, M. T., Chakka, P., 1998, "Unsteady Wake Effects on Boundary Layer Transition and Heat Transfer Characteristics of a Turbine Blade," ASME Paper No. 98-GT-291, presented at the ASME, IGTI, International Gas Turbine Congress, in Stockholm.

3.30. Schobeiri, M.T., Jose, J., and Pappu, K., 1996, "Development of Two Dimensional Wakes within Curved Channel: Theoretical Framework and Experimental Investigations," ASME *Journal of Turbomachinery*, Vol. 118, pp. 506-518.

3.31. Schobeiri, M. T., Chakka, P., "Prediction of turbine blade heat transfer and aerodynamics using unsteady boundary layer transition model," *International Journal of Heat and Mass Transfer,* 45 (2002) pp. 815-829.

4 Integral Balances in Turbomachinery

In the following sections, we summarize the conservation laws in integral form essential for applying to the turbomachinery flow situations. Using the Reynolds transport theorem explained in Chapter 2, we start with the continuity equation, which will be followed by the equation of linear momentum, angular momentum, and the energy. Vavra [1] utilized an alternative approach by directly integrating the differential balances. Both approaches are valid and lead to the same results.

4.1 Mass Flow Balance

We apply the Reynolds transport theorem by substituting the function *f(**X**,t)* in Chapter 2 by the density of the flow field:

$$m = \int_{v(t)} \rho(\boldsymbol{X}, t)dv \tag{4.1}$$

where the density generally changes with space and time. To obtain the integral formulation, Reynolds transport theorem from Chapter 2 is applied. The requirement that the mass be constant leads to:

$$\frac{Dm}{Dt} = \int_{v(t)} \frac{\partial}{\partial t}\rho(\boldsymbol{X}, t)dv + \int_{S(t)} \rho(\boldsymbol{X}, t)\boldsymbol{V}\cdot\boldsymbol{n}\,dS = 0 \tag{4.2}$$

If the density does not undergo a time change (steady flow), the above equation is reduced to:

$$\int_{S(t)} \rho(\boldsymbol{X}, t)\boldsymbol{V}\cdot\boldsymbol{n}\,dS = 0 \tag{4.3}$$

For practical purposes, a fixed control volume is considered, where the integration must be carried out over the entire control surface:

$$\int_{S} \rho\boldsymbol{V}\cdot\boldsymbol{n}\,dS = \int_{S_{in}} \rho\boldsymbol{V}\cdot\boldsymbol{n}\,dS + \int_{S_{out}} \rho\boldsymbol{V}\cdot\boldsymbol{n}\,dS + \int_{S_{wall}} \rho\boldsymbol{V}\cdot\boldsymbol{n}\,dS = 0 \tag{4.4}$$

The control surface may consist of one ore more inlets, one more exits, and may include porous walls, as shown in Fig. 4.1. For such a case Eq. (4.4) is expanded as:

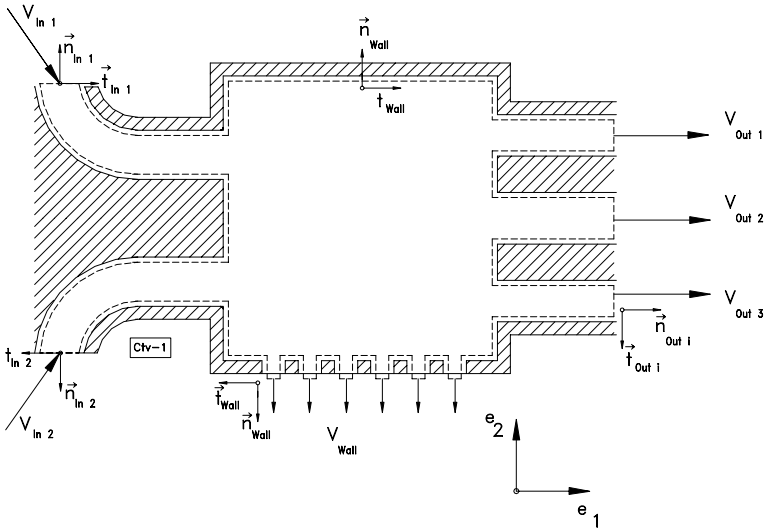

Fig. 4.1: Control volume, unit normal and tangential vectors

$$\int_{S_{in_1}} \rho V \cdot \boldsymbol{n}\, dS + \int_{S_{in_2}} \rho V \cdot \boldsymbol{n}\, dS + \int_{S_{out_1}} \rho \boldsymbol{V} \cdot \boldsymbol{n} dS + \int_{S_{out_2}} \rho \boldsymbol{V} \cdot \boldsymbol{n}\, dS + \int_{S_{out_3}} \rho \boldsymbol{V} \cdot n\, dS + \int_{S_{Wall}} \rho \boldsymbol{V} \cdot \boldsymbol{n}\, dS = 0 \tag{4.5}$$

As shown in Fig. 4.1 and by convention, the normal unit vectors, n_{in}, n_{out}, n_{Wall}, point away from the region bounded by the control surface. Similarly, the tangential unit vectors, t_{in}, t_{out}, t_{Wall}, point in the direction of shear stresses. A representative example where the integral over the wall surface does not vanish, is a film cooled turbine blade with discrete film cooling hole distribution along the blade suction and pressure surfaces as shown in Fig. 4.2. To establish the mass flow balance through a turbine or cascade blade channel, the control volume should be placed in such a way that it includes quantities that we consider as known, as well as those we seek to find. For the turbine cascade in Fig. 4.2, the appropriate control surface consists of the surfaces AB, BC, CD, and DA. The two surfaces, BC and DA, are portions of two neighboring streamlines. Because of the periodicity of the flow through the cascade, the surface integrals along these streamlines will cancel each other. As a result, the mass flow balance reads:

$$\int_{S_{in}} \rho \boldsymbol{V} \cdot \boldsymbol{n}\, dS + \int_{S_{out}} \rho \boldsymbol{V} \cdot \boldsymbol{n}\, dS + \int_{S_{Wall}} \rho \boldsymbol{V} \cdot \boldsymbol{n}\, dS = 0 \tag{4.6}$$

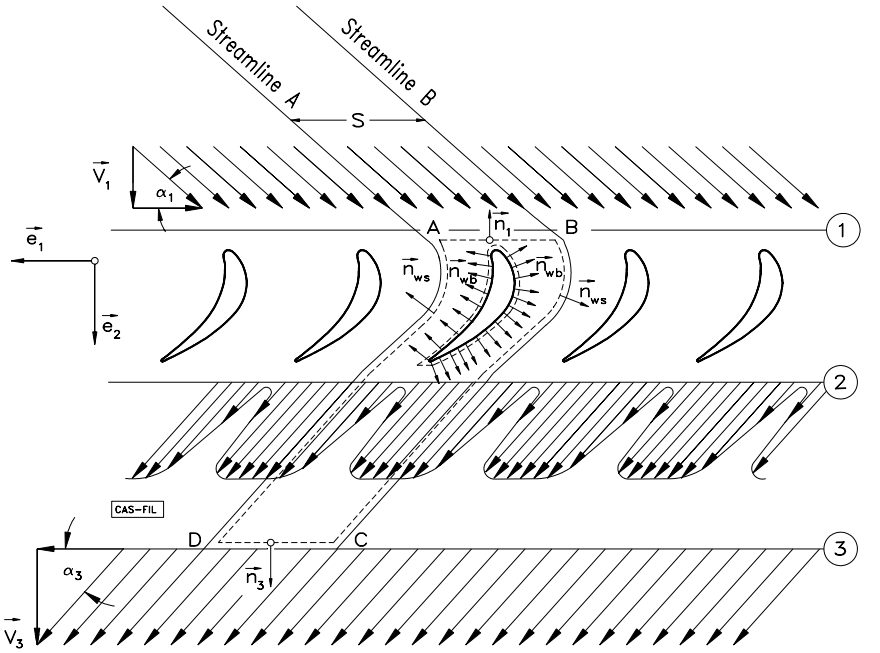

Fig. 4.2: Flow through a rectilinear turbine cascade with discrete film cooling holes.

The last surface integral accounts for the mass flow injection through the film cooling holes. If there is no mass diffusion through the wall surfaces, the last integral in Eq. (4.6) will vanish leading to:

$$\int_S \rho \boldsymbol{V}\cdot\boldsymbol{n}\,dS = \int_{S_{in}} \rho \boldsymbol{V}\cdot\boldsymbol{n}\,dS + \int_{S_{out}} \rho \boldsymbol{V}\cdot\boldsymbol{n}\,dS = 0 \tag{4.7}$$

4.2 Balance of Linear Momentum

The momentum equation in integral form applied to a control volume determines the integral flow quantities such as blade lift and drag forces, average pressure, temperature, and entropy. The motion of a material volume is described by the Newton's second law of motion, which states that mass times acceleration is the sum of all external forces acting on the system. In the absence of electrodynamic, electrostatic, and magnetic forces, the external forces can be summarized as the surface forces and the gravitational forces.

$$m\frac{D\boldsymbol{V}}{Dt} = \boldsymbol{F}_S + \boldsymbol{F}_G \tag{4.8}$$

Equation (4.8) is valid for a closed system with a system boundary that may undergo deformation, rotation, expansion or compression. In a turbomachinery component, however, there is no closed system with a defined system boundary. The mass is continuously flowing from one point within a turbomachinery component to another point. Thus, in general, we deal with *mass flow* rather than mass. Consequently, Eq. (4.8) must be modified in such a way that it is applicable to a *predefined control volume*, with mass flow passing through it. This requires applying the Reynolds transport theorem to a control volume, as we already discussed in the previous section. For this purpose, we prepare Eq. (4.8) before proceeding with the Reynolds transport theorem. In the following steps, we add a zero-term to Eq. (4.8):

$$\frac{Dm}{Dt} = 0, \quad \boldsymbol{V}\frac{Dm}{Dt} = 0 \tag{4.9}$$

Adding this term to Eq. (4.8) leads to:

$$m\frac{D\boldsymbol{V}}{Dt} + \boldsymbol{V}\frac{Dm}{Dt} = \boldsymbol{F}_S + \boldsymbol{F}_G \tag{4.10}$$

Using the Leibnitz's chain rule of differentiation, Eq. (4.10) can be rearranged:

$$\frac{D}{Dt}(m\boldsymbol{V}) = \boldsymbol{F}_S + \boldsymbol{F}_G \tag{4.11}$$

Applying the Reynolds transport theorem to the left hand side of Eq. (4.11), we arrive at:

$$\frac{D}{Dt}(m\boldsymbol{V}) = \int_{v(t)}\left(\frac{\partial(\rho\boldsymbol{V})}{\partial t} + \nabla\cdot(\rho\boldsymbol{V}\boldsymbol{V})\right)dv = \int_{v(t)}\left(\frac{\partial(\rho\boldsymbol{V})}{\partial t}\right)dv + \int_{v(t)}\nabla\cdot(\rho\boldsymbol{V}\boldsymbol{V})\,dv \tag{4.12}$$

and replace the second volume integral by a surface integral using the Gauss conversion theorem (see Chapter 2):

$$\frac{D}{Dt}(m\boldsymbol{V}) = \int_{v(t)}\left(\frac{\partial(\rho\boldsymbol{V})}{\partial t}\right)dv + \int_{S(t)}\boldsymbol{n}\cdot(\rho\boldsymbol{V}\boldsymbol{V})dS \tag{4.13}$$

We consider now the surface and gravitational forces acting on the moving material volume under investigation. The first term on right-hand side of Eq. (4.10), represents the resultant surface force acting on the entire control surface. It can be written as the integral of a scalar product of the normal unit vector with the total stress tensor acting on the surface element ds:

$$\boldsymbol{F}_S = \int_{S_C} d\boldsymbol{F}_S = \int_{S_C} \boldsymbol{n}\cdot\boldsymbol{\Pi}\, dS \tag{4.14}$$

The product of the normal vector and the stress tensor gives a stress vector, which can be decomposed into a normal and a shear stress force

$$\boldsymbol{n}\cdot\boldsymbol{\Pi} = -\boldsymbol{n}p \; -\boldsymbol{t}\tau \tag{4.15}$$

with $\boldsymbol{n}$ as the normal unit vector that points away from the surface and $\boldsymbol{t}$ as the tangential unit vector. The negative sign of $\boldsymbol{n}$ and $\boldsymbol{t}$ have been chosen to indicate that the pressure p and the shear stress τ are exerted by the surroundings *on the surface S*. Thus, the surface force acting on a differential surface is:

$$d\boldsymbol{F}_s = -\boldsymbol{n}p\, dS \; - \boldsymbol{t}\tau\, dS \tag{4.16}$$

Inserting Eq. (4.16) into Eq. (4.11) and considering Eq. (4.12), we arrive at:

$$\int_{v_C}\left(\frac{\partial(\rho\boldsymbol{V})}{\partial t}\right) dv + \int_{S_C} \boldsymbol{n}\cdot(\rho\boldsymbol{V}\boldsymbol{V})dS = \int_{S_C}(-\boldsymbol{n}p \; - \boldsymbol{t}\tau)dS + \boldsymbol{G} \tag{4.17}$$

Since the control volume does not change with time (fixed), Eq. (4.17) becomes with $\rho dv = dm$:

$$\frac{\partial}{\partial t}\int_{V_C} \boldsymbol{V} dm + \int_{S_C} \boldsymbol{n}\cdot(\rho\boldsymbol{V}\boldsymbol{V})dS = \int_{S_C}(-\boldsymbol{n}p \; - \boldsymbol{t}\tau)dS + \boldsymbol{G} \tag{4.18}$$

In Eq. (4.18) the integration must be carried out over the entire control surface. For a control surface consisting of inlet, exit, and wall surfaces, the second integral on the left-hand side gives:

$$\int_{S_C} \boldsymbol{n}\cdot(\rho\boldsymbol{V}\boldsymbol{V})dS = \int_{S_{Cin}} \boldsymbol{n}\cdot(\rho\boldsymbol{V}\boldsymbol{V})dS + \int_{S_{Cout}} \boldsymbol{n}\cdot(\rho\boldsymbol{V}\boldsymbol{V})dS + \int_{S_{CW}} \boldsymbol{n}\cdot(\rho\boldsymbol{V}\boldsymbol{V})dS \tag{4.19}$$

Evaluating the integrands on the right-hand side of Eq. (4.19) by considering the directions of the unit vectors shown in Fig. 4.3, we find for the single inlet cross section:

$$\int_{S_{Cin}} \boldsymbol{n}\cdot(\rho\boldsymbol{V}\boldsymbol{V})dS = \int_{S_{Cin}} \boldsymbol{V}(\rho\,\boldsymbol{n}\cdot\boldsymbol{V}dS) = \int_{S_{Cin}} \boldsymbol{V}(-\rho\boldsymbol{e}_1\cdot\boldsymbol{e}_1 V_{in}\, dS) = -\int_{S_{Cin}} \boldsymbol{V}\, \dot{dm} \tag{4.20}$$

In the case of a control volume with multiple inlets, as Fig. 4.1 shows, we need to integrate over the entire inlet cross sections. For the exit cross section we obtain:

$$\int_{S_{Cout}} \boldsymbol{n}\cdot(\rho \boldsymbol{V}\boldsymbol{V})dS = \int_{S_{Cout}} \boldsymbol{V}(\rho \boldsymbol{n}\cdot\boldsymbol{V}dS) = \int_{S_{Cout}} \boldsymbol{V}(\rho\, \boldsymbol{e}_1\cdot\boldsymbol{e}_1 V_{out}\, dS) = \int_{S_{Cout}} \boldsymbol{V}\, \dot{dm} \tag{4.21}$$

And finally for the wall:

$$\int_{S_{Cwall}} \boldsymbol{n}\cdot(\rho \boldsymbol{V}\boldsymbol{V})dS = \int_{S_{Cwall}} \rho\,(\boldsymbol{n}\cdot\boldsymbol{V})\,\boldsymbol{V}dS = \int_{S_{Cwall}} \rho\,(-\boldsymbol{e}_2)\cdot(-\boldsymbol{e}_2 V_{wall})\boldsymbol{V}\, dS = \int_{S_{Cwall}} \boldsymbol{V}\, \dot{dm} \tag{4.22}$$

Inserting the Eqs. (4.20) through (4.22) into Eq. (4.19) and the results into Eq. (4.18), we obtain a relation that includes the mass flow through the control volume:

$$\frac{\partial}{\partial t}\int_{V_C} \boldsymbol{V}dm + \int_{S_{Cout}} \boldsymbol{V}\dot{dm} - \int_{S_{Cin}} \boldsymbol{V}\dot{dm} + \int_{S_{Cwall}} \boldsymbol{V}\dot{dm} = \int_{S_C}(-\boldsymbol{n}p - \boldsymbol{t}\tau)dS + \boldsymbol{G} \tag{4.23}$$

The first term expresses the total momentum exchange of all particles contained in the region (control volume) under consideration, at the time *t*, because of velocity changes produced by a non-steady flow. For a steady flow, it vanishes. The second and third integral are *leaving* and *entering velocity momenta*. The fourth term exhibits the velocity momentum through the wall. This term is different from zero if the wall is porous (permeable) or has perforations or slots that may be used for different purposes such as cooled turbine blades, Fig. 4.2, boundary layer suction, etc. For a solid wall, this term of course vanishes identically. The first and the second integral on the right-hand side of Eq. (4.23) are momentum contributions due to the action of static pressure and the shear stresses. These integrals must be taken over the entire bounding surface that includes inlet, exit and wall surfaces, Fig. 4.3:

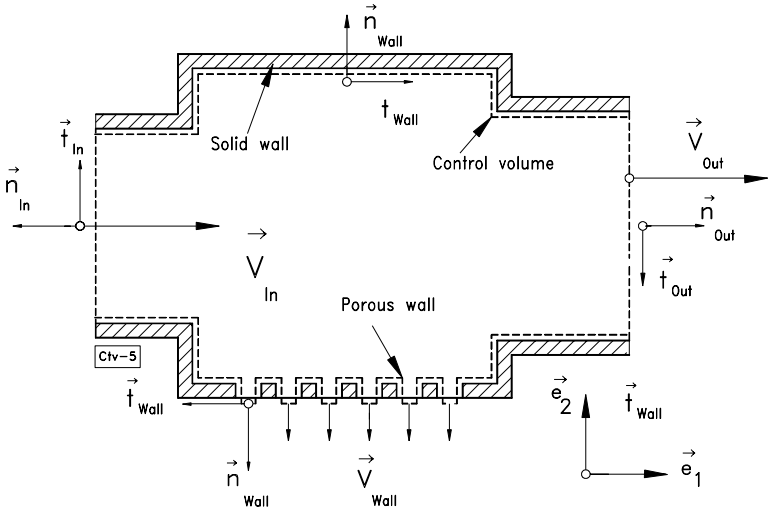

Fig. 4.3: Control volume, single inlet, single and outlet and porous wall.

$$\int_{S_C}(-\boldsymbol{n}p)dS + \int_{S_C}(-\boldsymbol{t}\tau)dS = \int_{S_{Cout}}(-\boldsymbol{n}p)dS + \int_{S_{Cout}}(-\boldsymbol{t}\tau)dS + \int_{S_{Cin}}(-\boldsymbol{n}p)dS + \int_{S_{Cin}}(-\boldsymbol{t}\tau)dS + \int_{S_{Cw}}(-\boldsymbol{n}p)dS + \int_{S_{Cw}}(-\boldsymbol{t}\tau)dS \tag{4.24}$$

According to the convention in ?, the direction of unit normal vectors $\boldsymbol{n}_{\text{in}}$, $\boldsymbol{n}_{\text{out}}$, and $\boldsymbol{n}_{\text{wall}}$ point away from the region bounded by the control surface S_C. The last two

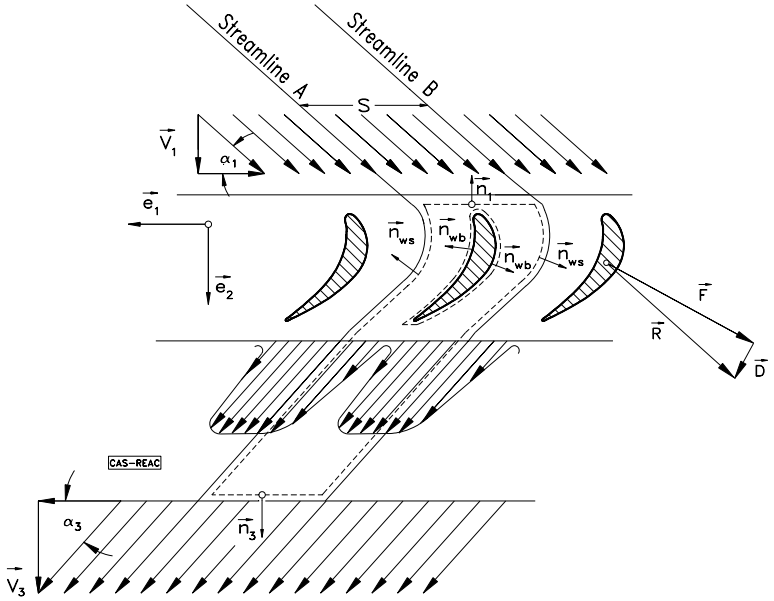

Fig. 4.4: Reaction force on a turbine blade with ***F*** and ***D*** as the lift, drag forces, and ***R*** the resultant force.

integrals in Eq. (4.24) determine the reaction forces. To demonstrate the physical significance of the reaction force, we consider a rectilinear turbine cascade, Fig. 4.4. The reaction force ***R*** which is exerted by the flow on the surface S_{Cw}, that is, on the turbine blade wall between the stations (1) and (2) and the body, is therefore:

$$\boldsymbol{F}_R = -\boldsymbol{F}_{Flow} = -\int_{S_{Cw}}(-\boldsymbol{n}p)dS - \int_{S_{Cw}}(-\boldsymbol{t}\tau)dS = \int_{S_{Cw}}(\boldsymbol{n}p)dS + \int_{S_{Cw}}(\boldsymbol{t}\tau)dS \tag{4.25}$$

As Eq. (4.25)indicates, the flow force equals the negative value of the two last integrals. Considering an steady flow and implementing Eq. (4.25) into (4.23), the reaction forces can be determined using the relationship:

$$\boldsymbol{F}_R = \int_{S_{Cin}} \boldsymbol{V} d\dot{m} - \int_{S_{Cout}} \boldsymbol{V} d\dot{m} - \int_{S_{Cwall}} \boldsymbol{V} d\dot{m} + \int_{S_{Cin}} (-\boldsymbol{n}p) dS + \int_{S_{Cin}} (-\boldsymbol{t}\tau) dS + \int_{S_{Cout}} (-\boldsymbol{n}p) dS + \int_{S_{Cout}} (-\boldsymbol{t}\tau) dS + \boldsymbol{G} \tag{4.26}$$

The vector equation (4.26) can be decomposed into three components. An order of magnitude estimation suggests that the shear stress terms at the inlet and outlet are, in general, very small compared to the other terms. It should be pointed out that the wall shear stress is already included in the resultant force $\boldsymbol{F}_R$.

4.3 Balance of Moment of Momentum

To establish the conservation law of moment of momentum for a time dependent material volume, we start from the second law of Newton, Eq. (4.18):

$$m\frac{D\boldsymbol{V}}{Dt} = \sum \boldsymbol{F} = \boldsymbol{F}_S + \boldsymbol{G} = = \int_{V(t)} \nabla \cdot \boldsymbol{\Pi} dv + \boldsymbol{G} \tag{4.27}$$

The moment of the force given by Eq. (4.27) is then

$$m\boldsymbol{X} \times \frac{D\boldsymbol{V}}{Dt} = \sum \boldsymbol{X} \times F \tag{4.28}$$

with $\boldsymbol{X}$ as the position vector originating from a fixed point. To rearrange Eq. (4.28) for further analysis, its left-hand side is extended by adding the following zero-term identities:

$$\boldsymbol{V} \times V = \frac{D\boldsymbol{X}}{Dt} \times \boldsymbol{V} = m\frac{D\boldsymbol{X}}{Dt} \times \boldsymbol{V} = 0 \tag{4.29}$$

and:

$$\frac{Dm}{Dt} = 0 = \boldsymbol{X} \times \boldsymbol{V} \frac{Dm}{Dt} = 0 \tag{4.30}$$

Introducing the identities (4.29) and (4.30) into Eq. (4.28), we arrive at:

$$m\boldsymbol{X} \times \frac{D\boldsymbol{V}}{Dt} + m\frac{D\boldsymbol{X}}{Dt} \times \boldsymbol{V} + \boldsymbol{X} \times \boldsymbol{V} \frac{Dm}{Dt} = \sum \boldsymbol{X} \times \boldsymbol{F} \tag{4.31}$$

Using the Leibnitz's chain differential rule, a simple rearrangement of Eq. (4.31) allows the application of the Reynolds transport theorem as follows:

$$\frac{D(m\,\boldsymbol{X}\times\boldsymbol{V})}{D\,t} = \sum \boldsymbol{X}\times\boldsymbol{F} \tag{4.32}$$

Since: $m = \int_{v(t)} \rho\, d\,v$, Eq. (4.32) can be written as:

$$\frac{D}{D\,t}\int_{v_C} (\rho\,\boldsymbol{X}\times\boldsymbol{V})\; d\,v = \sum \boldsymbol{X}\times\boldsymbol{F} \tag{4.33}$$

We apply the Reynolds transport theorem and the Gauss conversion theorem (Chapter 2) to the left-hand side of Eq. (4.33) and arrive at:

$$\frac{D}{D\,t}\int_{v_C} (\rho\,\boldsymbol{X}\times\boldsymbol{V})\; d\,v = \int_{V_C}\left(\frac{\partial\,(\rho\,\boldsymbol{X}\times\boldsymbol{V})}{\partial\,t}\; dv\right) - \int_{S_C} \boldsymbol{n}\cdot(\rho\,\boldsymbol{V}\,\boldsymbol{V}\times\boldsymbol{X})\; dS \tag{4.34}$$

We now interchange the sequence of multiplication for the vector product inside the parenthesis of the second integral in Eq. (4.34), $\rho\;\boldsymbol{V}\boldsymbol{V}\times\boldsymbol{X} = -\rho\,\boldsymbol{V}\times\boldsymbol{X}\,\boldsymbol{V}$ and obtain:

$$\frac{D}{D\,t}\int_{v_C} (\rho\,\boldsymbol{X}\times\boldsymbol{V})\; d\,v = \int_{V_C}\left(\frac{\partial\,(\rho\,\boldsymbol{X}\times\boldsymbol{V})}{\partial\,t}\; dv\right) + \int_{S_C} \boldsymbol{n}\cdot(\rho\,\boldsymbol{V}\,\boldsymbol{X}\times\boldsymbol{V})\, dS \tag{4.35}$$

Introducing the mass flow $\boldsymbol{n}\cdot\boldsymbol{V}ds = d\dot{m}$, Eq. (4.35) results in:

$$\frac{D}{D\,t}\int_{v_C} (\rho\,\boldsymbol{X}\times\boldsymbol{V})\; d\,v = \int_{V_C}\left(\frac{\partial\,(\rho\,\boldsymbol{X}\times\boldsymbol{V})}{\partial\,t}\; dv\right) + \int_{S_C} (\boldsymbol{X}\times\boldsymbol{V})\; d\dot{m} \tag{4.36}$$

The surface integral has to be carried out over the entire control surface S_C.

$$\frac{D}{D\,t}\int_{v_C}(\rho\,\boldsymbol{X}\times\boldsymbol{V})\,d\,v = \int_{V_C}\left(\frac{\partial\,(\rho\,\boldsymbol{X}\times\boldsymbol{V})}{\partial\,t}\,dv\right) + \int_{S_{C2}} (\boldsymbol{X}\times\boldsymbol{V})d\dot{m} - \int_{S_{C1}} (\boldsymbol{X}\times\boldsymbol{V})d\dot{m} \tag{4.37}$$

Now we consider the moment of momentum of all other forces on the right-hand side of Eq. (4.33):

$$\sum \boldsymbol{X}\times\boldsymbol{F} = \int_{S_c} \boldsymbol{X}\times(-\boldsymbol{n}\,p)\,d\,S + \int_{S_C} \boldsymbol{X}\times(-\boldsymbol{t}\tau)\,d\,S_C + \int_{V_C} \boldsymbol{X}\times\boldsymbol{g}\,d\,m \tag{4.38}$$

Since the right side of Eq. (4.33) is equal to the right side of Eq. (4.38), the equation of moment of momentum can be presented in a more compact form that contains the

contributions of velocity, pressure and shear stress momenta:

$$\int_{V_{(t)}} \left(\frac{\partial (\rho \boldsymbol{X} \times \boldsymbol{V})}{\partial t} \, dv \right) + \int_{S_{Cout}} (\boldsymbol{X} \times \boldsymbol{V}) \, \dot{dm} - \int_{S_{Cin}} (\boldsymbol{X} \times \boldsymbol{V}) \, \dot{dm} = \int_{S_c} \boldsymbol{X} \times (-\boldsymbol{n}\, p) \, dS + \int_{S_C} \boldsymbol{X} \times (-\boldsymbol{t}\tau) \, dS_C + \int_{V_C} \boldsymbol{X} \times \boldsymbol{g} \, dm \tag{4.39}$$

The integration of the first two integrals on the right hand side have to be performed over S_{Cin}, S_{Cout} and S_{CW}.

$$\int_{S_C} \boldsymbol{X} \times (-\boldsymbol{n}p) dS + \int_{S_C} \boldsymbol{X} \times (-\boldsymbol{t}\tau) dS = \int_{S_{Cout}} \boldsymbol{X}_{S_{Cout}} \times (-\boldsymbol{n}p) dS + \int_{S_{Cout}} \boldsymbol{X}_{S_{Cout}} \times (-\boldsymbol{t}\tau) dS + \int_{S_{Cin}} \boldsymbol{X}_{S_{Cin}} \times (-\boldsymbol{n}p) dS + \int_{S_{Cin}} S_{Cin} \boldsymbol{X}_{S_{Cin}} \times (-\boldsymbol{t}\tau) dS + \int_{S_{Cw}} \boldsymbol{X}_{S_{Cw}} \times (-\boldsymbol{n}p) dS + \int_{S_{Cw}} \boldsymbol{X}_{S_{Cw}} \times (-\boldsymbol{t}\tau) dS \tag{4.40}$$

Similar to the expression for the reaction force, the last two integrals on the right-hand side of Eq. (4.40) determine the reaction moment, $\boldsymbol{M}_R$.

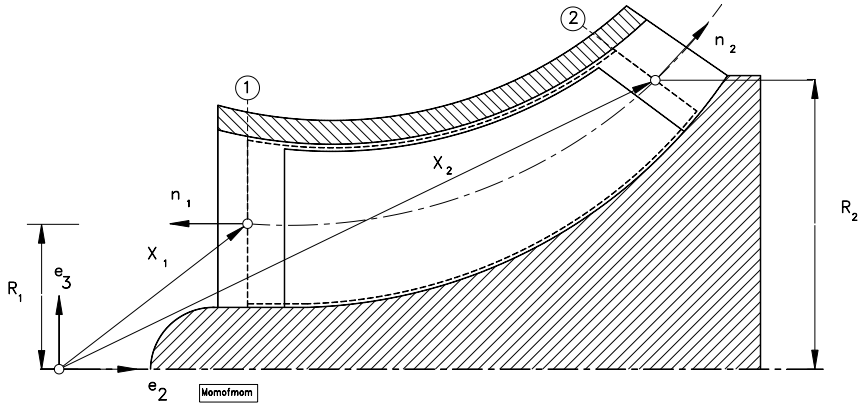

Fig. 4.5: A mixed flow compressor with control surfaces.

This reaction moment is exerted by the flow on the solid boundary S_W of the system with respect to a fixed point such as coordinate origin shown in Fig. 4.5. This figure exhibits the flow through a mixed axial-radial compressor stage, where the flow undergoes a change in radial direction associated with certain deflection from inlet at station 1 to the exit at station 2. A fixed control volume is placed on the rotor that includes a compressor blade. The normal unit vectors at the inlet and exit are used to establish the mass flow balances at station 1 and 2. The *wall surface* S_W represents one blade surface (pressure or suction surface) that is projected on the drawing plane.

The reaction moment consists of the moment by the surface shear and pressure forces:

$$\boldsymbol{M}_0 = \int_{S_W} \boldsymbol{X}_{S_W} \times (\boldsymbol{t}\tau)_W \, dS_W + \int_{S_w} \boldsymbol{X}_{S_W} \times (\boldsymbol{n}p)_W \, dS_W \tag{4.41}$$

From Eq. (4.41) it is seen that the last two integrals of Eq. (4.40) are equal to - $\boldsymbol{M}_0$. Therefore, from Eqs. (4.40) and (4.41), the moment $\boldsymbol{M}_0$ exerted by the flow on the solid boundary S_W with respect to a fixed point using the station numbers in Fig. 4.5 is:

$$\begin{aligned} \boldsymbol{M}_0 = & -\frac{\partial}{\partial t}\left(\int_{V_C} \boldsymbol{X} \times \boldsymbol{V} \, dm \right) + \int_{S_1} (\boldsymbol{X} \times \boldsymbol{V}) \, \dot{dm} - \int_{S_2} (\boldsymbol{X} \times \boldsymbol{V}) \, \dot{dm} \\ & \int_{S_1} (\boldsymbol{X} \times (-\boldsymbol{n}p) dS)_1 + \int_{S_1} (\boldsymbol{X} \times (-\boldsymbol{t}\tau) dS)_1 + \\ & \int_{S_2} (\boldsymbol{X} \times (-\boldsymbol{n}p) dS)_2 + \int_{S_2} (\boldsymbol{X} \times (-\boldsymbol{t}\tau) dS)_2 + \\ & \int_{V_C} \boldsymbol{X} \times \boldsymbol{g} \, d\, m \end{aligned} \tag{4.42}$$

Equation (4.42) describes the moment of momentum in general form. The first integral on the right-hand side expresses the angular momentum contribution due to the unsteadiness. The second and third term represents the contribution due to the velocity momenta at the inlet and exit. The forth and sixth term are formally the contributions of pressure momenta at the inlet and exit. The shear stress integrals, the fifth and seventh terms, representing the moment due to shear stresses at the inlet and exit, are usually ignored in practical cases. For applications to turbomachines, Eq. (4.42) can be used to determine the moment that the flow exerts on a turbine or compressor cascade. Of practical interest is the *axial moment* $M = M_a$ which acts on the cascade with respect to the axis of rotation. The moment $M = M_a$ is equal to the component of the moment vector parallel with the axis of surfaces of revolution. As shown in Fig. 4.6, the axial moment is :

$$\boldsymbol{M} = \boldsymbol{M}_a = e_2 \left(e_2 \cdot \boldsymbol{M}_0 \right) \tag{4.43}$$

Neglecting the contribution of the shear stress terms at the inlet and exit but not along the wall surfaces, S_W, and performing the above scalar multiplication, the pressure contributions vanish identically. Furthermore, the moment contribution of gravitational force will vanish. With this premise, Eq. (4.43) reduces to:

$$\boldsymbol{M}_a = -\frac{\partial}{\partial t}\left(\int_{V_{(t)}} \boldsymbol{X} \times \boldsymbol{V} \, dm \right) + \int_{S_1} \left(R_1 \, V_{u1} \right) \dot{dm} - \int_{S_2} \left(R_2 \, V_{u2} \right) \dot{dm} \tag{4.44}$$

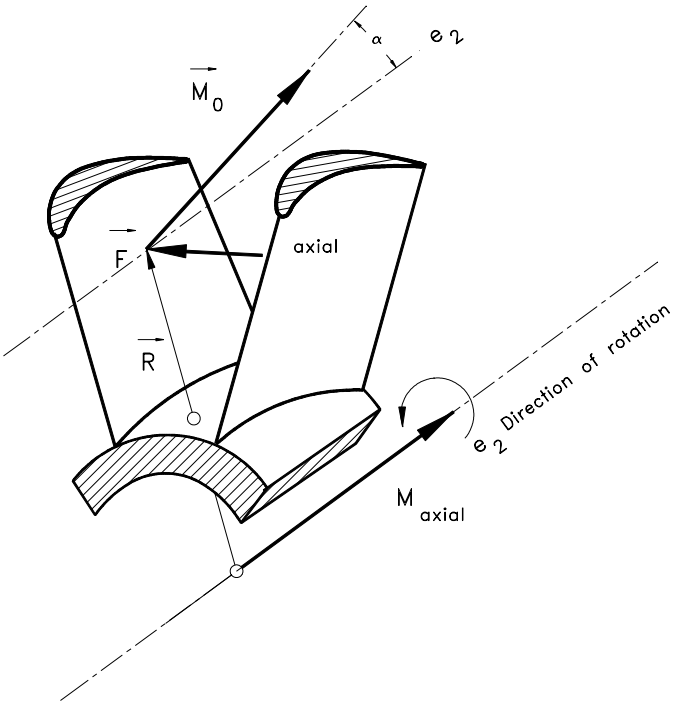

Fig. 4.6: Illustration of the axial moment by projecting the reaction moment $\vec{M}_0$ on the axial direction e_2 .

with V_u as the absolute velocity component in circumferential direction. For steady flow, Eq. (4.44) reduces to:

$$\boldsymbol{M}_a = \int_{S_1} \left(R_1 V_{u1}\right) d\dot{m} - \int_{S_2} \left(R_2 V_{u2}\right) d\dot{m} \tag{4.45}$$

For the case where the velocity distributions at the inlet and exit of the channel are fully uniform and the turbomachine is rotating with the angular velocity $\boldsymbol{\omega}$, the power consumed (or produced) by a compressor (or by a turbine) stage is calculated by:

$$P = \omega \cdot \boldsymbol{M}_a = \omega \cdot e_2 \dot{m} \left(R_1 V_{u1} - R_2 V_{u2}\right) = \dot{m}\left(U_1 V_{u1} - U_2 V_{u2}\right) \tag{4.46}$$

Although the application of conservation laws are extensively discussed in the following chapters, it is found necessary to present a simple example of how the moment of momentum is obtained by utilizing the *velocity diagram* of a single-stage axial compressor. Figure 4.7a represents a single stage axial compressor with the constant hub and tip diameters. We consider the flow situation at the mid- section. The flow is first deflected by the *stator row*. Entering the rotor row, the fluid particle

moves through a rotating frame, where the rotational velocity ***U*** is superimposed on the relative velocity ***W*** (for details see Chapters 5). The constant radii at the inlet and exit of the mid-section results in $\omega R_1 = \omega R_2 = U_1 = U_2 = U$ simplifying Eq. (4.46) to $P = \dot{m} U \left(V_{u1} - V_{u2} \right)$. The expression in the parenthesis, $(V_{u1} - V_{u2})$, is shown in the velocity diagram, Figure 4.7b. It states that the compressor power consumption is related to the flow deflection expressed in terms of the circumferential velocity difference. The larger the difference $(V_{u1} - V_{u2})$ is, the higher the pressure ratio that the compressor produces. However, for each type of compressor design (axial, radial, subsonic, super sonic) there is always a limit to this difference, which is dictated by the flow separation, as we will see later.

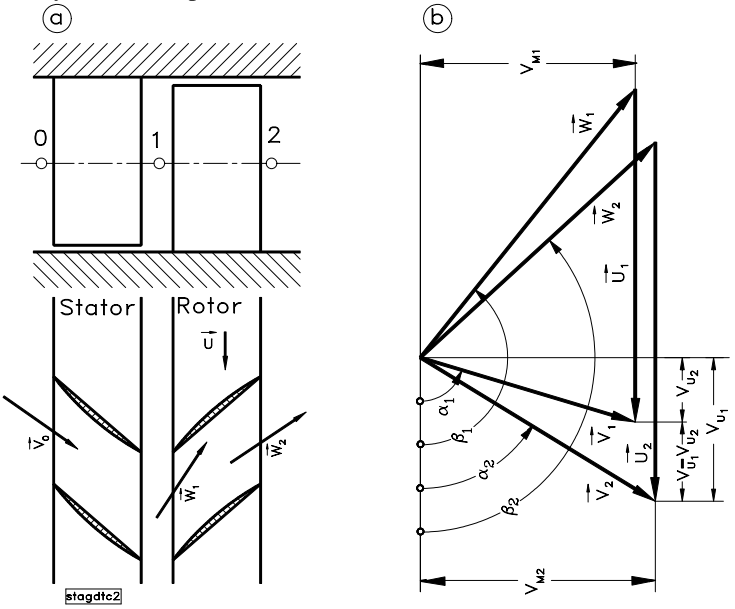

Fig. 4.7 A single-stage axial compressor (a), velocity diagram (b). The circumferential velocity difference $(V_{u1} - V_{u2})$ is responsible for the power consumption.

For the case where no blades are installed inside the channel and the axial velocity distributions at the inlet and exit of the channel are fully uniform, Eq. (4.45) is reduced to:

$$R_1 V_{u1} = R_2 V_{u2} = const. \tag{4.47}$$

This is the so called free vortex flow.

4.4 Balance of Energy

The conservation law of energy in integral form, that we discuss in the following sections, is based on the thermodynamic principals, primarily first law of

thermodynamics for open systems and time dependent control volume. It is fully independent from conservation laws of fluid mechanics. However, it *implicitly* contains the irreversibility aspects described by the dissipation process in the previous chapter. The contribution of the irreversibility is *explicitly* expressed by using the *Clausius-Gibbs* entropy equation, known as the second law of thermodynamics. The energy equation is applied to a variety of turbomachine components and describes a *chain of energy conversion process* that usually takes place in a thermo-fluid dynamics system. As an example, Fig. 4.8 shows a high performance gas turbine engine with several components to which we apply the results of our derivations.

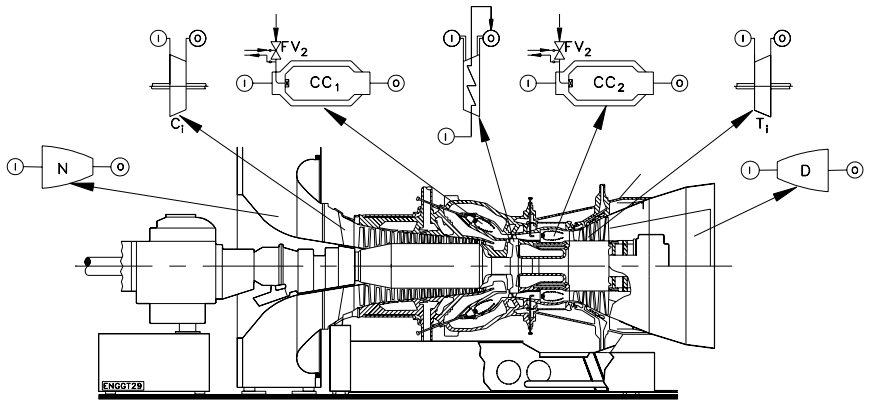

Fig. 4.8: A modern power generation gas turbine engine with a single shaft, two combustion chambers, a multi-stage compressor, a single-stage reheat turbine and a multi-stage turbine.

In this chapter, we apply the conservation law of energy to a material volume with a system boundary that moves through the space where it may undergo deformation, rotation and translation. The first law of thermodynamics in integral form states that if we add thermal energy (heat) Q and mechanical energy (work) W to a closed system, the total energy of the system E experiences a change from initial state E_1 to the final state E_2. Expressing in terms of energy balance, we have:

$$Q + W = E_2 - E_1 \tag{4.48}$$

The total energy E is the sum of internal, kinetic and potential energies,

$$E = U + \frac{1}{2}mV^2 + mgz \tag{4.49}$$

In order to apply the conservation law of energy to a control volume, we divide Eq. (4.49) by the mass m to arrive at the *specific total energy*,

$$E = me = m\left(u + \frac{1}{2}V^2 + gz \right) \tag{4.50}$$

with e as the specific total energy. Similar to the conservation laws of mass, momentum, and moment of momentum, we ask for substantial change of the total energy, i.e.:

$$\frac{D(Q + W)}{Dt} = \dot{Q} + \dot{W} = \frac{D\,E}{D\,t} = \frac{D(me)}{Dt} \tag{4.51}$$

with $\dot{Q}$ and $\dot{W}$as the thermal and mechanical energy flow, respectively. Since $m = \int_{v(t)} \rho\, dv$, Eq. (4.51) yields:

$$\dot{Q} + \dot{W} = \frac{D}{D\,t} \int_{v(t)} \rho\, e\, dv \tag{4.52}$$

To apply the the conservation of energy to a control volume, we use the Reynolds transport theorem. Using the Jacobi-transformation function $dv = J\, dv_0$, and introducing the time fixed volume v_0, we arrive at:

$$\dot{Q} + \dot{W} = \int_{v_0} \left(J\, \frac{D(\rho e)}{Dt} + \frac{DJ}{Dt} \rho e \right) dv_0 \tag{4.53}$$

We now introduce $DJ/Dt = J\,\nabla\cdot\boldsymbol{V}$ for the substantial derivative of the Jacobian

$$\dot{Q} + \dot{W} = \int_{v(t)} \left(\frac{D(\rho e)}{Dt} + \rho e\, \nabla\cdot\boldsymbol{V} \right) dv \tag{4.54}$$

Developing the first integral term:

$$\dot{Q} + \dot{W} = \int_{v(t)} \left(\frac{\partial(\rho e)}{\partial t} + \boldsymbol{V}\cdot\nabla(\rho e) + \rho e \nabla\cdot\boldsymbol{V} \right) dv \tag{4.55}$$

Application of the chain rule to the second and third term yields:

$$\dot{Q} + \dot{W} = \int_{v(t)} \frac{\partial(\rho e)}{\partial t}\, dv + \int_{v(t)} \nabla\cdot(\rho e \boldsymbol{V})\, dv \tag{4.56}$$

With Gauss-Divergence Theorem:

$$\dot{Q} + \dot{W} = \int_{v(t)} \frac{\partial(\rho e)}{\partial t} dv + \int_{S(t)} (\rho e \boldsymbol{n}\cdot\boldsymbol{V})\, dS \tag{4.57}$$

The above equation is valid for any volume $v(t)$ including $v(t=0)$, which might be a fixed control volume. In Eq. (4.57), the integration must be carried out over the entire control surface. For a control surface consisting of inlet, exit, and wall surfaces, (Fig. 4.4) the second integral on the left-hand side gives:

$$\int_{S_C} (\rho e \boldsymbol{n}\cdot\boldsymbol{V})\, dS = \int_{S_{Cin}} e(\rho \boldsymbol{n}\cdot\boldsymbol{V}) dS + \int_{S_{Cout}} e(\rho \boldsymbol{n}\cdot\boldsymbol{V}) dS \tag{4.58}$$

Evaluating the integrands on the right-hand side of Eq. (4.58) by considering the directions of the unit vectors shown in Fig. 4.4, $\boldsymbol{n}_{in} = -\boldsymbol{e}_1$, $\boldsymbol{n}_{out} = +\boldsymbol{e}_1$, we find for the inlet cross section:

$$\int_{S_{Cin}} e(\rho \boldsymbol{n}\cdot\boldsymbol{V}) dS = \int_{S_{Cin}} e(-\rho \boldsymbol{e}_1\cdot\boldsymbol{e}_1 V_{in}\, dS) = -\int_{S_{Cin}} e\, d\dot{m} \tag{4.59}$$

For the exit cross section we obtain:

$$\int_{S_{Cout}} e(\rho \boldsymbol{n}\cdot\boldsymbol{V}) dS = \int_{S_{Cout}} e(\rho \boldsymbol{e}_1\cdot\boldsymbol{e}_1 V_{in}\, dS) = \int_{S_{Cout}} e\, d\dot{m} \tag{4.60}$$

Inserting the Eqs. (4.59) and (4.60) into Eq. (4.57), we obtain the energy equation for a control volume:

$$\dot{Q} + \dot{W} = \int_{v(t)} \frac{\partial(\rho e)}{\partial t} dv + \int_{S_{Cout}} e\, d\dot{m} - \int_{S_{Cin}} e\, d\dot{m} \tag{4.61}$$

with the specific internal energy, $e = u + \frac{1}{2} V^2 + g z$,

$$\dot{Q} + \dot{W} = \int_{v(t)} \frac{\partial\left(\rho(u + \frac{1}{2}V^2 + gz\right)}{\partial t} dv + \\ + \int_{S_{Cout}} (u + \frac{1}{2}V^2 + gz)\dot{dm} - \int_{S_{Cin}} (u + \frac{1}{2}V^2 + gz)\dot{dm} \tag{4.62}$$

For uniform velocity distribution, Eq. (4.62) is reduced to:

$$\dot{Q} + \dot{W} = \int_{v(t)} \frac{\partial\left(\rho(u + \frac{1}{2}V^2 + gz\right)}{\partial t} dv + \\ + \dot{m}_{Out}(u + \frac{1}{2}V^2 + gz) - \dot{m}_{In}(u + \frac{1}{2}V^2 + gz) \tag{4.63}$$

The mechanical energy flow $\dot{W}$ consists of the shaft power $\dot{W}_{shaft}$ and the mechanical energy flow $\dot{W}_{flow}$ which is needed to overcome the shear and normal stresses at the system or control volume boundaries:

$$\dot{W} = \dot{W}_{Shaft} + \dot{W}_{Flow} \tag{4.64}$$

The shaft power is the sum of the net shaft power and the power dissipated by the bearings $\dot{W}_{shaft} = \dot{W}_{net} + \dot{W}_{bearings}$.

The second term is the power required to overcome the normal and shear stress forces at the inlet and exit of the system. It is the product of the flow force vector $\boldsymbol{F}$ and the displacement vector d$\boldsymbol{X}$

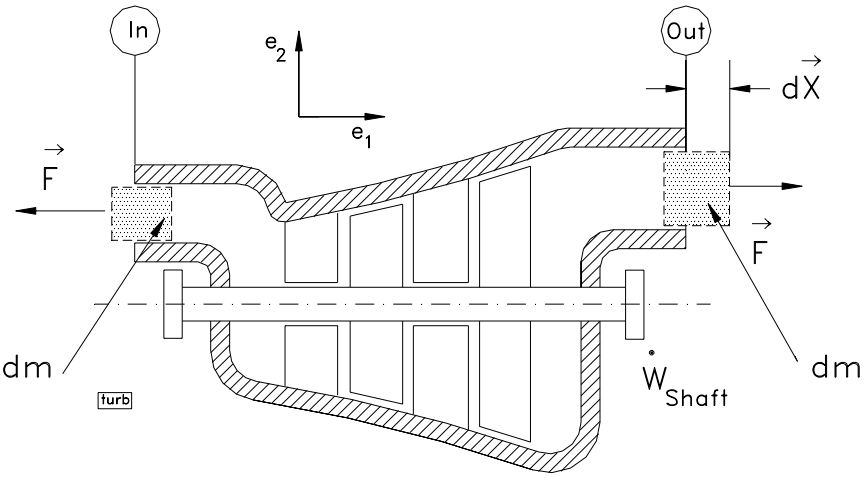

Fig. 4.9: Explanation of flow forces, sketch of a turbine component.

$$\dot{W}_{Flow} = \int_{In}^{Out} d\dot{W}_F = \int_{In}^{Out} d\left(\frac{\boldsymbol{F}\cdot d\boldsymbol{X}}{dt} \right) \tag{4.65}$$

Consider a turbine component, Fig. 4.9, where the working fluid (gas or steam) enters the inlet station. To force the differential mass *dm* into the turbine, which is under high pressure, a force is required that must compensate the pressure and the shear stress forces at the inlet. Figure. 4.9 exhibits a simplified schematic of one of the turbine components in Fig. 4.8. It shows the directions of the forces and the displacements. At the inlet, the force vector $\boldsymbol{F}$ is expressed in terms of pressure and the inlet area and is oriented toward negative $\boldsymbol{e}_1$-direction. The displacement vector d$\boldsymbol{X}$ has the positive direction. As a result, the product:

$$d(\boldsymbol{F}\cdot d\boldsymbol{X}) = d(-e_1 \cdot e_1 p\, s\, dx) = -p\, dV \tag{4.66}$$

is negative. The differential volume can be expressed as the product of the specific volume and the differential mass. Replacing, in Eq. (4.66), *dV* with *vdm* ($dV = vdm$) and dividing the result by *dt*, we arrive at:

$$\frac{\boldsymbol{F}\cdot d\boldsymbol{x}}{dt} = -p\, v \frac{dm}{dt} = -p\, v \dot{m} \tag{4.67}$$

Inserting Eq. (4.67) into (4.66), the integration from initial state to final state and assuming a constant mass flow, we find:

$$\dot{W}_{Flow} = -\int_{In}^{Out} d(\dot{m} p\, v) = -\left[\left(\dot{m}\, p\, v\right)_{Out} - \left(\dot{m}\, p\, v\right)_{In} \right] \tag{4.68}$$

To eliminate the internal energy from the equation of energy for open systems, we introduce the thermodynamic property enthalpy $h = u + p\, v$ into Eq. (4.63).

$$\begin{aligned} \dot{Q} + \dot{W}_{Shaft} = & \int_{v(t)} \frac{\partial}{\partial t}\left(\rho(u + \frac{1}{2}V^2 + gz) \right) dv + \\ & \dot{m}_{Out}(h + \frac{1}{2}V^2 + gz) - \\ & \dot{m}_{In}(h + \frac{1}{2}V^2 + gz) \end{aligned} \tag{4.69}$$

For a fixed control volume, the volume integral can be rearranged as:

$$\int_{v(t)} \frac{\partial}{\partial t}\left(\rho(u + \frac{1}{2}V^2 + gz)\right) dv = \int_{VC} \frac{\partial(\rho e)}{\partial t} dv = \frac{\partial}{\partial t}\int_{VC} (\rho e) dv \tag{4.70}$$

We set $\int_{CV} \rho e dv = E_{CV}$, and since E_{VC} can only change with time, the partial derivative is replaced by the ordinary one, $\partial/\partial t \equiv d/dt$. As a result, we obtain:

$$\dot{Q} + \dot{W}_{Shaft} = \frac{dE}{dt} + \dot{m}_{Out}(h + \frac{1}{2}V^2 + gz) - \dot{m}_{In}(h + \frac{1}{2}V^2 + gz) \tag{4.71}$$

Equation (4.71) exhibits the general form of energy equation for an open system with a fixed control volume. For technical applications, several special cases are applied which we will discuss in the following.

4.4.1 Energy Balance Special Case 1: Steady Flow

If a power generating machine such as a turbine, or a power consuming machine such as a compressor, operates in a steady design point, the first term on the right-hand side of Eq. (4.71) disappears, $dE/dt = 0$, which leads to:

$$\dot{Q} + \dot{W}_{Shaft} = \dot{m}_{Out}(h + \frac{1}{2}V^2 + gz) - \dot{m}_{In}(h + \frac{1}{2}V^2 + gz) \tag{4.72}$$

Equation (4.72) is the energy balance for a turbomachine with heat addition/rejection $\dot{Q}$ and the shaft power is supplied or consumed $\dot{W}_{shaft}$.

4.4.2 Energy Balance Special Case 2: Steady Flow, Constant Mass Flow

In many applications, the mass flow remains constant from the inlet to the exit of the machine. Examples are uncooled turbines and compressors where no mass flow is added during the compression or expansion process. In this case, Eq. (4.72) reduces to:

$$\dot{Q} + \dot{W}_{Shaft} = \dot{m}\left[(h + \frac{1}{2}V^2 + gz)_{out} - (h + \frac{1}{2}V^2 + gz)_{In}\right] \tag{4.73}$$

Now, we define the *specific total enthalpy*

$$H \equiv h + \frac{1}{2}V^2 + gz \tag{4.74}$$

and insert it into Eq. (4.73), from which we get:

$$\dot{Q} + \dot{W}_{Shaft} = \dot{m}\left(H_{Out} - H_{In}\right) \tag{4.75}$$

In Eq. (4.73) or (4.75), the contribution of Δgz compared to Δh and ΔV^2 is negligibly small. Using the above equation, the energy balance for the major components of the gas turbine engine shown in Fig. 4.8 can be established as detailed in the following section.

4.5 Application of Energy Balance to Turbomachinery Components

The gas turbine engine shown in Fig. 4.8 consists of a variety of components, to which the energy balance in different form can be applied. These components can be categorized in three groups. The first group entails all those components that serve either the mass flow transport from one point of the engine to another or the conversion of kinetic energy into the potential energy and vice versa. Pipes, diffusers, nozzles, and throttle valves are representative examples of the first group. Within this group no thermal or mechanical energy (shaft work) is exchanged with the surroundings. We in thermodynamic sense these components are assumed adiabatic. The second group contains those components, within which thermal energy is generated or exchanged with the surroundings. Combustion chambers or heat exchangers are typical examples of these components. Thermodynamically speaking, in this case we are dealing with diabatic systems. Finally, the third group includes components within which thermal and mechanical energy is exchanged. In the following sections, each group is treated individually.

4.5.1 Application: pipe, diffuser, nozzle

Pipes, nozzles, diffusers, compressor and turbine stator cascades as well as throttle devices are few examples. For this group Eq. (4.75) reduces to:

$$H_{out} - H_{In} = 0, \text{ or } H_{out} = H_{In} = Const \tag{4.76}$$

The h-s-diagrams of the pipe, nozzle, and diffuser are shown in Fig. 4.10. As this figure shows, the viscous flow causes entropy increase which results in a reduction of the total pressure from P_1 to P_2. The total pressure is the sum of static pressure, dynamic pressure and the pressure due to the change of height:

$$P = p + \frac{1}{2}\rho V^2 + \rho g z \tag{4.77}$$

neglecting the contribution of Δgz results in the following relation for total pressure loss:

$$\Delta P = P_{In} - P_{Out} = \left(p + \frac{1}{2}\rho V^2 \right)_{In} - \left(p + \frac{1}{2}\rho V^2 \right)_{Out} \tag{4.78}$$

The area under the process-line reflects the irreversibility due to the internal friction which results in total pressure drop.

4.5.2 Application: Combustion Chamber

As indicated, combustion chambers or heat exchangers are typical examples of the components belonging to this group, within which heat transfer or heat generation takes place. The energy balance is:

$$\dot{Q} = \dot{m}\left(H_{Out} - H_{In}\right) \tag{4.79}$$

As a result, the total enthalpy at the exit is the sum of the inlet total enthalpy plus the heat added to the system. Introducing the specific thermal energy, $q = \dot{Q}/\dot{m}$, we find

$$H_{Out} = H_{In} + q \tag{4.80}$$

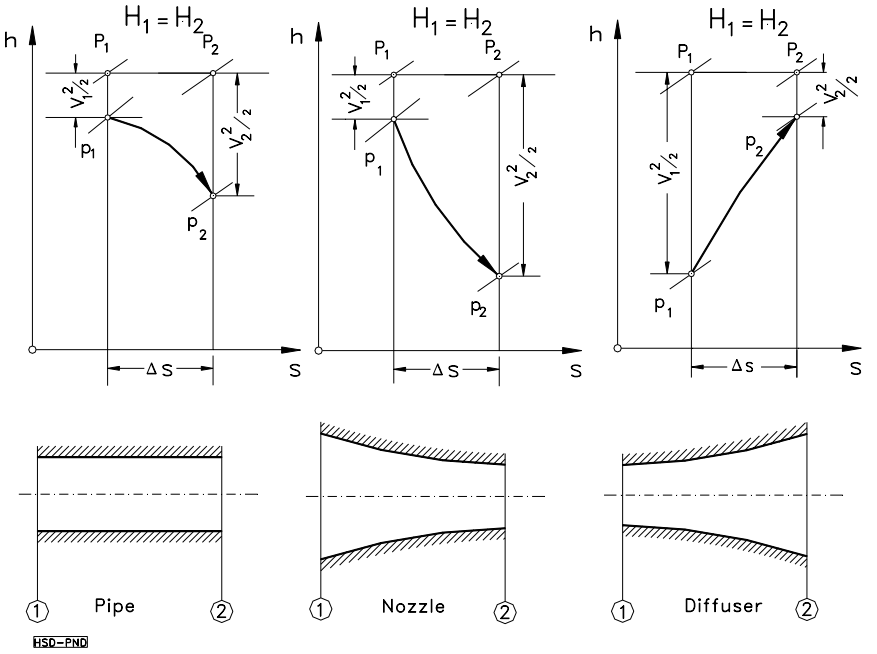

Fig. 4.10: Energy transfer in pipes, nozzles, and diffusers.

Figure. 4.11 shows a schematic of a gas turbine combustion chamber, where the combustion air and fuel are mixed leading to an increased exit temperature and enthalpy. The combustion process is shown in Fig. 4.11, where a simplified model of a combustion chamber is presented.

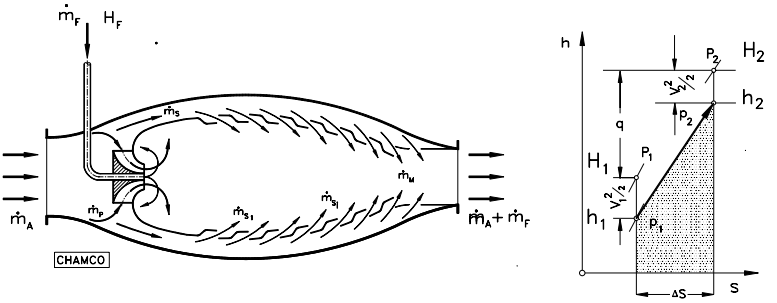

Fig. 4.11: Schematic of a gas turbine combustion chamber, h-s-diagram. Fuel mass flow $\dot{m}_F$, primary mass within the primary combustion zone, secondary mass flow $\dot{m}_s$.

The flow and combustion process within the combustion chamber is associated with entropy increases due to the heat addition and internal friction inside the chamber. The internal friction, the wall friction, and particularly the mixing process of the primary and secondary air mass flows $\dot{m}_p$, $\dot{m}_s$, causes pressure decreases of up to 5%. The thermal energy per unit mass flow is shown in Fig. 4.11 as *q*. It corresponds to the total enthalpy difference.

4.5.3 Application: Turbine, Compressor

Within this group, mechanical and thermal energy transfers to/from surroundings take place. Turbines and compressors are two representative examples. The energy balance in general form is:

$$\dot{Q} + \dot{W}_{Shaft} = \frac{dE}{dt} + \dot{m}_{Out}\left(h + \frac{1}{2}V^2 + gz\right) - \dot{m}_{In}\left(h + \frac{1}{2}V^2 + gz\right) \qquad (4.81)$$

We distinguish in the following cases, where we consider steady flow only. Thus, the first term on the right-hand side, $dE/dt = 0$, disappears.

4.5.3.1 Uncooled turbine. We start with adiabatic (uncooled) turbine component, where no heat exchange between the turbine blades with the surroundings, in this case the turbine working medium, takes place: $\dot{Q} = 0$. The mass flows at the inlet and exit are the same. Figure. 4.12 shows a turbine stage, which consists of a stator and a rotor row. The stator row with several blades deflects the flow to the following rotor row, which turns with angular velocity ω. The process of conversion of total energy into mechanical energy takes place within the rotor. Following the nomenclature in Fig. 4.12, we introduce the specific stage mechanical energy $l_m = \dot{W}_{Shaft}/\dot{m}$. Considering

the h-s-diagram in Fig. 4.12, for adiabatic turbine, $\dot{Q} = 0$, Eq. (4.81) reduces to:

$$-l_m = H_3 - H_1 = (h_3 - h_1) + \frac{1}{2}(V_3^2 - V_1^2) \tag{4.82}$$

The negative sign of l_m indicates that energy is rejected from the system (to the surroundings). The h-s-diagram in ? shows the expansion process within the stator, where the total enthalpy within the stator $H_1 = H_2$ remains constant.

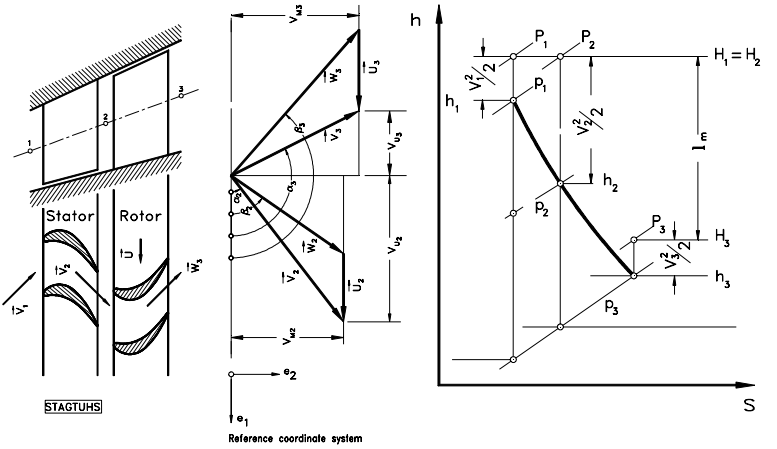

Fig. 4.12: Turbine stage consisting of a stator and a rotor row (left), velocity diagram (middle), h-s-diagram (right).

Changes of the total enthalpy occur within the rotor, where mechanical energy is produced. In addition, the *stage velocity diagram* is also shown in Fig. 4.12. This diagram shows the velocity deflection within both stator and rotor blades. As we saw from Eq. (4.46), the stage power is given by:

$$P = \omega \cdot \boldsymbol{M}_a = \omega \cdot e_2 \dot{m} \left(R_1 V_{u1} - R_2 V_{u2} \right) = \dot{m} \left(U_1 V_{u1} - U_2 V_{u2} \right) \tag{4.83}$$

Dividing the above equation by the mass flow, we find:

$$\frac{P}{\dot{m}} = l_m = U_1 V_{u1} - U_2 V_{u2} \tag{4.84}$$

This equation can be found using the energy Equation (4.82) by replacing the static enthalpies in Eq. (4.82) by the kinetic energies and trigonometric relations the velocity diagram in Fig. 4.12.

4.5.3.2 Cooled turbine. As the second case, we consider a cooled (diabatic) gas turbine blade, where a heat exchange between the turbine material and the cooling medium takes place. The schematic of such a gas turbine blade is shown in Fig. 4.13. In a high performance gas turbine engine, the front stages of the turbine component are exposed to temperatures that are close to the melting point of the turbine blade

material. In order to protect the blades, substantial amount of heat must be removed from the blades. One of the cooling methods currently used introduces cooling air into the turbine cooling channels. Inside these channels, intensive heat transfer from the blade material to the cooling medium takes place resulting in a substantial reduction of the blade surface temperature. The process of expansion and heat transfer is depicted in the h-s diagram shown in Fig. 4.13.

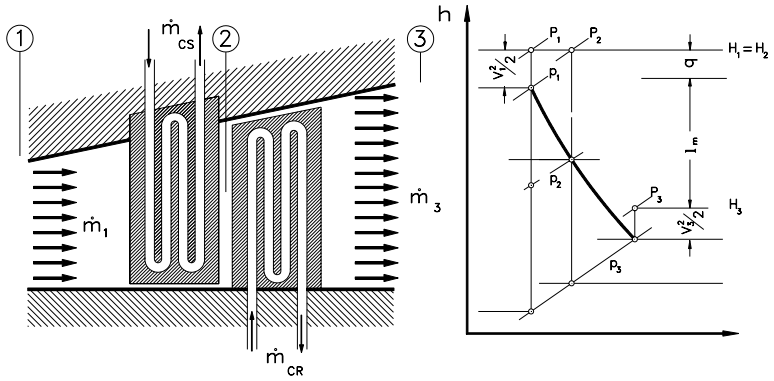

Fig. 4.13: A simplified schematic of a cooled turbine blade with internal cooling channels, hs-diagram.

Assuming a steady flow through the turbine and neglecting the energy by gravitational force, the energy equation reads:

$$\dot{Q} + \dot{W}_{Shaft} = \dot{m}_{Out}(h + \frac{1}{2}V^2) - \dot{m}_{In}(h + \frac{1}{2}V^2) \tag{4.85}$$

Since in this particular type of cooling scheme the cooling mass flows through the stator and rotor, $\dot{m}_{CS}$ and $\dot{m}_{CR}$, and does not join the main turbine mass flow, the inlet and exit mass flows are the same, $\dot{m}_{In} = \dot{m}_{Out} = \dot{m}$. We introduce the specific heat $q \equiv \dot{Q}/\dot{m}_{In}$ which is transferred from the stator and rotor blades to the cooling mass flows, $\dot{m}_{CS}$ and $\dot{m}_{CR}$. Considering the negative signs of the specific mechanical energy l_m and the heat q, we obtain from Eq. (4.85):

$$q + l_m = (h + \frac{1}{2}V^2)_{In} - (h + \frac{1}{2}V^2)_{Out} \tag{4.86}$$

The h-s diagram in Fig. 4.13 shows the specific stage mechanical energy l_m and the heat transferred from the turbine stage blade material q. From this diagram we can see that the turbine specific stage mechanical energy has been reduced by the amount of the heat rejected from the blades.

4.5.3.3 Uncooled compressor. Figure. 4.14 shows a compressor stage which consists of a stator and a rotor row. Similar to the turbine stage, the stator row with several

blades deflects the flow to the following rotor row, which is turning with an angular velocity ω. The process of conversion of total energy into mechanical energy takes place within the rotor. As in the case of a turbine component, we follow the nomenclature of Fig. 4.14 for mechanical energy transfer and introduce the specific stage mechanical energy $l_m = \dot{W}_{Shaft}/\dot{m}$. Considering the h-s-diagram in Fig. 4.14, Eq. (4.81) modifies as:

$$l_m = H_3 - H_1 \tag{4.87}$$

The positive sign of l_m indicates that energy is consumed by the system (from the surroundings).

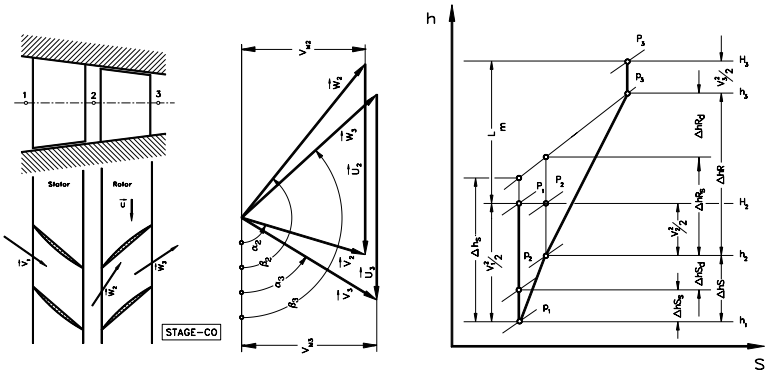

Fig. 4.14: Compressor stage consisting of stator and rotor rows (left), velocity diagram (middle), h-s- diagram (right).

4.6 Irreversibility and Total Pressure Losses

The total pressure losses within a component can be calculated using the second law of thermodynamics:

$$ds = \frac{\delta q}{T} = \frac{du + pdv}{T} = \frac{dh - vdp}{T} \tag{4.88}$$

Using the generalized thermodynamic relations, we find:

$$ds = \frac{c_v}{T}\,dT + \left(\frac{\partial p}{\partial T}\right)_v dv \tag{4.89}$$

or in terms of c_p:

$$ds = \frac{c_P}{T}\,dT - \left(\frac{\partial v}{\partial T}\right)_p dp \tag{4.90}$$

With:

$$dh = c_p dT + \left(v - T\left(\frac{\partial v}{\partial T} \right)_p \right) dp \tag{4.91}$$

For the working media used in thermal turbomachines such as steam, air, and combustion gases, the thermodynamic properties can be taken from appropriate gas and steam tables. In general, the specific heats at constant pressure c_p and constant specific volume c_v are functions of temperature. Figure 4.15 shows the specific heat at constant pressure as a function of temperature with the *fuel/air ratio* μ as

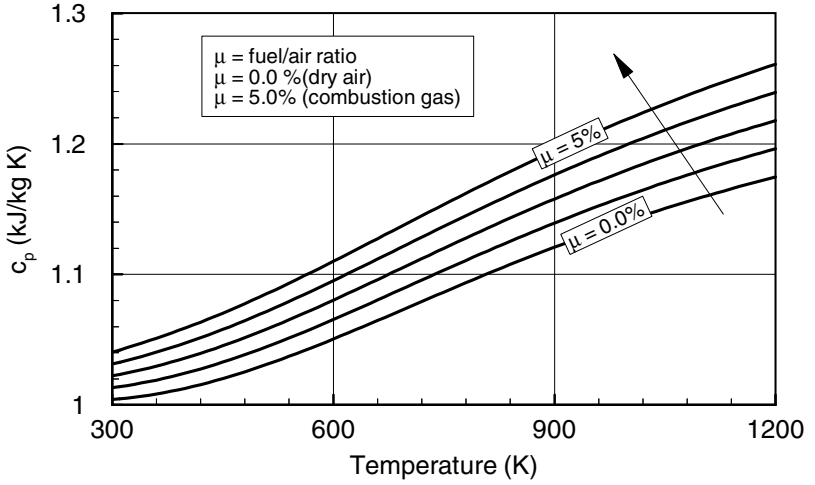

Fig. 4.15: Temperature dependency of the specific heat c_p for air and combustion gases at different fuel/air ratios.

parameter. The dry air is characterized by $\mu = 0$ and no moisture. As seen at lower temperatures, changes of c_p are not significant. However, increasing the temperature results in higher specific heat. In the case of combustion gases, the addition of fuel in a combustion chamber causes a change in the gas constant R and additional increase in c_p. At moderate pressures, the ideal gas relation can be applied

$$pv = RT \; ; \quad \frac{\partial v}{\partial T} = \frac{R}{p} \tag{4.92}$$

With this relation, the entropy change can be obtained using Eq. (4.89) in terms of enthalpy or internal energy,

$$ds = \frac{c_p}{T} dT - R\frac{dp}{p}, \quad ds = \frac{c_v}{T} dT + R\frac{dv}{v} \tag{4.93}$$

Assuming lower temperatures where c_p and c_v can be approximated as constant, the entropy change is calculated by integrating Eq. (4.93):

$$\Delta s = c_p \ln\left(\frac{T_2}{T_1}\right) - R \ln\left(\frac{p_2}{p_1}\right) = c_p \ln\left[\left(\frac{T_2}{T_1}\right)\left(\frac{p_1}{p_2}\right)^{\frac{\kappa-1}{\kappa}}\right] \tag{4.94}$$

$$\Delta s = c_v \ln\left(\frac{T_2}{T_1}\right) + R \ln\left(\frac{v_2}{v_1}\right) = c_v \ln\left[\left(\frac{T_2}{T_1}\right)\left(\frac{v_2}{v_1}\right)^{\kappa-1}\right] \tag{4.95}$$

Equations (4.94) and (4.95) are valid under perfect gas assumption, c_p and $c_v \neq f(T)$, for estimating the entropy changes. For dry or moist air as working media in compressors, and combustion gases as the working media in turbines and combustion chambers, appropriate gas tables must be used in order to avoid significant errors.

4.6.1 Application of Second Law to Turbomachinery Components

To calculate the entropy increase as a result of an irreversible process, a simple nozzle or turbine stator flow is considered. The expansion process is shown in Fig. 4.16.

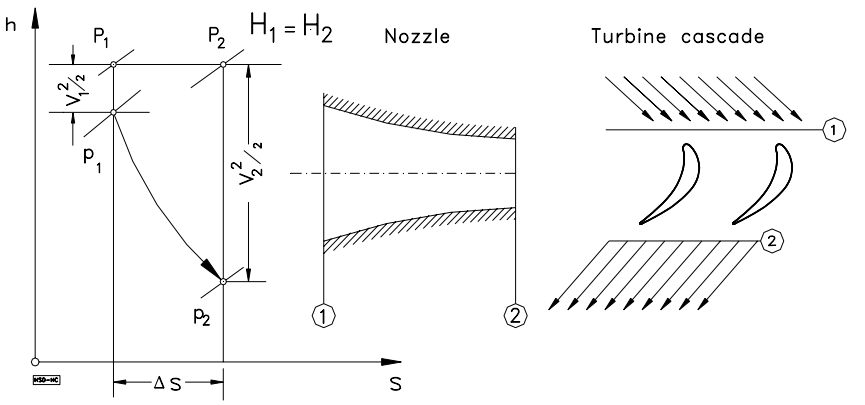

Fig. 4.16: Total pressure loss and entropy increase in a nozzle and a turbine cascade.

The entropy change is obtained using the second law:

$$\Delta s = c_p \ln\left(\frac{T_2}{T_1}\right) - R \ln\left(\frac{p_2}{p_1}\right) \tag{4.96}$$

where p_1, p_2 and T_1, T_2 are static pressures and temperatures. These quantities can be related to the total quantities by the following simple modification:

$$\frac{p_2}{p_1} = \frac{\left(\frac{p_2}{p_{o2}}\right)}{\left(\frac{p_1}{p_{o1}}\right)} \left(\frac{p_{o2}}{p_{o1}}\right) \tag{4.97}$$

Introducing the temperature relation by applying the isentropic relation with $p v^{\kappa} = const.$,

$$\left(\frac{p_2}{p_{o2}}\right) = \left(\frac{T_2}{T_{o1}}\right)^{\frac{\kappa}{\kappa-1}}, \quad \text{and} \quad \left(\frac{p_1}{p_{o1}}\right) = \left(\frac{T_1}{T_{o1}}\right)^{\frac{\kappa}{\kappa-1}} \tag{4.98}$$

and inserting Eq. (4.98) into Eq. (4.97) leads to:

$$\frac{p_2}{p_1} = \frac{\left(\frac{T_2}{T_{o2}}\right)^{\frac{\kappa}{\kappa-1}}}{\left(\frac{T_1}{T_{o1}}\right)^{\frac{\kappa}{\kappa-1}}} \left(\frac{p_{o2}}{p_{o1}}\right) \tag{4.99}$$

since $T_{o1} = T_{o2}$,

$$\frac{p_2}{p_1} = \left(\frac{T_2}{T_1}\right)^{\frac{\kappa}{\kappa-1}} \left(\frac{p_{o2}}{p_{o1}}\right) \tag{4.100}$$

The entropy changes obtained form:

$$\Delta s = c_p \ln\left(\frac{T_2}{T_1}\right) - R\frac{\kappa}{\kappa-1} \ln\left(\frac{T_2}{T_1}\right) - R \ln\left(\frac{p_{o2}}{p_{o1}}\right) \tag{4.101}$$

Since:

$$c_p = R \frac{\kappa}{\kappa-1} \tag{4.102}$$

$$\Delta s = R \ln\left(\frac{p_{o1}}{p_{o2}}\right) = -R \ln\left(\frac{p_{o2}}{p_{o1}}\right) = -R \ln \frac{p_{o1} - \Delta p_o}{p_{o1}} \tag{4.103}$$

Thus, the entropy change is directly related to the total pressure loss. We introduce the total pressure loss coefficient ζ:

$$\zeta = \frac{\Delta p_o}{p_{o1}} \tag{4.104}$$

then we have:

$$\Delta s = -R\ln(1 - \zeta) \tag{4.105}$$

or

$$\zeta = 1 - e^{\frac{-\Delta s}{R}} \tag{4.106}$$

If the total pressure loss coefficient is known, the entropy change can be calculated using Eq. (4.106). For compressor or turbine components, different loss correlations are available that are based on experimental investigations. We will discuss a few of these correlations later.

4.7 Flow at High Subsonic and Transonic Mach Numbers

The components of turbomachines are frequently subjected to higher subsonic, transonic, or supersonic Mach ranges. This is particularly true when the components operate at off-design conditions that may cause an increase in exit flow velocity. A typical example is the flow through a subsonic turbine stator blade shown in Fig. 4.17.

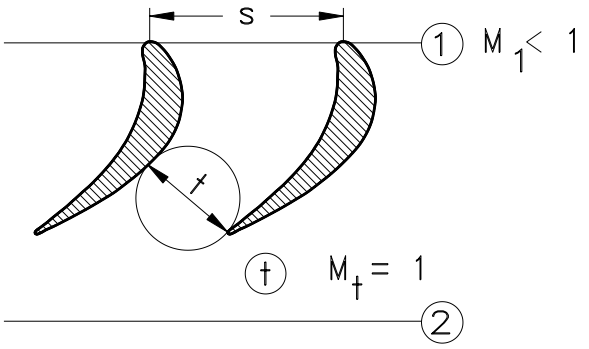

Fig. 4.17: Guided flow through a turbine cascade from inlet at station (1) to the throat (t). The flow is accelerated from subsonic M < 1 to sonic with M = 1.

Similar situations may occur in blade channels of turbine or compressor rotors, inlet guide vanes, and nozzles.

Figure 4.17 depicts a purely *convergent channel*. An increase in flow velocity at the exit of a turbine stator, shown in Fig. 4.17, necessitates an increase of the inlet pressure. Since the flow velocity is a function of the pressure difference across the turbine cascade, it will increase continuously until the speed of sound is reached. This happens at the smallest cross section, namely the blade *throat t*. For a convergent blade channel, as shown in Fig. 4.17, no further acceleration can take place with increasing the pressure difference between the inlet (1) and the exit (2). By reaching the speed of sound at the throat, the critical condition is established and the turbine blade channel is *choked*. If a higher velocity than the speed of sound is desired, then the blade geometry must change. In the following sections, we introduce the basic physics necessary to describe the flow behavior at high subsonic and transonic Mach numbers and their effect on channel geometry and thermodynamic properties.

4.7.1 Density Changes with Mach Number, Critical State

The changes in fluid density and the flow Mach number are closely related. To find the corresponding relationships, we apply the energy equation for an adiabatic system to a large adiabatic container, Fig. 4.18, where the exit diameter *d* is assumed to be negligibly small compared to the container diameter *D*.

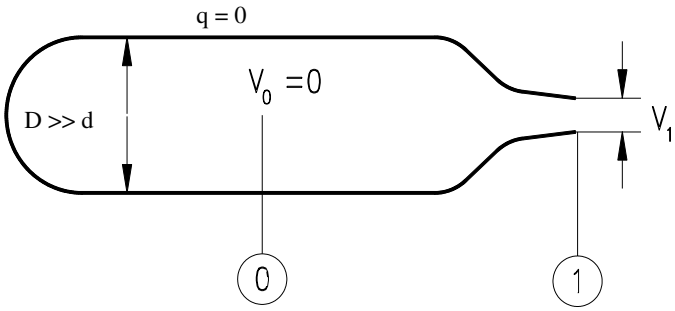

Fig. 4.18: Adiabatic system under pressure.

The energy equation is written as:

$$H \equiv h_t = h_0 + \frac{1}{2}V_0^2 = h_1 + \frac{1}{2}V_1^2 = const. \tag{4.107}$$

Since in this chapter we are dealing with one-dimensional flow, the velocity subscripts refer to the stations and not to the velocity components as we did in previous chapters. Thus, the subscript *0* and *t* refers to the *stagnation* condition, where the velocity is assumed to be zero. Assuming a perfect gas, we introduce, for enthalpy, the temperature and rewrite Eq. (4.107) in terms of total temperature:

$$\frac{T_t}{T} = 1 + \frac{1}{2c_p}\frac{1}{T}V^2 \tag{4.108}$$

The specific heats at constant pressure and volume are related by the specific gas constant:

$$c_p - c_v = R,\ \frac{c_p}{c_v} = \kappa,\ \text{and}\ \ c = \sqrt{\kappa RT} \tag{4.109}$$

Using the above relations, the total temperature ratio and the Mach number read:

$$\frac{T_t}{T} = 1 + \frac{1}{2}(\kappa - 1)M^2 \tag{4.110}$$

To obtain similar relationship for the density ratio, we assume an isentropic process described by:

$$pv^{\kappa} = p_t v_t^{\kappa} = con. \tag{4.111}$$

that we combine with the equation of state for ideal gases,

$$v = \frac{p}{RT} \tag{4.112}$$

Thus eliminating the specific volume results in:

$$\frac{p_t}{p} = \left(\frac{T_t}{T}\right)^{\frac{\kappa}{\kappa-1}} \tag{4.113}$$

Introducing Eq. (4.110) into (4.113) results in:

$$\frac{p_t}{p} = \left(1 + \frac{\kappa - 1}{2}M^2\right)^{\frac{\kappa}{\kappa-1}} \tag{4.114}$$

Likewise, we obtain the density ratio as:

$$\frac{\rho_t}{\rho} = \left(1 + \frac{\kappa - 1}{2}M^2\right)^{\frac{1}{\kappa-1}} \tag{4.115}$$

Equation (4.115) expresses the ratio of stagnation point density relative to the density at any arbitrary point in the container including the exit area. Assuming air as a perfect gas with $\kappa = 7/5$ at a temperature of $T = 300^0 K$, the ratios $\Delta\rho/\rho_t = (\rho_t - \rho)/\rho_t$, $\Delta p/p_t = (p_t - p)/p_t$, and $\Delta T/T_t = (T_t - T)/T_t$ from Eqs. (4.110), (4.114) and (4.115), are plotted in Fig. 4.19.

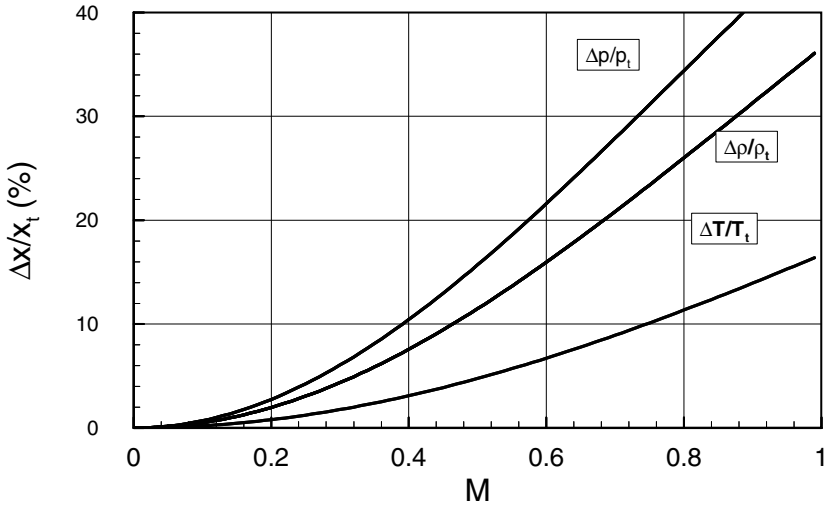

Fig. 4.19: Density, pressure, and temperature changes as a function of flow mach number.

We find that for very small Mach numbers , $M<0.1$, the density change, $\Delta\rho/\rho_t$, is small and the flow is considered incompressible. Increasing the Mach number, however, results in significant changes of the density ratio. In practical applications, flows with $M<0.3$ are still considered incompressible. Increasing the Mach number above $M>0.3$ results in higher density changes that cannot be neglected as Fig. 4.19 shows. Thus, the flow is considered as compressible with a noticeable change of density. If the velocity approaches the speed of sound, i.e. $V = c$ and $M = 1$, it is called the critical velocity and the flow state is called critical. In this case, the properties in Eqs. (4.110), (4.114) and (4.115) are calculated by setting $M = 1$. To distinguish this particular flow state, quantities are labeled with the superscript *. The critical temperature ratio is:

$$\frac{T_t^*}{T^*} = \frac{(\kappa + 1)}{2} \text{ for } \kappa = 7/5: \frac{T_t^*}{T^*} = 1.2 \tag{4.116}$$

The critical pressure ratio reads:

$$\frac{p_t^*}{p^*} = \left(\frac{\kappa + 1}{2}\right)^{\frac{\kappa}{\kappa-1}} \quad \text{for } \kappa = 7/5: \ \frac{p_t^*}{p^*} = 1.893 \tag{4.117}$$

and finally, the critical density ratio is obtained from:

$$\frac{\rho_t^*}{\rho_*} = \left(\frac{\kappa + 1}{2}\right)^{\frac{1}{\kappa-1}} \quad \text{for } \kappa = 7/5: \ \frac{\rho_t^*}{\rho^*} = 1.577 \tag{4.118}$$

From Eq. (4.117), it is obvious that in order to achieve the sonic flow ($M = 1$), the critical pressure ratio must be established first. In a system as in Fig. 4.18 with a *convergent exit nozzle* and air as the working medium with $\kappa = 1.4$, the critical pressure ratio is $p_t^*/p^* = 1.893$. At this pressure ratio the mass flow per unit area has a maximum and the flow velocity at the exit nozzle equals to the speed of sound. Any increase in pressure ratio above the critical one results in a *choking state* at the nozzle throat. In this case, the convergent nozzle produces its own exit pressure, such that the critical pressure ratio is maintained. To calculate the mass flow of a clerically perfect gas through a convergent nozzle in terms of pressure ratios, we first replace the enthalpy in the energy equation by:

$$h = c_p T = \frac{k}{k-1} RT = \frac{k}{k-1} pv = \frac{k}{k-1} \frac{p}{\rho} \tag{4.119}$$

Thus the energy equation for a clerically perfect gas reads:

$$\frac{V_1^2}{2} + \frac{\kappa}{\kappa - 1} \frac{p_1}{\varrho_1} = \frac{V_2^2}{2} + \frac{\kappa}{\kappa - 1} \frac{p_2}{\varrho_2} \tag{4.120}$$

To eliminate the density at the exit, we now apply the isentropic relation to the right-hand side of Eq. (4.120) and arrive at:

$$\frac{V_1^2}{2} + \frac{\kappa}{\kappa - 1} \frac{p_1}{\varrho_1} = \frac{V_2^2}{2} + \frac{\kappa}{\kappa - 1} \frac{p_1}{\varrho_1} \left(\frac{p_2}{p_1}\right)^{\frac{(\kappa-1}{\kappa}} \tag{4.121}$$

We assume that inside the container, because of $D \gg d$, the velocity V_1 is negligibly small compared to the velocity at the nozzle exit V_2. In this case, the static pressure p_1 would represent the total pressure at the same position $p_1 \equiv p_t$. We now set $p_2 \equiv p_e$ and call it the nozzle exit or back pressure. If the actual pressure ratio is less than the critical one, $p_t/p_e < p_t^*/p_e^*$ and the mass flow exits into the atmosphere, then the nozzle exit pressure is identical with the ambient pressure and the nozzle is not choked. On the other hand, if $p_t/p_e > p_t^*/p_e^*$, the convergent nozzle is choked indicating that it has established a back pressure for itself, which corresponds to the critical pressure. With the above assumption, the mass flow through a convergent

channel is calculated by:

$$\dot{m} = V\rho A = A\sqrt{\frac{2\kappa}{\kappa-1}p_t\rho_t\left[\left(\frac{p_e}{p_t}\right)^{\frac{2}{\kappa}}-\left(\frac{p_e}{p_t}\right)^{\frac{\kappa+1}{\kappa}}\right]} = A\psi\sqrt{\frac{2\kappa}{\kappa-1}p_t\rho_t} \tag{4.122}$$

where the *mass flow function* Ψ is defined as

$$\psi = \sqrt{\left(\frac{p_e}{p_t}\right)^{\frac{2}{\kappa}}-\left(\frac{p_e}{p_t}\right)^{\frac{\kappa+1}{\kappa}}} \tag{4.123}$$

thus the mass flow through the nozzle is calculated by,

$$\dot{m} = A\psi\sqrt{\frac{2\kappa}{\kappa-1}p_t\rho_t} \tag{4.124}$$

Figure 4.20 shows the mass flow function Ψ as a function of the ratio pressure ratio for different κ.
The maximum value of Ψ is obtained from:

$$\psi_{max} = \sqrt{\frac{\kappa-1}{\kappa+1}}\left(\frac{2}{\kappa+1}\right)^{\frac{1}{\kappa-1}} \tag{4.125}$$

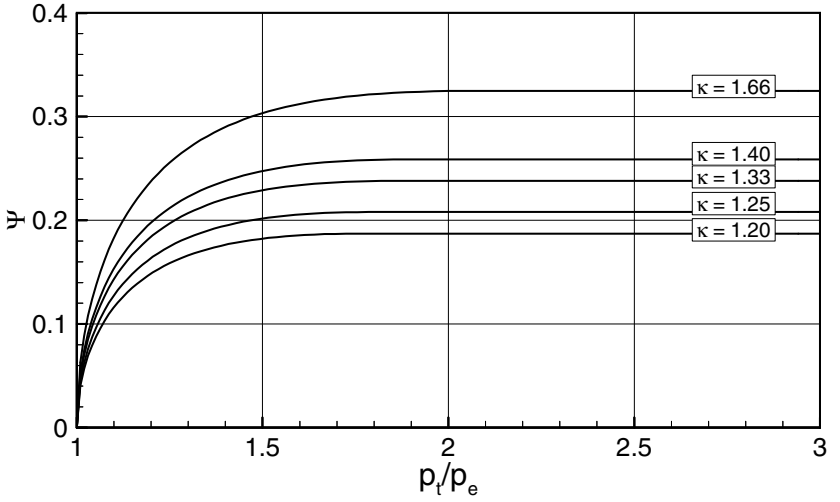

Fig. 4.20 Flow function ψ versus the pressure ratio with κ as parameter.

Figure 4.20 shows that increasing the pressure ratio results in an increase of the mass flow function Ψ until Ψ_{max} has been reached. Further increase in pressure ratio results in a choking state, where the flow function remains constant.

4.7.2 Effect of Cross-Section Change on Mach Number

The influence of the *Mach number* gives rise to further differences between compressible and incompressible flow. However, we first examine the effect that the Mach number has on the relation between the cross-sectional area A and the velocity V in isentropic flow. This relation is directly obvious in an incompressible flow from the continuity equation:

$$VA = const; \tag{4.126}$$

as A becomes large V must decrease, and vice versa. However, the continuity equation for compressible flow,

$$\varrho VA = const \tag{4.127}$$

contains the additional variable ϱ that changes with the Mach number as shown in Fig. 4.19. We differentiate Eq. (4.127) and divide the result by Eq. (4.127). As a result, we obtain the expression:

$$\frac{dV}{V} + \frac{dA}{A} + \frac{d\varrho}{\varrho} = 0 \tag{4.128}$$

for isentropic flow, thus $p = p(\varrho)$, we have from the definition of the speed of sound

$$c^2 = \left(\frac{\partial p}{\partial \varrho} \right)_s \tag{4.129}$$

in particular $dp/d\varrho = c^2$ and therefore, from Eq. (4.128)

$$\frac{dV}{V} + \frac{dA}{A} + \frac{dp}{c^2 \varrho} = 0 \,. \tag{4.130}$$

Using the component of Euler's equation for one-dimensional flow,

$$V\,dV = -\frac{dp}{\varrho} \tag{4.131}$$

We then obtain the modified Eq.(4.130) as:

$$\frac{dV}{V} + \frac{dA}{A} = \frac{V^2}{c^2} \frac{dV}{V} \tag{4.132}$$

which we reduce to:

$$\frac{dA}{A} = -\frac{dV}{V}\left(1 - M^2\right) \tag{4.133}$$

Introducing Eq. (4.133) into (4.131) results in:

$$\frac{dA}{A} = \frac{dp}{\rho V^2}\left(1 - M^2\right) \tag{4.134}$$

With Eqs. (4.133) and (4.134) we have established a relationship between the velocity change, the pressure change, and the Mach number. For $M < 1$ we obtain qualitatively the same behavior as in incompressible flow: a decrease in the cross-sectional area leads to an increase in velocity, leading to a subsonic nozzle flow, Fig. 4.21(left). On the other hand, an increase in the cross-sectional area (dA > 0) corresponds to a decrease in velocity (dV < 0), resulting in a subsonic diffuser flow, Fig. 4.21 (right). For M = 1, we obtain dA/dx = 0 and dp = 0. For M > 1 Eq. (4.133) and (4.134) show that if the cross-sectional area (dA/dx > 0) increases, the velocity must also increase (dV/dx > 0), or if the area decreases, so does the velocity. As a result, we have a supersonic nozzle and diffuser

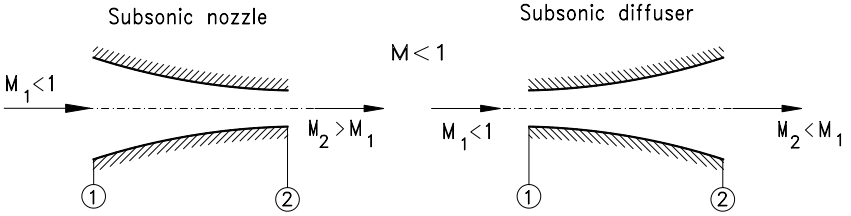

Fig. 4.21 Left: Subsonic nozzle with dA <0, dV > 0, dp < 0,
Right: Subsonic diffuser with dA > 0, dV < 0, dp > 0.

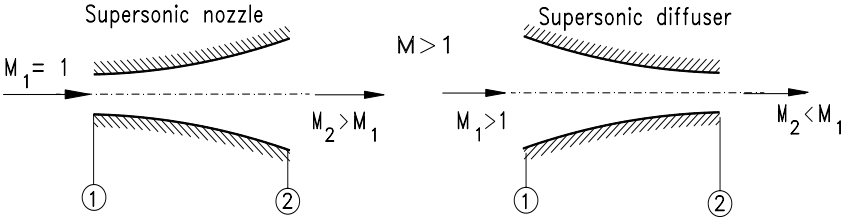

Fig. 4.22: Left: Supersonic nozzle with dA >0, dV > 0, dp < 0,
Right: Supersonic diffuser with dA > 0, dV < 0, dp > 0.

respectively, as shown in Fig. 4.22. Equations (4.132) and (4.133) indicate that in order to reach the sonic speed M = *1*, the area change *dA/dx* must vanish. This implies that the cross section must have a minimum. Considering the configurations shown in Fig. 4.21 and Fig. 4.22, channels can be constructed that satisfy the requirements stated in Eq. (4.133) and (4.134). A generic convergent-divergent nozzle known as the *Laval nozzle* shown in Fig. 4.23 (a), is an example. A similar configuration is used in the so called *control stage* of steam turbines, Fig. 4.23 (b).

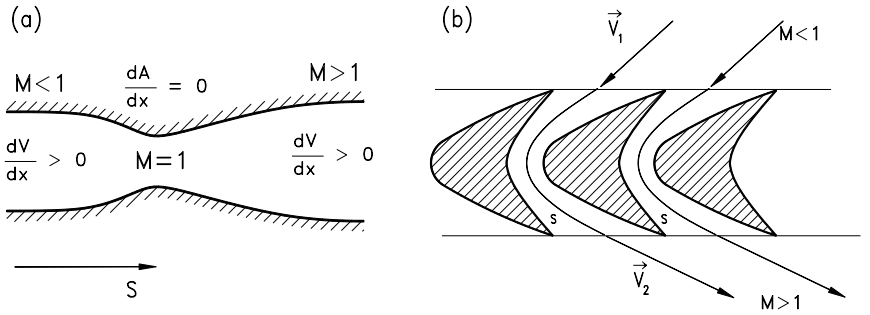

Fig. 4.23: (a) A generic Laval nozzle operating at the design pressure ratio, (b) Stator row of a control stage of a steam turbine.

This channel can accelerate the flow from a subsonic to a supersonic Mach range. The condition for a supersonic flow to be established is that the pressure ratio along the channel from the inlet to the exit must correspond to the nozzle design pressure ratio, which is above the super critical pressure ratio. In this case, the flow is accelerated in the convergent part, reaches the Mach number *M = 1* in the *throat*, and is further accelerated in the divergent portion of the nozzle. If the channel pressure ratio is less than the critical pressure ratio, the flow in convergent part is accelerated to a certain subsonic Mach number, M<1, and then decelerates in divergent parts. A supersonic diffuser, on the other hand, is characterized by convergent divergent channels with an inlet Mach number, M>1.

Figure 4.24 shows a supersonic flow through a supersonic inlet diffuser. The flow enters the inlet and is decelerated from *M > 1* to *M = 1* at the throat, where the sonic

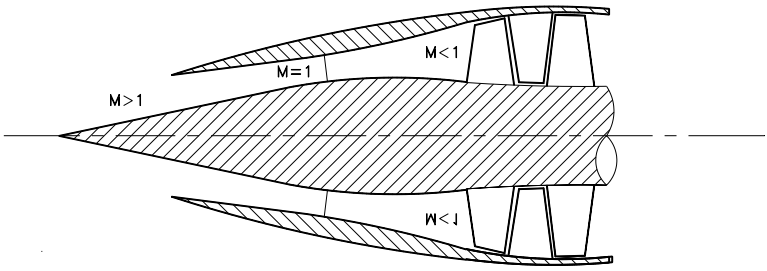

Fig. 4.24: Flow though a supersonic inlet: deceleration from M>1 to M<1.

velocity has been reached. Further deceleration occurs at the divergent part of the inlet.

Equation (4.133) and its subsequent integration, along with the flow quantities listed in Table 4.1, indicate the direct relation between the area ratio and the Mach number. These relations can be utilized as a useful tool for estimating the cross section distribution of a Laval nozzle, a supersonic stator blade channel, or a supersonic diffuser. If, for example, the Mach number distribution in the streamwise direction is given, $M(S) = f(S)$, the cross section distribution $A(S) = f(M)$ is directly calculated from Table 4.1. If, on the other hand, the cross section distribution in the streamwise direction is prescribed, then the Mach number distribution, and thus, all other flow quantities can be calculated using an inverse function. Since we assumed the isentropic flow with clerically perfect gases as the working media, important features such as flow separation as a consequence of the boundary layer development under adverse pressure gradient, will not be present. Therefore, in both cases, the resulting channel geometry or flow quantities are just a rough estimation, no more, no less. Appropriate design of such channels, particularly transonic turbine or compressor blades, require a detailed calculation where the fluid viscosity is fully considered.

In order to represent the thermodynamic variables as functions of a Mach number, we use the continuity and energy equations in conjunction with the isentropic relation, and the equation of state for the thermally perfect gases with $p = \varrho RT$. The isentropic flow parameters as a function of a Mach number are summarized in Table 4.1, which contains two columns. The first column gives the individual parameter ratios at arbitrary sections, whereas the second one gives the ratios relative to the critical state. The gas dynamics relations presented in Table 4.1 are depicted in Fig. 4.25.

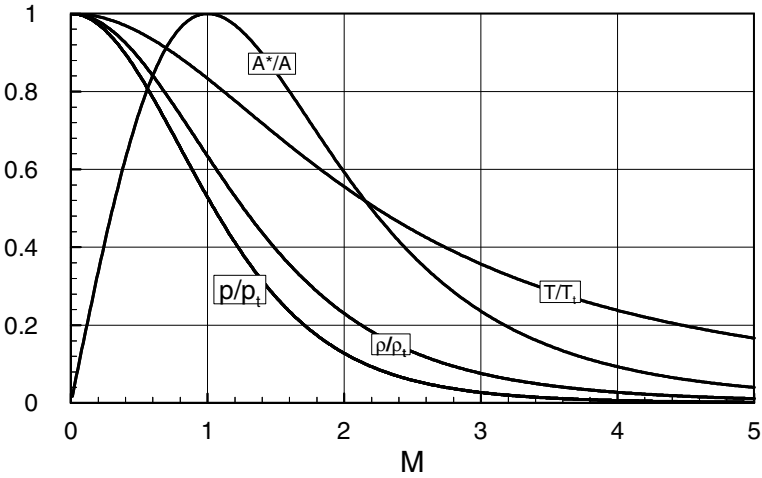

Fig. 4.25: Area ratio and the thermodynamic property ratios as a function of Mach number for $\kappa = 1.4$.

Table 4.1: Summary of the gas dynamic functions

Parameters for any two arbitrary sections	Parameters relative to the critical state
$\frac{A}{A_1} = \frac{1}{M}\left(\frac{1+\frac{\kappa-1}{2}M^2}{1+\frac{\kappa-1}{2}M_1^2}\right)^{\frac{1}{2}\frac{\kappa+1}{\kappa-1}}$	$\frac{A}{A*} = \frac{1}{M}\left(\frac{1+\frac{\kappa-1}{2}M^2}{\frac{\kappa+1}{2}}\right)^{\frac{1}{2}\frac{\kappa+1}{\kappa-1}}$
$\frac{p}{p_1} = \left(\frac{1+\frac{\kappa-1}{2}M_1^2}{1+\frac{\kappa-1}{2}M^2}\right)^{\frac{\kappa}{\kappa-1}}$	$\frac{p}{p*} = \left(\frac{\frac{\kappa+1}{2}}{1+\frac{\kappa-1}{2}M^2}\right)^{\frac{\kappa}{\kappa-1}}$
$\frac{T}{T_1} = \frac{1+\frac{\kappa-1}{2}M_1^2}{1+\frac{\kappa-1}{2}M^2}$	$\frac{T}{T*} = \frac{\frac{\kappa+1}{2}}{1+\frac{\kappa-1}{2}M^2}$
$\frac{h}{h_1} = \frac{1+\frac{\kappa-1}{2}M_1^2}{1+\frac{\kappa-1}{2}M^2}$	$\frac{h}{h*} = \frac{\frac{1+\kappa}{2}}{1+\frac{\kappa-1}{2}M^2}$
$\frac{V}{V_1} = \frac{M}{M_1}\left(\frac{1+\frac{k-1}{2}M_1^2}{1+\frac{\kappa-1}{2}M^2}\right)^{\frac{1}{2}}$	$\frac{V}{V*} = M\left(\frac{\frac{1+k}{2}}{1+\frac{\kappa-1}{2}M^2}\right)^{\frac{1}{2}}$
$\frac{\rho}{\rho_1} = \frac{v_1}{v} = \left(\frac{1+\frac{\kappa-1}{2}M_1^2}{1+\frac{\kappa-1}{2}M^2}\right)^{\frac{1}{\kappa-1}}$	$\frac{\rho}{\rho*} = \frac{v*}{v} = \left(\frac{\frac{1+\kappa}{2}}{1+\frac{\kappa-1}{2}M^2}\right)^{\frac{1}{\kappa-1}}$

Laval nozzles were first used in steam turbines, but many other applications for these nozzles have been found, for example, in rocket engines, supersonic steam turbines,

etc. In the following, we briefly discuss the operational behavior of a generic Laval nozzle, which is strongly determined by the pressure ratio. Detailed discussion of this topic can be found in excellent books by Spurk [2], Shapiro [3], Becker [4], Prandtl et al.[5]. Starting with the design operating point, where the exit pressure is set equal to the ambient pressure $p_e = p_a$, curve ①, that corresponds to the design area ratio (Fig. 4.26a).

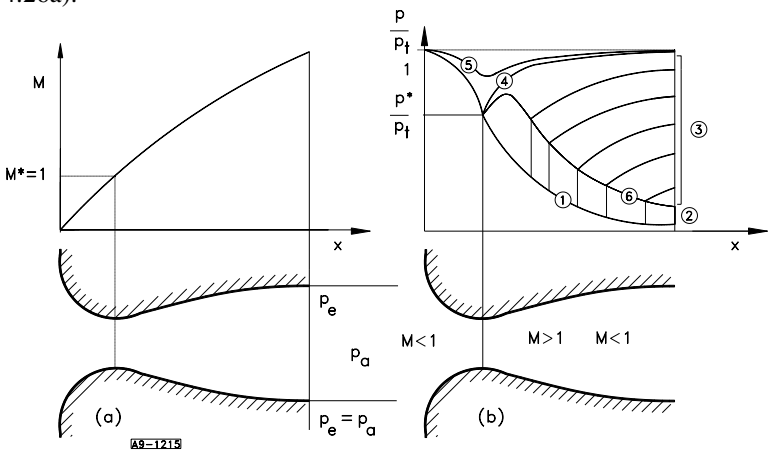

Fig. 4.26: Operational behavior of a generic Laval nozzle, (a) Expansion to the design exit pressure, (b) Overexpansion.

In this case, the Mach number continuously increases from the subsonic at the inlet to the supersonic at the exit. Increasing the ambient pressure results in an overexpanded jet, because the flow in the nozzle expands above a pressure that does not correspond to its design pressure: point ② with $p_e < p_a$. At this pressure condition, the flow pattern inside the nozzle does not change as curve ① indicates. However, outside the nozzle, the flow undergoes a system of *oblique shocks* that emanate from the rim of the nozzle, raising the lower nozzle discharge pressure discontinuously to the ambient pressure. The shock surfaces intersect and are reflected at the jet boundary as steady *expansion waves* (Fig. 4.27).

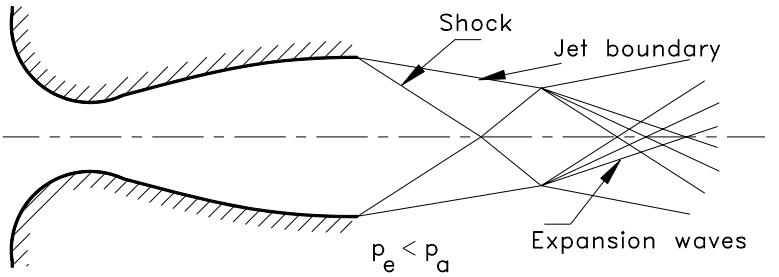

Fig. 4.27: Overexpanded jet

A rhombic pattern, characteristic of supersonic jets, arises and this is sometimes visible to the naked eye in exhaust jets of rocket engines. If the ambient pressure is further raised, the shock moves into the nozzle and forms a *normal shock wave* in the nozzle, curves ③. This discontinuous pressure increase positions itself in the nozzle just so that the required ambient pressure is reached. Behind the shock, the flow is subsonic. The section of the nozzle behind the shock then works as a subsonic diffuser, which theoretically raises the pressure behind the shock to the ambient pressure. However, in practice, a flow separation occurs and the actual gain in pressure is so small that the pressure behind the shock is actually about the same as the ambient pressure. If the ambient pressure is raised even further, it curves, the shock migrates into the nozzle, and it becomes weaker, since the Mach number in front of the shock becomes smaller. If the ambient pressure is increased such that the shock finally reaches the throat of the nozzle, the shock strength drops to zero and the whole nozzle contains subsonic flow, curve ④. If we increase p_a even further, the Mach number has a maximum at the throat, but $M = 1$ is no longer reached, curve ⑤. The geometric locations of all pressure discontinuities are also shown in Fig. 4.26, curve ⑥.

In under-expanded jets, the pressure at the nozzle exit p_e is larger than the ambient pressure p_a (Fig. 4.28). The pressure is reduced to the ambient pressure through a system of stationary *expansion waves*. The flow in the nozzle remains unaffected by this. The expansion waves penetrate into themselves and are then reflected at the boundary of the jet as *compression waves* and these often reform themselves into a shock. In this manner, a rhombi pattern is set up in the jet again, very much the same as for over-expanded jets.

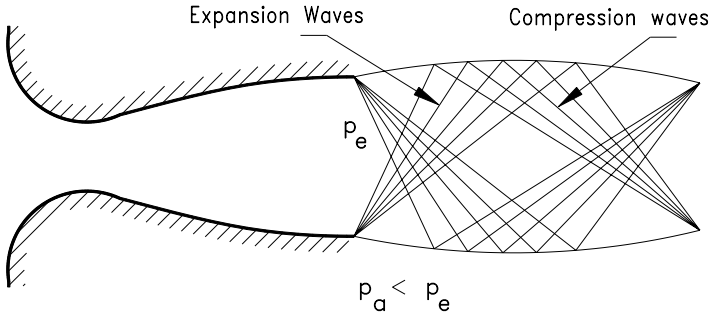

Fig. 4.28: Under-expanded jet

In a convergent nozzle, no steady supersonic flow can be formed in the above stated manner. As long as the ambient pressure p_a is larger than the critical pressure p^*, the pressure in the jet p_e is the same as the ambient pressure p_a (Fig. 4.29). If the Mach number, $M = 1$, is reached at the smallest cross-section, then $p_e = p^*$ and the ambient pressure can be decreased below this pressure ($p_a < p_e$). Next, an after-expansion takes place in the free jet and the pressure at the nozzle exit is expanded to the ambient pressure p_a again through stationary expansion waves (Fig. 4.30).

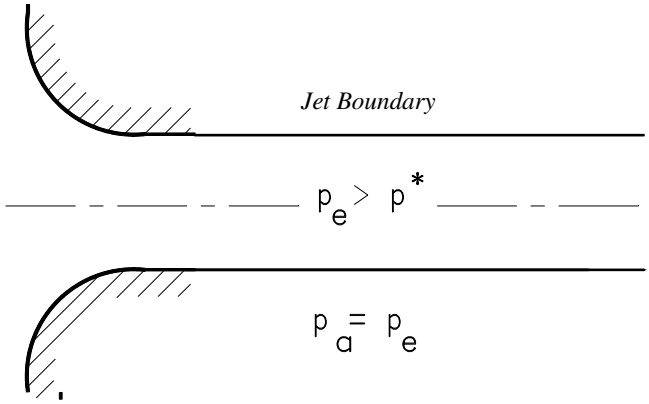

Fig. 4.29: Subsonic nozzle and subsonic jet

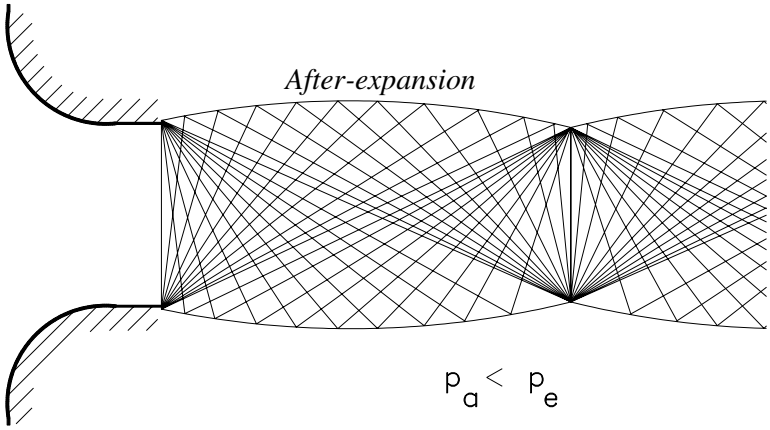

Fig. 4.30: Subsonic nozzle with after expansion

4.7.3 Compressible Flow though Channels with Constant Cross Section

This type of flow is encountered in several components of turbomachines such pipes, labyrinth seals, and to a certain degree of simplicity, in combustion chambers and afterburners of supersonic jet engines. In the case of pipes and labyrinth seals, we are dealing with an adiabatic flow process, where the total enthalpy remains constant. However, entropy increases are present due to the internal friction, shocks, or throttling. Combustion chambers and afterburners can be approximated by a constant cross section pipe with heat addition or rejection. The characteristic features of these devices are that the entropy changes are caused by heat addition, such that the friction contribution to the entropy increase can be neglected. This assumption leads to a major simplification that we may add heat to a constant cross section pipe and assume

that the impulse remains constant. The constant total enthalpy is described by the *Fanno process*, whereas the constant impulse case is determined by the *Rayleigh* process.

Starting with the Rayleigh process, we will specifically consider the flow in a duct with a constant cross-section, without surface or internal friction, but with heat transfer through the wall. In the absence of the shaft power, Eq. (4.73) is modified to:

$$\frac{V_2^2}{2} + h_2 = \frac{V_1^2}{2} + h_1 + q\,. \tag{4.135}$$

In the application of the momentum balance, we assume here that the contribution of the friction forces to the total entropy increase compared to the entropy increase by external heat addition is negligibly small, thus the friction in Eq. (4.26) is $\boldsymbol{F}_r = 0$. This results in:

$$\rho_2 V_2^2 + p_2 = \rho_1 V_1^2 + p_1 = \rho V^2 + p = const. \tag{4.136}$$

To find the flow quantities for the Rayleigh process, we present the calculation of a pressure ratio. The other quantities such as velocity ratio, temperature ratio, density ratio, etc., are obtained using a similar procedure. We start with the calculation of the pressure ratio by utilizing the following two steps.

Step 1: We combine the differential form of the momentum equation ,

$$dp + 2\rho V dV + d\rho V^2 = 0 \tag{4.137}$$

with the differential form of continuity equation for a constant cross section,

$$d\rho V + \rho dV = 0 \tag{4.138}$$

and obtain the modified momentum equation. This equation can immediately be found from the 1-D Euler equation.

$$v dp + V dV = 0 \tag{4.139}$$

We rearrange the modified momentum equation (4.139) and introduce the Mach number

$$\frac{dp}{p} = -\frac{VdV}{vp} = -\frac{VdV}{RT} = -\kappa M^2 \frac{dV}{V} \tag{4.140}$$

Step 2: We combine the differential form of the continuity equation (4.138) with the differential form of the equation of state for ideal gases. With this step we eliminate the density from Eq. (4.138), we have

$$\frac{dV}{V} + \frac{dp}{p} = \frac{dT}{T} \tag{4.141}$$

To eliminate the velocity ratio in Eqs. (4.140) and (4.141), we use the definition of the Mach number. Its differentiation yields

$$\frac{dV}{V} = \frac{dM}{M} + \frac{1}{2}\frac{dT}{T} \tag{4.142}$$

Step 3: Inserting the velocity ratio (4.142) into momentum equation (4.140) and the equation of motion (4.138), we obtain for the pressure ratio,

$$\frac{2}{\kappa M^2}\frac{dp}{p} - 2\frac{dM}{M} = \frac{dT}{T} \tag{4.143}$$

We also replace in continuity equation (4.141) the velocity ratio with Eq. (4.142) and find a second equation for temperature ratio,

$$\frac{2dp}{p} + \frac{2dM}{M} = \frac{dT}{T} \tag{4.144}$$

Step 4: Equating (4.143) and (4.144), we find

$$\frac{dp}{p} = \frac{2\kappa M dM}{1+\kappa M^2} \tag{4.145}$$

The above equation can be integrated between any two positions including the one where $M = 1$

$$\frac{p_2}{p_1} = \frac{1+\kappa M_1^2}{1+\kappa M_2^2} \tag{4.146}$$

and for the critical state

$$\frac{p}{p*} = \frac{1+\kappa}{1+\kappa M^2} \tag{4.147}$$

In a similar manner, the temperature ratio calculated as,

$$\frac{dT}{T} = 2\frac{dM}{M}\left(\frac{1-\kappa M_1^2}{1+\kappa M_2^2}\right) \tag{4.148}$$

Considering the initial assumption of cholerically perfect gas, the integration gives,

$$\frac{T_2}{T_1} = \frac{h_2}{h_1} = \frac{M_2^2}{M_1^2}\left(\frac{1+\kappa M_1^2}{1+\kappa M_2^2}\right)^2 \tag{4.149}$$

and relative to critical state, we have

$$\frac{T}{T*} = \frac{h}{h*} = M^2\left(\frac{1+\kappa}{1+\kappa M_2^2}\right)^2 \tag{4.150}$$

In the same manner, we find the flow quantities such as the velocity, density, and specific volume ratios for the Rayleigh process as functions of the Mach number. These quantities are listed in Table 4.1. With these quantities as functions of a Mach number, the entropy change is determined by using any of the two equations (4.94) or (4.95).

$$\Delta s = c_p \ln\left[\left(\frac{T_2}{T_1}\right)\left(\frac{p_1}{p_2}\right)^{\frac{\kappa-1}{\kappa}}\right] = c_v \ln\left[\left(\frac{T_2}{T_1}\right)\left(\frac{v_2}{v_1}\right)^{\kappa-1}\right] \tag{4.151}$$

In terms of critical state:

$$\Delta s = s - s* = c_p \ln\left[\left(\frac{T}{T*}\right)\left(\frac{p*}{p}\right)^{\frac{\kappa-1}{\kappa}}\right] = c_v \ln\left[\left(\frac{T}{T*}\right)\left(\frac{v}{v*}\right)^{\kappa-1}\right] \tag{4.152}$$

Replacing the temperature and pressure ratios by the corresponding functions listed in Table 4.1, we find,

$$\frac{s - s*}{c_p} = \ln\left(M^2\frac{(k+1)M^2}{(1+\kappa M^2)^2}\right)^{\frac{\kappa+1}{\kappa}} \tag{4.153}$$

The above properties can be determined by varying the Mach number. As mentioned previously, a Rayleigh curve is the location of all constant momentum processes. It can be easily constructed by varying the Mach number and finding the corresponding, enthalpy, pressure, or entropy ratios. Figure. 4.31 shows the enthalpy ratio as a function of entropy difference. Moving along the subsonic upper branch, the addition of heat causes the specific volume and, consequently, the velocity and the Mach number to increase until the speed of sound has been reached, where

$$V^2 = \left(\frac{dp}{d\varrho}\right)_R = \left(\frac{\partial p}{\partial \varrho}\right)_s = c^2, \tag{4.154}$$

and the Mach number approaches 1. On the upper branch of the curve (the subsonic branch), we see there is a region where the enthalpy decreases with increasing entropy. For a perfect gas this means that the temperature decreases there while the entropy increases. However, we cannot move through point $M = 1$ from either the subsonic or the supersonic branch by heating, since the entropy would then have to decrease under heating.

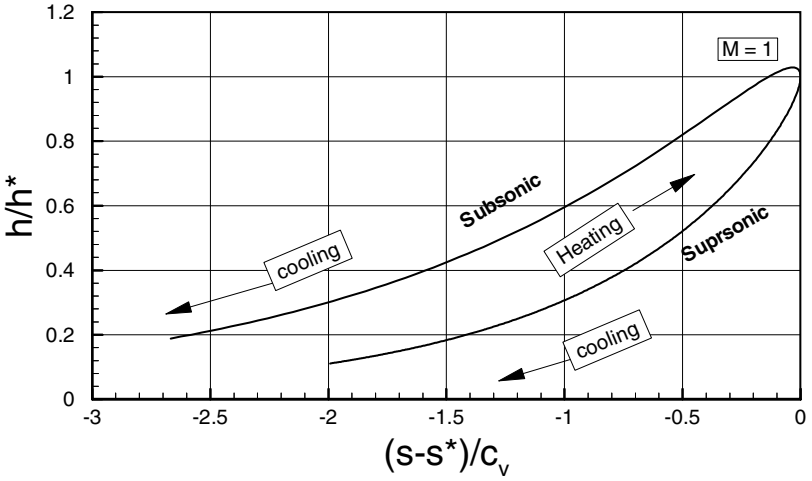

Fig. 4.31: Rayleigh curve for ideal two-atomic gases ($\kappa = 1.4$)

We now consider the case of Fanno process. It is characterized by constant total enthalpy, where no heat is supplied in a duct of constant cross-section. The flow is considered as non-isentropic, where internal, as well as, wall friction may exist. As a result, the static enthalpy experiences a continuous decrease, while the velocity increases. To generate the Fanno curve, first the flow quantities are expressed in terms of Mach number in a manner similar to the Rayleigh process presented above. The corresponding relations are summarized in Table 4.1.

Applying the energy, continuity, and impulse to an adiabatic constant cross-section duct flow, we find the pressure ration from

$$\frac{p}{p*} = \frac{1}{M}\left(\frac{\kappa + 1}{2(1 + \frac{\kappa-1}{2}M^2)}\right) \tag{4.155}$$

The other thermodynamic properties are calculated from:

$$\frac{T}{T*} = \frac{\frac{\kappa + 1}{2}}{1 + \frac{\kappa-1}{2}M^2}, \quad \frac{h}{h*} = \frac{\frac{1 + \kappa}{2}}{1 + \frac{\kappa-1}{2}M^2}, \quad \frac{\rho*}{\rho} = M\left(\frac{\frac{1 + k}{2}}{2(1 + \frac{\kappa-1}{2}M^2)}\right)^{\frac{1}{2}} \tag{4.156}$$

Finally, the velocity ratio is given by

$$\frac{V}{V*} = M\left(\frac{\frac{1+k}{2}}{2(1+\frac{\kappa-1}{2}M^2)}\right)^{\frac{1}{2}} \tag{4.157}$$

Taking the pressure and temperature ratios from Eqs. (4.155) and (4.156), we obtain the entropy difference from,

$$s - s* = \Delta s = c_p \ln\left[\left(\frac{T}{T*}\right)\left(\frac{p*}{p}\right)^{\frac{\kappa-1}{\kappa}}\right] \tag{4.158}$$

or in terms of Mach number, we obtain

$$\frac{\Delta s}{cp} = \frac{s - s*}{c_p} = \ln\left(M^2\frac{(k+1)M^2}{(1+\kappa M^2)^2}\right)^{\frac{\kappa+1}{\kappa}} \tag{4.159}$$

the Fanno curve in an *h-s* diagram plotted in Fig. 4.32. This curve is valid for a duct flow without heating, independent of the wall and internal friction.

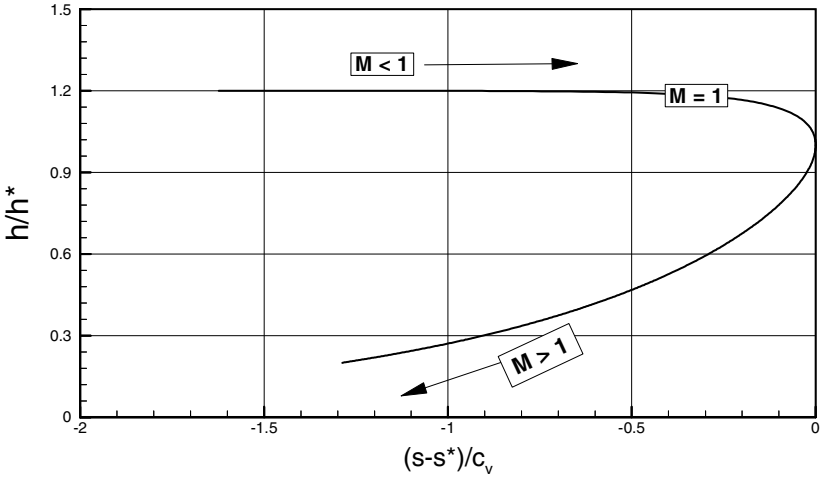

Fig. 4.32: Fanno curve for ideal two atomic gases (κ = 1.4).

The upper part of the curve is the subsonic branch and the lower is the supersonic branch. Considering a flow through a long pipe, because of the entropy increase, the static enthalpy, the static pressure, and the density decreases. As a consequence, the velocity increases until the speed of sound with Mach number $M = 1$ has been reached. A further increase of the velocity pass the speed of sound resulting in $M > 1$, requires a decrease in entropy which violates the second law. Therefore, the velocity cannot exceed the speed of sound. Figure. 4.33 shows a typical application of Fanno process. The high pressure side of a steam turbine shaft is sealed against the

atmospheric pressure. To reduce the mass flow that escapes from the process through the radial gap between the shaft and the casing, labyrinth seals are installed on the shaft and in the casing, Fig. 4.33 (a). High pressure steam enters the gap and expands through the clearance *C*, where its potential energy is converted into kinetic energy. By entering the cavity, the kinetic energy is dissipated causing a noticeable pressure decrease. The process of expansion and dissipation repeats in the following cavities resulting in a relatively small mass flow that leaves the turbine. The end points of all expansions through the clearances are located on a Fanno line, which corresponds to a constant total enthalpy.

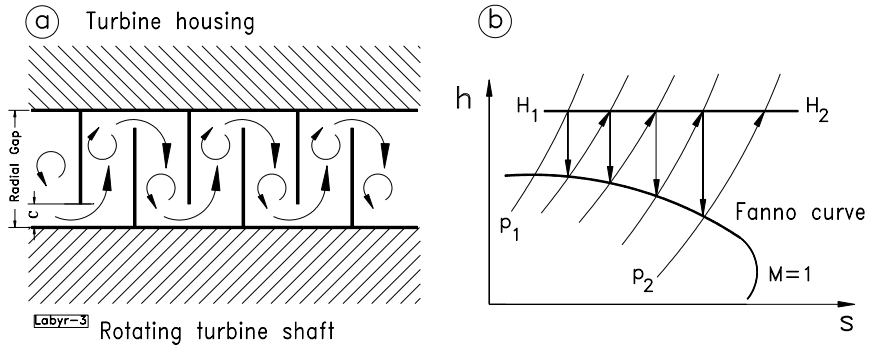

Fig. 4.33: Flow through a labyrinth seal of turbomachine (a) dissipation of kinetic energy, (b) Fanno process.

In Table 1, the equations are summarized and steps are marked that are necessary for construction of Rayleigh and Fanno lines. Fanno and Rayleigh curves are constructed using the following steps. In step ① the Mach number is varied and the corresponding thermodynamic properties are calculated from steps ② to ⑤. With the temperature and pressure ratios calculated in steps ① and ②, the entropy can be calculated. These steps were performed to plot Fig. 4.31 and Fig. 4.32. Once the thermodynamic properties are calculated, different versions of Fanno and Rayleigh curves can be constructed easily.

4.7.4 The Normal Shock Wave Relations

The shock wave mentioned in connection with the nozzle flow, i.e., the discontinuous transition from supersonic to subsonic velocity, occurs very often in supersonic flows. Here we present a brief discussion of the *normal shock wave*, in which the shock surface is perpendicular to the velocity. However, the more general relations of the *oblique shock wave* are obtained from the results and presented in the following section. Detailed discussion of this topic can be found in excellent books by Spurk [2], Shapiro [3], and Prandtl et al.[5].

For most purposes, it is enough to consider the shock wave as a surface of discontinuity across which the flow variables suddenly change. Strictly speaking, the shock is not a surface of discontinuity. The quantities actually change continuously

Table 4.2: Summary of steps and equations for construction of Rayleigh and Fanno curves

Rayleigh Characteristics	Fanno Characteristics
$\frac{A}{A*} = 1$	$\frac{A}{A*} = 1$
① $\frac{p}{p*} = \left(\frac{\kappa+1}{1+\kappa M^2}\right)$	$\frac{p}{p*} = \frac{1}{M}\left(\frac{\kappa+1}{2(1+\frac{\kappa-1}{2}M^2)}\right)^{1/2}$
$\frac{T}{T*} = M^2\left(\frac{\kappa+1}{(1+\kappa)M^2}\right)^2$ ②	$\frac{T}{T*} = \frac{\frac{\kappa+1}{2}}{1+\frac{\kappa-1}{2}M^2}$
$\frac{h}{h*} = M^2\left(\frac{\kappa+1}{(1+\kappa)M^2}\right)^2$ ③	$\frac{h}{h*} = \frac{\frac{1+\kappa}{2}}{1+\frac{\kappa-1}{2}M^2}$
④ $\frac{V}{V*} = \frac{(k+1)M^2}{1+\kappa M^2}$	$\frac{V}{V*} = M\left(\frac{\frac{1+k}{2}}{2(1+\frac{\kappa-1}{2}M^2)}\right)^{\frac{1}{2}}$
⑤ $\frac{\rho*}{\rho} = \frac{(k+1)M^2}{1+\kappa M^2}$	$\frac{\rho*}{\rho} = M\left(\frac{\frac{1+k}{2}}{2(1+\frac{\kappa-1}{2}M^2)}\right)^{\frac{1}{2}}$
⑥ $\Delta s = c_p \ln\left[\left(\frac{T}{T*}\right)\left(\frac{p*}{p}\right)^{\frac{\kappa-1}{\kappa}}\right]$	⑥ $\Delta s = c_p \ln\left[\left(\frac{T}{T*}\right)\left(\frac{p*}{p}\right)^{\frac{\kappa-1}{\kappa}}\right]$
$\frac{s-s*}{c_p} = \ln\left(M^2\frac{(k+1)M^2}{(1+\kappa M^2)^2}\right)^{\frac{\kappa+1}{\kappa}}$ ⑥	$\frac{s-s*}{c_p} = \ln\left(M^2\frac{(k+1)M^2}{(1+\kappa M^2)^2}\right)^{\frac{\kappa+1}{\kappa}}$ ⑥

over a distance which is of the order of magnitude of the mean free path, and thus can be taken as infinitesimally small in almost all technical problems. Inside the shock, the heat conduction and friction effects play a decisive role and the structure can be determined from, among other things, the Navier-Stokes equations.

We briefly present relations from which the quantities behind the shock can be determined knowing the corresponding ones in front of the shock. We assume that changes in velocity and temperature in front and behind the actual shock vanish, or are at least much smaller than the changes within the shock itself. Since the thickness of the shock is very small, we neglect all volume integrals in the application of the conservation laws to the shock. In addition, we neglect the external heating, since the surface of integration S_w in the balance of energy tends to be zero. Using the control volume in Fig. 4.34, we apply the continuity equation,

$$\varrho_1 V_1 = \varrho_2 V_2 , \tag{4.160}$$

the balance of momentum,

$$\varrho_1 V_1^2 + p_1 = \varrho_2 V_2^2 + p_2 , \tag{4.161}$$

and the balance of energy,

$$\frac{V_1^2}{2} + h_1 = \frac{V_2^2}{2} + h_2 , \tag{4.162}$$

where the subscript 1 denotes the position just in front of the shock and the subscript 2 the position just behind (Fig. 4.34). Since the thickness of the shock is assumed to be infinitesimally small, the areas A_1 and A_2 are the same, even if the cross-section of the duct varies. In addition to the conservation laws, we introduce the equation of state to have the corresponding number of equations necessary to find the unknowns. This can be taken from steam or gas tables

$$p = p(\varrho , h) \tag{4.163}$$

or else for the perfect gas

$$p = \varrho h \frac{\kappa - 1}{\kappa} . \tag{4.164}$$

With these, knowing the state in front of the shock, the state behind the shock can be determined, and the shock structure itself does not need to be known.

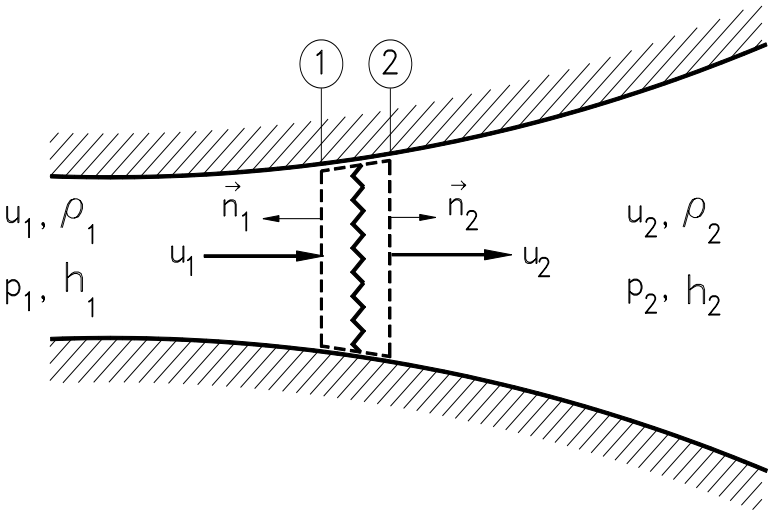

Fig. 4.34: Normal shock in a divergent channel

In general, only compression shock waves occur where $\varrho_2 > \varrho_1$, but expansion shock waves are also possible, according to the second law of thermodynamics if the inequality $(\partial^2 p/\partial v^2)_s < 0$ holds, as is possible, for example, near the critical point. Using a real gas whose p-v-T behavior is given by the Mollier diagram, we insert the continuity equation (4.160) into the balances of momentum (4.161) and of energy (4.162), we obtain:

$$p_2 - p_1 = \varrho_1 V_1^2 \left(1 - \frac{\varrho_1}{\varrho_2} \right) \tag{4.165}$$

and

$$h_2 - h_1 = \frac{V_1^2}{2} \left[1 - \left(\frac{\varrho_1}{\varrho_2} \right)^2 \right]. \tag{4.166}$$

For the calorically perfect gas, closed relations can be found eliminating the velocity V_1 from Eqs. (4.165) and (4.166) to obtain a relation between the thermodynamic quantities, the so-called *Hugoniot relation:*

$$h_2 - h_1 = \frac{1}{2}(p_2 - p_1) \left(\frac{1}{\varrho_1} + \frac{1}{\varrho_2} \right), \tag{4.167}$$

Using Eq. (4.164), we find for a perfect gas the following relation:

$$\frac{p_2}{p_1} = \frac{(\kappa + 1)\,\varrho_2/\varrho_1 - (\kappa - 1)}{(\kappa + 1) - (\kappa - 1)\,\varrho_2/\varrho_1}, \tag{4.168}$$

between the pressure and the density ratios. The maximum density ratio is obtained by the approaching the pressure ratio in Eq. (4.168) infinity:

$$\left(\frac{\varrho_2}{\varrho_1}\right)_{\max} = \frac{\kappa + 1}{\kappa - 1}. \tag{4.169}$$

Figure 4.35 shows the pressure ratio for normal shock as well as for the isentropic process. Contrary to this *Hugoniot* change of state, the isentropic change of state results for $p_2 / p_1 \to \infty$ in an infinitely large density ratio ϱ_2/ϱ_1. The maximum density ratio across a shock for diatomic gases with $\kappa = c_p/c_v = 7/5$ is then $\varrho_2/\varrho_1 = 6$. The limit for the temperature ration can also be obtained by using equation of state for the change of state:

$$\frac{p_2}{p_1} = \frac{\varrho_2}{\varrho_1}\frac{T_2}{T_1} \tag{4.170}$$

Setting in Eq. (4.170) the limit $p_2 / p_1 \to \infty$ results in $T_2 / Tp_1 = \infty$. From Eq. (4.165) the velocity can be obtained as:

$$V_1^2 = \frac{p_1}{\varrho_1}\left(\frac{p_2}{p_1} - 1\right)\left(1 - \frac{\varrho_1}{\varrho_2}\right)^{-1} \tag{4.171}$$

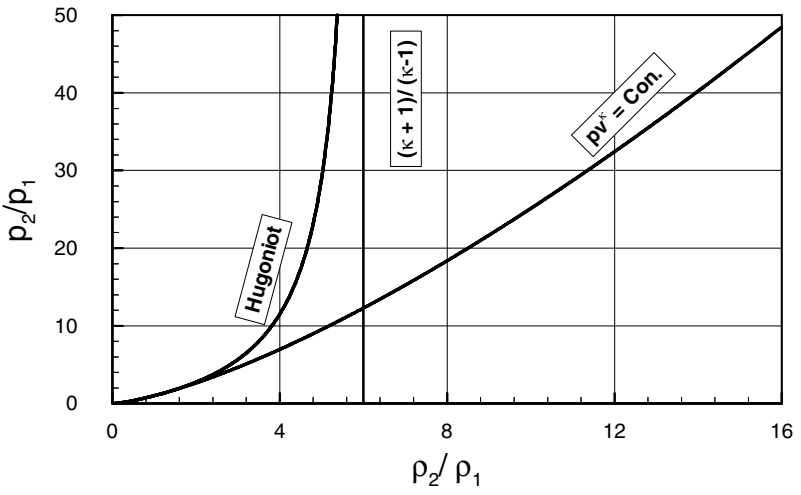

Fig. 4.35: Shock and isentropic compression.

Introducing the speed of sound $c^2 = \kappa p/\varrho$ for calorically perfect gases, Eq. (4.171) can be modified as:

$$\left(\frac{V_1}{c_1}\right)^2 = M_1^2 = \frac{1}{\kappa}\left(\frac{p_2}{p_1} - 1\right)\left(1 - \frac{\varrho_1}{\varrho_2}\right)^{-1} \tag{4.172}$$

from which we can eliminate ϱ_1/ϱ_2 using the Hugoniot relation (4.168). In this manner, we obtain an equation for the pressure ratio

$$\left(\frac{p_2}{p_1} - 1\right)^2 - 2\,\frac{\kappa}{\kappa + 1}\left(M_1^2 - 1\right)\left(\frac{p_2}{p_1} - 1\right) = 0\,, \tag{4.173}$$

Equation (4.173) has two solutions: $p_2/p_1 = 1$ (no shock) and

$$\frac{p_2}{p_1} = 1 + 2\,\frac{\kappa}{\kappa + 1}\left(M_1^2 - 1\right). \tag{4.174}$$

This is an explicit relation between the pressure ratio across the shock and the Mach number M_1 in front of the shock. For $M_1 = 1$, both solutions merge into one another and the shock becomes a sound wave. Equation (4.174) shows that, for a shock wave ($p_2/p_1 > 1$), the Mach number M_1 must be greater than one, and that for a very strong shock $M_1 \to \infty$, the pressure ratio tends to be infinity. If we replace p_2/p_1 in Eq. (4.174) using the Hugoniot relation (4.168), we acquire the equation for the jump in density,

$$\frac{\varrho_2}{\varrho_1} = \frac{(\kappa + 1)M_1^2}{2 + (\kappa - 1)M_1^2} \tag{4.175}$$

The temperature jump is obtained by using Eq. (4.174) and (4.175):

$$\frac{T_2}{T_1} = \frac{p_2}{p_1}\,\frac{\varrho_1}{\varrho_2} = \frac{\left(2\kappa M_1^2 - (\kappa - 1)\right)\left(2 + (\kappa - 1)M_1^2\right)}{(\kappa + 1)^2 M_1^2}\,. \tag{4.176}$$

To find the Mach number behind the shock, we use the continuity equation and the speed of sound to get

$$M_2^2 = \left(\frac{V_2}{a_2}\right)^2 = V_1^2\left(\frac{\varrho_1}{\varrho_2}\right)^2 \frac{\varrho_2}{\kappa p_2} = M_1^2\,\frac{p_1\varrho_1}{p_2\varrho_2}\,, \tag{4.177}$$

Introducing Eqs. (4.174) and (4.175) into (4.177), we finally find:

$$M_2^2 = \frac{\kappa + 1 + (\kappa - 1)\left(M_1^2 - 1\right)}{\kappa + 1 + 2\kappa\left(M_1^2 - 1\right)} . \tag{4.178}$$

We infer from this equation that in a normal shock wave, because $M_1 > 1$, the Mach number behind the shock is always lower than 1. In the case of a very strong shock M_2 takes on the limiting value

$$M_2\Big|_{(M_1 \to \infty)} = \sqrt{\frac{1}{2}\,\frac{\kappa - 1}{\kappa}} . \tag{4.179}$$

The shock relations are shown in Fig. 4.36.

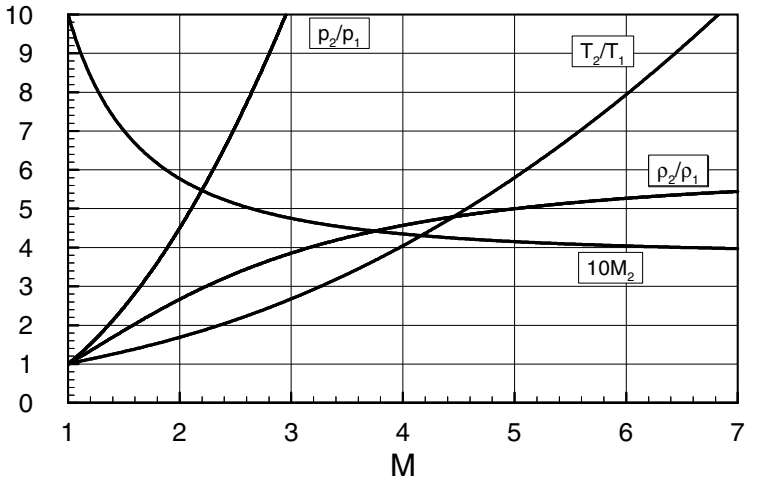

Fig. 4.36: Mach number and the thermodynamic properties behind the shock as a function of Mach number ahead of the shock.

Because of the irreversible processes (friction, heat conduction), the entropy increases through the shock. We can confirm this explicitly for the calorically perfect gases by using the second law:

$$s_2 - s_1 = c_v 1n\left[\frac{p_2}{p_1}\left(\frac{\varrho_2}{\varrho_1}\right)^{-\kappa}\right] \tag{4.180}$$

Eliminating the density ratio using the Hugoniot relation we find :

$$s_2 - s_1 = c_v 1n \left[\frac{p_2}{p_1} \left(\frac{(\kappa - 1)p_2/p_1 + \kappa + 1}{(\kappa + 1)p_2/p_1 + \kappa - 1} \right)^{\kappa} \right] . \tag{4.181}$$

For a strong shock $p_2 / p_1 \rightarrow \infty_1$, the entropy difference tends approaches infinity. However, for a weak shock with a pressure ratio in the order of $p_2/p_1 = 1 + \varepsilon$ and small ε, the right-hand side of Eq.(4.181) is expanded resulting in :

$$\frac{s_2 - s_1}{c_v} = \frac{\kappa^2 - 1}{12\kappa^2} \left(\frac{p_2 - p_1}{p_1} \right)^3 . \tag{4.182}$$

Equation. (4.182) shows that for calorically perfect gases, $p_2 - p_1$ must always be greater than zero so that only compression shock waves can occur, since otherwise the entropy would have to decrease across the shock.

4.7.5 Oblique Shock Wave Relations

In the previous section we dealt with the normal shock wave, a special type of shock that is perpendicular to the flow direction. The more prevalent shocks encountered in turbomachine flow paths such as transonic turbine or compressor blade channels are the oblique shocks. The basic mechanism of the oblique shock is shown in Fig. 4.37a.

Supersonic flow with uniform velocity V_1 approaches a wedge with a sharp angle 2δ. A surface discontinuity characterized by an oblique shock wave is formed that builds an angle Θ with the flow direction. This particular shock is called the attached shock. Following a streamline by passing through the shock front, the streamline is deflected by an angle which corresponds to the wedge angle $(2\delta)_a$. A different shock pattern is observed when the same supersonic flow approaches another wedge with $(2\delta)_b > (2\delta)_a$, as shown in Fig. 4.37b. Again, following an arbitrary streamline

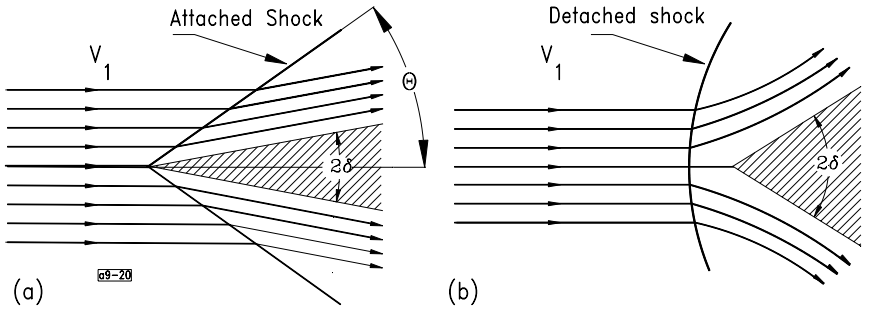

Fig. 4.37: A qualitative picture or two different shock patterns based on the same supersonic Mach number but different wedge angle 2δ

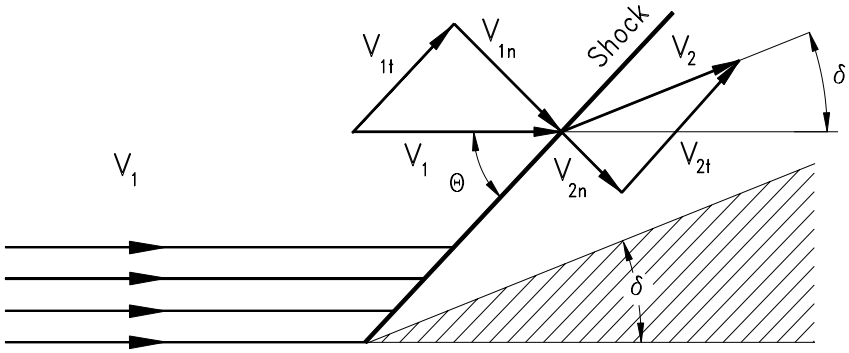

Fig. 4.38: Incoming velocity vector V_1 decomposed into normal and tangential components. Θ = Shock angle, δ = Half wedge angle.

upstream of the leading edge, a *strong shock* is formed which is detached. Figure 4.37(a) and (b) suggests that, depending on the magnitude of the incoming Mach number and the wedge angle or, generally body bluntness, attached or detached shocks may occur. To establish the corresponding relationships between the Mach number, the wedge angle, and the angle of the oblique shock, we use the same procedure that we applied to the normal shock waves. To do this, we decompose the velocity vector $\boldsymbol{V_1}$ in front of the shock into a component normal to the shock front V_{1n}, and a component tangential to the shock front V_{1t}, as shown in Fig. 4.38. The tangential component is

$$V_{1t} = V_1 \cos\Theta \,. \tag{4.183}$$

and the normal component follows from

$$V_{1n} = V_1 \sin\Theta \,, \tag{4.184}$$

Introducing the normal Mach number built with the normal component, we arrive at:

$$M_{1n} = \frac{V_{1n}}{a_1} = M_1 \sin\Theta \,. \tag{4.185}$$

The shock relations(4.174), (4.175) , and(4.176) , can then be carried over to the oblique shock wave, by replacing M_1, with M_{1n}, from (4.185) :

$$\frac{p_2}{p_1} = 1 + 2\frac{\kappa}{\kappa + 1}\left(M_1^2 \sin\Theta - 1\right), \tag{4.186}$$

$$\frac{\varrho_2}{\varrho_1} = \frac{(\kappa+1)M_1^2 \sin^2\Theta}{2+(\kappa-1)M_1^2 \sin^2\Theta}, \tag{4.187}$$

$$\frac{T_2}{T_1} = \frac{\left[2\kappa M_1^2 \sin^2\Theta - (\kappa-1)\right]\left[2+(\kappa-1)M_1^2 \sin^2\Theta\right]}{(\kappa+1)^2 M_1^2 \sin^2\Theta}. \tag{4.188}$$

Behind the oblique shock, the Mach number is formed with V_2, therefore $M_2 = V_2/a_2$. Since $V_{2n} = V_2 \sin(\Theta - \delta)$ holds, it follows that

$$M_{2n} = \frac{V_{2n}}{c_2} = M_2 \sin(\Theta - \delta). \tag{4.189}$$

Relative to the shock front, the normal component M_{1n}, which might be supersonic, experiences a drastic deceleration resulting in a subsonic normal component M_{2n} behind the shock. The Mach number M_2, however, can be supersonic. If we again replace M_1 and M_2 with M_{1n} and M_{2n} in the Eq. (4.178) valid for a normal shock, we find:

$$M_2^2 \sin^2(\Theta - \delta) = \frac{\kappa + 1 + (\kappa-1)\left(M_1^2 \sin^2\Theta - 1\right)}{\kappa + 1 + 2\left(M_1^2 \sin^2\Theta - 1\right)} \tag{4.190}$$

Using the continuity equation, we can transform this into a relation between the shock angle Θ and the wedge angle δ (Fig. 4.38):

$$\tan\delta = \frac{2\cot\Theta\left[M_1^2 \sin^2\Theta - 1\right]}{2+M_1^2\left[\kappa+1-2\sin^2\Theta\right]}. \tag{4.191}$$

Since the incoming Mach number M_1 and the wedge angle δ are supposed to be known, we have with Eqs. (4.190) and (4.191) two equations and two unknowns namely Θ and M_2. As shown in Fig. 39(a,b) for each given δ, two solutions, a strong shock and a weak shock, can be found based on the magnitude of the incoming M_1. A shock is called a *strong shock* if the shock angle Θ for a given Mach number M_1 is larger than the angle Θ_{max} (dashed curve in Fig 4.39a) associated with the maximum deflection δ_{max}; otherwise, we will talk of a *weak shock.* In a weak shock, the fluid velocity behind the shock can lie in either the subsonic or the supersonic range, but behind a strong shock, the flow is always subsonic. If the deflection angle δ is smaller than δ_{max}, there are then two possible solutions for the shock angle Θ. Which solution

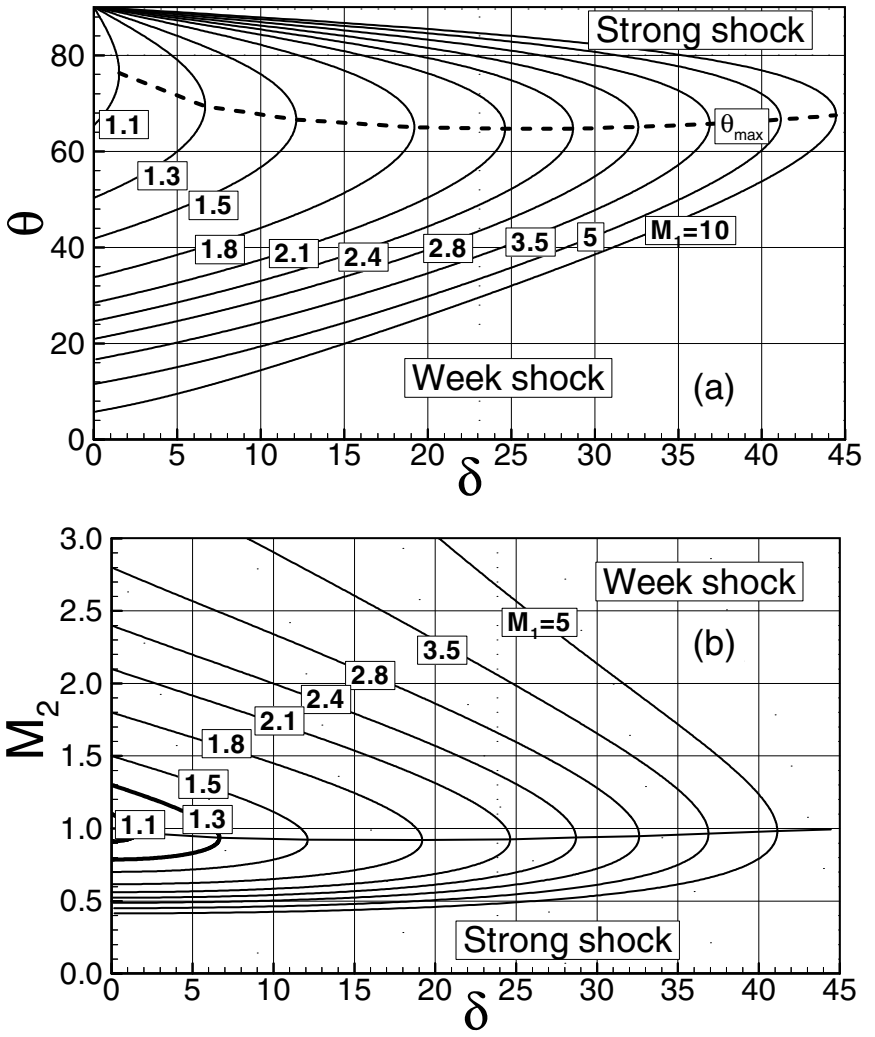

Fig. 4.39(a,b): Shock angle (a) and Mach number (b) as functions of deflection angle with incoming Mach number as parameter.

actually arises depends on the boundary conditions far behind the shock.Figure 4.39(b) displays the Mach number after the shock. Here again, strong shock leads to a subsonic mach number after the shock, whereas a week shock may maintain the supersonic character of the flow.

4.7.6 Detached Shock Wave

We now consider deflection angles $\delta > \delta_{max}$; these lead to flows past "blunt wedges". If, for a given Mach number M_1 a deflection angle δ larger than δ_{max} arises, a

detached shock is the only possibility. Both strong and weak shocks are then realized in the shock configuration as Fig. 4.39 reveals. Close to the stagnation streamline the wave angle is around 90° (strong shock, subsonic flow behind the shock), while at greater distances from the body the shock deteriorates into a Mach wave ($\Theta = \mu$). It is difficult to calculate the resulting flow behind the shock, since subsonic flow, supersonic flow and flow close to the velocity of sound all appear together (*transonic flow*).

4.7.7 Prandtl-Meyer Expansion

Unlike the supersonic flow along a concave surface which was associated with an oblique shock leading to a Mach number $M_2 < M_1$, the flow along a convex surface, Fig. 4.40, experiences an expansion process.

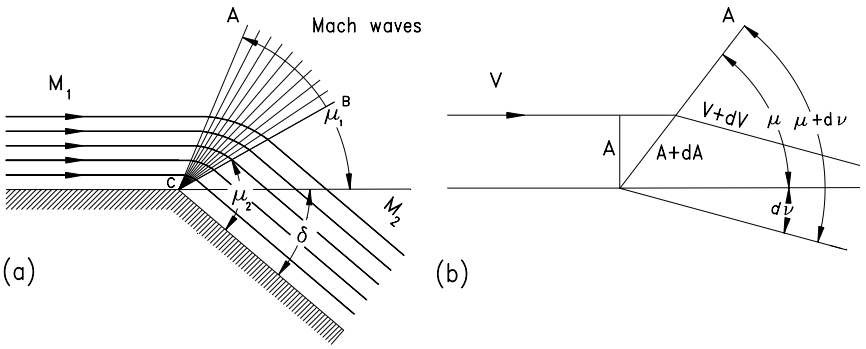

Fig. 4.40: Prandtl-Meyer Expansion around a corner

The parallel streamlines with the uniform Mach number M_1 passes through a system of expansion or Mach waves, thereby they move apart from each other and accelerate to a new Mach number $M_2 > M_1$. The expansion is associated with a deflection of the incoming supersonic flow with the Mach angle μ_1 to μ_2. To calculate the new Mach number, we first consider a supersonic flow around a corner of an infinitesimal deflection, *dA*, as shown in Fig. 4.40, and apply the continuity equation (4.133):

$$\frac{dA}{A} = -\frac{dV}{V}\left(1 - M^2\right) \tag{4.192}$$

The velocity ratio is expressed in terms of Mach number by utilizing the energy equation

$$\frac{dV}{V} = \frac{dM}{M\left(1 + \frac{\kappa - 1}{2}M^2\right)} \tag{4.193}$$

Inserting Eq. (4.193) into (4.192), we obtain:

$$\frac{dA}{A} = \frac{(M^2 - 1)\,dM}{M(1 + \frac{\kappa - 1}{2}M^2)} \tag{4.194}$$

The geometric relation from Fig. 4.40 reads:

$$\frac{A + dA}{A} = \frac{\sin(\mu + d\nu)}{\sin\mu} = \frac{\sin\mu\cos dv + \cos\mu\sin dv}{\sin\mu} = 1 + d\nu\cot\mu \tag{4.195}$$

In Eq. (4.195), we assumed dv as infinitesimally small allowing to set: $\cos dv = 1$ and $\sin dv = d\nu$. With this approximation, Eq. (4.195) becomes:

$$\frac{dA}{A} = d\nu\cot\mu = d\nu\sqrt{M^2 - 1} \tag{4.196}$$

with μ as the Mach angle that can be expressed as $\sin\mu = 1/M$. Equating (4.196) and (4.194) leads to:

$$d\nu = \frac{\sqrt{(M^2 - 1)}\,dM}{M(1 + \frac{\kappa - 1}{2}M^2)} \tag{4.197}$$

and its subsequent integration gives:

$$\nu = \sqrt{\frac{\kappa + 1}{\kappa - 1}}\arctan\left(\sqrt{\frac{\kappa + 1}{\kappa - 1}}\sqrt{M^2 - 1}\right) - \arctan\sqrt{M^2 - 1} \tag{4.198}$$

This deflection angle ν as well as the Mach angle μ equation are plotted in 4.41.As shown, each arbitrary supersonic Mach number is uniquely associated with a deflection angle ν. As an example, we assume that in Fig. 4.41the flow has the Mach number $M_1 = 1.5$ and turns around a corner with an angle $\delta = 40^o$. For this Mach number, the corresponding deflection angle $\nu_1 = 12.2$ is found. After turning around the corner, the deflection is $\nu_2 = \nu_1 + \delta = 52.2$, which results in a Mach number of $M_2 = 3.13$.

The Prandtl-Meyer expansion theory is widely used for design and loss calculation of transonic and supersonic compressor blades. Although this topic is treated in the corresponding chapter, in the context of this section, it is useful to point to a few interesting features from turbomachinery design point of view. Figure 4.42 shows a supersonic compressor cascade with an inlet Mach number $M_\infty > 1$. The incoming supersonic flow impinges on the sharp leading edge and forms a weak

oblique shock, followed by an expansion fan. Passing through the shock front, the Mach number, although smaller, remains supersonic. Expansion waves are formed along the suction surface (convex side) of the blade from the leading edge *L* to the point *e*, where the subsequent Mach wave at point *e* wave intercepts the adjacent blade leading edge. Since the angle Θ is known, Mach number M_e at position *e* can easily be calculated from Prandtl-Meyer relation.

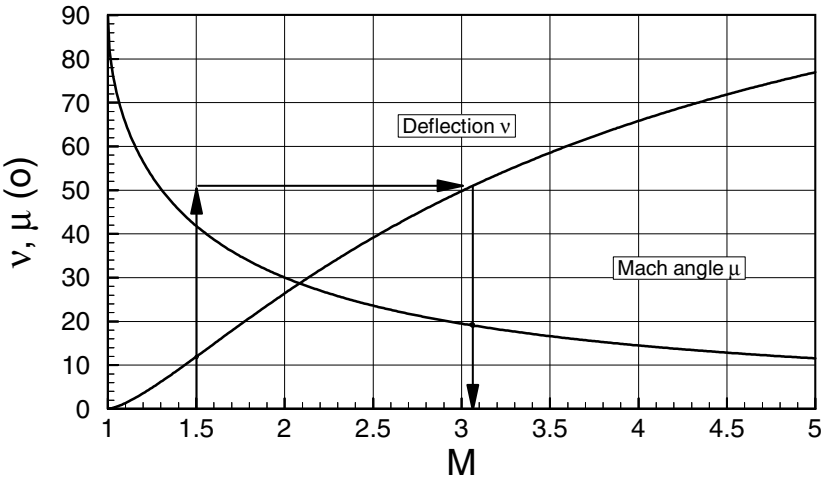

Fig. 4.41: Deflection angle ν and Mach angle μ as functions of Mach number.

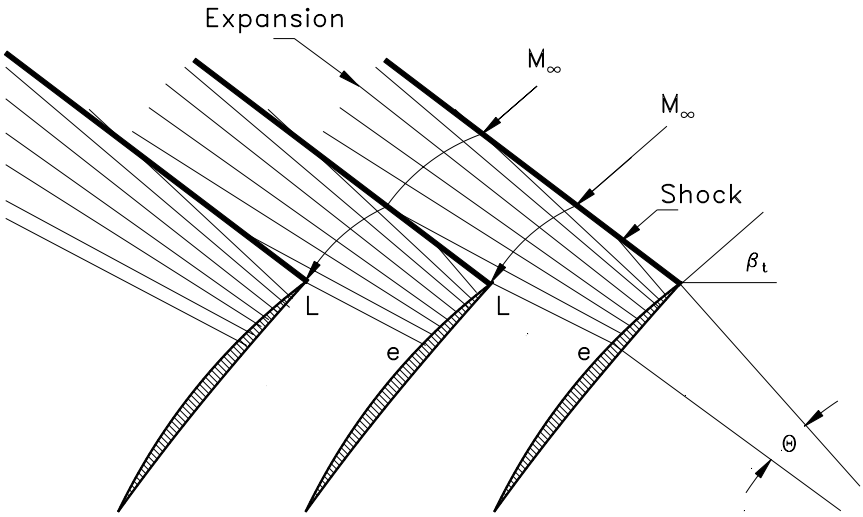

Fig. 4.42: A supersonic compressor cascade with supersonic inlet flow.

References, Chapter 4

4.1 Vavra, M.H, 1960, “Aero-Thermodynamics and Flow in Turbomachines,” John Wiley &S ons, Inc.
4.2 Spurk, J, 1997, “Fluid mechanics,” Springer-Verlag, berlin, Heidelberg, New York.
4.3 Shapiro, A.H., 1954, “The Dynamics and Thermodynamics of Compressible Fluid Flow,” Vol. I, Ronald Press Company, New York, 1954.
4.4 Becker, E., 1969, “Gasdynamik, Stuttgart, Teubner Studienbücher Mechanik, Leitfaden der angewandten Mathematik und Mechanik.
4.5 Prandtl, L., Oswatisch, K., Wiegarhd, K., 1984, “Führer durch die Strömung-lehre,” 8. Auflage, Branschweig, Vieweg Verlag.

5 Theory of Turbomachinery Stages

5.1 Energy Transfer in Turbomachinery Stages

The energy transfer in turbomachinery is established by means of the stages. A *turbomachinery stage* comprises a row of fixed, guide vanes called *stator blades*, and a row of rotating blades termed *rotor*. To elevate the total pressure of a working fluid, *compressor stages* are used that partially convert the mechanical energy into potential energy. According to the conservation law of energy, this energy increase requires an external energy input which must be added to the system in the form of mechanical energy. Figure 5.1 shows the schematic of an axial compressor stage that consists of one stator and two rotor rows. In general, a *compressor component* starts with a rotor row followed by a stator row. Compressor configurations are also found that start with an *inlet guide vane*. To define a unified station nomenclature for compressor and turbine stages, we identify with station number 1 as the inlet of the stator, followed by station 2 as the rotor inlet and 3, rotor exit. The absolute and relative flow angles are counted counterclockwise from a horizontal line. This convention allows an easier calculation of the off-design behavior of compressor and turbine stages during a transient operation, as we will see later. Different angle conventions are used in literature, [1], [2], [3], and [4] The working fluid enters the first rotor with an

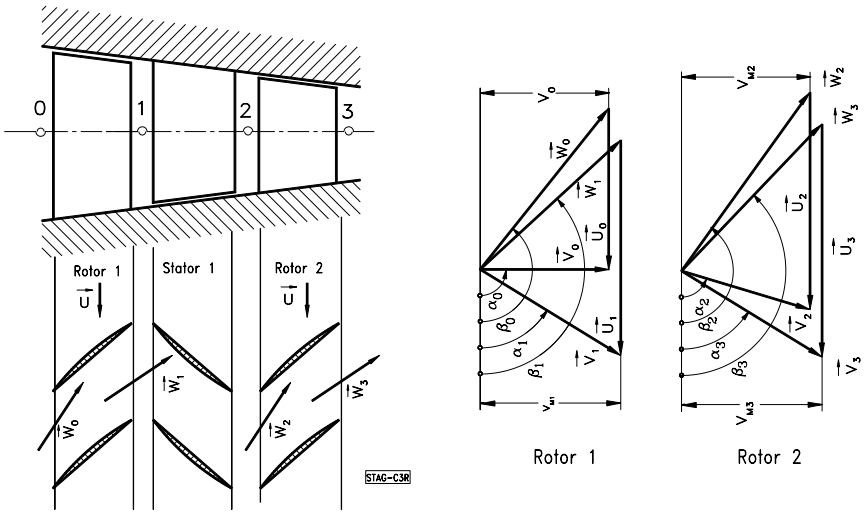

Fig. 5.1: An axial compressor stage with a rotor-stator-rotor configuration (left) and velocity diagrams for the first and second rotor (right).

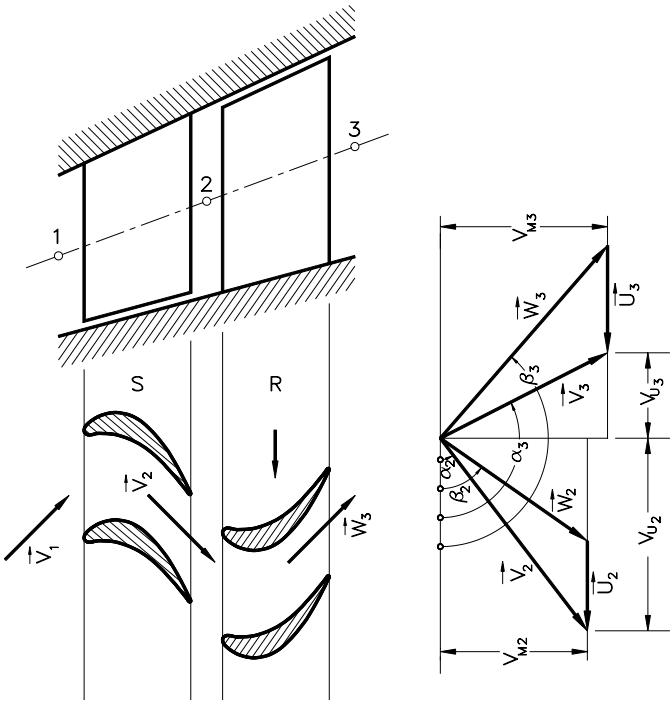

Fig. 5.2: An axial turbine stage with velocity diagram.

absolute velocity in the axial direction, Fig. 5.1 (right), where it is deflected in the direction of the rotor's leading edge. As a result of the rotational motion of the rotor, a major part of the mechanical energy input is converted into the potential energy of the working medium, causing the total pressure to rise. During the compression process, the absolute velocity within the stator and the relative velocity vector within the rotor decreases. To convert the total energy of a working medium into mechanical energy, *turbine stage*s are used. Figure 5.2 exhibits a turbine stage within a multi-stage environment. As shown, the mean diameter may change from inlet to exit. The continuous increase in flow path cross section is due to the continuity requirement.

5.2 Energy Transfer in Relative Systems

Since the rotor operates in a relative frame of reference (relative system), the energy conversion mechanism is quite different from that of a stator (absolute system). A fluid particle that moves with a relative velocity $\boldsymbol{W}$ within the relative system that rotates with the angular velocity ω, has an absolute velocity:

$$\boldsymbol{V} = \boldsymbol{W} + \boldsymbol{\omega}\times\boldsymbol{R} = \boldsymbol{W} + \boldsymbol{U}, \qquad \boldsymbol{\omega}\times\boldsymbol{R} = \boldsymbol{U} \tag{5.1}$$

with $\boldsymbol{R}$ in Eq. (5.1) as the radius vector of the particle in the relative system.

Introducing the absolute velocity vector ***V*** in the equation of motion, (3.37), and multiplying the results with a relative differential displacement *dR*, we get the energy equation for an adiabatic steady flow within a relative system:

$$d\left(h + \frac{1}{2}W^2 - \frac{\omega^2 R^2}{2} + gz \right) = 0 \tag{5.2}$$

or the relative total enthalpy (for details see Chapter 3):

$$H_r = h + \frac{1}{2}W^2 - \frac{\omega^2 R^2}{2} + gz = const. \tag{5.3}$$

Neglecting the gravitational term, gz ≈ 0, Eq. (5.3) can be written as:

$$h_1 + \frac{1}{2}W_1^2 - \frac{1}{2}U_1^2 = h_2 + \frac{1}{2}W_2^2 - \frac{1}{2}U_2^2 \tag{5.4}$$

Equation (5.4) is the energy equation transformed into a relative system. As can be seen, the transformation of kinetic energy undergoes a change while the transformation of static enthalpy is frame indifferent. With these equations in connection with the energy balance treated in Chapter 3, we can analyze the energy transfer within an arbitrary turbine or compressor stage.

5.3 General Treatment of Turbine and Compressor Stage

In this chapter, compressor and turbine stages are treated from a unified physical point of view. Figures 5.3 and 5.4 show the decomposition of a turbine and a compressor stage into their stator and rotor rows. The primes " / " and " // " refer to stator and rotor rows respectively. As seen, the difference between the isentropic and the polytropic enthalpy difference is expressed in terms of dissipation $\Delta h'_d = \Delta h_s - \Delta h'$. For the stator, the energy balance requires that $H_2 = H_{1:}$

$$h_1 - h_2 = \Delta h_s = \frac{1}{2}\left(V_2^2 - V_1^2\right) \tag{5.5}$$

Moving to the relative frame of reference, the relative total enthalpy $H_{r2} = H_{r3}$ remains constant. Thus, the energy equation for the rotor is according to Eq. (5.4), Fig. 5.4:

$$h_2 - h_3 = \Delta h_R = \frac{1}{2}\left(W_3^2 - W_2^2 + U_2^2 - U_3^2\right) \tag{5.6}$$

The stage specific mechanical energy balance requires (Fig. 5.5):

$$1_m = H_1 - H_3 = \left(h_1 - h_2\right) - \left(h_3 - h_2\right) + \frac{1}{2}\left(V_1^2 - V_3^2\right) \tag{5.7}$$

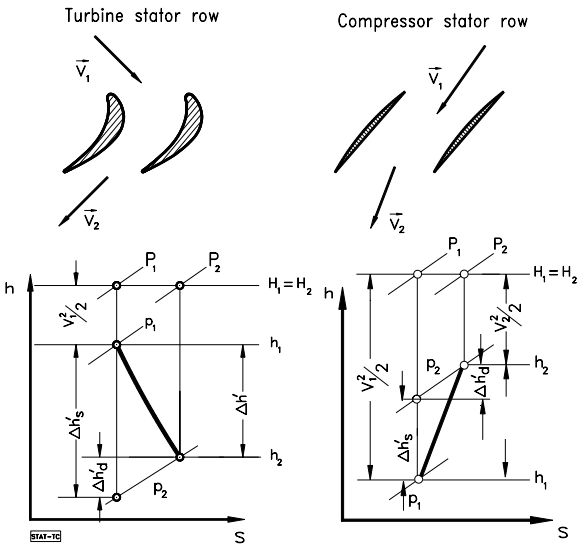

Fig. 5.3: Expansion and compression process through a turbine and a compressor stator row.

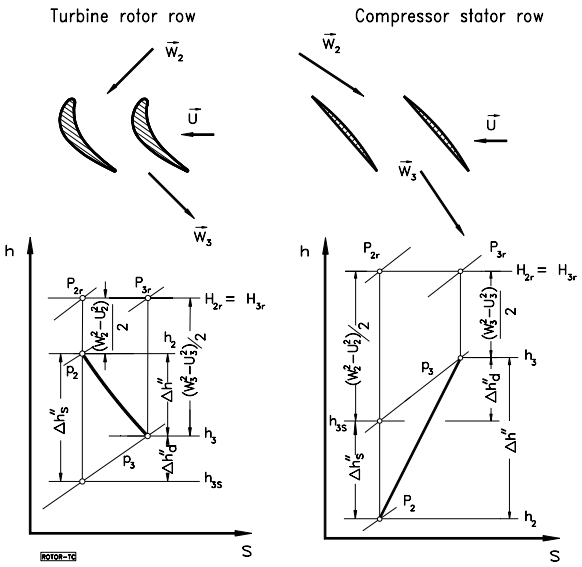

Fig. 5.4: Expansion and compression process through a turbine and a compressor rotor row.

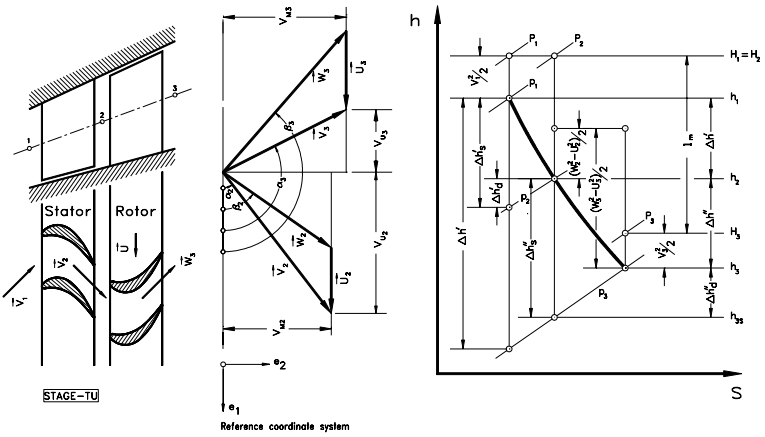

Fig. 5.5: A turbine stage (left) with the velocity diagram (middle) and the expansion process (right). The direction of the unit vector e_1 is identical with the rotational direction.

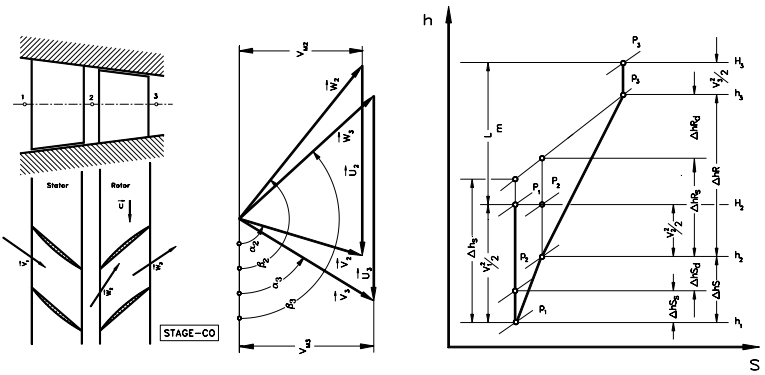

Fig. 5.6: A turbine stage (left) with the velocity diagram (middle) and the expansion process (right). The direction of the unit vector e_1 is identical with the rotational direction.

inserting Eq. (5.5) and (5.6) into (5.7) yields :

$$l_m = \frac{1}{2}\left[\left(V_2^2 - V_3^2\right) + \left(W_3^2 - W_2^2\right) + \left(U_2^2 - U_3^2\right)\right] \tag{5.8}$$

Equation (5.8), known as the *Euler Turbine Equation,* indicates that the stage work can be expressed simply in terms of absolute, relative, and rotational kinetic energies. This equation is equally applicable to turbine stages that *generate* shaft power and to compressor stages that *consume* shaft power. In the case of a turbine stage, the sign of the specific mechanical energy l_m is negative, which indicates that energy is removed from the system (power generation). In compressor cases, it is positive

because energy is added to the system (power consumption). Before proceeding with velocity diagrams, it is of interest to evaluate the individual kinetic energy differences in Eq. (5.8). If we wish to design a turbine or a compressor stage with a high specific mechanical energy l_m for a particular rotational speed, then we have two options: (1) We increase the *flow deflection* that leads to an increase in $(V_2^2 - V_3^2)$. (2) We increase the radial difference that leads to a larger $(U_2^2 - U_3^2)$. While option (1) is used in axial stages, option (2) is primarily applied to radial stages. These quantities are the characteristics of a stage velocity diagram at the corresponding radial section.

Using the trigonometric relation with the *angle convention* from the velocity diagram in Figs. 5.5 and 5.6, we determine the velocity components and vector relations from:

$$\begin{aligned} V_{m2} &= W_{m2}\,, \quad V_{m3} = W_{m3} \\ \boldsymbol{W}_2 &= e_1\left(V_{u2} - U_2\right) + \boldsymbol{e_2} V_{m2} \\ \boldsymbol{W}_3 &= -e_1\left(V_{u3} + U_3\right) + \boldsymbol{e_2} V_{m3} \end{aligned} \tag{5.9}$$

In Eq. (5.9) V_m, W_m and V_u, W_u are the meridional and circumferential components of the absolute and relative velocities, respectively. The corresponding kinetic energy contributions are determined from:

$$\begin{aligned} W_2^2 &= \left(V_{u2}^2 + V_{m2}^2\right) + U_2^2 - 2V_{u2}U_2 = V_2^2 + U_2^2 - 2V_{u2}U_2 \\ W_3^2 &= V_{u3}^2 + U_3^2 + 2V_{u3}U_3 + V_{m3}^2 \\ W_3^2 &= V_3^2 + U_3^2 + 2V_{u3}U_3 \end{aligned} \tag{5.10}$$

Incorporating Eq. (5.9) and (5.10) into (5.8) yields the *stage specific work*:

$$l_m = U_2 V_{u2} + U_3 V_{u3} \tag{5.11}$$

Equation (5.11) is valid for axial, radial, and mixed flow turbines and compressors. A similar relation was obtained in Chapter 4, Eq. (4.46), from the scalar product of moment of momentum and the angular velocity. There, we found the power: $P = \dot{m} U\left(V_{u1} - V_{u2}\right)$. In order to avoid confusions that may arise from different signs, it should be pointed out that in Chapter 4, no angle convention was introduced and the negative sign in Eq. (4.46) was the result of the formal derivation of the conservation law of moment of momentum. This negative sign implies that V_{u1} and V_{u2} point in the same direction. The unified angle convention introduced in Figs. 5.1 and 5.2, however, takes the actual direction of the velocity components with regard to a predefined coordinate system.

5.4 Dimensionless Stage Parameters

Equation (5.11) exhibits the direct relation between the specific stage work l_m and the kinetic energies. These velocities from which these kinetics are built can be taken from the corresponding stage velocity diagram. The objective of this chapter is to introduce dimensionless stage parameters that completely determine the stage velocity diagram. These stage parameters exhibit unified relations for compressor and turbine stages respectively.

Starting from a turbine or compressor stage with constant mean diameter and axial components, shown in Fig. 5.7, we define the dimensionless stage parameters that describe the stage velocity diagram of a *normal stage* introduced by Traupel [5]. A normal stage is encountered within the high pressure (HP) part of multi-stage turbines or compressor components and is characterized by $\boldsymbol{U}_3 = \boldsymbol{U}_2$, $\boldsymbol{V}_3 = \boldsymbol{V}_1$ and $V_{m1} = V_{m3}$, and $\alpha_1 = \alpha_3$. The similarity of the velocity diagrams allows using the same blade profile throughout the HP-turbine or compressor, thus significantly reducing manufacturing costs.

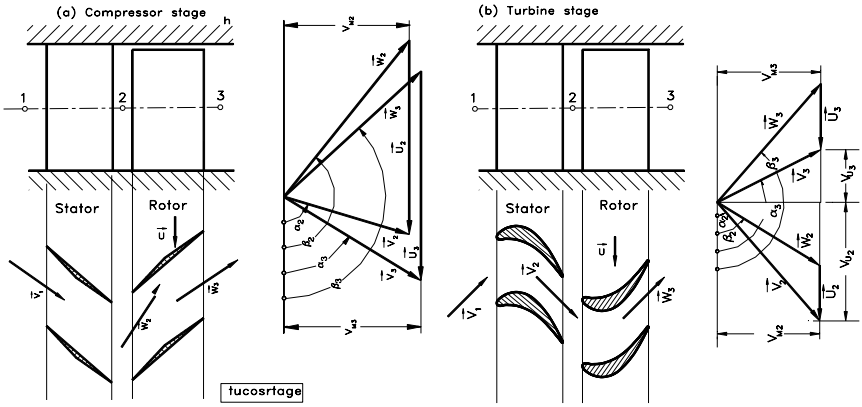

Fig. 5.7: Turbine and compressor stages with corresponding velocity diagrams.

We define the stage flow coefficient ϕ as the ratio of the meridional velocity components and the circumferential component. For this particular case, the meridional component is identical with the axial component:

$$\phi = \frac{V_{m3}}{U_3} \tag{5.12}$$

The stage flow coefficient ϕ in Eq. (5.12) is a characteristic for the mass flow behavior through the stage. The *stage load coefficient* λ is defined as the ratio of the specific stage mechanical energy l_m and the exit circumferential kinetic energy U_3^2. This coefficient directly relates the flow deflection given by the velocity diagram with the specific stage mechanical energy.

$$\lambda = \frac{l_m}{U_3^2} \tag{5.13}$$

The stage load coefficient λ in Eq. (5.13) describes the work capability of the stage. It is also a measure for the stage loading. The *stage enthalpy coefficient* ψ represents the ratio of the isentropic stage mechanical energy and the exit circumferential kinetic energy $U_3{}^2$.

$$\psi = \frac{l_s}{U_3^2} \tag{5.14}$$

The stage enthalpy coefficient represents the stage isentropic enthalpy difference within the stage. Furthermore, we define the *stage degree of reaction r*, which is the ratio of the static enthalpy difference used in rotor row divided by the static enthalpy difference used in the entire stage:

$$r = \frac{\Delta h''}{\Delta h'' + \Delta h'} \tag{5.15}$$

The degree of reaction r indicates the portion of energy transferred in the rotor blading. Using Eqs. (5.5) and (5.6), we arrive at:

$$r = \frac{\Delta h''}{\Delta h' + \Delta h''} = \frac{W_3^2 - W_2^2 + U_2^2 - U_3^2}{W_3^2 - W_2^2 + U_2^2 - U_3^2 + V_2^2 - U_1^2} \tag{5.16}$$

Since for the stage type under consideration, $V_1 = V_3$ and $U_2 = U_3$, Eq. (5.16) can be simplified as:

$$r = \frac{W_3^2 - W_2^2}{W_3^2 - W_2^2 + V_2^2 - V_3^2} \tag{5.17}$$

The velocity vectors and the corresponding kinetic energies are determined from the stage velocity diagram in connection with the angle and direction convention as follows :

$$\begin{aligned} \boldsymbol{V}_2 &= e_1(W_{u2} + U_2) + e_2 W_{m2}, \qquad V_2^2 = (W_{u2} + U_2)^2 + W_{m2}^2 \\ \boldsymbol{V}_3 &= -\boldsymbol{e_1}(W_{u3} + U_3) + \boldsymbol{e_2} W_{m3}, \qquad V_3^2 = (W_{u3} + U_3)^2 + W_{m3}^2 \end{aligned} \tag{5.18}$$

since $U_2 = U_3 = U$

$$V_2^2 - V_3^2 = W_2^2 - W_3^2 + 2UW_{u2} + 2UW_{u3} \tag{5.19}$$

Using Eqs. (5.18) and (5.19), Eq. (5.17) gives:

$$r = \frac{W_3^2 - W_2^2}{2U(W_{u2} + W_{u3})} = \frac{W_{u3}^2 - W_{u2}^2}{2U(W_{u2} + W_{u3})} \tag{5.20}$$

Re-arranging Equation (5.20) yields the final relationship for the particular stage we introduced above:

$$r = \frac{1}{2}\frac{W_{u3} - W_{u2}}{U} \tag{5.21}$$

5.5 Relation Between Degree of Reaction and Blade Height for a Normal Stage

In axial flow compressors or turbines, the working fluid has a rotational and translational motion. The rotating fluid is subjected to centrifugal forces that must be balanced by the pressure gradient in order to maintain the radial equilibrium. Consider an infinitesimal sector of an annulus with unit depth containing the fluid element which is rotating with tangential velocity V_u.

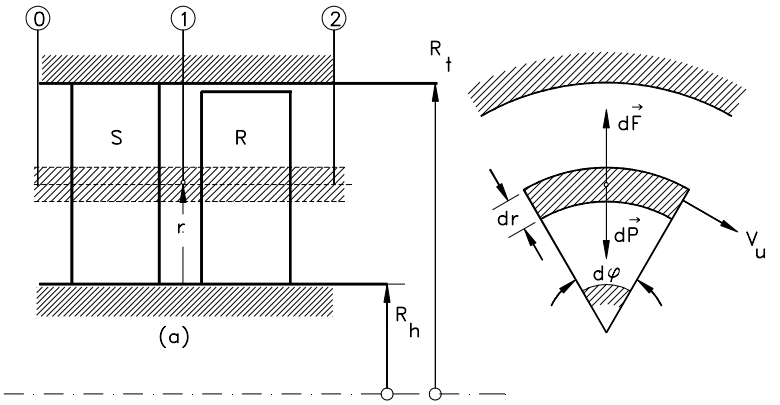

Fig. 5.8: Explanation for simple radial equilibrium

The centrifugal force acting on the element is shown in Fig. 5.8. Since the fluid element is in radial equilibrium, the centrifugal force is obtained from:

$$dF = dm\frac{V_u^2}{R} \tag{5.22}$$

with $dm = \rho R\, dR\, d\phi$. The centrifugal force is kept in balance by the pressure forces:

$$\frac{dp}{dR} = \rho\frac{V_u^2}{R} \tag{5.23}$$

This result can also be obtained by decomposing the Euler equation of motion (3.46) for inviscid flows in its three components in a cylindrical coordinate system. The Euler equation is expressed as:

$$\boldsymbol{V}\cdot\nabla\boldsymbol{V} = -\frac{1}{\rho}\nabla p \tag{5.24}$$

In the radial direction:

$$V_r\frac{\partial V_r}{\partial R} + V_u\frac{\partial V_r}{R\partial\phi} + V_z\frac{\partial V_r}{\partial z} - \frac{V_u^2}{R} = -\frac{1}{\rho}\frac{\partial p}{\partial R} \tag{5.25}$$

The assumptions needed to arrive at Eq. (5.23) are:

$$\frac{\partial V_r}{\partial R} \simeq 0 \quad , \quad \text{Axial symmetric:} \quad \frac{\partial V_r}{\partial\phi} = 0 \ , \quad \frac{\partial V_r}{\partial z} \simeq 0 \tag{5.26}$$

With these assumptions, Eq. (5.24) yields:

$$\frac{1}{\rho}\frac{\partial p}{\partial R} = \frac{V_u^2}{R} \ , \tag{5.27}$$

Equation (5.27) is identical to Eq. (5.23). Calculation of a static pressure gradient requires additional information from the total pressure relation. For this purpose, we apply the Bernoulli equation:

$$p_o = p + \frac{1}{2}\rho V^2 = p + \frac{1}{2}\rho(V_u^2 + V_{ax}^2) \tag{5.28}$$

Using Eq. (5.28), the change in radial direction is:

$$\frac{dp_o}{dR} = \frac{dp}{dR} + \rho V_u\frac{dV_u}{dR} + \rho V_{ax}\frac{dV_{ax}}{dR} \tag{5.29}$$

If the stagnation or total pressure $p_o = const.$ and $Vm = const.$, Eq.(5.29) yields:

$$\frac{dp}{dR} + \rho V_u\frac{dV_u}{dR} = 0 \ , \quad or \quad \frac{dp}{dR} = -\rho V_u\frac{dV_u}{dR} \tag{5.30}$$

Equating (5.30) and (5.23) results in:

$$V_u \frac{dV_u}{dR} + \frac{V_u^2}{R} = 0 \tag{5.31}$$

or

$$\frac{dV_u}{V_u} + \frac{dR}{R} = 0 \tag{5.32}$$

The integration of Eq. (5.32) leads to $V_u R = const.$ This type of flow is called free vortex flow and fulfills the requirement to be potential flow, $\nabla \times \boldsymbol{V} = const.$ We use this relation to rearrange the specific stage mechanical energy:

$$l_m = U_2 V_{u2} + U_3 V_{u3} = \omega\left(R_2 V_{u2} + R_3 V_{u3}\right) \tag{5.33}$$

At station (2) the swirl is $R_2 V_{u2} = const. = K_2$; likewise at station 3 the swirl is $R_3 V_{u3} = K_3$. Since $\omega = const.$, the specific stage mechanical energy is constant:

$$l_m = (K_2 + K_3)\omega = const. \tag{5.34}$$

Equation (5.34) implies that for a stage with constant spanwise meridional components and constant total pressure from hub to tip, the specific stage mechanical energy is constant over the entire blade height. To express the degree of reaction in spanwise direction, we replace the enthalpy differences in Eq. (5.15) by pressure differences. For this purpose we apply the first law for an adiabatic process through stator and rotor blades expressed in terms of $\Delta h'' = \bar{v}_R \Delta p''$ $\Delta h' = \bar{v}_S \Delta p'$ that lead to:

$$r = \frac{\bar{v}_R \Delta p_R}{\bar{v}_R \Delta p_R + \bar{v}_S \Delta p_s} = \frac{\Delta p_R}{\Delta p_R + \dfrac{\bar{v}_S}{\bar{v}_R}\Delta p_s} \cong \frac{p_2 - p_3}{p_1 - p_3} \tag{5.35}$$

In the above equation, the ratio of specific volumes was approximated as $\bar{v}_S / \bar{v}_R \cong 1$. This approximation is admissible for low Mach number ranges. Integrating Eq. (5.23) for station 1 from an arbitrary diameter R to the mean diameter R_m yields,

$$\left(p_1 - p_{m1}\right) = \frac{\rho}{2}\left(V_{um}\right)_1^2 \left(1 - \frac{R_m^2}{R^2}\right)_1 \tag{5.36}$$

At station (2) we have,

$$\left(p_2 - p_{m2}\right) = \frac{\rho}{2}\left(V_{um}\right)_2^2 \left(1 - \frac{R_m^2}{R^2}\right)_2 \tag{5.37}$$

and finally, at station (3) we arrive at:

$$\left(p_3 - p_{m3}\right) = \frac{\rho}{2}\left(V_{um}\right)_3^2 \left(1 - \frac{R_m^2}{R^2}\right)_3 \tag{5.38}$$

with $\left(R_m\right)_1 = \left(R_m\right)_2 = \left(R_m\right)_3$, and $V_{um3} = V_{um1}$. Introducing Eqs. (5.36) , (5.37) and (5.38) into (5.35), we finally arrive at a simple relationship for the degree of reaction:

$$\frac{1 - r}{1 - r_m} = \frac{R_m^2}{R^2} \tag{5.39}$$

From a turbine design point of view, it is of interest to estimate the degree of reaction at the hub and tip radius by inserting the corresponding radii into Eq. (5.39). As result, we find:

$$\frac{1 - r_h}{1 - r_m} = \left(\frac{R_m}{R_h}\right)^2 , \quad \frac{1 - r_t}{1 - r_m} = \left(\frac{R_m}{R_t}\right)^2 \tag{5.40}$$

Equation (5.40) represents a simple radial equilibrium condition which allows the calculation of the inlet flow angle in a radial direction by integrating Eq. (5.32):

$$V_u R = const.; \; R = \frac{const.}{V_u} \tag{5.41}$$

This leads to determination of the inlet flow angle in a spanwise direction,

$$\frac{R_m}{R} = \frac{cotg\,\alpha_1}{cotg\,\alpha_{1m}} \tag{5.42}$$

5.6 Effect of Degree of Reaction on the Stage Configuration

The distribution of degree of reaction can also be obtained by simply using the velocity ratio for *r*. If, for example, the degree of reaction at the mean diameter is set at *r = 50%*, Eq. (5.40) immediately calculates *r* at the hub and tip for the simple radial equilibrium condition $V_u R = const.$ as presented above. It should be mentioned that, for a turbine stage negative *r < 0* at the hub may lead to flow separation and is not desired. Likewise, for the compressor, *r* should not exceed the value of 100%. The value of *r* has major design consequences. For turbine blades with *r = 0,* as shown in Fig. 5.9(a) and 5.10, the flow is deflected in the rotor blades without any enthalpy changes. As a consequence, the magnitude of the inlet and exit velocity vectors are the same and the entire stage static enthalpy difference is partially converted within the stator row. Note that the flow channel cross section remains constant. For *r = 0.5*,

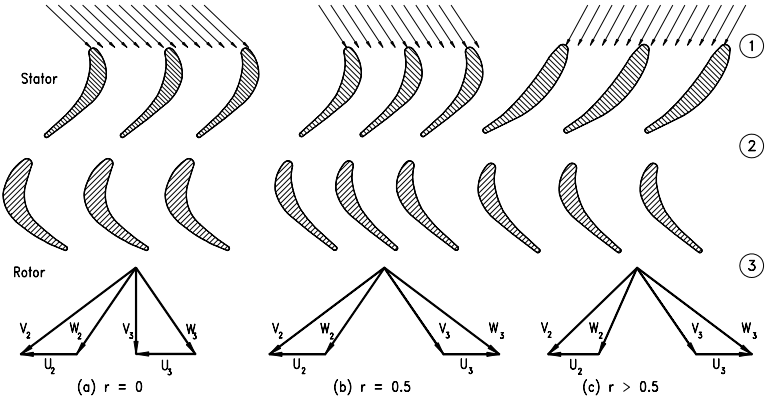

Fig. 5.9: Effect of degree of reaction on the stage configuration

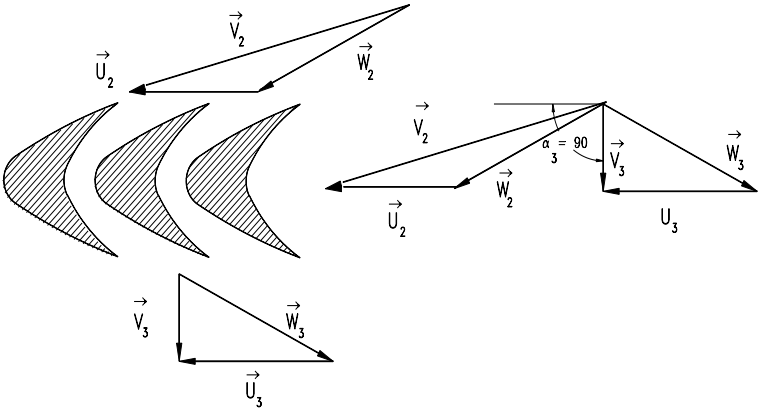

Fig. 5.10: Flow through a high speed turbine rotor with a degree of reaction r = 0.0, note that $\alpha_3 = 90^0$ and $\boldsymbol{V_2 = V_3}$

shown in Fig. 5.9(b), a fully symmetric blade configuration is established. Figure 5.9© shows a turbine stage with $r > 0.5$. In this case, the flow deflection inside the rotor row is much greater than the one inside the stator row. Figure 5.10 shows the flow deflection within a high speed rotor cascade. In the past, mainly two types of stages were common designs in steam turbines. The stage with a constant pressure across the rotor blading ($p_2 = p_3$) called *action stage*, was used frequently. This turbine stage was designed such that the exit absolute velocity vector $\boldsymbol{V_3}$ was swirl free. It is most appropriate for the design of single stage turbines and as the last stage of a multi-stage turbine. As we shall see in Chapter 8, the *exit loss*, which corresponds to the kinetic energy of the exiting mass flow, becomes a minimum by using a swirl free absolute velocity. The stage with $r = 0.5$ is called the *reaction stage.*

5.7 Effect of Stage Load Coefficient on Stage Power

The stage load coefficient λ defined in Eq. (5.13) is an important parameter, which describes the stage capability to generate/consume shaft power. A turbine stage with low flow deflection, thus, low specific stage load coefficient lower λ, generates lower specific mechanical energy. To increase the stage mechanical energy l_m , blades with higher flow deflection are used that produce higher stage load coefficient λ. The effect of an increased λ is shown in Fig. 5.11, where three different bladings are plotted.

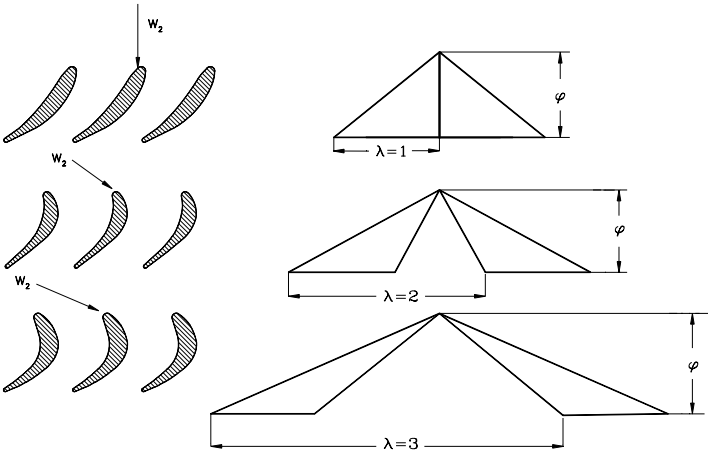

Fig. 5.11: Dimensionless stage velocity diagram to explain the effect of stage load coefficient λ on flow deflection and blade geometry, r = 0.5.

The top blading with the stage load coefficient $\lambda = 1$ has lower deflection. The middle blading has a moderate flow deflection and moderate $\lambda = 2$ which delivers the state power twice as high as the top blading. Finally, the bottom blading with $\lambda = 3$, delivers three times the stage power as the first one. In the practice of turbine design, among other things, two major parameters must be considered. These are the specific load coefficients and the stage polytropic efficiencies.

Lower deflection generally yields higher stage polytropic efficiency, but many stages are needed to produce the required turbine power. However, the same turbine power may be established by a higher stage flow deflection and thus, a higher λ at the expense of the stage efficiency. Increasing the stage load coefficient has the advantage of significantly reducing the stage number, thus, lowering the engine weight and manufacturing cost. In aircraft engine design practice, one of the most critical issues besides the thermal efficiency of the engine, is the thrust/weight ratio. Reducing the stage numbers may lead to a desired thrust/weight ratio. While a high turbine stage efficiency has top priority in power generation steam and gas turbine design, the thrust/weight ratio is the major parameter for aircraft engine designers.

5.8 Unified Description of a Turbomachinery Stage

The following sections treat turbine and compressor stages from a unified standpoint. Axial, mixed flow, and radial flow turbines and compressors follow the same thermodynamic conservation principles. Special treatments are indicated when dealing with aerodynamic behavior and loss mechanisms. While the turbine aerodynamics is characterized by negative (favorable) pressure gradient environments, the compression process operates in a positive (adverse) pressure gradient environment. As a consequence, partial or total flow separation may occur on compressor blade surfaces leading to partial stall or surge. On the other hand, with the exception of some minor local separation bubbles on the suction surface of highly loaded low pressure turbines blades, the turbine operates normally without major flow separation or breakdown. These two distinctively different aerodynamic behaviors are due to different pressure gradient environments. Turbine and compressor cascade aerodynamics and losses are extensively treated in Chapters 7 and 16. In this section, we will first present a set of algebraic equations that describes the turbine and compressor stages with constant mean diameter and extend the approach to general cases where the mean stage diameter changes.

5.8.1 Unified Description of Stage with Constant Mean Diameter

For a turbine or compressor stage with constant mean diameter (Fig. 5.7), we present a set of equations that describe the stage by means of the dimensionless parameters such as stage flow coefficient ϕ, stage load coefficient λ, degree of reaction r, and the flow angles. From the velocity diagram with the angle definition in Fig. 5.7, we obtain the flow angles:

$$
\begin{aligned}
cotg\,\alpha_2 &= \frac{U_2 + W_{u2}}{V_{ax}} = \frac{1}{\phi}\left(1 + \frac{W_{u2}}{U}\right) = \frac{1}{\phi}\left(1 - r + \frac{\lambda}{2}\right) \\
cotg\,\alpha_3 &= -\frac{W_{u2} - U_2}{V_{ax}} = -\frac{1}{\phi}\left(\frac{W_{u3} - U}{U}\right) = \frac{1}{\phi}\left(1 - r - \frac{\lambda}{2}\right)
\end{aligned}
\tag{5.43}
$$

Similarly, we find the other flow angles, thus, we summarize:

$$cotg\,\alpha_2 = \frac{1}{\phi}\left(1 - r + \frac{\lambda}{2}\right) \tag{5.44}$$

$$cotg\,\alpha_3 = \frac{1}{\phi}\left(1 - \frac{\lambda}{2} - r\right) \tag{5.45}$$

$$cotg\,\beta_2 = \frac{1}{\phi}\left(\frac{\lambda}{2} - r\right) \tag{5.46}$$

$$cotg\,\beta_3 = -\frac{1}{\phi}\left(\frac{\lambda}{2} + r\right) \tag{5.47}$$

The stage load coefficient can be calculated from:

$$\lambda = \phi\left(cotg\,\alpha_2 - cotg\,\beta_3\right) - 1 \tag{5.48}$$

The velocity diagram of the last stage of a compressor or a turbine differs considerably from the normal stage. As mentioned in the previous section, to minimize the *exit losses*, the last stage usually has an exit flow angle of $\alpha_3 = 90^0$. Figure 5.12 compares the velocity diagram of a normal stage with the one in the last stage of the same turbine component. As shown, by changing the exit flow angle to $\alpha_3 = 90^0$, substantial reduction in exit velocity vector $\boldsymbol{V_3}$ and thus, the exit kinetic energy V_3^2 can be achieved. This subject is treated in Chapter 7 in detail.

5.8.2 Generalized Dimensionless Stage Parameters

In this chapter, we extend the foregoing consideration to compressor and turbine

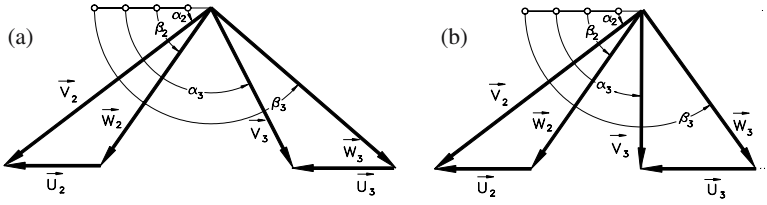

Fig. 5.12: Turbine stage velocity diagrams, (a) for normal stage, (b) for last stage.

stages where the diameter, circumferential velocities, and meridional velocities are not constant. Examples are axial flow turbine and compressors, Fig. 5.1 and 5.7, radial inflow (centripetal) turbines, Figs. 5.13, and centrifugal compressors, 5.14.

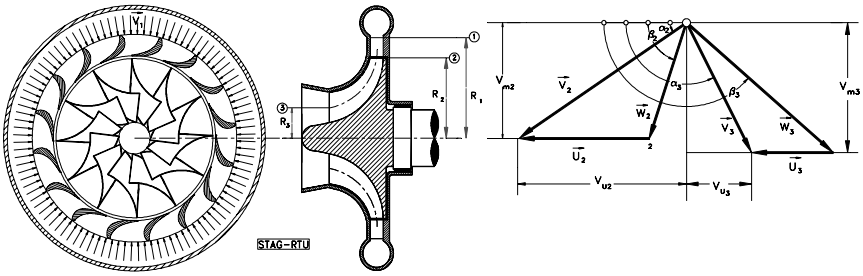

Fig. 5.13: A centripetal turbine stage with cross section and velocity diagram

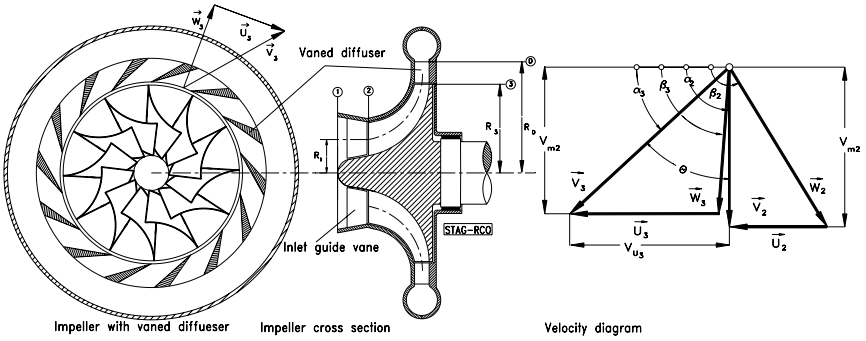

Fig.5.14: A centrifugal compressor stage with cross section and velocity diagram

In the following, we develop a set of unifying equations that describes the above axial turbine and compressor stages, as well as the centripetal turbine and centrifugal compressor stages shown in Figs. 5.13 and 5.14. We introduce new dimensionless parameters:

$$\mu = \frac{V_{m2}}{V_{m3}}\ ,\ \nu = \frac{R_2}{R_3} = \frac{U_2}{U_3}\ ,\ \phi = \frac{V_{m3}}{U_3}\ ,\quad \lambda = \frac{1_m}{U_3^2}\ ,\ r = \frac{\Delta h''}{\Delta h' + \Delta h''S} \tag{5.49}$$

with V_m, U from the velocity diagram, and $\Delta h''$ and $\Delta h'$, the specific static enthalpy difference in rotor and stator. The dimensionless parameters μ represents the meridional velocity ratio for the stator and rotor respectively, ν the circumferential velocity ratio, ϕ the stage flow coefficient, λ the stage load coefficient and r the degree of reaction. Introducing these parameters into the equations of continuity, moment of momentum, and the relation for degree of reaction, the stage is completely defined by a set of four equations:

$$cotg\alpha_2 - cotg\beta_2 = \frac{\nu}{\mu\phi} \tag{5.50}$$

$$cotg\alpha_3 - cotg\beta_3 = \frac{1}{\phi} \tag{5.51}$$

$$r = 1 + \frac{\phi^2}{2\lambda}\left[1 + cotg^2\alpha_3 - \mu^2\left(1 + cotg^2\alpha_2\right)\right] \tag{5.52}$$

$$\lambda = \phi(\mu\nu cotg\alpha_2 - cotg\beta_3) - 1 \tag{5.53}$$

The system of Eqs. (5.50), (5.51), (5.52), and (5.53) contains nine unknown stage parameters. To find a solution, five parameters must be guessed. Appropriate candidates for the first guess are: the diameter ratio $\nu = R_2/R_3 = U_2/U_3$, the stator and rotor exit angles α_2, and β_3, the exit flow angle α_3 and the stage degree of reaction r. In addition, the stage flow coefficient ϕ can be estimated by implementing the information about the mass flow and using the continuity equation. Likewise, the stage load coefficient λ can be estimated for turbine or compressor stages by employing the information about the compressor pressure ratio or turbine power. Once the five parameters are guessed, the rest of the four parameters are determined by solving the above equation system. In this case, the four parameters calculated fulfill the conservation laws for the particular compressor or turbine blade geometry for which five stage parameters were guessed. This preliminary estimation of stage parameters, however, is considered the first iteration toward an optimum design. A subsequent loss and efficiency calculation, presented in Chapter 8, will clearly show if the guessed parameters were useful or not. In fact, few iterations are necessary to find the optimum configuration that fulfills the efficiency requirement set by the compressor or turbine designer. Equations (5.50), (5.51), (5.53), and (5.52) can be expressed in terms of the flow angles α_2, α_3, β_2, and β_3 which lead to a set of four nonlinear equations:

$$\begin{aligned}
&\mu^2\phi^2\left(1-\nu^2\right)\cot^2\alpha_2 + 2\mu\nu\phi\lambda\cot\alpha_2 - \lambda^2 - 2(1-r)\lambda + \left(\mu^2-1\right)\phi^2 = 0\\
&\phi^2\left(1-\nu^2\right)\cot^2\alpha_3 + 2\phi\lambda\cot\alpha_3 + \lambda^2 - 2(1-r)\lambda\nu^2 + \left(\mu^2-1\right)\phi^2\nu^2 = 0\\
&\left(1-\nu^2\right)\left(\mu\phi\cot\beta_2 + \nu\right)^2 + 2\nu\lambda\left(\phi\mu\cot\beta_2 + \nu\right) - \lambda^2 - 2(1-r)\lambda + \left(\mu^2-1\right)\phi^2 = 0\\
&\left(1-\nu^2\right)\left(\phi\cot\beta_3 + 1\right)^2 + 2\lambda\left(\phi\cot\beta_3 + 1\right) + \lambda^2 - 2(1-r)\lambda\nu^2 + \left(\mu^2-1\right)\phi^2\nu^2 = 0
\end{aligned} \tag{5.54}$$

5.9 Special Cases

Equations (5.50) through (5.54) are equally valid for axial, radial, and mixed flow turbine and compressor stages. Special stages with corresponding dimensionless parameters are described as special cases as listed below.

5.9.1 Case 1, Constant Mean Diameter

In this special case, the diameter remains constant leading to the circumferential velocity ratio of $\nu = U_2/U_3 = 1$. The meridional velocity ratio $\mu = V_{m2}/V_{m3} \neq 1$. The flow angle expressed in terms of other dimensionless parameters are:

$$\begin{aligned}
\cot\alpha_2 &= \frac{1}{\phi\mu}\left[\frac{\lambda}{2} + (1 - r) - (\mu^2 - 1)\frac{\phi^2}{2\lambda}\right] \\
\cot\alpha_3 &= \frac{1}{\phi}\left[-\frac{\lambda}{2} - (1 - r) - (\mu^2 - 1)\frac{\phi}{2\lambda}\right] \\
\cot\beta_2 &= \frac{1}{\mu\phi}\left[\frac{\lambda}{2} + (1 - r) - (\mu^2 - 1)\frac{\phi^2}{2\lambda} - 1\right] \\
\cot\beta_3 &= \frac{1}{\phi}\left[-\frac{\lambda}{2} + (1 - r) - (\mu^2 - 1)\frac{\phi}{2\lambda} - 1\right]
\end{aligned} \tag{5.55}$$

The stage load coefficient is calculated from:

$$\lambda = \phi\left(\mu\cot\alpha_2 - \cot\beta_3\right) - 1 \text{ for } \nu = 1 \text{ and } \mu \neq 1 \tag{5.56}$$

5.9.2 Case 2, Constant Mean Diameter and Meridional Velocity Ratio

In this special case, circumferential and meridional velocities are equal leading to: $\nu = U_2/U_3 = 1$, $\mu = V_{m2}/V_{m3} = 1$. The flow angles are calculated from:

$$\begin{aligned}
\cot\alpha_2 &= \frac{1}{\phi}\left(\frac{\lambda}{2} - r + 1\right) \\
\cot\alpha_3 &= \frac{1}{\phi}\left(-\frac{\lambda}{2} - r + 1\right)
\end{aligned} \tag{5.57}$$

The stage load coefficient is calculated from:

$$\lambda = \phi\left(\cot\alpha_2 - \cot\beta_3\right) - 1 \text{ for } \nu = 1 \quad \text{and} \quad \mu = 1 \tag{5.58}$$

In the following, we summarize the generalized stage load coefficient for different μ, ν- cases,

$$\begin{aligned}
&\lambda = \phi\left[\mu\nu\cot\alpha_2 - \cot\beta_3\right] - 1 \qquad \textit{for } \nu \neq 1 \quad \textit{and} \quad \mu \neq 1\\
&\lambda = \phi\left[\mu\cot\alpha_2 - \cot\beta_3\right] - 1 \qquad \textit{for } \nu = 1 \quad \textit{and} \quad \mu \neq 1\\
&\lambda = \phi\left[\nu\cot\alpha_2 - \cot\beta_3\right] - 1 \qquad \textit{for } \nu \neq 1 \quad \textit{and} \quad \mu = 1\\
&\lambda = \phi\left[\cot\alpha_2 - \cot\beta_3\right] - 1 \qquad \textit{for } \nu = 1 \quad \textit{and} \quad \mu = 1
\end{aligned} \tag{5.59}$$

5.10 Increase of Stage Load Coefficient, Discussion

Following the discussion in Section 5.3 regarding the increase of the specific stage mechanical energy and the subsequent discussion in Section 5.8, we proceed with Eq. (5.53) where the stage load parameter λ is expressed in terms of μ, ν, and the blade angle α_2 and β_3 are presented below:

$$\lambda = \phi(\mu\nu\, cotg\alpha_2 - cotg\beta_3) - 1 \tag{5.60}$$

The effect of flow deflection on stage load coefficient of axial flow turbines was already discussed in Section 5.8. As we saw, turbine blades can be designed with a stage load coefficients λ as high as 3 or more. In turbine blades with high λ and Reynolds numbers $Re = V_{exit}\, c/\nu > 150{,}000$, the governing strong negative pressure gradient prevents the flow from major separation. However, if the same type of blade operates at lower Reynolds numbers, flow separation may occur that results in a noticeable increase of profile losses. For high pressure turbines (HP-turbines), the strong favorable pressure gradient within the blade channels prevents the flow from major separation. However, low pressure turbine (LPT) blades, particularly those of aircraft gas turbine engines that operate at low Reynolds numbers (cruse condition up to *Re = 120,000*), are subjected to laminar flow separation and turbulent re-attachment. While axial turbine blades can be designed with relatively high positive λ, the flow through axial compressor blade channels is susceptible to flow separation, even at relatively low λ. This is primarily due to a positive pressure gradient in the streamwise direction that causes the boundary layer to separate once a certain deflection limit or a *diffusion factor* (see Chapter 16) has been exceeded. To achieve a higher λ and thus, a higher stage pressure ratio, a smaller diameter ratio $\nu = D_2/D_3 = U_2/U_3$ can be applied. Using a moderate diameter ratio range of $\nu = 0.85 - 0.75$ results in a mixed flow configuration. At a lower range of ν such as $\nu = 0.75 - 0.4$, centrifugal compressor configuration is designed.

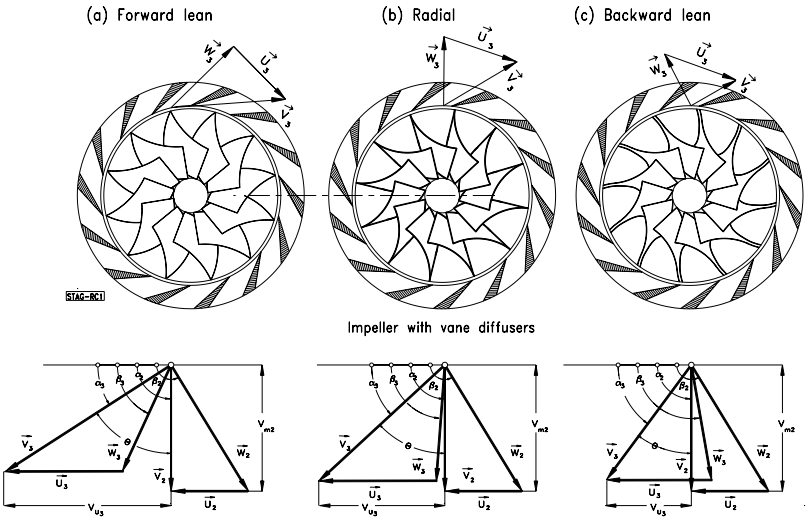

Fig. 5.15: Centrifugal compressor stage with velocity diagrams, a) forward lean, b) radial zero lean, c) backward lean.

Figure 5.15 shows, schematically, three centrifugal compressors with three different exit flow angles and the corresponding velocity diagrams. Figure 5.15a exhibits a centrifugal impeller with the trailing edge portion that is forward leaned and has a negative lean angle of $\Delta\beta = \beta_3 - 90^0 < 0$. The reference configuration, Fig. 5.15 b shows the impeller with a radial exit flow angle $\beta_3 = 90^0$ and thus $\Delta\beta = 0$. Finally, Fig. 5.15c shows the impeller with backward leaned trailing edge portion with a positive lean angle $\Delta\beta = \beta_3 - 90^0 > 0$. All three impellers have the same diameter ratio ν and the same rotational speed ω. The λ-behavior of these impellers is shown in Fig. 5.16, where the relative exit flow angle is varied in the range of $\beta_3 = 80^0 - 105^0$. As shown, forward lean results in higher deflection Θ, larger ΔV_u and thus, higher negative λ, which is associated with a higher profile loss. Backward lean, however, reduces the flow deflection Θ and ΔV_u. As a result, the stage load coefficient λ reduces. For the comparison, the radial exit case with $\beta_3 = 90^0$ is plotted. In calculating the stage load coefficient λ, the influence of the radius ratio $\nu = R_2/R_3 = U_2/U_3$ on the stage load coefficient becomes clear.

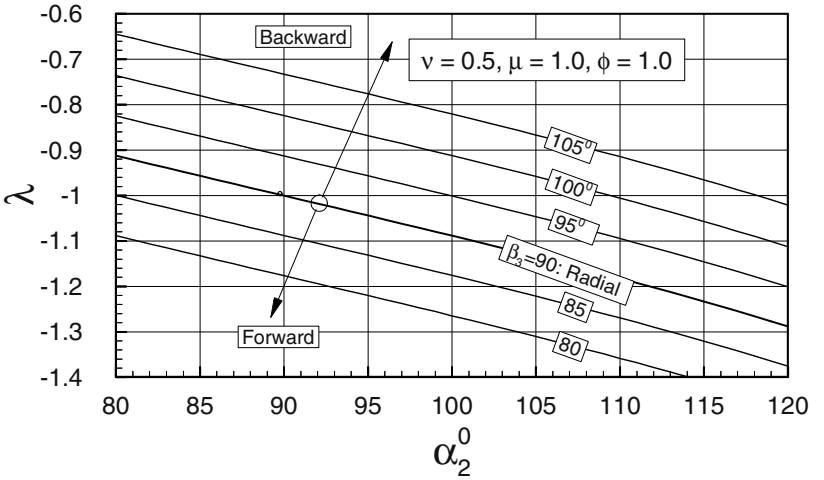

Fig.5.16: Influence of lean angle on λ: Forward lean with $\beta_3 < 90^0$, Backward lean $\beta_3 > 90^0$, Zero lean $\beta_3 = 90^0$.

References, Chapter 5

5.1 Vavra, M.H., Aero-Thermodynamics and Flow in Turbomachines, John Wiley & Sons, New York London, 1960.
5.2 Traupel, W., Thermische Turbomaschinen, Bd.I, 1977, Springer-Verlag Berlin Heidelberg New York.
5.3 Horlock, J.H.: Axial Flow Compressors. London, Butterworth 1966.
5.4 Horlock, J.H.: Axial Flow Turbine London, Butterworth 1966.

6 Turbine and Compressor Cascade Flow Forces

The last chapter was dedicated to the energy transfer within turbomachinery stages. The stage mechanical energy production or consumption in turbines and compressors were treated from a unified point of view by introducing a set of dimensionless parameters. As shown in Chapter 4, the mechanical energy, and therefore the stage power, is the result of the scalar product between the moment of momentum acting on the rotor and the angular velocity. The moment of momentum in turn was brought about by the forces acting on rotor blades. The blade forces are obtained by applying the conservation equation of linear momentum to the turbine or compressor cascade under investigation. In this chapter, we first assume an inviscid flow for which we establish the relationship between the *lift force* and *circulation*. Then, we consider the viscosity effect that causes friction or drag forces on the blading.

6.1 Blade Force in an Inviscid Flow Field

Starting from a given turbine cascade with the inlet and exit flow angles shown in Fig.6.1, the blade force can be obtained by applying the linear momentum principles

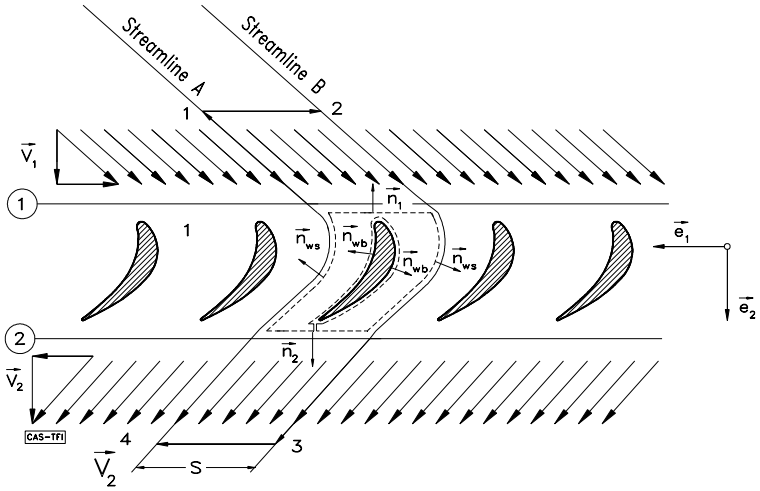

Fig. 6.1: Inviscid flow through a turbine cascade. The blades are assumed to have zero trailing edge thickness

to the control volume with the unit normal vectors and the coordinate system shown in Fig.6.1. As in Chapter 4, the blade force is:

$$\boldsymbol{F}_i = \dot{m}\boldsymbol{V}_1 - \dot{m}\boldsymbol{V}_2 - \boldsymbol{n_1} p_1 sh - \boldsymbol{n_2} p_2 sh \tag{6.1}$$

with h as the blade height that can be assumed as unity. The relationship between the control volume normal unit vectors and the unit vectors pertaining to the coordinate system is given by: $\boldsymbol{n}_1 = -\boldsymbol{e_2}$ and $\boldsymbol{n}_2 = \boldsymbol{e_2}$. The inviscid flow force is obtained by the linear momentum equation where no shear stress terms are present:

$$\boldsymbol{F}_i = \dot{m}\left(\boldsymbol{V}_1 - \boldsymbol{V}_2\right) + \boldsymbol{e_2}\left(p_1 - p_2\right)sh \tag{6.2}$$

The subscript i refers to inviscid flow. The above velocities can be expressed in terms of circumferential as well as axial components;

$$\boldsymbol{F}_i = -\boldsymbol{e_1}\dot{m}\left[\left(V_{u1} + V_{u2}\right)\right] + \boldsymbol{e_2}\left[\dot{m}\left(V_{ax1} - V_{ax2}\right) + \left(p_1 - p_2\right)sh\right] \tag{6.3}$$

With $V_{ax1} = V_{ax2}$ and $V_{u1} \neq V_{u2}$ from Fig. 6.1, Eq. (6.3) is rearranged as:

$$F_i = -\boldsymbol{e_1}\dot{m}\left(V_{u1} + V_{u2}\right) + \boldsymbol{e_2}\left(p_1 - p_2\right)sh = \boldsymbol{e_1}F_u + \boldsymbol{e_2}F_{ax} \tag{6.4}$$

with

$$F_u = -\dot{m}\left(V_{u1} + V_{u2}\right) \text{ and } F_{ax} = \left(p_1 - p_2\right)sh \tag{6.5}$$

The above static pressure difference is obtained from the following Bernoulli equation:

$$\begin{aligned} p_{o1} &= p_{o2} \\ p_1 - p_2 &= \frac{1}{2}\rho\left(V_2^2 - V_1^2\right) = \frac{1}{2}\rho\left(V_{u2}^2 - V_{u1}^2\right) \end{aligned} \tag{6.6}$$

Inserting the pressure difference along with the mass flow $\dot{m} = \rho V_{ax} sh$ into Eq. (6.5) with the blade height $h = 1$, we obtain the axial as well as the circumferential components of the lift force:

$$\left.\begin{aligned} F_{ax} &= \frac{1}{2}\rho\left(V_{u2} + V_{u1}\right)\left(V_{u2} - V_{u1}\right)s \\ F_{u} &= -\rho V_{ax}\left(V_{u2} + V_{u1}\right)s \end{aligned}\right\} \tag{6.7}$$

From Eq.(6.2) and considering (6.7), the lift force vector for the inviscid flow is:

$$\boldsymbol{F}_i = \rho s\left(V_{u2} + V_{u1}\right)\left(-\boldsymbol{e}_1 V_{ax} + \boldsymbol{e}_2 \frac{V_{u2} - V_{u1}}{2}\right) \tag{6.8}$$

This means that the direction of the blade force is identical with the direction of the vector within the brackets. In the next step, we evaluate the expression in the bracket. First, we calculate the mean velocity vector V_∞:

$$\boldsymbol{V}_\infty = \frac{\boldsymbol{V}_1 + \boldsymbol{V}_2}{2} = \frac{1}{2}\boldsymbol{e}_1\left(V_{u2} - V_{u1}\right) + \boldsymbol{e}_2 V_{ax} \tag{6.9}$$

and the circulation around the profile shown in Fig. 6.1 is:

$$\Gamma = \oint \boldsymbol{V} \cdot d\boldsymbol{c} \ , \tag{6.10}$$

where $d\boldsymbol{c}$ is a differential displacement along the closed curve and $\boldsymbol{V}$is the velocity vector. The closed curve is placed around the profile so that it consists of two streamlines that are apart by the spacing s. Performing the contour integral around the closed curve c, we find:

$$\Gamma = V_{u1}s + \int_2^3 \boldsymbol{V}\cdot d\boldsymbol{c} + V_{u2}s + \int_4^1 \boldsymbol{V}\cdot d\boldsymbol{c} \tag{6.11}$$

Since the following integrals cancel each other:

$$\int_2^3 \boldsymbol{V}\cdot d\boldsymbol{c} = -\int_4^1 \boldsymbol{V}\cdot d\boldsymbol{c} \tag{6.12}$$

We obtain the circulation and thus the circulation vector:

$$\Gamma = \left(V_{u2} + V_{u1}\right)s \text{ with the direction } \boldsymbol{e}_3 = -\boldsymbol{e}_2 \times \boldsymbol{e}_1$$
$$\boldsymbol{\Gamma} = \left(\boldsymbol{e}_2 \times \boldsymbol{e}_1\right)s\left(V_{u2} + V_{u1}\right) = \left(-\boldsymbol{e}_3\right)s\left(V_{u1} + V_{u2}\right) \tag{6.13}$$

We multiply the circulation vector with the mean velocity vector

$$\boldsymbol{V}_\infty \times \Gamma = \left\{\frac{1}{2}\boldsymbol{e}_2\left(V_{u2} - V_{u1}\right) - \boldsymbol{e}_1 V_{ax}\right\}\left(V_{u2} + V_{u1}\right)s \tag{6.14}$$

and compare Eq.(6.14) with (6.8) to arrive at the inviscid flow force:

$$\boldsymbol{F}_i = \rho \boldsymbol{V}_\infty \times \boldsymbol{\Gamma} \tag{6.15}$$

This is the well known Kutta-Joukowsky lift-equation for inviscid flow. Figure 6.2 exhibits a single blade taken from a turbine cascade with the velocities $\boldsymbol{V}_1$, $\boldsymbol{V}_2$, $\boldsymbol{V}_\infty$, as well as the circulation vector $\boldsymbol{\Gamma}$, and the force vector $\boldsymbol{F}_i$. As seen, the inviscid flow force vector $\boldsymbol{F}_i$ is perpendicular to the plane spanned by the mean velocity vector $\boldsymbol{V}_\infty$ and the circulation vector $\boldsymbol{\Gamma}$.

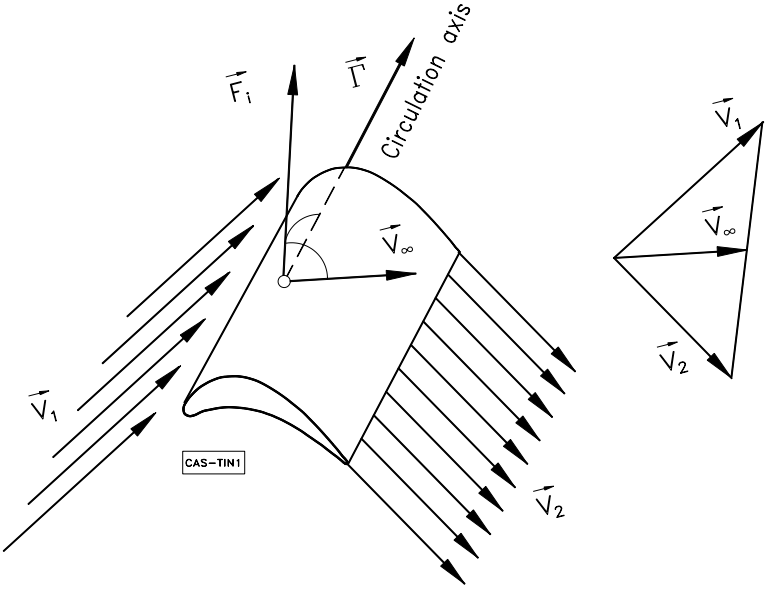

Fig. 6.2: A turbine blade in an inviscid low field with velocity, circulation, and lift force vectors.

Equation (6.15) holds for any arbitrary body that might have a circulation around it regardless of the body shape. It is valid for turbine and compressor cascades and exhibits the fundamental relation in inviscid flow aerodynamics. The magnitude of the force vector is obtained from:

$$F_i = \frac{F_{ax}}{\cos\alpha_\infty} = \frac{1}{2}\frac{\rho s\left(V_{u2} + V_{u1}\right)\left(V_{u2} - V_{u1}\right)}{\cos\alpha_\infty} \tag{6.16}$$

Expressing F_i in terms of V_∞, the inviscid lift force for a turbine cascade is:

$$F_i = \rho V_\infty \left(V_{u2} + V_{u1}\right)s \tag{6.17}$$

Figure 6.3 exhibits the inviscid flow forces acting on a turbine and a compressor cascade.

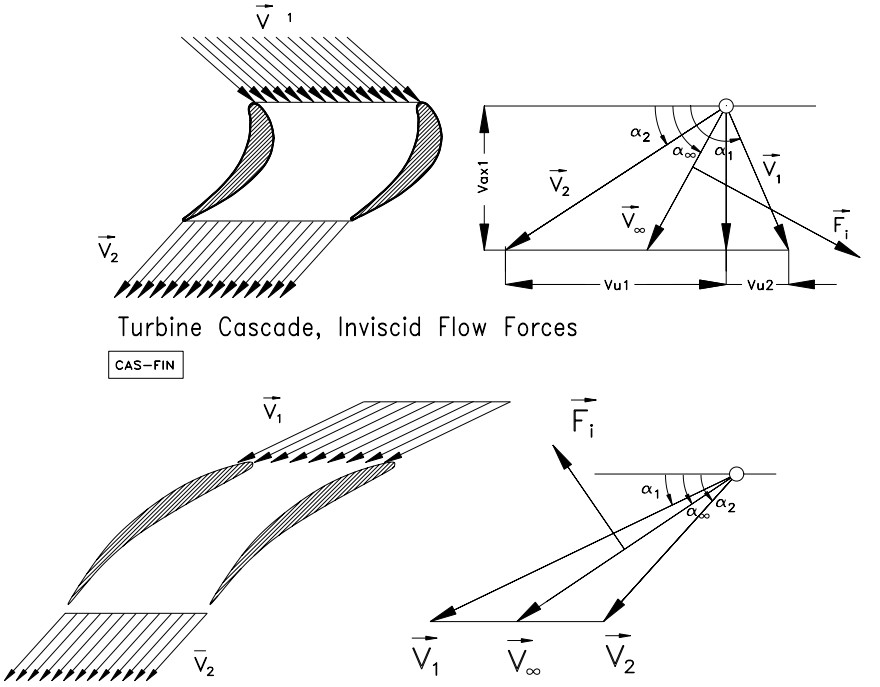

Fig. 6.3: Turbine (top) and Compressor cascade (bottom) with velocity diagram and inviscid flow forces

The flow deflection through the cascades are shown using the velocity diagram for accelerated flow (turbine) and decelerated flow (compressor). As shown in this Fig. 6.3, the inviscid flow force (inviscid lift) is perpendicular to the mean velocity vector $\boldsymbol{V}_\infty$. The lift force can be non-dimensionalized by dividing Eq. (6.17) by a product of the exit dynamic pressure $\rho V^2/2$ and the projected area $A = ch$ with the height h assumed $h = 1$. Thus, the *lift coefficient* is obtained from:

$$C_L = \frac{F_i}{\frac{\rho}{2} V_2^2 c} = \left[\frac{2\, V_\infty \left(V_{u2} + V_{u1}\right)}{V_2^2}\right]\frac{s}{c} \tag{6.18}$$

As shown in section 6.2, the above relationship can be expressed in terms of the cascade flow angles and the geometry.

6.2 Blade Forces in a Viscous Flow Field

The working fluids in turbomachinery, whether air, gas, steam or other substances, are always viscous. The blades are subjected to the viscous flow and undergo shear stresses with *no-slip condition* on the suction and pressure surfaces, resulting in boundary layer developments on both sides of the blades. Furthermore, the blades have certain definite trailing edge thicknesses. These thicknesses together with the boundary layer thickness, generate a spatially periodic wake flow downstream of each cascade as shown in Fig. 6.4. The presence of the shear stresses cause drag forces that reduce the total pressure. In order to calculate the blade forces, the momentum Eq. (6.1) can be applied to the viscous flows. As seen from Eq. (4.26) and Fig. 6.4, the circumferential component remains unchanged. The axial component, however, changes in accordance with the pressure difference as shown in the following relations:

$$\begin{aligned} F_u &= -\rho V_{ax}\left(V_{u2} + V_{u1}\right)s \\ F_{ax} &= \left(p_1 - p_2\right)s \end{aligned} \tag{6.19}$$

The blade height h may be assumed as unity. For a viscous flow, the static pressure difference cannot be calculated by the Bernoulli equation. In this case, the total pressure drop must be taken into consideration. We define the total pressure loss coefficient:

$$\zeta \equiv \frac{p_{o1} - p_{o2}}{\frac{1}{2}\rho V_2^2} \tag{6.20}$$

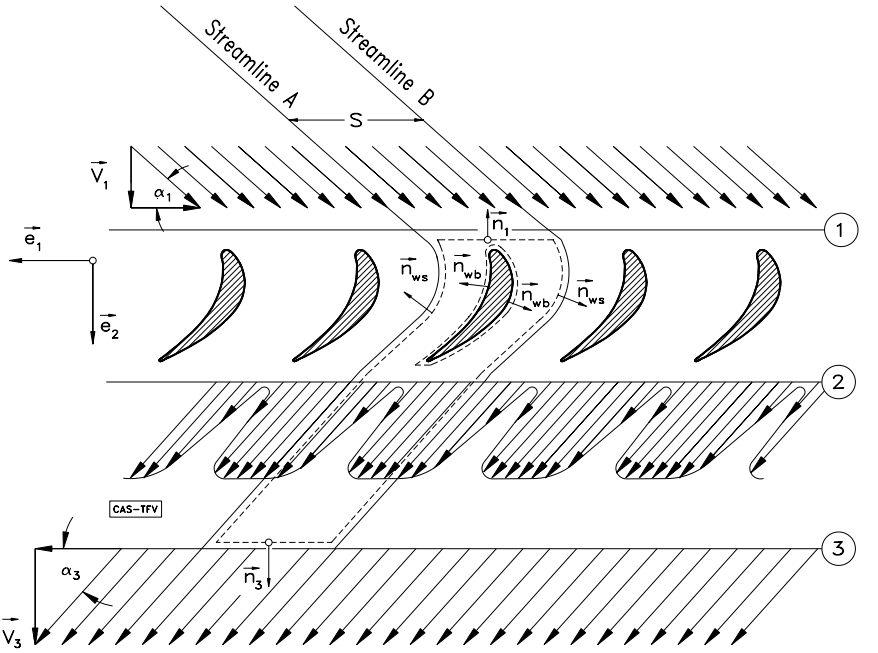

Fig. 6.4: Viscous flow through a turbine cascade. Station ① has a uniform velocity distribution. At station ② wakes are generated by the trailing edge thickness and the boundary layer thickness.

with p_{01} and p_{02} as the averaged total pressure at stations 1 and 2. Inserting for the total pressure the sum of static and dynamic pressure, we get the static pressure difference as:

$$p_1 - p_2 = \frac{\rho}{2}\left(V_2^2 - V_1^2\right) + \zeta \frac{\rho}{2} V_2^2 \tag{6.21}$$

Incorporating Eq. (6.21) into the axial component of the blade force in Eq. (6.19) yields:

$$F_{ax} = \frac{\rho}{2}\left(V_2^2 - V_1^2\right)s + \zeta \frac{\rho}{2} V_2^2 s \tag{6.22}$$

We introduce the velocity components into Eq. (6.22) and assume that the axial components of the inlet and exit flows are the same. As a result, Eq. (6.22) reduces to:

$$F_{ax} = \frac{\rho}{2}\left(V_{u2}^2 - V_{u1}^2\right)s + \zeta\frac{\rho}{2}V_2^2 s \tag{6.23}$$

The second term on the right-hand side exhibits the axial component of drag forces accounting for the viscous nature of a frictional flow shown in Fig. 6.5. Thus, the axial projection of the drag force is obtained from:

$$D_{ax} = \zeta\frac{\rho}{2}V_2^2 s \tag{6.24}$$

Figure 6.5 exhibits the turbine and compressor cascade flow forces, including the lift and drag forces on each cascade for viscous flow, where the periodic exit velocity distribution caused by the wakes and shown in Fig. 6.4, is completely mixed out resulting in an averaged uniform velocity distribution, Fig. 6.5.

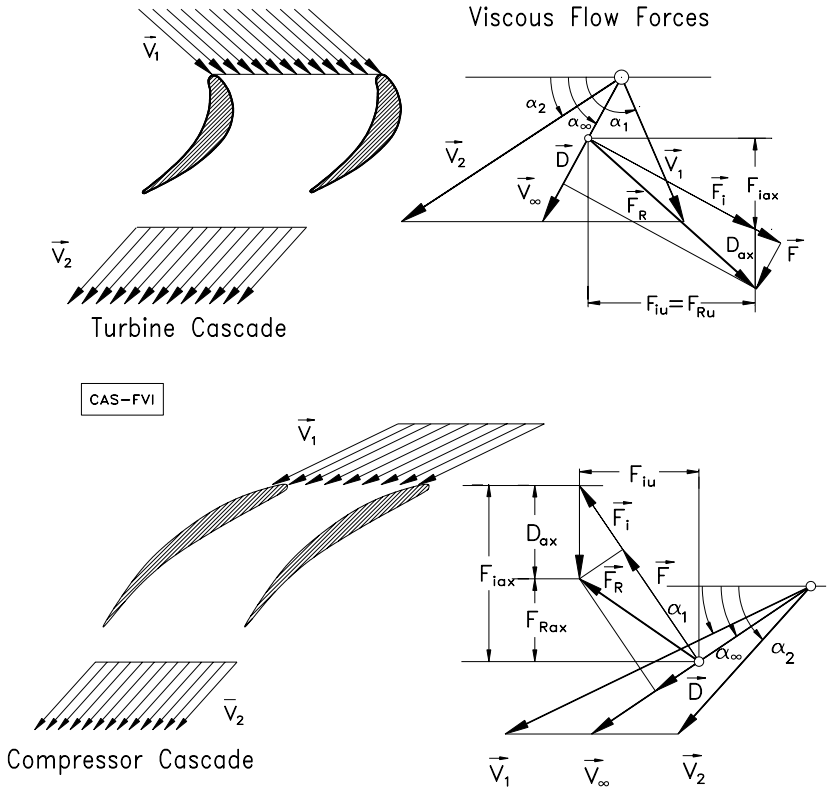

Fig. 6.5: Viscous flow forces on turbine blade (top) and a compressor blade (bottom). The resultant force is decomposed into a drag and a lift component

With Eq. (6.24), the loss coefficient is directly related to the drag force:

$$\zeta = \frac{D_{ax}}{\frac{\rho}{2} V_2^2 s} \tag{6.25}$$

Since the drag force D is in the direction of V_∞, its axial projection D_{ax} can be written as:

$$D_{ax} = \frac{D}{\sin \alpha_\infty} \tag{6.26}$$

We define the drag and lift coefficients as:

$$C_D = \frac{D}{\frac{\rho}{2} V_2^2 c}, \quad C_L = \frac{F}{\frac{\rho}{2} V_2^2 c} \tag{6.27}$$

introduce the drag coefficient C_D into Eq. (6.25), and obtain the loss coefficient

$$\zeta = C_D \frac{c}{s} \frac{1}{\sin \alpha_\infty} \tag{6.28}$$

The lift force is the projection of the resultant force F_R on the plane perpendicular to V_∞:

$$F = F_i + D_{ax} \cos \alpha_\infty \tag{6.29}$$

Using the lift coefficient defined previously and inserting the lift force, we find

$$C_L = \frac{2 V_\infty \left(V_{u2} + V_{u1} \right)}{V_2^2} \frac{s}{c} + \zeta \frac{s}{c} \cos \alpha_\infty \tag{6.30}$$

Introducing the cascade solidity σ = c/s into Eq. (6.30) results in:

$$C_L \frac{c}{s} = \frac{2 V_\infty \left(V_{u2} + V_{u1} \right)}{V_2^2} + \zeta \cos \alpha_\infty \tag{6.31}$$

The lift-solidity coefficient is a characteristic quantity for the cascade aerodynamic loading. Using the flow angles defined in Fig. 6.3, the relationship for the lift-solidity

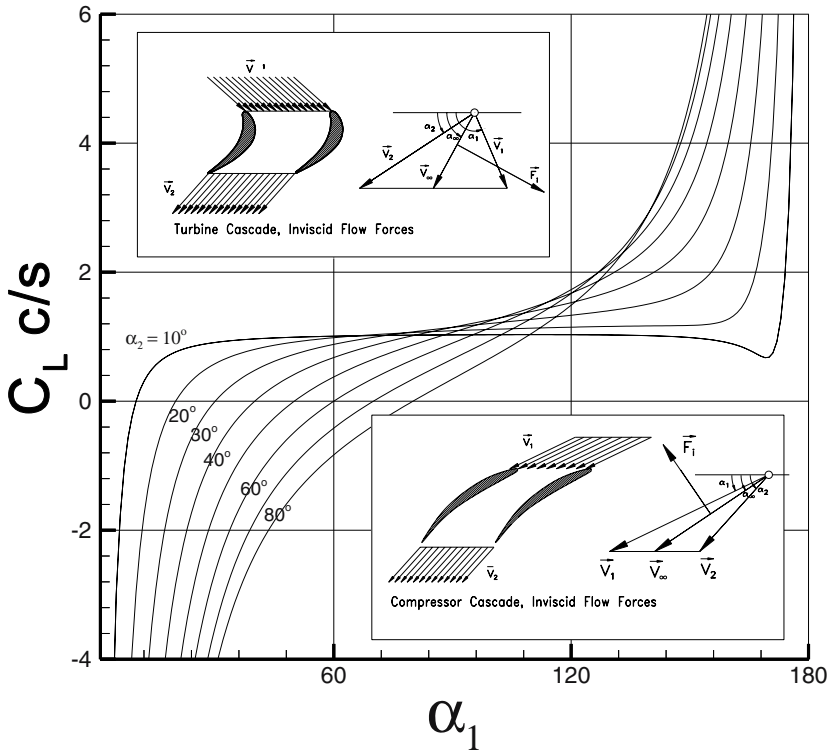

Fig. 6.6: Lift-solidity coefficient as a function of inlet flow angle α_1 with the exit flow angle α_2 as parameter for turbine and compressor cascades.

coefficient becomes:

$$C_L \sigma = 2 \frac{\sin^2 \alpha_2}{\sin \alpha_\infty} \left(cotg\, \alpha_2 - cotg\, \alpha_1 \right) + \zeta \cos \alpha_\infty \tag{6.32}$$

with:

$$cotg\, \alpha_\infty = \frac{1}{2} \left(cotg\, \alpha_2 + cotg\, \alpha_1 \right) \tag{6.33}$$

For the optimum design consideration, the contribution of the second term in Eq. (6.32) compared with the first term can be neglected. Figure 6.6 shows the results as a function of inlet flow angle with exit flow angle as the parameter for turbine and compressor cascades. As an example, a turbine cascade with an inlet flow angle of $\alpha_1 = 132^o$, and an exit flow of $\alpha_2 = 30^o$ resulting in a total flow deflection of $\Theta = 102^o$, has a positive lift-solidity coefficient of $C_L \sigma = 2.0$. This relatively high lift coefficient

is responsible for generating high blade forces and thus, a high blade specific mechanical energy for the rotor. In contrast, a compressor cascade with an inlet flow angle of $\alpha_1 = 60^o$ and an exit flow of $\alpha_2 = 80^o$ which result in a total compressor cascade flow deflection of only $\Theta = 20^o$, has a lift-solidity coefficient of $C_L\sigma = -0.8$. This leads to a much lower blade force and thus, lower specific mechanical energy input for the compressor rotor. The numbers in the above example are typical for compressor and turbine blades. The high lift-solidity coefficient for turbine cascade is representative of the physical process within a highly accelerated flow around a turbine cascade, where, despite a high flow deflection, no flow separation occurs. On the other hand, in case of a compressor cascade, a moderate flow deflection, such as the one mentioned above, may result in flow separation. The difference between the turbine and compressor cascade flow behavior is explained by the nature of boundary layer flow around the turbine and compressor cascades. In a compressor cascade, shown in Fig. (6.7) the boundary layer flow is subjected to two co-acting decelerating effects, the wall shear stress dictated by the viscous nature of the fluid and the positive pressure gradient imposed by the cascade geometry.

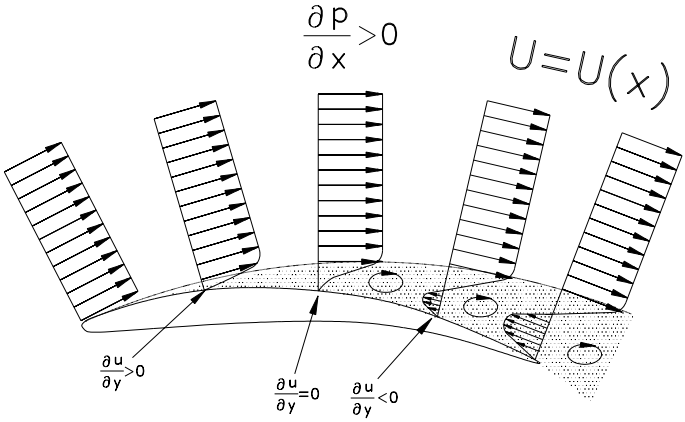

Fig. 6.7: Boundary layer development along the suction surface of a compressor cascade

A fluid particle within the boundary layer that has inherently lower kinetic energy compared to a particle outside the boundary layer, has to overcome the pressure forces due to the governing positive pressure gradient. As a result, this particle continuously decelerates, comes to a rest, and separates. In the case of a turbine cascade, the decelerating effect of the shear stress forces is counteracted by the accelerating effect of the negative pressure gradient that predominates a turbine cascade flow.

6.3 The Effect of Solidity on Blade Profile Losses

Equation (6.32) exhibits a fundamental relation between the lift coefficient, solidity, inlet and exit flow angle, and the loss coefficient ζ. At this stage, the question might arise as to how the profile loss ζ will change if the solidity σ changes. The solidity has the major influence on the flow behavior within the blading. If the spacing is too small, the number of blades is large and the friction losses dominate. Increasing the spacing, which is identical to reducing the number of blades, at first causes a reduction of friction losses. Further increasing the spacing, decreases the friction losses and also reduces the guidance of the fluid that may result in flow separation leading to separation losses. With definite spacing, there is an equilibrium between the separation and friction losses. At this point, the profile loss $\zeta = \zeta_{friction} + \zeta_{separation}$ is at a minimum. The corresponding spacing/chord ratio has an optimum, which is shown in Fig. 6.8.

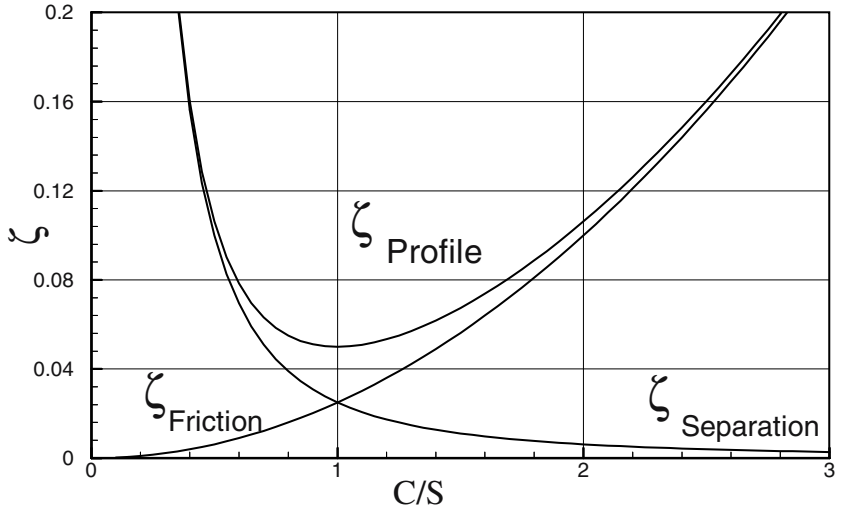

Fig. 6.8: Profile loss coefficient as a function of spacing/chord ratio

6.4 Relationship Between Profile Loss Coefficient and Drag

To establish a relationship for turbine cascade profile losses, which is based on a systematic turbine cascade investigations, we define the so-called drag-lift ratio:

$$\varepsilon = \frac{C_D}{C_L} \tag{6.34}$$

which is a characteristic for a profile. The drag and the loss coefficients are

$$\zeta = C_D \frac{c}{s} \frac{1}{\sin\alpha_\infty} \tag{6.35}$$

interconnected by Eq.(6.28) as:

$$C_L \frac{c}{s} = \frac{\zeta \sin\alpha_\infty}{\varepsilon} \tag{6.36}$$

Expressing the drag coefficient in Eq. (6.35) by the lift coefficient (6.34), we obtain: Introducing Eq.(6.36) into (6.32) leads to:

$$\zeta \frac{\sin\alpha_\infty}{\varepsilon} - \zeta\cos\alpha_\infty = 2 \frac{\sin^2\alpha_2}{\sin\alpha_\infty} \left(\cot\alpha_2 - \cot\alpha_1\right) \tag{6.37}$$

Rearranging Eq. (6.37) gives a direct relation between the loss coefficient ζ, the inlet and exit flow angles and the drag-lift ratio ε:

$$\zeta = \frac{2\varepsilon}{1 - \varepsilon\cot\alpha_\infty} \cdot \frac{\sin^2\alpha_2}{\sin\alpha_\infty} \left(\cot\alpha_2 - \cot\alpha_1\right) \tag{6.38}$$

Figure 6.9 shows a typical drag-lift ratio ε experimentally determined by Pfeil [1], for turbine and compressor cascades.

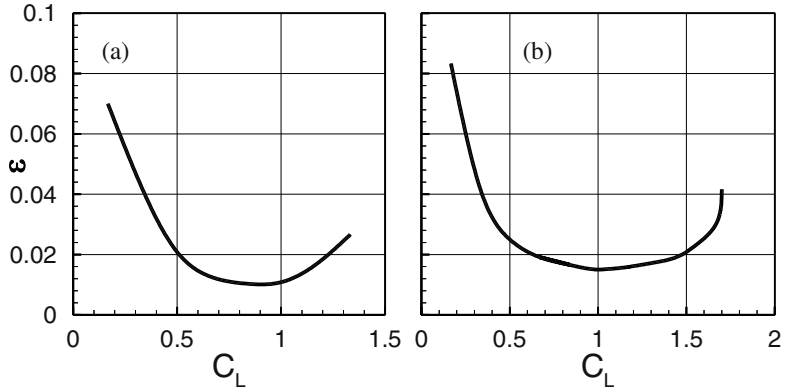

Fig. 6.9: Typical drag-lift ratio ε as a function of the lift coefficient (a) for a turbine cascade and (b) for a compressor cascade, from [1]

6.5 Optimum Solidity

To find the optimum solidity for a variety of turbine and compressor cascades, Pfeil [1] performed a series of comprehensive experimental studies where 8 compressor cascades with NACA-profiles and 8 turbine cascades were investigated. The blade profiles ranged from low to high flow deflection. In these studies, Pfeil extended his analysis, among others, to the existing data from Carter and Hounsell [2] , and Abbot, et al.[3]. According to the studies in [1], the ε versus C_L-diagram in Fig. 6.9 shows that the drag-lift ratios for compressor and turbine cascades have clearly defined optimum ranges. For the turbine cascades presented in [1] and in accord with the finding of Zweifel [4] the optimum lift coefficient range is $\left(C_L\right)_{opt} \approx 0.8-1.05$, whereas for the compressor cascades $C_{L_{opt}} \approx 0.9-1.25$. Investigating the ε-behavior of a single profile and building a relative ε-ratio, the studies in [1] reveals the following functional relationship:

$$\left(\frac{\varepsilon}{\varepsilon_s}\right)_{opt} = 1 + f\left(\frac{c}{s}\right)_{opt} \tag{6.39}$$

The above relationship is plotted in Fig. (6.10) and can be approximated by:

$$\left(\frac{\varepsilon}{\varepsilon_s}\right)_{opt} = 1 + K\left(\frac{c}{s}\right)^n_{opt} \tag{6.40}$$

with ε_s as the drag-lift ratio for a single blade. From experimental investigations for turbine and compressor cascades with hydraulically smooth blade surfaces, the thickness-chord ratio (t/c) = 0.15, 0.1 and the Reynolds number $Re = 3.5\times10^5$, the values for n, K, and $(\varepsilon_s)_{opt}$ were evaluated and are given in Fig.6.9 (a) and (b). Using Eq. (6.40), the optimum profile loss coefficient is calculated by :

$$\zeta = (\varepsilon_s)_{opt}\left[1 + K\left(\frac{c}{s}\right)^n_{opt}\right] C_L \frac{c}{s}\frac{1}{\sin\alpha_\infty} \tag{6.41}$$

Figures 6.10 (a) and (b) exhibit the optimum ε-ratios as a function of optimum chord-spacing ratio for turbine and compressor cascades investigated in [1]. As seen for up to $(c/s)_{opt} \approx 0.4$, the ratio $(\varepsilon/\varepsilon)_{opt}$ is almost constant.

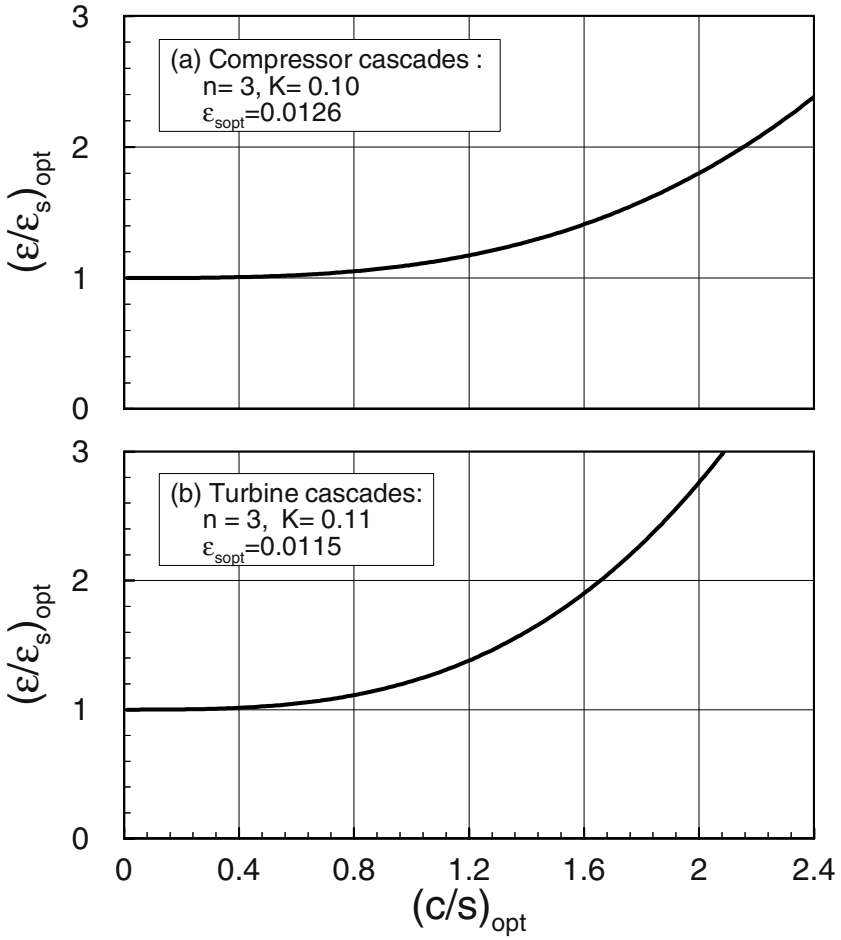

Fig. 6.10: Relative drag/lift-ratio as a function of optimum chord-spacing ratio for (a) compressor and (b) turbine cascades, [1]

6.6 Generalized Lift-Solidity Coefficient

The relationship for lift-solidity coefficient derived in section 6.2 is restricted to turbine and compressor stages with constant inner and outer diameters. This geometry is encountered in high pressure turbines or compressor components, where the streamlines are almost parallel to the machine axis. In this special case, the stream surfaces are cylindrical with almost constant diameter. In a general case such as the intermediate and low pressure stage, however, the stream surfaces have different radii, as shown in Fig. 6.11.

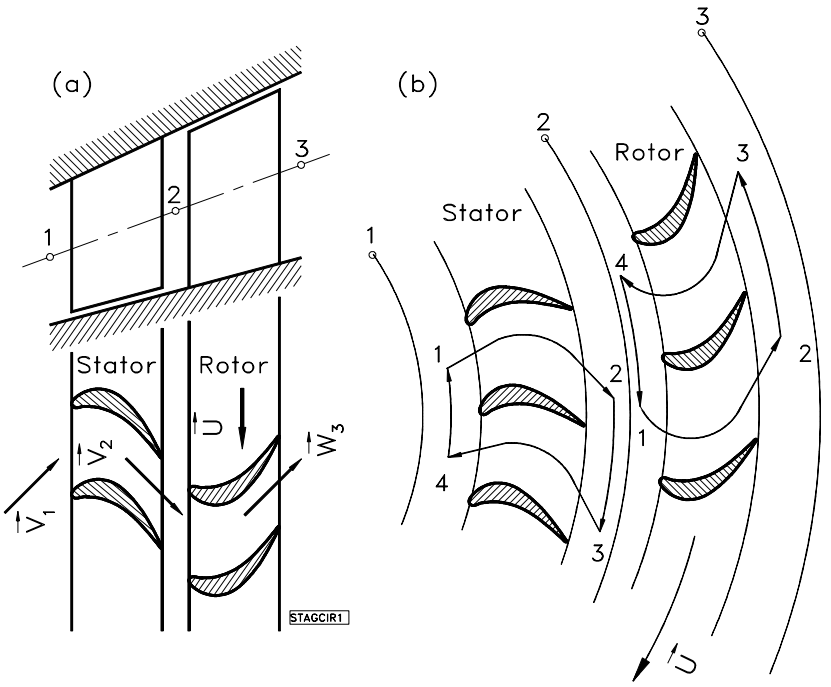

Fig. 6.11: Fig. 6.11: A turbine stage with different mean diameter (a), circulation around stator and rotor

The meridional velocity component might also change from station to station. In order to calculate the blade lift-solidity coefficient correctly, the radius and the meridional velocity changes must be taken into account. In the following sections, the corresponding relations for a turbine stator and rotor are derived. Extending the derivation to compressor stator and rotor leads to the same results.

Figure 6.11 shows a turbine stage with a meridional cross section where the mean radius changes from the inlet at station *1* to the exit at station *3* (Fig 6.11a). The same cross section unfolded exhibits the change of the spacing for the stator and the rotor cascade (6.11b). Before starting with the derivation of the generalized lift-solidity coefficient, we introduce a convention about the direction of the circulation around the stator and rotor blades. The reference configurations are the turbine stator and rotor. To treat both the turbine and compressor stator and rotor in a unified manner, we use the same direction convention that we assume for the reference configuration, namely turbine stator and rotor. Thus, the generalized lift-solidity coefficients that we obtain for turbine stator is fully identical with the one for compressor stator. Likewise, the lift-solidity coefficient for the turbine rotor is fully identical with the one for compressor rotor. This convention is depicted in Fig. 6.12.

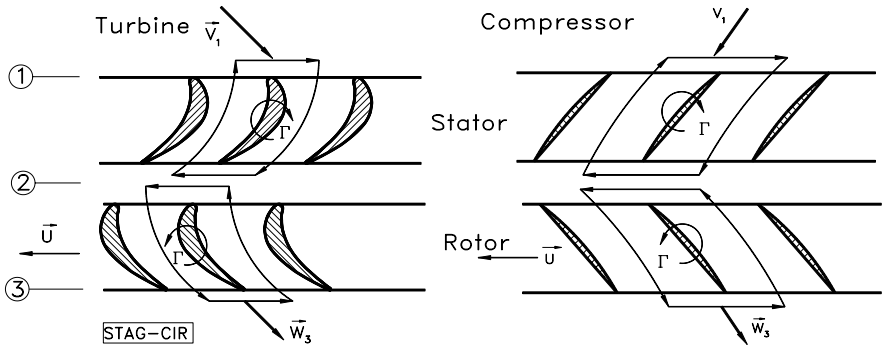

Fig. 6.12: Unified circulation convention for stator and rotor cascades.

6.6.1 Turbine Stator

To calculate the lift-solidity coefficient for the turbine stator shown in Fig. 6.12, first the circulation around the stator blade is calculated

$$\Gamma = \oint \boldsymbol{V} \cdot d\boldsymbol{c} = V_{u1} s_1 + V_{u2} s_2 + \int_1^2 \boldsymbol{V} \cdot d\boldsymbol{c} + \int_3^4 \boldsymbol{V} \cdot d\boldsymbol{c} \tag{6.42}$$

The last two integrals in Eq. (6.42) cancel each other resulting in

$$\Gamma = V_{u2} s_2 + V_{u1} s_1 \tag{6.43}$$

As shown in Fig. 6.11, the spacing s_1 is different from s_2. To establish a relationship between s_1 and s_2, we may introduce two planes that intersect each other on the machine axis at an angle $\Delta\theta$. The angle $\Delta\theta$ is chosen such that the planes contain at least one blade. The spacings are related through:

$$\frac{s_1}{s_2} = \frac{\Delta\theta r_1}{\Delta\theta r_2} = \frac{r_1}{r_2} \tag{6.44}$$

We introduce the dimensionless meridional velocity ratio and the diameter ratio for the stator

$$\mu = \frac{V_{m1}}{V_{m2}}, \qquad \nu = \frac{r_1}{r_2} = \frac{s_1}{s_2} \tag{6.45}$$

Since s_1 and s_2 are related by $s_1 = \nu s_2$, the circulation Γ in Eq. (6.43) becomes:

$$\Gamma = s_2\left(V_{u2} + \nu V_{u1}\right) \tag{6.46}$$

Similar to Eq. (6.9), the mean velocity vector is:

$$\boldsymbol{V}_\infty = \frac{1}{2}\left(\boldsymbol{V}_1 + \boldsymbol{V}_2\right) \tag{6.47}$$

The velocity vector $\boldsymbol{V}_\infty$, its corresponding components, and angles are presented in Fig. 6.13. Using the reference coordinate in Fig. 6.13, we express the velocity vector $\boldsymbol{V}_\infty$ in terms of its components

$$\boldsymbol{V}_\infty = \frac{1}{2}\left(\boldsymbol{V}_1 + \boldsymbol{V}_2\right) = \frac{1}{2}\left[(-\boldsymbol{e_1} V_{u1} + \boldsymbol{e_2} V_{m1}) + (\boldsymbol{e_1} V_{u2} + \boldsymbol{e_2} V_{m2})\right] \tag{6.48}$$

Rearranging Eq. (6.48) gives:

$$\boldsymbol{V}_\infty = \frac{1}{2}\left[\boldsymbol{e_1}(V_{u2} - V_{u1}) + \boldsymbol{e_2}(V_{m1} + V_{m2})\right] \tag{6.49}$$

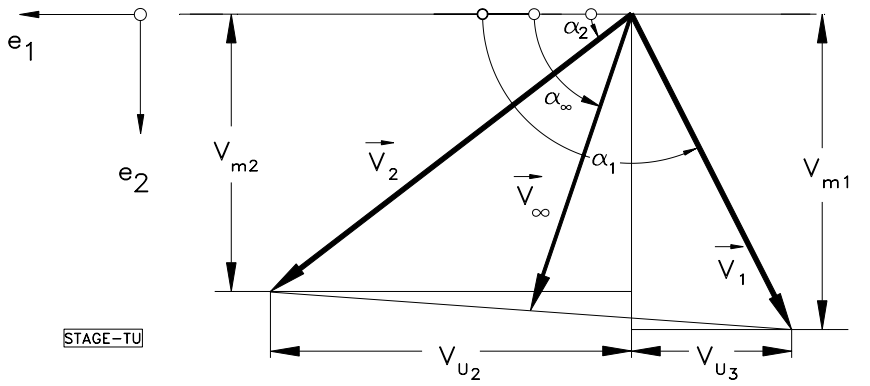

Fig. 6.13: Velocity diagram for a stator cascade with different radii at the inlet and exit.

Thus the components in circumferential and meridional directions are:

$$V_{u\infty} = \frac{1}{2}\left(V_{u2} - V_{u1}\right) \quad \text{and} \quad V_{m\infty} = \frac{1}{2}\left(V_{m1} + V_{m2}\right) \tag{6.50}$$

With $V_{m\infty}$ from Eq. (6.50), $V_{m\infty} = V_\infty \sin\alpha_\infty$, and (6.45) we obtain:

$$V_\infty = \frac{1}{2}\frac{V_{m2}(1+\mu)}{\sin\alpha_\infty} \tag{6.51}$$

where $\sin\alpha_\infty$ can be obtained from

$$\cot\alpha_\infty = \frac{V_{u_\infty}}{V_{m_\infty}} = \frac{V_{u2} - V_{u1}}{V_{m1} + V_{m2}} = \frac{\mu\cot\alpha_1 + \cot\alpha_2}{1+\mu} \tag{6.52}$$

Introducing Eq. (6.46) and (6.51) into the inviscid lift equation (6.15) , we find:

$$C_L = \frac{F_i}{\frac{1}{2}\rho_\infty V_2^2 c} = \frac{V_{m2}(1+\mu)}{V_2^2 \sin\alpha_\infty}\left(V_{u2} + \nu V_{u1}\right)\frac{s_2}{c} \tag{6.53}$$

or:

$$C_L \frac{c}{s_2} = \frac{\sin\alpha_2^2}{\sin\alpha_\infty}(1+\mu)\left[\cot\alpha_2 - \nu\mu\cot\alpha_1\right] \tag{6.54}$$

Equation (6.54) represents the generalized lift-solidity coefficient for a stator cascade with different inlet and exit radii, meridional and circumferential velocity components. Setting $\nu = 1$ and $\mu = 1$, Eq. (6.54) assumes the same form as Eq. (6.32).

The influence of the diameter ratio ν on the cascade lift coefficient can be seen from Fig. 6.14. It represents the plot of Eq. (6.54). Setting the exit flow angle $\alpha_2 = 70^o$, the lift coefficient is plotted as a function of the inlet flow angle α_1 for five different ν-vales. The curve with $\nu < 1.0$ corresponds to axial, radial cascades, where the exit diameter is larger than the inlet one. Such diameter ratios are found in multi-stage axial compressors. The curve with $\nu = 1$ corresponds to a cascade geometry with constant mean diameter, and finally the case $\nu > 1.0$ corresponds to a cascade geometry, where the inlet diameter is larger than the exit one. This type of cascade are encountered in radial inflow turbines. As Fig. 6.13 shows, a compressor cascade with an inlet flow angle $\alpha_2 = 60^o$ and $\nu = 1$ gives a lift coefficient $C_L c/s = -0.41643$. Reducing the diameter ratio to $\nu = 0.8$ results in much smaller lift-solidity coefficient of $C_L c/s = -0.19081$ and thus a relaxation of the cascade aerodynamic loading. As a

consequence, higher deflection may be achieved that leads to a higher stage pressure ratio. For this particular example, keeping the exit flow angle $\alpha_2 = 70^o$, the cascade flow will increase from 10 to 15.5°. These results are fully compatible with those presented in Chapter 5.

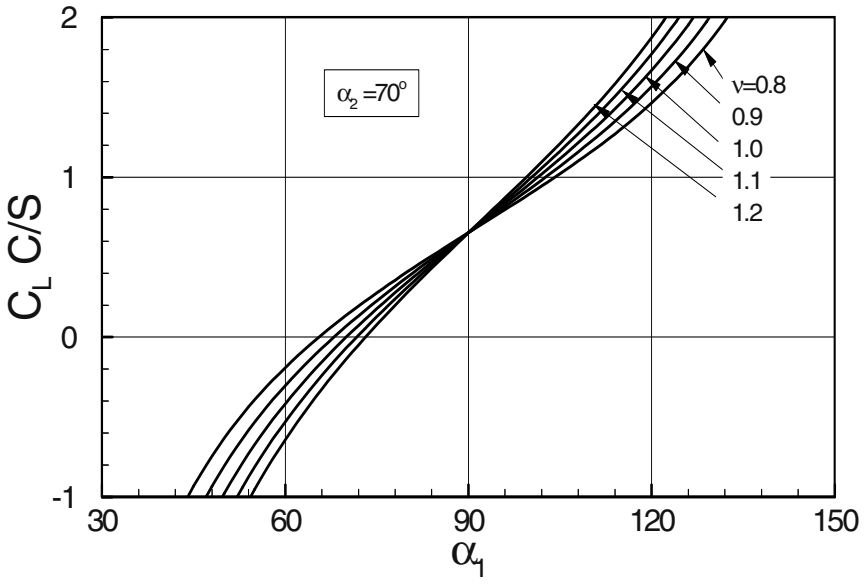

Fig. 6.14: On the influence of diameter ratio on the cascade lift-solidity coefficient.

6.6.2 Turbine Rotor

To determine the lift-solidity coefficient of a rotating cascade, two different types of circulations are distinguished. The first one is the *relative circulation* that is constructed by the circumferential components of the relative velocity vectors and the corresponding spacings. This relative circulation is registered by an observer who is placed within the rotating or relative frame of reference. The second one is the *absolute circulation*, which is observed by an observer located in a stationary or absolute frame of reference. Since the absolute circulation is responsible for energy transfer to/from the rotating cascade, it is used for calculating the lift-solidity coefficient of turbine/compressor rotor cascades. Using the nomenclature in Fig. 6.11 in conjunction with the stage velocity diagram, Fig. 6.15, the absolute circulation around the rotor blade is given by:

$$\Gamma = V_{u2} s_2 + V_{u3} s_3 \tag{6.55}$$

Considering the following relations:

$$\mu = \frac{V_{m2}}{V_{m3}}, \qquad \nu = \frac{r_2}{r_3}, \qquad \phi = \frac{V_{m3}}{U_3} \tag{6.56}$$

and applying similar procedure as in 6.6.1, the mean velocity is found:

$$V_\infty = \frac{1}{2} \frac{V_{m3}}{\sin \alpha_{\infty R}} (1 + \mu) \tag{6.57}$$

The subscript R in Eq. (6.57) refers to the rotor. Referring to the angle definition in Fig. 6.15, the absolute velocity components in circumferential direction V_{u2}, V_{u3} can be explained in terms of circumferential component of the relative velocities W_{u2}, W_{u3} and the circumferential velocities U_2, U_3. For the absolute and relative velocity vectors and their components we find:

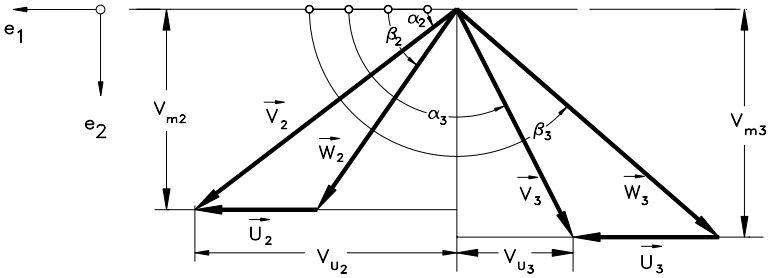

Fig. 6.15: Angle definition to determine the rotor cascade lift coefficient.

$$\begin{aligned} \boldsymbol{V_2} &= \boldsymbol{W_2} + \boldsymbol{U_2}, \qquad \boldsymbol{V_3} = \boldsymbol{W_3} + \boldsymbol{U_3} \\ V_{u2} &= W_{u2} + U_2, \qquad V_{u3} = W_{u3} - U_3 \end{aligned} \tag{6.58}$$

Introducing Eqs. (6.56), (6.57), and (6.58) into the following lift equation:

$$\boldsymbol{F} = \rho_\infty \boldsymbol{V}_\infty \times \boldsymbol{\Gamma} \tag{6.59}$$

we obtain the generalized inviscid lift-solidity coefficient for the rotor:

$$C_L = \frac{V_{m3}}{\sin\alpha_{\infty R}} \frac{(1 + \mu)(V_{u2} s_2 + V_{u3} s_3)}{V_3^2 c} \tag{6.60}$$

Replacing the exit velocity by $V_3 = V_{m3}/\sin\alpha_3$, we find:

$$C_L = \frac{\sin^2\alpha_3}{\sin\alpha_{\infty R}} (1 + \mu) \left(\nu \frac{V_{u2}}{V_{m3}} + \frac{V_{u3}}{V_{m3}} \right) \frac{s_3}{c} \tag{6.61}$$

In Eq. (6.61) we insert the corresponding components from Eq (6.58)

$$C_L = \frac{\sin^2\alpha_3}{\sin\alpha_{\infty R}} (1 + \mu) \left(\mu \nu \left(\frac{W_{u2}}{V_{m2}} + \frac{U_2}{V_{m2}} \right) + \frac{W_{u3}}{V_{m3}} - \frac{U_3}{V_{m3}} \right) \frac{s_3}{c} \tag{6.62}$$

For further rearrangement of Eq. (6.62), we implement the following relations

$$\frac{W_{u2}}{V_{m2}} = cotg\beta_2, \quad \frac{W_{u3}}{V_{m3}} = -cotg\beta_3, \quad \frac{U_2}{V_{m2}} = \frac{\nu}{\phi\mu}, \quad \frac{U_3}{V_{m3}} = \frac{1}{\phi} \tag{6.63}$$

and obtain the final relation for the lift-solidity coefficient for a rotor cascade as:

$$C_L \frac{c}{s_3} = \frac{\sin^2\alpha_3}{\sin\alpha_{\infty R}} (1 + \mu) \left[\mu \nu \cot\beta_2 - \cot\beta_3 + \frac{\nu^2 - 1}{\phi} \right] \tag{6.64}$$

Equation (6.64) is generally valid for calculating the lift coefficients of radial, mixed, and axial turbines and compressor rotors. The absolute angles α_3 and $\alpha_{\infty R}$ are related to the relative angles β_2 and β_3 by the following trigonometric relations:

$$\cot\alpha_2 = \cot\beta_2 + \frac{\nu}{\mu\phi}, \quad \cot\alpha_3 = \cot\beta_3 + \frac{1}{\phi}, \quad \cot\alpha_\infty = \frac{cotg\,\alpha_3 + \mu\, cotg\alpha_2}{1 + \mu} \tag{6.65}$$

With Eqs. (6.63) and (6.64) the generalized lift- solidity coefficient can be determined for turbine and compressor cascades with given geometry, flow angles, and velocity

ratios. As an example, Fig. 6.16 presents the lift-solidity coefficient for turbine and compressor rotor cascades as a function of rotor relative inlet flow angle β_2 with the relative exit flow angle β_3 as a parameter. As the figure shows, the positive lift-solidity coefficients represent the values for turbine rotor cascades, whereas the negative ones pertain to the compressor rotor cascades. Keeping the exit flow angle constant and decreasing the relative inlet flow angle leads to a higher flow deflection and thus a higher lift. In contrast, a higher lift-solidity coefficient for compressor rotor cascades is achieved by increasing the relative inlet flow angle. It should be pointed out that flow deflections above $\Delta\theta = 20^o$ may lead to flow separation along the suction surface of the compressor rotor blade.

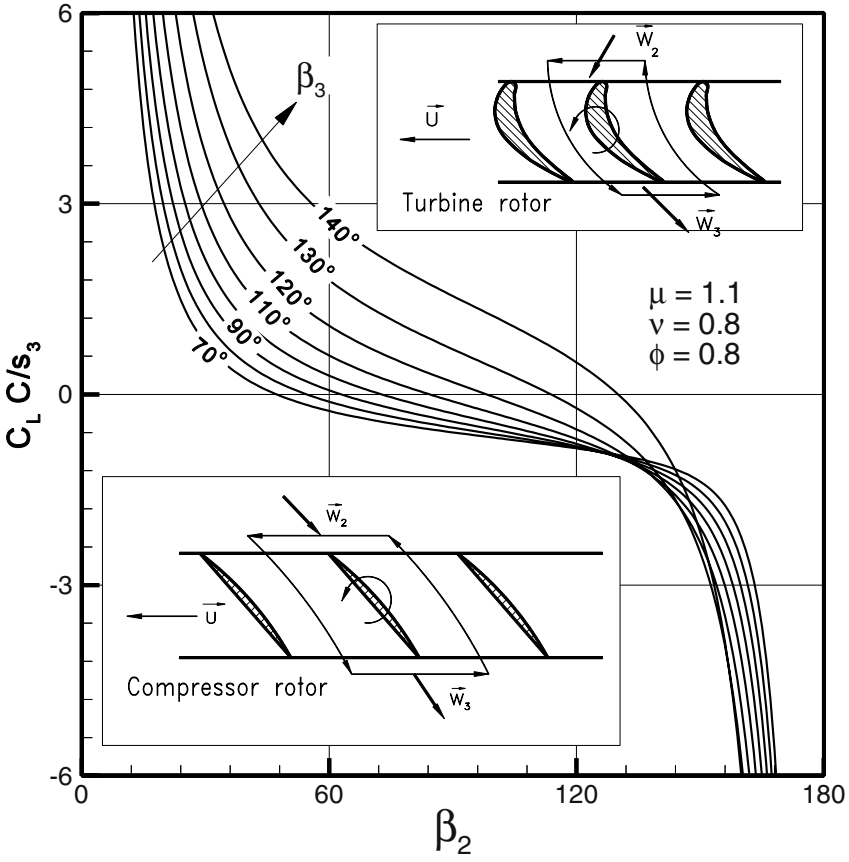

Fig. 6.16: Lift-solidity coefficient for turbine and compressor rotor cascades as a function of the relative inlet flow angle β_2 with β_3 as parameter

Equation (6.46) is generally valid for a rotating cascade, where the meridional and circumferential velocity ratios are different from zero. Special case for no-rotating cascade can easily be derived for $U \to 0$, and in the limit $\phi \to \infty$ we obtain the term $(v^2 - 1)/\phi \to 0$. In this case the relative flow angles are transformed into absolute flow angles. Considering the sign convention for circulation in Fig. 6.12, the resulting equation corresponds to Eq. (6.54).

References, Chapter 6

6.1 Pfeil, H., 1969, "Optimale Primärverluste in Axialgittern und Axialstufenvon Strömungsmaschinen," *VD-Forschungsheft* 535.

6.2 Carter, A.D.S., Hounsell, A.F., 1949, "General Performance Data for Aerofoils Having C1, C2 or C4 Base Profiles on Circular Arc Camberlines," National Gas Turbine Establishment (NGTE), Memorandum 62. London H.M. Stationary Office 1949

6.3 Abbot, J.H., Doenhoff, A.E., Stivers, L.S., 1945, "Summary of Airfoil Data," National Advisory Committee for Aeronautics (NACA) T.R. 824, Washington 1945.

6.4 Zweifel, O., 1945, "Die Frage der optimalen Schaufelteilung bei Beschaufelungen von Turbomaschinen, insebesondere bei grosser Ulenkung in den Schaufelreihen," Brown Boveri und Co., BBC-Mitteilung 32 (1945), S. 436/444.

7 Losses in Turbine and Compressor Cascades

The flow through a turbomachine is generally three-dimensional, viscous, highly unsteady, turbulent, and compressible. This complex flow is associated with total pressure losses caused by different flow and geometry parameters. To accurately predict the efficiency of a turbomachine, accurate flow calculation is required. The most accurate flow calculation method is the direct numerical simulation (DNS), which solves the Navier-Stokes equations without including any turbulence and transition models. This method is currently being applied to different turbomachinery components with great success. However, for the time being, the computational efforts and the required computation time makes the application of DNS as a design tool impractical. As an alternative, the Reynolds averaged version of the Navier-Stokes equations (RANS) is routinely applied in turbomachinery design. To simulate the flow relatively accurately by RANS, the turbomachinery aerodynamicist has to choose, among a variety of turbulence and transion models, the most suitable one that satisfactorily predicts the efficiency of the turbomachine under design. Since most of these models involve empirical correlations that are derived from simple flow experiments, they deliver efficiencies that significantly differ from the measured efficiency of the machine. To find an acceptable solution, the computer Navier-Stokes codes are frequently *calibrated*.

Before performing a CFD-simulation, however, the aerodynamicist has to estimate the magnitude of major component losses essential for the one-dimensional *mean line* calculations to arrive at the preliminary machine efficiency. For this purpose, different types of loss correlations are used that are of a purely empirical, semi-empirical, or theoretical nature. Such correlations are established by research centers, or individual turbomachinery manufacturers. What is interesting is that, regardless of the different natures of correlations and different design concepts and philosophies the machines are based on, their measured efficiencies are not far from the estimated ones. As Traupel [1] correctly indicated, a turbomachinery stage might have an efficiency of 85%, using five different major loss sources each associated with an uncertainty of ±20%. For a total stage loss coefficient, this leads to an uncertainty of ±10%. Since the normalized magnitude of the loss coefficient is considered to be 100%-85% = 15%, the uncertainty in efficiency estimation would be about 1.5% which is acceptable for a preliminary calculation. Considering these facts, the use of loss correlations is always a part of the preliminary design process.

In this chapter, attempt is made to present correlations for major individual loss coefficients that are described by the conservation laws of aero-thermodynamics and based on systematic experiments. Evidently these correlations are first approximations and cannot be considered as generally valid. However, they give insight into the mechanism of loss generation from a physical point of view and may be enhanced or corrected to suit the particular design needs. The major aerodynamic losses are:

1. Profile or primary losses
2. Losses due to the trailing edge thickness
3. Secondary flow losses
4. Losses due to trailing edge mixing in cooled gas turbine blades
5. Exit losses

Disc friction and wetness losses are minor losses. In t his chapter an attempt is made to present plausible correlations for the first five individual losses.

7.1 Profile Losses

For calculation of optimum chord-spacing, we learned that the optimum chord-spacing ratio exists at the point where the total pressure loss is a minimum. We then introduced the total pressure loss coefficient ζ, called the *profile loss coefficient* ζ_P. The profile losses are caused, among others, by the Reynolds- and Mach-number effects, geometry parameters, such as chord-spacing ratio c/s, maximum blade thickness-chord ratio *t/c*, and surface roughness. In Chapter 6, we presented the profile loss coefficient ζ_P by Pfeil [2] as:

$$\zeta_P = \left(\varepsilon_{opt}\right)_{single}\left[1 + K\left(\frac{c}{s}\right)^3_{opt}\right] C_L \frac{c}{s}\frac{1}{\sin\alpha_\infty} \tag{7.1}$$

where $(\varepsilon_{opt})_{single}$ = 0.0107 for a maximum blade thickness-chord ratio (t/c) = 0.15 for turbine, (t/c) = 0.1 for compressor blading, and K = 0.25. This equation gives a reasonably good estimation of turbine profile losses. However, for the compressor blade loss calculation, we resort to the calculation methods based on a comprehensive investigation by the National Advisory Committee for Aeronautics, NACA.

7.2 Viscous Flow in Compressor Cascade

In order to calculate the total pressure losses within a compressor cascade caused by viscous effects, the boundary layer calculation method can be applied. Such investigations were performed by NACA (1940-1965), where a great number of compressor blades have been investigated systematically. The results of those investigations are still valid for compressor design calculations and are published in the NASA-Technical Note, NASA-SP-36 [3].

7.2.1 Calculation of Viscous Flows

The viscous flow through turbine and compressor cascades or through any other turbomachinery component is described by the Navier-Stokes equations. These equations are obtained if the shear stress term in equation of motion is replaced by the Stokes relation, where the shear stress tensor is directly proportional to the deformation tensor. The solution of these equations require considerable computational effort and CPU-time. An alternative method, which leads to satisfactory results, combines the classical boundary layer method with an inviscid flow calculation procedure that is applied to the *potential core*. The basic concept of this method states that the viscosity has a significant effect within a thin *boundary layer*. Inside the boundary layer, the viscous flow causes drag forces that are associated with total pressure losses. Outside of the boundary layer, the viscosity effect might be neglected if the Reynolds number is high enough.

7.2.2. Boundary Layer Thicknesses

Before discussing the boundary layer integral equation, we introduce the boundary layer quantities such as the *displacement thickness,* δ_1, *momentum thicknesses* δ_2, *energy dissipation thickness* δ_3 and *form parameters*. Assuming the flow is incompressible, Fig. 7.1 shows the boundary layer growth on a flat plate.

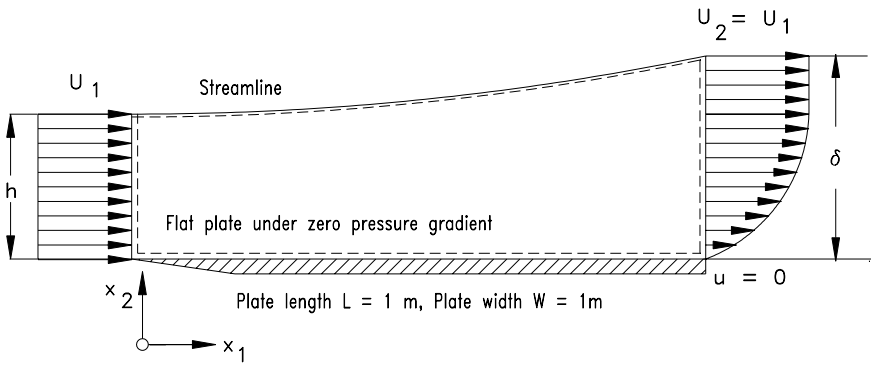

Fig. 7.1: Boundary layer development along a flat plate.

The displacement thickness is obtained by applying the continuity condition to the boundary layer flow:

$$\rho U h = \rho \int_{o}^{\delta} [(u - U) + U] dy = \rho \left[\int_{0}^{\delta} (u - U) dy + (h + \delta_1) U \right] \tag{7.2}$$

with $\delta = h + \delta_1$ and $U_1 = U_2 = U$ as the velocity at the edge of the boundary

layer shown in Fig. 7.1. As a result, we obtain the boundary layer displacement thickness:

$$\delta_1 = \int_o^{\delta} \left(1 - \frac{u}{U}\right) dy \tag{7.3}$$

The drag force in x-direction is obtained from:

$$D = \dot{m}U - \int_o^{\delta} u\, d\dot{m} \tag{7.4}$$

Using the continuity equation, the drag force becomes:

$$D = \rho \int_o^{\delta} (U - u) u dy \tag{7.5}$$

We introduce the drag coefficient C_D:

$$C_D = \frac{D}{\frac{1}{2}\rho U^2 l w} = \frac{2}{lw} \int_o^{\delta} \left(1 - \frac{u}{U}\right) \frac{u}{U} dy \tag{7.6}$$

with l and w as the length and the width of the plate. The integral in Eq. (7.7) is the the *momentum deficiency thickness* δ_2:

$$\delta_2 = \int_o^{\delta} \left(1 - \frac{u}{U}\right) \frac{u}{U} dy \tag{7.7}$$

the drag coefficient yields:

$$C_D = \frac{2\delta_2}{l} \tag{7.8}$$

Thus, the drag coefficient C_D is directly proportional to the boundary layer momentum thickness δ_2. In a similar manner, we find the *energy dissipation thickness*.

$$\delta_3 = \int_o^{\delta} \left(1 - \frac{u}{U}\right) \left(\frac{u}{U}\right)^2 dy \tag{7.9}$$

The energy dissipation thickness, especially defined for the compressor cascade, is not identical to the energy thickness in the external flow boundary layer calculation

method. We define further the form parameter:

$$H_{12} = \frac{\delta_1}{\delta_2} \quad and \quad H_{32} = \frac{\delta_3}{\delta_2} \tag{7.10}$$

7.2.3 Boundary Layer Integral Equation

We consider a two-dimensional incompressible viscous flow within the boundary layer. The equation of continuity is:

$$\frac{\partial u}{\partial x} + \frac{\partial v}{\partial y} = 0 \tag{7.11}$$

with u, and v as the velocity components in the x- and y-direction. The equations of momentum in x- and y-directions are:

$$\begin{aligned} \rho\left[u\frac{\partial u}{\partial x} + v\frac{\partial u}{\partial y}\right] &= -\frac{\partial p}{\partial x} + \mu\left[\frac{\partial^2 u}{\partial x^2} + \frac{\partial^2 u}{\partial y^2}\right] \\ \rho\left[u\frac{\partial v}{\partial x} + v\frac{\partial v}{\partial y}\right] &= -\frac{\partial p}{\partial y} + \mu\left[\frac{\partial^2 v}{\partial x^2} + \frac{\partial^2 v}{\partial y^2}\right] \end{aligned} \tag{7.12}$$

Ludwieg Prandtl deduced that if the Reynolds number is large enough, the shear layer must be very thin, so that the following approximations can be applied:

$$\delta \ll l, \quad v \ll u \quad \text{and} \quad \frac{\partial}{\partial x} \ll \frac{\partial}{\partial y} \tag{7.13}$$

Using these approximations, we arrive at:

$$\frac{\partial p}{\partial y} \simeq 0, \text{ this results in } p = p(x) \text{ and } \frac{\partial p}{\partial x} = \frac{dp}{dx} \tag{7.14}$$

The change of static pressure in Eq. (7.14) can be obtained by applying the Bernoulli relation to the region outside the boundary layer, with U as the velocity outside the boundary layer (*potential flow velocity*) that is obtained from Bernoulli equation:

$$\frac{\partial p}{\partial x} = -\rho U\frac{dU}{dx} \tag{7.15}$$

This requires that the distribution of U(x) outside the boundary layer be known. According to the previous assumptions, the following approximation can be made:

$$\frac{\partial^2 u}{\partial x^2} \ll \frac{\partial^2 u}{\partial y^2} \tag{7.16}$$

With the above approximations, the system of three Eqs. (7.11) and (7.12) is reduced to the following system of two boundary layer equations:

$$\frac{\partial u}{\partial x} + \frac{\partial u}{\partial y} = 0$$
$$u\frac{\partial u}{\partial x} + v\frac{\partial u}{\partial y} \simeq U\frac{dU}{dx} + \frac{\mu}{\rho}\frac{\partial^2 u}{\partial y^2} \tag{7.17}$$

Introducing the shear stress $\tau = \mu \frac{\partial u}{\partial y}$ and integrating Eq. (7.17) leads to:

$$\frac{d\delta_2}{dx} + \left(2 + H_{12}\right)\frac{\delta_2}{U}\frac{dU}{dx} = \frac{\tau_w}{\rho U^2} = \frac{1}{2}C_f \tag{7.18}$$

This is the boundary layer equation developed by von Kármán [4]. It expresses the change of the momentum thickness δ_2 as a function of variable x and contains the form parameter H_{12} and the friction factor C_f, which can be obtained from experimental data. The shear stress diminishes if the velocity slope approaches negligible values $\tau_w = \mu \frac{\partial u}{\partial y} \simeq 0$ if $\frac{\partial u}{\partial y} \to 0$. To solve the differential equation (7.18) for the momentum thickness δ_2, relationships for the form parameter H_{12} and the friction coefficient C_f are needed. Furthermore, the streamwise pressure gradient, which is expressed in terms of dU/dx, must be known.

7.2.4 Application of Boundary Layer Theory to Compressor Blades

The objective of the following consideration is to calculate the compressor profile losses by applying the boundary layer theory. We assume that: 1) outside the boundary layer, the total pressure is constant, inside there is a total pressure loss; 2) the working fluid is incompressible (M < 0.3); 3) at the exit, the static pressure and flow angles are constant. We define the profile loss coefficient as the total pressure loss due to the viscosity. With respect to the inlet kinetic energy it reads:

$$\zeta_P = \frac{\Delta p_o}{\frac{1}{2}\rho V_1^2} \tag{7.19}$$

with

$$\Delta p_o = \frac{1}{\dot{m}}\int_o^s \left(p_{o1} - p_{o2}\right) d\dot{m} \tag{7.20}$$

as the mass averaged total pressure loss.

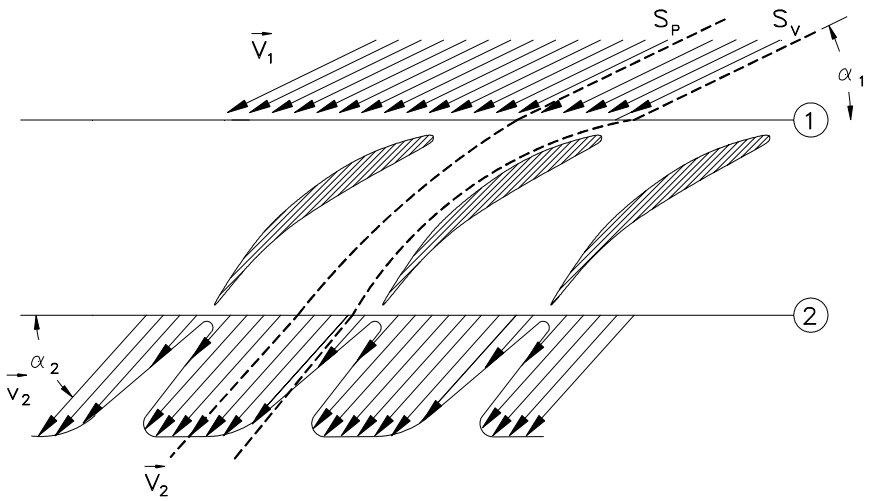

Fig. 7.2: Identification of total pressure losses due to the viscosity; S_P and S_V are streamlines within the potential core and the boundary layer

According to the above assumptions and Fig. 7.2, the total pressure outside the boundary layer, $p_{o1,}$ is:

$$p_{o1} = p_{o2} = p_2 + \frac{1}{2}\rho V_2^2 \tag{7.21}$$

The static pressure p_2 is constant within the boundary layer. Replacing the differential mass flow in Eq. (7.20) $d\dot{m} = \rho V_2 \sin\alpha_2 ds$, the total pressure loss is obtained from:

$$\Delta p_0 = \frac{\int_o^s \frac{1}{2}\rho\left(V_2^2 - v_2^2\right)\rho v_2 \sin\alpha_2 ds}{\int_o^s \rho v_2 \sin\alpha_2 ds} \tag{7.22}$$

Using the following boundary layer quantities:

$$\delta_1,\ \delta_2,\ \delta_3,\ H_{12} = \frac{\delta_1}{\delta_2} \quad and \quad H_{32} = \frac{\delta_3}{\delta_2} \tag{7.23}$$

where $\delta_1 = \delta_{1S} + \delta_{1P}$, $\delta_2 = \delta_{2S} + \delta_{2P}$, with S and P referring to suction and pressure sides. Thus, the profile loss coefficient yields:

$$\zeta_P = \sigma\left(\frac{\delta_2}{c}\right)\left(\frac{\sin^2\alpha_1}{\sin^3\alpha_2}\right)\left(\frac{1 + H_{32}}{1 - \frac{\delta_2}{c}\frac{\sigma H_{12}}{\sin\alpha_2}}\right) \tag{7.24}$$

For compressors with moderate flow deflection, the expression in the bracket is close to 2, thus Eq. (7.24) can be approximated as:

$$\zeta_P = 2\left(\frac{\delta_2}{c}\right)\left(\frac{\sigma}{\sin\alpha_2}\right)\left(\frac{\sin\alpha_1}{\sin\alpha_2}\right)^2 \tag{7.25}$$

The dimensionless momentum thickness δ_2/c can be obtained either from the von Karman's boundary layer equation or from experimental data. The solution of Eq. (7.25) for decelerated flow requires a number of empirical correlations. For design of compressor blading, it is more common to use the results of experimental investigations. Comprehensive experimental investigations concerning the optimal design of compressor blading were made in the United States by the National Advisory Committee for Aeronautics (NACA). NACA systematically investigated a number of cascade geometries, particularly the NACA-65 series published in [3]

The following uses the NACA correlations since they are still valid for low as well as high subsonic compressor blading. According to the NACA experimental observations, the velocity distribution on the blade suction surface is primarily responsible for the boundary layer development and consequently the velocity diffusion as shown in Fig. 7.3. Therefore, it is necessary to establish a relationship between the momentum thickness and the velocity distribution on the suction surface. The velocity diffusion can be expressed in terms of diffusion ratio V_{max}/V_2. Lieblein [5] introduced a functional relationship between the ratio V_{max}/V_1 and the circulation function G:

$$\frac{V_{\max}}{V_1} = C_1\, f(G) + C_2 \tag{7.26}$$

where the circulation function is

$$G = \frac{\sin^2\alpha_1}{\sigma}\left(\cot\alpha_2 - \cot\alpha_1\right) \tag{7.27}$$

Using the inlet and exit flow angles we set (for details see Chapter 16):

$$\frac{V_{\max}}{V_1} = C_1\frac{\sin^2\alpha_1}{\sigma}\left(\cot\alpha_2 - \cot\alpha_1\right) + C_2 \tag{7.28}$$

The constants C_1 and C_2 are evaluated from experiments. For NACA-65 and circular arc profiles they are $C_1 = 0.61$, $C_2 = 1.12$. Using the diffusion ratio, Eq. (7.28), the *diffusion* factor is then calculated from:

$$D = \frac{V_{max}}{V_2} = \left(\frac{V_{max}}{V_1}\right)\left(\frac{V_1}{V_2}\right)$$
$$D = \frac{\sin\alpha_2}{\sin\alpha_1}\left[0.61\,\frac{\sin^2\alpha_1}{\sigma}\left(\cot\alpha_2 - \cot\alpha_1\right) + 1.12\right] \tag{7.29}$$

Equation (7.29) is valid for the reference incidence angle i_{ref}. For incidence angle different from design incidence angle, the diffusion ratio can be obtained from [6]:

$$D = \frac{\sin\alpha_2}{\sin\alpha_1}\left[0.746\left(i - i_{ref}\right) + 0.65\left(i - i_{ref}\right)^2 + 0.61\frac{\sin^2\alpha_1}{\sigma}\left(\cot\alpha_2 - \cot\alpha_1\right) + 1.12\right] \tag{7.30}$$

With Eq.(7.30) as an independent variable, the correlation for momentum thickness is obtained experimentally. The results are plotted in Fig. 7.3. The profile loss is obtained by inserting δ_2 into Eq.(7.25).

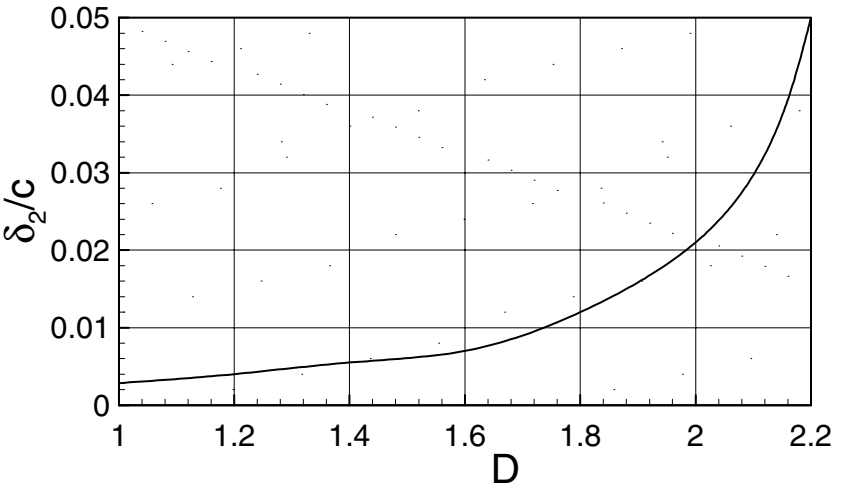

Fig. 7.3: Dimensionless momentum thickness as a function of diffusion factor.

7.2.5 Effect of Reynolds Number

As shown in Eq.(7.25), the total loss coefficient ζ is directly proportional to the momentum thickness, which in turn is inversely proportional to the Reynolds number

$$\zeta \sim \delta_2 \sim \frac{1}{Re^{m}} \tag{7.31}$$

If the Reynolds number of the blading under consideration is different from the reference Reynolds number at which the experimental measurements have been carried out, the loss coefficient must be corrected by the following relation:

$$\frac{\zeta}{\zeta_{ref.}} = \left(\frac{Re_{ref.}}{Re} \right)^{m}, \quad m = \frac{1}{5} = 0.2 \tag{7.32}$$

7.2.6 Stage Profile Losses

After determining the profile loss coefficient for stator and rotor blades, the stage profile loss coefficient Z_P can be calculated as follows:

$$Z_1 \equiv Z_P = \zeta_{PS} \left(\frac{V_n^2}{2l} \right) + \zeta_{PR} \left(\frac{W_n^2}{2l} \right) \tag{7.33}$$

with P as profile, S as stator, R as rotor, l as the specific stage mechanical energy, and n as the number of the reference plane, where ζ_P has been obtained.

7.3 Trailing Edge Thickness Losses

Downstream of a stator or a rotor cascade, the trailing edge thickness causes an exit velocity deficit, which produces a wake flow at the cascade trailing edge plane. Downstream of the cascade, at station 3 of Fig. 7.4, the non-uniform wake flow is assumed to be uniform because of the turbulent mixing. This mixing process causes additional total pressure losses that can be calculated by using the equations of continuity, momentum and energy. We start from the continuity equation:

$$\int_{o}^{s-d} \rho_2 V_2 \sin\alpha_2 dy = \rho_3 V_3 \sin\alpha_3 s \tag{7.34}$$

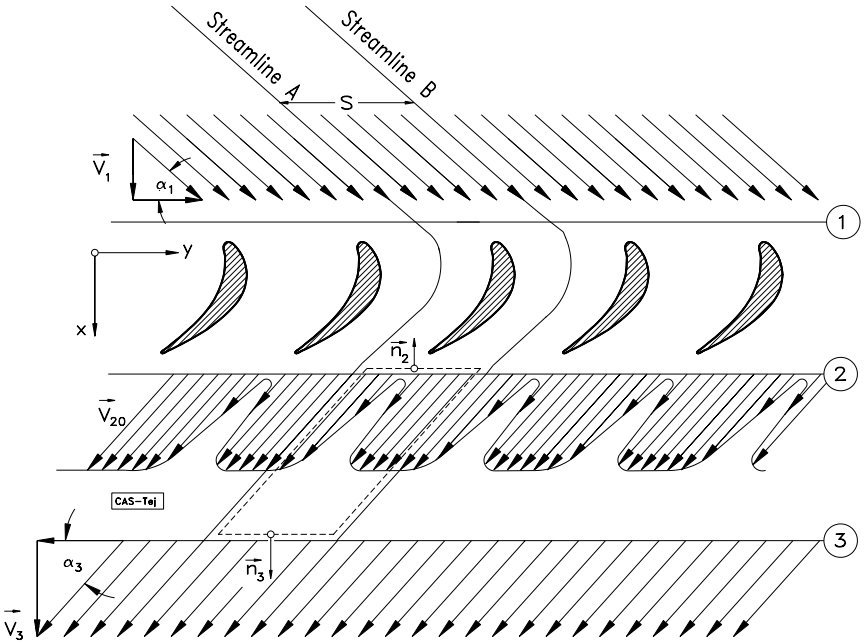

Fig. 7.4: Wake mixing downstream of a cascade with a finite trailing edge thickness.

The momentum equation in y-direction reads:

$$\int_o^{s-d} \rho_2 V_2^2 \sin\alpha_2 \cos\alpha_2 dy = \rho_3 V_3^2 \sin\alpha_3 \cos\alpha_3 s \tag{7.35}$$

and in x-direction

$$\int_o^{s-d} \rho_2 V_2^2 \sin^2\alpha_2 dy + \int_o^{s} p_2(y)\, dy = \rho_3 V_3^2 \sin^2\alpha_3 s + p_3 s \tag{7.36}$$

The energy equation yields:

$$\zeta = \frac{p_{o2} - p_{o3}}{\frac{1}{2}\rho V_3^2} \tag{7.37}$$

We introduce the boundary layer displacement and momentum thicknesses:

$$\delta_{1y} = \int_{o}^{s-d}\left(1 - \frac{V_2}{V_{2o}}\right) dy \;,\; \delta_{2y} = \int_{0}^{s-d}\frac{V_2}{V_{2o}}\left(1 - \frac{V_2}{V_{2o}}\right) dy \;,\; H_{12} = \frac{\delta_1}{\delta_2} \tag{7.38}$$

where δ_{1y} and δ_{2y} are displacement and momentum thicknesses in the y-direction. We introduce the following dimensionless variables with respect to the spacing:

$$D = \frac{d}{s} = \frac{b}{s\sin\alpha_2}, \quad \Delta_1 = \frac{\delta_{1y}}{s}, \quad \Delta_2 = \frac{\delta_{2y}}{s}$$

$$\delta_{1y} = \frac{\delta_{1S} + \delta_{1P}}{\sin\alpha_2}, \quad \text{and} \quad \delta_{2y} = \frac{\delta_{2S} + \delta_{2P}}{\sin\alpha_2} \tag{7.39}$$

with D as the dimensionless trailing edge thickness. Figure 7.5 shows the boundary layer thicknesses at the trailing edge.

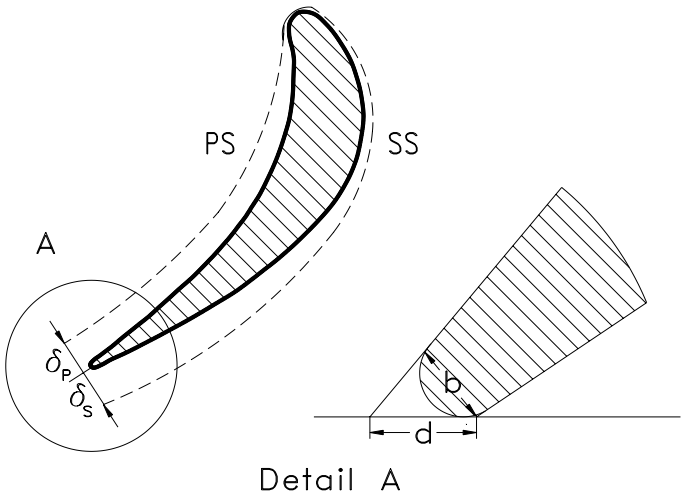

Fig. 7.5: Boundary layer thickness on suction, pressure surface, trailing edge geometry

In Eq. (7.39), the indices *P* and *S* refer to the pressure and suction side. Introducing relations in Eq. (7.39) into (7.34), (7.35) and (7.36), the equation of continuity yields:

$$\frac{\rho_3 V_3}{\rho_2 V_{2o}} = \frac{\sin\alpha_2}{\sin\alpha_3}\left[1 - D - \Delta_1\right] \tag{7.40}$$

The momentum equation in y-direction:

$$\rho_2 \sin\alpha_2 \cos\alpha_2 \int_o^{s-d} \frac{V_2^2}{V_{2o}^2}\, dy = \rho_3 \sin\alpha_3 \cos\alpha_3 \frac{V_3^2}{V_2^2}\, s$$

$$I = \int_o^{s-d} \left(\frac{V_2}{V_{2o}}\right)^2 dy = \int_o^{(s-d)} \left[-\left(1 - \frac{V_2}{V_{2o}}\right) + 1 - \frac{V_2}{V_{2o}}\left(1 - \frac{V_2}{V_{2o}}\right) \right] dy$$

$$I = s - d - \delta_{1y} - \delta_{2y} \tag{7.41}$$

With respect to s, the above integral yields:

$$\frac{\rho_3}{\rho_2} \frac{\sin\alpha_3}{\sin\alpha_2} \frac{\cos\alpha_3}{\cos\alpha_2} \left(\frac{V_3}{V_{2o}}\right)^2 = 1 - D - \Delta_1 - \Delta_2 \tag{7.42}$$

For further treatment, Eq. (7.42) is rearranged as:

$$\left(\frac{\rho_3}{\rho_2}\right)^2 \left[\frac{\rho_2}{\rho_3} \frac{\sin\alpha_3}{\sin\alpha_2} \frac{\cos\alpha_3}{\cos\alpha_2}\right] \left(\frac{V_3}{V_{2o}}\right)^2 = 1 - D - \Delta_1 - \Delta_2 \tag{7.43}$$

Dividing Eq. (7.43) by Eq. (7.40) results in:

$$\frac{\rho_2}{\rho_3} \frac{\sin\alpha_2}{\cos\alpha_2} \frac{\cos\alpha_3}{\sin\alpha_3} = \frac{1 - D - \Delta_1 - \Delta_2}{\left(1 - D - \Delta_1\right)^2} \tag{7.44}$$

Thus, the equation of momentum in y-direction is rearranged as:

$$\frac{\rho_2}{\rho_3} \cot\alpha_3 = \cot\alpha_2 \frac{1 - D - \Delta_1 - \Delta_2}{\left(1 - D - \Delta_1\right)^2} \tag{7.45}$$

For further treatment of the equation of momentum in x-direction:

$$\int_o^s p_2(y)\, dy - p_3 s = \rho_3 V_3^2 \sin^2\alpha_3 s - \int_o^{s-d} \rho_2 V_2^2 \sin^2\alpha_2\, dy \tag{7.46}$$

we look at the first integral. At the trailing edge plane, the static pressure generally changes in the y-direction. However, we introduce an average $\bar{p}_2$ that represents an integral average of the static pressure along the trailing edge area. Inserting the relationship for the integral term on the right-hand side of Eq.(7.46), we arrive at:

$$\left(\bar{p}_2 - p_3\right) = \rho_3 \sin\alpha_3^2 V_3^2 - \rho_2 \sin\alpha_2^2 V_{2o}^2 \left[1 - D - \Delta_1 - \Delta_2\right] \tag{7.47}$$

Finally, the dimensionless pressure difference reads:

$$\frac{\bar{p}_2 - p_3}{\frac{1}{2}\rho_3 V_3^2} = 2\sin\alpha_3^2 \left[1 - \frac{\rho_3}{\rho_2} \frac{1 - D - \Delta_1 - \Delta_2}{(1 - D - \Delta_1)^2}\right] \tag{7.48}$$

The total pressure loss coefficient is determined from:

$$\zeta = \frac{p_{o2} - p_{o3}}{\frac{1}{2}\rho_3 V_3^2} = \frac{p_2 - p_3}{\frac{1}{2}\rho_3 V_3^2} + \frac{\rho_2}{\rho_3}\left(\frac{V_{2o}}{V_3}\right)^2 - 1 \tag{7.49}$$

Now we introduce the following auxiliary functions:

$$\begin{aligned} G_1 &= 1 - D - \Delta_1 \\ G_2 &= 1 - D - \Delta_1 - \Delta_2 \\ \Delta_2 &= \Delta 1/H \quad R = \rho_3/\rho_2 \end{aligned} \tag{7.50}$$

with $H = H_{12}$ as the form parameter. The total pressure loss coefficient is then:

$$\zeta = \frac{G_1^2 - 2RG_2 + R}{G_1^2} - \cos\alpha_3^2 \left\{\frac{2G_1^2 - 2G_2 + R}{G_1^2} - \frac{1}{R}\frac{G_1^2}{G_2^2}\right\} \tag{7.51}$$

For the case that $R = 1$ it reduces to:

$$\zeta = \frac{G_1^2 - 2G_2 + 1}{G_1^2} - \cos\alpha_3^2 \left\{\frac{2G_1^2 - 2G_2 + 1}{G_1^2} - \frac{G_1^2}{G_2^2}\right\} \tag{7.52}$$

This equation is shown in Fig. 7.6, where the total pressure loss coefficient ζ is plotted against the dimensionless trailing edge thickness D. As shown, the total pressure losses increase with increasing trailing edge thickness. The figure also shows the effect of boundary layer thickness on the mixing process. The case $\Delta_1 = 0.0$ represents the zero-boundary layer thickness.Increasing the boundary layer thickness results in higher mixing losses. To demonstrate the effect of the trailing edge thickness on the mixing losses, we define the difference $\zeta - \zeta_0$ with ζ_0 as the loss coefficient at zero trailing edge thickness. The results, plotted in Fig. 7.7, show the mixing losses due to the trailing edge thickness only.

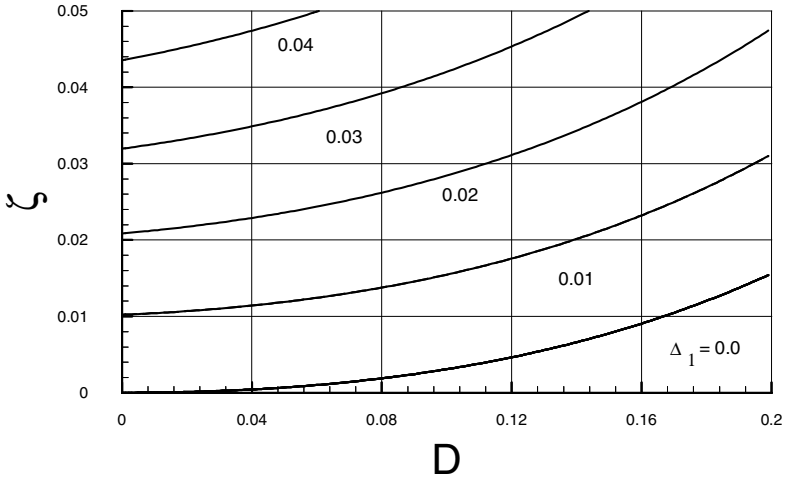

Fig. 7.6: Trailing edge loss coefficient ζ as a function of dimensionless trailing edge thickness D with dimensionless boundary layer thickness Δ_1 as a parameter.

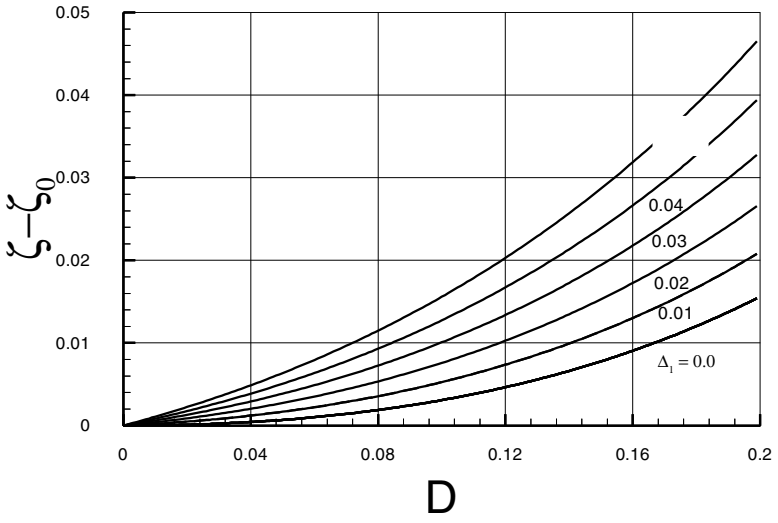

Fig. 7.7: Trailing edge loss coefficient ζ as a function of dimensionless trailing edge thickness D with dimensionless boundary layer thickness Δ_1 as a parameter.

Figures 7.6 and 7.7 display the trailing edge mixing loss coefficient with the relative boundary layer displacement thickness as parameter. This parameter can be easily determined using boundary layer calculation procedure.

7.4 Losses Due to Secondary Flows

Secondary flow losses are caused by secondary flows within the blade passage, which is a result of boundary layer development on the hub and casing walls. Between the suction and pressure surface, there is a static pressure difference. In the mid-section of the channel where the flow is assumed to be quasi potential flow (at high Re-No.), there is an equilibrium condition between the forces due to the above pressure differences and the convective flow forces. In the near of the side walls (hub or casing) where the velocity is generally affected by viscous effects, the flow forces are not able to maintain this equilibrium condition. As a result, the fluid particles in the boundary layers tend to move from the pressure side (concave) to the suction side and forms on both sides a system of secondary vortices. This phenomenon is schematically explained in Fig. 7.8. These vortex tubes induce, according to the Bio-Savart Law, a velocity field with the corresponding induced drag forces, especially drag forces. These additional drag forces must be overcome by convective forces, which result in additional total pressure losses.

7.4.1 Calculation of Secondary Flow Losses for Unshrouded Blades

Consider now a turbine cascade that undergoes an inviscid flow. Since there is no viscosity effect within the flow field, the corresponding drag forces are zero. Instead there is an induced drag force which is caused by the secondary flow field. For a wing with finite span and an elliptical lift distribution, Prandtl established a relationship

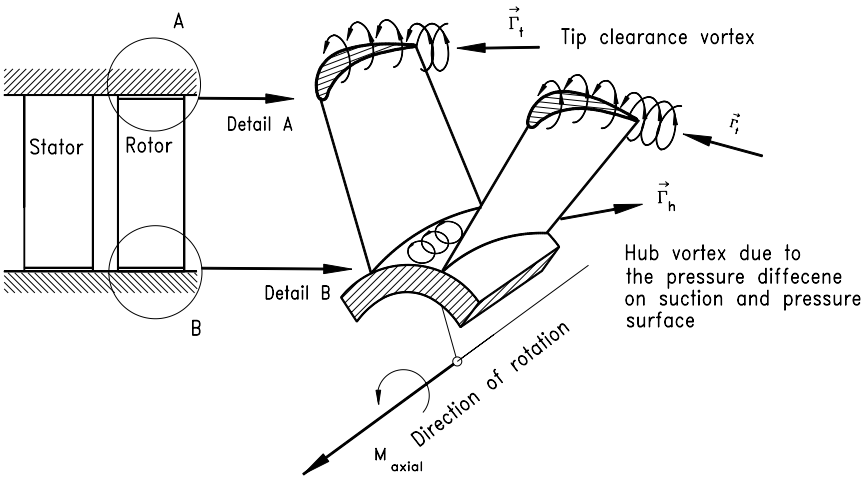

Fig. 7.8: Schematic explanation of secondary flows in a turbine stage.

between the induced drag force and the lift force. This relation can also be applied to the compressor or turbine with small aspect ratio, where the secondary flow effects

are dominant. For the turbine and compressor cascades, the induced drag forces cause a total pressure loss which is similar to the viscous pressure loss:

$$D_{axin} = sh\Delta p_{os} = \frac{D_{in}}{\sin\alpha_\infty} \tag{7.53}$$

where, h represents the blade height, s the spacing and the subscripts s and n refer to secondary flow and induced quantities. According to the Prandtl's theory, for a wing with a finite span and an elliptical lift distribution, the induced drag is directly proportional to the quadrate of lift force:

$$D_{in} \sim \frac{F_i^2}{\frac{1}{2}\rho V_\infty^2 sh} \tag{7.54}$$

since

$$\zeta_s = \frac{\Delta p_{os}}{\frac{1}{2}\rho V_2^2}\ ,\ C_L = \frac{F_i}{\frac{1}{2}\rho V_2^2 ch}\ ,\ \text{and}\quad \Delta p_{os} = \frac{D_{in}}{\sin\alpha_\infty}\frac{1}{sh} \tag{7.55}$$

where, c is the blade chord.

$$\zeta_s = \frac{1}{\frac{1}{2}\rho V_2^2}\frac{D_{in}}{\sin\alpha_\infty}\frac{1}{sh} \tag{7.56}$$

Introducing Eq.(7.54) into (7.56) yields:

$$\zeta_s \sim \frac{F^2}{\left(\frac{\rho}{2}\right)^2 V_2^2 V_\infty^2 (sh)^2}\frac{1}{\sin\alpha_\infty} = \left(C_L\frac{c}{s}\right)^2\frac{\sin\alpha_\infty}{\sin^2\alpha_2} \tag{7.57}$$

For an inviscid flow, as we saw in Chpter 6, the lift coefficient is:

$$C_L\frac{c}{s} = 2\frac{\sin^2\alpha_2}{\sin\alpha_\infty}\left(\cot\alpha_2 - \cot\alpha_1\right) \tag{7.58}$$

Incorporating Eq. (7.58) into (7.57):

$$\zeta_s \sim 4\left(cotg\alpha_2 - cotg\alpha_1\right)^2\frac{\sin^2\alpha_2}{\sin\alpha_\infty} = \Lambda \tag{7.59}$$

We introduce the load function

$$\Lambda = 4\frac{\sin^2\alpha_2}{\sin\alpha_\infty}\left(\cot\alpha_2 - \cot\alpha_1\right)^2 \tag{7.60}$$

where α_∞ can be obtained from:

$$\cot\alpha_\infty = \frac{1}{2}\left(\cot\alpha_2 + cotg\alpha_1\right) \tag{7.61}$$

The experimental results obtained from unshrouded blades by [7]show that the secondary loss coefficient is directly proportional to the load function Λ and also to the dimensionless tip clearance:

$$\zeta_s \sim \Lambda\ ,\ \zeta_s \sim f\left(\frac{\delta - \delta_o}{c}\right) \tag{7.62}$$

where δ is the actual tip clearance and δ_o the smallest tip clearance that does not cause a tip clearance flow. It was found from experiments that:

$$\zeta_s = K\Lambda\left(\frac{\delta - \delta_o}{c}\right)^m \tag{7.63}$$

where $K = 0.169$ and $m = 0.6$. We finally have for the stator:

$$\zeta_s = 0.676\left(\cot\alpha_2 - \cot\alpha_1\right)^2\frac{\sin^2\alpha_2}{\sin\alpha_\infty}\left[\frac{\delta - \delta_o}{c}\right]^m \tag{7.64}$$

and rotor:

$$\zeta_s = 0.676\left(cotg\beta_3 - cotg\beta_2\right)^2\frac{\sin^2\beta_3}{\sin\beta_\infty}\left[\frac{\delta - \delta_o}{c}\right]^m \tag{7.65}$$

The tip and hub clearance flows have two different effects. First, they generate secondary flow vortices which induce additional drag forces and secondly they cause a mass flow defect which does not participate in power production. These two effects result in a decrease of the stage efficiency and also the overall efficiency of turbomachines. The losses caused by tip clearance and secondary flow affect significantly the efficiency of those stages with a small ratio of blade height to chord, (aspect ratio). Figure 7.9 shows the secondary flow loss coefficient ζ_s as a function of dimensionless tip clearance δ/c with the blade deflection θ as the parameter.

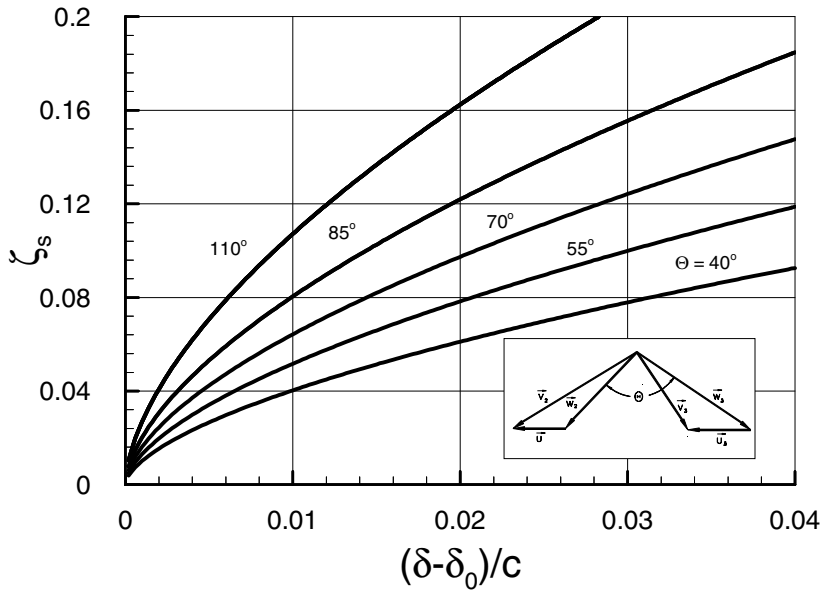

Fig. 7.9: Tip clearance total pressure loss coefficient as a function of dimensionless tip clearance with the flow deflection Θ as parameter.

As shown in Fig. 7.9, the total pressure loss coefficient increases as the tip clearance increases. Increasing the flow deflection causes the tip clearance increase considerably.

7.4.2 Secondary Flow Losses in Shrouded Blading

To reduce the tip clearance losses, shrouds with integrated labyrinth seals can be applied. The purpose of the labyrinths are to reduce the pressure difference across each labyrinth, thus reducing the clearance mass flow by using the dissipation of kinetic energy of the leakage mass flow through the clearance. Figure 7.10 shows a turbine stage with the labyrinth seals. Since the shrouded blading has no tip clearances, there is no secondary flow vortices due to tip clearance, but there are still secondary flows which originate from the boundary layer development on hub and casing walls. The following empirical correlation predicts the losses accurately:

$$\zeta_{sb} = K_2 \frac{\delta_2}{h} \left(C_L \frac{c}{s} \right)^2 \frac{\sin\alpha_\infty}{\sin^2\alpha_2} \tag{7.66}$$

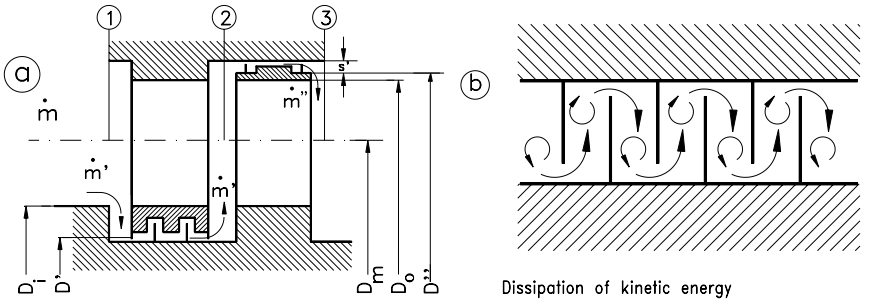

Fig. 7.10: a) A turbine stage with stator and rotor shrouds with labyrinth seals, b) Reduction of pressure across a labyrinth by means of dissipation of kinetic energy.

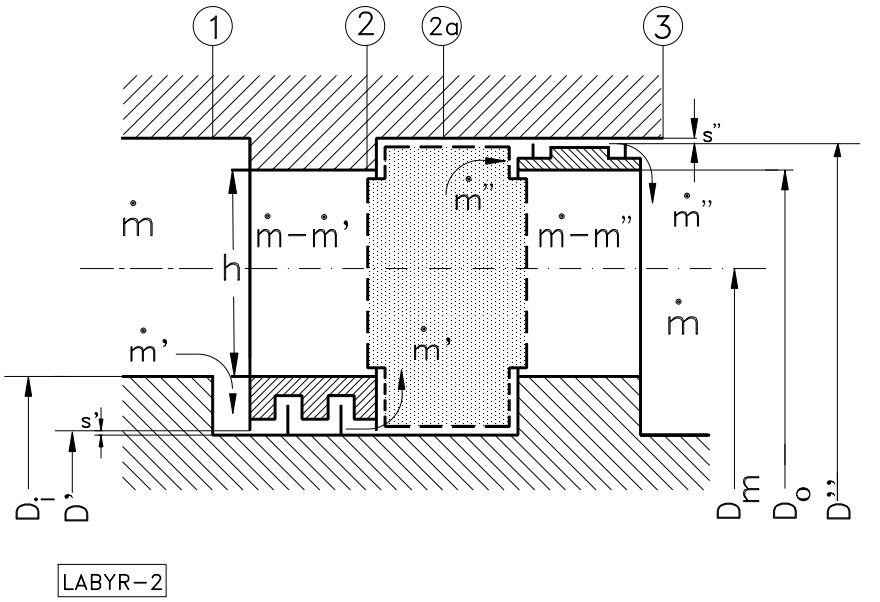

Fig. 7.11: Flow through a labyrinth seal with mixing process within the axial clearance. Quantities with ‘ and “ refer to stator and rotor respectively

In Eq. (7.66) δ_2 is the momentum thickness of the wall boundary layer, h the blade height, and the subscript *sb* refers to the secondary flow that originates from boundary layer development near the hub respectively casing. For a fully developed turbulent flow, the momentum thickness can be related to the Reynolds number:

$$\frac{\delta_2}{c} = 0.074\ R_e^{-0.2}\ ,\ K_2 = 0.444 \tag{7.67}$$

The friction forces due to the viscous flow, which occurs in the near of side walls, cause additional total pressure losses. The corresponding loss coefficient of both side walls (hub and casing) is:

$$\zeta_{fw} = K_1 \frac{\delta_2}{h} \tag{7.68}$$

Consider Eq. (7.66) and (7.68), the secondary flow and the wall friction loss coefficient is:

$$\zeta_s = 2\left(\frac{c}{h}\right)\left(\frac{0.074}{R_e^{0.2}}\right)\left(K_1 + K_2\left(C_L\frac{c}{s}\right)^2 \frac{\sin\alpha_\infty}{\sin^2\alpha_2}\right) \tag{7.69}$$

with the constants $K_1 = 3.06$, $K_2 = 0.444$, and $\zeta_s = \zeta_{sb} + \zeta_{fw}$. For shrouded blading, the stage secondary loss coefficient is:

$$Z_s = \zeta_{Ss}\frac{V_2^2}{2l} + \zeta_{Rs}\frac{W_3^2}{2l} \tag{7.70}$$

with ζ_{Ss} and ζ_{SR} as the stator and rotor secondary flow loss coefficients. In Eq. (7.70) l represents the specific mechanical energy of stage, the subscripts, *s*, *S*, and *R* stand for secondary, stator, and rotor.

7.4.3 Losses Due to Leakage Flow in Shrouds

As mentioned previously, the tip clearance losses can be reduced by applying shrouds to the stator hub and rotor tip, Fig. 7.10. The flow through the rotor shroud labyrinth does not participate in power generation. It also causes additional mixing losses. This section deals with the calculation of mixing losses. Consider a stage with shroud, Fig. 7.11, upstream of the stator blade, the stage mass flow is $\dot{m}'$. Immediately at the inlet of the stator, a fraction of the this mass flow, $\dot{m}'$, flows through the stator labyrinths.

In the axial gap, there is a mixing process between the remaining mass flow $\dot{m} - \dot{m}'$ and the leakage flow $\dot{m}'$ which is supposed to be completed immediately upstream to the rotor blading. After the mixing at station 2, a small portion, $\dot{m}''$, flows through the rotor labyrinth and therefore does not contribute to poser generation. At station 3 mixing of $\dot{m}''$ and the remaining $\dot{m} - \dot{m}''$ takes place. This mixing process is repeated for all rows and causes a total pressure loss that can be calculated by using the conservation equations. The continuity equation at station 2 in Fig. 7.11 yields:

$$\left(\dot{m} - \dot{m}'\right) = \pi\rho D_m h V_{ax2} \tag{7.73}$$

with $\dot{m}'$ as the mass flow through the stator labyrinth. At station 2a after mixing, we have:

$$\dot{m} = \rho\pi D_m h V_{ax2a} \tag{7.74}$$

Assuming an axisymmetric flow, the momentum in circumferential direction is:

$$(\dot{m} - \dot{m}')V_{u2} = \dot{m}V_{u2a} \tag{7.75}$$

and in axial direction

$$(\dot{m} - \dot{m}')V_{ax2} + \pi D_m h p_2 = \dot{m}V_{ax2a} + p_{2a} D_m h\pi \tag{7.76}$$

For stator, the total pressure loss due to the mixing is then:

$$(\Delta p_o)_S = p_{o2} - p_{o2a} = p_2 - p_{2a} + \frac{\rho}{2} V_2^2 - \frac{\rho}{2} V_{2a}^2 \tag{7.77}$$

Incorporating the above continuity and the momentum equations into Eq.(7.77), we get for stator:

$$(\Delta p_o)_S = \frac{2\dot{m}'}{\dot{m}} \frac{\rho}{2} V_2^2 \tag{7.78}$$

and rotor:

$$(\Delta p_o)_R = \frac{2\dot{m}''}{\dot{m}} \frac{\rho}{2} W_3^2 \tag{7.79}$$

where $\dot{m}'$ and $\dot{m}''$ represents the mass flow through the stator and rotor labyrinths. To find the mass flows $\dot{m}'$ and $\dot{m}''$ we consider the flow through a labyrinth seal, which consists of *n* teeth, Fig. 7.12. We assume that the flow passing through the labyrinth clearance is isentropic. After entering the labyrinth chamber, its kinetic energy is dissipated as heat isobarically:

$$\left(p + \frac{1}{2}\rho V\right)_A^2 = \left(p + \frac{1}{2}\rho V^2\right)_B \tag{7.80}$$

where *A* represents the station in labyrinth chamber and *B* refers to the station in the labyrinth tooth. Since the cross section area $a_B << a_A$, the velocity $V_B >> V_A$. Therefore V_A can be neglected compared to V_B. As a result, we get:

$$p_A - p_B = \Delta p = \frac{1}{2}\rho V_B^2 \tag{7.81}$$

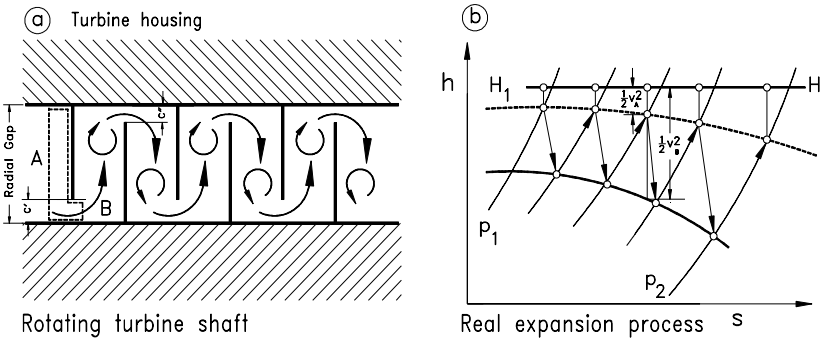

Fig. 7.12: Expansion and dissipation process through a labyrinth tooth and chamber. (a) Expansion from the labyrinth chamber with the area a_A through the tooth clearance C with the area a_B and the following dissipation in the labyrinth chamber. (b) Polytropic expansion, where the velocity inside the chamber is negligible compared with the tooth velocity.

since $\dot{m}' = a_B \rho V_B$ we find:

$$V_B = \left(\frac{\dot{m}'}{a_B} \right) \frac{1}{\rho} \tag{7.82}$$

Introducing Eq. (7.82) into Eq. (7.81) yields:

$$\Delta p = \frac{1}{2\rho} \left(\frac{\dot{m}'}{a_B} \right)^2 \tag{7.83}$$

For better understanding, the pressure distribution along a labyrinth is shown if Fig. 7.12. For an equal pressure drop in each labyrinth, the pressure difference can be expressed as:

$$\Delta p = \frac{p_1 - p_2}{n'} \tag{7.84}$$

where n' is the number of stator labyrinths

$$\frac{p_1 - p_2}{n'} = \frac{1}{2\rho} \left(\frac{\dot{m}'}{a_B} \right)^2 \tag{7.85}$$

or

$$\dot{m}' = a_B \sqrt{\frac{2(p_1 - p_2)}{n'}\rho} \tag{7.86}$$

For an incompressible flow through the stator, the density is approximated as $\rho_1 \approx \rho_2 = \rho$. This approximation allows the introduction of the enthalpy difference:

$$(p_1 - p_2)v = h_1 - h_2 = \Delta h' \tag{7.87}$$

Inserting Eq. (7.87) into (7.86), the stator leakage mass flow is calculated as:

$$\dot{m}' = a_B \rho \sqrt{\frac{2\Delta h'}{n'}} \tag{7.88}$$

We introduce relative mass flows by using main mass flow and the stage flow coefficient:

$$\dot{m} = A \rho V_{ax1} = A \rho \phi U \tag{7.89}$$

In the following, first the relative mass flow through the stator labyrinth is given followed by the mass relative flow through the rotor labyrinth. The following re-arrangement establishes a relationship between the relative mass flow through the stator- and rotor-labyrinths and the stage parameters:

$$\frac{\dot{m}'}{\dot{m}} = \frac{a_B}{A}\sqrt{\frac{2\Delta h'}{n'}}\frac{1}{\phi}\frac{1}{U}$$

$$\frac{\dot{m}'}{\dot{m}} = \frac{a_B}{A}\sqrt{\frac{2\,\Delta h'\Delta h}{n'\Delta h\; U^2}}\frac{1}{\phi}$$

$$\frac{\dot{m}'}{\dot{m}} = \frac{a_B}{A}\sqrt{\frac{2(1-r)\lambda}{n'\phi^2}} = \frac{\alpha' D' C'}{D_m h}\sqrt{\frac{2(1-r)\lambda}{n'\phi^2}} \tag{7.90}$$

with the clearance area $a_B = \pi D' C' \alpha'$, the blade cross section $A = \pi D_m h$, and the stator tooth clearance C' from Fig. 7.12. Similarly for the rotor labyrinth, we find:

$$\frac{\dot{m}''}{\dot{m}} = \frac{\alpha'' D'' C''}{D_m h}\sqrt{\frac{2r\lambda}{n''\phi^2}} \tag{7.91}$$

The values of the labyrinth flow contraction coefficients α' and α'' depend strongly on the labyrinth shape. Typical values are 0.8-0.93. For a stage with the given ϕ, λ, r, and labyrinth geometry, Figures 7.13 exhibits the relative mass flows through stator- and rotor-labyrinths $M_{Stator} = \dot{m}'/\dot{m}$ and $M_{Rotor} = \dot{m}''/\dot{m}$ respectively with the degree of reaction r as parameter. For the stator, Fig. 7.13(a), the largest leakage occurs at

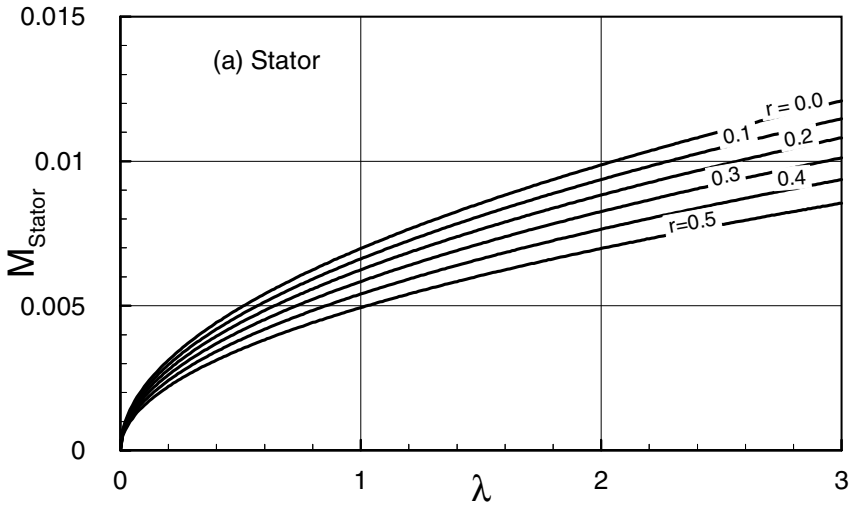

Fig. 7.13a: Relative mass flow $M_{Stator} = \dot{m}'/\dot{m}$ through the stator as function of stage load coefficient λ with degree of reaction r as parameter with $\phi = 1.0$, $\alpha' = 0.9$, D'/D_m=0.95, D''/D_m=1.05, and $s/h = 0.01$

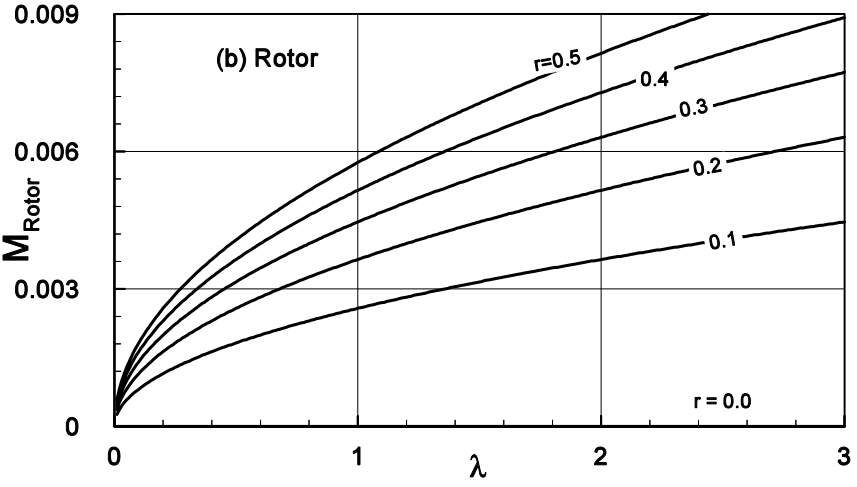

Fig. 7.13b: Relative mass flow $M_{Rotor} = \dot{m}''/\dot{m}$ through the rotor-labyrinths as function of stage load coefficient λ with degree of reaction r as parameter with ϕ=1.0, α'=0.9, D'/D_m=0.95, D''/D_m=1.05, and $s/h = 0.01$.

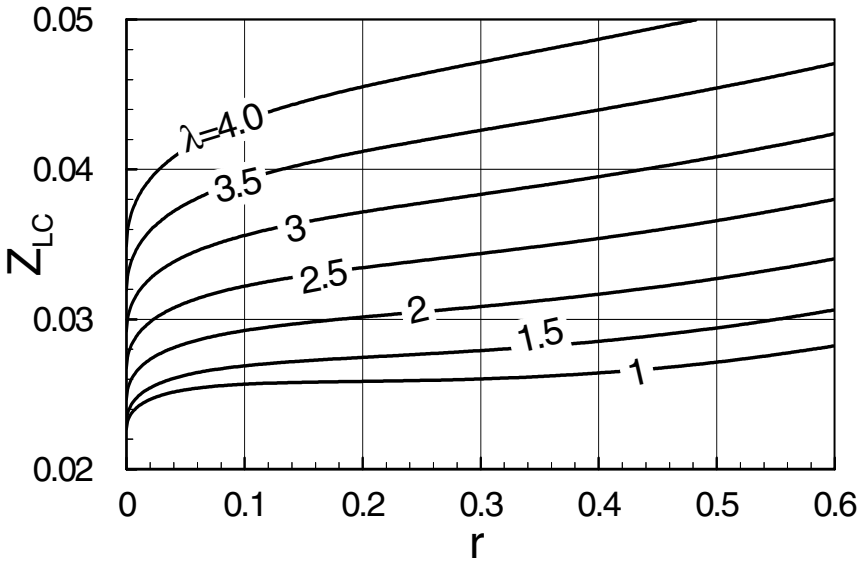

Fig. 7.14: Stage clearance leakage loss coefficient Z for a shrouded stage as a function of degree of reaction with the stage load coefficient as parameter.

r = 0. Increasing the degree of reaction leads to smaller relative mass flow through the labyrinths. This corresponds to the pressure difference across the stator labyrinths. For *r = 0* , the largest pressure difference occurs across the stator blade and thus stator labyrinths, while the pressure difference across the rotor is zero.

Increasing the degree of reaction to *r = 0.5* reduces the pressure difference across the stator blades and thus the stator labyrinths to 50%, resulting in smaller relative mass flow through the stator labyrinths. The relative mass flow through the rotor labyrinths presented in Fig. 7.13(b), however shows the opposite picture. Largest leakage flow occurs at *r = 0.5*, since it has the largest pressure difference across the rotor blading and thus the rotor labyrinths. Reducing the degree of reaction lowers the pressure difference across the rotor blading and thus the labyrinth causing the relative leakage mass flow to decrease. The stage loss coefficient due to mass flow loss is:

$$Z_{\dot{m}} = \frac{\Delta H \dot{m}^{//}}{l\dot{m}} = \frac{\dot{m}^{//}}{\dot{m}} \tag{7.92}$$

With the specific mechanical energy $\Delta H = l$. The stage clearance leakage loss comprises of stator and rotor mixing losses, described by Eqs. (7.78) and (7.79) with the mass flow rations given by Eqs. (7.90) and (7.91) and rotor mass flow loss (7.92). It is summarized as $Z_{LC} = Z_M + Z_{\dot{m}}$ and is detailed as:

$$Z_{LC} = \frac{\dot{m}^{/}}{\dot{m}} \frac{\phi^2}{\lambda} \frac{1}{\sin\alpha_2^2} + \frac{\dot{m}^{//}}{\dot{m}} \frac{\phi^2}{\lambda} \frac{1}{\sin\beta_3^2} + \frac{\dot{m}^{//}}{\dot{m}} \tag{7.94}$$

Equation (7.94) has been evaluated and is presented in Fig. 7.14 as a function of the degree of reaction *r* with the stage load coefficient λ as parameter. As seen, the lowest leakage loss is found at *r = 0*. Keeping the stage load coefficient λ constant and increasing the degree of reaction results in higher stage clearance leakage losses. Steeper increases are shown at higher λ- values.

7.5 Exit Loss

This loss represents the total energy loss caused by exit kinetic energy. For multi-stage turbomachines, it occurs only at the last stage. For a single stage machine, the exit loss has a significant influence on the overall drop of the stage efficiency. The exit loss coefficient Z_E is defined as the ratio of the exit kinetic energy with respect to specific mechanical energy of the stage:

$$Z_E = \frac{V_3^2}{2l} = \frac{V_3^2}{2\lambda U_3^2} \tag{7.95}$$

Expressing the exit velocity vector V_3 in terms of axial velocity component and using the stage dimensionless parameter from Chapter 5, we get:

$$Z_E = \frac{\phi^2}{2\lambda \sin^2\alpha_3} \tag{7.96}$$

Replacing the exit flow angle α_3 by the stage parameters from Chapter 5 yields:

$$Z_E = \frac{\phi^2 + \left(1 - \frac{\lambda}{2} - r\right)^2}{2\lambda} \tag{7.97}$$

The stage flow coefficient ϕ can be expressed as a function of the stator exit flow angle α_2, which is known as one of the stage design parameters.

$$\phi = tg\alpha_2 \left[1 - r + \frac{\lambda}{2}\right] \tag{7.98}$$

Introducing Eq. (7.98) into Eq. (7.96), the result is:

$$Z_E = \frac{1}{2\lambda}\left[tg^2\alpha_2\left(1 - r + \frac{\lambda}{2}\right)^2 + \left(1 - \frac{\lambda}{2} - r\right)^2\right] \tag{7.99}$$

This relation shows the influence of the stage load coefficient λ, the stator exit flow angle α_2 and the degree of reaction *r* on the exit loss coefficient Z_E. The results are presented in Fig. 7.15. For each pair of stator exit flow angle α_2 and degree of

reaction r, there is a minimum exit loss coefficient. at a particular λ. Since the exit kinetic energy of the last stage in a multi-stage turbine does not contribute to generation of shaft power, it must be kept as small as possible. For an stator exit flow angle of $\alpha_2 = 20^o$, the degree of reaction of $r = 50\%$ yields a minimum at $\lambda = 1$. The rotor row with this stage characteristic has an absolute exit flow angle of $\alpha_3 = 90^o$.

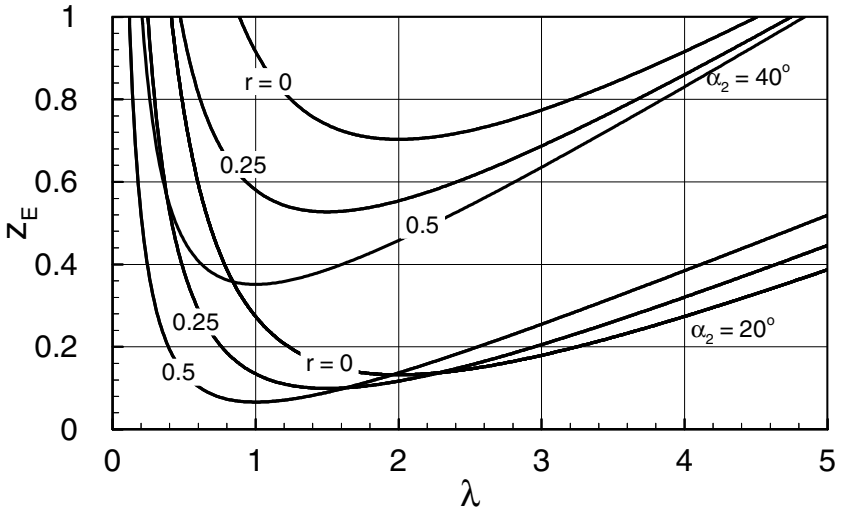

Fig. 7.15: Exit loss coefficient Z_E as a function of stage load coefficient λ with degree of reaction r as a parameter.

7.6 Trailing Edge Ejection Mixing Losses of Gas Turbine Blades

Increasing the thermal efficiency of power or thrust generating gas turbine engines requires high turbine inlet temperatures. For conventional turbine blade materials, cooling of the front stages allows an increase of the turbine inlet temperature. The required cooling mass flow is injected partially or entirely through the trailing edge slots into the downstream axial gap where the cooling and main mass flows are mixed. The trailing edge ejection affects the flow regime downstream to the cooled blade, especially the losses associated with the mixing of the cooling mass flow and the main mass flow. The ejection velocity ratio, the cooling mass flow ratio, the slot-width ratio, and the ejection angle affects the mixing losses and therefore the efficiency of cooled blades. Improper selection of these parameters results in higher mixing losses that reduce the efficiency of the cooled turbine stage. Experimental research work by Prust [8], [9] on a two-dimensional turbine stator cascade shows that the trailing edge ejection significantly affects the blade efficiency. Analytical and experimental investigations by Schobeiri [10] and Schobeiri and Pappu [11], aim at identifying and optimizing the crucial design parameters to significantly reduce the aerodynamic losses that originate from trailing edge ejection mixing processes.

7.6.1 Calculation of Mixing Losses

Starting from the conservation laws of fluid mechanics, relations are derived that accurately describes the influence of the above parameters on the flow field downstream of the cooled turbine blade. Fig. 7.16 shows the flow stations upstream of the blade, immediately at the trailing edge plane and at the mixing plane. The continuity equation can be written as:

$$\int_0^{s-d} \rho_2 V_2 \sin\alpha_2 \, dy + \rho_c V_c \sin\alpha_c \, fd = \rho_3 V_3 \sin\alpha_3 s \tag{7.100}$$

The momentum equation in y-direction is:

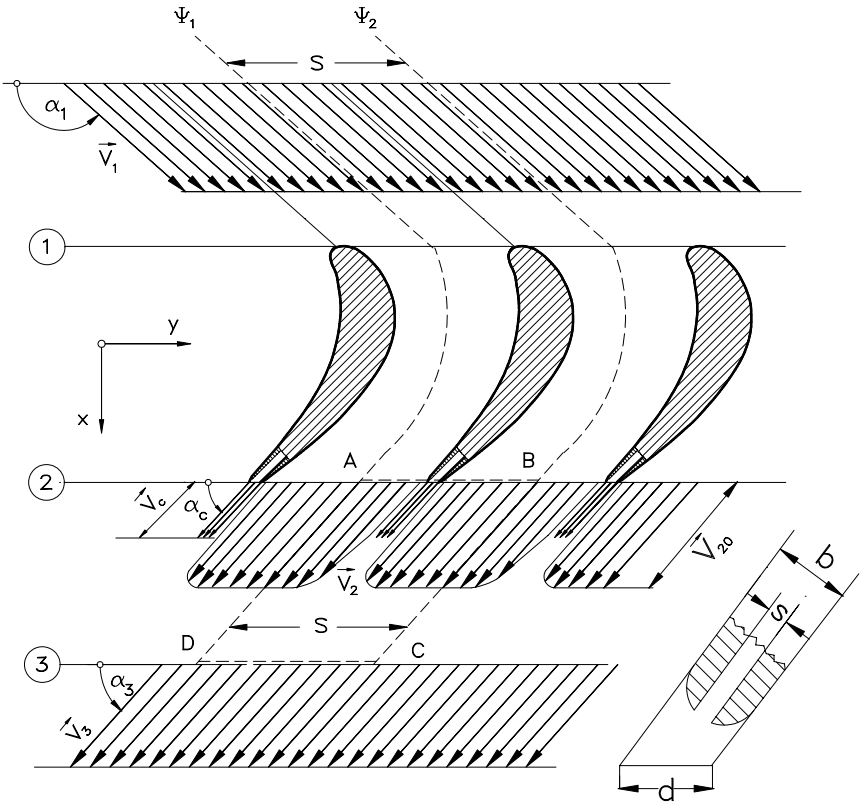

Fig. 7.16: Trailing edge ejection and mixing downstream of a cooled gas turbine blade.

$$\int_0^{s-d} \rho_2 V_2^2 \sin\alpha_2 \cos\alpha_2 \, dy + \rho_c V_c^2 \sin\alpha_c \cos\alpha_c \, fd = \rho_3 V_3^2 \sin\alpha_3 \cos\alpha_3 s \quad (7.101)$$

The momentum equation in x-direction is:

$$\int_0^{s-d} \rho_2 V_2^2 \sin\alpha_2^2 dy + \rho_c V_c^2 \sin\alpha_c^2 fd + \int_0^{s} p_2(y) dy = \rho_3 V_3^2 \sin\alpha_3^2 t + p_3 s \quad (7.102)$$

In Eqs. (7.l00) through (7.102), the parameter $f = s/b$ represents the ratio of slot width s and the trailing edge thickness b; α_2 and α_c are the exit flow angle and ejection angle, respectively, of the cooling mass flow; V_2 and V_c c are the blade exit velocity and mean ejection velocity; $p_2(y)$ is the static pressure distribution along the spacing t. The angles α_2 and α_c are assumed to be constant. Outside the trailing edge region, the static pressure $p_2(y) = p_{20}$ can be assumed as constant. As shown by Sieverding [12], inside the trailing edge region, p_2 has a nonlinear distribution whose average might differ from p_{20}. Since this pressure difference occurs only in a relatively small trailing edge region, its contribution compared with the other terms in Eq. (7.102), can be neglected. At the exit of the slot, the pressure $p_2(y)$ is determined by the static pressure p_c of the cooling mass flow. By presuming $p_c = p_{20}$ and considering the above facts, the static pressure can be approximated over the entire spacing by $p_2 = p_{20}$. For further treatment of Eqs. (7.l00) through (7.102), the boundary layer parameters, namely displacement thickness, momentum thickness and the shape parameter, are introduced:

$$\delta_1 = \int_0^{s-d} \left(1 - \frac{V_2}{V_{20}}\right) dy, \quad \delta_2 = \int_0^{s-d} \frac{V_2}{V_{20}} \left(1 - \frac{V_2}{V_{20}}\right) dy \quad (7.103)$$

The dimensionless thicknesses are found by:

$$\Delta_1 = \frac{\delta_1}{s} \; with \; \delta_1 = \frac{\delta_{1S} + \delta_{1P}}{\sin\alpha_2}$$

$$\Delta_2 = \frac{\delta_2}{s} \; with \; \delta_2 = \frac{\delta_{2S} + \delta_{2P}}{\sin\alpha_2} \quad (7.104)$$

$$D = \frac{b}{\sin\alpha_2} = \frac{d}{s}$$

where the indices S and P refer to the suction and pressure surfaces. Introducing the dimensionless parameters (7.104) into the dimensionless versions of Eqs. (7.l00)

through (7.102), the continuity relation yields:

$$\frac{\rho_3}{\rho_2}\frac{V_3}{V_2} = \frac{\sin\alpha_2}{\sin\alpha_3}\left[1 - \Delta^* - D\left(1 - \frac{\sin\alpha_c}{\sin\alpha_2}\mu\tau f\right)\right] \tag{7.105}$$

The momentum equation in y-direction is:

$$\frac{\rho_2}{\rho_3}\,cotg\alpha_3 = cotg\alpha_2\left\{\frac{1 - \Delta_1 - \Delta_2 - D(1 - \frac{\sin 2\alpha_c}{\sin 2\alpha_2}\mu\tau f)}{\left[1 - \Delta_1 - D(1 - \frac{\sin\alpha_c}{\sin\alpha_2}\mu\tau f)\right]^2}\right\} \tag{7.106}$$

The momentum equation in x-direction determines the static pressure difference:

$$\frac{p_{20} - p_3}{\frac{1}{2}\rho_3 V_3^2} = 2\sin^2\alpha_3\left\{1 - \frac{\rho_3}{\rho_2}\frac{1 - \Delta^* - \Delta^{**} - D(1 - \frac{\sin^2\alpha_c}{\sin^2\alpha_2}\mu^2\tau f)}{\left[1 - \Delta^* - D(1 - \frac{\sin\alpha_c}{\sin\alpha_2}\mu\tau f)\right]^2}\right\} \tag{7.107}$$

with: $\mu = \frac{\overline{V_c}}{V_{20}}$, $\tau = \frac{T_2}{T_c}$, $R = \frac{\rho_3}{\rho_2}$ as velocity, temperature, and density ratio.

To define the energy dissipation due to the mixing process, it is necessary to consider not only the contribution of the main flow, but also the cooling mass flow. For this purpose we combine the mechanical and thermal energy balances and arrive at a relationship that represents the change of total pressure within a system where an exchange of thermal and mechanical energy with the surroundings takes place (for detail see Chapter 12). For an adiabatic steady flow with no mechanical energy exchange, this equation is reduced to:

$$\nabla\cdot(\boldsymbol{V}P) = \frac{\kappa - 1}{\kappa}\nabla\cdot(\boldsymbol{V}\cdot\boldsymbol{T}) \tag{7.108}$$

where $P = p + \frac{1}{2}\rho V^2$ is the total pressure, **T** the shear stress tensor, and κ the ratio of the specific heats. Eq. (7.108) states that the rate of work done on fluid per unit volume by viscous forces causes a defect of total pressure work per unit volume. For an inviscid flow, Eq. (7.108) reduces to a Bernoulli equation. Integrating Eq. (7.108)

over the control volume and converting the volume integrals into the surface integrals by means of Gauss' divergence theorem leads to.

$$\int_S (n\cdot VP)dS = \int_{S_{in}} (n\cdot VP)dS + \int_{S_{out}} (n\cdot VP)dS = \Delta \dot{E} \tag{7.109}$$

The second and third integral are carried out over the entire inlet and exit surfaces under consideration. Introducing the individual mass flows $\dot{m}_c$, $\dot{m}_2$ and substituting the inlet total pressure by the total pressure of the potential core at station 2, the total energy dissipation is obtained from:

$$\Delta\dot{E} = \dot{m}_2\left(\frac{p_{20}}{\rho_2} + \frac{1}{2}V_{20}^2\right) + \dot{m}_c\left(\frac{p_c}{\rho_c} + \frac{1}{2}V_c^2\right) - \dot{m}_3\left(\frac{p_3}{\rho_3} + \frac{1}{2}V_3^2\right) \tag{7.110}$$

With respect to the exit kinetic energy, the loss coefficient is defined as:

$$\zeta = \frac{\Delta\dot{E}}{\frac{1}{2}\dot{m}_3 V_3^2} \tag{7.111}$$

Incorporating the mass flow ratios:

$$\frac{\dot{m}_2}{m_3} = \frac{1 - \Delta_1 - D}{1 - \Delta_1 - D\left(1 - \frac{\sin\alpha_c}{\sin\alpha_2}\mu\tau f\right)}, \quad \frac{\dot{m}_c}{m_3} = \frac{\sin\alpha_c \mu\tau f D}{\sin\alpha_2\left[1 - \Delta_1 - D\left(1 - \frac{\sin\alpha_c}{\sin\alpha_2}\mu\tau f\right)\right.}. \tag{7.112}$$

into Eq. (7.111), using Eqs. (7.105) through (7.107) and introducing the following auxiliary functions:

$$\begin{aligned}
G_1 &= 1 - \Delta^* - D\left(1 - \frac{\sin\alpha_c}{\sin\alpha_2}\mu\tau f\right)\\
G_2 &= 1 - \Delta^* - \Delta^{**} - D\left[\left(1 - \frac{\sin^2\alpha_c}{\sin^2\alpha_2}\mu\tau f\right)\right]\\
G_3 &= 1 - \Delta^* - D\left[\left(1 - \frac{\sin\alpha_c}{\sin\alpha_2}\mu^3\tau f\right)\right]\\
G_4 &= \frac{\sin\alpha_c \sin(\alpha_c - \alpha_2)}{\sin^2\alpha_2 \cos\alpha_2}\mu^2\tau f D
\end{aligned} \tag{7.113}$$

The loss coefficient ζ is completely described by:

$$\zeta = \frac{G_1^3 - 2RG_1^2G_2 + R2G_3}{G_1^3} - \cos^2\alpha_3 \left(\frac{2G_1^3 - 2RG_2G_1^2 + R^2G_3}{G_1^3} - \frac{G_1G_3}{(G_2 - G_4)^2} \right) \tag{7.114}$$

where all the significant parameters determining the influence of trailing edge ejection are present. With this relation, it is possible to predict the energy dissipation due to the trailing edge thickness, the boundary layer thickness at the trailing edge, and the trailing edge ejection. In this connection, the contribution of the trailing edge ejection to the energy dissipation is of particular interest. For this purpose, a typical gas turbine cascade is considered where its geometry, exit flow angle α_2, and the boundary layer parameters are known. To show the effect of trailing edge ejection, the loss coefficient ζ is calculated from Eq. (7.114) as a function of cooling mass flow ratio $\dot{m}_c/\dot{m}_2$.

The loss coefficient ζ includes the profile losses that are caused by viscosity effects. To eliminate this contribution, a cascade with the same flow conditions and boundary layer parameters, but with an infinitesimally thin trailing edge and no ejection is considered. This cascade has almost the same pressure distribution on the suction and pressure sides and also the same profile loss coefficient. The difference (ζ-ζ_o) in this case illustrates the effect of trailing edge ejection for a given trailing edge thickness.

7.6.2 Trailing Edge Ejection Mixing Losses

Equation (7.114) includes three major ejection parameters that influence the mixing loss coefficient ζ. These are the cooling velocity ratio $\mu = \bar{V}_c/V_2$, the cooling mass flow ratio $\dot{m}_c / \dot{m}_2$, the slot thickness ratio $f = s/b$, and the temperature ratio $\tau = T_c/T_2$. The effects of these parameters were theoretically investigated by Schobeiri [13] and experimentally verified by Schobeiri and Pappu [11] for two different turbines, namely the Space Shuttle Main Engine (SSME) turbine and an industrial gas turbine. For both the cascades, the cooling mass flow ratio $\dot{m}_c / \dot{m}_2$ was varied from *0.0* to *0.04* that corresponds to the cooling velocity ratio range of $\mu = 0.00 - 1.40$.

7.6.3 Effect of Injection Velocity Ratio on Trailing Edge Mixing Loss

Figure (7.17) shows the total pressure mixing loss coefficient as a function of the velocity ratio, $\mu = \bar{V}_c/V_2$, with the non-dimensional slot thickness ratio *f* as the parameter for the SSME blade. The symbols represent results from experimental

measurements and the solid, dashed lines represent results from theoretical evaluations.

For no injection $\mu = 0.0$, there is pressure loss due to finite thickness of the trailing edge and also from the boundary layer development along the pressure and suction surfaces of the blade. With increasing the cooling jet velocities, the losses initially increase until a maximum is reached. Further increase in cooling jet velocities results in the decrease of ζ to a minimum, and then increasing thereafter. For $\mu < 0.7$, the losses due to injection of cooling mass flow are higher than for the no injection case. This is caused by the low momentum of the cooling jet being unable to sustain the strong dissipative nature of the wake flow downstream of the trailing edge. So, the main mass flow entrains the cooling mass flow resulting in a complete dissipation of the energy of the jet. Therefore, higher mixing losses occur at low injection velocities until a maximum ζ is reached, which occurs around $\mu = 0.3$ beyond which ζ begins to decrease. For injection velocity ratios $\mu > 0.7$, the momentum of a cooling jet is sufficient to overcome the wake flow without being dissipated completely. Owing to this phenomenon, a significant reduction in mixing losses is evident from Figs. 7.17. This reduction proceeds until ζ reaches a minimum, which is around $\mu = 1$. Further increase of μ above 1.1 increases the losses again for similar reasons explained earlier.

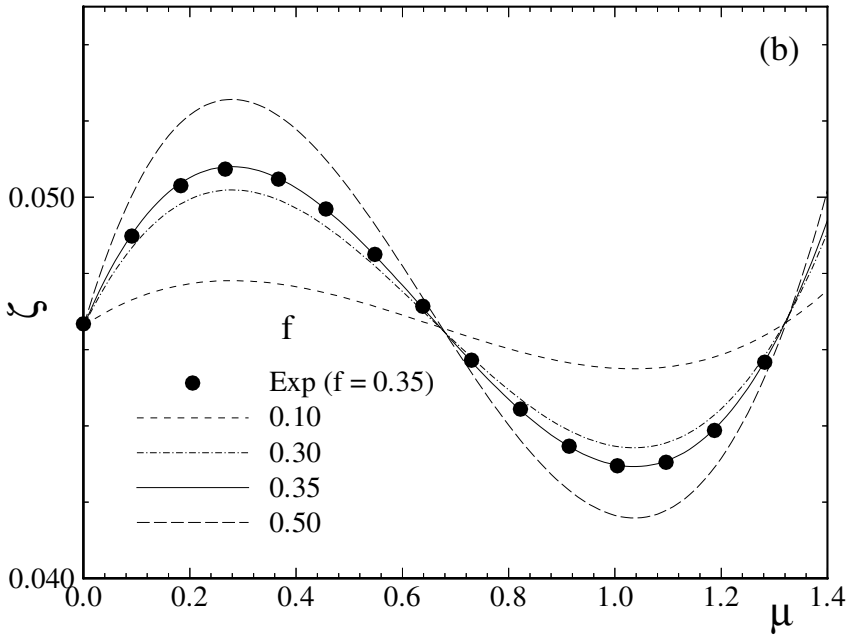

Fig. 7.17: Loss coefficient ζ as a function of velocity ratio μ with slot-with ratio *f* as a parameter for SSME blade, [11]. Experiments shown as solid circles.

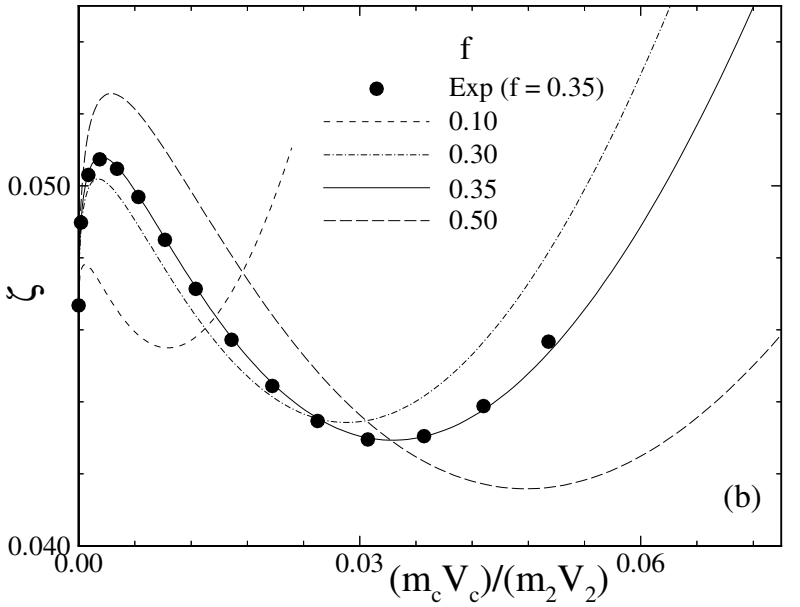

Fig. 7.18: Loss coefficient ζ as a function of momentum ratio $(\dot{m}_c \bar{V}_c)/(\dot{m}_2 V_2)$ with slot-width as parameter for SSME blades [11].

Figures 7.18 shows the mixing loss coefficient as a function of cooling jet momentum ratio $(\dot{m}_c \bar{V}_c)/(\dot{m}_2 V_2)$ with slot- thickness ratio *f* as the parameter for the SSME blade. Also, it is evident from this figure that for a given *f*, the mixing loss coefficient has a pronounced optimum.

7.6.4 Optimum Trailing Edge Mixing Losses

Of particular interest to the turbine blade aerodynamicist and designer is how small the slot-thickness ratio *f* should be for a given cooling mass flow which is dictated by the heat transfer requirements to meet the optimum conditions for ζ. Figures 7.19 provides this crucial information. This figure show the miing loss coefficient ζ as a function of sloth thickness ratio with the mass flow ratio $\dot{m}_c/\dot{m}_2$ as the parameter. Optimum mixing loss can easily be found by choosing the appropriate slot-thickness ratio.

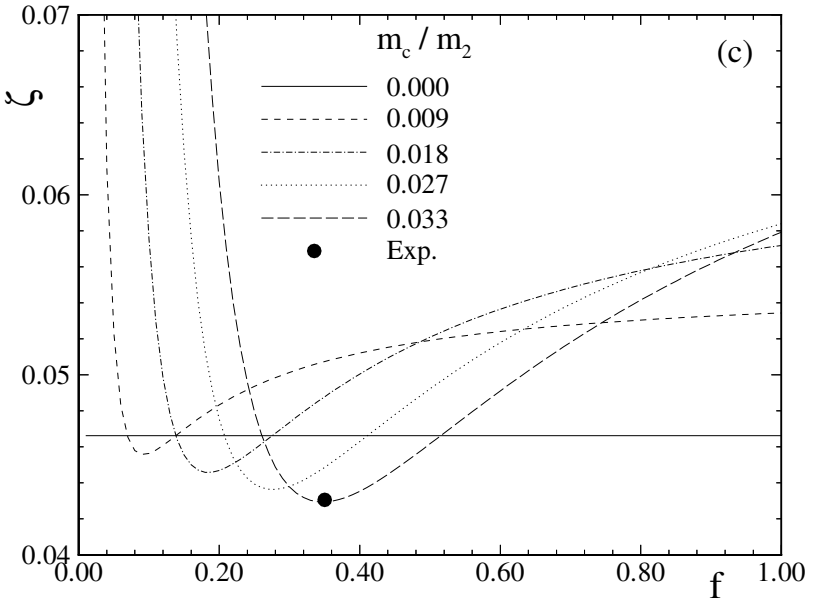

Fig. 7.19: Loss coefficient ζ as a function of slot- thickness ratio f for SSME blade

7.7 Stage Total Loss Coefficient

After calculating the individual stage loss coefficients Z_i, the total stage coefficient is calculated as:

$$Z = \sum_{i=1}^{n} Z_i = Z_1 + Z_2 + \ldots \tag{7.115}$$

where, index *i* represents the individual stage losses, for example, profile losses, secondary losses, etc. We define the total isentropic stage loss coefficient Z_s:

$$Z_s = \frac{\Delta h_{loss}}{\Delta H_s} \tag{7.116}$$

where Δh_{loss} represents all the enthalpy losses due to the different loss mechanisms discussed in this chapter, and ΔH_s the available stage isentropic enthalpy difference. For the turbine stage, Eq. (7.116) is written as:

$$Z_s = \frac{\Delta h_{loss}}{l + \Delta h_{loss}} = \frac{Z}{Z + 1} \tag{7.117}$$

and for compressor stage:

$$Z_s = \frac{\Delta h_{loss}}{l - \Delta h_{loss}} = \frac{Z}{1 - Z} \tag{7.118}$$

The isentropic efficiency for turbine stage is defined as the ratio of actual total enthalpy difference, which is identical with stage mechanical energy and the isentropic stage total enthalpy difference. The isentropic stage efficiency in terms of Z_s is:

$$\eta_s = \frac{\Delta H}{\Delta H_s} = \frac{l}{\Delta H_s} = \frac{\Delta H_s - \Delta h_{loss}}{\Delta H_s} = 1 - Z_s \tag{7.119}$$

and in terms of Z:

$$\eta_s = \frac{\Delta H}{\Delta H_s} = \frac{l}{\Delta H_s} = \frac{l}{l + \Delta h_{loss}} = \frac{1}{1 + Z} \tag{7.120}$$

Equation (7.120) represents the isentropic turbine stage efficiency in terms of the actual total stage loss coefficient Z. Similar relations are derived for compressor stage in terms of Z_s:

$$\eta_s = \frac{\Delta H_s}{\Delta H} = \frac{\Delta H_s}{\Delta H} = \frac{\Delta H_s}{\Delta H_s + \Delta h_{loss}} = \frac{1}{1 + Z_s} \tag{7.121}$$

and in terms of Z:

$$\eta_s = \frac{\Delta H_s}{\Delta H} = \frac{\Delta H_s}{l} = \frac{l - \Delta h_{loss}}{l} = 1 - Z \tag{7.122}$$

References, Chapter 7

7.1 Traupel, W., Thermische Turbomaschinen, Bd.I, 1977, Springer-Verlag Berlin Heidelberg New York.

7.2 Pfeil, H., Verlustbeiwerte von optimal ausgelegten Beschaufelungsgittern, Energie und Technik 20, Jahrgang 1968, Heft 1, L.A. Klepzig Verlag Düsseldorf.

7.3 NASA SP-36 NASA Report, 1965.

7.4 von Kármán , Th., Über laminare und turbulenteReibung,ZAMM, 1, 233-253, (1921).

7.5 Lieblein, S., Schwenk, F., Broderick, R.L., Diffusions factor for estimating losses and limiting blade loadings in axial flow compressor blade elements, *NACA RM E53D01* June 1953.

7.6 Schobeiri, M. T., 1998, A New Shock Loss Model for Transonic and Supersonic Axial Compressors With Curved Blades," *AIAA, Journal of Propulsion and Power,* Vol. 14, No. 4, pp. 470-478.

7.7 Berg, H., Untersuchungen über den Einfluss der leistungsyahl auf Verluste in Axialturbinen, Dissertation, Technische Hochschule Darmstadt, 1973, D 17.

7.8 Prust, H., 1974, "Cold-air study of the effect on turbine stator blade aerodynamic performance of coolant ejection from various trailing-edge slot geometries," NASA-Reports I: TMX 3000.

7.9 Prust, H., 1975, "Cold-air study of the effect on turbine stator blade aerodynamic performance of coolant ejection from various trailing-edge slot geometries," NASA-Reports II: TMX 3190.

7.10 Schobeiri, T.,1985, "Einfluss der Hinterkantenausblasung auf die hinter den gekuehlten Schaufeln entstehenden Mischungsverluste," Forschung im Ingenieurwesen Bd.51 Nr.1, pp.25-28.

7.11 Schobeiri, M. T., Pappu, K., 1999, "Optimization of Trailing Edge Ejection Mixing Losses Downstream of Cooled Turbine Blades: A theoretical and Experimental Study," ASME Transactions, *Journal of Fluids Engineering*, 1999, Vol. 121, pp. 118-125 Schobeiri and pappu

7.12 Sieverding, C.H., 1982, "The Influence of Trailing Edge Ejection on the Base Pressure in Transonic Cascade," ASME Paper: 82-GT-50.

7.13 Schobeiri, M. T., 1989, "Optimum Trailing Edge Ejection for Cooled Gas Turbine Blades," ASME Transaction, *Journal of Turbo machinery*, Vol. 111, No. 4, pp.510-514, October 1989.

8 Efficiency of Multi-stage Turbomachines

In Chapter 7, we derived the equations for calculation of different losses that occur within the stage. As shown, the sum of those losses determines the stage efficiency, which shows the capability of energy conversion within the stage. The stage efficiency, however, is not fully identical to the efficiency of the entire turbomachine. In a multi-stage turbomachine, the expansion or compression process within individual stages causes an entropy production, which is associated with a temperature increase. For an expansion process, this temperature increase leads to a heat recovery, Fig. 8.1 ; for a compression process, it is associated with a reheat. As a consequence, the turbine efficiency is higher and the compressor efficiency smaller than the stage efficiency. The objective of this chapter is to describe this phenomenon by means of classical thermodynamic relations. The approach is adopted by many authors, among others, Traupel [1] and Vavra [2].

8.1 Polytropic Efficiency

For an infinitesimal expansion and compression shown in Fig. 8.1, we *define the small polytropic efficiency:*

$$\eta_p = \frac{dh}{dh_s}\ (expansion),\ \eta_p = \frac{dh_s}{dh}\ (compression),\ dh = c_p dT,\ dh_s = c_p dT_s \tag{8.1}$$

For an infinitesimal expansion, c_p can be considered as constant:

$$\eta_p = \frac{(T + dT) - T}{T + dT_s - T} = \frac{\frac{T + dT}{T} - 1}{\frac{T + dT_s}{T} - 1} \tag{8.2}$$

For a polytropic process it generally holds pv^n = const. Inserting Eq. (8.2) into Eq. (8.1):

$$\eta_p = \frac{dh}{dh_s} = \frac{\left(\frac{p + dp}{p}\right)^{\frac{n-1}{n}} - 1}{\left(\frac{p + dp}{p}\right)^{\frac{k-1}{k}} - 1} \tag{8.3}$$

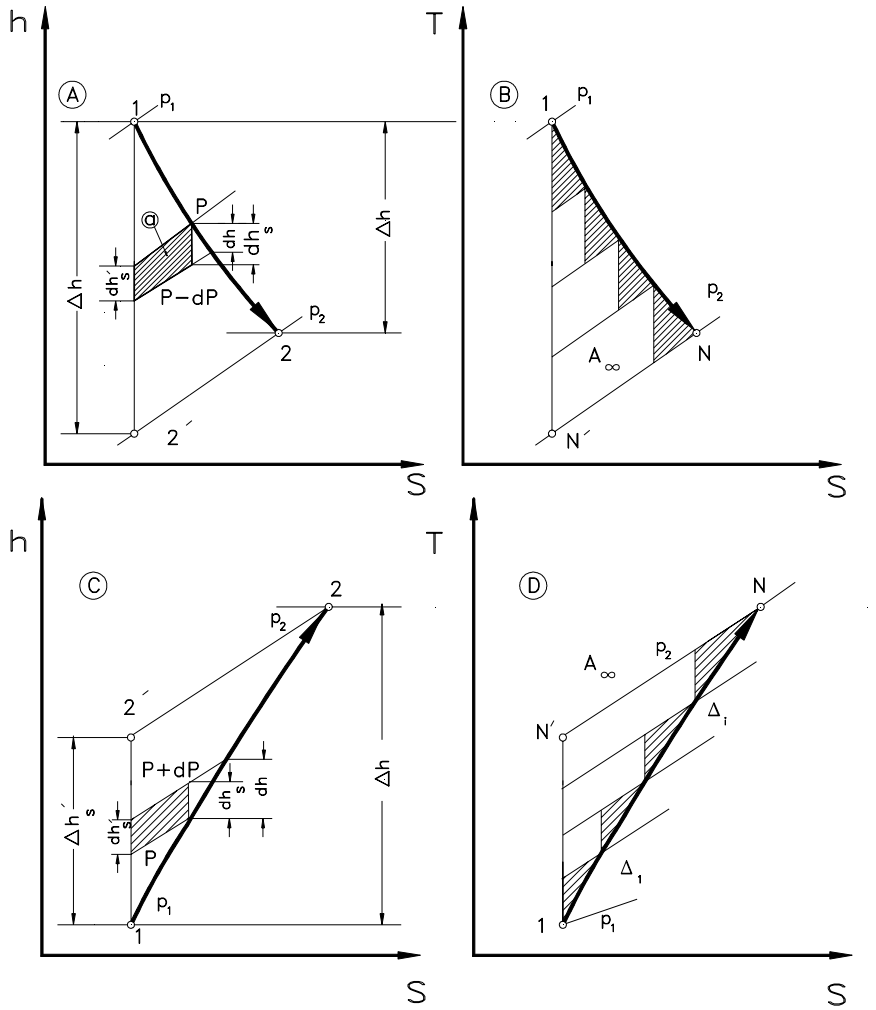

Fig. 8.1: A)Heat recovery in a turbine with $N_{stage}=\infty$, B)Heat recovery in a turbine with $N_{stage}=4$, C) Reheat process in a compressor with $N_{stage}=\infty$, D) Reheat process in a compressor with $N_{stage}=4$

After expanding the expressions in the parentheses in Eq. (8.3):

$$\left(\frac{p+dp}{p}\right)^{\frac{n-1}{n}} \quad and \quad \left(\frac{p+dp}{p}\right)^{\frac{\kappa-1}{\kappa}} \tag{8.4}$$

and neglecting the higher order terms, we find:

$$\left(1 + \frac{dp}{p}\right)^{\frac{n-1}{n}} \simeq 1 + \left(\frac{n-1}{n}\right)\frac{dp}{p} \tag{8.5}$$

Now, we introduce Eq. (8.5) into (8.3) and obtain the small polytropic efficiency:

$$\eta_p = \frac{dh}{dh_s} = \frac{1 + \frac{dp}{p}\frac{n-1}{n} - 1}{1 + \frac{dp}{p}\frac{\kappa-1}{\kappa} - 1} \tag{8.6}$$

For the expansion process, Eq. (8.6) reduces to:

$$\eta_p = \left(\frac{\kappa}{\kappa-1}\right)\left(\frac{n-1}{n}\right) \tag{8.7}$$

likewise for a compression process we find:

$$\eta_p = \left(\frac{n}{n-1}\right)\left(\frac{\kappa-1}{\kappa}\right) \tag{8.8}$$

With n as the polytropic and κ as isentropic exponents. Equations (8.7) and (8.8) express the direct relation between the polytropic efficiency η_p and the polytropic exponent n for *infinitesimally small* expansion and compression, where n and κ are considered constant. In a multi-stage environment, both exponents change from the start of expansion or compression to the end. As a result, Eqs. (8.7) and (8.8) are not valid for finite expansion or compression processes. However, if the end points of these processes are known, averaged polytropic efficiency for multi-stage compression and expansion can be found. For a process with known beginning and end points, we may use the polytropic relation:

$$p_1 v_1^{\bar{n}} = p_2 v_2^{\bar{n}} \tag{8.9}$$

and the following enthalpy relation:

$$h = \frac{\bar{\kappa}}{\bar{\kappa}-1} p v \tag{8.10}$$

where $\bar{n}$ and $\bar{\kappa}$ are the averaged polytropic and isentropic exponents. From Eq. (8.9), we find:

$$\overline{n} = \frac{\ln\frac{p_2}{p_1}}{\ln\frac{v_1}{v_2}} \tag{8.11}$$

Inserting Eq. (8.11) into Eqs. (8.7) and (8.8), we find

$$\overline{\eta_{p_C}} = \frac{\overline{\kappa} - 1}{\overline{\kappa}} \frac{\ln\frac{p_2}{p_1}}{\ln\frac{T_2}{T_1}}, \qquad \overline{\eta_{p_T}} = \frac{\overline{\kappa}}{\overline{\kappa} - 1} \frac{\ln\frac{T_2}{T_1}}{\ln\frac{p_2}{p_1}} \tag{8.12}$$

As mentioned previously, calculating the above polytropic efficiencies require the knowledge of the process end points, which are at the beginning of a design process, unknown, but can be determined after the individual losses are calculated. The averaged isentropic exponent in Eq. (8.12) is calculated from:

$$\overline{c_p} = \frac{h_2 - h_1}{T_2 - T_1}, \quad \frac{\overline{c_p}}{\overline{c_v}} = \overline{\kappa}, \quad \text{and} \quad \overline{c_p} - \overline{c_v} = R \tag{8.13}$$

8.2 Isentropic Turbine Efficiency, Recovery Factor

Assuming the turbine has an infinite number of stages, we start from an infinitesimal expansion to define the isentropic stage efficiency, Fig. 8.1:

$$\eta_s = \frac{dh}{dh_{s'}} \Rightarrow dh = \eta_s dh_{s'} \tag{8.14}$$

Using the definitions in Eq. (8.1), we find the enthalpy differential:

$$dh = \eta_p dh_s \tag{8.15}$$

As shown in Fig. 8.1, for an infinitesimally small cycle with the area a, the isentropic enthalpy differentials are interrelated by the first law as: $dh_s = dh_{s'} + a$. Using Eq. (8.15), we arrive at:

$$dh = \eta_p \left(dh_{s'} + a \right) \tag{8.16}$$

Integration of Eq. (8.15) and (8.16) yields:

$$\Delta h = \overline{\eta}_s \Delta h_{s'} \tag{8.17}$$

and:

$$\Delta h = \overline{\eta}_p \Delta h_s = \overline{\eta}_p \left(\Delta h_{s'} + A_\infty \right) \tag{8.18}$$

with A_∞ as the area 122'1, and $\bar{\eta}_s$ and $\bar{\eta}_p$ as the mean isentropic turbine and mean polytropic efficiencies. Equating (8.17) and (8.18) results in:

$$\overline{\eta_s} = \overline{\eta_p} \frac{\left(\Delta h_s' + A_\infty \right)}{\Delta h_{s'}} = \overline{\eta_p} \left[1 + \frac{A_\infty}{\Delta h_{s'}} \right] \tag{8.19}$$

We introduce the heat recovery factor for a turbine with the stage number N = ∞:

$$1 + f_{\infty T} = 1 + \frac{A_\infty}{\Delta h_{s'}} \tag{8.20}$$

With this definition, Eq. (8.19) becomes:

$$\overline{\eta}_s = \overline{\eta}_p \left(1 + f_{\infty T} \right) \tag{8.21}$$

To find the recovery factor, we divide Eq. (8.17) by (8.18):

$$\frac{\overline{\eta_s}}{\overline{\eta_p}} = \frac{\Delta h_s}{\Delta h_{s'}} = \frac{\int_{p_2}^{p_1} v dp}{\int_{p_2}^{p_1} v_s dp} = 1 + f_{\infty T} \tag{8.22}$$

The integral in the numerator must be performed along the polytropic expansion, whereas the integral expression in the denominator must be performed along the isentropic expansion. We insert in Eq. (8.22)) for the specific volume, the relationship for polytropic and isentropic processes:

$$v_s = v_1 \left[\frac{p_1}{p_2} \right]^{\frac{1}{\kappa}} \quad , \quad v = v_1 \left[\frac{p_1}{p} \right]^{\frac{1}{n}} \tag{8.23}$$

and arrive at:

$$1 + f_{\infty T} = \frac{\dfrac{\bar{n}}{\bar{n} - 1}}{\dfrac{\bar{\kappa}}{\bar{\kappa} - 1}} \frac{\left(1 - \left[\dfrac{p_2}{p_1} \right]^{\frac{\bar{n} - 1}{\bar{n}}} \right)}{\left(1 - \left[\dfrac{p_2}{p_1} \right]^{\frac{\bar{\kappa} - 1}{\bar{\kappa}}} \right)} \tag{8.24}$$

The polytropic exponent $\bar{n}$ in Eq. (8.23) can be expressed in terms of $\bar{\kappa}$ and η_p using Eq. (8.8). With this modification, the recovery factor is obtained from:

$$1 + f_{\infty T} = \frac{1}{\bar{\eta}_p} \frac{\left(1 - \left[\dfrac{p_2}{p_1} \right]^{\frac{\kappa - 1}{\kappa} \frac{1}{\eta_p}} \right)}{\left(1 - \left[\dfrac{p_2}{p_1} \right]^{\frac{\kappa - 1}{\kappa}} \right)} \tag{8.25}$$

For a multi-stage turbine with N stages, Fig. 8.1B, the following geometrical approximations may be made:

$$\begin{aligned} A_N &= A_\infty - \sum_{i=0}^{N} \Delta_i \\ \Delta_i &\simeq \Delta_{i+1} \simeq \Delta_m \end{aligned} \tag{8.26}$$

with Δ_m as the area that represents an average of all triangular areas Δ_i. With this approximation, we obtain $A_N = A_\infty - N\Delta_m$ and define the ratio:

$$f_T = \frac{A_N}{\Delta h_s} = \frac{A_\infty}{\Delta h_s} \left(1 - \frac{N\Delta_m}{A_\infty} \right) \tag{8.27}$$

Since A_∞ and Δ_m are similar, we may approximate

$$\Delta_m \simeq \frac{A_\infty}{N^2} \tag{8.28}$$

As a result, Eq. (8.27) reduces to:

$$f_T = f_{\infty T}\left(1 - \frac{NA_\infty}{N^2 A_\infty}\right) = f_{\infty T}\left(1 - \frac{1}{N}\right) \tag{8.29}$$

Using the same procedure that has lead to Eq. (8.22), for a turbine component with a finite number of stages we find:

$$\overline{\eta_s} = \overline{\eta_p}\left(1 + f_T\right) \tag{8.30}$$

Since f_T is > 0, the turbine isentropic efficiency is greater than the polytropic efficiency. This is a consequence of stage entropy production that results in heat recovery. For a turbine component with a pressure ratio $\pi_T = p_2/p_1$, the recovery factor f_{∞_T} is plotted in Fig. 8.2, where the averaged turbine polytropic efficiency $\overline{\eta_P}$ is varied from 0.7 to 0.95. As seen, the lowest efficiency of $\overline{\eta_P} = 0.7$ causes the highest dissipation that leads to a high recovery factor. Increasing the polytropic efficiency to $\overline{\eta_P} = 0.95$, causes a much less dissipative expansion. As a result, the heat recovery for the turbine with $\overline{\eta_P} = 0.95$ is much lower than the previous one with $\overline{\eta_P} = 0.7$.

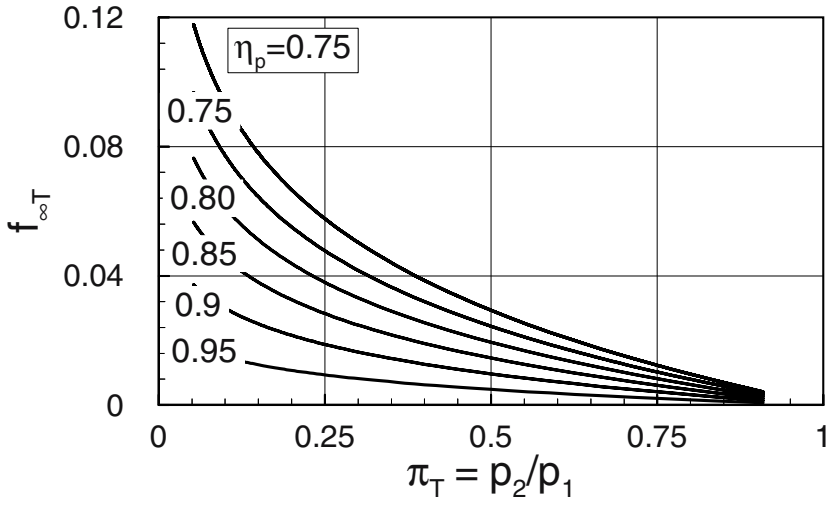

Fig. 8.2: Recovery factor of a multi-stage turbine for κ = 1.4.

8.3 Compressor Efficiency, Reheat Factor

To obtain the reheat factor for a multi-stage compressor, we apply a similar procedure as outlined in section 8.2. The isentropic efficiency of an infinitely small compression, shown in Fig. 8.1, is defined as:

$$\eta_s = \frac{dh_{s'}}{dh} \quad , \quad dh = \frac{dh_{s'}}{\eta_s} \tag{8.31}$$

Polytropic efficiency is:

$$\eta_p = \frac{dh_s}{dh} \quad , \quad dh = \frac{dh_s}{\eta_p} \tag{8.32}$$

For a compressor with an infinite number of stages, the mean isentropic efficiency is:

$$\overline{\eta_s} = \overline{\eta_p} \frac{1}{1 + f_{\infty C}} \tag{8.33}$$

where the expression $1 + f_{\infty C}$ is the reheat factor and the subscript C refers to a compressor. The reheat factor is obtained from:

$$1 + f_{\infty C} = \overline{\eta_p} \frac{\left(\frac{p_2}{p_1}\right)^{\frac{1}{\eta_p}\frac{\bar{\kappa}-1}{\bar{\kappa}}} - 1}{\left(\frac{p_2}{p_1}\right)^{\frac{\bar{\kappa}-1}{\bar{\kappa}}} - 1} \tag{8.34}$$

For a multi-stage high pressure compressor component with a pressure ratio $\pi_C = p_2/p_1$, the reheat factor f_{∞_C} is plotted in Fig. 8.3, where the averaged compressor polytropic efficiency $\overline{\eta_P}$ is varied from 0.7 to 0.95. Similar to the turbine component discussed in Section 9.2, the lowest efficiency of $\overline{\eta_P} = 0.7$ causes the highest dissipation that leads to a high reheat factor. Increasing the polytropic efficiency to $\overline{\eta_P} = 0.95$ causes much less dissipation. As a result, the reheat for the compressor with $\overline{\eta_P} = 0.95$ is much lower than the previous one with $\overline{\eta_P} = 0.7$. Using the same procedure discussed in the previous section, we find the following relationship between f_C and $f_{\infty C}$ for a multi-stage compressor with N stages:

$$f_C = f_{\infty C}\left(\frac{N-1}{N}\right) = f_{\infty C}\left(1 - \frac{1}{N}\right) \tag{8.35}$$

Once the reheat factor for a compressor with an infinite number of stages $f_{\infty C}$ is determined, the reheat factor of a compressor with a finite number of stages is calculated using Eq.(8.35).

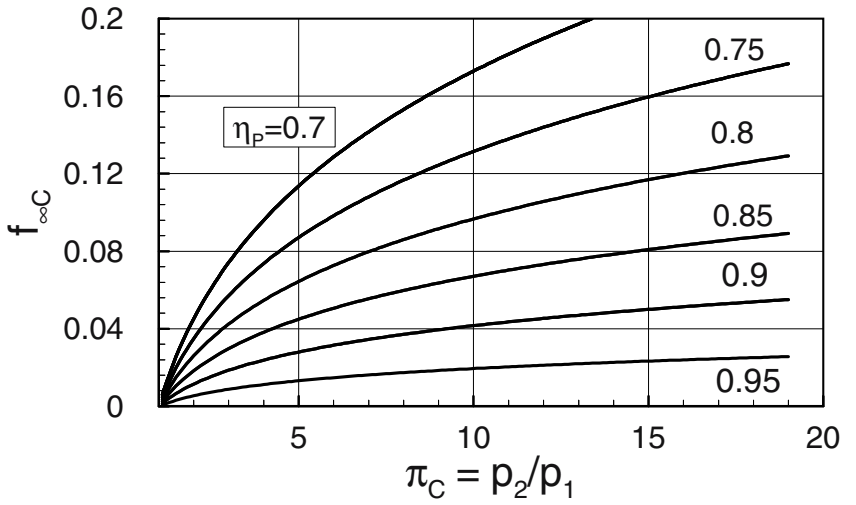

Fig. 8.3: Reheat factor of a multistage compressor for κ = 1.4.

8.4 Polytropic vs. Isentropic Efficiency

As shown in Eqs. (8.18) and (8.34), the polytropic efficiency accounts for the energy dissipation within a turbine and a compressor component. Furthermore, the polytropic efficiency can be used to compare turbine or compressor components that are operating under different initial conditions or have different working media. In these cases, both polytropic and isentropic efficiencies change. However, the rate of change for polytropic efficiency is much smaller than that of an isentropic one. It is indeed 3possible for two compressor or turbine components to have the same polytropicefficiency if certain similarity conditions are met. This is not the case for isentropic efficiency. Therefore, the isentropic efficiency is not appropriate for comparison purposes. Another major advantage of polytropic efficiency is the use of row-efficiencies to calculate the row-by-row expansion or compression process. Calculating the polytropic efficiency, however, requires the knowledge of expansion or compression end points, which are generally unknown at the stage of design. The isentropic efficiency, on the other hand, exhibits a simple and practical tool, since the isentropic enthalpy difference is calculated from the inlet and exit conditions at constant entropy. As we saw in this chapter, these two efficiencies are related to each other. Figure 8.4 exhibits, for a multi-stage turbine component, the dependency of the isentropic efficiency upon the polytropic efficiency with the pressure ratio $\pi_T = p_1/p_2$

as the parameter. As shown in Fig. 8.4, the isentropic efficiency is always greater than the poytropic one. The difference diminishes by increasing the polytropic efficiency, which reflects a reduction in dissipation. Figure 8.5 exhibits an opposite tendency for a multi-stage compression process. In this case, the polytropic efficiency is always greater than the isentropic one.

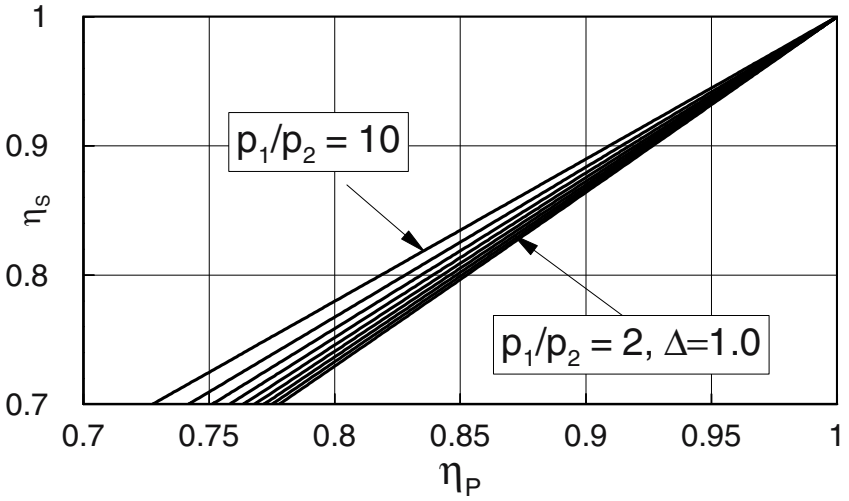

Fig. 8.4: Turbine isentropic efficiency as a function of polytropic efficiency with turbine pressure ratio p_1/p_2 as parameter for $\kappa = 1.4$

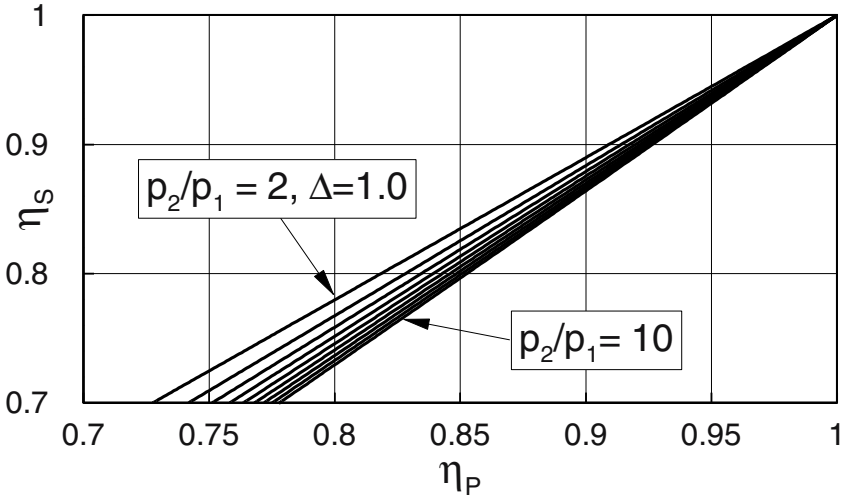

Fig. 8.5: Compressor isentropic efficiency as a function of polytropic efficiency with compressor pressure ratio $\pi_C = p_2/p_1$ as a parameter for $\kappa = 1.4$.

References, Chapter 8

8.1 Traupel, W., Thermische Turbomaschinen, Bd.I, 1977, Springer-Verlag Berlin Heidelberg New York.
8.2 Vavra, M.H., 1960, “Aero-Thermodynamics and Flow in Turbomachinees,” John Wiley & Sons, Inc.

9 Incidence and Deviation

Up to this point, the relationships developed for a turbomachinery stage have been strictly correct for given velocity diagrams with known inlet and exit flow angles. We assumed that the flow is fully congruent with the blade profile. This assumption implies that the inlet and exit flow angles coincide with the camber angles at the leading and trailing edges. Based on the operation condition and the design philosophy, there might be a difference between the camber and flow angle at the leading edge, which is called the incidence angle. The difference between the blade camber angle and the flow angle at the exit is termed the deviation angle. Since the incidence and deviation affect the required total flow deflection, the velocity diagram changes. If this change is not predicted accurately, the stage operates under a condition not identical with the optimum operation condition for which the stage is designed. This situation affects the efficiency and performance of the stage and thus the entire turbomachine. In order to prevent this, the total flow deflection must be accurately predicted. The compressor and the turbine flows react differently to a change of incidence. For instance, a slight change of incidence causes a partial flow separation on the compressor blade suction surface that can trigger a rotating stall; a turbine blade is less sensitive even to greater incidence change. To obtain the incidence and deviation angle for compressor and turbine blades, we use two different calculation methods. The first method deals with the application of conformal transformation to cascade flows with low deflection as in compressor blades. The second method concerns the calculation of deviation in high loaded cascades as in turbine blades.

9.1 Cascade with Low Flow Deflection

9.1.1 Conformal Transformation

Conformal transformation is one of the areas in classical complex analysis. Its application to fluid dynamics and cascade aerodynamics can be found, among others, in [1], [2], and [3]. Weinig [4] applied the conformal transformation method to turbomchinery blading and developed a simple procedure for calculating the exit flow angle of cascades with low flow deflection such as compressor cascades. Further treatment of cascade aerodynamics using method of conformal transformation by Weinig is found in [5], [6], [7], and [8].

Starting from the simplest case, consider the physical plane where a cascade consisting of identical straight-line profiles is located (Fig. 9.1). The profiles are staggered at an angle ν_m and have a spacing s. The flow is parallel to the cascade profiles. In other words, the profiles themselves are stream lines. Furthermore, assume that the flow originates from - ∞ and flows to + ∞. Since the flow from one cascade strip to another remains the same, it is sufficient to map only one of the profiles into the complex plane ζ on the unit circle. This unit circle exhibits one Riemann's sheet in the complex plane. The ζ-plane consists of an infinite number of

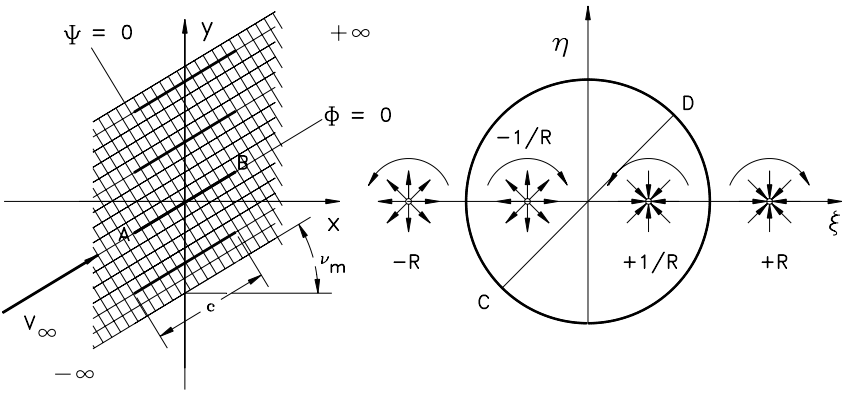

Fig. 9.1: Conformal transformation of a straight cascade. The cascade in z-plane is mapped onto the unit circle in ζ-plane.

Riemann's sheets, which correspond to the number of straight-line profiles within the cascade. The origin and end of the flow field, located ± ∞ in z-plane, must be mapped onto the real axis of ζ-plane at ± R (Fig.9.1). The complex potential in z-plane may be written as:

$$X(z) = \Phi + i\Psi \tag{9.1}$$

where Φ and ψ are the potential and stream functions. The function $X(z)$ is holomorphic if it is on the closed curve ABA continuous and differentiable, in other words, it must be an analytic function with the derivative

$$\frac{dX(z)}{dz} = \frac{\partial\Phi}{\partial x} + i\frac{\partial\Psi}{\partial x} \tag{9.2}$$

that satisfies the Cauchy-Riemann's condition:

$$\frac{\partial\Phi}{\partial x} = \frac{\partial\Psi}{\partial y} \equiv u, \qquad \frac{\partial\Phi}{\partial y} = -\frac{\partial\Psi}{\partial x} \equiv v \tag{9.3}$$

Inserting Eqs. (9.3) into Eq. (9.2), we find

$$\frac{dX(z)}{dz} = u - iv \tag{9.4}$$

If the velocity in z-plane is V_∞, its components in x- and y-directions are:

$$u = V_\infty \cos \nu_m \quad ; \quad v = V_\infty \sin \nu_m \tag{9.5}$$

Introducing Eq. (9.5) into (9.4) yields:

$$\frac{dX(z)}{dz} = V_\infty \left(\cos \gamma_m - i \sin \gamma_m \right) = V_\infty e^{-i\nu_m} \tag{9.6}$$

The integration of Eq. (9.6) leads to :

$$X(z) = zV_\infty e^{-i\nu_m} \quad \text{where} \quad z = re^{i\theta} \quad \text{or} \quad :X(z) = V_\infty re^{i(\theta - \nu_m)} \tag{9.7}$$

which is:

$$X(z) = V_\infty r \left[\cos(\theta - \nu_m) + i \sin(\theta - \nu_m) \right] \tag{9.8}$$

Comparing Eq. (9.8) with (9.1) delivers:

$$\begin{aligned} \Phi &= V_\infty r \cos(\theta - \nu_m) \\ \Psi &= V_\infty r \sin(\theta - \nu_m) \end{aligned} \tag{9.9}$$

with Φ in Eq. (9.9) as the complex velocity potential (potential function) and Ψ the stream function. Moving from one profile to another, as shown in Fig. 9.1, the potential and stream functions experience the following changes:

at $r = 0, \ \Phi = \Phi_0 = 0, \ and \ \Psi = \Psi o = 0$

at $r = s, \quad \Phi = \Phi 1 = V_\infty s \cos(\pi/2 - \nu_m) = V_\infty s \sin \nu_m$

and $\Psi = \Psi_1 = V_\infty s \sin(\pi/2 - \nu_m) = V_\infty s \cos \nu_m$

Using Eq. (9.9), the potential difference can be expressed as:

$$\Delta\Phi = \Phi_1 - \Phi_o = V_\infty s \sin \nu_m \tag{9.10}$$

and the stream function difference is:

$$\Delta\Psi = \Psi_1 - \Psi_o = V_\infty s \cos \nu_m \tag{9.11}$$

The stream function difference, Eq. (9.11), represents the volume flow through a strip of the cascade with spacing s and height h=1. This volume flow originates from a source at $z = -\infty$ and has a source strength Q with $Q = \Delta\Psi = V_\infty s \cos \nu m$. To generate such $\Delta\Psi$ and $\Delta\Phi$ in z-plane, the corresponding conformal transformation in ζ-plane at $-R$ must contain a source and a vortex with the strengths Q and Γ. Similarly at $+R$, a sink and a vortex with the strengths $-Q$ and $-\Gamma$ must be placed that correspond to the station $+\infty$ in z-plane. Thus, a system of sources, sinks, and vortices is arranged on the real ζ-axis outside (exterior) the unit circle. This system fulfills the boundary condition at $+\infty$ and also $\pm R$, but the most important requirement that the unit circle must itself be a streamline, is not fulfilled. This problem can be solved simply by reflecting the singularities onto the unit circle. The locations of the reflected singularities are then $\pm 1/R$ inside (interior) the unit circle. The next step is to find the corresponding transformation function in ζ-plane.

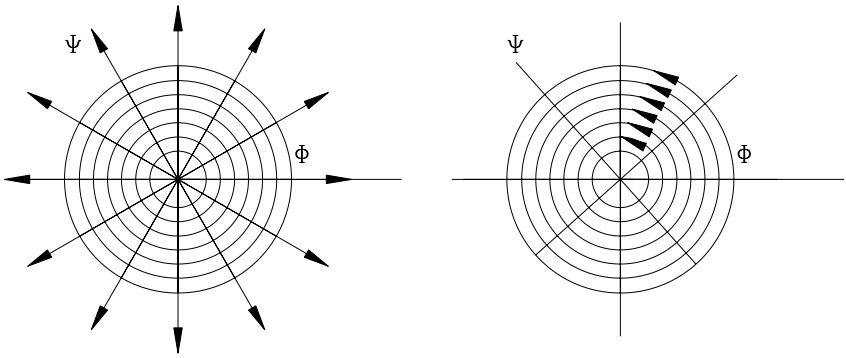

Fig. 9.2: Singularities source and circulation distribution with stream function Ψ and potential function Φ.

The *complex potential for a source located* at $\zeta = 0$ and has a strength Q is (Fig. 9.2):

$$X = \phi + i\Psi \equiv \frac{Q}{2\pi} \ln\zeta \tag{9.12}$$

In Eq. (9.12) the complex function ζ is:

$$\zeta = \xi + i\eta \text{ and since}$$

$$\xi = r\cos\theta, \quad \eta = r\sin\theta, \quad e^{i\theta} = \cos\theta + i\sin\theta \tag{9.13}$$

$$\zeta = r(\cos\theta + i\sin\theta) = re^{i}\theta$$

Introducing Eq. (9.13) into (9.12) and decomposing the result into its real and imaginary parts Φ, Ψ respectively, we find

$$X = \Phi + i\Psi = \frac{Q}{2\pi}\ln(re^{i\theta}) = \frac{Q}{2\pi}(\ln r + i\theta)$$

$$\Phi = \frac{Q}{2\pi}\ln r, \quad \Psi = \frac{Q}{2\pi}\theta \tag{9.14}$$

with the radius in Eq.(9.14) as

$$r = \sqrt{\xi^2 + \eta^2}, \quad \theta = arctg\,\frac{\eta}{\xi} \tag{9.15}$$

By moving around the center of the source along a closed curve, θ in Eq. (9.15) will change from 0 to 2π and as a result, the change of stream function is:

$$\Delta\Psi = \frac{Q}{2\pi}2\pi = Q = V_\infty s\cos\nu_m \tag{9.16}$$

which corresponds to the source strength. For a source located at $\zeta = R$, the complex potential is:

$$X = \frac{Q}{2\pi}\ln(\zeta - R) \tag{9.17}$$

where for sources $Q > 0$ and for sinks $Q < 0$. The potential lines of source, at $\zeta = 0$ are concentric circles, Fig. 9.2. The vortex flow can be established by generating stream lines from these concentric circles, inserting $Q = i\Gamma$ in Eq. (9.14):

$$X = \frac{i\Gamma}{2\pi}\ln\zeta = \frac{i\Gamma}{2\pi}(\ln r + i\theta) \tag{9.18}$$

The variables in the parentheses of Eq. (9.18) are expressed in terms of

$$\Phi = -\frac{\Gamma}{2\pi}\theta\,, \qquad \Psi = \frac{\Gamma}{2\pi}\ln r \tag{9.19}$$

Using Φ and Ψ as the potential and stream function from Eq. (9.19), the velocity can be obtained from Eq. (9.20)

$$V = -\frac{d\Phi}{ds} = -\frac{\Gamma}{2\pi}\frac{1}{r} \tag{9.20}$$

where the differential arc length $ds = rd\theta$. By moving around the vortex center from $\theta = 0$ to 2π, the potential difference is $\Delta\Phi = \Gamma = V_\infty s \sin\nu_m$, where Γ is the circulation. For a vortex located at $\zeta = R$, the complex potential is:

$$X = \frac{i\Gamma}{2\pi}\ln(\zeta - R) \tag{9.21}$$

If the source is located at an arbitrary point ζ_o, Eq. (9.21) can be written as:

$$X = \frac{Q}{2\pi}\ln(\zeta - \zeta_o) \tag{9.22}$$

For a vortex flow, Eq. (9.22) yields:

$$X = \frac{i\Gamma}{2\pi}\ln(\zeta - \zeta_o) \tag{9.23}$$

The required complex potential consists of sinks, sources and vortices located at $\pm R$ and $\pm 1/R$ which we summarize as $X(\zeta) = \Sigma X(\zeta)_{\text{sources}} + \Sigma X(\zeta)_{\text{sinks}} + \Sigma X(\zeta)_{\text{vortices}}$ is given as

$$\begin{aligned} X(\zeta) = {} & \frac{s}{2\pi}\cos\nu_m \ln(\zeta + R) + \frac{s}{2\pi}\cos\nu_m \ln\left(\zeta + \frac{1}{R}\right) - \\ & - \frac{is}{2\pi}\sin\nu_m \ln(\zeta + R) + \frac{is}{2\pi}\sin\nu_m \ln\left(\zeta + \frac{1}{R}\right) - \\ & - \frac{s}{2\pi}\cos\nu_m \ln(\zeta - R) - \frac{s}{2\pi}\cos\nu_m \ln\left(\zeta - \frac{1}{R}\right) + \\ & + \frac{is}{2\pi}\sin\nu_m \ln(\zeta - R) - \frac{is}{2\pi}\sin\nu_m \ln\left(\zeta - \frac{1}{R}\right) \end{aligned} \tag{9.24}$$

Rearranging Eq. (9.24):

$$X(\zeta) = \frac{s}{2\pi}\left\{ e^{-i\nu_m} \ln\frac{R+\zeta}{R-\zeta} + e^{i\nu_m} \ln\frac{\zeta+\frac{1}{R}}{\zeta-\frac{1}{R}} \right\} \tag{9.25}$$

Setting $|V_\infty| = 1$ and equating Eq. (9.7) and (9.25) yields:

$$X(Z) = X(\zeta) \tag{9.27}$$

resulting in:

$$z = \frac{s}{2\pi}\left\{ \ln\frac{R+\zeta}{R-\zeta} + e^{2i\nu_m} \ln\frac{\zeta+\frac{1}{R}}{\zeta-\frac{1}{R}} \right\} \tag{9.28}$$

With Eq. (9.28), the transformation function is completely defined. As shown, the complex potential X(ζ) fulfills the streamline requirement on the unit circle. The contributions of all the singularities outside (exterior) the circle are exactly equal to the contributions of the singularities inside (interior) the circle. The complex potential on the unit circle that characterizes the equilibrium state between the singularities is expressed as:

$$X(\zeta_c) = \frac{s}{\pi} e^{i\nu_m} \ln\frac{\zeta_c+\frac{1}{R}}{\zeta_c-\frac{1}{R}} \tag{9.29}$$

where the subscript c in Eq. (9.29) refers to circle contour with $\zeta_c = 1.e^{i\alpha}$. Decomposing Eq. (9.29) into its real and imaginary parts, the real part is :

$$\Phi_c = \frac{s}{2\pi}\left\{ \cos\nu_m \ln\frac{R^2+2R\cos\alpha+1}{R_2-2R\cos\alpha+1} + 2\sin\nu_m \, arctg\left[\frac{2R\sin\alpha}{R^2-1}\right] \right\} \tag{9.30}$$

The velocity distribution on the unit circle can be obtained by differentiating Eq. (9.30) around the circle:

$$V = \frac{d\Phi_c}{rd\alpha} \qquad \text{where} \quad r = 1 \tag{9.31}$$

The stagnation points on the unit circle requires that in Eq. (9.31) the velocity vanishes, $V = 0$. This requirement leads to:

$$tg\alpha_s = \frac{R^2 - 1}{R^2 + 1} tg\nu_m \tag{9.32}$$

In Eq. (9.32) α_s is the first stagnation angle. To find the potential difference between the stagnation points α_s and $\alpha_s + \pi$, the angle α in Eq. (9.30) is replaced successively by α_s and $\alpha_s + \pi$. In ζ-plane:

$$\Delta\Phi_{CD} = \Phi_C - \Phi_D = \Phi_{\alpha_s} - \Phi_{(\alpha_s + \pi)} \tag{9.33}$$

In z-plane:

$$\begin{aligned} \Phi_A &= V_\infty \frac{c}{2} \cos(\theta_A - \nu_m) = V_\infty \frac{c}{2}, \quad since \ \theta_A = \nu_m \\ \Phi_B &= V_\infty \frac{c}{2} \cos(\theta_E - \nu_m) = -V_\infty \frac{c}{2}, \quad since \ \theta_E = \nu_m + \pi \end{aligned} \tag{9.34}$$

As a result, we obtain the potential difference from Eq. (9.34):

$$\Delta\Phi_{AB} = \Phi_A - \Phi_B = V_\infty c = c \quad , \qquad \text{where} \quad V_\infty = 1 \tag{9.35}$$

Equating the potential differences in ζ- and z-plane from Eq. (9.33) and (9.35) yields:

$$\Delta\Phi_{CD}(\zeta) = \Delta\Phi_{AB}(z) \tag{9.36}$$

and with Eq. (9.30) we have:

$$\frac{c}{s} = \frac{1}{\pi} \left\{ \cos\nu_m \ln \frac{R^2 + 2R\cos\alpha + 1}{R_2 - 2R\cos\alpha + 1} + 2 \sin\nu_m \, arctg \left[\frac{2R\sin\alpha}{R^2 - 1} \right] \right\} \tag{9.37}$$

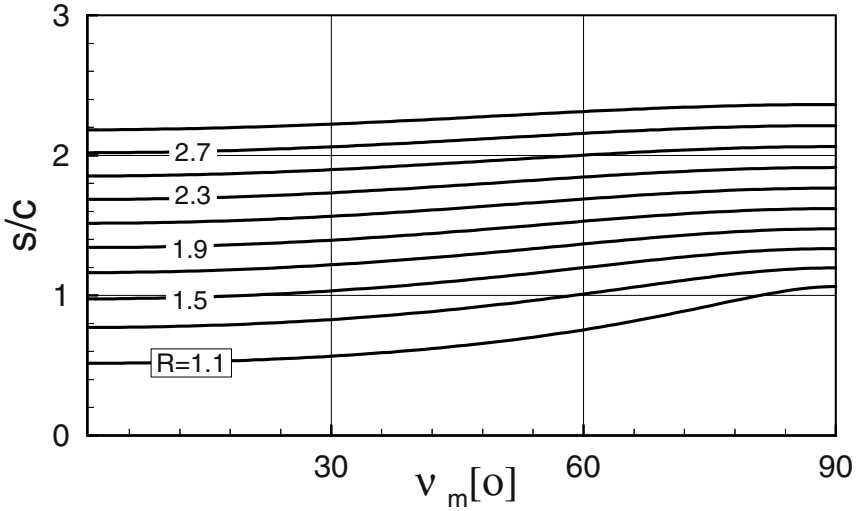

Fig. 9.3: Spacing/chord ration s/c as a function of the cascade stagger angle ν_m with the mapping parameter *R* as parameter.

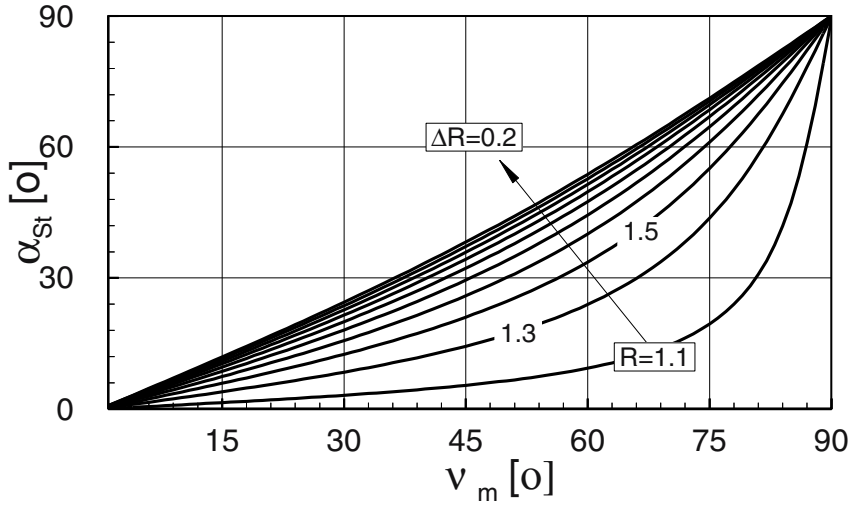

Fig. 9.4: Stagnation angle α_{st} as a function of the cascade stagger angle ν_m with the mapping parameter *R* as parameter.

The cascade parameter ν_m and c/s from Eq. (9.37) that belong to z-plane correspond to the α_s and R in ζ-plane. Equations (9.32) and (9.37) can be computed easily. The result of such a computation is shown in Figs. 9.3 and 9.4. As Fig. 9.3 shows, to each given pair of s/c and ν_m only one value is allocated to the transformation parameter R. Taking this parameter and the stagger angle ν_m, the stagnation angle α_{St} is determined from Fig. 9.4. With the aid of Eqs. (9.24) to (9.37), it is possible to calculate exactly the potential flow through cascades that consist of straight-line profiles. Since the turbomachinery blading has always curved camber lines, the derived conformal transformation methods must be extended to the profiles with curved camber lines. Since the compressor blade profiles have usually low deflection, their camber line can be approximated by a circular arc. In the following section, we replace the straight-line cascade by circular arc one.

9.1.2 Flow Through an Infinitely Thin Circular Arc Cascade

Consider a potential flow through a cascade consisting of a number of circular arcs. The potential flow condition requires that the contour of the circular arc follow the stream lines. This requirement implies that the flow direction must be identical to the contour direction ν of the circular arc profiles under consideration. To simplify the problem, replace the circular arc cascade by a straight cascade, EA, with prescribed flow directions that correspond to the contour direction ν as shown in Fig. 9.5.

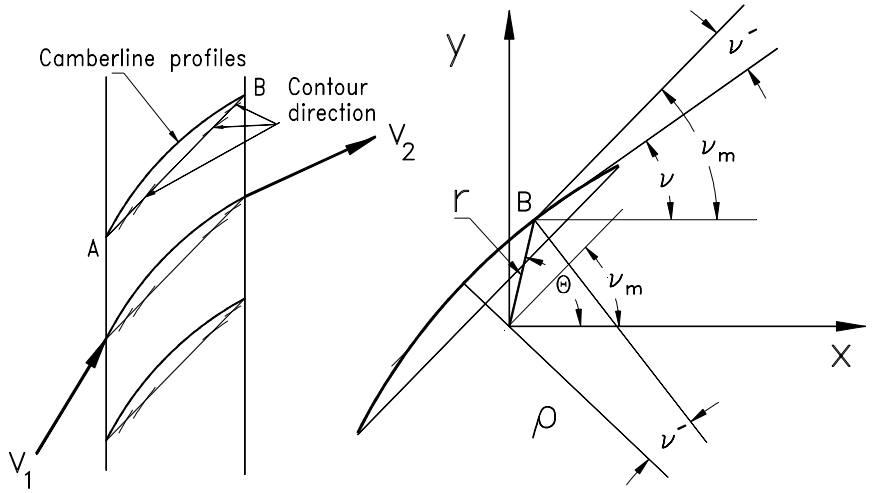

Fig. 9.5: Prescribed velocity directions on straight line cascade

To establish the corresponding analytical relations, we start from the conformal transformation relations derived in the previous section and extend them to an infinitely thin cascade with variable direction. For the cascade with the prescribed direction ν, the complex potential, Eq (9.7) is rewritten as:

$$X(z) = zVe^{-i\nu} \tag{9.38}$$

with V as contour velocity and ν its direction. Differentiating Eq. (9.38), its logarithm yields:

$$\ln\left[\frac{dX(z)}{dz}\right] = \ln V - i\nu \tag{9.39}$$

Since $X(z)$ in Eq. (9.39) is an analytic function, its derivative and the logarithm of its derivative must be analytic functions also. It follows that:

$$\bar{X}(z) = \bar{\Phi} + i\bar{\Psi} \tag{9.40}$$

where

$$\bar{X}(z) = \ln\left[\frac{dX(z)}{dz}\right], \quad \bar{\Phi} = \ln V, \quad and \quad \bar{\Psi} = -\nu \tag{9.41}$$

Similar to Eq. (9.9), the velocity potential from Eq. (9.41) at an arbitrary point B, shown in Fig. 9.5 can be found:

$$\Phi = Vr\cos(\Theta - \nu_m) \tag{9.42}$$

The position vector r in Eq. (9.42) shown in Fig. 9.5 is obtained from

$$r \approx \frac{\rho\nu'}{\cos(\theta - \nu_m)} \text{ with } \nu' = \frac{\Phi}{V\rho}, \text{ and } \nu' = \nu_m - \nu \tag{9.43}$$

Considering Eqs. (9.40) and (9.43), we find :

$$\bar{\Psi} = \frac{\Phi}{V\rho} - \nu_m \tag{9.44}$$

Equation (9.44) states that the stream function $\bar{\Psi}$ which according to Eq. (9.40) exhibits the flow direction, is up to the additive constant ν_m proportional to the potential function Φ. It follows that the complex potential X(z) is also up to an

additive constant directory proportional to Φ resulting in:

$$\bar{X}(z) = \bar{\Phi} + i\bar{\Psi} = i\left[\frac{\Phi}{V\rho} - \nu_m\right] + \ln V = \frac{i\Phi}{V\rho} + \left(\ln V - i\nu_m\right) \tag{9.45}$$

for $V = 1$ and $(\ln V - i\nu_m) = const. = C$, Eq. (9.45) is reduced to

$$\bar{X}(z) = \frac{i\Phi}{V\rho} + C \tag{9.46}$$

The new complex potential $\bar{X}(z) \sim \Phi(z)$ is now mapped into the ζ-plane. The potential Φ represents in ζ-plane vortices, which are located at $\pm R$ and reflected on the unit circle $\pm 1/R$. Since on the unit circle, the contribution of the vortices outside the circle is exactly equal to the contribution of those vortices located inside the circle, the new complex potential Eq. (9.46) can be written as:

$$\bar{X}(\zeta) = \frac{i}{\rho}\frac{s}{\pi} e^{i\nu_m} \ln \frac{\zeta + \frac{1}{R}}{\zeta - \frac{1}{R}} \tag{9.47}$$

The imaginary part of Eq. (9.47) corresponds to the imaginary part of Eq. (9.40) that contains the angle ν. After decomposition of Eq. (9.47), we find:

$$Im\left\{\bar{X}(\zeta)\right\} = \frac{s}{\rho\,\pi} \cos\nu_m \ln \frac{\zeta + \frac{1}{R}}{\zeta - \frac{1}{R}} \tag{9.48}$$

Along the unit circle we set in Eq. (9.48) $\zeta = 1$ and replace the left-hand side of (9.48) by Eq. (9.46) and consider Eq. (9.43) that contains ν', we find

$$\left.\begin{matrix}\nu'_1\\ \nu'_2\end{matrix}\right\} = \mp \frac{s}{\pi\rho} \cos\nu_m \ln \frac{R^2 - 1}{R^2 + 1} \tag{9.49}$$

In Eq. (9.49) we replace $\nu' = \nu_m - \nu$ from Eq. (9.43) and arrive at

$$\left.\begin{matrix}\nu_1\\ \nu_2\end{matrix}\right\} = \nu_m \mp \frac{1}{\pi}\left(\frac{s}{c}\frac{c}{\rho}\right) \cos\nu_m \ln \frac{R^2 - 1}{R^2 + 1} \tag{9.50}$$

For a circular arc, the chord-curvature radius ratio c/ρ in Eq. (9.50) can be approximated by the flow deflection $c/\rho \approx \theta$. As a result, Eq. (9.50) is modified as

$$\left.\begin{matrix}\nu_1\\ \nu_2\end{matrix}\right\} = \nu_m \pm \frac{\theta}{\pi}\frac{s}{c}\cos\nu_m \ln\frac{R^2+1}{R^2-1} \tag{9.51}$$

For the second term on the right-hand side of Eq. (9.51), we now introduce the following auxiliary function:

$$\frac{\mu}{2} = \frac{1}{\pi}\frac{s}{c}\cos\nu_m \ln\frac{R^2+1}{R^2-1} \tag{9.52}$$

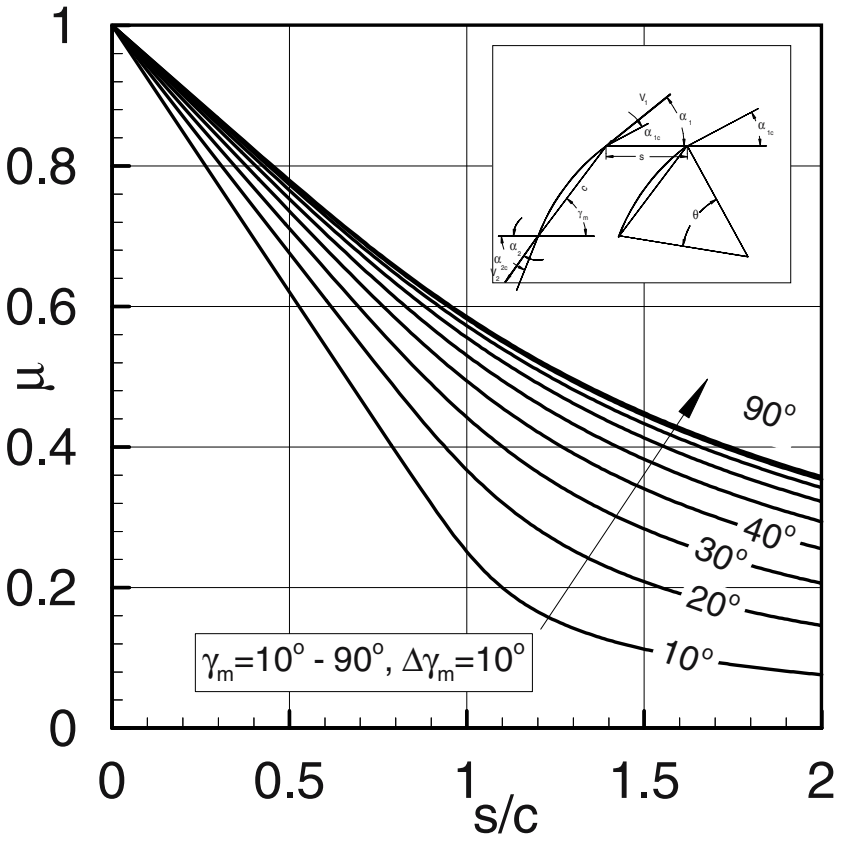

Fig. 9.6: Weinig μ-factor as a function of *s/c* with γ_m as parameter.

For a straight cascade with the given cascade solidity *(c/s)* and stagger angle $\nu_{m,}$ the transformation parameter *R* in Eq. (9.52) is completely defined by Eqs. (9.32) and (9.37). Thus, in the auxiliary function, Eq. (9.52), μ is uniquely determined. Figure 9.6 exhibits the values for μ as a function of space/chord ratio with the cascade stagger angle ν_m as a parameter. Using α_2, and γ_m instead of ν_1, ν_2, and ν_m for a profile, the result for a compressor cascade or decelerated flow is:

$$\alpha_2 = \alpha_1 + \mu\Theta - A\left(\alpha_1 - \gamma_m + \frac{\Theta\mu}{2}\right) \tag{9.53}$$

and for accelerated flow:

$$\alpha_2 = \alpha_1 - \mu\Theta - A\left(\alpha_1 - \gamma_m - \frac{\Theta\mu}{2}\right) \tag{9.54}$$

Factor *A* is a correction factor that was introduced by Traupel [6] and accounts for a non-zero incidence. It depends on the cascade parameter *s/c* and the stagger angle γ_m as is shown in Fig.9.7.

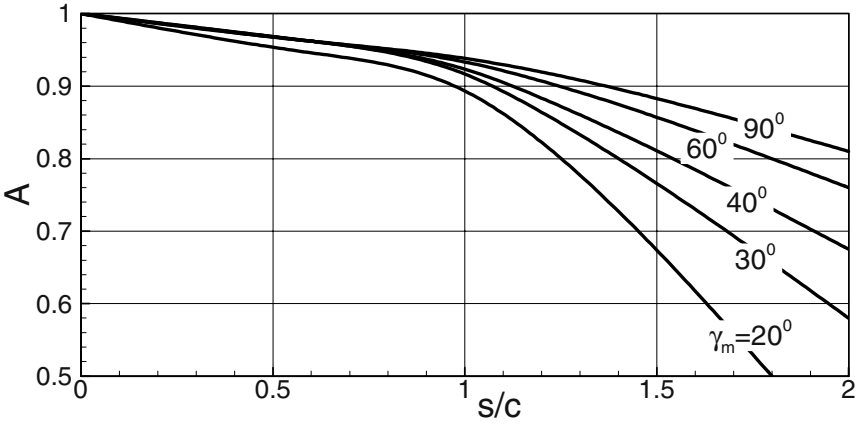

Fig. 9.7: Correction factor *A* as a function of s/c with γ_m as parameter.

For $A = 1$:

$$\alpha_2 = \gamma_m \pm \frac{\mu\Theta}{2} \tag{9.55}$$

with (+) and (-) signs for compressor and turbine cascade, respectively. For an infinitely thin blade, the exit flow angle is identical to the camber angle α_{2c} since $\mu = 1$. It is calculated from:

$$\alpha_{2c} = \gamma_m \pm \frac{\Theta}{2} \tag{9.56}$$

The deviation angle $\delta\alpha_2$ is obtained as follows:

$$\delta\alpha_2 = \alpha_{2c} - \alpha_2 = \left(\gamma_m - \alpha_1\right)(1 - A) + \Theta\left[\frac{1}{2} - \mu\left(1 - \frac{A}{2}\right)\right] \tag{9.57}$$

with α_{2c} as the exit camber angle, the correction factor A from Fig. 9.7, and μ from Fig. 9.5. Once the deviation angle is calculated from Eq. (9.57), (9.58), the exit flow angle α_2 is calculated as the difference $\alpha_2 = \alpha_{2c} - \delta\alpha_2$.

Table 9.1: Cascade parameters

γ_m	c/s	A_α	A_t	γ_m	c/s	A_α	A_t
30	0.5	1.096	-0.084	45	0.5	0.982	-0.076
	1.0	1.130	-0.351		1.0	0.814	-0.211
	1.5	0.849	-0.448		1.5	0.602	-0.245
	2.0	0.663	-0.443		2.0	0.451	-0.233
30	0.5	1.052	-0.17	45	0.5	0.942	-0.154
	1.0	0.948	-0.399		1.0	0.720	-0.242
	1.5	0.657	-0.368		1.5	0.506	-0.222
	2.0	0.489	-0.310		2.0	0.367	-0.182
60	0.5	0.901	-0.056	75	0.5	0.845	-0.027
	1.0	0.672	-0.115		1.0	0.605	-0.056
	1.5	0.484	-0.135		1.5	0.430	-0.060
	2.0	0.365	-0.128		2.0	0.327	-0.060
60	0.5	0.872	-0.125	75	0.5	0.830	-0.090
	1.0	0.620	-0.145		1.0	0.581	-0.088
	1.5	0.434	-0.133		0.5	0.408	-0.069
	2.0	0.321	-0.109		2.0	0.307	-0.055

A purely empirical correlation for deviation angle known as the Carter's rule is:

$$\delta\alpha_2 = \frac{\Theta}{4\sqrt{\sigma}} \tag{9.58}$$

with Θ as the difference between the and inlet and exit camber angles. Carter [9] modified the correlation for compressor cascades as $\delta\alpha_2 = m(\Theta/\sigma)$ with m as an empirical functions of stagger angle.

9.1.3 Thickness Correction

For a profile with finite thickness *t*, the stagger angle is corrected by:

$$\gamma_{mt} = \gamma_m + \Delta_\gamma \quad \text{where} \quad \Delta_\gamma = 57.3 \frac{|A_t|}{A_\alpha} \frac{t}{c} \tag{9.59}$$

with A_t and A_α from Table 9.1. For compressor cascades, the range of thickness/chord ratio is $t/c = 0.1 - 0.15$.

9.1.4 Optimum Incidence

To obtain the optimum incidence angle i_{opt} for an arbitrary blade thickness, Johnsen and Bullock [10] introduced an empirical correlation that relates the optimum incidence angle i_{opt} to the incidence angle i_{10} of a NACA-type blade, Fig. 9.8, with the maximum thickness $t/s=0.1$.

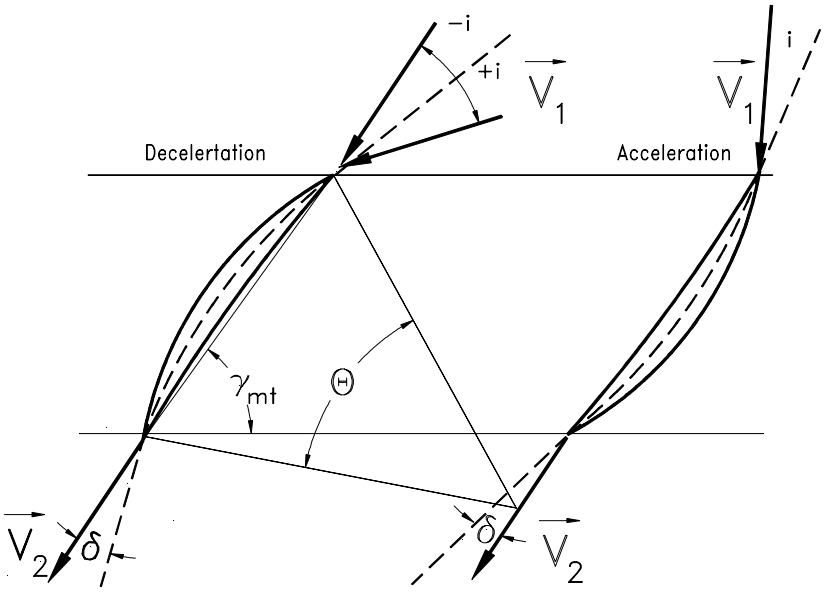

Fig. 9.8: Incidence and deviation for a DCA-profile

Taking i_{10} from Fig. 9.9, i_{opt} can be estimated from:

$$i_{opt} = K_p K_{th} i_{10} - K_\theta \Theta \tag{9.60}$$

where i_{10} is the optimum incidence for a profile with *t/c = 0.1*. The coefficients K_p and K_{th} account for the profile type and profile thickness. For DCA and NACA profile types, the following empirical values $K_p = 0.7$ for NACA profiles and $K_p = 1.0$ for DCA profiles are suggested. Figure 9.9 shows the variation of i_{10} and n with the inlet flow angle α_1. Figure 9.10 shows the thickness factor K_{th} as a function of thickness-chord ratio t/c.

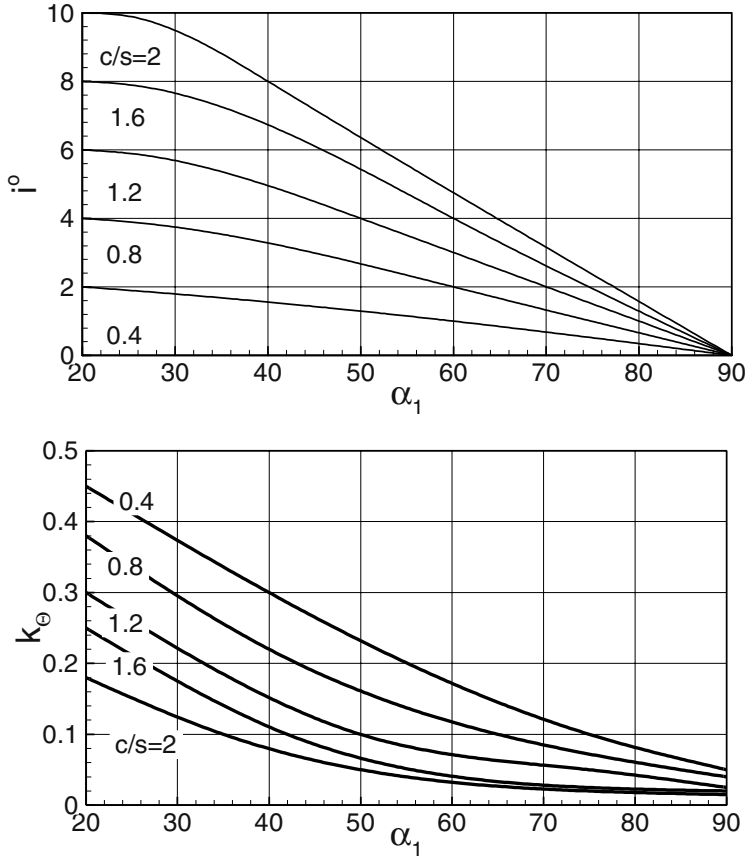

Fig. 9.9: Coefficients i_0 and K_θ as functions of inlet flow angle α_1 with *c/s* as parameter

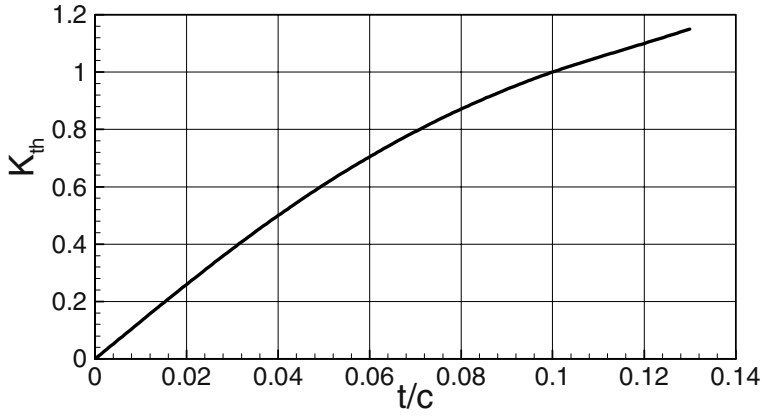

Fig. 9.10: Coefficients K_{th} as a function of the relative thickness

9.1.5 Effect of Compressibility

For intermediate to high subsonic inlet flow with *M = 0.6 - 0.8*, the incidence and the deviation angle are affected by the compressibility. The deviation angle of a compressible flow may be related to the deviation angle of an incompressible flow by using the following correlation proposed by Wennerström [11]:

$$\delta_{com} = K_C \, \delta_{inc} \tag{9.61}$$

with K_c as the compressibility function from Fig. 9.11.

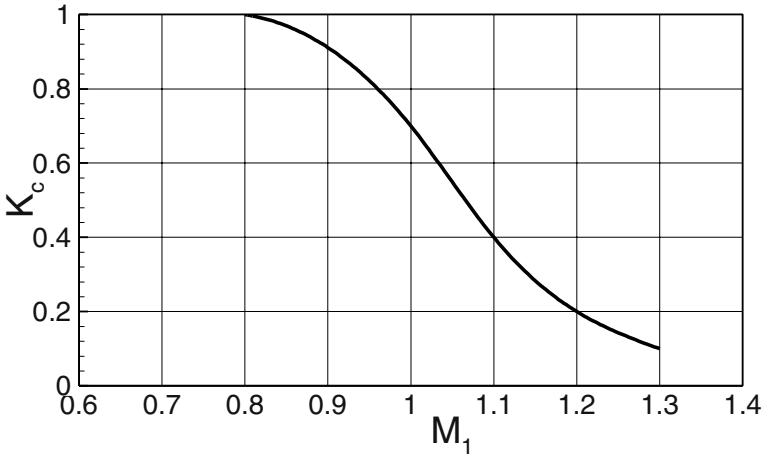

Fig. 9.11: Influence of mach number on deviation factor K_C

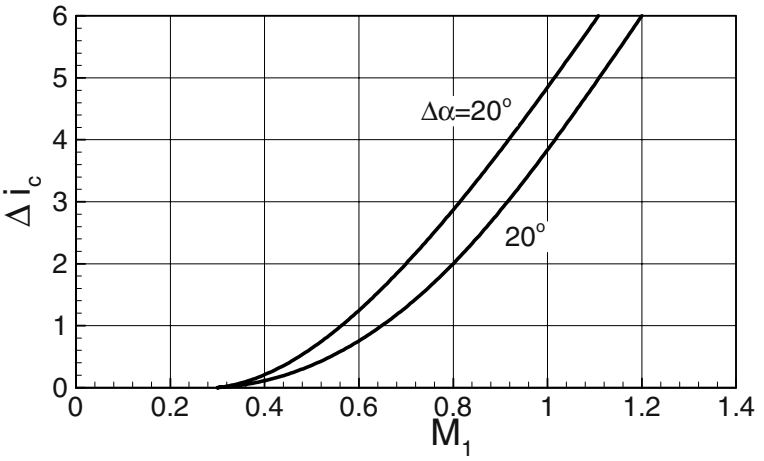

Fig. 9.12: Influence of Mach number on optimum incidence factors Δi_C

The compressibility effect causes an increase in incidence angle, which can be corrected using the empirical correlation suggested in [11] and [6]:

$$i_{opt}\left(M_1\right) = i_{opt}(0) + \Delta i_c \tag{9.62}$$

with $i_{opt}(0)$ from Eq. (9.59) and Δi_c from Fig. 9.12.

9.2 Deviation for High Flow Deflection

The accelerated flow through the turbine blades generally undergoes higher deflection than the decelerated flow through the compressor blades. The major parameter affecting the behavior of an accelerated flow with respect to the change of inlet flow direction is the Mach number, which determines the cascade flow geometry. If the flow has a low subsonic Mach number, such as in high pressure or intermediate pressure steam turbines, then the flow behavior is affected by the change of incidence if the blade profile has a small leading edge thickness. This fact enables the application of relatively thicker profiles that are less sensitive to changes of the inlet flow direction. In the rear stages of a low pressure steam turbine or a modern gas turbine, however, the inlet flow in the tip region is high subsonic that requires relatively thin profiles. Fig. 9.13 depicts the blade sections at the hub and the tip of a typical gas turbine rotor blade.

Since the flow at the hub is low subsonic with high deflection, a thick profile with a relatively large leading edge radius is applied, Fig. 9.13. Its corresponding profile loss coefficient is plotted in Fig. (9.14) against the inlet flow angle.

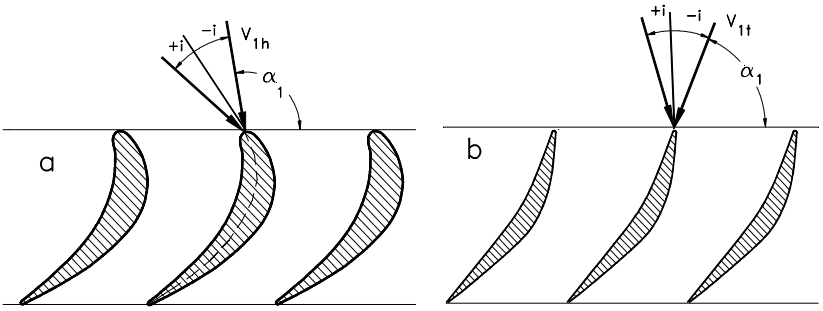

Fig. 9.13: Hub (a) and tip (b) section of a turbine blade

Starting from the optimum flow angle α_{1opt}, Fig. 9.14, curve (a) shows that the loss coefficient is not affected by the change of the inlet flow angle within an incidence range of $-15^o < i < +15^o$. Thus the change of incidence for a high deflected turbine cascade with a relatively large leading edge diameter that operates at a low subsonic mach number does not significantly increase the profile loss at moderate off-design operation conditions. The situation changes drastically towards the tip where the blade profile is subjected to a high subsonic even transonic inlet flow condition. For the profile at the tip section, Fig. 9.14b, the loss coefficient in Fig. 9.14, curve b changes considerably if the inlet flow direction departs from the design point. As seen in Fig.9.14b, the flow has a comparatively low deflection, so that the calculation procedure derived in Chapter 9.1 can be applied. Based on the above facts for an accelerated flow, only the changes of deviation angles need to be considered. Since a high deflected turbine cascade cannot be approximated by a straight-line

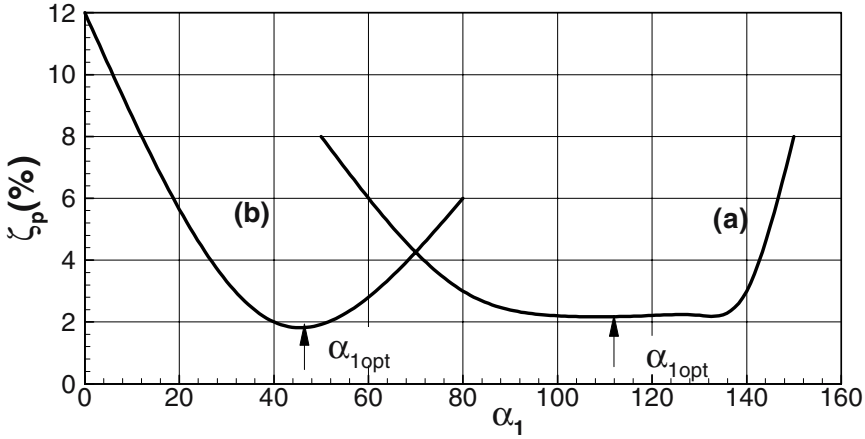

Fig. 9.14: Profile loss coefficient as a function of inlet flow angle for (a) hub section and (b) tip section

cascade, the conformal transformation method discussed in Chapter 9.1 can not be used for the calculation of exit flow angle. Based on conservation laws, Traupel [6] derived the following simple method that allows an accurate prediction of the deviation angle for cascades with high flow deflection.

9.2.1 Calculation of Exit Flow Angle

Consider the pressure distribution on the suction and pressure surface of a turbine cascade shown in Fig. 9.15.

The pressure difference:

$$\Delta F_y = h_a \int_C^D p dy - h_2 \int_E^D p dy \simeq 0 \tag{9.63}$$

With the approximation described by Eq. (9.63), the momentum balance in circumferential direction yields:

$$V_2 \cos\beta_2 = V_a \cos\beta_a \tag{9.64}$$

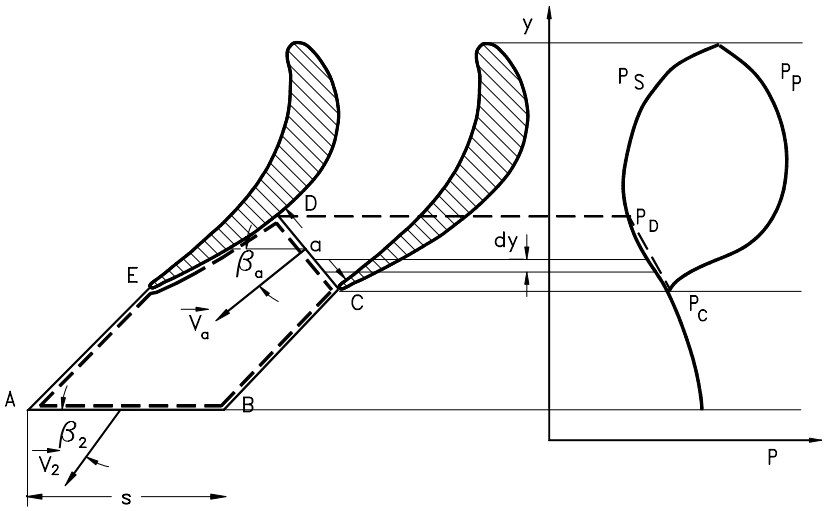

Fig. 9.15: On the estimation of pressure momentum along the throat *CD* and the suction surface blade portion *DE* by Traupel method [6]

From the continuity equation we find:

$$sh_2 \rho_2 V_2 \sin\beta_2 = ah_a \rho_a V_a \tag{9.65}$$

where h_2 and h_a in Eq. (9.65) are the blade heights at stations *2* and *a*. For an isentropic flow, Eqs. (9.64) and (9.65) are written as:

$$\sin\beta_2 = \frac{ah_a \rho_a \cos\beta_2}{sh_2 \rho_s \cos\beta_a} = \frac{ah_a \cos\beta_2}{sh_2 \cos\beta_a}\left[\frac{p_a}{p_2}\right]^{\frac{1}{k}} \tag{9.66}$$

Further, we assume an isentropic expansion process between *a* and *2* and calculate the isentropic enthalpy difference:

$$\frac{V_a^2 - V_2^2}{2} = \left[\Delta h_s\right]_a^2 = h_2\left[1 - \left(\frac{p_a}{p_2}\right)^{\frac{\kappa - 1}{\kappa}}\right] - 1 \tag{9.67}$$

introducing the exit Mach number $M_2 = V_2 / c_2$ and the static enthalpy $h_2 = c_2^2/(k-1)$ with *c* as the speed of sound at the exit, Eq. (9.67) becomes:

$$\frac{V_a^2}{V_2^2} = \frac{2}{M_2^2(\kappa - 1)}\left[1 - \left(\frac{P_a}{p_2}\right)^{\frac{\kappa - 1}{\kappa}}\right] - 1 \tag{9.68}$$

Introducing Eq. (9.64) into (9.68):

$$\frac{\cos^2\beta_2}{\cos^2\beta_a} = \frac{2}{M_2^2(k - 1)}\left[1 - \left(\frac{P_a}{p_2}\right)^{\frac{k - 1}{k}}\right] - 1 \tag{9.69}$$

The solution of Eq. (9.69) for pressure ratio is:

$$\frac{p_a}{p_2} = \left[1 - M_2^2\left(\frac{\kappa - 1}{\kappa}\right)\left(\frac{\cos^2\beta_2}{\cos^2\beta_a} - 1\right)\right]^{\frac{\kappa}{\kappa - 1}} \tag{9.70}$$

Incorporating Eq. (9.70) into (9.66):

$$tg\beta_2 = \frac{a}{s}\frac{h_a}{h_2}\frac{1}{\cos\beta_a}\left\{1 - M_2^2\left(\frac{\kappa - 1}{2}\right)\left[\frac{\cos^2\beta_2}{\cos^2\beta_a} - 1\right]\right\}^{\frac{1}{\kappa - 1}} \tag{9.71}$$

For a Mach number approaching unity and a constant blade height $h_2 = h_a$, the exit flow angle β_2 approaches β_a, which leads to

$$tg\beta_2 = \frac{a}{s}\frac{1}{\cos\beta_2}$$
$$\sin\beta_2 = \frac{a}{s} \tag{9.72}$$

For incompressible flow, δ_2 can be obtained from:

$$\sin\beta_2 = \frac{a}{s}\frac{\cos\beta_2}{\cos\beta_a} \quad \text{or:} \quad tg\beta_2 = \frac{a}{s}\frac{1}{\cos\beta_a} \tag{9.73}$$

where the exit flow angle β_2 is:

$$\beta_2 = arctg\left[\frac{a}{s}\frac{1}{\cos\beta_a}\right] \tag{9.74}$$

The deviation is obtained from the difference

$$\delta_2 = \beta_{2c} - \beta_2 \tag{9.75}$$

with β_{2c} as the camber angle at the trailing edge.

References, Chapter 9

9.1 Gostelow, J.P., 1984, " Cascade Aerodynamics," Prgamon Press.
9.2 Scholz, N, 1965," Aerodynamik der Schaufelgitter," Brwon-Verlag, Karlsruhe.
9.3 Betz, A., 1948,"Konforme Abbildung," Berlin, Göttingen, Springer-Verlag.
9.4 Weinig, F., 1935," Die Strömung um die Scahufeln von Turbomaschinen," Leipzig, Barth-Verlag.
9.5 Eckert, B., Schnell, E., 1961, "Axial-und Radialkompressoren," 2. Auflage, Berlin, Göttingen, Heidelberg, Springer- Verlag.

9.6 Traupel, W., “Thermische Turbomaschinen,” Bd.I, 1977, Springer-Verlag Berlin.
9.7 Lakschminarayana, B., 1995, “Fluid Dynamics and Heat Transfer of Turbomchinery,” John Wiley and Sons, Inc.
9.8 Cumpsty, N. A., 1989, “Compressor Aerodynamics,” Longman Group, New York.
9.9 Carter, A.D. , 1950,“The Low Speed Performance of Related Airfoils in Cascades, Aeronautical Research Council.
9.10 Johnsen, I. A, Bullock, R., O., 1965: “Aerodynamic Design of Axial Flow Compressors, ”NASA SP 36.
9.11 Wennerström, A., 1965,“Simplified design Theory of highly loaded axial Compressor Rotors and Experimental Study of two Transonic Examples,” Diss. ETH-Zürich.

10 Simple Blade Design

Flow deflection in turbomachines is established by stator and rotor blades with prescribed geometry that includes inlet and exit *camber angles*, *stagger angle*, camber line, *and thickness distribution*. The blade geometry is adjusted to the stage velocity diagram which is designed for specific turbine or compressor flow applications. Simple blade design methods are available in the open literature (see References). More sophisticated, high efficiency blade designs developed by engine manufacturers are generally not available to the public. In the following, a simple method is presented that is equally applicable for designing compressor and turbine blades. The method is based on (a) constructing the blade *camber line* and (b) superimposing a predefined *base profile* on the camber line.

10.1 Compressor Blade Design

The major parameter for determining the shape of a compressor blade is the Mach number. For low-subsonic to intermediate-subsonic Mach range (M_1 = 0.1 to 0.6), NACA-65 profiles [1] give a relatively high pressure at a reasonably high efficiency. For intermediate Mach numbers, *double circular arc* (DCA) and *multi circular arc* (MCA) profiles may be used. Surface pressure measurements by Cumpsty [2] show that at an inlet Mach number of M_1= 0.6 and at design incidence, the NACA-65 and DCA profiles have comparable pressure distributions. However, due to a sharp leading edge, the DCA-profiles may have higher profile losses than the NACA-65 series. For high subsonic Mach range (M_1 > 0.6), DCA or MCA profiles are used. Controlled diffusion profiles CD are used for transonic Mach range in order to reduce the shock losses. Supersonic compressors require s-shaped blades with sharp leading edge to keep to avoid the shock detachment.

10.1.1 Low Subsonic Compressor Blade Design

In Chapter 6.2, it was shown that for an inviscid flow, the lift force can be expressed as:

$$\boldsymbol{F} = \rho \boldsymbol{V}_\infty \, X \, \boldsymbol{\Gamma}, \quad \text{where} \quad \Gamma = \oint \boldsymbol{V} \cdot d\boldsymbol{c} \tag{10.1}$$

This relation shows that the lift force can exist if there is circulation around the airfoil.

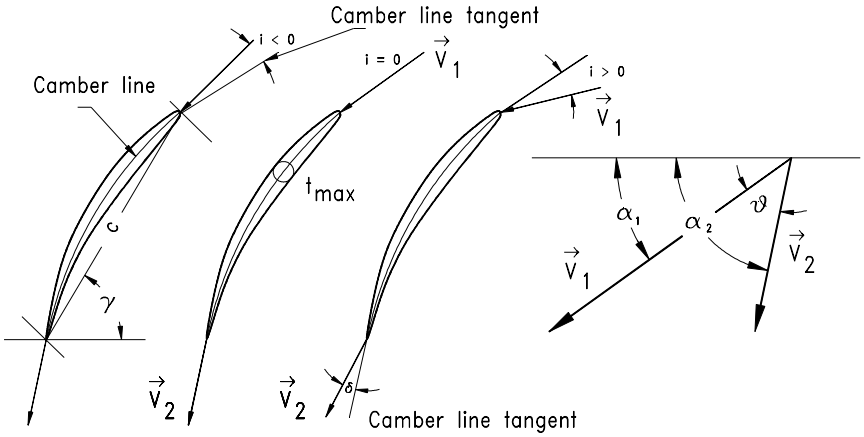

Fig. 10.1: Compressor cascade nomenclature, c = cascade chord length, t_{max} = maximum thickness, γ = cascade stagger angle, ϑ = cascade flow deflection, i = incidence, δ = deviation

As we saw, the circulation was directly related to the flow deflection from the cascade inlet to the exit, which is shown in Fig. 10.1. For an incidence free (*i = 0*) flow, the velocity vector at the inlet is tangent to the camber line. Likewise, for a deviation free (δ = 0) exit flow, the velocity vector is tangent to the camber line at the cascade exit, as seen in Fig. 10.1. Once the compressor stage velocity diagram is constructed, the deflection angle θ and thus, the circulation Γ is known. The problem now is to find the corresponding blade profile for a given circulation. For a compressor blade which generally has a small flow deflection, the circulation Γ can be thought of as the sum of infinitesimal vortices with the intensity dΓ. If we distribute the vortices along the blade chord and consider the specific circulation at an arbitrary point x to be:

$$\gamma(x) = \frac{d\Gamma}{dx} \tag{10.2}$$

Integrating Eq. (10.2) yields:

$$\Gamma = \int_o^c \gamma(x)\,dx \tag{10.3}$$

The vortex dΓ, located at the point ζ, induces a velocity at an arbitrary point *x*, that can be calculated from Bio-Sawart's law. Figure 10.2 shows the distribution of discrete vortices along the chord (left) and their induced velocity (right). An induced velocity in *y*-direction is:

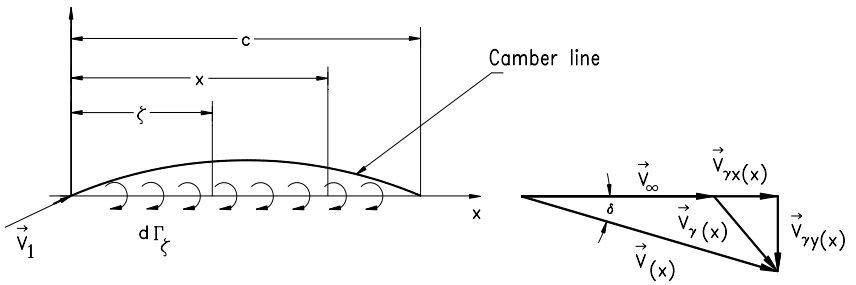

Fig. 10.2: Vortex distribution along the blade chord and induced velocity

$$dV_{\gamma y}(x) = -\frac{d\Gamma_\zeta}{2\pi(x - \zeta)} \tag{10.4}$$

and in the *x*-direction:

$$V_{\gamma x}(x) = \pm\frac{\gamma(x)}{2}\ , \quad (- \textit{ sign for } x > \zeta) \tag{10.5}$$

The integration of Eq. (10.4) gives the total velocity induced at *x* by the vortices distributed at ζ:

$$V_{\gamma y}(x) = -\frac{1}{2\pi}\int_0^c \frac{\gamma(\zeta)d\zeta}{(x - \zeta)} \tag{10.6}$$

The induced velocity for the incidence angle $i = 0$ is shown in Fig. 10.1. Superimposing the induced velocity $V_\gamma(x)$ on V_1, we get the contour velocity $V(x)$ around the profile. Since the direction of this velocity must be identical to the slope of the camber line,

$$tg\delta = \frac{dy(x)}{dx} = \frac{V_{\gamma y}(x)}{V_1 + V_{\gamma x}(x)} \tag{10.7}$$

since the induced velocity component $V_{\gamma x}(x) << V_1$, it follows that

$$\frac{dy(x)}{dx} = \frac{V_{\gamma y}(x)}{V_1} \tag{10.8}$$

Introducing Eq. (10.4) into (10.8):

$$\frac{dy(x)}{dx} = -\frac{1}{2\pi V_1}\int_o^c \frac{\gamma(\zeta)d\zeta}{x-\zeta} \quad for\ i = 0 \tag{10.9}$$

and for considering a small incidence angle I, we find:

$$i + \frac{dy(x)}{dx} = -\frac{1}{2\pi V_1}\int_o^c \frac{\gamma(\zeta)d\zeta}{x-\zeta} \tag{10.10}$$

Now, we introduce the lift coefficient for the camber line and label it with the superscript *:

$$C_L^* = \frac{F^*}{\frac{\rho}{2}V_1^2 c} = \frac{\rho\Gamma V_1}{\frac{\rho}{2}V_1^2} = \frac{2\Gamma}{V_1 c} \tag{10.11}$$

We assume that the lift force induced by a discrete vortex is linearly proportional to the blade lift. This uniform lift distribution assumption results in:

$$\frac{d\Gamma_\zeta}{d\zeta} = \frac{\Gamma}{c} \tag{10.12}$$

and so:

$$\frac{d\Gamma_\zeta}{d\zeta} = \gamma(\zeta) = \frac{C_L^*}{2}V_1 \tag{10.13}$$

Inserting Eq. (10.13) into (10.10) and setting for $i = 0$:

$$\frac{dy(x)}{dx} = \frac{C_L^*}{4\pi}\int_0^c \frac{d\zeta}{x-\zeta} \tag{10.14}$$

The first integration of Eq. (10.14) yields:

$$\frac{dy(x)}{dx} = \frac{C_L^*}{4\pi} \ln\left(\frac{1 - \frac{x}{c}}{\frac{x}{c}} \right) \tag{10.15}$$

The second integration determines the coordinate for the camber line:

$$\frac{y(x)}{c} = -\frac{C_L^*}{4\pi}\left[\left(1 - \frac{x}{c}\right) \ln\left(1 - \frac{x}{c}\right) + \frac{x}{c} \ln\left(\frac{x}{c}\right) \right] \tag{10.16}$$

This is the equation of the camber line for the NACA-compressor blades. The maximum camber is at $x/c = 0.5$

$$\frac{y_{\max}}{c} = \frac{C_L^*}{4\pi} \ln 2 \tag{10.17}$$

With Eq. (10.17), we are able to design the compressor blade camber line at a particular position where the lift coefficient is already calculated. To construct the profile, we need a base profile to superimpose on the camber. The base profile is given for NACA-65 series. For a profile with chord c the camber line coordinates are:

$$\begin{aligned} x_c &= \frac{x}{c} c \\ y_c &= \frac{y}{c} c \end{aligned} . \tag{10.18}$$

where the subscript c represents the camber line. The next step is to superimpose the base profile (for example, from Table 10.1) on the camber. If the maximum thickness $(t/c)_{\max}$ of the actual blade is different from the reference maximum thickness $(t/c)_{\max ref}$ of the base profile, the thickness distribution of the actual profile can be determined by:

$$\frac{t}{c} = \left(\frac{t}{c}\right)_{ref} \frac{\left(\frac{t}{c}\right)_{\max}}{\left(\frac{t}{c}\right)_{\max\, ref}} \tag{10.19}$$

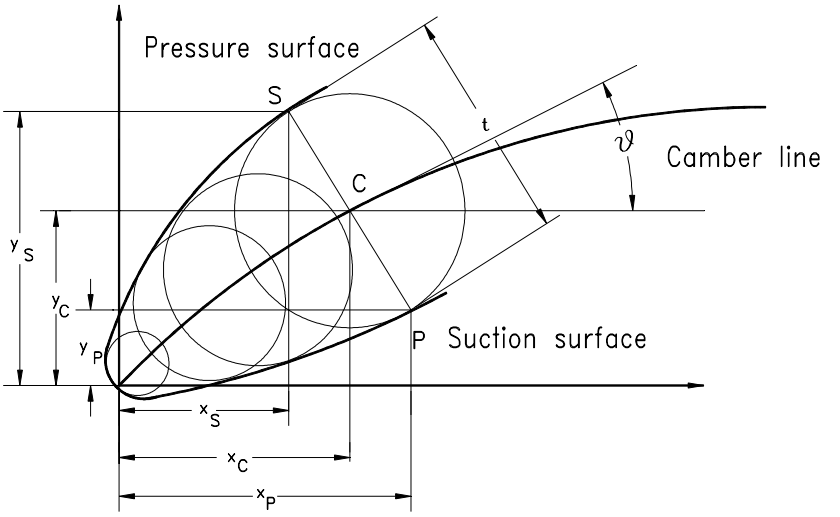

Fig. 10.3: Superposition of base profile on camber line

The superposition procedure is sketched in Fig. 10.3 where a piece of the camber line is shown, on which the thickness is superimposed. For the section side, Fig.10.3, where $\bar{s}\bar{c} = t/2$:

$$\left.\begin{aligned} x &= x_c - \left(\frac{t}{2}\right)\sin\vartheta \\ y &= y_c + \left(\frac{t}{2}\right)\cos\vartheta \end{aligned}\right\} \qquad (10.20)$$

and for the pressure side, where $\bar{c}\bar{p} = t/2$:

$$\left.\begin{aligned} x &= x_c + \left(\frac{t}{2}\right)\sin\vartheta \\ y &= y_c - \left(\frac{t}{2}\right)\cos\vartheta \end{aligned}\right\} \qquad (10.21)$$

The angle ϑ is calculated from Eq. (10.15):

$$\frac{dy(x)}{dx} = tg\,\vartheta = \frac{C_L^*}{4\pi} \ln \left(\frac{1 - \frac{x_c}{c}}{\frac{x_c}{c}} \right) \tag{10.22}$$

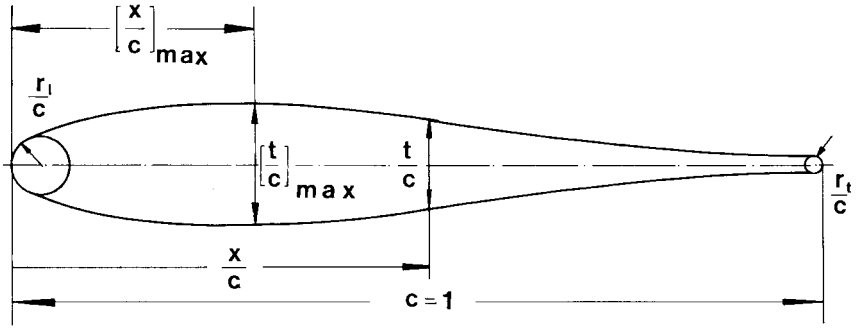

Fig. 10.4: Schematic of a base profile to be superimposed on a camber line

Table 10.1: Thickness distribution of a NACA-65 compressor base profile, $\xi = x/c$, $t = t_{max}\, f(\xi)$

ξ	0	0.0125	0.0250	0.0500	0.0750	0.1000	0.1500	0.200	
f(ξ)	0.	0.2338	0.3148	0.4354	0.5294	0.6080	0.7333	0.8268	
ξ	0.30	0.4000	0.5000	0.6000	0.7000	0.8000	0.9000	0.9500	1.00
f(ξ)	0.952	0.9992	0.9624	0.8292	0.6312	0.3974	0.1620	0.0612	0.00

The base profile listed in Table 10.1 is shown in Fig. 10.4

Summary, simple compressor blade design steps:

1. Calculate C_L^* from velocity diagram.
2. To find (y/c), calculate y(x)/c from Eq. (10.16).
3. Calculate ϑ from Eq. (10.11) and Eq. (10.22).
4. If $(t/c)_{max}$ is different from $(t/c)_{max\,ref.}$, then introduce new $(t/c)_{max}$ into Eq. (10.19) and use the data for the reference base profile.

5. With the actual *t*, calculate from Eq. (10.20) the suction surface, and from Eq. (21) the pressure surface.
6. Use smoothing if needed.

10.1.2 Intermediate Subsonic Compressor Blades

Double circular arc (DCA) and multi-circular arc (MCA) profiles are used particularly for compressors operating at intermediate subsonic inlet Mach numbers (M > 0.5). Considering a particular cross section through a compressor cascade as shown in Fig. 10.5, the suction and pressure surfaces of a DCA-profile consist of two circular arcs. The suction and pressure surfaces of a MCA-profiles however, may consists of several circular arc.

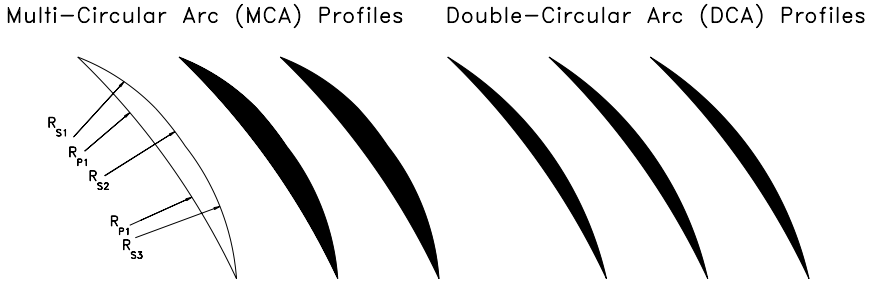

Fig. 10.5: DCA and MCA profiles for high subsonic Mach number applications, R_{si} = suction surface radii, R_{Pi} = pressure surface radii

Following criteria dictate the selection of a particular profile for a compression application:

1) The inlet Mach number
2) Incidence tolerance with regard to the profile losses
3) Pressure distribution that directly determines the lift coefficient
4) Drag forces that determines the blade profile loss

(1) and (4) can be combined to arrive at the optimum lift/drag ratio, which we treated in Chapter 6.

10.1.3 Transonic, Supersonic Compressor Blades

For compressors operating at transonic and supersonic Mach numbers, blades design efforts are concentrated at keeping the shock losses at a minimum level. Regarding the transonic compressors, the research efforts resulted in design of *controlled diffusion blades* that almost eliminate shock losses ([3], [4], [5].

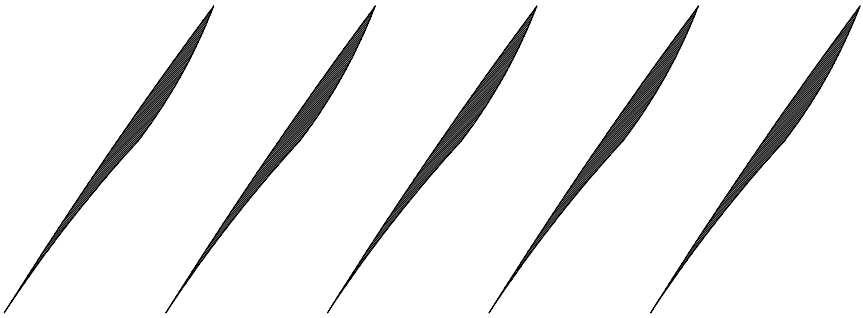

Fig. 10.6: Supersonic compressor blades composing of multi-circular arcs, sharp leading edges, convergent inlet and divergent exit regions.

For compressors operating in supersonic Mach range, the so called S-profiles with sharp leading edges are used. Such profiles are shown in Fig. 10.6. As seen, the pressure and suction surfaces consists of several multi circular arcs with very small curvatures(large radii). Particular attention must be paid to the shock losses, as discussed in Chapter 7 and in [6].The flow decelerates within the convergent part by a system of oblique shock waves followed by a normal shock. Further deceleration is achieved by diffusion within the divergent part. As seen, these profiles have a slightly convergent inlet tangent to a throat which is followed by a slightly divergent channel.

10.2 Simple Turbine Blade Design

Different turbine blade designs are discussed in literature among others, [7], [8], [9], [10], and [11]. For turbine blade design, the camber line can be estimated from the inlet and exit flow angles, Fig.10.7. This can be done graphically or numerically. Given a chord length c, the tangents to the leading- and trailing-edge of the chord are constructed by the inlet and exit flow angles as shown in Fig. 10.7. The tangents are brought to an intersection with each other and subdivided into equal distances. The envelope to the inner region of the connecting lines is the camber line, as shown in Fig.10.7. Once the camber line is constructed, a turbine base profile is superimposed and the profile is generated, Fig.10.8. For the numerical description of the camber line, the following dimensionless quantities are defined: $\eta = y(x)/c, \zeta = x/c$ The camber line can be described by a polynomial:

$$\eta = \sum_{\nu=0}^{n} a_\nu \xi^\nu \tag{10.23}$$

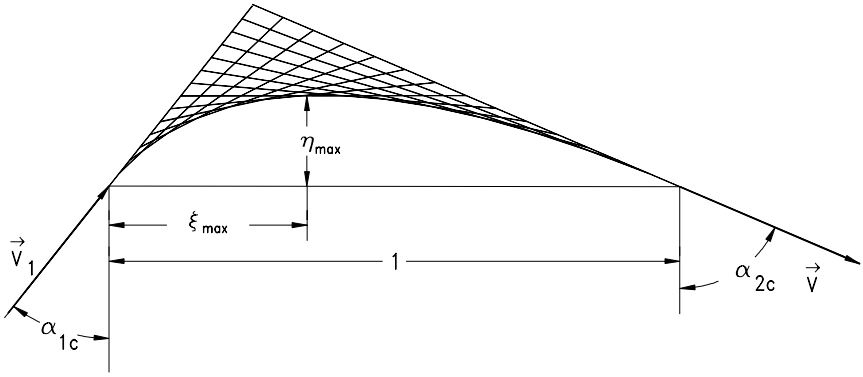

Fig. 10.7: Graphical design of a turbine blade camber line with the given $\eta_{max} = t_{cmax}/c$ and $\xi_{max} = x_{t_c max}/c$

The coefficients a_v are obtained from the following boundary conditions:

$$\text{At } \xi = \frac{x}{c} = 0 \Rightarrow \eta = 0, \quad \text{and } \frac{d\eta}{d\xi} = tg\alpha_{1c} \qquad \text{BC1}$$

$$\text{At } \xi = \frac{x}{c} = 1 \Rightarrow \eta = 0, \quad \text{and } \frac{d\eta}{d\xi} = tg\alpha_{2c} \qquad \text{BC2}$$

$$\text{At } \xi = \xi_{max} \Rightarrow \frac{\partial\eta}{\partial\xi} = 0 \qquad \text{BC3}$$

where x_{max} and $t_{c\,max}$ are given. With the boundary conditions BC1 to BC3, five coefficients can be determined. The corresponding polynomial is of the fourth order:

$$\eta = \sum_{v=0}^{4} a_v \xi^v \qquad (10.25)$$

or

$$\eta = a_0 + a_1\xi + a_2\xi^2 + a_3\xi^3 + a_4\xi^4 \qquad (10.26)$$

From BC1, it follows immediately that $a_0 = 0$. To find the turbine profile, the base profile must be superimposed on this camber line, Fig. 10.8. It is important to ensure that there is no discontinuity on the profile surfaces. For this purpose, the final profile should be smoothed mathematically.

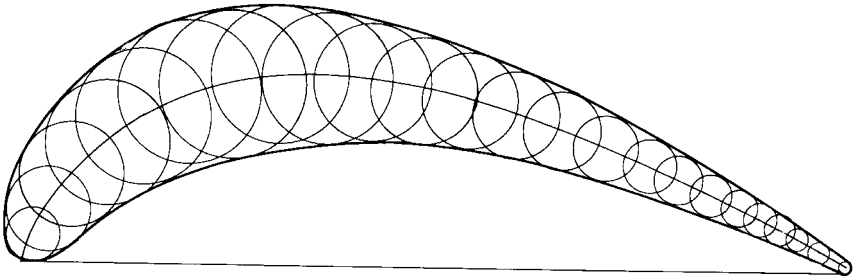

Fig. 10.8: Superposition of a base profile on the camber line.

References, Chapter 10

10.1 NASA SP-36 NASA Report, 1965.

10.2 Cumpsty, N. A., 1989, "Compressor Aerodynamics," Longman Group, New York.

10.3 Hobson, D. E., 1979, "Shock Free Transonic Flow in Turbomachinery cascade," Ph.D-Thesis, Cambridge University Report CUED/A Turbo/65.

10.4 Schmidt, J. F., et al., 1984, "Redesign and Cascade tests of a Supercritical Controlled Diffusion stator Blade Section," AIAA Paper 84-1207.

10.5 Lakschminarayana, B., 1995, "Fluid Dynamics and Heat Transfer of Turbomchinery," John Wiley and Sons, Inc.

10.6 Schobeiri, M. T., 1998, A New Shock Loss Model for Transonic and Supersonic Axial Compressors With Curved Blades," *AIAA, Journal of Propulsion and Power,* Vol. 14, No. 4, pp. 470-478.

10.7 Teufelberger, A. Choice of an optimum blade profile for steam turbines. *Rev. Brown Boveri*, 1976, (2), 126-128.

10.8 Kobayashi, K., Honjo, M., Tashiro, H. and Nagayama, T. Verification of flow pattern for three-dimensional-designed blades. IMechE paper C423/0l5, 1991.

10.9 Jansen, M. and Ulm, W. Modern blade design for improving steam turbine efficiency. *VDI Ber.*, 1995, 1185.

10.10 Emunds, R., Jennions, I.K., Bohn, D. and Gier, J. The computation of adjacent blade-row effects in a 1.5 stage axial flow turbine. ASME paper 97-GT-81, Orlando, Florida, June 1997.

10.11 Dunavant, J.C. and Erwin, J.R. Investigation of a related series of turbine-blade profiles in cascade. NACA TN-3802, 1956.

11 Radial Equilibrium

In Chapter 5 we briefly described a simple radial equilibrium condition necessary to determine the radial distribution of the stage parameters such as, ϕ, λ, r, α_i, and β_i. Assuming an axisymmetric flow with constant meridional velocity and total pressure distributions, we arrived at free vortex flow as a simple radial equilibrium condition with $rv_u = const.$ In practice, from aerodynamics design point of view a constant meridional velocity component or constant total pressure may not be desirable. As an example, consider the flow field close to the hub or tip of a stage, where secondary flow vortices predominate. As discussed in Chapter 6, these secondary vortices induce drag forces leading to secondary flow losses which reduce the efficiency of the stage. To reduce the secondary flow losses, specific measures can be taken that are not compatible with the simple radial equilibrium condition. In this case the simple radial equilibrium method needs to be replaced by a general one. Wu [1] proposed a general theory for calculating the three-dimensional flow in turbomachines. He introduced two sets of surfaces: Blade to blade surfaces called S_{1i} and hub-to-tip surfaces labeled with $S_{2j.}$ Utilizing S_{1i} and S_{2j} surfaces, Wu [1] proposed an iterative method to solve the three-dimensional inviscid flow field in turbomachinery stages. Coupling both surfaces, however, is associated with computational instabilities that gives rise to replacing the technique by complete Euler or Navier-Stokes solver, [2]. A computationally more stable method for solving the flow field is the streamline curvature technique. This method is widely used in turbomachinery industry and is the essential tool for generating the basic design structure necessary to start with CFD application. Streamline curvature method can be used for design, off-design, and analysis. Vavra [3] presented the theoretical structure for inviscid axisymmetric flow in turbomachines that can be used to derive the streamline curvature equations. A thorough review of the streamline curvature method can be found in Novak and Hearsey [4], Wilkinson [5], and Lakshminarayana [2].Wennerstrom [6] presented a concise description of this technique, which is given in this section in its original form.

Rapid calculation procedures used in the turbomachinery industry determining the distribution of flow properties within the turbomachinery assume steady adiabatic flow and axial symmetry. The more sophisticated of these procedures include calculation stations within blade rows as well as the more easily treated stations at the blading leading and trailing edges. The assumption of axial symmetry in the bladed region implies an infinite number of blades. The blade forces acting between the

blades and the fluid are taken into consideration by body force terms in equation of motion. The streamlines are not straight lines as could be supposed. They usually have certain curvatures that are maintained if the forces exerted on the fluid particle are in equilibrium state, described by the equilibrium equation. This equation includes various derivatives in the meridional plane and is solved in this plane along the computing stations which are normal to the average meridional flow direction. The equilibrium equation in its complete form cannot be solved analytically, therefore numerical calculation methods are necessary. For the application of the equilibrium equation to the stage flow with streamline curvature, Hearsey [7] developed a comprehensive computer program, which is successfully used in the turbomachinery industry for design of advanced compressors and turbines. Since the treatment of the corresponding numerical method for the solution of this equation is given in [7], this chapter discusses the basic physical description of the calculation method. As a result, streamline curvature method can be used as design tool and for the post design analysis. An advanced compressor design is presented followed by a brief discussion of special cases.

11.1 Derivation of Equilibrium Equation

The starting point for this derivation is the formulation of the equations of motion for an axisymmetric flow in intrinsic coordinates fixed in space along streamlines as shown in Fig.11.1.

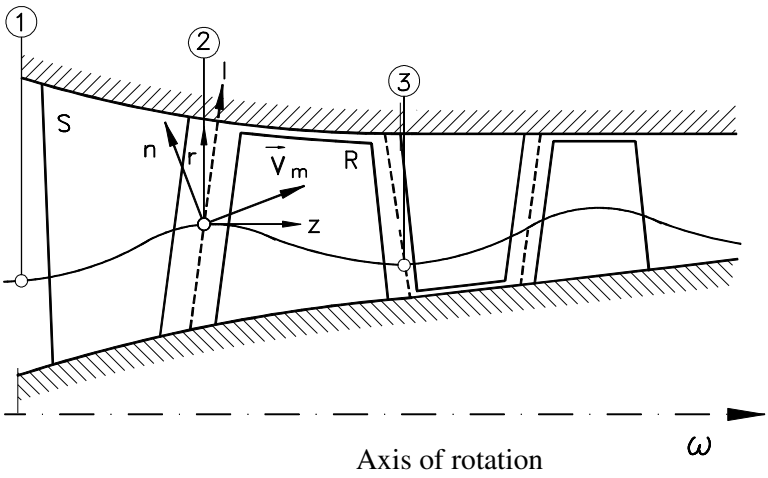

Fig. 11.1: Flow through axial compressor, streamline, directions are: n = normal, m = meridional, r = radial, z = axial, and l = computing station

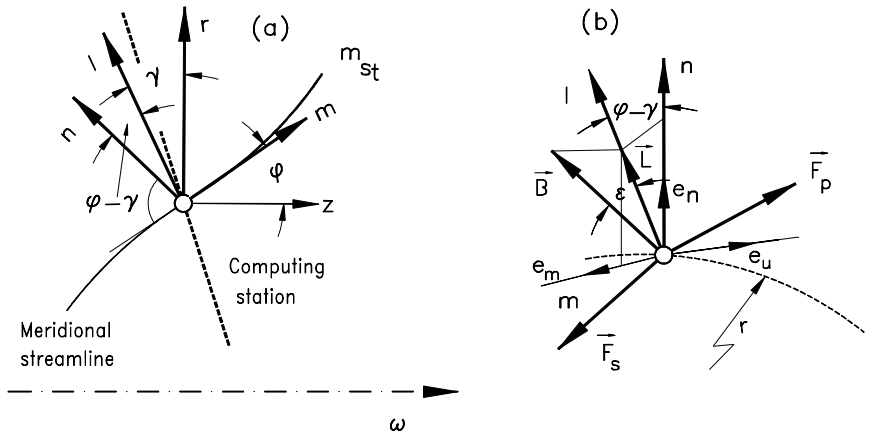

Fig. 11.2: (a) Coordinate directions in the meridional plane, (b) orientation of vectors with respect to m, u, n orthogonal coordinate system, redrawn from [6].

The momentum equation in meridional direction:

$$V_m \frac{\partial V_m}{\partial m} - \frac{V_u^2}{r} \sin\phi = -\frac{1}{\rho}\frac{\partial p}{\partial m} + F_m \tag{11.1}$$

in stream surface normal direction:

$$\frac{V_m^2}{r_c} - \frac{V_u^2}{r} \cos\phi = -\frac{1}{\rho}\frac{\partial p}{\partial n} + F_n \tag{11.2}$$

and in circumferential direction:

$$\frac{V_m}{r}\frac{\partial (rVu)}{\partial m} = F_u \tag{11.3}$$

Thermodynamic equations required are the energy equation for steady adiabatic flow:

$$H = h + \frac{V^2}{2} \tag{11.4}$$

and the Clausius-Gibbs relation:

$$\frac{1}{\rho} dp = dh - Tds \tag{11.5}$$

Since, in intrinsic coordinates, there is no velocity component in the n-direction (by definition),

$$V^2 = V_m^2 + V_u^2 \tag{11.6}$$

Equations (11.4), (11.5), and (11.6) are combined to give:

$$\frac{1}{\rho} dp = dH - Tds - V_m dV_m - V_u dV_u \tag{11.7}$$

Since the computation station lies in the space between the stator and the rotor usually not normal to the meridional stream surface, the derivatives must be defined with respect to the l-direction along a computing station, Fig.11.2:

$$\frac{d}{dl} = \frac{dn}{dl}\frac{\partial}{\partial n} + \frac{dm}{dl}\frac{\partial}{\partial m} = \cos(\phi - \gamma)\frac{\partial}{\partial n} + \sin(\phi - \gamma)\frac{\partial}{\partial m} \tag{11.8}$$

Rearranging Eq.(11.8) to eliminate the derivatives with respect to the normal direction:

$$\frac{\partial}{\partial n} = \sec(\phi - \gamma)\frac{d}{dl} - tg(\phi - \gamma)\frac{\partial}{\partial m} \tag{11.9}$$

Introducing Eq.(11.7) into Eq.(11.1) and (11.2), eliminating derivatives with respect to *n* with Eq.(11.9), the resulting equations are combined to eliminate

$$\frac{\partial H}{\partial m} - T\frac{\partial s}{\partial m} \tag{11.10}$$

The equation obtained after algebraic rearrangement and trigonometric substitution is:

$$V_m \frac{dV_m}{dl} = \sin(\phi - \gamma) V_m \frac{\partial V_m}{\partial m} + \cos(\phi - \gamma)\frac{V_m^2}{r_c} - \frac{V_u}{r}\frac{d(rV_u)}{dl} +$$

$$\frac{dH}{dl} - T\frac{ds}{dl} - \sin(\phi - \gamma)F_m - \cos(\phi - \gamma)F_n \tag{11.11}$$

In some cases, it is more convenient to work in a similar system of coordinates which is stationary with respect to a rotating blade row. As shown in Chapter 3, Eq.(11.11) is easily transformed into the rotating frame of reference by introducing the substitution:

$$V_u = W_u + \omega r \tag{11.12}$$

for the circumferential velocity component. The corresponding relative total enthalpy[1] H_r from Eq. (3.104) is:

$$H_r = h + \frac{W^2}{2} - \frac{U^2}{2} \tag{11.13}$$

Combining Eqs. (11.12), and (11.13) leads to:

$$H = H_r + \omega r\left(W_u + \omega r\right) \tag{11.14}$$

Introducing Eqs.(11.12) and (11.14) into Eq. (11.11), the corresponding radial equilibrium equation is:

$$V_m \frac{dV_m}{dl} = \sin(\phi - \gamma)\, V_m \frac{\partial V_m}{\partial m} + \cos(\phi - \gamma)\, \frac{V_m^2}{r_c} - \frac{W_u}{r} \frac{d(rW_u)}{dl} +$$

$$\frac{dH_r}{dl} - T\frac{ds}{dl} - 2\omega W_u \cos\gamma - \sin(\phi - \gamma)\, F_m - \cos(\phi - \gamma)\, F_n \tag{11.15}$$

Equations.(11.11) and (11.15) represent the radial equilibrium condition. The point of principal interest in this derivation are associated with the treatment of the body forces, F_m and F_n. Note that the complete body force field contains a third component F_u which is orthogonal to the other two mutually orthogonal components F_m and F_n and can be directly calculated from Eq. (11.3). The reminder of this derivation is aimed at obtaining expressions for F_m and F_n which relate to geometric properties of the blading. Combining Eqs.(11.1) and (11.7) gives:

$$T\frac{\partial s}{\partial m} = \frac{\partial H}{\partial m} - \frac{V_u^2}{r}\sin\phi - V_u \frac{\partial V_u}{\partial m} - F_m \tag{11.16}$$

---

[1] Wennerstrom [6] calls this quantity rothalpy which was introduced by Wu [1], who termed the sum of the static enthalpy and the kinetic energy of the relative flow $h_R = h + W^2/2$ as the relative total enthalpy (see also Lakshminarayana [2]). In a rotating frame of reference, the expression h_R changes along a streamline that varies in radial direction. In contrast, the relative total enthalpy given by Eq. (11.13) derived in Chapter 3 (Eq. 3.104) remains constant and is generally valid within a rotating frame of reference, where the streamlines may change in radial direction (see also Vavra [3]).

or

$$T\frac{\partial s}{\partial m} = \frac{\partial H}{\partial m} - \frac{V_u}{r}\frac{\partial (rV_u)}{\partial m} - F_m \tag{11.17}$$

Equation (11.3) and the thermodynamic definition of work (applied to a turbomachine) may be combined to give

$$\frac{\partial H}{\partial m} = \frac{U}{r}\frac{\partial (rV_u)}{\partial m} \tag{11.18}$$

a differential form of the Euler equation of turbomachinery. Combining Equations (11.17) and (11.18), noting from the velocity triangle that

$$tg\beta = \frac{W_u}{V_m} \tag{11.19}$$

and introducing Equation (11.3) again leads to

$$F_m = -F_u \tan\beta - T\frac{\partial s}{\partial m} \tag{11.20}$$

Equation (11.20) is sufficient to solve Eqs. (11.11) or (11.15) for some bladeless cases but, in order to solve the equations within a bladed region, more information is required concerning the direction and nature of the force components. For this purpose, it is convenient to resort to vector analysis to relate the various force components and coordinate directions. Fig.11.2b illustrates the vectors described in the following discussion. The variables *m, u, n* are the principal orthogonal axes of a right handed, streamline coordinate system. In this system, F_s is the body force vector acting to oppose motion of the fluid; i.e. the body force which produces an irreversible increase in entropy. It lies in the m-u plane and at the angle β (relative flow angle) from the meridional direction. The vector $\boldsymbol{L}$ is coincident with the l-direction and lies in the n-m plane at the angle (ϕ-γ) from the n-direction. The vector B is tangent to the mean blade surface and lies in the l-u plane at an angle ε from the l-direction. Planes such as the m-u plane and l-u plane are understood as planes tangent to the curved surface described by the respective coordinates at the point in question. The equation of the unit vector in F_s-direction is:

$$\frac{\boldsymbol{F_s}}{F_s} = \cos\beta\, e_m + \sin\beta\, e_u + (0)\, e_n \tag{11.21}$$

and the equation of the unit vector $\boldsymbol{B}$ is

$$\boldsymbol{B} = \cos\varepsilon\sin(\phi - \gamma)e_m - \sin\varepsilon\, e_u + \cos\varepsilon\cos(\phi - \gamma)e_n \tag{11.22}$$

The force due to a pressure difference across a blade acts in a direction normal to both vectors $\boldsymbol{F}_s$ and $\boldsymbol{B}$, which together define the local plane of the mean blade surface at a point. Therefore, pressure force vector can be defined by the cross product of $\boldsymbol{F}_s$ and $\boldsymbol{B}$. Since $\boldsymbol{F}_s$ and $\boldsymbol{B}$ are usually not perpendicular but at an angle $(\pi/2 - (\phi - \gamma))$ to one another, the product of these vectors differs from a unit vector by $\cos(\phi - \gamma)$. Therefore to obtain a unit vector for the force due to pressure across a blade and because $\boldsymbol{F}_p$ must be positive direction of rotation, this is written

$$\frac{\boldsymbol{F}_p}{F_p} = \frac{1}{\cos(\phi - \gamma)}\left[\frac{\boldsymbol{B}\times\boldsymbol{F}}{F_s}\right]$$

$$\frac{\boldsymbol{F}_p}{\boldsymbol{F}_p} = -\sin\beta\cos\varepsilon\, e_m + \cos\beta\cos\varepsilon\, e_u + \left[\frac{\cos\beta\sin\varepsilon}{\cos(\phi-\gamma)} + \sin\beta\cos\varepsilon\, tg(\phi - \gamma)\right] \tag{11.23}$$

From Fig.11.2b, note that $\boldsymbol{F}_m$ is composed of the m-components of $\boldsymbol{F}_s$ and $\boldsymbol{F}_p$. Consequently, from Eqs.(11.21) and (11.23):

$$F_m = F_s\cos\beta - F_p\sin\beta\cos\varepsilon \tag{11.24}$$

Similarly, $\boldsymbol{F}_u$ and $\boldsymbol{F}_n$ are composed respectively of the u and n components of $\boldsymbol{F}_s$ and $\boldsymbol{F}_p$

$$F_u = F_s\sin\beta + F_p\cos\beta\cos\varepsilon \tag{11.25}$$

$$F_n = F_p\left[\cos\beta\sin\varepsilon\sec(\phi - \gamma) + \sin\beta\cos\varepsilon\, tg(\phi - \gamma)\right] \tag{11.26}$$

Since the orthogonal components of the force field have been defined in terms of components acting along and perpendicular to the relative flow direction, it is possible to solve for these two components. By inserting Eqs.(11.24) and (11.25) into Eq. (11.20) and simplifying, one obtains:

$$F_s = -\cos\beta\, T\frac{\partial s}{\partial m} \tag{11.27}$$

Subsequently, Eqs.(11.25) and (11.27) can be combined to give

$$F_p = \frac{F_u}{\cos\beta\cos\varepsilon} + \frac{\sin\beta}{\cos\varepsilon} T\frac{\partial s}{\partial m} \tag{11.28}$$

If Eqs.(11.27) and (11.28) are now inserted into Eqs.(11.24) and (11.26) , the body forces appropriate to the intrinsic coordinate system are defined in terms of parameters readily calculated. The most useful form of the radial equilibrium equation is the form in relative system, Equation (11.15), since it becomes identical to Eq.(11.11) in the absolute system when the angular velocity of the coordinates is set equal to zero. Combining Eq.(11.24), (11.26), (11.27) and (11.28) into Eq.(11.15) puts the radial equilibrium equation in the form:

$$V_m \frac{dV_m}{dl} = \sin(\phi - \gamma) V_m \frac{\partial V_m}{\partial m} + \cos(\phi - \gamma) \frac{V_m^2}{r_c} -$$

$$\frac{W_u}{r} \frac{d\left(r W_u\right)}{dl} + \frac{dH_r}{dl} - T\frac{ds}{dl} - 2\omega W_u \cos\gamma - tg\varepsilon F_u +$$

$$\left[\sin(\phi - \gamma)\cos^2\beta - tg\varepsilon \sin\beta \cos\beta\right] T\frac{\partial s}{\partial m} \tag{11.29}$$

The force $\boldsymbol{F_u}$ can be obtained from Eq.(11.3) or from

$$F_u = \frac{V_m}{r} \frac{\partial (r W_u)}{\partial m} + 2\omega V_m \sin\phi \tag{11.30}$$

applicable to the relative system. If working in a relative system with specified flow angle, it is convenient to employ Eq.(11.19) to eliminate W_u. The result of this substitution included in a combined form of Eq.(11.29) and (11.30) is

$$V_m \frac{dV_m}{dl} = \cos^2\beta \left[\left(\sin(\phi - \gamma) - tg\varepsilon\, tg\beta\right) V_m \frac{\partial V_m}{\partial m} + \cos(\phi - \gamma) \frac{V_m^2}{r_c} \right] -$$

$$\cos^2\beta \left[V_m^2 \frac{tg\beta}{r} \frac{d(rtg\beta)}{dl} - 2\omega V_m \left(tg\varepsilon \sin\phi + tg\beta \cos\gamma\right) \right] +$$

$$\cos^2\beta \left[\left(\sin(\phi - \gamma)\cos^2\beta - tg\varepsilon \sin\beta \cos\beta \right) T\frac{\partial s}{\partial m} \right] +$$

$$\cos^2\beta \left[\frac{dH_r}{dl} - T\frac{ds}{dl} - V_m^2 \frac{tg\varepsilon}{r} \frac{\partial (rtg\beta)}{\partial m} \right] \tag{11.31}$$

The form of the radial equilibrium equation most appropriate for a particular calculation depends on a number of factors. The most important of these are the nature of the numerical scheme for analysis and the choice of parameters to be specified. This derivation was guided by the intent to apply the results to a streamline curvature type of computing procedure wherein the meridional velocity was the primary variable for which solutions were sought. In this type of procedure, the radial equilibrium equation is solved along each computing station for an assumed set of streamlines. The streamlines are then refined and this process repeated until a satisfactory degree of convergence is attained. This calculation method is used successfully in turbomachinery industry for design of advanced compressors and turbines.

Before discussing applications in bladed regions of a turbomachine, consider applications involving bladefree spaces. The body force due to a pressure difference across a blade was defined by the vector F_p in Eq.(11.23). In a bladefree space, this component is zero. The remaining body force, F_s, associated with the entropy increase was defined by Eq.(11.26). Hence, Eqs.(11.24), (11.25) and (11.26) describing the three orthogonal body forces of the intrinsic coordinate system reduce to

$$F_m = -\cos^2\beta\, T\frac{\partial s}{\partial m} \tag{11.32}$$

$$F_u = -\sin\beta\cos\beta T\frac{\partial s}{\partial m} \tag{11.33}$$

$$F_n = 0 \tag{11.34}$$

In addition, all terms involving the blade lean angle, ε, drop out of the radial equilibrium equation. Equation (11.29) then reduces to:

$$V_m\frac{dV_m}{dl} = \sin(\phi-\gamma)V_m\frac{\partial V_m}{\partial m} + \cos(\phi-\gamma)\frac{V_m^2}{r_c} -$$

$$-\frac{W_u}{r}\frac{d(rW_u)}{dl} + \frac{dH_r}{dl} - T\frac{ds}{dl} - 2\omega W_u\cos\gamma +$$

$$+\sin(\phi-\gamma)\cos^2\beta\, T\frac{\partial s}{\partial m} \tag{11.35}$$

It is interesting to note that according to Eq.(11.32) and (11.33) in a swirling flow, an entropy rise in the direction of flow always leads to body force terms both in — and

u-directions. This is obvious for the vaneless diffuser and a centrifugal machine where most of the entropy rise occurs from wall friction. It is much less obvious for an axial turbomachine of high aspect ratio where annulus wall friction may be negligibly small in relation to losses due to wake mixing. However, it appears that a change in angular momentum occurs in both cases if the entropy is assumed to be increasing in flow direction.

Considering bladed regions, the choice of parameters specified initially generally falls into one of two categories. The first involves cases where total temperature or circumferential velocity component is specified. Practically these variables are for all practical purposes interchangeable, being simply related through Eq.(11.18). The most convenient solution for these cases is usually obtained in stationary frame of reference using Eq.(11.29) with $\omega = 0$, $W_u = V_u$, and $H_r = H$. During each calculation pass, the only variables in Eq.(11.29) are usually V_m and β, since all the other parameters distributed along the *l*-direction are either input data or upgraded between passes. The second important category of calculation within the bladed region involves specified relative flow angles. For this purpose it is most expedient to work in a relative frame of reference, specifying ω within the rotors and zero elsewhere. The most convenient radial equilibrium equation is Eq.(11.31). In this instance, the only variable in Eq.(11.31) during a calculation pass is V_m and all other variations in *l*-direction are either input data or upgraded only between calculation passes.

11.2 Application of Streamline Curvature Method to Turbomachinery

Utilizing the equations derived in section 11.1, Hearsey [7] developed a computational tool that can be used for design and analysis of turbomachines. This section summarizes the computational aspects of the streamline curvature technique by Hearsey [7].

As discussed in the previous section, the streamline curvature method offers a flexible method of determining an Euler solution of the axisymmetric flow through a turbomachine. The computational grid comprises the streamlines, as seen in a meridional view of the flow path, and quasi-normals that are strategically located in the flow, Figs. 11.1. Several stations are generally placed in the inlet duct upstream of the turbomachine proper, and several more are generally placed downstream. Within the turbomachine, the minimum number of quasi-normals, or "stations", is simply one between each adjacent pair of blade-rows, which would then represent both outlet conditions from the previous row and inlet conditions to the next. A better choice is one at each edge of each blade-row. For some calculations, additional stations are added within the blade-rows. This is a relatively coarse grid (compared with that used for CFD computations), making for calculations that typically take just seconds to complete (when run on a typical year-2003 PC).

By virtue of being an axisymmetric, Euler solution, the basic method is inherently incapable of predicting entropy rises, that is pressure losses and efficiency. This is handled by invoking a cascade performance prediction scheme to estimate losses and, in some situations, discharge flow angles from blading. Complicated boundary layers form on the flow path inner and outer walls of turbomachinery, causing "blockage" and participating in secondary flows. Especially for multi-stage axial compressors, a good estimate of blockage is required in order to correctly predict stage matching.

The equation system that is used broadly caters to two situations: when the variation of absolute tangential velocity component along a computing station is known, and when the relative flow angle distribution is known. The former generally arises in "design" calculations, and the latter in "analysis", or performance prediction, cases. Thus the streamline curvature procedure may be used for design calculations, off-design performance predictions and test-data analysis. This versatility, combined with the speed of solution, makes the method a work-horse tool. Many designs can be accomplished using only the streamline curvature method, and while some CFD computations are now offering design capability, even then a good candidate design is generally required as a starting point.

Although the Euler equations are the basis of the method, properly accounting for the change in entropy that is super-imposed from station to station, that is, in the streamwise direction, requires some care. This was highlighted in Horlock [8] in which several previously-published equation systems were examined and found to be missing what is usually a small term.

For the case where tangential velocities are known, the appropriate equation is Eq. (11.29). When relative flow angles are known, Eq. (11.31) is used. In conjunction with one of these equations, the continuity equation and the energy equation are required. Fluid properties are also required; these are best computed in a discreet sub-program to allow for easy replacement. The continuity equation takes the form:

$$\dot{m} = \int_{r_h}^{r_t} V_m \rho \cos(\phi - \gamma) 2\pi r dl \tag{11.36}$$

The rate of change of flow with meridional velocity will also be required. This is given by:

$$\frac{d\dot{m}}{dV_m} = \int_{r_h}^{r_t} (1 - M_m^2) \frac{d\dot{m}}{V_m} \tag{11.37}$$

when tangential velocity component is specified, or:

$$\frac{d\dot{m}}{dV_m} = \int_{r_h}^{r_t} \left[1 - M_{m_{rel}}^2 \left(1 + \frac{\zeta \kappa p/P_{rel}}{1 + \zeta(1 - p/P_{rel})} \right) \right] \frac{d\dot{m}}{V_m} \tag{11.38}$$

when relative flow angle is given. The loss coefficient ζ included in Eq. (11.38) is the total pressure loss coefficient normalized by *exit* dynamic pressure. If not used, it is set zero in Eq. (11.38). The Euler equation of turbomachinery relates total enthalpy change to angular momentum change:

$$\Delta H = H_3 - H_2 = \omega(r_3 V_{u3} - r_2 V_{u2}) \tag{11.39}$$

11.2.1 Step-by-Step Solution Procedure

Given these equations, a step-by-step procedure to obtain a solution is as follows:

(1) An initial estimate of the streamline pattern is made. An obvious choice is to divide the flow path into equal areas at each station. Slightly more uniform (final) streamline spacing may be achieved by dividing the inlet (or some other) station into equal increments, and then using the resulting area fractions to guide the remaining estimates.

(2) Initial estimates of the streamwise gradients that occur in Eqs.(11.29) and (11.31) are made. These are all second-order terms, and zero is the usual first estimate.

(3) The streamline slopes and curvatures are computed at all mesh points (although alternatively this can be done station-by-station as the calculation proceeds). Curvatures are normally set to zero for the first and last stations.

(4) At the first station, the user is required to specify the variation of total enthalpy, entropy and angular momentum or flow angle along the station. Enthalpy and entropy are typically implied by total pressure and temperature in the users input data. The fluids package can then be used to obtain enthalpy and entropy on each streamline.

(5) A first estimate of the meridional velocity on one streamline is made, from the inlet flow and the first station area. It is recommended that the mid-streamline value be defined. High accuracy is not required. (This will not be required after the first pass).

(6) Depending upon whether angular momentum or flow angle was given in the input data, Eq. (11.29)or (11.31) is integrated from the mid-streamline to the inner wall, and from the mid-streamline to the outer wall. This yields a meridional velocity distribution that is consistent with the momentum equation, the assumed streamline characteristics and the estimated mid-line velocity estimate. Although this is not likely to occur at Station 1, extreme values can lead to negative velocities, or values greater than the speed of sound. Provisions must be made for such occurrence.

(7) Equations (11.36) and (11.37) or (11.38) are integrated across all streamlines, to yield the achieved flow and its rate of change with meridional velocity.

(8) The sign of the flow gradient indicates on which branch of the continuity equation the current velocity profile lies, a positive value indicating the subsonic branch and a negative value the supersonic branch. If tangential velocity is specified, only the subsonic branch is valid for a streamline curvature solution but if flow angle is specified, the user must specify which branch is required; both are potentially valid. (The criterion for a valid solution is actually that the meridional velocities be less than the speed of sound. Thus if zero or small flow angles are specified, the supersonic solution will not be valid). If the profile lies on the correct branch, and the achieved flow is within the desired tolerance of the specified flow, control passes to Step 9. Otherwise a new estimate of the mid-line meridional velocity is required. If the profile lies on the wrong branch, a semi-arbitrary change in the mid-line meridional velocity estimate is made, and control returns to Step 6 (subject to some limit on the permitted number of iterations). Otherwise, the mid-line meridional velocity is re-estimated using:

$$V_{m_{new}} = V_{m_{old}} + \frac{\left(\dot{m}_{specified} - \dot{m}_{achieved}\right)}{\frac{d\dot{m}}{dV_m}} \tag{11.40}$$

and again, control returns to Step 6 (subject to some limit on the permitted number of iterations). Several potential difficulties exist when applying Eq. (11.40). The gradient $d\dot{m}/dV_m$ becomes ever smaller as the junction between the two branches of the continuity equation is approached. Thus very large changes in *Vm*-mid may be calculated (although usually not at Station 1, but this same procedure will be used at stations). Some logic should therefore be employed to ensure that the result of applying Eq. (11.39) is plausible.

(9) The process moves on to the next station. Although Station 2 will usually be in an inlet duct, a general description applicable to all stations after the first will be given.

(10) If the station follows a blade-free space, total enthalpy, entropy and angular momentum are convected along streamlines from the previous station (these

may have to be computed following a solution at the previous station if Eq. (11.29) or (11.31) in rotating coordinates was used). Equation (11.29) will be applied whenever absolute angular momentum is given or implied by the user input data. Equation (11.39) will usually be used to determine total enthalpy from angular momentum, or vice versa. Entropy is determined from the efficiency or pressure loss, however expressed. In some cases, for example when a total pressure loss coefficient relative to the exit dynamic pressure is given, entropy can only be estimated because the loss depends upon the as-yet unknown velocity distribution. Then an initial estimate of meridional velocities on all streamlines is required; this can be made by assuming the values determined at the previous station. Note that this is done on the first pass through all stations only. There are numerous possible combinations of data. Total temperature, total enthalpy, total temperature or enthalpy change from the previous station, total pressure or pressure ratio from the previous station are some of the possibilities. In conjunction with these, various efficiencies or loss coefficients may be prescribed. For test data analysis, and following a rotor, total temperature and total pressure will be the inputs. A significant amount of programming logic is required to navigate the choices. Equation (11.31) will be applied when relative flow angle is given or implied. A design calculation might specify flow angle rather than angular momentum at a stator discharge station, where test data will normally be total pressure and flow angle. (If total temperature is also measured, there is a choice to be made between convecting the temperatures from the leading edge station, or abandoning them and imposing the newly measured values. Some care would then be required with the overall thermodynamics of the calculation). Relative flow angle will be implied by any off-design performance calculation when blade geometry is the input data. This will require the estimation of losses and discharge flow angles by a cascade performance prediction scheme. Depending upon the scheme selected, the losses and/or flow angles may be dependant upon the as-yet unknown meridional velocities, leading only to estimates. Equation (11.29) or (11.31) is integrated, as was done in Step 6. If any of the data required for Eq. (11.29) or (11.31) could only be estimated, an iterative loop should be performed to obtain a meridional velocity distribution that is consistent with the performance modeling, although once a few overall passes have been performed any discrepancy should become very small.

(11) The continuity equation is applied as in Steps 7 and 8, with control passing back to Step 10 until the specified flow is achieved (or all permitted iterations have been performed). The stream function on each streamline will be required later.

(12) Control passes repeatedly back to Step 9 until the last station has been processed.

(13) The overall convergence of the calculation is checked, unless this point has been reached at the completion of the first pass. The following two criteria should be applied:
(a) The stream functions along each streamline should be constant, and
(b) The meridional velocities computed at each mesh point should not change from one pass to the next.
If convergence has been achieved, the desired output data may be generated (tolerances are discussed bellow). If convergence has not been achieved, and subject to a maximum permitted number of passes, control is passed to Step 14.

(14) The estimated streamline pattern for the entire machine may now be updated, the intent being to have the stream functions established at Station 1 maintained throughout. A simple interpolation of the streamline coordinates at each computing station using the Station 1 stream functions provides the new, raw streamline coordinates. In order to ensure a stable, convergent procedure a relaxation factor must be applied to the coordinate changes that the interpolation provides. This is discussed further below.

(15) All streamwise gradients are updated.

(16) Control passes back to Step 3, to start another pass.

(17) The relaxation factor required when relocating the streamlines is:

$$RF = \frac{1}{1 + \frac{A}{6}\left(\frac{h}{\Delta m}\right)^2} \tag{11.41}$$

where $h/\Delta m$ is the ratio of the station length to the meridional distance to the closest adjacent station, $A = (1 - M_m^2)$ if tangential velocity component is given, and $A = \cos^2\beta\,(1 - M_m^2)$ if relative flow angle is given. Occasionally the constant shown as 6 in Eq.(11.41) needs setting to 4. Typically this occurs when many stations are placed relatively close together, for example when multiple stations are placed within blade-rows. Although not supported by theory, it seems reasonable to limit the Mach numbers to maximum values of perhaps 0.7. These equations are based on Wilkinson [9].

Nested iterative calculations are involved in the solution procedure, and appropriate tolerances to judge convergence of each loop are needed. A master

tolerance should be defined by the input data, and this can be used for the outermost loop, that is, the streamline location and meridional velocity convergence check. For normal engineering purposes, a tolerance of 1 or 2 parts in 10^4 is adequate and easily obtained. If the results are to be used in a gradient-based optimization scheme, it may be necessary to reduce the master tolerance to 1 part in 10^7 or less.

Tolerances should be reduced by a factor of 5 or 10 for each successive nesting level. Several additional calculations can be integrated in the above procedure. Bleed flows can be modeled by arranging that at the first station, the desired bleed flows be contained within the outermost streamtubes. One or more streamlines are then removed at appropriate stations along the flow path. Overall pressure ratio can be specified for off-design calculations by estimating the corresponding flow, and then refining the estimate as the solution proceeds. Logic is required to handle the various failure situations that may occur, for example, choking of the machine when the estimated flow is too large. Loss models may be incorporated so that when a converged solution is achieved it includes losses consistent with the derived flow, both for design and off-design calculations. During design calculations, blade geometry may also be simultaneously generated.

A major shortcoming of the basic streamline curvature method lies in its use of the Euler equations: no transfer of momentum or heat occurs in the transverse direction. This is in contrast to both real flows and CFD solutions of the Navier-Stokes equations. The result is that realistic span-wise variations of losses cannot be specified through multi-stage machines because extreme profiles of properties typically develop. This can be largely overcome by superimposing a "mixing" calculation upon the basic streamline curvature calculation. While there is evidence that some of the transverse effects, such as radial wake movement in axial compressors, are not random (Adkins and Smith [10]), a simple turbulent mixing calculation, as suggested in Gallimore [11], seems to capture most important effects. With this addition to the flow-model, off-design calculations can be performed that include realistic span-wise variations of losses, and which result in realistic profiles of properties.

A momentum equation of somewhat different form to Eq.(11.29) and (11.31) is shown in Smith [12] . Here the gradient of meridional velocity in the meridional direction is eliminated through use of the continuity equation and streamline characteristics. This is aesthetically pleasing (at least) as it removes a streamwise gradient from those that must be updated from pass to pass. Further, for cases with few stations, such as when there are stations at blade-row edges only, intuitively it seems that the local streamwise velocity gradient might be better estimated from the streamline pattern than from velocities at points beyond a blade-row. In a case with many stations within all blade-rows, the differences should be very small. As presented, Smith's equation is less useful because it is framed in the radial rather than an arbitrary direction.

11.2.2 Examples

In this section some representative examples of the use of a streamline curvature program are shown. A design is pursued that aims to meet the targets defined by the NASA UEET project (as of 2003) for a four-stage aero-engine HP-compressor with an overall pressure ratio of 12:1.

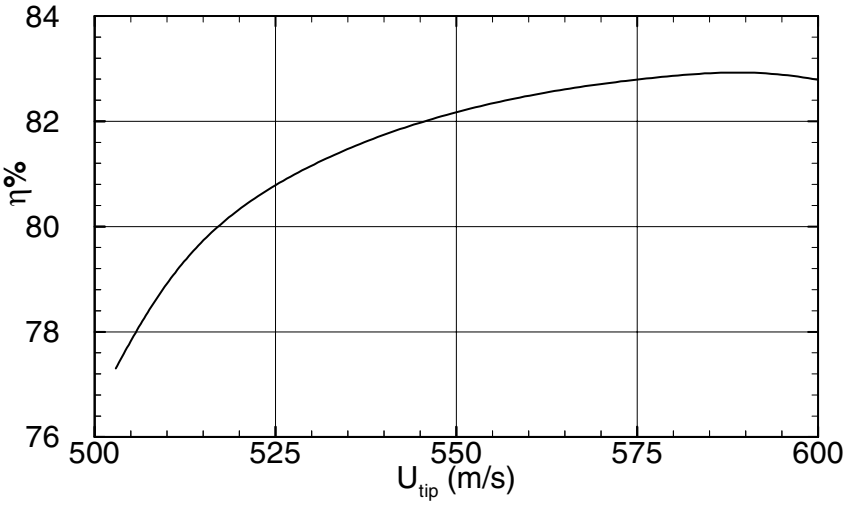

Fig. 11.3: Efficiency versus tip speed for NASA -UEET four stage compressor with pressure ratio 12:1

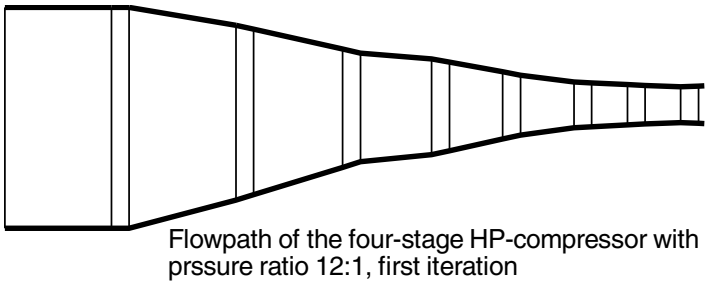

Fig. 11.4: Preliminary flow path of NASA -UEET four stage compressor.

The first calculations use the compressor preliminary design (CPD) procedure that is included in the program. In this mode of operation, streamline slope and curvature are assumed zero, and the blade forces acting in the station-wise direction are ignored. Radial stations are placed at each blade-row edge, so that a greatly simplified form of the momentum equation applies. These simplifications are made in order to stabilize and speed the solution. An optimizer package is used to derive the design of maximum efficiency that meets various constraints that the designer specifies. Figure 11.3 shows the resulting variation of design-point efficiency with first rotor tip speed. The optimum corrected tip of 589 m/sec results from the over-ambitious project goals. For the purposes of this rather academic exercise, a tip speed of 548 m/sec was selected as a possible compromise between mechanical and aerodynamic considerations. Figure 11.4 is the corresponding flow-path.

The next calculation made is a "first detail design". As for the CPD, total pressure is specified at rotor exits and tangential velocity component is specified at stator exits. Whereas for the CPD losses are estimated based solely on flow angles and Mach numbers, in the detail design blading, albeit generic, is derived by the design procedure. The flow model simplifications that were used for the CPD are

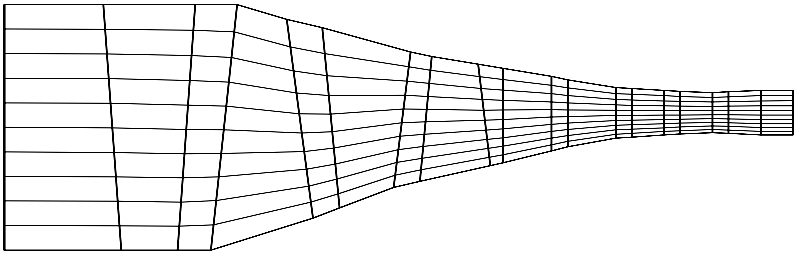

Fig. 11.5: Second iteration flow path of NASA UEET four-stage HP-compressor with pressure ration 12:1

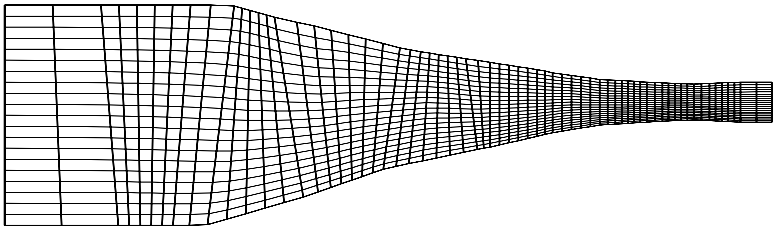

Fig. 11.6: Refined final flow path of NASA UEET four-stage HP-compressor with pressure ration 12:1

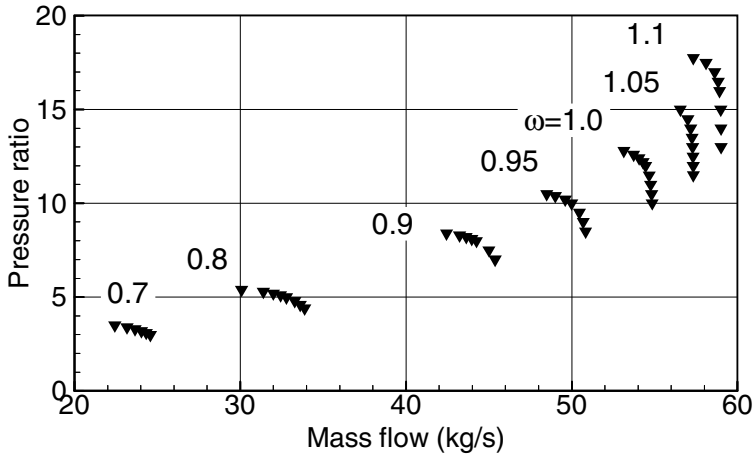

Fig. 11.7: Performance map of NASA UEET four-stage HP-compressor

removed. Figure 11.5 shows the computed streamline pattern. The first detail design assumed generic blading (DCA profiles), but with a first rotor tip Mach number approaching 1.5, a more sophisticated design is required.
This is accomplished by adding stations within the blade-rows, and then distributing the effects of the blade-rows amongst the station-to-station intervals. Figure 11.6

Fig. 11.8: Solid model of two adjacent blades.

shows the streamline pattern that is computed. Given the blading specification that the calculation created, an off-design calculation can now be performed; Figure 11.7 shows the resulting performance map. Figure 11.8 shows a solid-model of two adjacent blades, looking from downstream. The procedure described may be used to produce a final design, although nowadays it will generally be used to create a "first candidate" for further analysis using CFD.

11.3 Special Cases

The radial equilibrium calculation method derived in section 11.2 was applied to design compressor stages using numerical procedures. The method is also applicable to turbine stages. For few special cases analytical solutions can be found. For this purpose, simplifications are necessary to achieve analytical solutions.

11.3.1 Free Vortex Flow

The flow under consideration is assumed to fulfill the conditions: isentropic: $\nabla s = 0$, isoenergetic: $\nabla H = 0$, and constant meridional velocity, $dV_m = 0$. With these conditions and the assumption that the streamlines have no curvature, (cylindrical stream surfaces), Eq.(11.11) reduces for a bladeless channel, where $F_m = F_n = o$, and $(\phi - \gamma) = 0$, to:

$$d\left(rV_u\right) = 0,\ rV_u = \text{const.} \tag{11.45}$$

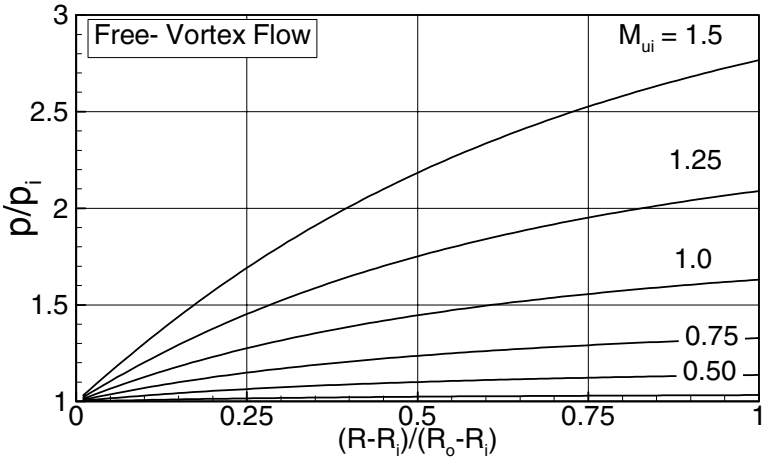

Fig. 11.9: Radial pressure distribution of a free-vortex flow with the hub circumferential Mach number M_u as parameter.

Eq.(11.45) is the radial equilibrium equation for a free vortex flow, called Beltrami free vortex flow. Figure11.9 shows the radial pressure distribution within an annular channel for different circumferential Mach number.

11.3.2 Forced vortex flow

This type of flow is assumed to satisfy the following conditions: isentropic, $\nabla s = 0$ isoenergetic, $\nabla H = 0$, and circumferential velocity is proportional to the radius: $V_u \propto r$ *or* $V_u = K$ r, where K is a constant.
With these conditions and the assumption that the streamlines have no curvature, (cylindrical stream surface), Eq.(11.11) reduces for a bladeless channel, where $F_m = F_n = o$, and $(\phi - \gamma) = 0$, to:

$$V_m \frac{dV_m}{dr} = - \frac{Krd(Kr^2)}{rdr} = -2K^2 \frac{rdr}{dr} \tag{11.46}$$

Integration of Eq.(11.46) gives:

$$V_m^2 = 2K^2\left(r_i^2 - r^2\right) + V_{mi}^2 \tag{11.47}$$

The constant K is:

$$K = \frac{V_u}{r} = \frac{V_{ui}}{r_i} \tag{11.48}$$

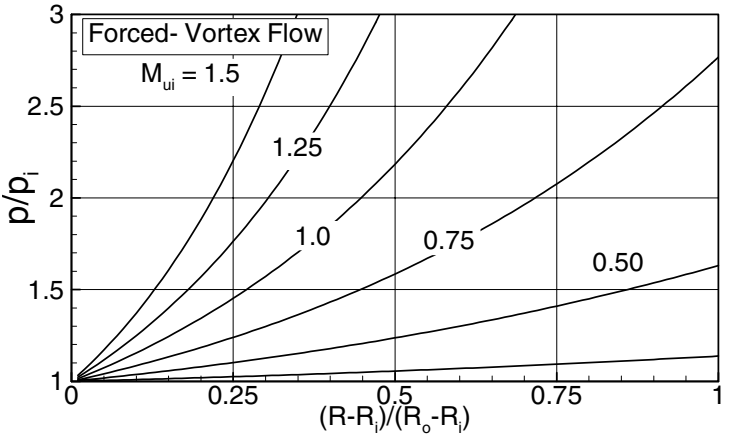

Fig. 11.10: Pressure distribution of a forced-vortex flow with the hub circumferential Mach number M_u as parameter.

Using the angle definition in Fig. 11.3, where β is replaced by α and $V_{ui} = V_{mi} tg\alpha_i$ and introducing Eq.(11.48) into (11.47) gives:

$$\left[\frac{V_m}{V_{mi}}\right]^2 = 1 - 2tg^2\alpha_i\left[\left(\frac{r}{r_i}\right)^2 - 1\right] \tag{11.49}$$

Figure 11.10 shows the radial distribution of meridional velocity ratio.

11.3.3 Flow with Constant Flow Angle

The flow under consideration is assumed to fulfill the conditions: isentropic, $\nabla s = 0$ isoenergetic, $\nabla H = 0$, and constant inlet flow angle, $d\alpha_1 = 0$. With these conditions and the assumption that the streamlines have no curvature, (cylindrical stream surface), Eq.(11.11) then reduces for a bladeless channel, where $F_m = F_n = o$, and $(\phi - \gamma) = 0$, to:

$$V_m \frac{dV_m}{dr} = -\frac{V_u}{r}\frac{d(rV_u)}{dr} \tag{11.50}$$

Since

$$V_u = V_m tg\alpha_1 \tag{11.51}$$

introducing Eq.(11.50) into (11.51) leads to:

$$\frac{dV_m}{V_m} = -\sin^2\alpha_1 \frac{dr}{r} \tag{11.52}$$

Integrating Eq.(11.52) gives:

$$\frac{V_m}{V_{mi}} = \left(\frac{r_i}{r}\right)^{\sin^2\alpha_1} \tag{11.53}$$

Figure 11.11 depicts the axial velocity ratio as a function of the radius ratio with α_1 as parameter.

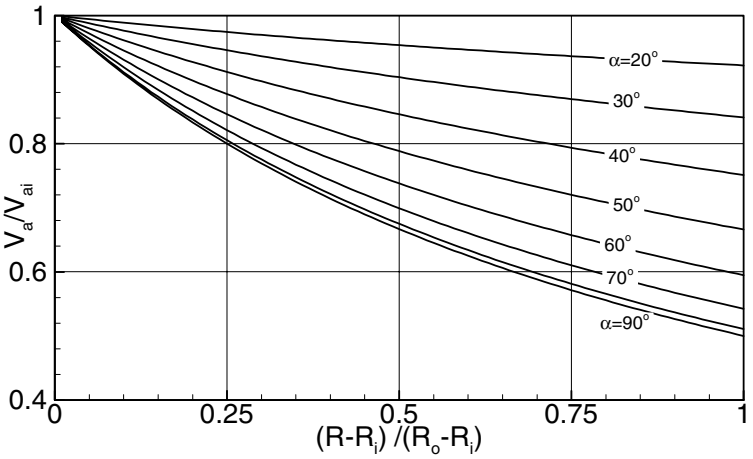

Fig. 11.11: Axial velocity ratio as a function of dimensionless blade height with the inlet angle as parameter.

References, Chapter 11

11.1 Wu, Chung-Hua, 1952, "A general Theory of Three-Dimensional Flow in Subsonic and Supersonic Turbomachines of Axial-, Radial, and mixed-Flow Types,"NACA technical Note 2604, Washington, D.C., January 1952.

11.2 Lakshminarayana, B., 1996, "Fluid Dynamics and Heat Transfer of Turbomachinery," John Wiley & Sons.

11.3 Vavra, M.H., 1960, "Aero-Thermodynamics and Flow in Turbomachines," John Wiley & Sons, Inc.

11.4 Novak, R. A., and Hearsey, R. M., " A Nearly Three Dimensional Intra blade Computing System for Turbomachinery, Part I & II," *Journal of Fluid Engineering*, Vol 99, pp. 154-166.

11.5 Wilkinson, D.H., 1972, "Calculation of Blade-to-Blade Flow in Turbomachine by Streamline Curvature," British ARC R&M 3704.

11.6 Wennerstrom, A. J., 1974, "On the Treatment of body Forces in the radial Equilibrium Equation of Turbomachinery," Traupel-Festschrift, Juris-Verlag, Zürich.

11.7 Hearsey, R. M., 2003, "Computer Program HT 0300 version 2.0," Hearsey technology, Bellevue, Washington

11.8 Horlock, J.H., 1971, "On Entropy Production in Adiabatic Flow in Turbomachines," *ASME Journal of Basic Engineering*, pp. 587-593.

11.9 Wilkinson, D.H., 1969, Stability, Convergence and Accuracy of 2-Dimensional Streamline Curvature Methods Using Quasi-Orthogonals, Proceedings of the Institution of Mechanical Engineers, Volume 184, 1979-1970.

11.10 Adkins, G. G., Smith L. H., 1982, "Spanwise Mixing in Axial-Flow Turbomachines," *ASME Journal of Engineering for Gas Turbines and Power*, Vol. 104, pp. 97-110.

11.11 Gallimore, S.J., 1986, "Spanwise mixing in Multistage Axial Flow Compressors: Part II – Throughflow Calculations Including Mixing," ASME Journal of Turbomachinery, Vol. 108, pp. 10-16.

11.12 Smith, L.H. Jr., 1966, "The Radial-Equilibrium Equation of Turbomachinery," *ASME Journal of Engineering for Power*, January, 1966, pp. 1-12.

12 Nonlinear Dynamic Simulation of Turbomachinery Components and Systems

The following chapters deal with the nonlinear transient simulation of turbomachinery systems. Power generation steam and gas turbine engines, combined cycle systems, aero gas turbine engines ranging from single spool engines to multi-spool high pressure core engines with an afterburner for supersonic flights, rocket propulsion systems and compression systems for transport of natural gas with a network of pipeline systems are a few examples of systems that heavily involve turbomachinery components.

Considering a power generation gas turbine engine as a turbomachinery system that is designed for steady state operation, its behavior during routine startups, shot downs, and operational load changes significantly deviates from the steady state design point. Aero gas turbine engines have to cover a relatively broad operational envelope that includes takeoff, low and high altitude operation conditions, as well as landing. During these operations, the components are in a continuous dynamic interaction with each other, where the aero-thermodynamic as well as the mechanical load conditions undergo temporal changes. As an example, the acceleration/deceleration process causes a dynamic mismatch between the turbine and compressor power resulting in temporal change of the shaft speed.

In the above cases, the turbomachinery systems are subjected to the operating modes that are specific to the system operation. Besides these foreseeable events, there are unforeseeable operation scenarios that are not accounted for when designing the system. System failures, such as, blade loss during a routine operation, loss of cooling mass flow through the cooled turbine blades, adverse operation conditions that force the compressor component to surge, and failure of the control system, are a few examples of adverse operational conditions. In all of these operations, the system experiences adverse changes in total fluid and thermodynamic process leading to greater aerodynamic, thermal and mechanical stress conditions.

The trend in the development of gas turbine technology during the past decades shows a continuous increase in efficiency, performance, and specific load capacities. This trend is inherently associated with increased aerodynamic, thermal, and mechanical stresses. Under this circumstance, each component operates in the vicinity of its aerodynamic, thermal and mechanical stress limits. Adverse operational conditions that cause a component to operate beyond its limits can cause structural

damages as a result of increased aerodynamic, thermal, and structural stresses. To prevent this, the total response of the system, including aerodynamic, thermal, and mechanical responses, must be known in the stage of design and development of new turbomachinery systems.

This chapter describes the physical basis for the non-linear dynamic simulation of gas turbine components and systems. A brief explanation of the numerical method for solution is followed by detailed dynamic simulation of several components described in the following chapters.

12.1 Theoretical Background

Dynamic behavior of turbomachinery components and systems can generally be described by conservation laws of fluid mechanics and thermodynamics ([1], [2], [3], [4]. The fluid dynamic process that takes place within an inertial system is, as a rule, unsteady. The steady state, a special case, always originates from an unsteady condition during which the temporal changes in the process parameters have largely come to a standstill. The following accounts this fact by formulation of the fluid and thermodynamic conservation laws in a 4-dimensional temporal-spatial coordinate system. For this purpose the conservation laws we discussed in Chapter 3 must be rearranged such that temporal changes of thermo-fluid dynamic quantities are expressed in terms of spatial changes. A summary of relevant equations are found in [5]. For an unsteady flow, the conservation of mass derived in Chapter 3, Eq. (3.4), is called upon:

$$\frac{\partial \rho}{\partial t} = -\nabla \cdot (\rho \boldsymbol{V}) \tag{12.1}$$

Equation (12.1) expresses the *temporal change* of the density in terms of *spatial change* of the specific mass flow. Neglecting the gravitational force, the Cauchy equation of motion (3.22) was derived as:

$$\frac{\partial \boldsymbol{V}}{\partial t} + \boldsymbol{V} \cdot \nabla \boldsymbol{V} = \frac{1}{\rho} \nabla \cdot \boldsymbol{\Pi} \tag{12.2}$$

We rearranging Eq. (12.2) to include the density in the temporal and spatial derivatives

$$\frac{\partial (\rho \boldsymbol{V})}{\partial t} + \nabla \cdot (\rho \boldsymbol{V} \boldsymbol{V}) = \nabla \cdot \boldsymbol{\Pi} \tag{12.3}$$

where the stress tensor $\boldsymbol{\Pi}$ can be decomposed into the pressure and shear stress tensor as follows:

$$\Pi = \boldsymbol{I}p + \boldsymbol{T} \tag{12.4}$$

with $\boldsymbol{I}p$ as the normal stress and $\boldsymbol{\Pi}$ as the shear stress tensor. Inserting Eq. (12.4) into (12.3) results in

$$\frac{\partial(\rho \boldsymbol{V})}{\partial t} + \nabla \cdot (\rho \boldsymbol{V}\boldsymbol{V}) = -\nabla p + \nabla \cdot \boldsymbol{T} \tag{12.5}$$

Equation (12.5) directly relates the temporal changes of the specific mass flow to the spatial changes of the velocity, pressure, and shear stresses. For the complete description of the unsteady flow process, the total energy equation that includes mechanical and thermal energy balance is needed. Referring to Eq. (3.58) and neglecting the gravitational contribution, we find for mechanical energy that:

$$\rho \frac{D}{Dt}\left(\frac{V^2}{2}\right) = -\boldsymbol{V} \cdot \nabla p + \nabla \cdot (\boldsymbol{T} \cdot \boldsymbol{V}) - \boldsymbol{T} : \boldsymbol{D} \tag{12.6}$$

Equation (12.6) exhibits the mechanical energy balance in differential form. The first term on the right-hand side represents the mechanical energy contribution due to the pressure gradient. The second term is the contribution of the shear stress work. The third term represents the production of the irreversible mechanical energy due to the shear stress. It dissipates as heat and increases the internal energy of the system. Before rearranging Eq. (12.6) and performing the material differentiation, we revert to the thermal energy balance, Eq. (3.66),

$$\rho \frac{Du}{Dt} = -\nabla \cdot \dot{\boldsymbol{q}} - p \nabla \cdot \boldsymbol{V} + \boldsymbol{T} : \boldsymbol{D} \tag{12.7}$$

The combination of the mechanical and thermal energy balances, Eq. (12.6) and (12.7), results in:

$$\rho \frac{D}{Dt}\left(u + \frac{V^2}{2}\right) = -\nabla \cdot \dot{\boldsymbol{q}} + \nabla \cdot (\Pi \cdot \boldsymbol{V}) \tag{12.8}$$

Since all components of a turbomachinery system are considered open systems, it is appropriate to use enthalpy h rather than internal energy u. The state properties h and u can be expressed as a function of other state properties such as T, v, p etc.

$$u = u(T,v),\ du = \left(\frac{\partial u}{\partial T}\right)_v dT + \left(\frac{\partial u}{\partial v}\right)_T dv \tag{12.9}$$

$$h = h(T,p),\ dh = \left(\frac{\partial h}{\partial T}\right)_p dT + \left(\frac{\partial h}{\partial p}\right)_T dp \tag{12.10}$$

where T and h are the absolute static temperature and enthalpy. With the definitions:

$$c_v = \left(\frac{\partial u}{\partial T}\right)_v,\ c_p = \left(\frac{\partial h}{\partial T}\right)_p \tag{12.11}$$

and the application of the first law, the following relation between c_p and c_v is established:

$$c_p = c_v + \left[\left(\frac{\partial u}{\partial v}\right)_T + p\right]\left(\frac{\partial v}{\partial T}\right)_p \tag{12.12}$$

For the open cycle gas turbines and also jet engines with moderate pressure ratios, the working fluids air and combustion gases behave practically like ideal gases whose internal energy is only a function of temperature and not volume. This circumstance considerably simplifies the interconnection of different thermodynamic properties if the equation of state of ideal gases is considered:

$$pv = RT \tag{12.13}$$

Introducing the Gibbs's enthalpy function:

$$h = u + pv \tag{12.14}$$

the differentiation gives:

$$dh = \frac{\kappa}{\kappa - 1} d(pv) \text{ and } dh = \kappa du \tag{12.15}$$

with

$$c_p - c_v = R \quad \text{and} \quad \frac{c_p}{c_v} = \kappa \tag{12.16}$$

As a consequence, for ideal gases, the result of this operation leads to:

$$\left(\frac{\partial v}{\partial T}\right)_p = \frac{R}{p} \tag{12.17}$$

Thus, the state properties, u and h, as well as the specific heat capacities c_p, and c_v and their ratio κ are solely functions of temperature. This is also valid for combustion gases with approximately ideal behavior. For combustion gases, there is a parametric dependency of the above stated properties and the fuel-air ratio. After this preparation, Eq. (12.7) can be written in terms of h and p:

$$\rho \frac{Dh}{Dt} = -\nabla \cdot \dot{\boldsymbol{q}} + \frac{Dp}{Dt} + \boldsymbol{T}:\boldsymbol{D} \tag{12.18}$$

with Eq. (12.15) and considering the continuity equation (12.1), the substantial change of the static pressure is:

$$\frac{Dp}{Dt} = \frac{\kappa - 1}{\kappa} \rho \frac{Dh}{Dt} - p \nabla \cdot \boldsymbol{V} \tag{12.19}$$

Introducing Eq. (12.19) into (12.18):

$$\frac{\rho}{\kappa} \frac{Dh}{Dt} = -\nabla \dot{\boldsymbol{q}} - p \nabla \cdot \boldsymbol{V} + \boldsymbol{T}:\boldsymbol{D} \tag{12.20}$$

The combination of thermal energy equation (12.20) and mechanical energy equation (12.6) leads to:

$$\begin{aligned} \frac{\partial H}{\partial t} = -k\boldsymbol{V} \cdot \nabla H - (\kappa - 1)\left(\frac{1}{\rho} \nabla \cdot (\rho \boldsymbol{V})(H + K) + \frac{\boldsymbol{V} \cdot \partial(\rho \boldsymbol{V})}{\rho \partial t} \right) \\ + \left(-\frac{\kappa \nabla \cdot \boldsymbol{q}}{\rho} + \frac{\kappa}{\rho} \nabla \cdot (\boldsymbol{V} \cdot \boldsymbol{T}) \right) \end{aligned} \tag{12.21}$$

with $H = h + V^2/2$ as the total enthalpy and $K = V^2/2$ the kinetic energy. Equation (12.21) can also be obtained by introducing the relationship between the pressure and enthalpy into Eq.(12.21). The total enthalpy can be expressed in terms of total temperature:

$$c_p \frac{\partial T^*}{\partial t} = -k\boldsymbol{V}\cdot\nabla\left(c_p T^*\right) - (\kappa - 1)\left(\frac{1}{\rho}\nabla\cdot(\rho\boldsymbol{V})\left(c_p T^* + K\right) + \frac{\boldsymbol{V}\cdot\partial(\rho\boldsymbol{V})}{\rho\partial t}\right) + \left(-\frac{\kappa\nabla\cdot\dot{\boldsymbol{q}}}{\rho} + \frac{\kappa}{\rho}\nabla\cdot(\boldsymbol{V}\cdot\boldsymbol{T})\right) \tag{12.22}$$

Finally, the total energy equation in terms of total pressure can be established by inserting Eqs. (12.14) and (12.16) into Eq. (12.8):

$$\frac{\partial P}{\partial t} = -k\nabla\cdot(\boldsymbol{V}P) + (\kappa - 1)[-\nabla\cdot(\dot{\boldsymbol{q}}) + \nabla\cdot(\boldsymbol{V}\cdot T)] - (\kappa - 2)\left[\frac{\partial(\rho K)}{\partial t} + \nabla\cdot(\rho K\boldsymbol{V})\right] + \rho\boldsymbol{g}\cdot\boldsymbol{V} \tag{12.23}$$

where $P = p + \rho V^2/2$ is the total pressure. Equations (12.2), (12.22) and (12.23) express the same physical principles, namely the law of conservation of energy in two different forms. In physical terms, they are fully equivalent and mathematically convertible to each other. As shown in the following chapters, one or the other of these equations is called upon in conjunction with the other laws to deal with various dynamic problems. For example, in dealing with an unsteady exchange of energy and impulse, it is useful to apply the differential equation for total temperature. If the principal goal of a problem is the determination of the unsteady changes in pressure, the total pressure differential equation should be used. A summary of the working equations is given in Table 12.1.

Table 12.1: Summary of thermo-fluid dynamic equations.

Equations In terms of substantial derivatives D/Dt	Eq.No.
Continuity $\frac{D\rho}{Dt} = -\rho\nabla\cdot\boldsymbol{V}$	(3.4) (12.1)
Motion $\rho\frac{D\boldsymbol{V}}{Dt} = \nabla\cdot\boldsymbol{\Pi} + gz$	(3.22) (12.2)
Mechanical Energy $\rho\frac{D}{Dt}\left(\frac{V^2}{2}\right) = -\boldsymbol{V}\cdot\nabla p + \nabla\cdot(\boldsymbol{T}\cdot\boldsymbol{V}) - \boldsymbol{T}:\boldsymbol{D} + \rho\boldsymbol{V}\cdot\boldsymbol{g}$	(3.58) (12.6)

Equations in terms of substantial and local derivatives D/Dt, $\partial/\partial t$	Eq. No.
Equation of thermal energy in terms of u $\rho\frac{Du}{Dt} = -\nabla\cdot\dot{\boldsymbol{q}} - p\nabla\cdot\boldsymbol{V} + \boldsymbol{T}:\boldsymbol{D}$	(3.66) (12.7)
Equation of thermal energy in terms of h for ideal gas $\rho\frac{Dh}{Dt} = -\nabla\cdot\dot{\boldsymbol{q}} + \frac{Dp}{Dt} + \boldsymbol{T}:\boldsymbol{D}$	(12.18)
Equation of total enthalpy $\rho\frac{DH}{Dt} = \rho\frac{D}{Dt}(h + \frac{V^2}{2}) = \frac{\partial p}{\partial t} + -\nabla\cdot\dot{\boldsymbol{q}} + \nabla\cdot(\boldsymbol{T}\cdot\boldsymbol{V}) + \rho\boldsymbol{V}\cdot\boldsymbol{g}$	(3.73) (12.21)
Equation of thermal energy in terms of c_v and T for ideal gas $\rho c_v\frac{DT}{Dt} = -\nabla\cdot\dot{\boldsymbol{q}} - p\nabla\cdot\boldsymbol{V} + \boldsymbol{T}:\boldsymbol{D}$	(3.66) (12.7)
Equation of thermal energy in terms of c_p and T for ideal gas $\rho c_p\frac{DT}{Dt} = -\nabla\cdot\dot{\boldsymbol{q}} + \frac{Dp}{Dt} + \boldsymbol{T}:\boldsymbol{D}$	(12.7)
Equation of continuity $\frac{\partial\rho}{\partial t} = -\nabla\cdot(\rho\boldsymbol{V})$	(3.4) (12.1)
Equation of motion in terms of total stress tensor $\frac{\partial(\rho\boldsymbol{V})}{\partial t} + \nabla\cdot(\rho\boldsymbol{V}\boldsymbol{V}) = \nabla\cdot\Pi$	(3.22) (12.2)
Equation of motion, stress tensor decomposed $\frac{\partial(\rho\boldsymbol{V})}{\partial t} + \nabla\cdot(\rho\boldsymbol{V}\boldsymbol{V}) = -\nabla p + \nabla\cdot\boldsymbol{T}$	(12.5)
Equation of mechanical energy including ρ $\frac{\partial(\rho K)}{\partial t} = -\nabla\cdot(\rho K\boldsymbol{V}) - V\cdot\nabla p + \nabla\cdot(\boldsymbol{T}\cdot\boldsymbol{V}) + \rho\boldsymbol{V}\cdot\boldsymbol{g}$	(3.58) (12.6)
Equation of thermal energy in terms of u for ideal gas $\frac{\partial(\rho u)}{\partial t} = -\nabla\cdot(\rho u\boldsymbol{V}) - \nabla\dot{\boldsymbol{q}} - p\nabla\cdot\boldsymbol{V} + \boldsymbol{T}:\nabla\boldsymbol{V}$	(12.7) Re- arranged

Equations in terms of local derivatives $\partial/\partial t$	Eq. No.
Equation of thermal energy in terms of h for ideal gas $\frac{\partial(\rho h)}{\partial t} = -\nabla\cdot(\rho h \boldsymbol{V}) - \nabla\dot{\boldsymbol{q}} + \frac{Dp}{Dt} + \boldsymbol{T}:\nabla\boldsymbol{V}$	(12.7) Rearranged
Equation of thermal energy in terms of c_v and T $\frac{\partial(\rho c_v T)}{\partial t} = -\nabla\cdot(\rho u \boldsymbol{V}) - \nabla\dot{\boldsymbol{q}} - p\nabla\cdot\boldsymbol{V} + \boldsymbol{T}:\nabla\boldsymbol{V}$	(12.7) Re-arranged
Equation of thermal energy in terms of static h for ideal gases $\frac{\partial(\rho c_p T)}{\partial t} = -\nabla\cdot(\rho h \boldsymbol{V}) - \nabla\dot{\boldsymbol{q}} + \frac{Dp}{Dt} + \boldsymbol{T}:\nabla\boldsymbol{V}$	(12.7) Re-arranged
Energy equation in terms of total enthalpy $\frac{\partial H}{\partial t} = -k\boldsymbol{V}\cdot\nabla H - (\kappa - 1)\left(\frac{1}{\rho}\nabla\cdot(\rho\boldsymbol{V})(H + K) + \frac{\boldsymbol{V}\cdot\partial(\rho\boldsymbol{V})}{\rho\partial t}\right) + \left(-\frac{\kappa\nabla\cdot\boldsymbol{q}}{\rho} + \frac{\kappa}{\rho}\nabla\cdot(\boldsymbol{V}\cdot\boldsymbol{T})\right)$	(12.21)
Energy equation in terms of total temperature $c_p\frac{\partial T_0}{\partial t} = -k\boldsymbol{V}\cdot\nabla\left(c_p T_0\right) - (\kappa-1)\left(\frac{1}{\rho}\nabla\cdot(\rho\boldsymbol{V})\left(c_p T_0 + K\right) + \frac{\boldsymbol{V}\cdot\partial(\rho\boldsymbol{V})}{\rho\partial t}\right) - \left(\frac{\kappa\nabla\cdot\dot{\boldsymbol{q}}}{\rho} - \frac{\kappa}{\rho}\nabla\cdot(\boldsymbol{V}\cdot\boldsymbol{T})\right)$	(12.22)
Energy equation in terms of total pressure $\frac{\partial P}{\partial t} = -k\nabla\cdot(\boldsymbol{V}P) - (\kappa - 1)\left[\nabla\cdot\dot{\boldsymbol{q}} + \nabla\cdot(\boldsymbol{V}\cdot T)\right] - (\kappa - 2)\left[\frac{\partial(\rho K)}{\partial t} + \nabla\cdot\left(\rho K\boldsymbol{V}\right)\right]$	(12.23)

12.2 Preparation for Numerical Treatment

The thermo-fluid dynamic equations discussed above constitute the theoretical basis describing the dynamic process that takes place within a turbomachinery component

during a transient operation. A four-dimensional time space treatment that involves the Navier solution is, at least for the time being, out of reach. For simulation of dynamic behavior of a turbomachine that consists of many components, it is not primarily important to calculate the unsteady three-dimensional flow processes in great detail. However, it is critical to accurately predict the response of each individual component as a result of dynamic operation conditions. A one-dimensional time dependent calculation procedure provides sufficiently accurate results. In the following, the conservation equations are presented in index notation. For the one-dimensional time dependent treatment, the basic equations are prepared first by setting the index $i = 1$ in Eqs. (12.24-12.27).

12.3 One-Dimensional Approximation

The thermo-fluid dynamic equations discussed above constitute the theoretical basis describing the dynamic process that takes place within a turbomachinery component during a transient operation. A four-dimensional time space treatment that involves Navier solution is, at least for the time being, out of reach. For simulation of the dynamic behavior of a turbomachine that consists of many components, it is not primarily important to calculate the unsteady three-dimensional flow processes in great detail. However, it is critical to accurately predict the response of each individual component as a result of dynamic operation conditions. A one-dimensional time dependent calculation procedure provides sufficiently accurate results. For this purpose, firstly the basic equations are prepared for the one-dimensional treatment.

12.3.1 Time Dependent Equation of Continuity

In Cartesian coordinate system the continuity equation (12.1) is:

$$\frac{\partial \rho}{\partial t} = - \frac{\partial}{\partial x_i} \left(\rho V_i \right) \tag{12.24}$$

Equation (12.24) after setting $\rho V_1 = \dot{m}/S$ becomes:

$$\frac{\partial \rho}{\partial t} = - \frac{\partial}{\partial x_1} \left(\frac{\dot{m}}{S} \right) \tag{12.25}$$

with x_1 as the length in streamwise direction and $S = S(x)$ the cross sectional area of the component under investigation. Equation (12.25) expresses the fact that the temporal change of the density is determined from the spatial change of the specific mass flow within a component. The partial differential Eq. (12.25) can be approximated as an ordinary differential equation by means of conversion into a difference equation. The ordinary differential equation can then be solved numerically

with the prescribed initial and boundary conditions. For this purpose, the flow field is equidistantly divided into a number of discrete zones with prescribed length, ΔX, inlet and exit cross sections S_i and S_{i+1} as Fig. 12.1 shows.

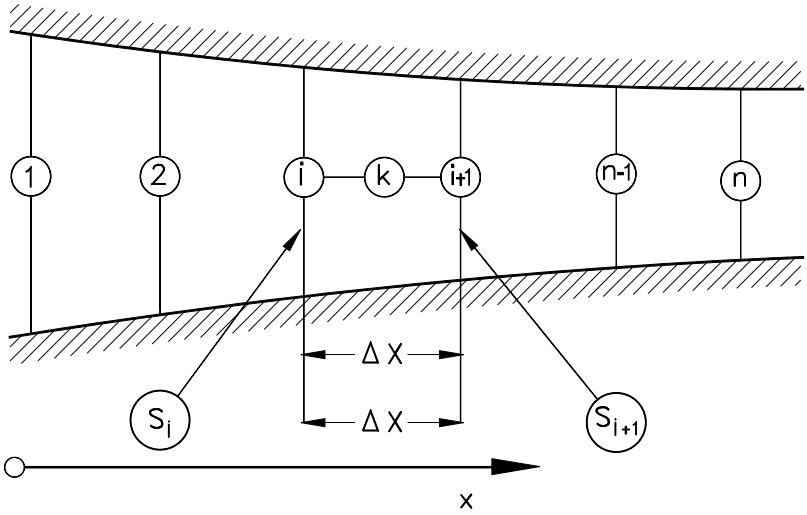

Fig. 12.1: Discretization of an arbitrary flow path with changing cross section $S = S(x)$.

Using the nomenclature in Fig. 12.1, Eq. (12.25) is approximated as:

$$\frac{\partial \rho_k}{\partial t} = -\frac{1}{\Delta x}\left(\frac{\dot{m}_{i+1}}{S_{i+1}} - \frac{\dot{m}_i}{S_i}\right) \tag{12.26}$$

with $\dot{m}_i$ and $\dot{m}_{i+1}$ as the mass flows at stations i and $i+1$ with the corresponding cross sections. For a constant cross section, Eq.(12.26) reduces to:

$$\frac{\partial \rho_k}{\partial t} = -\frac{1}{\Delta x S}\left(\dot{m}_{i+1} - \dot{m}_i\right) = -\frac{1}{\Delta V}\left(\dot{m}_{i+1} - \dot{m}_i\right) \tag{12.27}$$

with ΔV as the volume of the element. The index k refers to the position at $\Delta x/2$, Fig. 12.1

12.3.2 Time Dependent Equation of Motion

The index notation of the momentum equation (12.5) is:

$$\frac{\partial(\rho V_i)}{\partial t} = -\frac{\partial}{\partial x_j}\left(\rho V_i V_j\right) - \frac{\partial p}{\partial x_i} + \frac{\partial T_{ij}}{\partial x_j} \tag{12.28}$$

In the divergence of the shear stress tensor in Eq. (12.28), $\nabla \cdot \boldsymbol{T} = e_i \partial T_{ij}/\partial x_j$ represents the shear force acting on the surface of the component. For a one-dimensional flow, the only non-zero term is $\partial \tau_{21}/\partial x_2$. It can be related to the wall shear stress τ_w which is a function of the friction coefficient c_f.

$$\tau_w = c_f \frac{\rho}{2} V^2 \tag{12.29}$$

In the near of the wall, the change of the shear stress can be approximated as the difference between the wall shear stress $\tau_W$and the shear stress at the edge of the boundary layer, which can be set as $\tau_e \approx 0$

$$\left(\frac{\partial \tau_{12}}{\partial x_2}\right)_{x_2=0} = \frac{\tau_e - \tau_w}{\Delta x_2} = -\frac{\tau_w}{\Delta x_2} \tag{12.30}$$

The distance in Δx_2 can be replaced by a characteristic length such as the hydraulic diameter D_h. Expressing the wall shear stress in Eq. (12.30) by the skin friction coefficient

$$\left(\frac{\partial \tau_{12}}{\partial x_2}\right)_{x_2=0} = -c_f \frac{\rho}{D_h}\frac{V^2}{2} = -c_f \frac{\dot{m}^2}{2 D_h \rho S^2} \tag{12.31}$$

and inserting Eq. (12.31) into the one-dimensional version of Eq. (12.28), we obtain

$$\frac{\partial \dot{m}}{\partial t} = -\frac{\partial}{\partial x_1}(\dot{m} V_1 + pS) + (\dot{m} V_1 + pS)\frac{1}{S}\frac{\partial S}{\partial x_1} - c_f \frac{\dot{m}^2}{2 D_h \rho S} \tag{12.32}$$

Equation (12.32) relates the temporal change of the mass flow to the spatial change of the velocity, pressure and shear stress momentums. As we will see in the following sections, mass flow transients can be accurately determined using Eq. (12.32). Using the nomenclature from Fig. 12.1, we approximate Eq. (12.32) as:

$$\frac{\partial \dot{m}_k}{\partial t} = -\frac{1}{\Delta x}\left(\dot{m}_{i+1}V_{i+1} - \dot{m}_i V_i + p_{i+1}S_{i+1} - p_i S_i\right) + \left(\frac{\dot{m}_k V_k + P_k S_k}{S_k}\right)\left(\frac{S_{i+1} - S_i}{\Delta x}\right) - c_f \frac{\dot{m}_k^2}{2\, D_{h_k}\rho_k S_k} \tag{12.33}$$

For a constant cross section, Eq. (12.33) is modified as:

$$\frac{\partial \dot{m}_k}{\partial t} = -\frac{1}{\Delta x}\left[\dot{m}_{i+1}V_{i+1} - \dot{m}_i V_i + (p_{i+1} - p_i)S\right] - c_f \frac{\dot{m}_k^2}{2\, D_{h_k}\rho_k S_k} \tag{12.34}$$

12.3.3 Time Dependent Equation of Total Energy

The energy equation in (12.21), in terms of total enthalpy, is written in index notation

$$\frac{\partial H}{\partial t} = -kV_i\frac{\partial H}{\partial x_i} - \frac{\kappa - 1}{\rho}\left[(H + K)\frac{\partial(\rho V_i)}{\partial x_i} + \frac{V_i \cdot \partial(\rho V_i)}{\partial t}\right] - \frac{\kappa}{\rho}\left[\frac{\partial \dot{q}_i}{\partial x_i} - \frac{\partial(V_j T_{ij})}{\partial x_i}\right] \tag{12.35}$$

expressing the total enthalpy, Eqs. (12.35), in terms of total temperature results in:

$$\frac{\partial(c_p T_0)}{\partial t} = -kV_i\frac{\partial(c_p T_0)}{\partial x_i} - \frac{\kappa - 1}{\rho}\left[\left(c_p T_0 + K\right)\frac{\partial(\rho V_i)}{\partial x_i} + \frac{V_i \cdot \partial(\rho V_i)}{\partial t}\right] - \frac{\kappa}{\rho}\left[\frac{\partial \dot{q}_i}{\partial x_i} - \frac{\partial(V_j T_{ij})}{\partial x_i}\right] \tag{12.36}$$

For calculating the total pressure, the equation of total energy is written in terms of total pressure already derived as Eq. (12.23) which is presented for the Cartesian coordinate system as:

$$\frac{\partial P}{\partial t} = -\kappa\frac{\partial}{\partial x_i}\left(PV_i\right) - (\kappa - 1)\left(\frac{\partial \dot{q}_i}{\partial x_i} - \frac{\partial}{\partial x_i}\left(V_j T_{ij}\right)\right) - (\kappa - 2)\left(\frac{\partial\left(\rho K V_i\right)}{\partial x_i} + \frac{\partial(\rho K)}{\partial t}\right) \tag{12.37}$$

Before treating the energy equation, the shear stress work needs to be evaluated:

$$\nabla\cdot\left(\boldsymbol{T}\cdot\boldsymbol{V}\right) = \delta_{ij}\delta_{km}\frac{\partial(\tau_{jk}V_m)}{\partial x_i} = \frac{\partial(\tau_{ij}V_j)}{\partial x_i} \tag{12.38}$$

For a two-dimensional flow, Eq. (12.38) gives

$$\nabla\cdot\left(\boldsymbol{T}\cdot\boldsymbol{V}\right) = \frac{\partial(\tau_{ij}V_j)}{\partial x_i} = \frac{\partial(\tau_{11}V_1 + \tau_{12}V_2)}{\partial x_1} + \frac{\partial(\tau_{21}V_1 + \tau_{22}V_2)}{\partial x_2} \tag{12.39}$$

Assuming a one-dimensional flow with $V_2 = 0$, the contribution of the shear stress work Eq. (12.39) is reduced to

$$\nabla\cdot\left(\boldsymbol{T}\cdot\boldsymbol{V}\right) = \frac{\partial(\tau_{11}V_1)}{\partial x_1} \approx \frac{(\tau_{11\,inlet}V_{inlet} - \tau_{11\,exit}V_{1exit})}{\Delta x_1} \tag{12.40}$$

The differences in τ_{11} at the inlet and exit of the component under simulation stems from velocity deformation at the inlet and exit. Its contribution, however, compared to the enthalpy terms in the energy equation, is negligibly small. Thus, the one-dimensional approximation of total energy equation (12.35) in terms of total enthalpy reads:

$$\frac{\partial H}{\partial t} = -\frac{\kappa\dot{m}}{\rho S}\frac{\partial H}{\partial x_1} - \frac{\kappa - 1}{\rho}\left[(H + K)\frac{\partial}{\partial x_1}\left(\frac{\dot{m}}{S}\right) + \frac{1}{2\rho S^2}\frac{\partial \dot{m}^2}{\partial t}\right] - \frac{\kappa}{\rho}\frac{\partial q}{\partial x} \tag{12.41}$$

For a steady state case, without changes of specific mass $\dot{m}/S$ Eq. (12.41) leads to:

$$\frac{\partial H}{\partial x_1} = -\frac{S}{\dot{m}} \frac{\partial \dot{q}_i}{\partial x_i} \tag{12.42}$$

Assuming a constant cross section and mass flow, Eq. (12.42) gives

$$\frac{\partial H}{\partial x_1} = -\frac{\partial}{\partial x_1}\left(\frac{S\,\dot{q}_i}{\dot{m}} \right) \tag{12.43}$$

Integrating Eq. (12.43) in a streamwise direction results in:

$$H_{out} - H_{in} = -\left(\frac{S}{\dot{m}} \right) \Delta\dot{q} \tag{12.44}$$

for Eq. (12.44) to be compatible with the energy equation, a modified version of Eq. (4.75) is presented.

$$H_{Out} - H_{In} = q + w_{Shaft} \tag{12.45}$$

Equating (12.44) and (12.45) in the absence of a specific shaft power, the following relation between the heat flux vector and the heat added or rejected from the element must hold:

$$q = -\left(\frac{S}{\dot{m}} \right) \Delta\dot{q} \tag{12.46}$$

From (12.46) it immediately follows that

$$\Delta\dot{q} = -\frac{q\dot{m}}{S} = -\frac{\dot{Q}}{S} \tag{12.47}$$

where $\dot{Q}$ is the thermal energy flow added to or rejected from the component. In the presence of shaft power, the specific heat in Eq. (12.47) may be replaced by the sum of the specific heat and specific shaft power:

$$\Delta\dot{q} = -\frac{\dot{m}q + \dot{m}l_m}{S} = -\left(\frac{\dot{Q} + L}{S}\right) \tag{12.48}$$

Equation (12.48) in differential form in terms of $\dot{Q}$ and $\boldsymbol{L}$ is

$$\frac{\partial\dot{q}}{\partial x} = -\frac{\partial}{\partial x}\left(\frac{\dot{m}q + \dot{m}l_m}{S}\right) = -\frac{\partial}{\partial x}\left(\frac{\dot{Q} + L}{S}\right) \tag{12.49}$$

With Eq. (12.49), we find:

$$\begin{aligned}\frac{\partial H}{\partial t} = &-\frac{\kappa\dot{m}}{\rho S}\frac{\partial H}{\partial x_1} - \frac{\kappa - 1}{\rho}\left[(H + K)\frac{\partial}{\partial x_1}\left(\frac{\dot{m}}{S}\right) + \frac{1}{2\rho S^2}\frac{\partial\dot{m}^2}{\partial t}\right] \\ &- \frac{\kappa}{\rho}\frac{\partial}{\partial x}\left(\frac{\dot{Q} + L}{S}\right)\end{aligned} \tag{12.50}$$

Using the nomenclature in Fig. 12.1, Eq. (12.50) is written as:

$$\begin{aligned}\frac{\partial H}{\partial t} = &-\kappa_k\frac{\dot{m}_k}{\rho_k S_k}\left(\frac{H_{i+1} - H_i}{\Delta x}\right) - \\ &-\left(\frac{\kappa - 1}{\rho}\right)_k\left[\left(\frac{H_k + K_k}{\Delta x}\right)\left(\frac{\dot{m}_{i+1}}{S_{i+1}} - \frac{\dot{m}_i}{S_i}\right) + \frac{\dot{m}_k}{\rho_k S_k^2}\frac{\partial\dot{m}_{i+1}}{\partial t}\right] - \\ &-\frac{\kappa_k}{\rho_k}\left(\frac{\Delta\dot{Q} + \Delta L}{\Delta V}\right)\end{aligned} \tag{12.51}$$

In terms of total temperature, Eq. (12.51) is rearranged as:

$$\frac{\partial c_p T_0}{\partial t} = -\kappa_k \frac{\dot{m}_k}{\rho_k S_k}\left(\frac{c_p T_{0_{i+1}} - c_p T_{0_i}}{\Delta x}\right) - \\ - \left(\frac{\kappa - 1}{\rho}\right)_k \left[\left(\frac{c_p T_{0_k} + K_k}{\Delta x}\right)\left(\frac{\dot{m}_{i+1}}{S_{i+1}} - \frac{\dot{m}_i}{S_i}\right) + \frac{\dot{m}_k}{\rho_k S_k^2}\frac{\partial \dot{m}_{i+1}}{\partial t}\right] - \\ - \frac{\kappa_k}{\rho_k}\left(\frac{\Delta \dot{Q} + \Delta L}{\Delta V}\right) \tag{12.52}$$

In terms of total pressure, Eq. (12.37) is:

$$\frac{\partial P}{\partial t} = -\kappa \frac{\partial}{\partial x_1}\left(P V_1\right) - (\kappa - 1)\left(\frac{\partial \dot{q}_1}{\partial x_1} - \frac{\partial}{\partial x_1}\left(V_j T_{1j}\right)\right) \\ - (\kappa - 2)\left(\frac{\partial\left(\rho K V_1\right)}{\partial x_1} + \frac{\partial(\rho K)}{\partial t}\right) \tag{12.53}$$

which is approximated as:

$$\frac{\partial P_k}{\partial t} = -\frac{\kappa_k}{\Delta x}\left(\frac{\dot{m}_{i+1} p_{i+1}}{\rho_{i+1} S_{i+1}} - \frac{\dot{m}_i p_i}{\rho_i S_i}\right) - \left(\kappa_k - 1\right)\left(\frac{\dot{m}_k q_k}{\Delta V} + c_{f_k}\frac{\dot{m}_{i+1}\,\dot{m}^2{}_k}{2 D_{h_{i+1}} S_{i+1} \rho_k^2}\right. \\ \left. -\left(\kappa_k - 2\right)\frac{\dot{m}_k}{\rho_k S_k^2}\left(\frac{1}{2}\frac{\dot{m}_k}{\rho_k}\frac{1}{\Delta x}\left(\frac{\dot{m}_{i+1}}{S_{i+1}} - \frac{\dot{m}_i}{S_i}\right) + \frac{\partial \dot{m}_{i+1}}{\partial t}\right)\right. \\ \left. - \frac{\left(\kappa_k - 2\right)}{2\Delta x}\left(\frac{\dot{m}_{i+1}^3}{\rho_{i+1}^2 S_{i+1}^3} - \frac{\dot{m}_i^3}{\rho_i^2 S_i^3}\right)\right) \tag{12.54}$$

with:

$$\rho_k = \frac{1}{R}\frac{p_{i+1} + p_i}{T_{i+1} + T_i}, \quad c_{p_k} = \frac{H_{i+1} - H_i}{T^*{}_{i+1} - T^*{}_i}, \quad \kappa_k = \frac{c_{p_k}}{c_{p_k} - R}$$

12.4 Numerical Treatment

The above partial differential equations can be reduced to a system of ordinary differential equations by a 1-dimensional approximation. The simulation of a complete gas turbine system is accomplished by combining individual components that have been modelled mathematically. The result is a system of ordinary differential equations that can be dealt with numerically. For weak transients, Runge-Kutta or Predictor-Corrector procedures may be used for the solution. When strong transient processes are simulated, the time constants of the differential equation system can differ significantly so that difficulties must be expected with stability and convergence with the integration methods. An implicit method avoids this problem. The system of ordinary differential equations generated in a mathematical simulation can be represented by:

$$\frac{d\boldsymbol{X}}{dt} = G(\boldsymbol{X},t) \tag{12.55}$$

with **X** as the state vector sought. If the state vector **X** is known at the time t, it can be approximated as follows for the time t+dt by the trapezoidal rule:

$$\boldsymbol{X}_{t+\Delta t} = \boldsymbol{X}_t + \frac{1}{2}\Delta t(G_{t+\Delta t} + G_t) \tag{12.56}$$

Because the vector **X** and the function G are known at the time t, i.e., $\mathbf{X}_t$ and G_t are known, Eq. (12.56) can be expressed as:

$$\boldsymbol{X}_{t+\Delta t} - \boldsymbol{X}_t - \frac{1}{2}\Delta t(G_{t+\Delta t} + G_t) = F(\boldsymbol{X}_{t+\Delta t}) \tag{12.57}$$

As a rule, the function F is non-linear. It can be used to determine $\mathbf{X}_{t+dt}$ by iteration when $\mathbf{X}_t$ is known. The iteration process is concluded for the time t+dt when the convergence criterion

$$\frac{\boldsymbol{X}_i^{(k+1)} - \boldsymbol{X}_i^{(k)}}{\boldsymbol{X}_i^{(k+1)}} < \varepsilon \tag{12.58}$$

is fulfilled. If the maximum number of iterations, $k = k_{max}$, is reached without fulfilling the convergence criterion, the time interval Δt is halved, and the process of iteration is repeated until the criterion of convergence is met. This integration process, based on the implicit one-step method described by Liniger and Willoughby [6] is reliable for the solution of stiff differential equations. The computer time

required depends, first, on the number of components in the system and, second, on the nature of the transient processes. If the transients are very strong, the computer time can be 10 times greater than the real time because of the halving of the time interval. For weak transients, this ratio is less than 1.

References, Chapter 12

12.1 Schobeiri M. T., 1985 “Aero-Thermodynamics of Unsteady Flows in Gas Turbine Systems,” Brown Boveri Company, Gas Turbine Division Baden Switzerland, BBC-TCG-51.

12.2 Schobeiri T., 1985b “COTRAN, the Computer Code for Simulation of Unsteady Behavior of Gas Turbines,” Brown Boveri Company, Gas Turbine Division Baden Switzerland, BBC-TCG-53.

12.3 Schobeiri T., 1986: “A General Computational Method for Simulation and Prediction of Transient Behavior of Gas Turbines,” ASME-86-GT-180.

12.4 Schobeiri, M. T., Abouelkheir, M., Lippke, C., 1994, “GETRAN: A Generic, Modularly Structured Computer Code for Simulation of Dynamic Behavior of Aero-and Power Generation Gas Turbine Engines,” an honor paper, ASME Transactions, *Journal of Gas Turbine and Power*, Vol. 1, pp. 483-494.

12.5 Bird, R. B., Stewart, W.E., and Lightfoot, E.N., 1960, “Transport Phenomena,”John Wiley and Sons, Inc.

12.6 Liniger W., Willoughby R., 1970, "Efficient integration methods for stiff systems of ordinary differential equations," SIAM. Numerical Analysis Vol. 7, No. 1.

13 Generic Modeling of Turbomachinery Components and Systems

A turbomachinery *system* such as a power generation gas turbine engine, a thrust generation aero- engine, rocket propulsion, or a small turbocharger, consist of several *sub-systems* that we call *components* ([1],[2],[3], [4]). Each component is an autonomous entity with a defined function within the system. Inlet nozzles, exit diffusers, combustion chambers, compressors, and turbines are a few component examples. A component may consist of several *sub-components*. A turbine or a compressor stage exhibits such a sub-component. The numerical models of components are called *modules*.

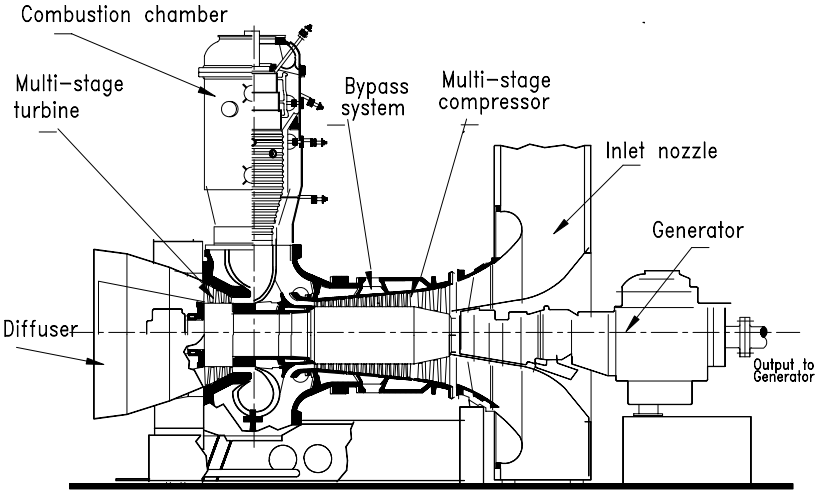

Fig. 13.1: Single-spool power generation gas turbine engine, BBC-GT-9 with major components

The gas turbine engine shown in Fig. 13.1 composed of an inlet nozzle, a multistage compressor component with three bypass systems that provide cooling mass flow for the shaft, the high pressure turbine, and the mixing air for reducing the combustion chamber exit temperature. To reduce the compressor exit flow losses, the remaining

compressor mass flow passes through a diffuser before entering the combustion chamber. In the following combustion chamber component, fuel is added to establish the required turbine inlet temperature. The following multistage turbine component placed on the same shaft as the compressor, drives the compressor and the generator. The configuration of the compressor and the turbine components placed on the same shaft is called a *spool*. As seen in Fig. 13.1, the spool shaft is coupled with the generator shaft, which converts the net turbine power into electrical power.

Figure 13.2 illustrates the decomposition of a *twin-spool* engine into its major components. It consists of (1) a *high pressure-spool*, the so-called gas generator that encompasses the multistage high pressure compressor (HP-compressor), combustion chamber component, and the high pressure turbine (HP-turbine) component, (2) a *low pressure-spool* shaft connects the low pressure compressor with the low pressure turbine component, (3) the combustion chamber, (4) an inlet diffuser and exit nozzle. The two spools are connected aerodynamically. The mass flow, with high kinetic energy exiting from the last stage of the HP-turbine stage, impinges on the first stator of the LP-turbine, and is further expanded within the LP-component and the following thrust nozzle, that provides the required kinetic energy for thrust generation.

Besides the major components shown in Fig. 13.1 and 13.2, there are several other components such as pipes that serve the transport of mass flow from compressor to turbine for cooling purposes, valves with the operation ramp defined by the control system, control systems, lubrication systems, bearings, electric motors for power supply, etc.

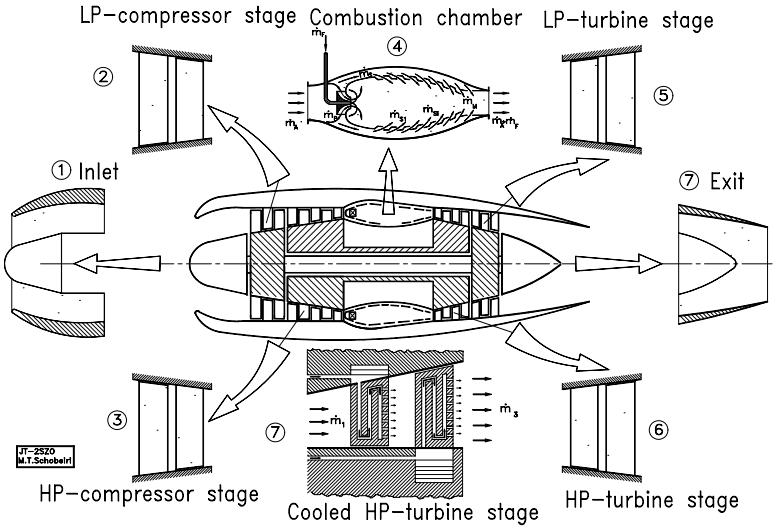

Fig. 13.2: A twin-spool aero gas turbine system with its major components.

13.1 Generic Component Configuration

These components shown in Fig. 13.1 and 13.2 are common to a small or large gas turbine engine regardless if it is a power generation engine, a thrust generation, or an engine that serves as a turbocharger. They can be modeled as modules to assemble a complete system ranging from a single spool power generation gas turbine to the most complicated of rocket propulsion systems. The components can be categorized into three groups according to their functions. The representatives of each of these groups are described below.

13.1.1 Group 1: Modular Configuration of Inlet, Exhaust, Pipe

Group 1 includes those components in which no transfer of thermal energy with the surrounding environment takes place. Their function consists, among other things, of transporting the mass, accelerating the mass flow through the nozzle, and reducing the kinetic energy through a diffuser. Figure 13.3 exhibits the physical as well as the modular representation of the component's nozzle, pipe, and diffuser. Each module is surrounded by an inlet and an outlet plenum. These plena serve as the coupling element between two or more modules. Detailed physical and mathematical modeling of these modules are presented in Chapter 14.

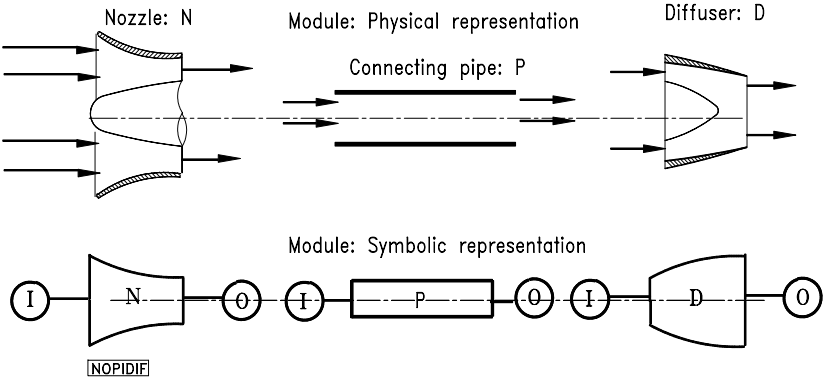

Fig. 13.3: Component and modular representation of inlet nozzle N, connecting pipe P, and Diffuser D

13.1.2 Group 2: Heat Exchangers, Combustion Chamber, After- Burners

Group 2 includes those components within which the processes of thermal energy exchange or heat generation take place. Heat exchangers are encountered in different

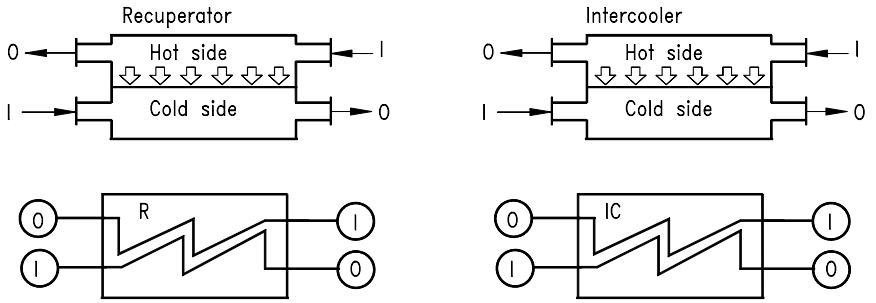

Fig. 13.4: Component and modular representations of a recuperator and an inter-cooler with the inlet and exit plena

forms such as recuperators, regenerators, inter-coolers, and after-coolers. Combustion chambers and afterburners share the same function. They convert the chemical energy of the fuel into thermal energy. As an example, Fig. 13.4 shows the component and modular representation of a recuperator and an inter-cooler. Recuperators are used to improve the thermal efficiency of power generation gas turbines. While hot gas from the exhaust system enters the low pressure side (hot side) of the recuperator, compressor air enters the high pressure side (cold side). By passing over a number of contact surfaces, the hot side of the recuperator transfers thermal energy with the compressor air that passes through the recuperator cold side. After exiting the recuperator air side, preheated air enters the following combustion chamber.

The component combustion chamber is exhibited in Fig. 13.5. It generally consists of a primary combustion zone, a secondary zone, and a mixing zone. The primary zone, surrounded by *n* rows of ceramic segments, separates the primary combustion zone from the secondary zone and protects the combustion chamber

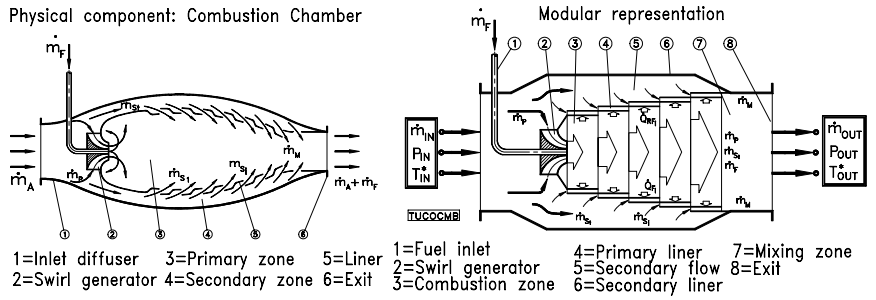

Fig. 13.5: Component and modular representation of a typical combustion chamber.

casing from being exposed to high temperature radiation. The actual process of combustion occurs in the primary zone. The mixing in of the secondary air passing through mixing nozzles and holes reduces the gas temperature in the mixing zone to a level acceptable for the gas turbine that follows. The rows of segments in the combustion zone are subjected to a severe thermal loading due to direct flame radiation. Film and convective cooling on both the air and the gas sides cools these segments. The air mass flows required to cool these hot segments flow through finned cooling channels, thereby contributing to the convection cooling of the segments on the air side. The cooling air mass flow exiting from the j^{th} segment row, effects a film cooling process on the gas side within the boundary layer in the next row of segments. At the end of that process, the cooling air mass flow is mixed with the primary air mass flow, thus, reducing the exit temperature.

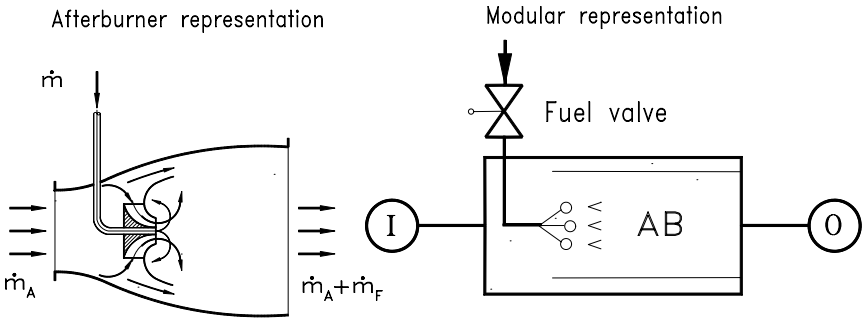

Fig. 13.6: Component and modular representation of a typical after burner

The afterburner (AF) component is applied to supersonic aero-engines that require supersonic exit velocities. Figure 13.6 exhibits a typical after-burner component with its modular representation. After leaving the low pressure turbine component, fuel is added to the mass flow inside the afterburner component causing an increase in temperature. The combustion gas is accelerated from subsonic to supersonic in a Laval nozzle that follows the afterburner. The principle function of the after-burner component and its modular simulation is very similar to the one discussed for combustion chambers.

13.1.3 Group 3: Modular Configuration of Adiabatic Compressor and Turbine Components

This group includes components within which an exchange of mechanical energy (shaft power) with the surroundings takes place. The representatives of this group are the compressors and turbines. Figure 13.6 shows a compressor stage with a

corresponding velocity diagram and its modular representation. The module represents one stage within a multi-stage environment. It is decomposed into a stator and a rotor row that are separated by the corresponding plena. Figure 13.7 shows the compressor stage with the corresponding modular representation.

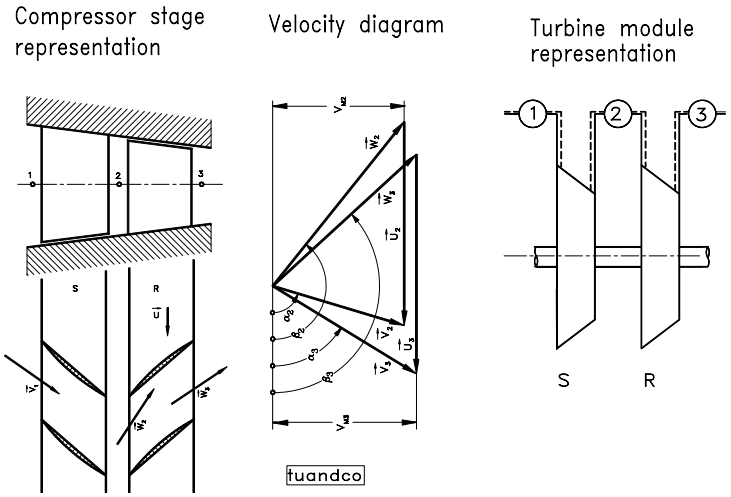

Fig. 13.7: Representation of an adiabatic compressor stage, module. The stage is decomposed into two rows that are connected via plenum No. 2

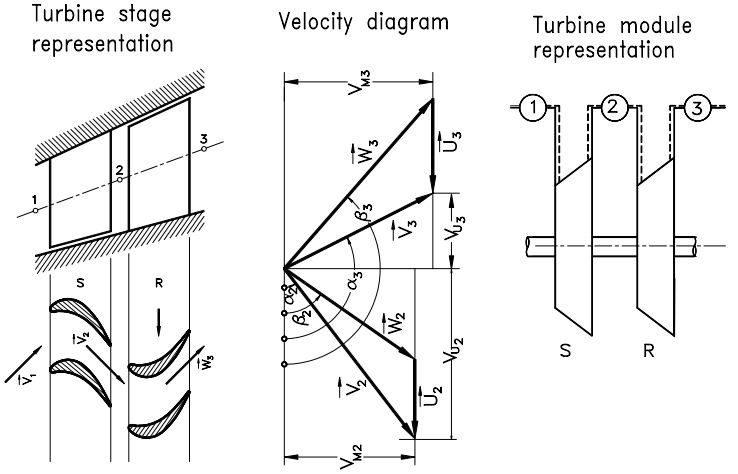

Fig. 13.8: Representation of an adiabatic turbine stage, module. The stage is decomposed into two rows that are connected via plenum No. 2

The row-by-row adiabatic compression process is described by the conservation laws in conjunction with the known stage characteristics as shown in shown in Chapter 5. Figure13.8 shows the component representation of a turbine stage along with its velocity diagram and the module representation. The turbine stage is decomposed into its stator and rotor row that are separated by plenum 2. The row-by-row adiabatic expansion process is described by the conservation laws in conjunction with the known stage characteristics detailed in Chapter 5.

13.1.4 Group 4: Modular Configuration of Diabatic Turbine and Compressor Components

Unlike the adiabatic turbine and compressor components discussed in Section 13.1.3, this group includes turbine and compressor components within which not only the exchange of mechanical energy (shaft power) with the surroundings takes place, but also thermal energy exchange with the working fluid occurs. This group encompasses cooled turbines and compressors as well as those that are not cooled. Figure 13.9 shows a cooled turbine stage with the corresponding modular representation. It is considered a special module that is usually utilized in the first three rows of the high pressure part of gas turbine engines. Its modular representation shows the decomposition of the stage into its stator and rotor row that are separated by the corresponding plenum 2. As Fig. 13.9 shows, a fraction of air, $\dot{m}_{cS}$, extracted from an HP-compressor is diverted into the first stator row and enters the cooling channels that might have several pin-fin and rib turbulators. Heat is transferred from the blade surface to the cooling air which may exit through several film cooling holes, slots at the trailing edge, and other holes. After exiting the blade surface, the cooling mass flow joins the turbine main mass . The same procedure may repeat in the subsequent

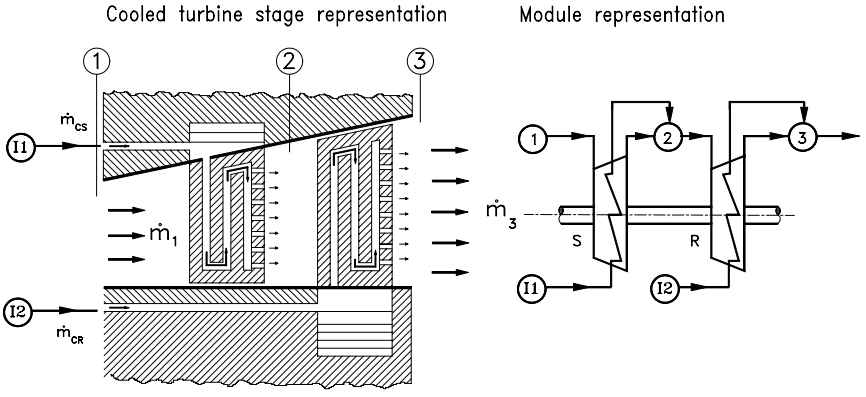

Fig. 13.9: Schematic of a cooled turbine stage and its modular representation.

rotor and stator rows as shown in Fig. 13.9. The module representation in Fig. 13.9 reflects the cooling and mixing procedure in the turbine stage. The main mass flow, with certain fuel/air and humidity/air ratios, enters the upstream station 1 that correspond to plenum (1) and expands through the stator row. The cooling mass flow from plenum (I1), with certain humidity/air ratios but zero fuel/air ratios, passes though the cooling channel and mixes with the mainstream combustion gas in plenum (2). The mixing process changes the fuel/air and humidity/air ratios, which is precisely calculated.

Similar heat transfers and mixing occurs within the rotor row with rotor cooling mass flow $\dot{m}_{cR}$ that enters the plenum at (I2). The non-linear dynamic behavior of the cooled turbine stage represented by the above module, is described by three differential equations for the gas side, three differential equations for the cooling air side, and one differential equation for the turbine material heat conduction as the closure condition. The same number of differential equations are generated for the rotor row. A diabatic expansion is not necessarily limited to the cooled turbine component. Uncooled blades are also subjected to diabatic processes whenever there is a temperature difference between the working medium and the turbine blade material. In steady state operations, which is specific to power generation gas turbine systems, there is a temperature equilibrium between the combustion gas and the blade material. Changing the engine load condition disrupts this equilibrium leading to a temperature difference between the turbine mass flow and the blade material. In the case of load addition, opening the fuel valve causes an instantaneous gas temperature increase. Since the blade temperature response significantly lags behind the response of the gas temperature, heat is transferred from the gas to the turbine material. Reducing the load by closing the fuel valve causes a portion of the thermal energy stored in the turbine blade material to be transferred to the working medium, causing a reduction of the turbine blade temperature. In case of aero-gas turbine engines, where acceleration and deceleration is the routine operational procedure, the turbine operates under diabatic conditions. A similar diabatic process is encountered in uncooled compressor components. However, the temperature differences are significantly lower.

The same cooling and simulation principle can be applied to compressor stages. However, it is a common practice for compressor trains consisting of several compressor components, and a high pressure ratio to intercool the mass flow. The process of intercooling serves to substantially reduce the temperature of the working medium. Figure 13.10 shows the modular configuration of an inter- mediate pressure compressor (IP-C), an intercooler (IC), and a high pressure compressor (HP-C). The *h-s* diagram shows the two-stage compression process with intercooling.

After the compression in IP-C, the working medium is intercooled to the initial temperature and is compressed in HP-C to arrive at the final pressure. Usually, the intercooling process is applied to industrial processes, where compression ratios above $\pi > 30$ is required. Without intercooling, a substantial efficiency drop is anticipated.

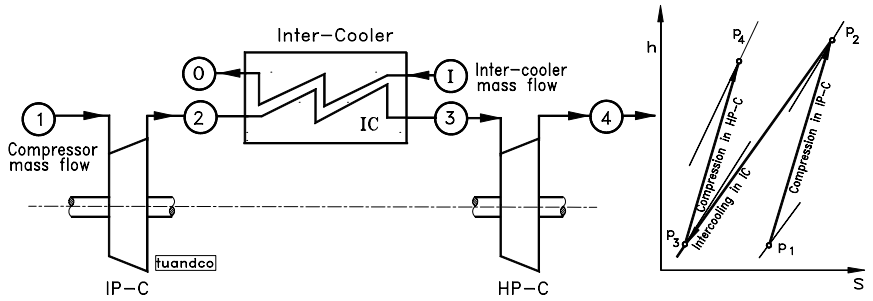

Fig. 13.10: Modular configuration of an intermediate pressure compressor, intercooler, and a high pressure compressor.

13.1.5 Group 5: Control System, Valves, Shaft, Sensors

This group of modules consist of shafts, sensors, control systems, and fuel and load schedule generators, shown in Fig. 13.11. The control system is a major module that controls the entire engine. Input information may contain rotor speed transferred by the speed sensors, turbine inlet temperature, pressure, and compressor inlet and exit pressures and temperatures. This information may trigger closing or opening of the fuel valves and several bypass valves, and can perform other control functions, such as the adjustment of compressor stator blades to perform active surge protection.

13.1.6 Coupling Module Plenum

The plenum is the coupling module between two or more successive components. Its primary function is to couple the dynamic information of entering and exiting

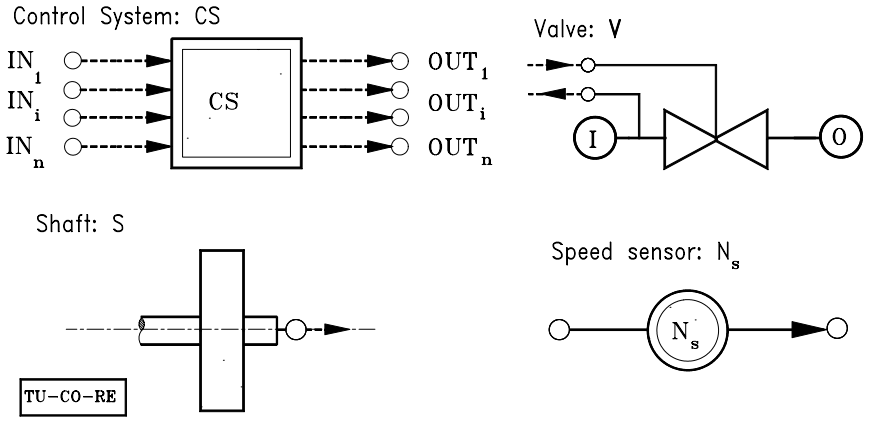

Fig. 13.11: Schematics of the modules: control system, valve, shaft, and sensor.

components. The volume of the plenum consists of partial volumes of components that enter and exit the plenum. The inlet components transfer information about mass flow $\dot{m}_i$, total pressure P, total temperature T_0, fuel/air f ratio, and water/air ratio w to the plenum. After entering the plenum, a mixing process takes place, where the aforementioned quantities reach their equilibrium values. These values are the same for all outlet components exiting the plenum. Each component represented by a module is uniquely defined by its name, inlet and outlet plena.

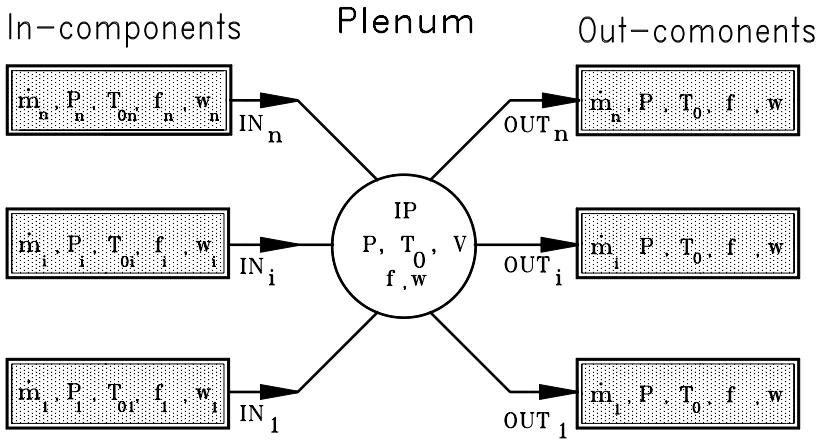

Fig. 13.12: Plenum as the coupling module between components.

13.2 Modular System Configuration Concept for Nonlinear Dynamic Simulation

From the conceptual dynamic simulation point of view, the previous survey has led to the practical conclusion that any arbitrary aircraft or power generation gas turbine engine and its derivatives, regardless of configuration, i.e., number of spools and components, can be generically simulated by arranging the modules according to the engine of interest. The nonlinear dynamic simulation method discussed in this and the next following chapters, is based on this modular configuration concept, and is a generic, modularly structured computational procedure that simulates the transient behavior of individual components, gas turbine engines, and their derivatives. The modules are identified by their names, spool numbers, and the inlet and outlet plena. This information is vital for automatically generating the system of differential equations that represent individual modules. Modules are then combined into a complete system that correspond to the system configuration. Each module is physically described by the conservation laws of thermo-fluid mechanics, which result in a system of nonlinear partial differential or algebraic equations. Since an engine

consists of a number of components, its modular arrangement leads to a system containing a number of sets of equations. The above concept can be systematically applied to any aircraft or power generation gas turbine engine. The modular concept allows the choice of generating a wide variety of simulation cases from single spool, power generation engines to twin, and multi spool thrust or combined thrust-power generation engines. The following three examples explain the modular design and simulation capability.

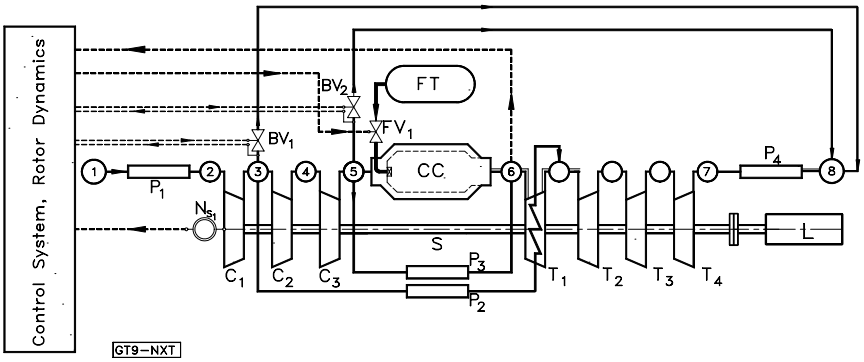

Fig. 13.13: Modular configuration of the gas turbine engine presented in Fig. 13.1

Figure 13.1 shows a cutaway of a power generation gas turbine. To simulate this engine, first, a modular representation is constructed for the purpose of module addressing and plena assignments. Fig. 13.13 presents the schematic simulation scheme for this engine. The first plenum, plenum 1, is open to the atmosphere, and is the entrance to the engine. The entrance to the compressor is represented by a pipe, P1. The compression system is divided into three compressors, the low pressure compressor stage group, C1, which is assigned plenum 2 as the inlet plenum and plenum 3 as the exit plenum, the intermediate pressure stage group, C2, and the high pressure stage group, C3. Upon exiting the first compressor, a portion of the flow is removed via the second pipe of the engine system, P2, and is assigned plenum 3 as its inlet plenum, and plenum 7 as its exit plenum. The temperature of the flow at this point is relatively low and the second pipe mass flow serves for the turbine cooling. A portion of the flow is removed upon exiting the high pressure compressor, C3, via the third pipe, P3, and is transferred to the turbine inlet without passing through the combustion chamber. Fuel is added to the combustion chamber at a rate which is given in the input data. The flow then exits the combustion chamber, is mixed with the exiting flow from the third pipe, P3, for the purpose of temperature control, and enters the turbine which resides between plena 6 and 7. The fourth pipe, P4, leads to plenum 8 which is also open to the atmosphere. The control system input variables are the rotational speed of the shaft and the turbine inlet temperature. Output from the control system is the opening and closing of the fuel valve to control fuel flow into

the combustion chamber (Fig. 13.13). Each component corresponds to a simulation module consisting of a main routine and several assistant subroutines, which determine the complete thermo-fluid dynamic profile of the component during the transient.

Figure 13.14 schematically exhibits a twin spool aircraft engine with its derivatives. The base engine (middle) is modified to construct a ducted bypass engine, where the exit jets are not mixed (top left) and an unducted bypass engine (bottom left). The same base engine also serves to design a power generation and a turboprop engine. While in the case of the power generation example a third shaft has been added, in the turboprop example, the low pressure turbine drives the propeller.

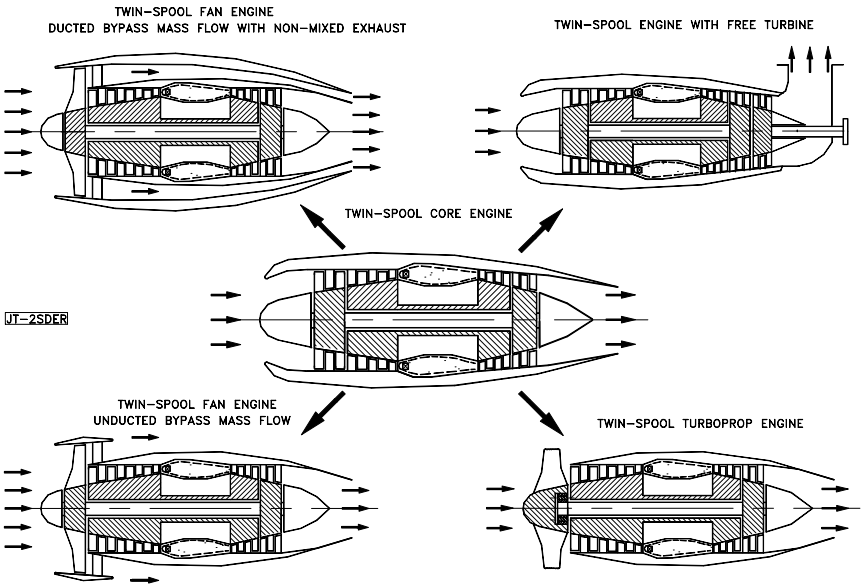

Fig. 13.14: A twin spool base engine (middle) with four different derivatives

Figure 13.14 presents an appropriate example of generic, modularly structured, component and system modeling. The schematic of the base engine is shown in Fig. 13.15. Two shafts are defined as S1 and S2. The flow passes through the engine in the following manner: first its velocity is reduced and its pressure is increased in the inlet diffuser (D1) which is between plena 1 and 2. The low pressure compressor group (C11 - C15) will then further increase the flow pressure. Next, the high pressure compressor group (C21 - C25), which resides on the second shaft, S2, further raises the pressure. Fuel is injected into the combustion chamber (CC1), which is located between plena 13 and 14, thus, raising its temperature. High pressure and temperature gas is expanded through the HP-turbine group (T21 - T23) which is

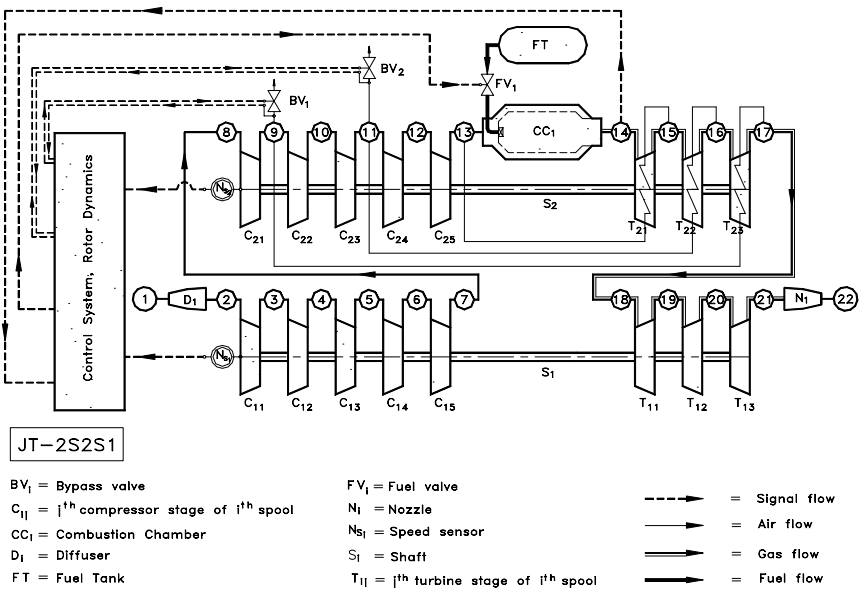

Fig. 13.15 Modular configuration of the twin spool base engine of Fig.13.14

resided on the second shaft (S2) that drives the HP-compressor. Due to high thermal loading on the blades, the Hp-turbine requires cooling. The combustion gas further expands through the LP- turbine group (T11 - T13) before it is exhausted into the atmosphere through the exit nozzle (N1), which is between plena 21 and 22. As shown in Fig. 13.15, signal flow from each module to the control system is represented by dashed lines, air flow is represented by single lines, gas flow is represented by the double lines, and fuel flow is represented by thick single lines.
An example of a modular composition of a helicopter gas turbine engine charged with a wave rotor is shown in Fig. 13.16. Compared to a single spool engine, Fig.13.16 reveals two new features: (1) a wave rotor super charger component is installed between the compressor and the combustion chamber that further increases the compression ratio leading to higher thermal efficiency, and (2) a propeller is driven by the spool shaft, whose rotational speed is reduced by a gear transmission.

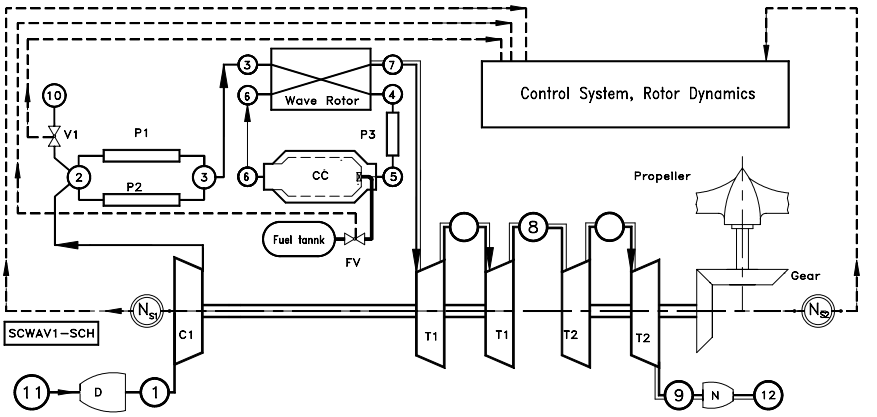

Fig. 13.16: Modular configuration of a helicopter gas turbine engine supercharged by a wave rotor.

13.3 Configuration of Systems of Non-linear Partial Differential Equations

Each component of the above modular system configuration is completely described by a set of partial differential equations and algebraic equations. These modules are connected via plena that are described by two differential equations. Thus, the modular system configuration consists of a set of differential equation systems. The solution of these equations depend on the initial and boundary conditions that trigger the nonlinear dynamic event. This and other related issues will be comprehensively discussed in the following chapters.

References, Chapter 13

13.1 Schobeiri, M. T., Abouelkheir, M., Lippke, C., 1994, “GETRAN: A Generic, Modularly Structured Computer Code for Simulation of Dynamic Behavior of Aero-and Power Generation Gas Turbine Engines,” an honor paper, ASME Transactions, *Journal of Gas Turbine and Power*, Vol. 1, pp. 483-494.

13.2 Schobeiri T., 1986: "A General Computational Method for Simulation and Prediction of Transient Behavior of Gas Turbines." ASME-86-GT-180.

13.3 Schobeiri M. T., 1985 "Aero-Thermodynamics of Unsteady Flows in Gas Turbine Systems." Brown Boveri Company, Gas Turbine Division Baden Switzerland, BBC-TCG-51.

13.4 Schobeiri T., 1985b "COTRAN, the Computer Code for Simulation of Unsteady Behavior of Gas Turbines." Brown Boveri Company, Gas Turbine Division Baden Switzerland, BBC-TCG-53.

14 Modeling of Inlet, Exhaust, and Pipe Systems

14.1 Unified Modular Treatment

This chapter deals with the numerical modeling of the components pertaining to group 1 discussed in section 13.1.1 The components pertaining to this category are the connecting pipes, inlet and exhaust systems, as shown in Fig. 14.1.

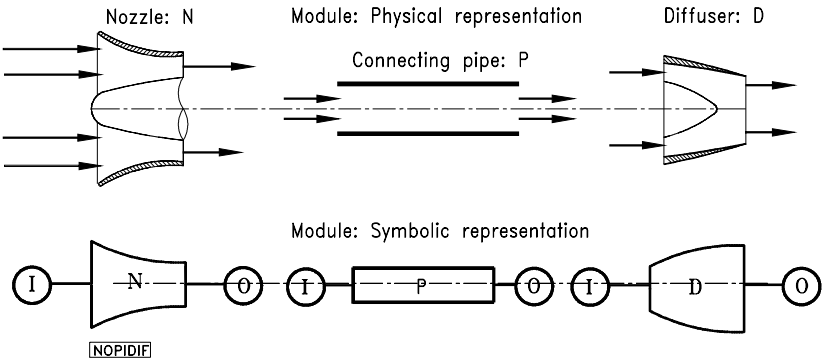

Fig. 14.1: Component and modular representation of inlet nozzle N, connecting pipe P, and Diffuser D

The function of this group consists, among other things, of the transportation of mass flow, and of converting the kinetic energy into potential energy and vice versa. Their geometry differs only in the sign of the gradient of the cross section in streamwise direction $\partial S/\partial x$. For $\partial S/\partial x < 0$, flow is accelerated for subsonic and decelerated for supersonic Mach numbers. On the other hand, for $\partial S/\partial x > 0$, the flow is decelerated for subsonic and accelerated for supersonic Mach numbers.

14.2 Physical and Mathematical Modeling of Modules

For modeling ducts with the varying cross sections, we apply the conservation laws derived in Chapter 12 ([1], [2], [3], [4]). The temporal change of the density at position *k,* shown in Fig. 14.2, is determined from Eq. (12.26) as is given below:

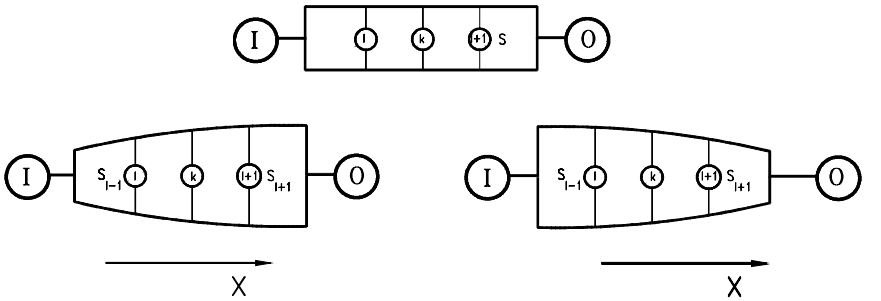

Fig. 14.2: Modeling the components diffuser $\partial S/\partial x > 0$, pipe $\partial S/\partial x = 0$, and nozzle $\partial S/\partial x < 0$

$$\frac{\partial \rho_k}{\partial t} = -\frac{1}{\Delta x}\left(\frac{\dot{m}_{i+1}}{S_{i+1}} - \frac{\dot{m}_i}{S_i}\right) \tag{14.1}$$

The mass flows $\dot{m}_i$ and $\dot{m}_{i+1}$ at stations i and $i+1$ are determined in conjunction with the momentum equation (12.33):

$$\begin{aligned}\frac{\partial \dot{m}_k}{\partial t} = & -\frac{1}{\Delta x}\left(\dot{m}_{i+1}V_{i+1} - \dot{m}_i V_i + p_{i+1}S_{i+1} - p_i S_i\right) \\ & + \left(\frac{\dot{m}_k V_k + P_k S_k}{S_k}\right)\left(\frac{S_{i+1} - S_i}{\Delta x}\right) - c_f \frac{\dot{m}_k^2}{2\, D_{h_k}\rho_k S_k}\end{aligned} \tag{14.2}$$

The energy equation in terms of total pressure Eq. (12.54) in the absence of heat addition is modified as follows:

$$\begin{aligned}\frac{\partial P_k}{\partial t} = & -\frac{\kappa_k}{\Delta x}\left(\frac{\dot{m}_{i+1}p_{i+1}}{\rho_{i+1}S_{i+1}} - \frac{\dot{m}_i p_i}{\rho_i S_i}\right) - (\kappa_k - 1)\left(\frac{\dot{m}_k q_k}{\Delta V} + c_{f_k}\frac{\dot{m}_{i+1}\,\dot{m}^2{}_k}{2D_{h_{i+1}}S_{i+1}\rho_k^2 S_k^2}\right) \\ & -(\kappa_k - 2)\frac{\dot{m}_k}{\rho_k S_k^2}\left[\frac{1}{2}\frac{\dot{m}_k}{\rho_k}\frac{1}{\Delta x}\left(\frac{\dot{m}_{i+1}}{S_{i+1}} - \frac{\dot{m}_i}{S_i}\right) + \frac{\partial \dot{m}_{i+1}}{\partial t}\right] \\ & - \frac{(\kappa_k - 2)}{2\Delta x}\left(\frac{\dot{m}_{i+1}^3}{\rho_{i+1}^2 S_{i+1}^3} - \frac{\dot{m}_i^3}{\rho_i^2 S_i^3}\right)\end{aligned} \tag{14.3}$$

For a constant cross-section, the equation of continuity (14.1) and motion (14.2) are written respectively as:

$$\frac{\partial \rho}{\partial t} = - \frac{1}{\Delta x \, S} \left(\dot{m}_{i+1} - \dot{m}_i \right) \tag{14.4}$$

$$\frac{\partial \dot{m}_k}{\partial t} = - \frac{1}{\Delta x} \left[\frac{\dot{m}^2_{i+1}}{\rho_{i+1} S} - \frac{\dot{m}^2_i}{\rho_i S} + S \left(P_{i+1} - P_i \right) \right] - c_f \frac{\dot{m}^2_k}{2 \rho_k S D_h} \tag{14.5}$$

Similarly, the equation of energy in terms of total pressure is simplified to:

$$\begin{aligned} \frac{\partial P_k}{\partial t} = & - \frac{\kappa_k}{\Delta x S} \left(\frac{\dot{m}_{i+1} p_{i+1}}{\rho_{i+1}} - \frac{\dot{m}_i p_i}{\rho_i} \right) - \left(\kappa_k - 1 \right) \left(\frac{\dot{m}_k q_k}{\Delta V} + c_{f_k} \frac{\dot{m}_{i+1} \dot{m}^2_k}{2 D_{h_{i+1}} \rho^2_k S^3} \right) \\ & - \left(\kappa_k - 2 \right) \frac{\dot{m}_k}{\rho_k S^2} \left[\frac{1}{2} \frac{\dot{m}_k}{\rho_k} \frac{1}{\Delta x S} \left(\dot{m}_{i+1} - \dot{m}_i \right) + \frac{\partial \dot{m}_{i+1}}{\partial t} \right] \\ & - \frac{\left(\kappa_k - 2 \right)}{2 \Delta x S^3} \left(\frac{\dot{m}^3_{i+1}}{\rho^2_{i+1}} - \frac{\dot{m}^3_i}{\rho^2_i} \right) \end{aligned} \tag{14.6}$$

Equations (14.4), (14.5), and (14.6) describe the transient process of a compressible flow within a tube with a constant cross section. For an incompressible flow Eq. (14.5) can be reduced to a simple differential equation:

$$\frac{\partial \dot{m}}{\partial t} = \frac{R \dot{m}^2}{L S} \left(\frac{T_1}{P_1} - \frac{T_n}{P_n} \right) + \frac{S}{L} \left(P_1 - P_n \right) - c_f \frac{\dot{m}^2}{\rho S D_h} \tag{14.7}$$

The friction coefficient c_f can be determined from the known steady-state condition, where the temporal change of the mass flow is set equally to zero. The indices *1* and *n* refer to the first and last station of the component. The solution of Eqs. (14.1) - ?, and (14.4) - (14.7) can be performed using the implicit integration method discussed later. However, considerable calculation speed is reached if the component under investigation is subdivided into several subsections that are connected to each other via plena. In this case, for each discrete section, the mass flow can be considered as spatially independent, which leads to further simplification of the above equations.

14.3 Example: Modeling of a Shock Tube

Simulation of a high frequency compression-expansion process within a shock tube is an appropriate example to demonstrate the nonlinear dynamic behavior of the above components. The shock-expansion process within shock tubes has been the subject of classical gas dynamics for many decades ([5], [6], [7],[8]). With the introduction of fast response surface mounted sensors, shock tubes have gained practical relevance for calibrating the high frequency response pressure and temperature probes. In classical gas dynamics, shock-expansion process are treated using the method of characteristics. Results of studies presented in [9] show substantial disagreement between calculations using method of characteristics and experiments. In this and the subsequent chapters, we simulate the dynamic behavior of each individual component using the simulation code GETRAN [2]. In GETRAN, the system of non-linear differential equations is solved using the implicit solution method described in Chapter 12.

The shock tube under investigation has a length of L=1m and a constant diameter D = 0.5m. The tube is divided into two equal length compartments separated by a membrane. The left compartment has a pressure of $p_l = 100\,bar$, while the right one has a pressure of $p_l = 50\,bar$. Both compartments are under the same temperature of $T_l = T_r = 400\,K$. The working medium is dry air, whose thermodynamic properties, specific heat capacities, absolute viscosity, and other substance quantities change during the process and are calculated using a gas table integrated in GETRAN. The pressure ratio of 2 to 1 is greater than the critical pressure ratio and allows a shock propagation with the speed of sound. Two equivalent schemes can be used to predict the compression-expansion process through the tube. These are shown in Fig. 14.3. In schematic (a), each half of the tube is subdivided into 10 equal pieces. The corresponding coupling plane 1, 2, and thus, the left half of the tube are under pressure of 100 bar, while the right half with the

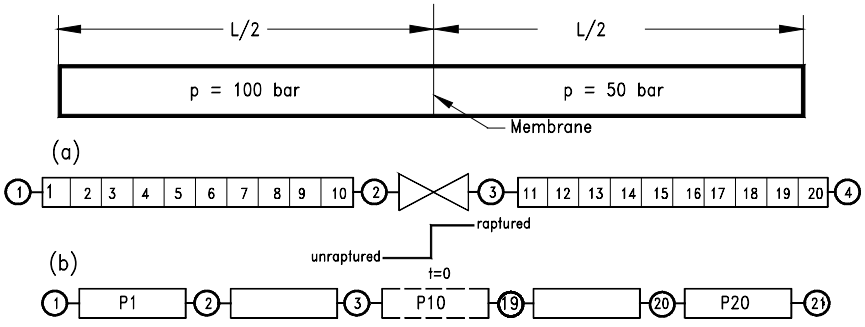

Fig. 14.3: Simulation schematics for a shock tube: the physical tube (top), and the simulation schematics (a) and (b)

plenums 3 and 4 are under the pressure of 50 bar. The membrane is modeled by a throttle system with a ramp that indicates the cross sectional area shown underneath the throttle. The sudden rupture of the membrane is modeled by a sudden jump of the ramp. The schematic (b) offers a simpler alternative. Here, as in case (a), the tube is subdivided into 20 pieces that are connected via plenums 1 to 21.

14.3.1 Shock Tube Dynamic Behavior

Pressure Transients: The process of expansion and compression is initiated by suddenly rupturing the membrane. At time t = 0, the membrane is ruptured which causes strong pressure, temperatures, and thus, mass flow transients. Since the dynamic process is primarily determined by pressure, temperature, and mass flow transients, only a few representative results are discussed as shown in Figs. 14.4 through 14.9.

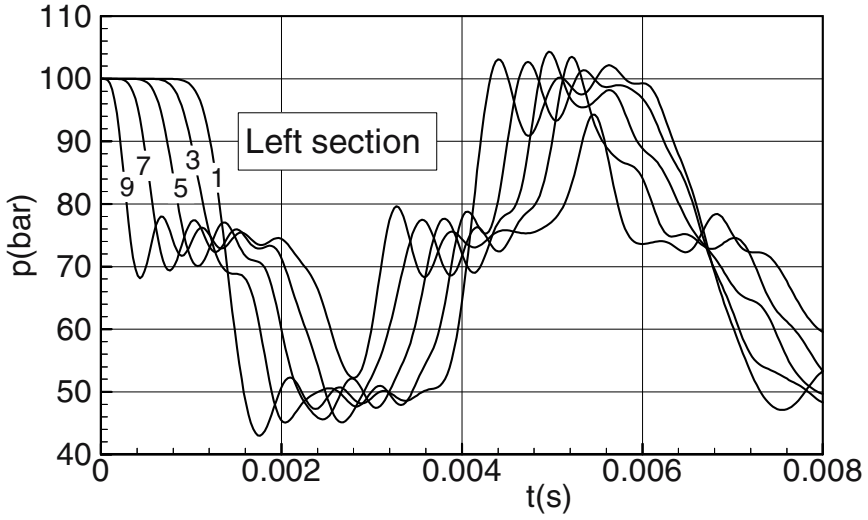

Fig. 14.4: Pressure transients within the shock tube. Left section includes all tube sections initially under high pressure of 100 bar, while the right section include those initially at 50 bar

Figure 14.4 shows the pressure transients within the left sections 1 to 9. As curve 9 shows, the section of the tube that is close to the membrane reacts with a steep expansion wave. On the other hand, the pressure within the pipe section ahead of the shock, Fig. 14.5, curve 11, increases as the shock passes through the section. Oscillatory behavior is noted as the shock strength diminishes. The pipe sections that are farther away from the membrane, represented by curves 7, 5, 3, and 1 on the left and curves 13, 15, 17, and 19 on the right section, follow the pressure transient with certain time lags. Once the wave fronts have reached the end wall of the tube, they are

reflected as compression waves. The aperiodic compression-expansion process is associated with a propagation speed which corresponds to the speed of sound. The expansion and compression waves cause the air, which was initially at rest, to perform an aperiodic oscillatory motion. Since the viscosity and the surface roughness effects are accounted for by introducing a friction coefficient, the transient process is of dissipative nature.

Temperature Transients: Figure 14.6 shows the temperature transients within the left sections 1 to 9. As curve 9 shows, the section of the tube that is close to the membrane reacts with a steep temperature decrease. The pipe sections that are farther away from the membrane, represented by curves 7, 5, 3, and 1 on the left and curves 13, 15, 17, and 19 on the right section, follow the temperature transient with certain time lags. Once the shock waves have reached the end wall of the tube, they are reflected as compression waves where the temperature experience a continuous increase.

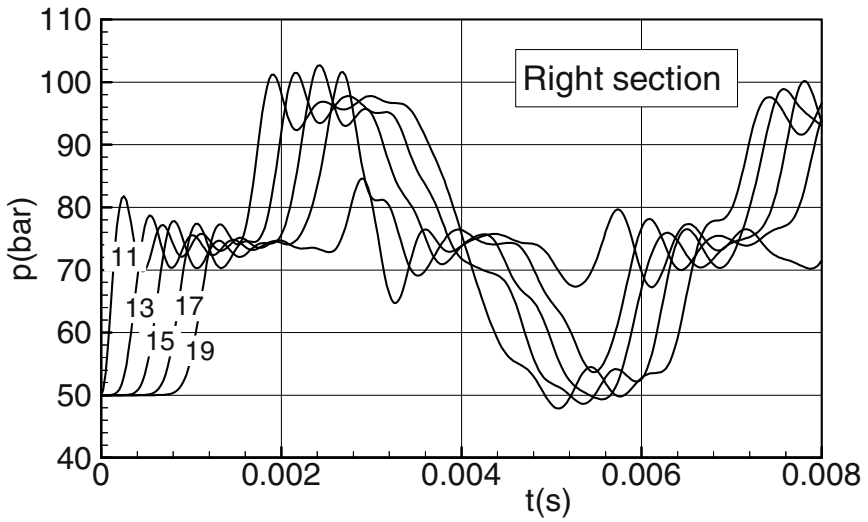

Fig. 14.5: Pressure transients within the shock tube. Right section includes all tube sections initially under high pressure of 50 bar, while the left section includes those initially at 100 bar

Slightly different temperature transient behavior of the right sections are revealed in Fig. 14.7. Compared to the temperature transients of the left sections, the right sections temperature transients seem to be inconsistent. However, a closer look at the pressure transients explains the physics underlying the temperature transients. For this purpose we consider the pressure transient curve 11, in Fig. 14.5. The location of this pressure transient is in the vicinity of the membrane's right side with

the pressure of 50 bar. Sudden rapture of the membrane simulated by a sudden ramp (Fig. 14.2) has caused a steep pressure rise from 50 bar to slightly above 80 bar.

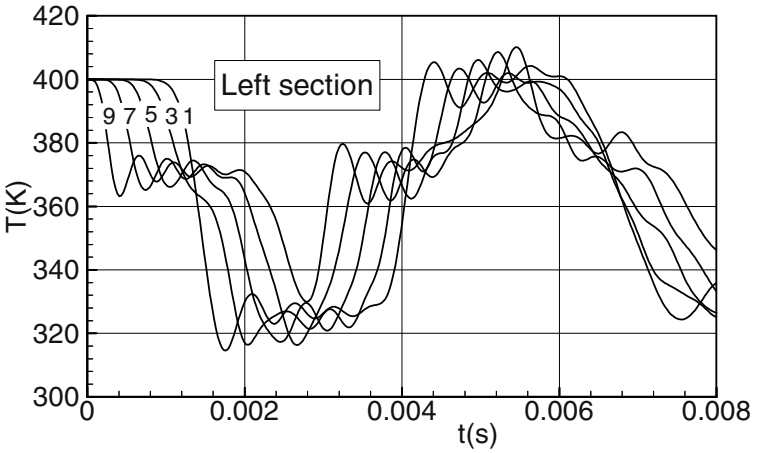

Fig. 14.6: Temperature transients within the left sections of the tube. Left and right sections includes all tube sections initially under temperature of 400 K

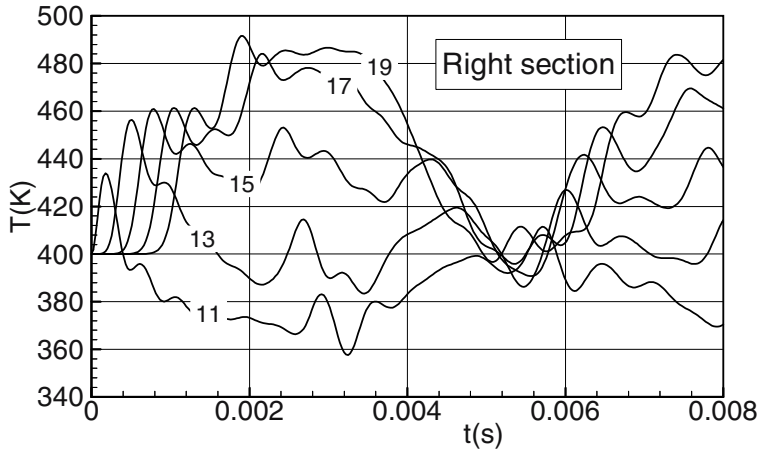

Fig. 14.7: Temperature transients within the right sections of the tube. Left and right sections includes all tube sections initially under temperature of 400 K

This pressure rise is followed by a damped oscillating wave that hits the opposite wall and reflects back with an initially increased pressure followed by a

damped oscillation. This behavior is in temperature distribution, where the pressure rise causes a temperature increase and vice versa. The temperature transients at downstream locations 12 to 20 follow the same trend.

Mass flow Transients: Figures 14.8 and 14.9 show the mass flow transients within the left section of the tube. The steep negative pressure gradient causes the mass

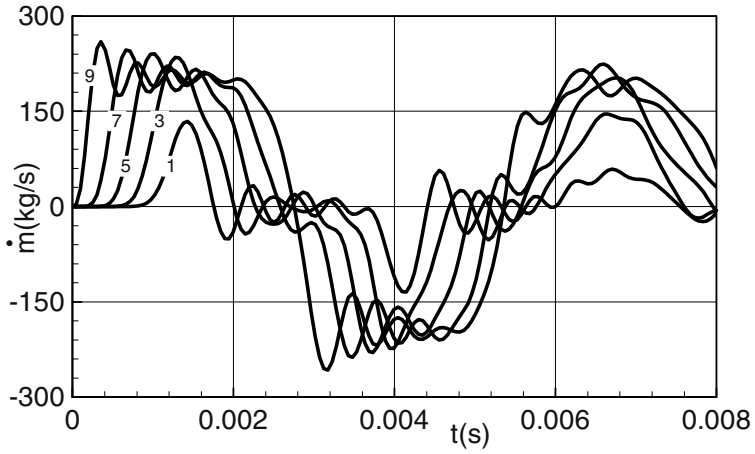

Fig. 14.8: Mass flow transients within left section of shock tube

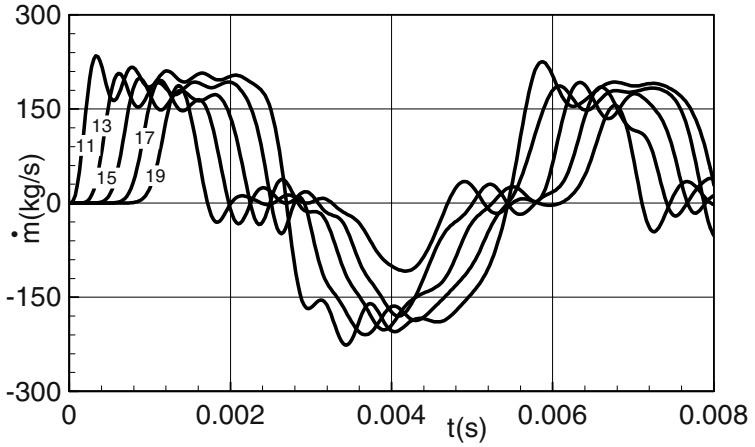

Fig. 14.9: Mass flow transients within the shock tube. The right section include all tube sections initially under high pressure of 50 bar, while the left section include those initially at 100 bar.

contained within the tube to perform aperiodic oscillatory motions. During the expansion process, curve 1, mass flows in the positive x-direction. It continues to stay positive as long as the pressure in individual sections are above their minimum. This means that the shock front has not reached the right wall yet. Once the shock front hits the right wall, it is reflected initiating a compression process that causes the mass flows in the negative x-direction. Figures 14.8 through 14.9 clearly show the dissipative nature of the compression and expansion process that results in diminishing the wave amplitudes and damping the frequency. The degree of damping depends on the magnutude of the friction coefficient c_f that includes the Re-number and surface roughness effects. For a sufficiently long computational time, the oscillations of pressure, temperature, and mass flow will decay. For $c_f = 0$, the a-periodic oscillating motion persists with no decay.

References, Chapter 14

14.1 Schobeiri T., 1986: "A General Computational Method for Simulation and Prediction of Transient Behavior of Gas Turbines," ASME-86-GT-180.

14.2 Schobeiri, M. T., Abouelkheir, M., Lippke, C., 1994, "GETRAN: A Generic, Modularly Structured Computer Code for Simulation of Dynamic Behavior of Aero-and Power Generation Gas Turbine Engines," an honor paper, ASME Transactions, *Journal of Gas Turbine and Power*, Vol. 1, pp. 483-494.

14.3 Schobeiri, M. T., Attia, M, Lippke, C., 1994, "Nonlinear Dynamic Simulation of Single and Multi-spool Core Engines, Part I: Theoretical Method," *AIAA, Journal of Propulsion and Power*, Volume 10, Number 6, pp. 855-862, 1994.

14.4 Schobeiri, M. T., Attia, M, Lippke, C., 1994, "Nonlinear Dynamic Simulation of Single and Multi-spool Core Engines, Part II: Modeling and Simulation Cases," *AIAA Journal of Propulsion and Power*, Volume 10, Number 6, pp. 863-867, 1994.

14.5 Prandtl, L., Oswatisch, K., Wiegarhd, K., 1984, "Führer durch die Strömung-lehre," 8. Auflage, Branschweig, Vieweg Verlag.

14.6 Shapiro, A.H., 1954, "The Dynamics and Thermodynamics of Compressible Fluid Flow," Vol. I, Ronald Press Company, New York, 1954.

14.7 Spurk, J, 1997, "Fluid mechanics," Springer-Verlag, berlin, Heidelberg, New York.

14.8 Becker, E., 1969, "Gasdynamik, Stuttgart, Teubner Studienbücher Mechanik, Leitfaden der angewandten Mathematik und Mechanik.

14.9 Kentfield, J. A. C., 1993, " Nonsteady, One-Dimensional, Internal, Compressible Flows, Theory and Applications,"Oxford University Press.

15 Modeling of Heat Exchangers, Combustion Chambers, Afterburners

This category of components includes recuperators, pre-heaters, regenerators, intercoolers, and aftercoolers. Within these components the process of heat exchange occurs between the high and low temperature sides. The working principle of these components is the same ([1], [2], [3], [4]). However, different working media are involved in the heat transfer process. More recently recuperators are applied to small and medium size gas turbine engines to improve their thermal efficiency. The exhaust thermal energy is used to warm up the compressor exit air before it enters the combustion chamber. A typical recuperator consists of a low pressure hot side flow path, a high pressure cold side flow path, and the wall that separates the two flow paths. A variety of design concepts are used to maximize the heat exchange between the hot and the cold side by improving the heat transfer coefficients. A cold side flow path may consist of a number of tubes with turbulators, fin pins, and other features that enhance the heat transfer coefficient. Based on the individual recuperator design concept, hot gas impinges on the tube surface in cross flow or counter flow directions. The working media entering and exiting the recuperator is generally combustion gas that exits the diffuser (hot side) and air that exits the compressor (cold side).

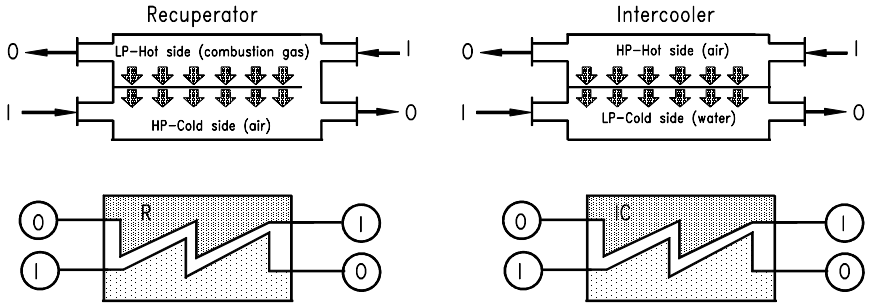

Fig. 15.1: Schematics of a recuperator and an intercooler and their modular representation, recuperator heat exchange between low pressure hot combustion gas from exhaust and high pressure cold air from compressor.

Intercooler is applied for intercooling the compressor mass flow before it enters the next stage of compression. In contrast to recuperators, the working medium on the intercooler hot side is air that exits the intermediate pressure compressor before entering the high pressure compressor. On the low pressure side, the working medium is water that removes the heat from the compressed air before entering the high pressure compressor for further compression. Aftercooler is used to aftercool the high pressure working medium for storage purposes in order to reduce the specific volume, thereby increasing the amount of stored air mass. This procedure is used, among other things, in compressed air storage facilities. Figure 15.1 shows schematics of a recuperator and an intercooler and their modular representation.

15.1 Modeling the Recuperators

Within this component, the heat exchange occurs between the high temperature low pressure combustion gas, and low temperature high pressure air. A schematic representation of a counter flow heat exchanger is given in Fig. 15.2. As shown, the heat exchange zone between the inlet, and exit plena on the hot, and cold sides is divided into (n-1) sections. The flow direction as well as the direction of the heat flow is shown in Fig.15.2. Since both the cold and hot gas streams have low subsonic velocities, they can be considered as incompressible, resulting in $D\rho/Dt$. For the sake of unifying treatment, we adopt the positive sign for heat transfer whenever heat is added to the wall. Furthermore, no cross section changes occur, so that $\nabla S = 0$. These specifications lead to a significant simplification of Eq. (12.33) and (12.52) that described the mass flow and temperature transients on the hot side.

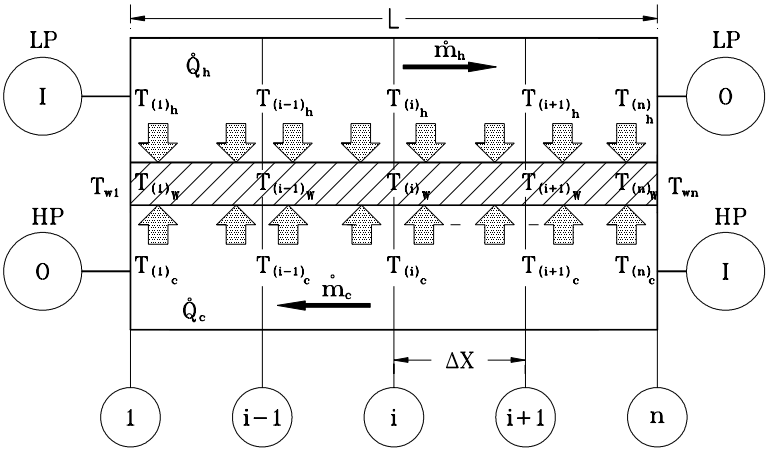

Fig. 15.2: A schematic segment of a heat exchanger with heat transfer, inlet and outlet plena on *hot* and *cold* sides

15.1.1 Recuperator Hot Side Transients

Starting from the equation of motion, the above simplifications lead to the following relations that describe the mass flow and temperature transients on the hot side. The mass flow dynamics is obtained by rearranging Eq. (12.34) to:

$$\frac{\partial \dot{m}_h}{\partial t} = \frac{R_h \, \dot{m}_h^2}{L_h \, S_h} \left(\frac{T_{h1}}{P_{h1}} - \frac{T_{hn}}{P_{hn}} \right) + \frac{S_h}{L_h} \left(P_{h1} - P_{hn} \right) - c_{fh} \frac{\dot{m}_h^2}{2 \, \rho_{hn} \, S_h \, D_{hn}} \tag{15.1}$$

The temperature transients are calculated by rearranging Eq. (12.52) as follows:

$$\begin{aligned} \frac{\partial T_{o,h,i+1}}{\partial t} = {} & \frac{-\kappa_{hk}}{c_{p,h,i+1} \, \rho_{hk} \, \Delta V_h} \left[\dot{m}_h \left(c_{p,h,i} \, T_{o,h,i} - c_{p,h,i+1} \, T_{o,h,i+1} \right) - \dot{Q}_{h_k} \right] \\ & - \left(\frac{\kappa_{hk} - 1}{c_{p,h,i+1}} \right) \frac{\dot{m}_h}{\rho_{hk}^2 \, S_h^2} \frac{\partial \dot{m}_h}{\partial t} \end{aligned} \tag{15.2}$$

15.1.2 Recuperator Cold Side Transients

The dynamic behavior of the recuperator cold side is determined from the equation of motion and energy, adopting the same simplification as for the flow on the hot side. The mass flow dynamics is obtained by rearranging Eq. (14.34) for the cold side as:

$$\frac{\partial \dot{m}_c}{\partial t} = \frac{R_c \, \dot{m}_c^2}{L_c \, S_c} \left(\frac{T_{c1}}{P_{c1}} - \frac{T_{cn}}{P_{cn}} \right) + \frac{S_h}{L_c} \left(P_{c1} - P_{cn} \right) - c_{fc} \frac{\dot{m}_c^2}{2 \, \rho_{cn} \, S_c \, D_{cn}} \tag{15.3}$$

The temperature transients are calculated by rearranging from Eq. (14.52) as:

$$\begin{aligned} \frac{\partial T_{o,c,i+1}}{\partial t} = {} & \frac{-\kappa_{ck}}{c_{p,c,i+1} \, \rho_{ck} \, \Delta V_h} \left[\dot{m}_h \left(c_{p,c,i} \, T_{o,c,i} - c_{p,c,i+1} \, T_{o,c,i+1} \right) - \dot{Q}_{c_k} \right] \\ & - \left(\frac{\kappa_{ck} - 1}{c_{p,c,i+1}} \right) \frac{\dot{m}_c}{\rho_{ck}^2 \, S_c 2} \frac{\partial \dot{m}_c}{\partial t} \end{aligned} \tag{15.4}$$

The subscripts *h* and *c* in Eqs. (15.1), (15.2) , (15.3) ΔX, and (15.4) refer to the *hot* and *cold* sides. The subscripts *i, i+1* refer to computational stations in Fig. 15.2. The

quantities with the subscript k are averaged between i and $i+1$. Equations (15.1), (15.2), (15.3), and (15.4) describe the mass flow transient as well as the temperature transients within volume elements of the width . The thermal energy flow portions $\dot{Q}_{h_k}$ and $\dot{Q}_{c_k}$ assume positive or negative signs based on the direction of the heat flow that pertain to the individual volume elements. They are calculated using the heat transfer coefficient and the temperature difference:

$$\dot{Q}_c = \bar{\alpha}_c A_c \Delta\bar{T}_c, \quad \dot{Q}_h = \bar{\alpha}_h A_h \Delta\bar{T}_h, \tag{15.5}$$

In Eq. (15.5), $\bar{\alpha}_c$, $\bar{\alpha}_h$ are the averaged heat transfer coefficients, $\Delta\bar{T}_c$, $\Delta\bar{T}_h$ the mean temperature and A_c, A_h the contact surfaces on the cold and hot sides, respectively. The mean temperatures are

$$\Delta\bar{T}_h = \bar{T}_{S_h} - \bar{T}_{\infty_h}, \quad \Delta\bar{T}_c = \bar{T}_{S_c} - \bar{T}_{\infty_c} \tag{15.6}$$

The subscripts S and ∞ in Eq. (15.6) refer to the *surfaces* outside the boundary layer respectively.

15.1.3 Coupling Condition Hot, Cold Side

The coupling condition between the cold and hot side is provided by the material temperature differential equation:

$$\frac{dT_w}{dt} = \frac{1}{\rho_w \, c_w \, \Delta v_w} \left(\dot{Q}_c + \dot{Q}_h \right) \tag{15.7}$$

where the $\dot{Q}_c$ and $\dot{Q}_{hc}$ assume negative values if the heat is rejected. For the special steady state case, Eq. (15.7) is reduced to:

$$\dot{Q}_c + \dot{Q}_h = 0 \tag{15.8}$$

15.1.4 Recuperator Heat Transfer Coefficient

The heat transfer coefficients on both sides are determined by using Nusselt based correlations:

$$Nu = 0.023 \, Re^{0.8} \, Pr^{0.4} \tag{15.9}$$

Kays and London [5] give a summary of empirical correlations for heat exchangers

with different geometries. The *Re*-number in Eq. (15.9), which must be individually determined for each side, is determined using the individual mass flow and hydraulic diameter

$$Re = \frac{V D_{hyd}}{\nu} = \frac{\dot{m} D_{hyd}}{S\mu} \tag{15.10}$$

With Eq. (15.9) and (15.10), the Statnon number can be calculated that determines the heat transfer coefficient:

$$St = \frac{Nu}{Re\,Pr} = \frac{\alpha}{\rho c_p V} \tag{15.11}$$

From Eq. (15.11), the individual heat transfer coefficient α is calculated as:

$$\alpha = St\,\rho c_p V = \frac{St\, c_p \dot{m}}{S} \tag{15.12}$$

with c_p as the specific heat at constant pressure and S the cross section. To account for the thermal resistance on the cold and hot side of the recuperator, the surface temperatures in Eqs. (15.5) and (15.6) must be replaced by the wall mean temperature. This is done by introducing the combined thermal resistance into Eq. (15.5)

$$\dot{Q}_c = \frac{A_c(\bar{T}_{S_c} - \bar{T}_{\infty_c})}{R_{w_c} + \dfrac{1}{\alpha_c}}, \quad \dot{Q}_h = \frac{A_h(\bar{T}_{S_h} - \bar{T}_{\infty_h})}{R_{w_h} + \dfrac{1}{\alpha_h}} \tag{15.13}$$

In most of the recuperators' high pressure sides, the working medium passes through a number of tubes. It is appropriate to approximate the thermal resistance R_{w_c} and R_{w_h} by an equivalent cylindrical pipe resistance. For determining the material temperature transients, Eq. (15.13) is inserted into (15.7). With the above equations and the following boundary conditions (15.14)

$$\begin{array}{llll} P_{h1} = P_{Ih} & P_{hn} = P_{Oh} & T_{o,h1} = T_{o,Ih} & T_{o,hn} = T_{o,Oh} \\ P_{c1} = P_{Oc} & P_{cn} = P_{Ic} & T_{o,c1} = T_{o,Oc} & T_{o,cn} = T_{o,Ic} \end{array} \tag{15.14}$$

the transient behavior of the recuperators is completely described.

15.2 Modeling Combustion Chamber

A generic representation of three different types of combustion chambers used in aero- and power generation gas turbine engines is given in Fig. 15.3. Key design features of gas turbine combustion chambers are given in [6] While the annular (a) and tubular type (b) combustion chambers are encountered in both aircraft and power generation gas turbines, the single cylindrical type (c) is utilized only in power generation gas turbine engines. All three types, regardless of their size and application field, share the following features: (1) Primary combustion zone, (2) secondary air zone for protecting the combustion chamber casing against high excessive flame radiation temperature, (3) mixing zone, where the hot gas and the rest of the secondary air are mixed, and (4) the fuel/air inlet nozzle. Since these features are common to the above, almost all of the other types of combustion chambers, a generic module can be designed that entails the above features. Figure 15.4 exhibits such a generic module. Figure 15.4 is a modular representation of a gas turbine component. It consists of a primary combustion zone, or primary zone, surrounded by *n* rows of segments, the secondary air zone, and the mixing zone. The actual combustion process occurs in the primary zone. The secondary air zone separates the hot primary combustion zone. The rows of segments in the combustion zone are subjected to a severe thermal loading due to direct flame radiation. Film and/or convection cooling on both the air and the gas sides cools these segments. The air required to cool these

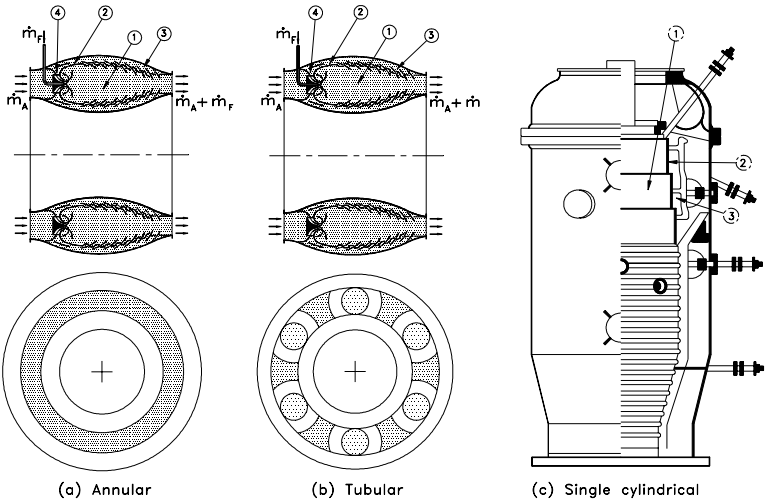

Fig. 15.3: Three different types of combustion chambers utilized in aircraft and power generation gas turbines. (a) Annular type, (b) tubular type, (c) heavy duty, single cylindrical power generation (BBC)

hot segments flows through finned cooling channels, thereby contributing to the convection cooling of the segments on the air side. The cooling air flow exiting from the j^{th} segment row effects the film cooling process on the gas side within the boundary layer in the next row of segments. At the end of that process, the cooling air mass flow is mixed completely with the primary air mass flow. The mass flow relationships prevailing in the primary, the cooling, and the mixing zones are substituted into the energy equation, already formulated. Their effect is significant, particularly in the case of energy balance, because they determine temperature distribution in the individual combustion chamber stations. For that reason, we first determine the mass flow relationships and then deal with the energy balance.

15.2.1. Mass Flow Transients

The combustion chamber mass flow is divided into primary mass flow, secondary (cooling) mass flow, and mixing mass flow, as shown in Fig. 15.4.

$$\dot{m}_{S_j} = \mu_j \dot{m}_S = \mu_j \mu_S \dot{m} \tag{15.15}$$

In Eq. (15.15), μ_p , μ_s, and μ_M denote the primary, secondary, and mixing mass flow ratios. If the primary zone consists of n rows of segments, the cooling mass flow for the j^{th} row of segments is:

$$\dot{m}_{S_j} = \mu_j \dot{m}_S = \mu_j \mu_S \dot{m} \tag{15.16}$$

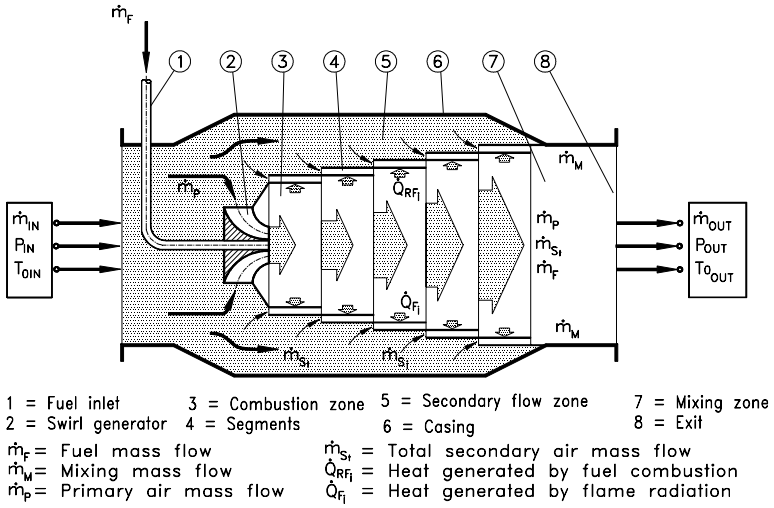

Fig. 15.4: Generic modular representation of a combustion chamber

Considering the fuel/air ratio, $\mu_F = \dot{m}_F / \dot{m}$, the mass flow within the j^{th} row of segments is:

$$\dot{m}_j = \sigma_j \dot{m} , \quad \sigma_j = \mu_F + \mu_P + \mu_S \sum_{\nu=1}^{j} \mu_\nu \tag{15.17}$$

To determine the transient behavior of a combustion chamber that has already been designed, it is necessary to start from the given ratios μ_P, μ_S, μ_M, and σ_j. For a new design, it is possible to vary these ratios until the desired solution is attained. The mass flow in the combustion chamber is obtained as the solution to the modified version of Eq. (14.34):

$$\frac{\partial \dot{m}}{\partial t} = \frac{R\dot{m}^2(1+\mu_F)^2}{\Delta x\, S}\left[\left(\frac{T}{P}\right)_I - \left(\frac{T}{P}\right)_O\right] + \\ + \frac{S}{\Delta x}\left(\frac{P_{o_I} - P_{o_O}}{1+\mu_F}\right) - c_f \frac{\dot{m}^2(1+\mu_F)}{2\rho S D_h} \tag{15.18}$$

In Eq. (15.18), the subscript *i* and *o* stand for the inlet and outlet plenum respectively. The volume of the combustion chamber is replaced here with an equivalent volume, a constant cross section *S* and length Δx. Thus, the pressures and temperatures in Eq. (15.18) represent inlet and outlet quantities, which must be known at the design point.

15.2.2. Temperature Transients

To determine the temperature transients for gas within the primary combustion zone and air within the secondary zone, we start from Eq. (14.52). Considering the air, fuel, and eventually, water as the main combustion components, Eq. (14.52) needs to be rearranged as follows:

$$\frac{\partial T_{o_{i+1}}}{\partial t} = \frac{1}{V\rho_{i+1}c_{p_{i+1}}}\left\{\sum_{k=1}^{K} \dot{m}_{ik}\left[\kappa_{i+1}(c_{p_i}T_{o_i})_k - c_{p_{i+1}}T_{o_{i+1}}\right]\right\} \\ + \frac{1}{V\rho_{i+1}c_{p_{i+1}}}\left[(1-\kappa_{i+1})\dot{m}_{i+1}\, c_{p_{i+1}}\, T_{o_{i+1}} - \kappa_{i+1}\dot{Q}_G\right] \\ - \left(\frac{1-\kappa_{i+1}}{c_{p_{i+1}}}\right)\left(\frac{\dot{m}}{\rho^2 S^2}\right)_{i+1} \frac{\partial \dot{m}_{i+1}}{\partial t} \tag{15.19}$$

with $\dot{Q}_G = V\,\Delta\dot{Q}$. The index *i* refers to the computation station in question. The mixing components are identified with the sequential index *k*, the upper summation limit for which *K* represents the number of constituents involved in a mixing and combustion process. The mixing components at the inlet station are the cooling air from secondary zone, the combustion air, and the fuel. For the cooling zone, Eq. (14.52) yields:

$$\frac{\partial T_{o_{i+1}}}{\partial t} = \frac{\kappa}{V\rho c_p}\left[\dot{m} c_p (T_{o_i} - T_{o_{i+1}}) - \dot{Q}_A\right] + \frac{1-\kappa}{c_p}\left(\frac{\dot{m}}{\rho^2 S^2}\right)\frac{\partial \dot{m}}{\partial t} \qquad (15.20)$$

with $\dot{Q}_A = V\,\Delta\dot{Q}$ .The temperature distribution within the segment material can be determined as follows using the heat conductance equation:

$$\frac{\partial \bar{T}_w}{\partial t} = \frac{1}{\rho_w c_w v_w}[\dot{Q}_h + \dot{Q}_c] \qquad (15.21)$$

The heat flows $\dot{Q}_G$, $\dot{Q}_A$, $\dot{Q}_h$, and $\dot{Q}_c$, are those supplied to or carried off from the part of the system. For the primary zone surrounded by a row of segments, $\dot{Q}_G$ is made up of the fuel heat, $\dot{Q}_F$, the flame radiation heat, $\dot{Q}_{RF}$, and the convection heat, $\dot{Q}_{CG}$, on the gas (or hot) side:

$$\dot{Q}_G = \dot{Q}_F + \dot{Q}_{RF} + \dot{Q}_{CG} \qquad (15.22)$$

The increased temperature level produced in the segments from the direct flame radiation is reduced to an acceptable level by an intensive film cooling on the gas side and convective heat removal on the air side. The segments are therefore subjected to the following thermal loading on the gas side (or hot side):

$$\dot{Q}_h = \dot{Q}_{RF} + \dot{Q}_{Fi} \qquad (15.23)$$

with $\dot{Q}_{Fi}$ standing for the amount of heat carried off by the film cooling. The heat flow carried off on the air side, $\dot{Q}_c$, consists of a convection and a radiation component. The latter is due to the difference in temperature between the cold air enclosure liner and the hot surface of the fins. As a result we find:

$$\dot{Q}_A = \dot{Q}_c = \dot{Q}_{CA} + \dot{Q}_{RA} \qquad (15.24)$$

For the film cooling:

$$\dot{Q}_{Fi} = \bar{\alpha}_{Fi} S_G (\bar{T}_{Fi} - \bar{T}_w) \tag{15.25}$$

with $\bar{\alpha}_{Fi}$ as the average heat transfer coefficient and $\bar{T}_{Fi}$ the average film temperature (Schobeiri, 1987). The convective heat removal on the air side is obtained from:

$$\dot{Q}_{CA} = \bar{\alpha}_A S_A (\bar{T}_w - \bar{T}_A) \tag{15.26}$$

The radiation heat flows, $\dot{Q}_{RA}$, $\dot{Q}_{RF}$, have been determined from Schobeiri (1987).

15.2.3 Combustion Chamber Heat Transfer

Heat transfer processes in combustion chambers involve several mechanisms. To distinguish these mechanisms, we consider a section of the heavy duty combustion chamber shown in Fig. 15.3 with the corresponding generic module Fig. 15.4. Different heat transfer mechanisms are shown in Fig. 15.5.

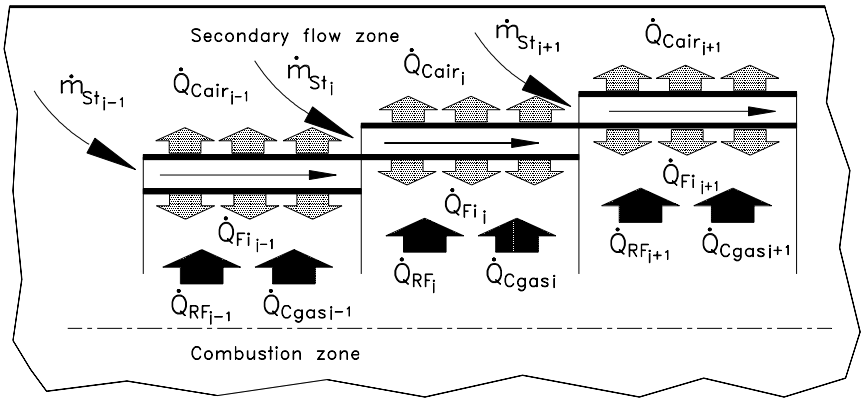

Fig. 15.5: Details of heat transfer radiation, conduction, and convection heat transfer along a generic segment of a gas turbine combustion chamber

Considering the combustion zone on the hot (or gas side) of a segment that separates the primary combustion zone from the secondary flow zone, as shown in Fig. 15. 5, the following heat transfer types are distinguished: (1) $\dot{Q}_{Cgas_i}$ is added to the segments by convection, (2) $\dot{Q}_{RF_i}$ is added by the flame radiation, (3) $\dot{Q}_{Fl_i}$ is removed from the gas side by film jets, (4) $\dot{Q}_{Cair_i}$ is removed from the segment on the air side by convection, and (5) the conduction through the segment wall couples the heat transfer portions on both sides of the segment. Convective and conductive heat transfer types are discussed in Section 15.1. For the jet film cooling heat transfer, correlations by Juhasz and Marek [7]can be used. On the primary combustion side,

the flame radiation is, by far, the major contributor to the radiation heat transfer. There is also radiation on the secondary air side between the segment material, enclosed secondary air, and the casing. However, its contribution compared to the flame radiation is negligibly small. The basis for radiative heat transfer is the Planck's [8] spectral distribution of radiation for an ideal radiating body, called *black body*

$$E_{\lambda,b}(T) = \frac{C_1}{\lambda^5\left(Exp(C_2/\lambda T) - 1\right)} \quad W/m^2\mu m \tag{15.27}$$

In Eq. (15.27), $E_{\lambda,b}(T)$ is the spectral emissive power of a black body as a function of wave length and temperature of the emitting surface, λ is the wave length in microns (or meters), T the absolute temperature of the body, and the subscript b stands for black ideal body. The constants are $C_1 = 3.742\times10^8\, W\mu m^4/m^2$ and $C_1 = 1.439\times10^4\mu mK$. Equation (15.27) is derived for an emitting surface in a vacuum, where the index of refraction is unity. This index is defined as the ratio of velocity of light in a vacuum to the velocity of light in a non-vacuum environment. The spectral distribution described by Eq. (15.27) is plotted in Fig. 15.6 with body temperature as a parameter.

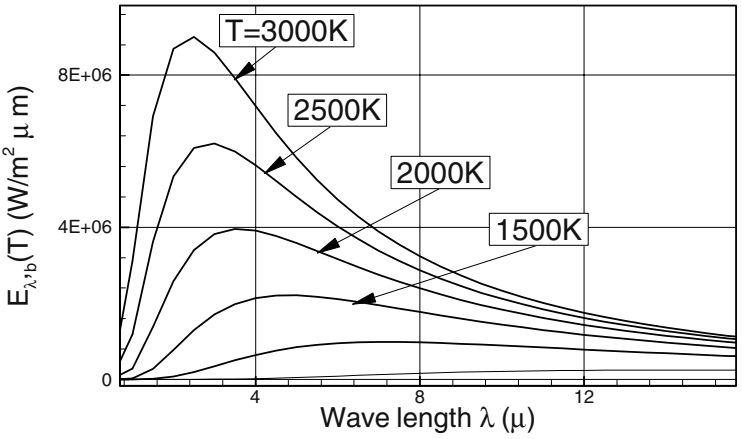

Fig. 15.6: Spectral emissive power as a function of wave length with body temperature as parameter described by Planck's Eq. (15.27)

Equation (15.27) describes the radiation power for each given wave length $\lambda = c/\nu$ with c as the speed of light and ν wave frequency. For combustion chamber application, it is necessary to find the total energy emitted by the body. This can be found by integrating Eq. (15.27):

$$E_b(T) = \int_0^\infty E_{\lambda,b}(T)\,d\lambda = \sigma T^4 \tag{15.28}$$

with σ as the Stefan-Bolzmann constant. Equation (15.28), (15.29) can be applied to two or more bodies that are in radiative interaction. Consider the simplest case of two parallel black surfaces that are at different temperatures. The net rate of heat transfer between these two surfaces is:

$$\dot{Q} = \sigma\left(T^4_1\, A_1 - T^4_2\, A_2\right) \tag{15.29}$$

For radiative heat transfer, the flame shape may be approximated as a cylinder.

15.3 Example: Startup and Shutdown of a Combustion Chamber-Preheater System

The example deals with the startup and shutdown process of a system consisting of a combustion chamber and pre-heater as shown in Figure 15.7. The combustion chamber is connected to plenum (1), which is at constant pressure and temperature. Constant air flow enters the combustion chamber which is connected to plenum (2). A major portion of the air passes through a pipe and exits the system at plenum (6). A minor portion of air enters the hot side of the pre-heater and leaves it at plenum (3). The cold side of the pre-heater continuously receives air at constant pressure and

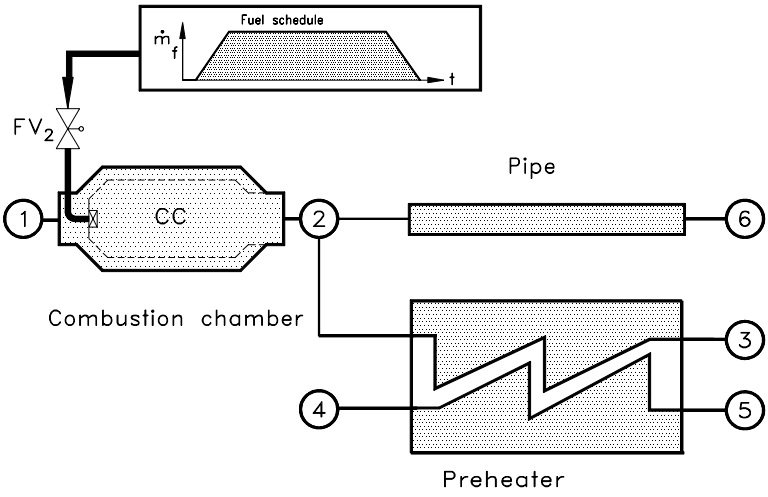

Fig. 15.7: A system consisting of a combustion chamber, a pre-heater and a pipe

room temperature from plenum (4) and exits the cold side pre-heater at plenum (5). The fuel valve is programmed to provide the combustion chamber with the fuel schedule $\dot{m} = \dot{m}(t)$. The fuel schedule is qualitatively shown in Fig. 15.7.

Similar to the cases discussed previously, each component of the above system represented by the corresponding module is described by a system of differential equations we discussed above. Prescribing the following boundary conditions:

$$\begin{array}{lllll} P_1 = const. & P_3 = const. & P_4 = const. & P_5 = const & P_6 = const. \\ T_{01} = const. & T_{03} = const. & T_{04} = const. & T_{05} = const. & T_{06} = const. \end{array} \quad (15.30)$$

the systems of the differential equations can be solved. Using the boundary conditions (15.30), we first simulate a cold start followed by design point operation and the subsequent shutdown. This process is controlled by the fuel schedule shown in Fig. 15.8.

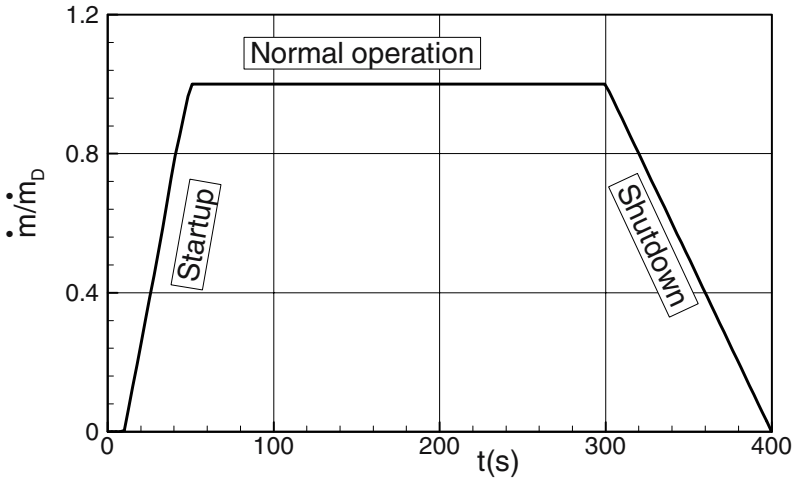

Fig. 15.8: Combustion chamber fuel schedule: Startup, design operation, shutdown

Starting from a cold combustion chamber and pre-heater, cold air flows through the entire system for about 10 seconds. At $t = 10\ s$, the fuel valve starts to open adding fuel continuously until the design fuel mass flow of has been reached. During the fuel addition, the temperature of the entire system starts to rise. The combustion chamber gas temperature, Fig. 15.9, reacts to this event with a corresponding increase. Curve 1 exhibits the temperature of the core flow. Mixing with the secondary air significantly reduces the gas temperature to the exit temperature level of slightly above 1000 K, curve 2.

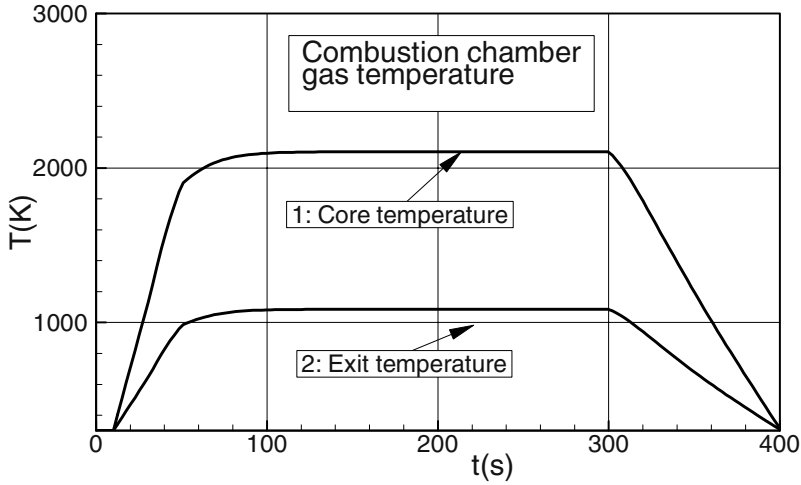

Fig. 15.9: Combustion chamber gas temperature, startup, design operation, shutdown

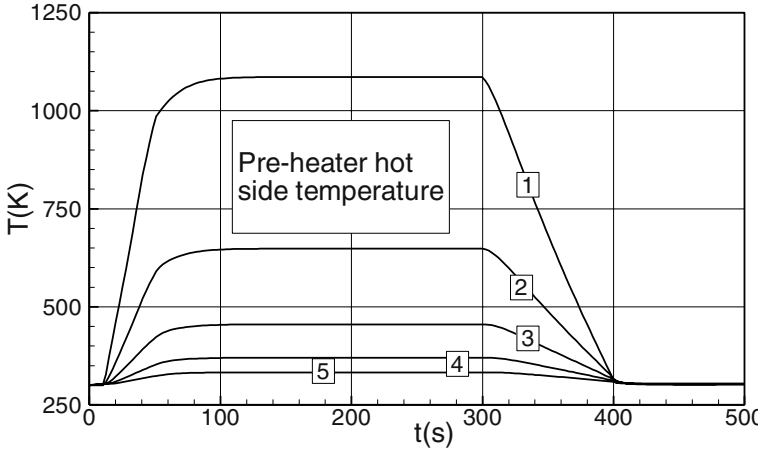

Fig. 15.10: Pre-heater hot side temperature distribution for startup, design operation, shutdown

The combustion gas enters the hot side of the pre-heater and increases its temperature as seen in Fig. 15.9. Curves 1 and 2 represent the gas temperature of the pre-heater front portion, while curves 3 and 4 represent the mid-section gas temperature. The exit temperature is represented by curve 5.

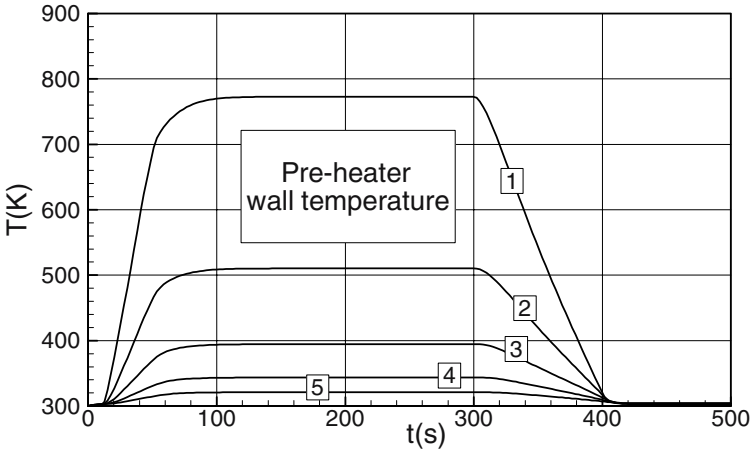

Fig. 15.11: Pre-heater wall temperature at five different locations

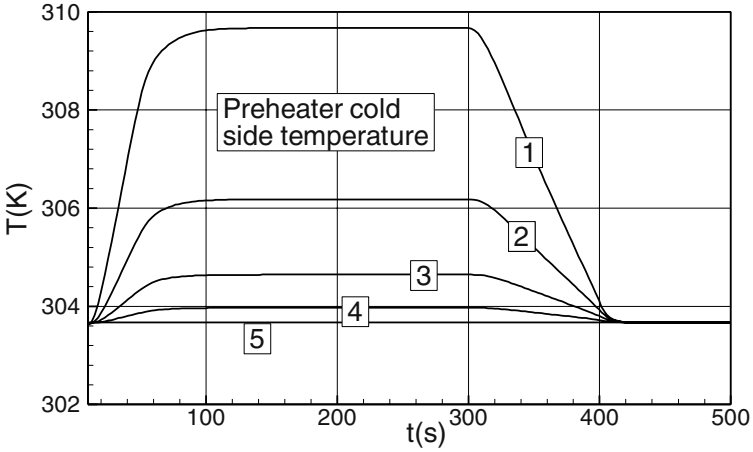

Fig. 15.12: Pre-heater cold side temperature

Heat is transferred from the hot side to the cold side of the pre-heater by means of convection and conduction through the pre-heater material plotted in Fig. 15.10. Curves 1 and 2 represent the gas temperature of the pre-heater metal front portion, while curves 3 and 4 represent the mid-section metal temperature. The metal temperature of the rear portion is represented by curve 5. The metal temperature distributions in Fig. 15.11 correspond to the temperatures on the hot side. The heat transferred to the cold side causes the cold side temperature to rise as seen in Fig. 15.12.

15.4 Modeling of Afterburners

This component, from a modeling point of view, exhibits a simplified version of the combustion chamber discussed in the previous section. This component, and its modular representation is shown in Fig. 15.13. The modeling of this component follows the same procedure as the combustion chamber. However, because of the absence of secondary flow, the mass flow ratios μ_p, μ_s, and μ_M have the following values: $\mu_p = 1$, $\mu_s = 0$, and $\mu_M = 0$.

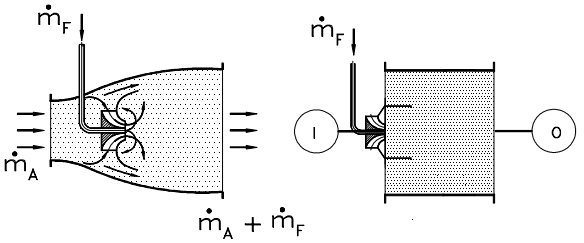

Fig. 15.13: Schematic of an afterburner module

References, Chapter 15

15.1 Schobeiri T., 1986: "A General Computational Method for Simulation and Prediction of Transient Behavior of Gas Turbines," ASME-86-GT-180.

15.2 Schobeiri, M. T., Abouelkheir, M., Lippke, C., 1994, "GETRAN: A Generic, Modularly Structured Computer Code for Simulation of Dynamic Behavior of Aero-and Power Generation Gas Turbine Engines," an honor paper, ASME Transactions, *Journal of Gas Turbine and Power*, Vol. 1, pp. 483-494.

15.3 Schobeiri, M. T., Attia, M, Lippke, C., 1994, "Nonlinear Dynamic Simulation of Single and Multi-spool Core Engines, Part I, II: Theoretical Method, Simulation Cases " *AIAA, Journal of Propulsion and Power*, Volume 10, Number 6, pp. 855-867, 1994.

15.4 Kays, W.M, London, A. L., 1984, "Compact Heat Exchangers," McGraw-Hill Book Company, third Edition.

15.5 Lefebvre, AS.H., 1983, "Gas Turbine Combustion,"Hemisphere Publishing Corporation.

15.6 Marek, C. J., and Huhasz, A. J., 1974, "Simulataneous Film and Convection Cooling of a Plate inserted in the Exhaust Stream of a Gas Turbine Combustor, NASA TND-7689.

15.7 Planck, M., 1959, " Theory of Heat Radiation," Dover Publication, Inc, New York.

16 Modeling the Compressor Component, Design and Off-Design

As mentioned in Chapter 1, the function of a compressor is to increase the total pressure of the working fluid. According to the conservation law of energy, this total pressure increase requires external energy input, which must be added to the system in the form of mechanical energy. The compressor rotor blades exert forces on the working medium thereby increasing its total pressure. Based on efficiency and performance requirements, three types of compressor designs are applied. These are axial flow compressors, radial or centrifugal compressors, and mixed flow compressors. Axial flow compressors are characterized by a negligible change of the radius along the streamline in the axial direction. As a result, comparison of the contribution of the circumferential kinetic energy difference $(U_3^2 - U_2^2)/2$ to the pressure buildup is marginal. In contrast, the above difference is substantial for a radial compressor stage, where it significantly contributes to increasing the total pressure as discussed in Chapter 5.

During the compression process, the fluid particles are subjected to a positive pressure gradient environment that may cause the boundary layer along the compressor blade surface to separate. To avoid separation, the flow deflection across each stage and thus the stage pressure ratio is kept within certain limits discussed in the following section. Compared to an axial stage, much higher relative stage pressure ratios $\pi_{rad}/\pi_{ax} > 5$ at relatively moderate flow deflections can be achieved by centrifugal compressors. However, geometry, mass flow, efficiency, and material constraints place limits on utilizing radial compressors. Radial compressors designed for high stage pressure ratios and mass flows comparable to those of axial compressors require substantially larger exit diameters. This can be considered an acceptable solution for industrial applications, but is not a practical solution for implementing into gas turbine engines. In addition, for gas turbine applications, high compressor efficiencies are required to achieve acceptable thermal efficiencies. While the die efficiencies of advanced axial compressors have already exceeded 91.5% range, those of advanced centrifugal compressors are still below 90%. Power generation gas turbine engines of 10 MW and above as well as medium and large aircraft engines use axial compressor design. Small gas turbines, turbochargers for small and large Diesel engines have radial impellers that generate pressure ratios above 5. Compact engines for turboprop applications may have a combination of both. In this case a relatively high efficiency multi-stage axial compressor is followed

by a lower efficiency centrifugal compressor to achieve the required engine pressure ratio at smaller stage numbers.

Further stage pressure buildup is achieved by increasing the inlet relative Mach number $M_{2rel.} = W_2 / c_2$. In case of subsonic axial flow compressors with $M_{2rel.} < 1$, the compression process is primarily established by *diffusion* and *flow deflection*. However, in the case of supersonic relative Mach number $M_{2rel.} > 1$ that occupies the entire compressor blade height from hub to tip, the formation of oblique shock waves followed by normal shocks as discussed in Chapter 4 substantially contributes to a major pressure increase. However, the increase of stage pressure ratio as a result of compression shocks is associated with additional shock losses that reduce the stage efficiency. To achieve a higher stage pressure ratio at an acceptable loss level, the compressor stage can be designed as *transonic compressor stage*. In this case, the relative Mach number at the hub is subsonic and at the tip supersonic, with transonic Mach range in between. Transonic compressor stage design is applied to the first compressor stage with a relatively low aspect ratio of high performance gas turbine engines.

In this chapter, we first investigate several loss mechanisms and correlations that are specific to compressor component. Using these correlations, first the basic concept for a row-by-row adiabatic calculation method is presented that accurately predicts the design and off-design behavior of single and multi-stage compressors. With the aid of this method, efficiency and performance maps are easily generated. The chapter is then enhanced to calculate the diabatic compression process where the blade rows exchange thermal energy with the working medium and vice versa. The above methods provide three different options for dynamically simulating the compressor component. The first option is to utilize the steady state compressor performance maps associated with dynamic coupling. The second option considers the row-by-row adiabatic calculation. Finally, the third option uses the diabatic compression process. Examples are presented.

16.1 Compressor Losses

In Chapter 7 we attempted to provide the basic physics of different loss mechanisms for accelerating and decelerating cascades from a unifying point of view. This section deals with particular loss mechanisms encountered in compressors. Because of its significance to aircraft gas turbine engines, manufacturers and research centers have been focusing their attention on developing compressor components with higher efficiency. To predict the compressor stage efficiency accurately, compressor designers often use loss correlations that reflect different loss mechanisms within the compressor stage flow field. In the early fifties, Lieblein and his co-workers [1], [2], [3], [4], [5] conducted fundamental research in compressor cascade and stage aerodynamics. Their research work, NASA-Report SP-36 [6], is a guideline for compressor designers. Miller and Hartmann [7], Miller et al. [8], and Schwenk et al.

[9] initiated their fundamental research on transonic compressors where they primarily investigated the shock losses. Gostelow et al. [10], Gostelow [11], Seylor and Smith [12], Seylor and Gostelow [13], Gostelow and Krabacher [14], Krabacher and Gostelow [15], [16] focused their experimental research on single-stage high Mach number compressor stages. Their comprehensive experimental research includes the performance evaluation of several rotors. Monsarrat et al. [17] performed similar investigations on single-stage high Mach number compressor stages. Koch and Smith [18] presented a method for calculating the design point efficiency potential of a multi-stage compressor. Schobeiri [19] investigated the individual loss mechanisms that occur in an advanced compressor stage. He developed a new shock loss model, introduced a modified diffusion factor and re-evaluated the relevant experimental data published by NASA. Recent investigations by König et al. [20] investigate the loss and deviation angles for transonic blading.

The total pressure losses encountered in an advanced compressor stage are: (1a) The blade primary losses generated by the wall shear stress, which is proportional to the local velocity deformation. Since the blade mid-section is not affected by the secondary flow that originates from the hub and casing, the primary losses are dominant. (1b) The trailing edge mixing losses are due to the thickness of the trailing edge and the boundary layer thicknesses on the suction and pressure surfaces that causes wake defect, mixing, and thus additional entropy increase. From an experimental point of view, these two losses are not separable since the total pressure measurements occur at a certain distance downstream of the trailing edge plane and inherently include the wake total pressure defect. The combination of these two losses is frequently called profile loss. (2) Shock losses are encountered in compressor stages with high transonic to supersonic inlet relative flow conditions. Based on an angle incidence and the shock position, these losses may generate considerable entropy increases that result in significant deterioration of the stage efficiency. The shock losses are approximately of the same order of magnitude as the profile losses. (3) Secondary losses due to the end wall boundary layer development and blade-wall clearances. (4) Secondary flow losses are also present for compressor blades with shrouds. A comprehensive treatment of losses is found in Schobeiri [21], [22].

This chapter focuses on three issues: (1) A new modified diffusion factor that describes the blade loading for the rectilinear and annular cascades, as well as for the entire compressor stage. This new diffusion factor, which includes the compressibility effects, allows the loss parameters to be systematically correlated with the diffusion factor. (2) A new shock loss model is presented that overcomes the weakness of the existing loss models described by Levine [23], Balzer [24] and Swan [25]. (3) The existing published data are re-evaluated and detailed correlations are presented.

16.1.1 Profile Losses

Lieblein and Roudebusch [26] derived the expression for profile loss coefficient as a function of cascade geometry, flow angles, and the boundary layer parameters

shown in Eq. (16.1):

$$\zeta_P = \sigma \left(\frac{\delta_2}{c} \right) \left(\frac{\sin\beta_1}{\sin\beta_2} \right)^2 \left(\frac{1 + H_{32}}{\left(1 - \frac{\delta_2}{c} \sigma H_{12} \right)^3} \right) \tag{16.1}$$

with the form factor $H_{32} = f(H_{12})$. Among the boundary layer parameters in Eq. (16.1), the momentum thickness δ_2 is of primary importance. It gives a direct relationship between the separation point and the free-stream velocity gradient (or pressure gradient) shown in the following von Kàrmàn integral equation for incompressible flow:

$$\frac{\tau_o}{\rho V^2} = \frac{d\delta_2}{dx} + \left(2 + H_{12} \right) \frac{\delta_2}{V} \frac{dV}{dx} \tag{16.2}$$

with τ_o as the wall shear stress and H_{12} the form parameter. For a highly loaded compressor blade, the velocity distribution may separate. Consequently, the wall shear stress vanishes and Eq. (16.2) may reduce to:

$$\frac{d\delta_2}{dx} = -\left(2 + H_{12} \right) \frac{\delta_2}{V} \frac{dV}{dx} \tag{16.3}$$

Equation (16.3) shows a direct relation between the blade velocity gradient and the momentum thickness. Appropriate differences can approximate the above differentials. As an appropriate measure for the velocity gradient, Lieblein et al. [27] introduced the equivalent diffusion factor:

$$D_{eq} = \frac{V_{\max}}{V_2} = \frac{V_1}{V_2} \frac{V_{\max}}{V_1} \tag{16.4}$$

with V_{max} as the maximum velocity on the suction surface shown in Fig. 16.1. This velocity ratio, which changes by changing the flow deflection given by the velocity triangle, properly reflects the blade loading situation. However, it requires the knowledge of the maximum velocity at different flow deflections, which is not always given. From a compressor designer point of view, relating the blade loading to the actual velocity triangle is most appropriate.

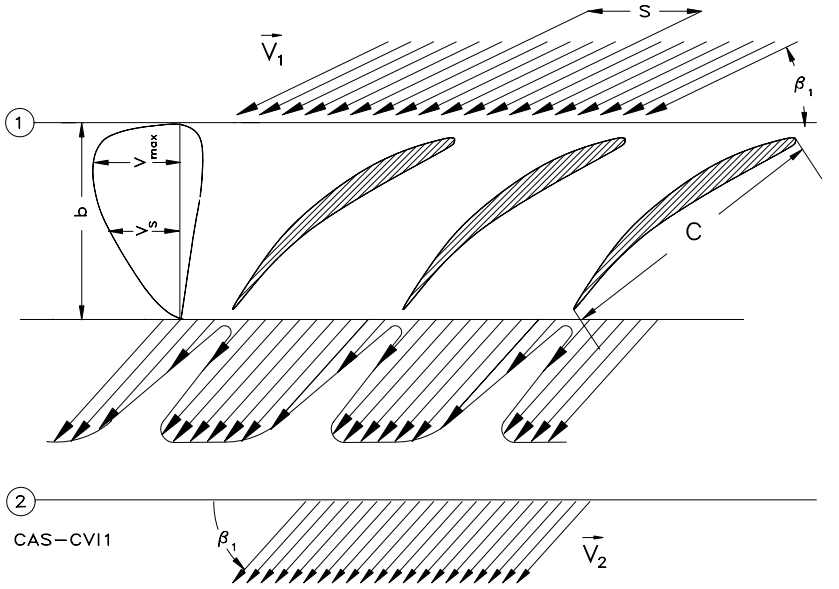

Fig. 16.1: Schematic representation of a compressor cascade flow

16.1.2 Diffusion Factor

We introduce the dimensionless parameter $\eta = V_S / V_1$, $\xi = x/b$ and approximate the dimensionless velocity distribution η by a polynomial

$$\eta = \sum_{n=0}^{N} a_n \xi^n = a_0 + a_1 \xi + a_2 \xi^2 + \cdots\cdots\cdots + a_n \xi^n \tag{16.5}$$

The Taylor expansion in the near of ξ_{max} results in:

$$\eta = \eta_{max} + \frac{d\eta}{d\xi} \Delta\xi + \frac{1}{2} \frac{d^2\eta}{d\xi^2} \Delta\xi^2 + \cdots\cdots \tag{16.6}$$

with $\Delta\xi = \xi - \xi_{max}$. Neglecting the higher order terms, Eq. (16.6) can reduce to

$$\eta = \eta_{max} + \left(\frac{d\eta}{d\xi}\right)_{\xi_{max}} \left(\xi - \xi_{max}\right) \tag{16.7}$$

The velocity slope is found from Eq. (16.5):

$$\left(\frac{d\eta}{d\xi}\right)_{\xi_{max}} = a_1 + 2a_2\,\xi_{max} \tag{16.8}$$

Incorporating Eq. (16.8) into Eq. (16.7) results in:

$$\eta = \eta_{max} + C_1\xi + C_2 \tag{16.9}$$

with the constants: $C_1 = a_1 + 2a_2\,\xi_{max}$ and $C_2 = -C_1\xi_{max}$. The tangential component of the force acting on the blade (see Fig. 16.1) is calculated by integrating the pressure distribution along the blade suction and pressure surfaces using the Bernoulli equation:

$$T = T_P - T_S = \int_o^b \left(p_P - P_S\right) dx = \frac{1}{2}\rho \int_o^b \left(V_S^2 - V_P^2\right) dx \tag{16.10}$$

Since only the contribution of the suction surface is considered for estimating the diffusion factor, the second term in the integrand may be set equal to zero. Incorporating Eq. (16.9) into Eq. (16.10) results in:

$$\frac{T}{\frac{1}{2}\rho V_1^2 b} = \eta_{max}^2 + \left(C_1 + 2C_2\right)\eta_{max} + \frac{1}{3}C_1^2 + C_1C_2 + C_2^2 \tag{16.11}$$

The force component T can also be calculated using the momentum equation in the tangential direction:

$$T = s\rho V_a \left(V_{t1} - V_{t2}\right) \tag{16.12}$$

with s and ρ as the blade spacing and the flow density, V_a and V_t as the axial and tangential velocity components. Inserting the velocity components defined in Fig. 16.1 into Eq. (16.12), it becomes:

$$\frac{T}{\frac{1}{2}\rho V_1^2 b} = 2\frac{s}{b}\sin^2\beta_1\left(\cot\beta_1 - \cot\beta_2\right) \tag{16.13}$$

Equating Eq. (16.11) and (16.13) results in the following relationship:

$$\eta_{max}^2 + D_1 \eta_{max} + D_3 = 0 \tag{16.14}$$

with the coefficients D_i as:

$$\begin{aligned} D_1 &= C_1 + 2\,C_2 \\ D_2 &= C_1\,C_2 + C_2^2 + \frac{1}{3}\,C_1^2 \\ D_3 &= D_2 - \frac{2s}{b}\,\sin^2\beta_1\left(\cot\beta_1 - \cot\beta_2\right) \end{aligned} \tag{16.15}$$

The solution of Eq. (16.14) after neglecting the higher order terms in D_3 yields:

$$\eta_{max} = \frac{V_{max}}{V_1} = K_1\,\frac{\sin^2\beta_1}{\sigma}\left(\cot\beta_1 - \cot\beta_2\right) + K_2 = K_1 G + K_2 \tag{16.16}$$

Equation (16.16) exhibits a special case of Eq. (16.14) and gives an explicit relationship between the maximum velocity V_{max} and the cascade circulation function $G = \frac{\sin^2\beta_1}{\sigma}\left(\cot\beta_1 - \cot\beta_2\right)$ in the bracket. Using the NACA-65(A10) series and the circular arc blade C.4, for the optimum flow condition denoted by (*), the constants in Eq. (16.16) are experimentally determined by Lieblein [28]:

$$\eta_{max}^* = -\left(\frac{V_{max}}{V_1}\right)^* = K_1 G^* + K_2 = 1.12 + 0.6\,\frac{\sin^2\beta_1}{\sigma}\left(\cot\beta_1 - \cot\beta_2\right) \tag{16.17}$$

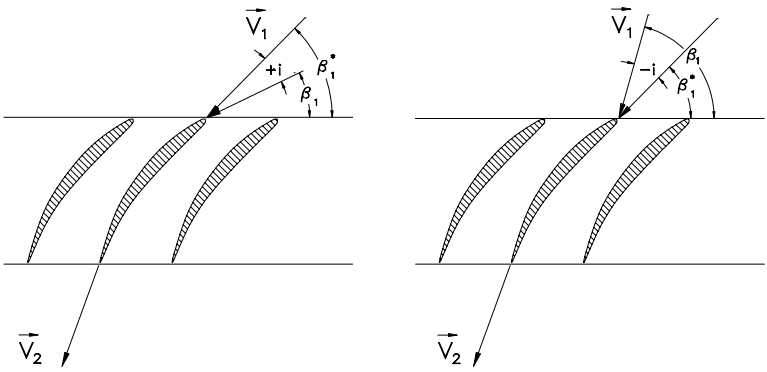

Fig. 16.2: Compressor cascade actual and optimum inlet flow angles with positive and negative incidence angle i. condition.

Equation (16.14) is generally valid for any arbitrary inlet flow angle including the off-design incidence angles. However, the compressor designer prefers to relate the off-design η_{max} to the design point. For this purpose, Lieblein [29] (??1975 or 1957) introduced an empirical correlation for V_{max}/V_1 for positive angles of attack as a function of the incidence angle $i = \beta_1 - \beta^*_{1,}$, Fig. 16.2.

$$\eta_{max} = \left(\frac{V_{max}}{V_1} \right) = 1.12 + 0.61\, G^* + a \left(\beta_1 - \beta_1^* \right)^{1.42} \tag{16.18}$$

where a = 0.0117 for the NACA 65(A10) and a = 0.0070 for the C.4 circular arc blades. Equation (16.18) accurately estimates the maximum velocity ratio for a positive incidence. However, it cannot be used for negative incidence angles $i = \beta - \beta^*$ because of the rational exponent of the argument $\beta - \beta^*$. Introducing the angle $\beta = \beta^* + i$ into Eq. (16.14) eliminates this deficiency, and after some rearranging we obtain:

$$\eta_{max} = \eta^*_{max} + \sum_{n=1}^{N} a_n \left(\beta_1 - \beta_1^* \right)^n \tag{16.19}$$

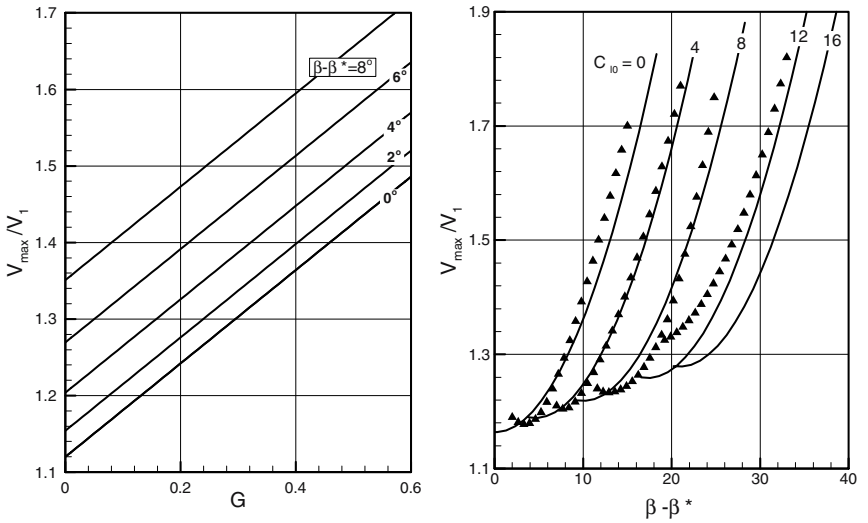

Fig. 16.3: Velocity ratio (left) as a function of the circulation function G with the incidence angle $i = \beta - \beta^*$ as parameter, and (right) as a function of incidence angle $i = \beta - \beta^*$ with lift coefficient C_{l0} as parameter, experiments represented by symbols from taken from Lieblein.

Neglecting terms with n > 2, Eq. (16.19) becomes:

$$\eta_{max} = \left(\frac{V_{max}}{V_1}\right) = \left(\frac{V_{max}}{V_1}\right)^* + a_1(\beta_1 - \beta_1^*) + a_2(\beta_1 - \beta_1^*)^2 \qquad (16.20)$$

Re-evaluating the experimental results by Lieblein [30] leads to $a_1 = 0.746$ and $a_2 = 6.5$. Equation (16.20) enables the calculation of the velocity ratio and thus the diffusion factor for any off-stall operation range. Fig. 16.3 shows the results of Eq. (16.20), where the velocity ratio is plotted against the circulation function G with the incidence angle $i = \beta_1 - \beta^*_1$ as a parameter.

Compared with Lieblein's correlation Eq. (16.18), the new correlation Eq. (16.20) yields more accurate results. This statement is also true for Fig. 16.3, where the maximum velocity ratio is plotted versus the incidence angle with the lift coefficient C_{l0} as parameter.

16.1.3 Generalized Maximum Velocity Ratio for Cascade, Stage

Lieblein's correlations for the maximum velocity ratio and their experimental verifications were based exclusively on the two-dimensional incompressible cascade flow situation. Significant effects such as compressibility and three-dimensionality were not considered. Furthermore, changes of axial velocity component and streamline curvature, which are always present in a modern compressor, were ignored. Finally, the effect of rotational motion on circulation was disregarded. This section includes the above-mentioned effects in the maximum velocity ratio by employing a generalized circulation concept that leads to a modified diffusion factor. Starting from the Kutta-Joukowsky's lift equation (lift force/unit span) with ρ_∞, V_∞ as the free stream density, velocity, and Γ as the circulation:

$$\boldsymbol{A} = \rho_\infty \boldsymbol{V}_\infty \times \boldsymbol{\Gamma} \qquad (16.21)$$

Using the definition in Fig. 16.4 for linear and annular compressor cascade, the circulation is expressed as:

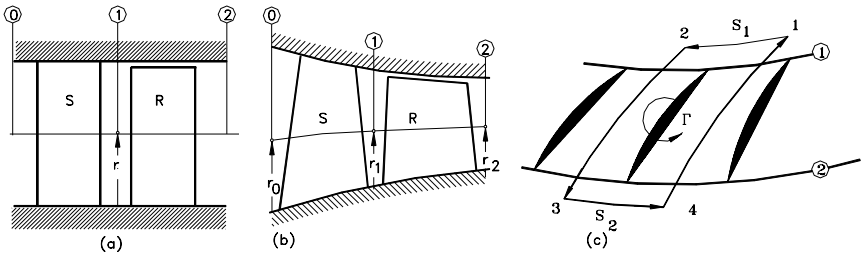

Fig. 16.4: Cross section of (a) compressor stage with constant and (b) with variable mean diameter. Fig. 16.4c relates the spacing at the inlet the one at the exit.

$$\Gamma = \oint \vec{V}.d\vec{s} \equiv \Gamma_{12} + \Gamma_{23} + \Gamma_{34} + \Gamma_{41} = V_{t1}\, s_1 - V_{t2}\, s_2 \tag{16.22}$$

where V_{t1} and V_{t2} represent the tangential velocity components at the inlet and exit and $\Gamma_{23} = -\Gamma_{41}$. For a rectilinear cascade with constant height or a stator cascade with a constant radius cylindrical streamlines, the spacings are equal at the inlet and exit, $s_1 = s_2 = s$. For a stator cascade with conical streamline (Fig. 16.4b,c and Fig. 16.5), different spacings at the inlet and exit are present that relate to each other by the radius of the streamline curvature, $s_1 = \Delta\vartheta\, r_1$, $s_2 = \Delta\vartheta\, r_2$. Using the following velocity ratios:

$$\phi = \frac{V_{a2}}{U_2}, \quad \nu = \frac{U_1}{U_2} = \frac{r_1}{r_2} = \frac{S_1}{S_2}, \quad \mu = \frac{V_{a1}}{V_{a2}} = \frac{W_{a1}}{W_{a2}} \tag{16.23}$$

and defining the specific circulation function γ, we obtain the following relations for the linear cascade γ_C, stator γ_S and rotor γ_R:

$$\gamma_C = \frac{A_C}{\rho_\infty V_\infty V_{a1}\, s} = \left(V_{t1} - V_{t2}\right)\frac{1}{V_{a1}} = \cot\beta_1 - \cot\beta_2 \tag{16.24}$$

$$\gamma_S = \frac{A_S}{\rho_\infty V_\infty V_{a1}\, s_1} = \left(V_{t1} - V_{t2}\,\frac{r_2}{r_1}\right)\frac{1}{V_{a1}} = \cot\beta_1 - \frac{1}{\nu\mu}\cot\beta_2 \tag{16.25}$$

$$\begin{aligned} \gamma_R &= -\frac{U_1}{V_{a1}} + \frac{W_{t1}}{V_{a1}} + \frac{r_2}{r_1}\frac{U_2}{V_{a1}} - \frac{r_2}{r_1}\frac{W_{t2}}{V_{z1}} \\ \gamma_R &= \frac{1}{\nu\,\phi\,\mu}\left(1 - \nu^2\right) + \cot\beta_1 - \frac{1}{\nu\,\mu}\cot\beta_2 \end{aligned} \tag{16.26}$$

Equation (16.26) exhibits a generalized relation for the specific circulation function. As seen, to calculate the circulation, the absolute velocity components V_{t1} and V_{t2} are utilized and refer to the absolute circulation rather than the relative one. Special cases such as the linear cascade, stator with cylindrical streamlines, and stator with axisymmetric streamlines can follow immediately by setting:

case 1: $u = 0$, $\phi = \infty$, $\mu = 1$, $\nu = 1$(linear cascade, cylinderical stator)
case2: $u = 0$, $\phi = \infty$, $\mu \neq 1$, $\nu \neq 1$(axisymmetric stator)
case 3: $u \neq 0$, $\phi \neq \infty$, $\mu = 1$, $\nu = 1$(cylinderical rotor)
case 4: $u \neq 0$, $\phi \neq \infty$, $\mu \neq 1$, $\nu \neq 1$(axisymmetric rotor)

Using the most general case (16.26), we obtain the circulation function for the rotor as:

$$G_R = \frac{\sin^2\beta_1}{\sigma}\gamma_R = \frac{\sin^2\beta_1}{\sigma}\left(\frac{1}{\mu\nu\phi}(1-\nu^2) + \cot\beta_1 - \frac{1}{\mu\nu}\cot\beta_2\right) \tag{16.27}$$

With Eqs. (16.24)-(16.27), the maximum velocity ratio at the optimum point for cascade (C), stator (S), and rotor (R) are calculated from:

$$\left(\frac{V_{\max}}{V_1}\right)^*_{C,S,R} = b_1 + b_2 G^*_{C,S,R} \tag{16.28}$$

Correspondingly, we obtain the off-design maximum velocity ratio by using Eq. (16.20):

$$\left(\frac{V_{\max}}{V_1}\right)_{C,S,R} = a_1\left(\beta_1 - \beta_1^*\right) + a_2\left(\beta_1 - \beta_1^*\right)^2 + b_1 + b_2 G^*_{C,S,R} \tag{16.29}$$

In Eqs. (16.28) and (16.29), the individual quantities denoted by the subscripts C, S, and R pertain to cascade, stator and rotor, respectively. The Lieblein's equivalent diffusion factor is then:

$$\begin{aligned} D_{eq} &= \frac{V_{\max}}{V_2} = \mu\frac{\sin\beta_2}{\sin\beta_1}\left(\frac{V_{\max}}{V_1}\right) \\ D_{eq} &= \mu\frac{\sin\beta_2}{\sin\beta_1}\left[a_1\left(\beta_1 - \beta_1^*\right) + a_2\left(\beta_1 - \beta_1^*\right)^2 + b_1 + b_2 G^*_{C,S,R}\right] \end{aligned} \tag{16.30}$$

16.1.4 Compressibility Effect

To consider the effect of compressibility on the maximum velocity ratio and thus on the diffusion factor, we modify the specific circulation function for the simplest case,

namely a linear cascade, by introducing the inlet density ρ_1:

$$\gamma_{C_c} = \frac{A_c}{\rho_1 V_\infty V_{a1} s} = \frac{\rho_\infty}{\rho_1} \left(V_{t1} - V_{t2}\right) \frac{1}{V_{a1}} \tag{16.31}$$

The second subscript c refers to compressible flow. The freestream density ρ_∞ can be expressed in terms of the density at the inlet and a finite increase $\rho_\infty = \rho_1 + \Delta\rho$. Outside the boundary layer we assume a potential flow that is not influenced by small perturbations. With this assumption, the Euler equation combined with the speed of sound may be applied:

$$VdV = -C^2 \frac{d\rho}{\rho} \tag{16.32}$$

with C as the speed of sound. For small changes, the flow quantities can be related to the quantities at the inlet:

$$\begin{aligned} V &= V_1 + \Delta V; \quad C = C_1 + \Delta C \\ \rho &= \rho_1 + \Delta\rho; \quad d\rho \cong \Delta\rho \end{aligned} \tag{16.33}$$

We introduce the above relations into Eq. (16.32) and approximate the differentials by differences and neglect the higher order terms. After some rearranging we obtain the density changes by:

$$\frac{\Delta\rho}{\rho_1} = -M_1^2 \left(\frac{V_2}{V_1}\right) \left(\frac{V_2}{V_1} - 1\right) \tag{16.34}$$

Introducing Eq. (16.34) into the relation $\rho_\infty = \rho_1 + \Delta\rho$ results in:

$$\frac{\rho_\infty}{\rho_1} = \left[1 - M_1^2 \left(\frac{\sin\beta_1}{\sin\beta_2}\right) \left(\frac{\sin\beta_1}{\sin\beta_2} - 1\right)\right] \tag{16.35}$$

Implementing Eq. (16.35) into Eq. (16.31) obtains the specific circulation functions for linear cascade and stators with cylindrical streamlines:

$$\gamma_{C_c} = \left[1 - M_1^2 \left(\frac{\sin\beta_1}{\sin\beta_2}\right) \left(\frac{\sin\beta_1}{\sin\beta_2} - 1\right)\right] \left[\cot\beta_1 - \cot\beta_2\right] \tag{16.36}$$

The expression in the above bracket reflects the Mach number effect on the specific circulation function. Using the same principle, the generalized circulation function for the rotor is obtained by:

$$\gamma_{R_c} = \left[1 - M_1^2 \left(\frac{1}{\mu}\frac{\sin\beta_1}{\sin\beta_2}\right)\left(\frac{1}{\mu}\frac{\sin\beta_1}{\sin\beta_2} - 1\right)\right] \times \left[\frac{1}{\mu\nu\phi}\left(1 - \nu^2\right) + \cot\beta_1 - \frac{1}{\mu\nu}\cot\beta_2\right] \tag{16.37}$$

This equation allows calculation of the specific circulation function for *cases 1 to 4*. As seen from Eqs. (16.36) and (16.37) and comparing them with Eqs. (16.24) and (16.26), the specific circulation of compressible and incompressible flows are related to each other by the density ratio and thus the Mach number. Considering the simplest case, namely the linear cascade described by Eq. (16.36), because of the compression process with $V_2 < V_1$, the bracket representing the compressibility effect is always greater than unity. With Eq. (16.36) and the conditions for *case 1 to case 4*, the circulation function for cascade, stator, and rotor with compressible flow are:

$$\left(G_{C,S,R}\right)_c = \frac{\sin^2\beta_1}{\sigma}\left(\gamma_{C,S,R}\right)_c \tag{16.38}$$

The subscripts C, S and R refer to the cases discussed above. Using Eq. (16.38) for optimum conditions, the velocity ratio for compressible flow is obtained from:

$$\left(\frac{V_{\max}}{V_1}\right)_{(G,S,R)C} = a_1\left(\beta_1 - \beta_1^*\right) + a_2\left(\beta_1 - \beta_1^*\right)^2 + b_1 + b_2\, G^*_{(G,S,R)C} \tag{16.39}$$

Introducing Eq. (16.39) into the relationship for the equivalent diffusion factor for the rotor as a generalized case, reads:

$$D_{eq} = \left\{ a_1 \left(\beta_1 - \beta_1^* \right) + a_2 \left(\beta_1 - \beta_1^* \right)^2 + b_1 \right.$$
$$+ b_2 \frac{\sin^2 \beta_1}{\sigma} \left[\frac{1}{\mu \nu \phi} \left(1 - \nu^2 \right) + \cot \beta_1 - \frac{1}{\mu \nu} \cot \beta_2 \right] \times \tag{16.40}$$
$$\left. \times \left[1 - \frac{1}{\mu} \frac{\sin \beta_1^*}{\sin \beta_2} M_1^2 \left(\frac{1}{\mu} \frac{\sin \beta_1^*}{\sin \beta_2} - 1 \right) \right] \right\} \frac{\sin \beta_2}{\sin \beta_1} \mu$$

The angles used in the above equations correspond to those defined in Fig. 16.1 and Fig. 16.5. Equations (16.39) and (16.40) show the direct relationship between the maximum velocity ratio and the specific circulation function. Equation (16.40) inherently includes the compressibility effect and the actual and optimum flow angles. An alternative diffusion factor, which was first proposed by Smith [31], is:

$$D = 1 - \frac{W_2}{W_1} + \frac{1}{\sigma} \frac{r_2 V_{t2} - r_1 V_{t1}}{\left(r_1 + r_2 \right) W_1} \tag{16.41}$$

This relation has been accepted and widely used by compressor aerodynamicists. It includes the effect of the rotation in its third term.

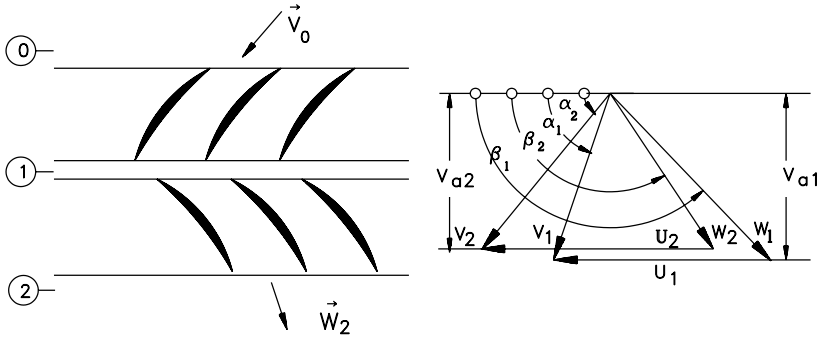

Fig. 16.5: Velocity triangle, angle definition

Using the angle definition in Fig. 16.5 and the dimensionless parameters previously defined, the re-arrangement of Eq. (16.41) results in:

$$D = 1 - \frac{1}{\mu} \frac{\sin \beta_1}{\sin \beta_2} + \frac{\nu \sin \beta_1}{\sigma(\nu + 1)} \left[\frac{1}{\mu \nu \phi} \left(1 - \nu^2 \right) - \cot \beta_1 + \frac{1}{\mu \nu} \cot \beta_2 \right] \tag{16.42}$$

The crucial part of this equation is the expression in the bracket, which is identical to the specific circulation function in Eqs.(16.38) and (16.39). Introducing the compressibility effect results in a modified version of Eq. (16.42):

$$D_m = 1 - \frac{1}{\mu}\frac{\sin\beta_1}{\sin\beta_2} + \frac{\nu\sin\beta_1}{\sigma(\nu+1)}\left[\frac{1}{\mu\nu\phi}\left(1-\nu^2\right) - \cot\beta_1 + \frac{1}{\mu\nu}\cot\beta_2\right] x \\ x\left[1 - \frac{1}{\mu}\frac{\sin\beta_1}{\sin\beta_2} M_1^2\left(\frac{1}{\mu}\frac{\sin\beta_1}{\sin\beta_2} - 1\right)\right] \tag{16.43}$$

The diffusion factors previously discussed are used to establish correlations for the individual losses as well as the total losses.

The theoretical background and the above discussion showed a direct correlation between the profile losses and the boundary layer quantities, particularly the boundary layer momentum thickness. Investigations by NACA, summarized in NASA SP-36 [32] and briefly reviewed in this chapter, showed that measuring the total pressure losses can experimentally determine the momentum thickness. Further investigations by Gostelow and Krabacher [33], Gostelow [34], Seylor and Smith [35], Seylor and Gostelow [36], Gostelow et al. [37], Krabacher and Gostelow [38], [39], and Monsarrat et al. [40] deal with the spanwise distribution of the total pressure and the total pressure loss coefficient. For the aerodynamic design of a single-stage compressor, Monsarrat et al. [41] presented correlations between the profile loss parameter and the diffusion factor using the experimental data by Sulam et al. [42]. The loss correlations by Monsarrat et al. [43] are frequently used as a guideline for designing compressor stages with the profile similar to that described by Monsarrat et al. [44]. Gostelow et al. [45] performed systematic and detailed experimental investigations on four different rotors to determine the optimum blade camber line shape. Although the experimental data revealed certain systematic tendencies, no attempt was made to develop a correlation to describe the loss situation in a systematic manner. These facts gave impetus to consider the above experimental data in the present analysis.

16.1.5 Shock Losses

Several studies have discussed experimental and theoretical shock loss investigations. As indicated previously, Miller and Hartmann [46], Miller et al. [47], and Schwenk et al. [48] initiated their fundamental research on transonic compressors where they investigated shock losses. Schwenk et al. [49] considered a normal shock in the entrance region of the cascade using a Prandtl-Meyer expansion. Levine [50], Balzer [51], and Swan [52] made efforts to calculate shock losses by estimating the shock position. Their proposed methods, particularly, Levine's [53] and Swan's [54] found their application in compressor design. Similar to Schwenk [55], the methods by

Levine, Balzer and Swan include the assumption of a normal shock. While Levine and Swan considered the acceleration on the suction surface by using the continuity and Prandtl-Meyer expansion, Balzer disregarded the expansion completely and used the continuity requirement. The deficiencies in the existing methods can be summarized as: a) They cannot accurately calculate the shock position, which is a prerequisite for accurately predicting the shock losses. b) The Mach number calculated by the Prandtl-Meyer expansion on the suction surface does not represent the shock Mach number along the channel width. Swan partially corrected this deficiency by building an average Mach number. c) The description of the physical process is not complete: the Prandtl-Meyer expansion combined with the continuity requirement is not sufficient to describe the physics. The above deficiencies gave impetus to generate the following new shock loss model. For the development of this model we assume the passage shock as an oblique shock, whose position changes according to the operating point and may include normal shock as a special case. Furthermore, we assume that the blading has a sufficiently sharp leading edge, where the shocks are attached at least at the design point with no detached bow waves expected. Fig. 16.6 shows the shock situation with the inlet flow angle β_1 , the metal angle β_t (camber angle), and the incidence angle I. To determine the shock position we use the continuity equation, the Prandtl-Meyer expansion, and the momentum equation. For the control volume in Fig. 16.6, the continuity requirement for a uniform flow is:

$$\rho_1 V_1 S_1 \sin\beta_1 = \rho_s V_s S_s \cos\delta \frac{h_s}{h_1} \tag{16.44}$$

with h_1 and h_S as the height of the stream tube at the inlet and at the shock position. Using the gas dynamics relationships, Eq. (16.44) is written as:

$$\frac{h_1}{h_s}\frac{S_1 \sin\beta_1}{S_s \cos\delta} = \frac{\rho_s}{\rho_1}\frac{V_s}{V_1} = \frac{M_s}{M_1}\left(\frac{1+\frac{\kappa-1}{2}M_1^2}{1+\frac{\kappa-1}{2}M_s^2}\right)^{\frac{1}{2}\frac{\kappa+1}{\kappa-1}} \tag{16.45}$$

with the geometric relation:

$$\delta = \frac{\pi}{2} + \beta_s - \gamma \tag{16.46}$$

The incidence and expansion angle are coupled by:

$$i = \theta - \nu_s + \nu_1 \tag{16.47}$$

where ν is determined from the Prandtl-Meyer expansion law:

$$\nu = \left(\frac{\kappa+1}{\kappa-1}\right)^{\frac{1}{2}} \tan^{-1}\left[\frac{\kappa-1}{\kappa+1}\left(M^2-1\right)\right]^{\frac{1}{2}} - \tan^{-1}\left(M^2-1\right)^{\frac{1}{2}} \tag{16.48}$$

The momentum equation in tangential (circumferential) direction is given by:

$$\int_{S_1} V_1 \cos\beta_1 \, d\dot{m}_1 - \int_{S_S} V_S \cos\beta_S \, d\dot{m}_S - \int_{S_S} p_S \cos\left(\beta_S - \delta\right) dS_S - \int_{S_V} p_W \cos\alpha_W \, dS_W = 0 \tag{16.49}$$

As Fig. 16.6 shows, because of the cascade periodicity, the pressure at point A is identical to the pressure at point C. Furthermore, point B on the suction surface represents the common end point for both distances, AB and CB. This means that the pressure distributions along AB and CB have exactly the same beginning and ending values, but may have different distributions between the points AB and CB. Assuming that the pressure integrals along the shock front AB and the blade contour portion CB are approximately equal, their projections in circumferential direction may cancel each other and lead to:

$$\frac{V_1}{V_s} = \frac{\cos\beta_s}{\cos\beta_1} = \frac{M_1}{M_s}\left(\frac{1+\frac{\kappa-1}{2}M_s^2}{1+\frac{\kappa-1}{2}M_1^2}\right)^{\frac{1}{2}} \tag{16.50}$$

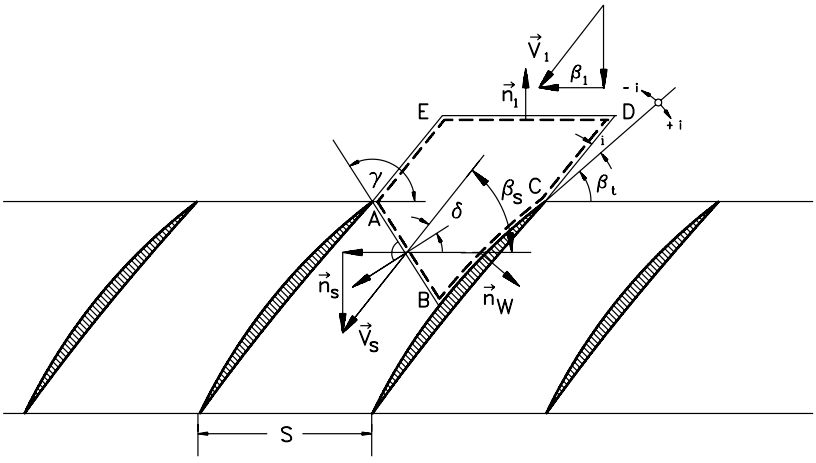

Fig. 16.6: Shock position and angle definition, n_1 , n_s, n_w are normal unit vectors at the inlet, shock location and the wall.

Finally, we arrive at a geometric closure condition that uses the mean stream line, which is assumed to be identical to the mean camber line of the blade with the radius R as shown in Fig. 16.7.

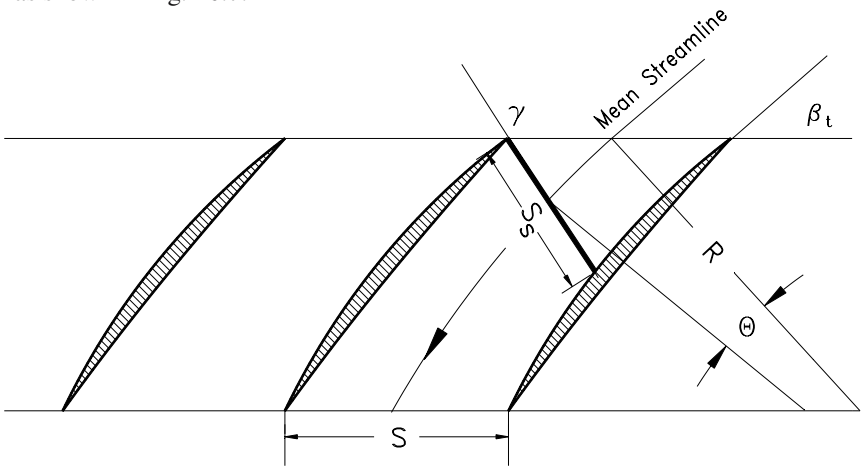

Fig. 16.7: Introduction of mean streamline with curvature radius

From Fig. 16.7, it follows immediately that

$$R\left[+\cos\beta_t - \cos\left(\beta_t + \theta\right)\right] = \frac{S_s}{2}\sin\gamma \tag{16.51}$$

and

$$R\left[-\sin\beta_t + \sin\left(\beta_t + \theta\right)\right] = \frac{S_s}{2}\cos\gamma + \frac{S_1}{2} \tag{16.52}$$

The shock angle is determined from:

$$tg\,\gamma = \frac{\cos\beta_t - \cos\left(\beta_t + \theta\right)}{-\sin\beta_t + \sin\left(\beta_t + \theta\right) - \frac{1}{2}\frac{S_1}{R}} \tag{16.53}$$

Considering the above procedure, the continuity equation yields:

$$\frac{h_1}{h_s}\,\frac{\sin\left(\beta_t + i\right)\sin\gamma}{2\,\frac{R}{S_1}\left[\cos\beta_t - \cos\left(\beta_t + \theta\right)\right]\sin\left(\gamma - \beta_s\right)} = \frac{M_s}{M_1}\left(\frac{1 + \frac{\kappa - 1}{2}M_1^2}{1 + \frac{\kappa - 1}{2}M_s^2}\right)^{\frac{1}{2}\frac{\kappa+1}{\kappa-1}} \tag{16.54}$$

With Eqs. (16.46), (16.47), (16.50), and (16.54), we have a system of four equations that easily calculates the four unknowns, namely: δ, β_s, γ, and M_s. The shock loss is:

$$\zeta_S = \frac{P_b - P_a}{P_b}$$

$$\zeta_S = 1 - \left[\frac{(\kappa+1)M_s^2\cos^2\delta}{2+(\kappa-1)M_s^2\cos^2\delta}\right]^{\frac{\kappa}{\kappa-1}}\left[1+\frac{2\kappa}{\kappa+1}\left(M_s^2\cos^2\delta-1\right)\right]^{\frac{-1}{\kappa-1}} \tag{16.55}$$

where P_b and P_a represent the total pressure before and after the shock. For $\beta_t = 30^o$ and the incidence angle $i = 0^0$, the above equation system is used to calculate the shock Mach number, the expansion angle θ, the shock position γ, the total pressure ratio, and the shock losses.Fig. 16.8 shows the shock Mach number as a function of spacing ratio *S/R* with the inlet Mach number M_1 as the parameter. This figure shows that increasing the spacing ratio cause the shock Mach number to continuously increase and approach an asymptotic value. These results are similar to those presented by Levine [56]. However, the values are slightly different because of the simplifying assumptions by Levine. Keeping the inlet Mach number constant, the increase of spacing ratio leads to higher expansion angle θ as shown in Fig. 16.9. However, increasing the inlet Mach number at a constant spacing ratio *S/R* leads to a smaller expansion angle.

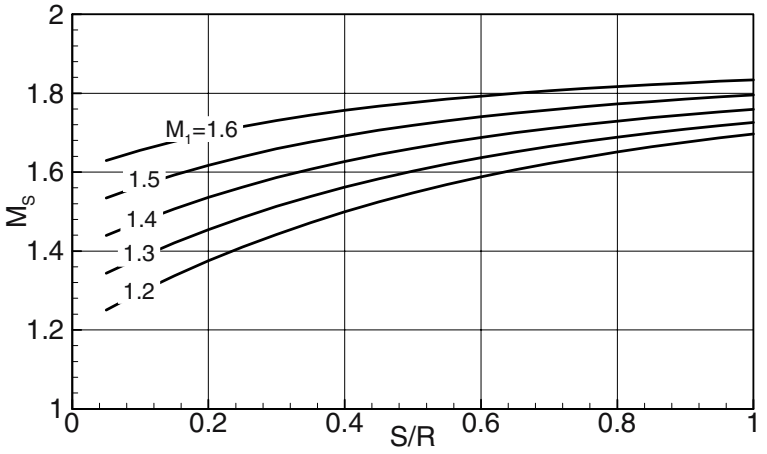

Fig. 16.8: Shock Mach number as a function of the spacing ratio S/R with the inlet Mach number M_1 as parameter with $\beta_t = 30^0$, and the incidence angle $i = 0^o$

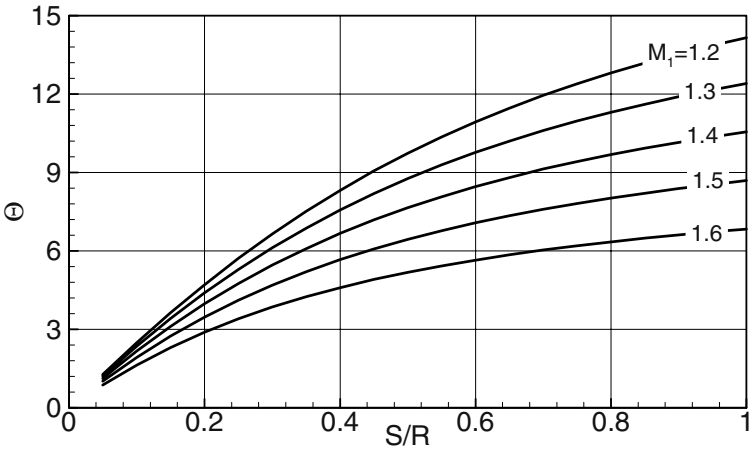

Fig. 16.9: Expansion angle Θ as a function of S/R with inlet Mach number M^1 as parameter with $\beta_2 = 30$ and incidence angle i = 0°

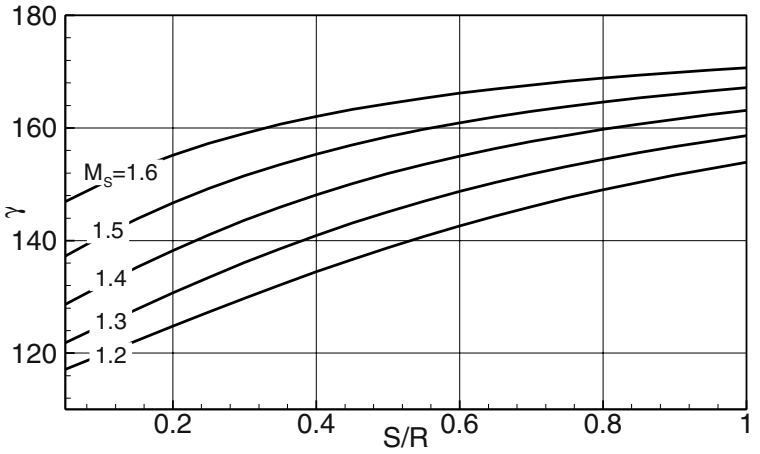

Fig. 16.10: Shock angle γ as a function of S/R with shock Mach number as parameter.

The same tendency can be read from the charts by Levine. For an inlet Mach number $M_1 = 1.2$ and $S/R = 0.5$, the Levine's method gives an expansion angle $\theta = 8^0$, while the method presented in here calculates $\theta = 9.7^0$. Fig. 16.10 shows the shock angle γ as a function of spacing ratio *S/R*. This figure shows the significant effect of the inlet Mach number on the shock position. Once the shock angle is calculated at the

design point, it may undergo changes during an off-design operation. The off-design operation may place a limitation on the shock angle range as Fig. 16.11 illustrates. Beginning with a design point speed line, Fig. 16.11a, the operating point (a) is given by the inlet Mach number M_1 with a uniquely allocated inlet flow angle β_l that satisfies the *unique incidence criterion*. Increasing the back pressure from the design point back pressure to a higher level (b) causes the passage shock to move toward the cascade entrance. By further increasing the back pressure from (b) to (c), a normal shock is established, which is still attached. The corresponding shock angle γ can be set equal to $\gamma_{\text{lim}} \equiv \gamma_{at}$. Decreasing the mass flow beyond this point, causes the shock to detach from the leading edge, as shown in Fig. 16.11d. Reducing the rotational speed change the incidence and may lead to further moving the shock from the leading edge as shown in Fig. 16.11d. These operating points are plotted schematically in a compressor performance map, shown in Fig. 16.12, with a surge limit and an attached normal shock line.

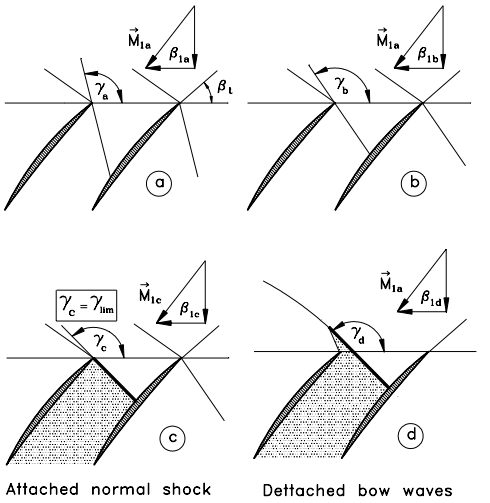

Fig. 16.11: Change of the shock angle γ for a given cascade geometry at different operation points.

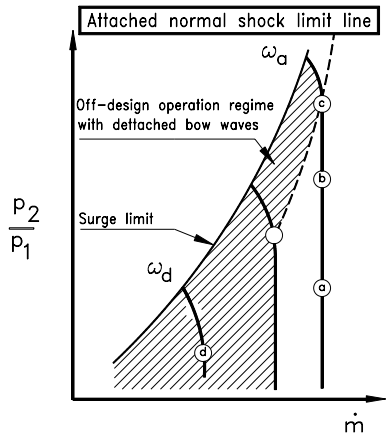

Fig. 16.12: Effect of shock angle γ change described in Fig. 16.8 on compressor performance map.

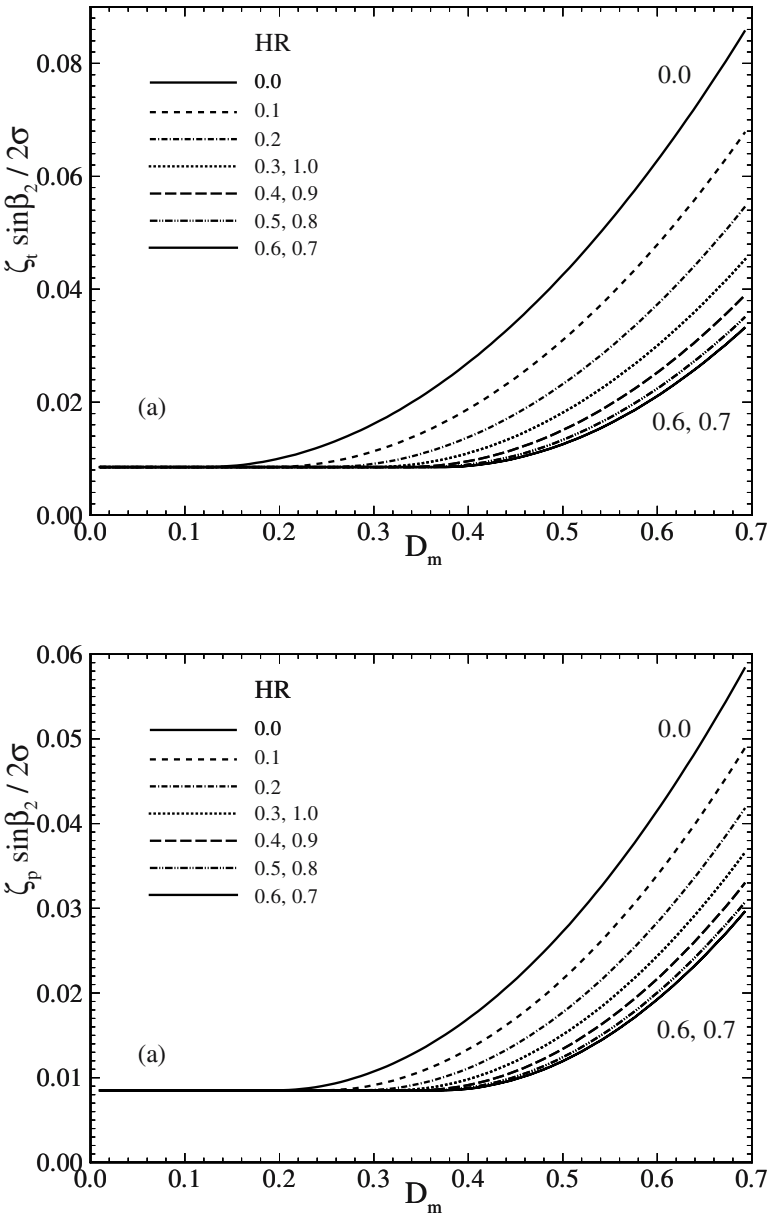

Fig. 16.13: Total loss parameter (top) and profile loss parameter (bottom) as a function of modified diffusion factor

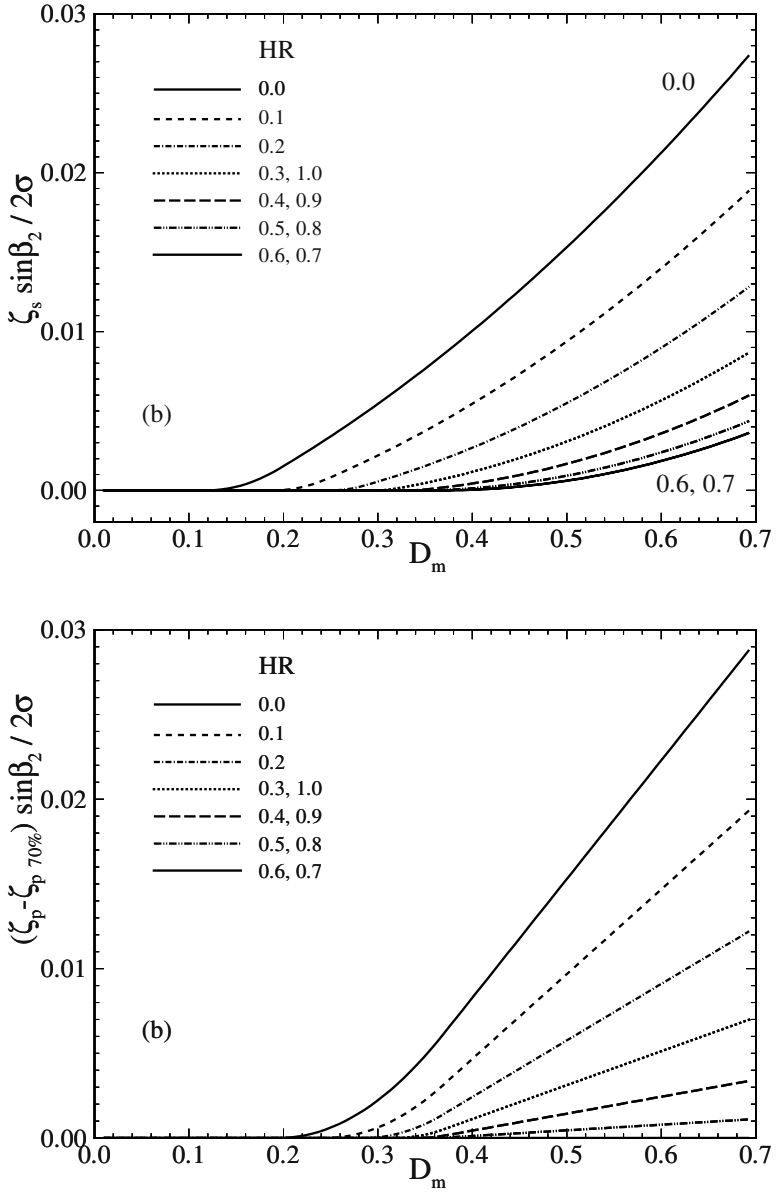

Fig. 16.14: Shock loss (top) and difference in profile loss parameter with respect to minimum profile loss parameter (bottom) as a function of modified diffusion factor

To establish the loss correlations, the existing available experimental data were re-evaluated, particularly those in Gostelow et al. [57] and Krabacher and Gostelow [58], [59], which used four single-stage compressors with multi-circular-arc profiles. A detailed description of the compressor facility and the stages are found in their reports. The data analysis used the following information: (1) the total pressure losses as a function of diffusion factor in the spanwise direction, (2) inlet, exit, and incidence angles, (3) Mach numbers, (4) velocities, and (5) geometry. To consider the compressibility effect discussed previously, the modified diffusion factor D_m was obtained using the information from Gostelow's report mentioned previously.

Figures 16. 13 and16.14 show the results. Starting from the tip with an immersion ratio of $H_R = (R_t - R)/(R_t - R_h) = 0$, Fig. 16.13 (top) shows the total loss parameter as a function of the modified diffusion factor. As shown, the highest total pressure loss that consists of shock loss, profile loss, and secondary flow loss is encountered at the tip region, with shock and secondary flow losses as the predominant losses. Subtracting the shock loss coefficients from the total loss coefficients provides loss coefficients that contain the primary and the secondary loss effects. The resulting loss coefficients are plotted in Fig. 16.14 (bottom) and are approximately 30% smaller than the total pressure loss coefficient.

Figure 16.14 (top) exhibits the shock losses as a function of modified diffusion factor with the immersion ratio as a parameter. Highest shock losses occur at the tip region, with the relative Mach number above unity and decrease toward the hub.

The fact that the sum of primary and secondary flow losses exhibit a minimum range of $H_{R\min} = 0.5 - 0.7$, where the secondary flow effects diminish, enables the compressor designer to estimate the secondary flow losses. This is done by subtracting the losses at $H_{R\min}$ from the loss distribution at different spanwise locations. As a result, these losses include the effect of the secondary flows associated with wall boundary layer development and clearance vortices. Figure 16.14 (bottom) shows the distribution of the secondary loss parameter as a function of the modified diffusion factor. It exhibits a linear dependency of the secondary loss parameter as a function of the modified diffusion factor with the immersion ratio as a parameter. Since the diffusion factor is directly related to the lift force and thus to the lift coefficient $(C_L c/s)$ as a linear function, one may conclude that the secondary flow losses are linearly proportional to $(C_l c/s)$. This is in agreement with the measurements by Grieb et al. [60] and in contrast to the correlation proposed earlier by Carter [61] that includes the term $(C_L c/s)^2$ and is adopted by many other researchers. A similar dependency for H_R = 50, 70 and 90%, where the smallest losses are encountered at H_r = 60 - 70. Moving further toward the hub at H_R = 90%, the total pressure losses experience a continuous increase attributed to higher friction losses and the secondary flow caused by the secondary vortices at the hub. A comparison of the loss parameters plotted in Fig. 16.14(top) shows that the total pressure losses in the tip region (H_r = 10%) are much higher than those in the hub region (H_r = 90%). The higher losses at the tip are due to an increased secondary flow effect that is attributed to the tip clearance vortices.

16.1.6 Correlations for Boundary Layer Momentum Thickness

As shown, the profile loss coefficient and the boundary layer momentum thickness are interrelated by:

$$\zeta_p = \sigma \left(\frac{\theta}{c} \right) \left(\frac{\sin\beta_1}{\sin\beta_2} \right)^2 F\left(H_{12}, H_{32}, \theta, \sigma, c\right) \tag{16.56}$$

The momentum thickness in Eq. (16.56) is the projection of the suction surface and pressure surface momentum thicknesses given by:

$$\theta \sin\beta_2 \equiv \theta_{SP} = \theta_S + \theta_P \tag{16.57}$$

where the subscripts S and P refer to the suction and pressure surface, respectively, and the function F is given by:

$$F = \frac{1 + H_{32}}{\left(1 - \frac{\delta_2}{c} \sigma H_{12} \right)^3} \tag{16.58}$$

with H_{12}, H_{32} as the displacement and energy form factors, θ as the boundary layer momentum thickness, σ as the solidity, and c as the blade chord. In the literature (see also Hirsch [62] and Swan [63]), the function F is frequently approximated as a constant with the value $F = 2$. For a realistic velocity distribution, Schobeiri [64] showed that the value of F may differ from 2. To arrive at a better estimation for F, the boundary layer velocity profile is approximated by several simple functions such as a linear function, a power law, a sine function, and an exponential function. A close examination of the results and their comparison with the experiments showed that the velocity approximation by a power function yields better results. However, the exponential approximation would be more appropriate for those profiles that are close to separation. Using the law function approximation, we arrive at:

$$H_{32} = \frac{H_{12} + 1}{3H_{12} - 1} \tag{16.59}$$

Introducing Eq. (16.59) into Eq. (16.58) and the results into Eq. (16.56) leads to:

$$\zeta_P = \sigma \left(\frac{\delta_2}{c} \right) \left(\frac{\sin\beta_1}{\sin\beta_2} \right)^2 \left[\frac{\frac{4H_{12}}{3H_{12} - 1}}{\left(1 - \frac{\delta_2}{c} \sigma H_{12} \right)^3} \right] \tag{16.60}$$

With Eq. (16.60) and (16.58), the momentum thickness is determined from:

$$\frac{\theta}{c} = \frac{\zeta_p \sin\beta_2}{\sigma}\left(\frac{\sin\beta_2}{\sin\beta_1}\right)^2 \frac{1}{F} \tag{16.61}$$

Using the profile losses as previously discussed, the correlation for the momentum thickness as a function of modified equivalent diffusion factor are plotted in Fig. 16.5 with the immersion ratio as a parameter. The highest value for the momentum thickness is encountered in the vicinity of the tip that includes the viscosity effects as well as the secondary flow effects. Similar to the profile losses, the momentum thickness continuously decreases by moving toward the blade mid-section up to $H_r = 0.6$. It assumes a minimum at $H_r = 0.7$. At this radius, the secondary flow effect apparently diminishes completely so that the momentum thickness corresponds to the one generated by the blade surface friction only. For immersion ratios greater that $H_r = 0.7$, the momentum thickness starts increasing again, which indicates the strong effect of the secondary flow.

16.1.7 Influence of Different Parameters on Profile Losses

The correlations presented above are based on experimental results performed on typical high performance compressors with specific flow characteristics and blade geometries similar to those discussed previously. These correlations may be applied to other compressors with similar geometries but different flow conditions by considering the effect of the following individual parameters.

16.1.7.1 Mach Number Effect: Estimating the Mach number effect requires calculating the critical Mach number. When the Mach number reaches unity locally in a compressor cascade, the corresponding inlet Mach number is said to have reached its critical value. Jansen and Moffat [65] made the assumptions that below the critical Mach number, the total pressure losses and the turning angle are essentially constant. The pressure losses increase rapidly beyond this value. Using the gas dynamics relations, Jansen and Moffat [66] determined the local critical Mach number by the following implicit relation:

$$\left(\frac{V_{\max}}{V_1}\right)^2 - 1 = \frac{1 - \left(\frac{2}{k+1} + \frac{k-1}{k+1} M_{1\,cr}^2\right)^{\frac{k}{(k-1)}}}{-1 + \left(1 + \frac{k-1}{2} M_{1\,cr}^2\right)^{\frac{k}{(k-1)}}} \tag{16.62}$$

To estimate the critical Mach number directly, Davis [67] suggested the following explicit relation:

$$M_{1\,cr} = 2.925 - 2.948\left(\frac{V_{\max}}{V_1}\right) + 1.17\left(\frac{V_{\max}}{V_1}\right)^2 - 0.1614\left(\frac{V_{\max}}{V_1}\right)^3 \qquad (16.63)$$

As seen in Part I, the velocity ratio V_{max}/V_1 is directly related to the circulation function and thus the diffusion factor. With the critical Mach number from Eq. (16.7) or (16.8), the profile loss coefficient can be corrected as:

$$\zeta_{pcor} = \zeta_p\left[A\left(M_1 - M_{1\,cr}\right) + 1.0\right] \qquad (16.64)$$

with A = 1.8-2.0 (see Moffat [68] and Davis [69]). For DCA-profiles, Dettmering and Grahl [70] found that Eq. (16.9) underestimates the correction and suggested the following modified approximation:

$$\zeta_{pcor} = \zeta_p\left\{14.0\left[M_1 - \left(M_{1\,cr} - 0.4\right)^3\right] + 1.0\right\} \qquad (16.65)$$

16.1.7.2 Reynolds number effect: This effect is only at lower Reynolds number ranges of practical significance. For high performance compressors, the Reynolds number is high enough so that its changes do not affect the profile losses. The following profile loss correction is suggested for Reynolds number ranges $Re < 2.5 \times 10^5$:

$$\zeta_{pcor} = \zeta_p\left(\frac{Re}{Re_{cor}}\right)^{0.2} \qquad (16.66)$$

16.1.7.3 Blade thickness effect: To consider the effect of the thickness ratio *t/c,* the boundary layer momentum thickness may be corrected using the correlation by Fottner [71].

$$\left(\frac{\theta}{c}\right)_{cor} = \frac{\theta}{c}\left(6.6\,\frac{t}{c} + 0.34\right) \qquad (16.67)$$

16.2 Compressor Aerodynamic Design and Off-Design Performance

The prerequisite for simulating the dynamic behavior of a compressor is a detailed knowledge of the design point properties as well as the overall performance characteristics. Three levels of simulation are discussed. The *first level* deals with steady state performance maps. It provides global information about the design and

off-design efficiency and performance behavior of a compressor. It does not contain any detailed information about the individual stage parameters such as stage flow, load coefficients, degree of reaction, absolute and relative flow angles. However, this information is necessary to construct the compressor performance map. The map can be generated either by a stage-by-stage or by a row-by-row compression calculation procedure, which treats the compression procedure fully adiabatic, neglecting the heat transfer to/from the blade material. The following row-by-row adiabatic compression calculation method, which provides the basis for the *second level* simulation will be followed by the diabatic compression process that is necessary for the *third level* comprehensive dynamic simulation.

16.2.1 Stage-by-stage and Row-by-Row Adiabatic Compression Process

The stage-by-stage and row-by-row methods for calculating the compression process within a multi-stage compressor, Fig. 16.15, presented in this chapter are equally applicable to axial and radial turbines and compressors, as discussed in Chapter 6.

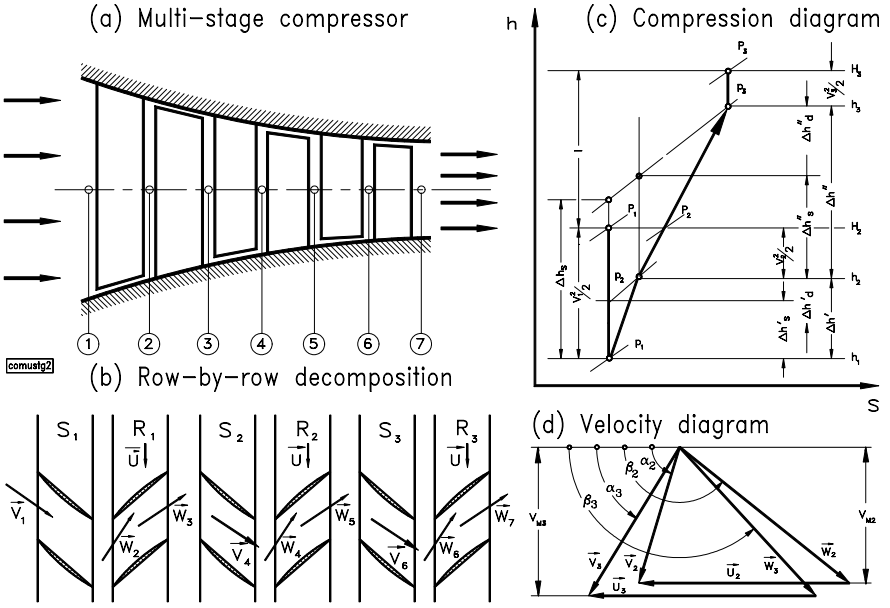

Fig. 16.15: Multi-stage compressor (a) flow path, (b) row-by-row arrangement, (c) compression diagram, (d) velocity diagram.

These methods are based on a one-dimensional calculation of the compression or expansion process using a set of dimensionless stage or row characteristics. These characteristics, along with loss correlations discussed in Section 16.1 describe the

design and off-design behavior of the compressor or turbine component under consideration. In the following we discuss and evaluate both methods. The equation derived for the stage-by-stage calculation method follows the nomenclature in Fig. 16.15.

16.2.1.1 Stage-by-stage calculation of compression process: The performance behavior of the compressor stage is completely described by the stage characteristics. The meridional view, blade configuration, compression diagram and velocity diagram of a typical compressor are shown in Fig. 16.15. For stage-by-stage analysis, we resort to the following dimensionless variables introduced in Chapter 6 in conjunction with the stage-by-stage arrangement, Fig. 16.15b, compression diagram, Fig. 16.15c and , velocity diagram in Fig. 16.15.

$$\mu = \frac{V_{m2}}{V_{m3}}, \quad \nu = \frac{U_2}{U_3}, \quad \phi = \frac{V_{m3}}{U_3}, \quad \lambda = \frac{1_m}{U_3^2}, \quad r = \frac{\Delta h_R}{\Delta h_R + \Delta h_S} \tag{16.68}$$

As shown in Chapter 6, these dimensionless variables were incorporated into the conservation equations of mass, momentum, moment of momentum, and energy leading to the following relations (6.40) to (6.43):

$$cotg\alpha_2 - cotg\beta_2 = \frac{\nu}{\mu\phi} \tag{16.69}$$

$$cotg\alpha_3 - cotg\beta_3 = \frac{1}{\phi} \tag{16.70}$$

$$\lambda = \phi(\mu\nu cotg\alpha_2 - cotg\alpha_3) - 1 \tag{16.71}$$

$$r = 1 + \frac{\phi^2}{2\lambda}\left[1 + cotg^2\alpha_3 - \mu^2\left(1 + cotg^2\alpha_2\right)\right] \tag{16.72}$$

Using the above set of stage characteristics in conjunction with the stage loss coefficients discussed in Chapter 8, the compression process is accurately calculated. This process, however, requires few assumptions and several iterations. The four equations (16.69) to (16.72) contain nine unknowns. The following quantities are assumed to be known: (1) the compressor mass flow, (2) the compressor pressure ratio, (3) the type of blades, their exit metal angles α_2 and β_3 for each individual stage, and their configuration in terms of degree of reaction. Further, we may assume the absolute inlet flow angle of the first stage and the exit flow angle of the last stage to be 90°. With these assumptions, all nine stage characteristics are estimated in the first iteration step, which usually does not deliver the required compression pressure ratio and exit enthalpy. The process of iteration is continued until the enthalpy and

pressure convergence have been reached. This stage-by-stage compression calculation method delivers accurate results, however, it requires some experience in guessing the initial values for unknown characteristics. The row-by-row calculation is discussed in more detail in the following section. It is computationally more efficient and does not require a lot of iterations.

16.2.1.2 Row-by-row adiabatic compression: As discussed in Chapter 6, the compression process within stator and rotor row, shown in Fig. 16.16, is summarized as:

$$\begin{aligned}
\Delta h' &= h_1 - h_2 = \frac{1}{2}\left(V_2^2 - V_1^2 \right) \\
\Delta h_s' &= h_1 - h_{2s} = \frac{1}{2}\left(V_{2s}^2 - V_1^2 \right) \\
\Delta h'' &= h_2 - h_3 = \frac{1}{2}\left(W_3^2 - W_2^2 + U_2^2 - U_3^2 \right) \\
\Delta h_s'' &= h_2 - h_{3s} = \frac{1}{2}\left(W_{3s}^2 - W_2^2 + U_2^2 - U_3^2 \right)
\end{aligned} \tag{16.73}$$

The quantities in Eqs. (16.73), the decomposition of a compressor stage in its stator and rotor rows, and the compression diagram are presented in Fig. 16.16.
In the above and the following, all quantities with superscripts "/ " and "// " refer to stator androtor rows, respectively. For the stator row, the compression diagram shows the details of an adiabatic compression, where the absolute total enthalpy remains

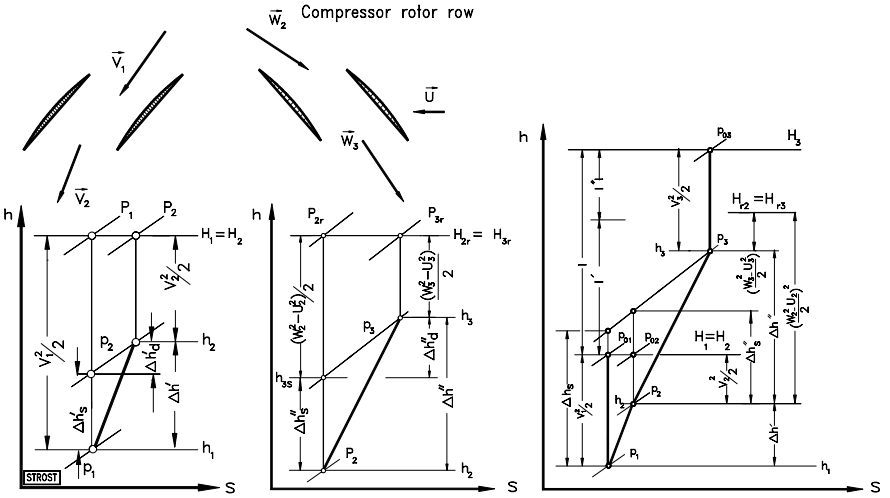

Fig. 16.16: Stator, rotor, stage compression diagram.

constant. The following rotor row with the corresponding compression diagram exhibits the details of energy balance in relative frame of reference with constant relative total enthalpy. The compression diagram for the entire stage exhibits a composite picture of energy balance within stator and rotor row. Introducing the efficiency definition for the stator and rotor row, respectively:

$$\eta' = \frac{\Delta h_s'}{\Delta h'} \quad , \quad \eta'' = \frac{\Delta h_s''}{\Delta h''} \tag{16.74}$$

Incorporating Eq. (16.74) into Eqs. (16.73), the isentropic enthalpy difference for stator and rotor row, respectively, is expressed by:

$$\begin{aligned} \Delta h_s' &= \frac{\eta'}{2} \left(V_2^2 - V_3^2 \right) \\ \Delta h_s'' &= \frac{\eta''}{2} \left(W_3^2 - V_2^2 + 2V_{u2}U_2 - U_3^2 \right) \end{aligned} \tag{16.75}$$

The expression for the dimensionless isentropic enthalpy difference is obtained by dividing Eqs. (16.75) by the circumferential kinetic energy at the exit of the stage. The dimensionless isentropic enthalpy difference is written in terms of the stage parameters of Eq. (16.68) as:

$$\begin{aligned} \chi' &= \frac{\Delta h_s'}{U_3^2} = \frac{\eta'}{2} \left(\frac{\phi^2 \quad \mu^2}{\sin^2\alpha_2} - \frac{\phi^2}{\sin^2\beta_3} - 2\phi\cot\beta_3 - 1 \right) \\ \chi'' &= \frac{\Delta h_s''}{U_3^2} = \frac{\eta''}{2} \left(\frac{\phi^2}{\sin^2\beta_3} - \frac{\mu^2\phi^2}{\sin^2\alpha_2} + 2\phi\mu\nu\cot\alpha_2 - 1 \right) \end{aligned} \tag{16.76}$$

Further analysis of Eqs. (16.76) show that knowledge of the entire stage parameter is necessary to determine the row isentropic enthalpy difference, which is similar to the stage-by-stage procedure discussed in the previous section, and requires many iterations. To avoid the iterative procedure, we subdivide the stage specific polytropic mechanical energy l, as well as the isentropic mechanical energy l_s, into two virtual contributions l' and l'' that we allocate to stator and rotor row as shown in Fig. 16.16. This step does not imply that the stator row is performing shaft power, which would violate the energy balance. It merely provides a smooth transition from stator row to rotor row when calculating the compression process. With this re-arrangement, we arrive at the contributions allocated to the stator and rotor rows as:

$$l' = \frac{1}{2} V_2^2 - \frac{1}{2} W_2^2$$
$$l'' = \frac{1}{2} (W_3^2 - U_3^2 + U_2^2 - V_3^2) \tag{16.77}$$

Similarly we find:

$$l_s' = \frac{1}{2} V_{2s}^2 - \frac{1}{2} W_2^2$$
$$l_s'' = \frac{1}{2} (W_{3s}^2 - U_3^2 + U_2^2 - V_3^2) \tag{16.78}$$

As seen, the sum of stator and rotor contributions leads to the stage specific mechanical energy. Using the polytropic specific mechanical energy expressions given in Eqs. (16.78) and dividing them by the circumferential kinetic energy at the exit of the individual row, the dimensionless row polytropic load coefficients for stator and rotor are:

$$\lambda' = \frac{l'}{U_2^2} = \phi' \cot\alpha_2 - \frac{1}{2}$$
$$\lambda'' = \frac{l''}{U_3^2} = - \phi'' \cot\beta_3 - 1 + \frac{\nu^2}{2} \tag{16.79}$$

where, $\phi' = V_{ax2} / U_2$, and $\phi'' = V_{ax3} / U_3$.Combining Eqs. (16.79) with the efficiency definition for the stator and rotor rows, Eq. (16.74), the following expressions for the efficiency are obtained:

$$\eta' = \frac{2l_s' - 2l' + V_2^2 - V_1^2}{V_2^2 - V_1^2}$$
$$\eta'' = \frac{2l_s'' - 2l'' + W_3^2 - W_2^2}{W_3^2 - W_2^2} \tag{16.80}$$

The isentropic row load coefficient ψ is defined as the dimensionless isentropic specific mechanical energy for the row. Implementing the efficiency expressions from Eqs. (16.80), the isentropic row load coefficients for the stator and rotor rows are obtained:

$$\psi' = \frac{l_s'}{U_2^2} = \lambda' + \frac{\phi^2}{2} \left(\frac{1}{\sin^2\alpha_2} - \frac{1}{\mu^2 \sin^2\alpha_3} \right) (\eta' - 1) \tag{16.81}$$

$$\psi'' = \frac{l_s''}{U_3^2} = \lambda'' + \frac{\phi^2}{2}\left(\frac{1}{\sin^2\beta_3} - \frac{\mu^2}{\sin^2\beta_2}\right)(\eta'' - 1) \tag{16.82}$$

All the information necessary to pursue the compression process on the h-s diagram is now available to predict the compressor behavior with sufficient accuracy and reliability. Given the pressure and temperature at the inlet, the remaining thermodynamic properties are calculated using the property tables of the working medium that can be implemented as a subroutine within the calculation procedure. The row flow coefficients ϕ' ϕ'' are calculated from the continuity equation:

$$\phi = \frac{V_{ax}}{U} = \frac{\dot{m}}{\rho A U} = \frac{\dot{m}}{\rho A \omega R} \tag{16.83}$$

Given the exit stator and rotor blade angle (α_2, β_3) as input data necessary to describe the geometry and the above flow coefficient, we determine the flow angles (α_3, β_2) for the stator and rotor rows, respectively:

$$\begin{aligned} \beta_2 &= \tan^{-1}\frac{\phi'}{\phi'\cot\alpha_2 - 1} \\ \alpha_3 &= \tan^{-1}\frac{\phi''}{\phi''\cot\beta_3 + 1} \end{aligned} \tag{16.84}$$

The incidence and deviation angles are calculated according to the procedure described in Chapter 11. Upon determining all the angles involved in the velocity diagram, the velocities and their components are completely known. The velocity triangle at the exit of the row is calculated and the flow behavior is completely described by the velocity diagram. The flow coefficient, ϕ' and ϕ'', and the flow angles (α_3, β_3, α_2, β_2,) are necessary tools to determine the polytropic and isentropic enthalpy differences between the inlet and exit of the row. The amount of mechanical energy consumed by the flow to increase its total pressure is represented by the polytropic load coefficients, λ', λ'', and the isentropic load coefficients ψ', ψ'' as presented above. Finally, from the energy balance relationships, the complete compression process for the stage is determined by the following set of equations:

$$\begin{aligned} h_2 &= h_1 - l' - \frac{1}{2}\left(W_2^2 - V_1^2\right) \\ h_3 &= h_2 - l'' - \frac{1}{2}\left(V_3^2 - W_2^2\right) \end{aligned} \tag{16.85}$$

$$h_{2s} = h_1 - l_s' - \frac{1}{2}\left(W_2^2 - V_1^2 \right)$$
$$h_{3s} = h_2 - l_s'' - \frac{1}{2}\left(V_3^2 - W_2^2 \right) \tag{16.86}$$

the above procedure can be easily repeated for all the stages of the compressor in question. However, it should be pointed out that the above analysis is completely dependent on an accurate and reliable method for determining the off-design efficiency. This is the subject of the next section.

16.2.1.3 Off-design efficiency calculation: The off-design efficiency calculation is based on the analysis of the diffusion factor. The modified diffusion factor, Eq. (16.45), includes compressibility effects and, therefore, is capable of handling highly compressible flow such as in transonic compressors. To apply the diffusion factor definition to stators and rotors on an individual basis, separate expressions were derived in terms of known stage and row quantities. The expression for the stator row given is:

$$D_m' = 1 - \frac{\sin\alpha_1}{\mu\sin\alpha_2} + \frac{\nu\sin\alpha_1}{\sigma(\nu + 1)}\left(\cot\alpha_1 - \frac{\cot\alpha_2}{\mu\nu} \right) \left[1 - M_1^2 \left(\frac{\sin\alpha_1}{\mu\sin\alpha_2} \right)\left(\frac{\sin\alpha_1}{\mu\sin\alpha_2} - 1 \right) \right] \tag{16.87}$$

and for the rotor row:

$$D_m'' = 1 - \frac{\sin\beta_2}{\mu\sin\beta_3} + \frac{\nu\sin\beta_2}{\sigma(\nu + 1)}\left(\frac{1-\nu^2}{\mu\nu\phi''} - \cot\beta_2 + \frac{\cot\beta_3}{\mu\nu} \right) \left[1 - M_2^2 \left(\frac{\sin\beta_2}{\mu\sin\beta_3} \right)\left(\frac{\sin\beta_2}{\mu\sin\beta_3} - 1 \right) \right] \tag{16.88}$$

The parameters μ, ν, and σ in Eqs. (16.87) and (16.88) pertain to the individual row under consideration. Using the above modified diffusion factor, the total loss parameter can be taken as a function of modified diffusion factor with the immersion ratio defined in Fig. 16.17 as a parameter. As shown, a set of curves representing the blade total loss parameter $\zeta t \sin(\alpha_{in}, \beta_{in})/2\sigma$ is plotted, with α_{in}, β_{in} as the inlet flow angle of stator or rotor row and σ as the blade solidity ratio. These curves may be presented in the form of polynomials to be implemented into a calculation procedure. The highest loss is encountered close to the tip at an immersion ratio of $H_r = 0.0$, where secondary flow and tip clearance losses predominate the loss picture. These

losses decrease as the immersion ratio approaches the blade mid height. However, for this particular compressor blade, the lowest loss is located around $H_r = 0.6 - 0.7$. Approaching the hub, the secondary losses dominate the losses leading to higher total loss parameter.

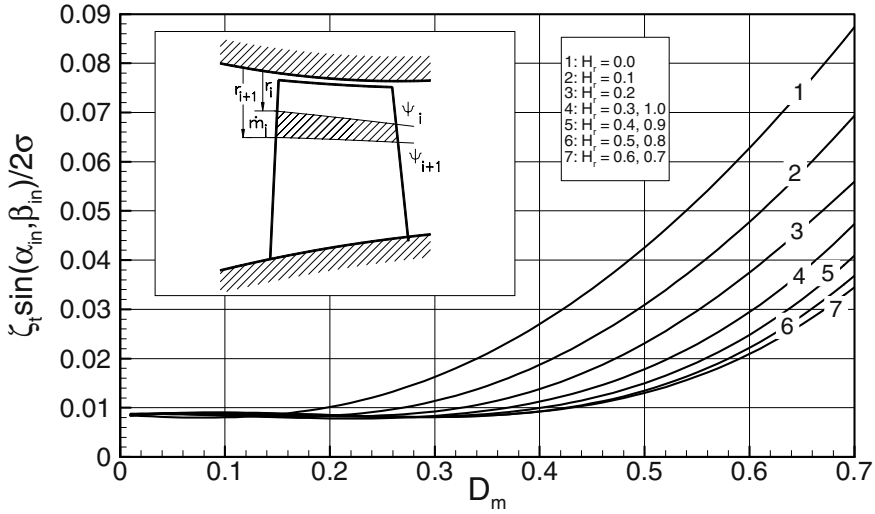

Fig. 16.17: Total loss parameter as a function of modified diffusion factor with immersion ratio as parameter from Schobeiri (1986).

It should be pointed out that, the loss parameter presented in Fig. 16.17 represents only the loss situation for a particular compressor, whose efficiency and performance are calculated and presented in this section. As indicated previously, the generation of compressor efficiency performance maps requires knowledge of the individual losses of the stator and rotor rows. The loss parameter curves of Fig. 16.17 are not symmetric and, therefore, must be applied to the blade in a manner compatible with their distribution over the blade spanwise direction. For this purpose, we apply energy balance to the blade, which results in:

$$\sum_{j=1}^{n} \dot{m}_j \left(\frac{\Delta h_{sj}}{\eta_j} \right) = \dot{m} \left(\frac{\Delta h_s}{\eta} \right) \tag{16.89}$$

where the index j refers to the blade spanwise positions from tip to hub. The efficiency is defined in terms of the row loss coefficient Z, introduced in Chapter 8, which is a function of ζ_t and may be written for the stator and rotor, respectively:

$$Z_t' = \frac{\zeta_t'\ V_1^2}{2\ l'}, \quad Z_t'' = \frac{\zeta_t''\ W_2^2}{2\ l''} \tag{16.90}$$

Using Eq. (16.90), the row efficiency can be expressed as:

$$\eta' = 1 - Z_t' \quad , \quad \eta'' = 1 - Z_t'' \tag{16.91}$$

Eq. (16.91), coupled with the total loss definition, can be reduced to:

$$Z_t = \frac{1}{\Delta h_s\ A_t} \left(\sum_{j=1}^{n} \Delta h_{sj}\ A_j\ Z_j \right) \tag{16.92}$$

Equation (16.92) is an integral representation of the loss distribution in the spanwise direction.

An alternative calculation method for calculating the efficiency is using the entropy change as a result of a row-by-row compression process. The design and off-design efficiency is then determined as an outcome of the loss calculation which reduces the number of iterations involved. Applying Eq. (4.103) to the stator row, the entropy change is directly related results in:

$$s_2 - s_1 = R \ln \left(\frac{p_{01}}{p_{02}} \right) \tag{16.93}$$

With the given initial entropy s_1 and total pressure p_{01}, the row exit entropy is calculated by using the row loss coefficient. For the stator row it is expressed by:

$$\zeta' = \frac{P_{o1} - P_{o2}}{\frac{1}{2}\ \rho_1\ V_1^2} = \frac{P_{o1}}{\frac{1}{2}\ \rho_1\ V_1^2} \cdot \left[1 - \left(\frac{P_{o2}}{P_{o1}} \right) \right] \tag{16.94}$$

Substituting Eq. (16.94) into (16.93) after some rearrangement, we obtain the entropy at the exit of the row:

$$s_2 = s_1 - R \ln \left[1 - \frac{\zeta'\ \rho_1\ V_1^2}{2\ P_{o1}} \right] \tag{16.95}$$

With the exit entropy and the corresponding enthalpy, the stator row exit thermodynamic condition is fully determined. The following rotor row is treated similarly considering the relative frame of reference. The entropy increase is related to the change of the relative total pressure which is expressed in the following relation:

$$s_3 - s_2 = R \ln \left(\frac{P_{o2r}}{P_{o3r}} \right) \tag{16.96}$$

Similar to the stator, with the given initial entropy s_1 and relative total pressure p_{r01}, the row exit entropy is calculated by using the rotor row loss coefficient. For the rotor row it is expressed by:

$$\zeta' = \frac{P_{o2r} - P_{o3r}}{\frac{1}{2} \rho_2 W_2^2} = \frac{P_{o2r}}{\frac{1}{2} \rho_2 W_2^2} \cdot \left[1 - \left(\frac{P_{o3r}}{P_{o2r}} \right) \right] \tag{16.97}$$

Substituting Eq. (16.90) into (16.89), we obtain

$$s_3 = s_2 - R \ln \left[1 - \frac{\zeta'' \rho_2 W_2^2}{2 P_{o2r1}} \right] \tag{16.98}$$

With the exit entropy and the corresponding enthalpy, the rotor row exit thermodynamic condition is fully determined. The row-by-row calculation is continued until the compression process for the entire compressor is completed.

16.2.3 Generation of Steady State Performance Map

Using the row-by-row calculation method described above, the compression process for design and off-design operation conditions can be accurately calculated. As a result, the calculation procedure provides efficiency and performance maps for single-stage axial, radial, and multi-stage axial compressors. The prerequisite for an accurate efficiency and performance prediction is the knowledge of the compressor blade's loss behavior. Given the geometry of a nine-stage subsonic axial compressor, steady state calculations are performed by varying the rotational speed and the compressor mass flow. Figures 16.18 and 16.19 exhibit the performance and efficiency behavior of a 3-stage subsonic compressor at its design and off-design operating points. The rotational speed is non-dimensionalized by the design angular velocity. Fig. 16.19 shows the compressor pressure ratio versus the non-dimensionalized mass flow ratio. Starting with the design speed ratio of $\omega/\omega_D = 1$, we first reduce the mass flow.

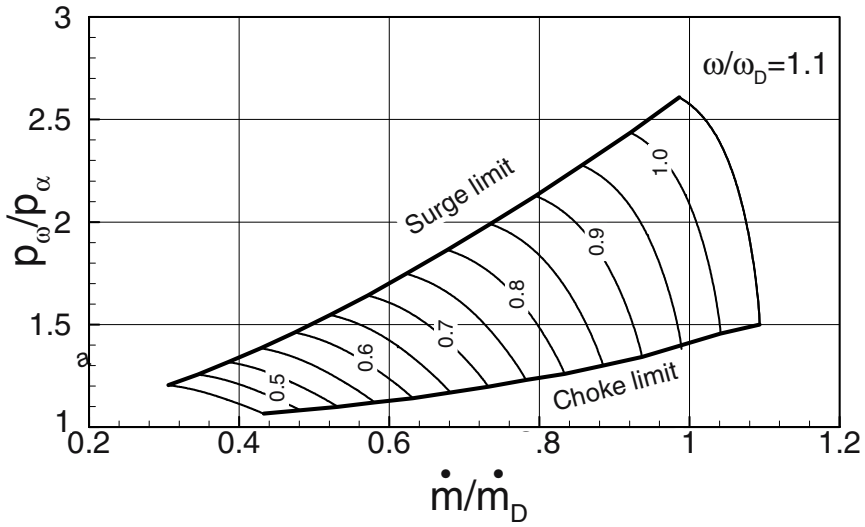

Fig. 16.18: Compressor pressure ratio as a function of relative mass flow with relative angular velocity as parameter.

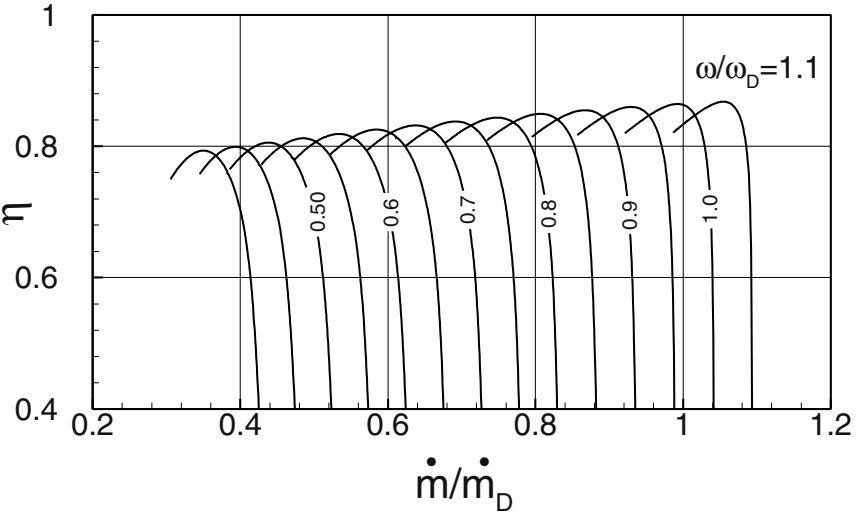

Fig. 16.19: Efficiency as a function of relative mass flow with relative angular velocity as parameter.

This in turn changes the stage velocity diagrams, and thus, the incidence angle of blades resulting in higher flow deflection, greater stage load coefficient, and therefore, higher pressure ratio. The mass flow reduction may be caused by specific operation conditions such as closing a valve of a compression system or increasing the compressor back pressure of a gas turbine system. For the case that mass flow at a constant speed is further reduced, a subsequent increase in inlet flow incidence will cause *a partial or total flow separation* resulting in a compressor *surge*. On the other hand, if at a constant rotational speed the compressor back pressure is reduced, the incidence angle assumes negative values causing the axial velocity component to increase. Further reducing the back pressure results in higher velocity that may approach the speed of sound. In this case, the compressor operates in a state of *choke*. Thus, the operational envelope of the compressor is bounded by a *surge limit* and a *choke limit* plotted in Fig. 16.18.

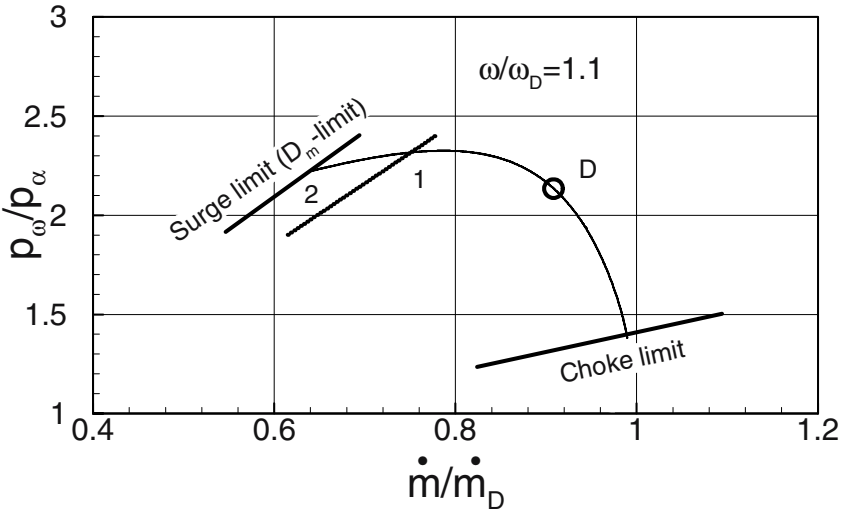

Fig. 16.20:Construction of surge and choke limits, point D refers to design point, point 2 corresponds to the maximum diffusion factor, 1-2 precautionary surge margin set by compressor designer.

Details of the performance map is shown in Fig. 16.20. After passing through the design point *D*, by further decreasing the compressor mass flow rate, the pressure ratio first reaches a maximum followed by a continuous decrease. Further decreasing the mass flow may trigger a sequence of events, sketched in Fig. 16.21. First, a boundary layer separation inception may occur at a few blades, as sketched in Fig. 16.21(1). While the channel of these blades are occupied by low energetic stall cells, the rest of the blades operate at normal flow condition, however, at a different incidence angle, as shown in Fig. 16.21(2). Since the stall cells have blocked a portion of the cross sectional area, a redistribution of the mass flow in circumferential

direction occurs, leading to a redistribution of the incidence angles. Based on the separation extent, the cells may partially occupy the tip and hub region, as well as the entire blade channels from hub to tip, as shown in Fig. 16.21(3).

(1) Boundary layer separation, inception of stall cells

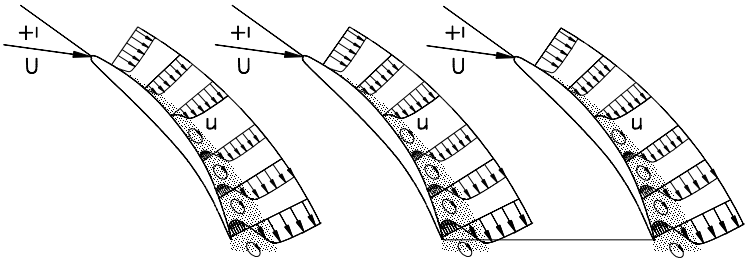

(2) Separation zones, manifestation of stall cells

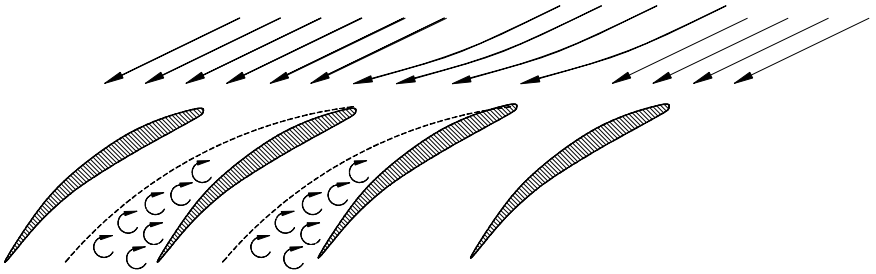

(3a)Partial span stall (3b)Full span stall (3c) Surge

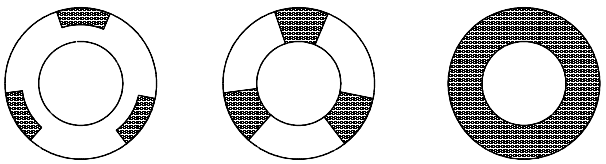

Fig. 16.21: Inception of rotating stall and surge

If these stall cells are located within rotor blades, they rotate with the corresponding frequency causing the compressor to *operate in rotating stall* mode. This operating mode is characterized by temporal fluctuations of the mass flow. Further reducing the mass flow may lead to a complete breakdown of the compressor operation that is called compressor *surge*. In this case, the compressor mass flow periodically oscillates between positive and negative. This non-linear dynamic operation causes

the blades to be subjected to severe periodic forces that may result in a complete de-blading of the compressor rows if immediate actions are not taken. In conjunction with the combustion chamber, the compressor surge may suck hot gas and eject it in a counter flow direction. To prevent the compressor from getting into surge operation, the compressor designer places a *surge limit* on the performance map. This limit may be experimentally determined or empirically estimated by setting certain flow deflection limits, diffusion factor limits, or even boundary layer separation criterion. For the performance map presented in Fig. 16.20, we set the diffusion factor to $D_m = 0.65$ as the limiting criterion for the beginning of a rotating stall. This is shown in Fig. 16.20 as the surge limit that intersects the pressure curve at point 2. The compressor aerodynamicist wishes to have certain margins to this limit, and may construct a second surge limit. This is illustrated in Fig. 16.20, where the diffusion factor limit was set at $D_m = 0.45$, point 1.

16.3. Modeling the Compressor Module for Non-linear Dynamic Performance

Three levels of compressor modeling are presented in this section. The first level utilizes the steady performance map. The second level uses the row-by-row adiabatic compression process, and the third level employs a diabatic row-by-row calculation method. The first level exhibits the global performance behavior of a compression system under dynamic operation condition. The second level delivers a detailed calculation of the adiabatic compression process under any dynamic operation condition . In addition to the information provided by the second level model, the third level provides detailed information about the blade temperature and the effect of the heat transfer on an operation envelope that includes the performance, surge, and choke limits.

16.3.1 Module Level 1: Using Performance Maps

The efficiency and performance maps generated in section16.2.3 can be used for a first level compressor simulation. This simulation level obviously does not provide details regarding the dynamic events within compressor stages. However, it is capable of globally reflecting the state of the compressor during a dynamic event. The global compressor module is modeled mathematically by a set of algebraic equations. It receives the dynamic information from the inlet plenum, performs off-design calculations, and transfers the results to the exit plenum. This arrangement allows a quasi dynamic simulation of the compressor component. The set of algebraic equations determines the off-design values of the mass flow rate $\dot{m}$, total temperature *To*), power consumption $\dot{E}$, efficiency, volume flow $\dot{V}$ as functions of the efficiency, pressure ratio, inlet temperature, and angular velocity (ω), as follows:

$$\begin{aligned} \dot{E} &= \dot{m}\ \bar{c}_p\ (\ T_{oO} - T_{oI}\ ) \\ T_{oD} &= T_{oD}\ (\pi,\ \eta, T_{oI}, \omega) \\ \dot{m} &= \dot{m}\ (\pi, \eta, T_{oI}, \omega) \\ \dot{V} &= \dot{V}\ (\pi, T_{oI}, \omega) \\ \dot{E} &= \dot{E}\ (\pi, \eta, T_{oI}, \omega) \end{aligned} \tag{16.99}$$

To account for the effect of temperature on the results obtained from performance map, we introduce a non-dimensional *relative* volume flow rate, $\dot{V}_R$

$$\dot{V}_R = \frac{\dot{V}}{\dot{V}_D} \sqrt{\frac{T_D}{T}} \tag{16.100}$$

a relative rotational speed,

$$\omega_R = \frac{\omega}{\omega_D} \sqrt{\frac{T_D}{T}} \tag{16.101}$$

and a relative pressure ratio,

$$\pi_R = \frac{\pi}{\pi_D} - 1 \tag{16.102}$$

where, the subscript *R* and *D* refer to relative and design point values, respectively. By introducing the above non-dimensionalized parameters into Eqs. (16.99), we obtain two functional relations for the efficiency and the volume flow rate:

$$\eta = \eta\ (\ \pi_R\ ,\ \omega_R\ ) \tag{16.103}$$

$$\dot{V}_R = \dot{V}_R \quad (\pi_R , \omega_R) \tag{16.104}$$

As seen from Eqs. (16.103) and (16.104), the number of the parameters has reduced by one, resulting in simpler functionality that can be expressed in terms of two-dimensional polynomials as functions of π_R, and ω_R as given below:

$$\dot{V}_R = \Pi_R \; . \; A \; . \; \Omega = \Pi_i \; A_{ij} \; \Omega_j \tag{16.105}$$

$$\eta = \Pi_R \; . \; C \; . \; \Omega = \Pi_i \; C_{ij} \; \Omega_j \tag{16.106}$$

with $\Pi_i = \pi_R^{i-1}$ and $\Omega_j = \omega_R^{j-1}$. The matrices A_{ij}, and C_{ij} represent the coefficients of the two dimensional polynomial describing the behavior of the volume flow rate and efficiency, respectively, as functions of the given pressure ratio and angular velocity. Considering the non-dimensionalized Eqs. (16.104)-(16.106), the first element of the matrices A and C are determined by the map as $A_{11} = \dot{V}_{R_D}$, $C_{11} = \eta_D$. Developing Eq. (16.105) and (16.106) finds the volume flow rate $\dot{V}$:

$$\begin{aligned} \dot{V}_R = {} & \Pi_1 \; A_{11} \; \Omega_1 + \Pi_1 \; A_{12} \; \Omega_2 + \cdots\cdots\cdots + \Pi_1 \; A_{1n} \; \Omega_n \\ & + \Pi_2 \; A_{21} \; \Omega_1 + \Pi_2 \; A_{22} \; \Omega_2 + \cdots\cdots\cdots + \Pi_2 \; A_{2n} \; \Omega_n \\ & + \Pi_m \; A_{m1} \; \Omega_1 + \Pi_m \; A_{1m} \Omega_m + \cdots\cdots\cdots + \Pi_m \; A_{mn} \; \Omega_n \end{aligned} \tag{16.107}$$

and the efficiency:

$$\begin{aligned} \eta = {} & \Pi_1 \; C_{11} \; \Omega_1 + \Pi_1 \; C_{12} \; \Omega_2 + \cdots\cdots\cdots + \Pi_1 C_{1n} \; \Omega_n \\ & + \Pi_2 \; A_{21} \; \Omega_1 + \Pi_2 \; C_{22} \; \Omega_2 + \cdots\cdots\cdots + \Pi_2 C_{2n} \; \Omega_n \\ & + \Pi_m \; A_{m1} \; \Omega_1 + \Pi_m \; C_{1m} \; \Omega_m + \cdots\cdots\cdots + \Pi_m \; C_{mn} \; \Omega_n \end{aligned} \tag{16.108}$$

The elements are

$$\Pi_1 = \pi_R,\ \Pi_2 = \pi_R^1,\ \Pi_3 = \pi_R^2,\ \Pi_i = \pi_R^{i-1}$$
$$\Omega_1 = \omega_R,\ \Omega_2 = \omega_R^1, \Omega_3 = \omega_R^2,\ \Omega_j = \omega_R^{j-1} \tag{16.109}$$

Utilizing Eq. (16.107) to (16.109) , the off-design mass flow rate, the total exit temperature and the power consumption $\dot{E}$ are calculated as follows:

$$\dot{m} = \rho \dot{V} \tag{16.110}$$

$$T_{oO} = T_{oI} \quad \pi^{\frac{\kappa-1}{\kappa}} \quad \frac{1}{\eta} \tag{16.111}$$

$$\dot{E} = \dot{m}\ \bar{c}_p\ (\ T_{oO} - T_{oI}\ ) \tag{16.112}$$

where, $\dot{V}$ is the volume flow rate, $\bar{c}_p$ is the average specific heat at constant pressure, $T_{o,I}$ is the inlet stagnation temperature, T_{oO} is the exit stagnation temperature, and η is the compressor efficiency.

16.3.1.1 Quasi dynamic modeling using performance maps: The compressor components are modeled quasi-dynamically using a steady state performance map enclosed within two plena as Fig. 16.22 reveals.

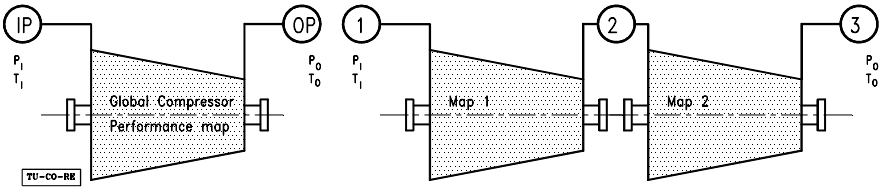

Fig. 16.22: Modeling of dynamic performance of a multi-stage compressor using (a) one performance map, (b) two or more maps.

For a compressor with up to three-stages, a single performance is sufficient to calculate the global transient behavior of the compressor. However, if the compressor has more than three stages, two or more performance maps may be necessary to satisfactorily predict the transient behavior of the compressor. The steady performance map is obviously not able to handle transient events. However, if it is

placed between two plena that continuously feed the steady map with unsteady data, it may deliver reasonable dynamic results. The inlet plenum transfers the time dependent pressure and temperature to the global map which calculates the compressor performance and transfers the information to the outlet plenum. For this purpose, the following system of differential and algebraic equation are used: (1) The inlet and outlet plena are described by Eq. (16. 10) and (16.11). For the sake of completeness, these equations are listed below:

$$\frac{\partial T_0}{\partial t} = \frac{1}{\rho V}\left[\sum_{i=1}^{n} \dot{m}_{I_i}\left(\kappa \frac{c_{pI_i}}{c_p} T_{0_{I_i}} - T_0\right) - (\kappa - 1)\sum_{j=1}^{m} \dot{m}_{O_j} T_0\right] \tag{16.113}$$

$$\frac{\partial P}{\partial t} = \frac{\kappa R}{V}\left[\sum_{i=1}^{n} \dot{m}_{I_i} \frac{c_{pI_i}}{c_p} T_{0_{I_i}} - \sum_{j=1}^{m} \dot{m}_{O_j} T_0\right] \tag{16.114}$$

with Eqs. (16.113) and (16.114) and the performance map described by algebraic equations (16.107), (16.108), (16.110), (16.111) and (16.112), we are now able to quasi-dynamically model the compressor component.

16.3.1.2 Simulation example: As an example, the global dynamic performance of a three-stage compressor is investigated. The compressor running at a constant rotational speed is connected to a large air storage facility. It continuously pumps air

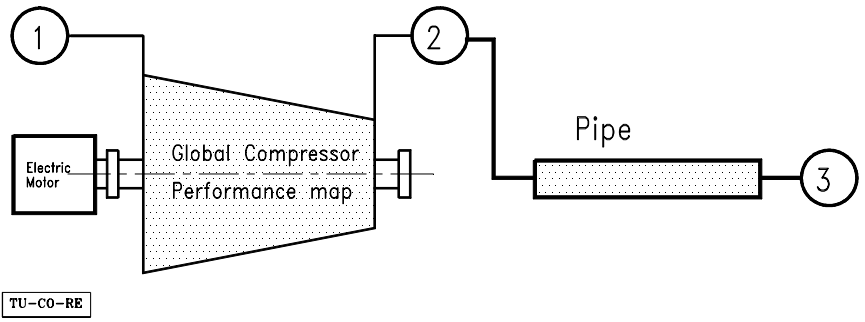

Fig. 16.23: Simulation schematic using a compressor performance map.
into the storage.

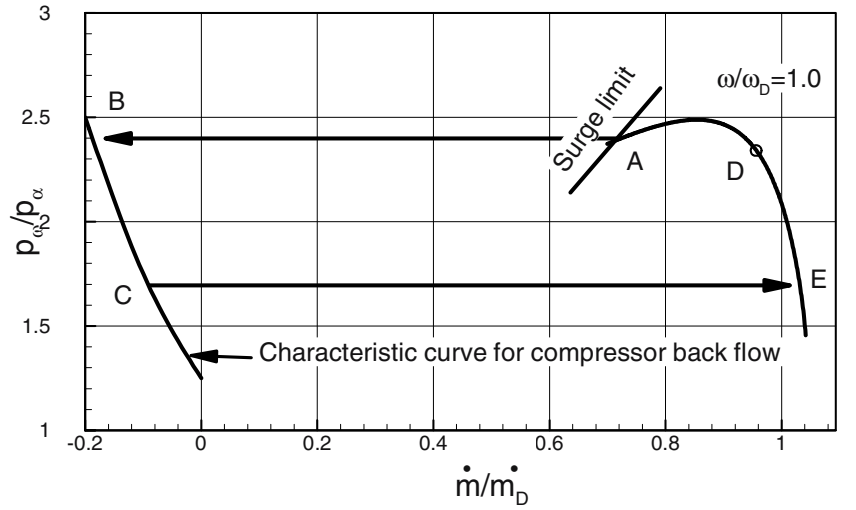

Fig. 16.24: Compression, surge, and recovery plotted in performance map

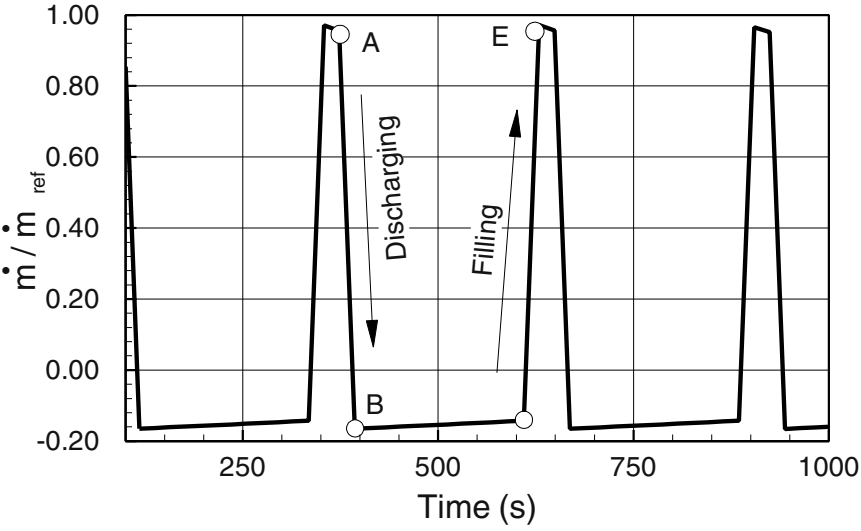

Fig. 16.25: Quantitative details of surge cycle

The system, schematically shown in Fig. 16.23, consists of an electric motor drive, a three-stage compressor with the performance maps shown in Fig. 16.19 and Fig. 16.18, which is a pipe that connects the compressor exit with the storage. Air is sucked from the environment at a constant pressure and temperature which is modeled

by plenum 1. The storage is represented by plenum 3. Starting from a storage pressure of one bar, air is pumped raising the pressure, Fig. 16.23. Approaching the surge limit at point A, the compressor operation experiences an instantaneous breakdown that causes the mass flow to reverse the direction, point B. At this point the compressor functions as a dissipater with the characteristic curve shown in Fig. 16.24.

The system rapidly starts to depressurize to arrive at point C, which is below the compressor design point D. The mass flow jumps to the right side, passes through the design point D and repeats the cycle. It should be pointed out that the characteristic curve for compressor back flow is not a part of the performance map that can be accurately predicted. It is merely an approximation that assumes the compressor channel as a pipe filled with blades that are exposed to back flow and function as dissipaters. Figure 16.25 reflects the details of the surge cycle that includes discharging and filling.

16.3.2 Module Level 2: Row-by-Row Adiabatic Calculation Procedure

This compressor module provides detailed information about the compressor behavior during dynamic events. Two methods can be used for describing this module. The first method utilizes the time dependent conservation laws for continuity, momentum, and energy Eqs. (14. 26), (14.33), and (14.51) derived in Chapter 14. For adiabatic stage compression calculation, Eq. (14.51) is reduced to:

$$\frac{\partial H}{\partial t} = -\kappa_k \frac{\dot{m}_k}{\rho_k S_k}\left(\frac{H_{i+1} - H_i}{\Delta x}\right) + \frac{\kappa_k}{\rho_k}\left(\frac{L}{\Delta V}\right) - \\ - \left(\frac{\kappa - 1}{\rho k}\right)_k \left[\left(\frac{H_k + K_k}{\Delta x}\right)\left(\frac{\dot{m}_{i+1}}{S_{i+1}} - \frac{\dot{m}_i}{S_i}\right) + \frac{\dot{m}_k}{\rho_k S_k^{\,2}}\frac{\partial \dot{m}_{i+1}}{\partial t}\right] \tag{16.115}$$

The stage power L in Eq. (16.115) is directly related to the specific stage mechanical energy $L = \dot{m} l$ with $l = \lambda U_3^2$. For row- by-row dynamic calculation, Eq. (16.115) may be decomposed using the row-parameters discussed in section 16.2.1.2. This method allows a detailed, dynamic calculation of row properties. The second method is based on the row-by-row adiabatic calculation procedure outlined in section 16.2.1.2 under utilization of plena Eqs.(16.113) and (16.114) for dynamic coupling. Three alternative coupling configurations for a two-stage compressor are shown in Fig. 16.26, Fig. 16.27. In configuration (a) each row has an inlet and an exit plenum, whereas in (b) each stage is enclosed by an exit and an inlet plenum. In (c) the entire compressor is placed between an inlet and an exit plenum. This configuration provides satisfactory results for small size compressors such as those of a helicopter gas turbine as shown in Fig 16.27. To accurately account for the volume dynamics of

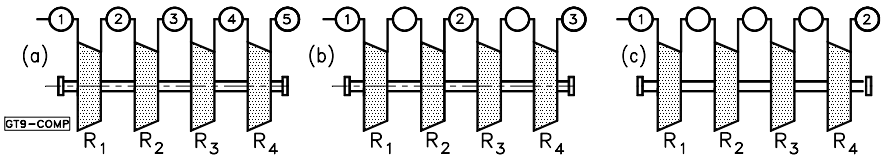

Fig. 16.26: Row-plena configuration, (a) each row enclosed by two plane, (b) each stage enclosed by two plena, (c) the entire compressor enclosed by two plena.

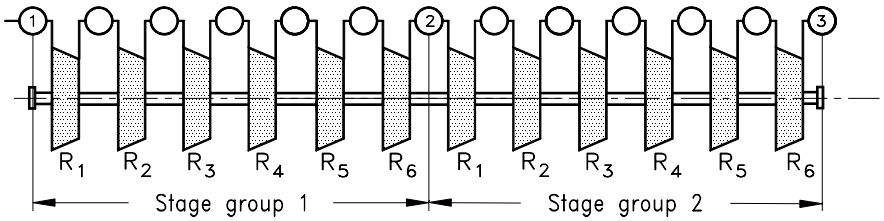

Fig. 16.27: Decomposition of a six stage compressor into two three-stage groups. Each group is enclosed by two plena.

a multi-stage compressor, it is more appropriate to decompose the compressor into several stage groups, where each group may consist of two to three stages that have configuration (b).

16.3.2.1 Active Surge Prevention by Adjusting the Stator Blades:

The row-by-row calculation procedure not only provides a detailed information about the compression process of individual rows and the entire compressor, but it also enables an active control of compressor instability and surge by adjusting the stagger angles of the stator rows. It is probably the most effective active aerodynamic control mechanism. The configuration of a multi-stage compressor with adjustable stator blade rows is shown schematically in Figure 16.28.

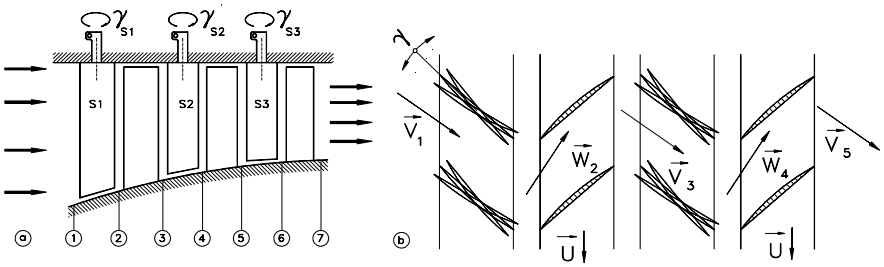

Fig. 16.28: (a) Multistage compressor with adjustable stator blades, (b) Stagger angle adjustment.

As shown in Fig. 16.28(b), the stagger angle of each individual stator row γ_{Si} can be changed according to a γ-scheme controlled by a multi-variable control system with the row exit pressure as one of its input variables. The effect of the adjustment on the stage velocity diagram is shown in Fig. 16.29.

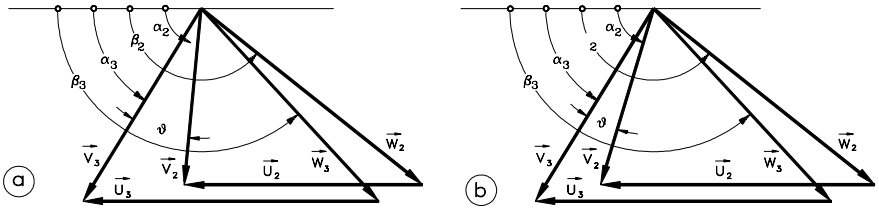

Fig. 16.29(a): Velocity with increased flow deflection ϑ as a result of an adverse dynamic operation, (b) adjusted stator blades causing a reduction in flow deflection ϑ, thus preventing rotating stall and surge.

Figure 16.29(a) exhibits the stator row in its design stagger position under an adverse operation condition which is associated with an increase in compressor pressure ratio. This pressure ratio, however, is established by a deflection angle ϑ that may cause a boundary layer separation on stator and rotor blades thus, leading to an inception of rotating stall and surge condition. To prevent this, the stagger angle γ is adjusted resulting in a reduced ϑ as Fig. 16.29(b) shows.

16.3.2.2 Simulation example: surge and its prevention: This example demonstrates the surge prevention capability of the row-by-row calculation method by simulating the dynamic behavior of an actual single spool gas turbine engine, Fig. 16.30, under an adverse transient operation condition.

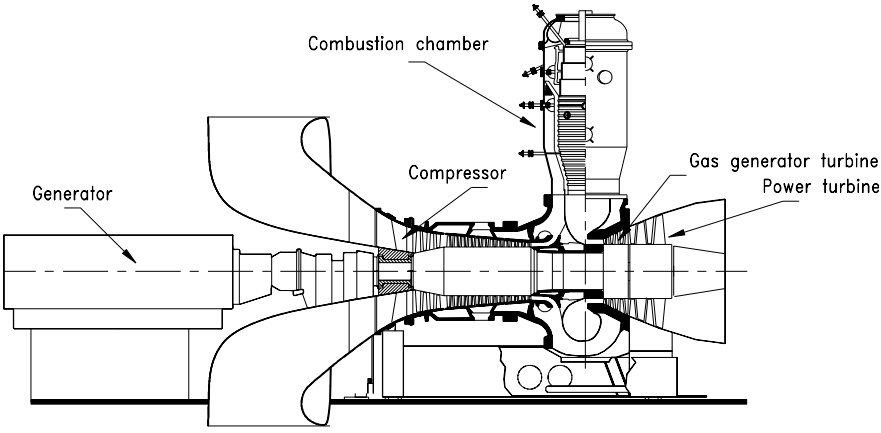

Fig. 16.30: A split shaft gas turbine engine for simulating rotating stall and surge.

To force the compressor into an unstable regime, we reconfigured the engine by splitting the shaft and decomposing the gas turbine into a gas generator and a power generator part, as shown in Fig. 16.30. The gas generator unit incorporates a multi-stage compressor that we decompose into a low pressure, an intermediate pressure, and a high pressure compressor, as discussed earlier. The compressor is followed by a combustion chamber, a three-stage turbine that drives the compressor, and a two-stage power turbine connected with a generator. The LP, IP, and HP-compressors are modeled using the row-by-row method presented in this paper. The simulation schematic of the engine is shown in Fig. 16.31, where the individual components are placed between the plena. It also shows the interaction of individual components with the control system.

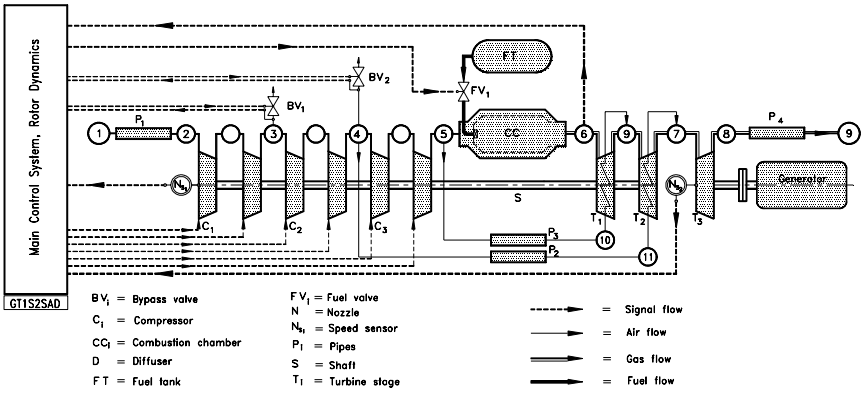

Fig. 16.31: Simulation schematic of gas turbine shown in Fig. 16.30.

As seen in Fig. 16.31, the speed controller is connected to the power shaft, thus sensing the rotational speed and the temperature of the power shaft and its time derivative to control the fuel mass flow.

Case I: Simulation of Compressor Surge: Starting from a steady state operating point, the dynamic behavior of the above engine is simulated for a transient operation which is controlled by the prescribed generator power schedule that acts on the power shaft as shown in Fig. 16.30. This increase in rotational speed causes the controller to trigger a rapid throttling of the fuel mass flow. The throttling process lasts until a constant idling speed of the power shaft is attained. After about seven seconds, full load is suddenly added and then reduced slowly such that after the completion of load addition, the gas turbine is supplying 25% of its rated load, as shown in Fig. 16.32. The rotor reacts to this sudden addition of load with a sharp decrease in rotational speed as displayed in Fig. 16.32. That, in turn, causes a quick opening of the fuel valve.

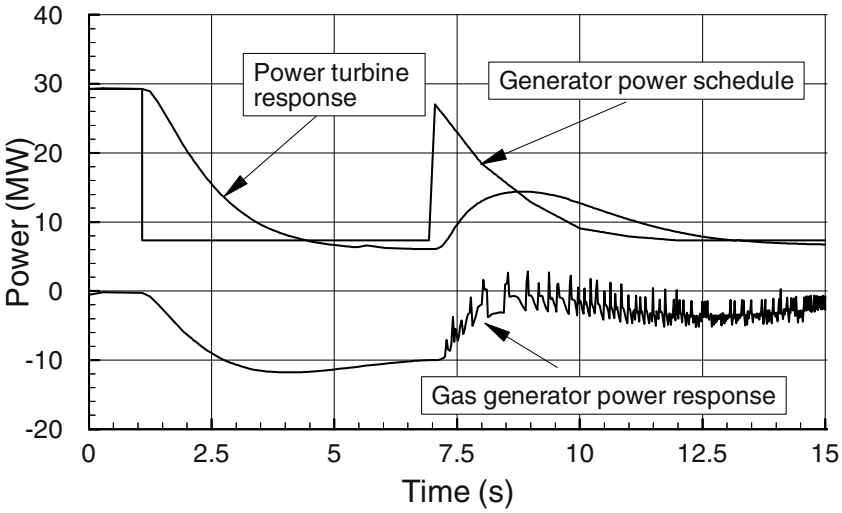

Fig. 16.32: Generator power schedule, response of power turbine and gas generator

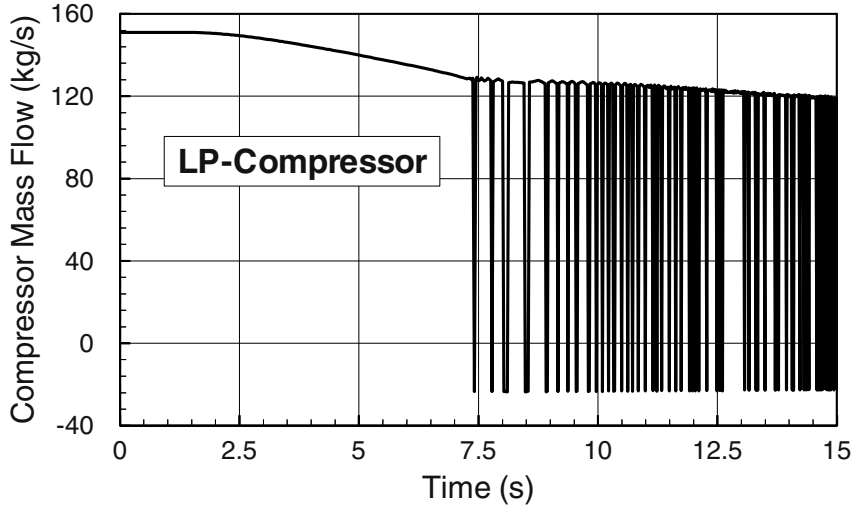

Fig. 16.33: LP-compressor operating in surge mode

During this process, the power generation capability of the gas generation turbine deteriorates significantly causing a major power imbalance between the turbine and compressor components. This imbalance results in a continuous decrease of the

compressor rotor speed, causing the compressor to operate partially in rotating stall and surge regimes. As shown in Fig. 16.33, reducing the rotor speed below 90% forces the LP-compressor stage group into rotating stall and a short duration surge process with reversal in the mass flow direction. Since the magnitude of the reversed mass flow is relatively small and of very short duration, a total engine mass flow reversal does not occur. The IP-compressor stage group exhibits similar instability behaviors, where the compressor mass flow reversal occurs at slightly lower frequency and almost the same amplitude. The HP-stage group displays a distinctively different behavior. While the mass flow experiences fluctuation at a similar frequency, the amplitude remains always positive. These fluctuations apparently are not caused by the HP-stage group itself and are propagated downstream from the LP- and IP-parts respectively. This behavior is fully consistent with the continuity requirement that leads to an integrally positive mass flow rate because of the high frequency and short duration mass flow reversal in LP- and IP-compressors.

Case II: Surge Prevention by Stator Stagger Angle Adjustment: To prevent the compressor instability and surge described in Case I, the stagger angles of the LP- and IP-compressor stage groups were dynamically adjusted. Similar to Case I, the engine was forced into an adverse off-design operation condition with the same load schedule as shown in Fig. 16.32. Starting from the steady state point, in accordance with the load schedule displayed in Fig. 16.34, a generator loss of load was simulated first.

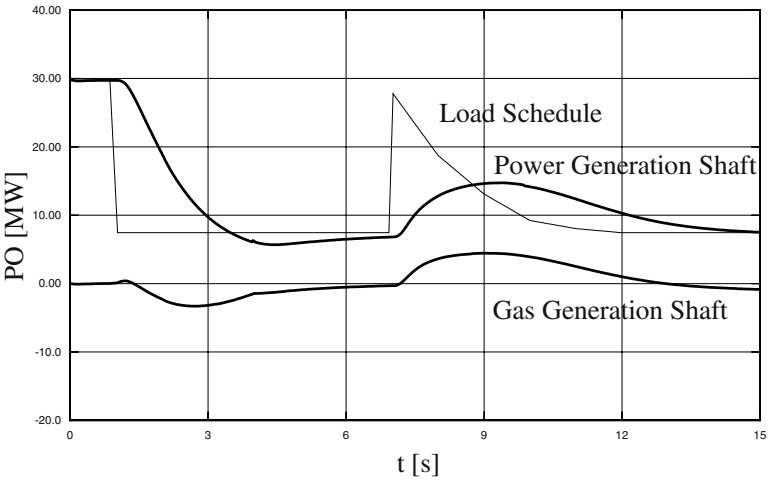

Fig. 16.34: Power response of the gas generator and power turbine shaft following a dynamic stator stagger angle adjustment

The power generation shaft responds to this event with a rapid increase in rotational speed, Fig. 16.35, which triggers closing of the fuel valve.

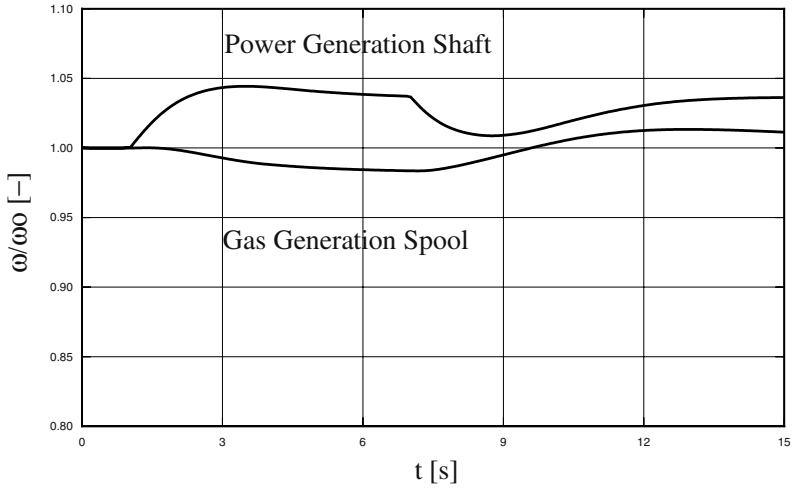

Fig. 16.35: Rotational speed of gas generator and power turbine shaft following a dynamic adjustment of stator stagger angle.

As a consequence, without active control, the power of the gas generation turbine would not be sufficient to cover the power consumption of the compressor. As observed in Case I this imbalance of power has led to a decrease in rotational speed of the gas generation shaft, which forced the first two compressor stage groups into an unstable regime. In order to avoid the power imbalance of the gas generation shaft as in Case I, the stagger angle pertaining to the stator blades of the LP- and IP- stage groups are continuously reduced according to the prescribed schedule. This procedure starts immediately at the time where the loss of load occurs and lasts until the prescribed γ- values at $t = 4s$ are reached. These values are kept constant for the rest of the simulation. As shown, it is sufficient to reduce the stagger angle of the LP- and IP-compressors, while the stagger angle of the HP-compressor remained unchanged. This intervention causes a substantial shift in the surge limit preventing all three compressor stage groups from entering into the instability regime. As Fig. 16.36 shows, the compressor mass flow does not experience any fluctuations. The stable operation of the compressors is reflected in Fig. 16.34, where the load schedule and the response of the power generator and gas generator turbines are displayed. In contrast to the unadjusted Case I shown in Fig. 16.32, no power fluctuations are encountered. The rotational speed behavior of the gas generator shaft shown in Fig.

16.35 is substantially different from the one shown in case I. The positive power difference of the gas generation spool plotted in Fig. 16.34 is the result of a decreased compressor load caused by stator angle adjustment. It prevents the rotational speed of the gas generation spool in Fig. 16.35 from decreasing and moves the compressor operation into a more stable operation regime. The power generator shaft, however, behaves very similar to Case I.

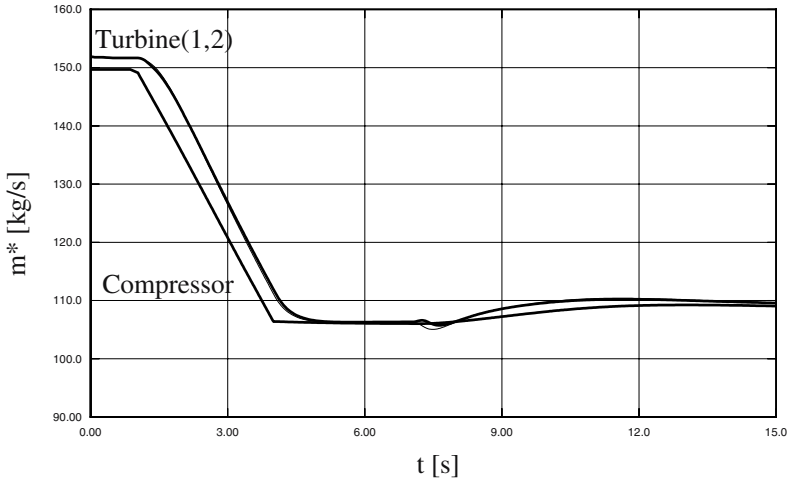

Fig. 16.36: Mass flow transient after stator blade adjustment.

16.3.3 Module Level 3: Row-by-Row Diabatic Compression

As briefly mentioned, during startup, shutdown, load change, or any other transient operation, there is a temperature difference between the compressor blade, hub, casing, discs, and the compressor working medium. This temperature difference causes a heat transfer from the working medium to the blade material and vice versa. In case of high pressure compressor trains utilized in the industry, the working medium exiting the IP-compressor passes through an inter-cooler, thus substantially reducing its temperature before entering the HP-compressor. Moreover, the trend in the development of future generation high performance gas turbine engines point toward higher pressure ratios that inherently result in higher temperature requiring cooling of rear stages. In these cases, the compression process is no longer adiabatic, it is termed *diabatic compression*. Figure 16.37 displays a diabatic compressor stage with the corresponding instantaneous velocity diagram during a transient event, where heat from a working medium at a higher temperature is transferred to stator and rotor blade material, thus, increasing the blade temperature. The total heat added to the

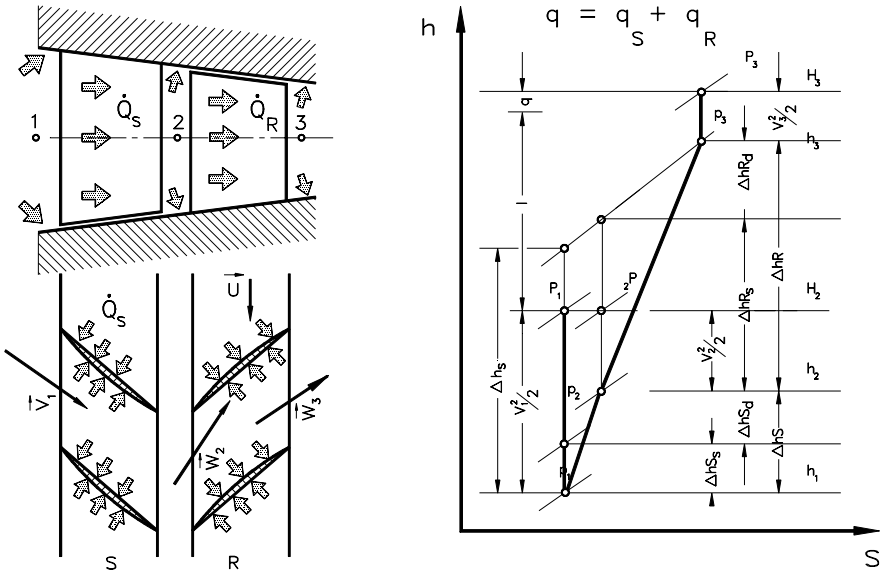

Fig. 16.37: Diabatic compression process within a compressor stage, compression process.

stage is the sum of the heat transferred to the stator and to the rotor. Heat transfers from a working medium to the compressor structure and thus, blading, hubbing, and casing occurs when the compressor is required to increase the higher pressure ratio. Heat rejection from the blading occurs when the compressor is relaxed. The process of heat transfer described in this section automatically captures both directions of heat transfer.

16.3.3.1 Description of diabatic compressor module: This compressor module provides detailed information about the compressor behavior during dynamic events and the heat transferred to/from the blade during a transient event. Similar to the adiabatic case discussed in Section 16.3.2, two methods can be used for describing this module. The first method utilizes the time dependent conservation laws for continuity, momentum, and energy Eqs. (14. 26), (14.33), and (14.51) derived in Chapter 14. For diabatic stage compression calculation, Eq. (14.51) is:

$$\frac{\partial H}{\partial t} = -\kappa_k \frac{\dot{m}_k}{\rho_k S_k}\left(\frac{H_{i+1} - H_i}{\Delta x}\right) - \left(\frac{\kappa - 1}{\rho k}\right)_k \times$$
$$\times\left[\left(\frac{H_k + K_k}{\Delta x}\right)\left(\frac{\dot{m}_{i+1}}{S_{i+1}} - \frac{\dot{m}_i}{S_i}\right) + \frac{\dot{m}_k}{\rho_k S_k^2}\frac{\partial \dot{m}_{i+1}}{\partial t}\right] \qquad (16.116)$$
$$+ \frac{\kappa_k}{\rho_k}\left(\frac{\Delta \dot{Q} + \Delta L}{\Delta V}\right)$$

The stage power ΔL in Eq. (16.116) is directly related to the specific stage mechanical energy $\Delta L \equiv L = \dot{m} l$ with $l = \lambda U_3^2$. The heat added to the stage is $\Delta \dot{Q} = \dot{m} q$ with q as the specific heat transferred to the stage. For steady state case with a constant mass flow, Eq. (16.116) immediately yields the conservation of energy $q + l = H_\omega - H_\alpha$. Thus, the equation of energy is rearranged as:

$$\frac{\partial H}{\partial t} = -\kappa_k \frac{\dot{m}_k}{\rho_k}\left(\frac{H_{i+1} - H_i}{\Delta V}\right) + \frac{\kappa_k \dot{m}_k}{\rho_k}\left(\frac{q + l}{\Delta V}\right)$$
$$- \left(\frac{\kappa - 1}{\rho k}\right)_k \left[\left(\frac{H_k + K_k}{\Delta x}\right)\left(\frac{\dot{m}_{i+1}}{S_{i+1}} - \frac{\dot{m}_i}{S_i}\right) + \frac{\dot{m}_k}{\rho_k S_k^2}\frac{\partial \dot{m}_{i+1}}{\partial t}\right] \qquad (16.117)$$

Equation. (16.117) together with equations of continuity and momentum, and additional information about the heat transfer, describes the dynamic behavior of the diabatic compressor stage. For a row-by-row analysis it can be decomposed into two equations that describe the individual stator and rotor rows. For stator row, because $l_S = 0$ and $q = q_S$, we find:

$$\frac{\partial c_{p_{i+1}} T_{0_{i+1}}}{\partial t} = -\kappa_k \frac{\dot{m}_k}{\rho_k}\left(\frac{c_{p_{i+1}} T_{0_{i+1}} - c_{p_{i+1}} T_{0_i}}{\Delta V}\right) + \frac{\kappa_k \dot{m}_k}{\rho_k}\left(\frac{q_S}{\Delta V}\right)$$
$$- \left(\frac{\kappa - 1}{\rho k}\right)_k \left[\left(\frac{c_{p_k} T_{0_k} + K_k}{\Delta x}\right)\left(\frac{\dot{m}_{i+1}}{S_{i+1}} - \frac{\dot{m}_i}{S_i}\right) + \frac{\dot{m}_k}{\rho_k S_k^2}\frac{\partial \dot{m}_{i+1}}{\partial t}\right] \qquad (16.118)$$

For the rotor row, because $l_R = l$ and $q = q_R$, we find:

$$\frac{\partial c_{p_{i+1}} T_{0_{i+1}}}{\partial t} = -\kappa_k \frac{\dot{m}_k}{\rho_k}\left(\frac{c_{p_{i+1}} T_{0_{i+1}} - c_{p_i} T_{0_i}}{\Delta V}\right) + \frac{\kappa_k \dot{m}_k}{\rho_k}\left(\frac{q_R + l}{\Delta V}\right) - \left(\frac{\kappa - 1}{\rho k}\right)_k \left[\left(\frac{c_{p_k} T_{0_k} + K_k}{\Delta x}\right)\left(\frac{\dot{m}_{i+1}}{S_{i+1}} - \frac{\dot{m}_i}{S_i}\right) + \frac{\dot{m}_k}{\rho_k S_k^2}\frac{\partial \dot{m}_{i+1}}{\partial t}\right. \tag{16.119}$$

with l as the stage mechanical energy. To completely describe the diabatic compression process with stator and rotor rows, heat transfer equations as well as blade material temperature equations must be added to the set of equations (16.118), (16.119), Eqs. (14. 26), and (14.33). The terms in the brackets in Equations (16.118) and (16.119) are of second order, therefore, may be neglected. As a result we obtain for stator:

$$\frac{\partial c_{p_{i+1}} T_{0_{i+1}}}{\partial t} = -\frac{\kappa_k}{\rho_k \Delta V}\left(\dot{m}_k c_{p_{i+1}} T_{0_{i+1}} - \dot{m}_k c_{p_i} T_{0_i} - \Delta \dot{Q}_S\right) - \left(\frac{\kappa - 1}{\rho k}\right)_k \frac{\dot{m}_k}{\rho_k S_k^2}\frac{\partial \dot{m}_{i+1}}{\partial t} \tag{16.120}$$

and for the rotor row

$$\frac{\partial c_{p_{i+1}} T_{0_{i+1}}}{\partial t} = -\frac{\kappa_k}{\rho_k \Delta V}\left(\dot{m}_k c_{p_{i+1}} T_{0_{i+1}} - \dot{m}_k c_{p_i} T_{0_i} - \Delta \dot{L} - \Delta \dot{Q}_R\right) - \left(\frac{\kappa - 1}{\rho k}\right)_k \frac{\dot{m}_k}{\rho_k S_k^2}\frac{\partial \dot{m}_{i+1}}{\partial t} \tag{16.121}$$

with ΔV as net volume of row space occupied by the working medium. The heat added to or rejected from the working medium in Equations (16.120) and (16.121) is transferred to the stator and rotor blade material. The heat transfer aspect is treated in the subsequent section.

16.3.3.2 Heat transfer closure equations: Details of a heat transfer mechanism are shown in Fig. 16.38. We assume that the stator blades are cooled internally. The compressor working medium transfers certain amounts of thermal energy flow or heat flow $\dot{Q}_S$ to the stator blades. To maintain a

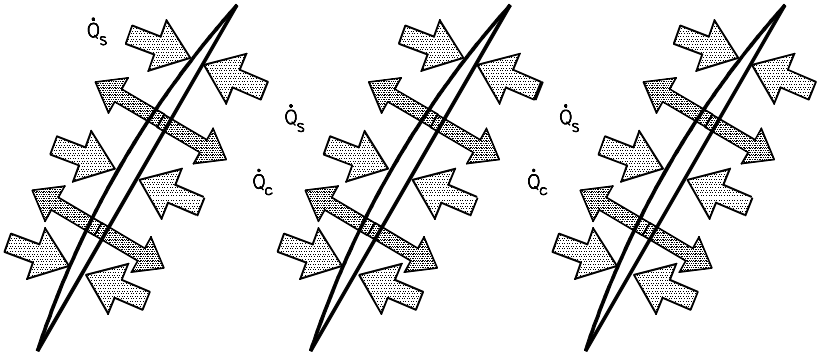

Fig. 16.38: Heat flow is transferred from compressor working medium to compressor blades $\dot{Q}_S$, the amount of $\dot{Q}_C$ is removed by the cooling medium.

desired blade temperature, the cooling mass flow through the blade internal channels have to remove the heat flow $\dot{Q}_C$ from the blade. The transferred thermal energies on hot and cold sides are:

$$\begin{aligned} \dot{Q}_S &= \bar{\alpha}_S A_S \, (\, \bar{T}_S - \bar{T}_W \,) \\ \dot{Q}_C &= \bar{\alpha}_C \, A_C (\, \bar{T}_W - \bar{T}_C) \end{aligned} \tag{16.122}$$

In Eq. (16.122) $\bar{\alpha}_C, \bar{\alpha}_S$ are the averaged heat transfer coefficients for internal cooling channels and the stator flow path, $\bar{T}_C$, $\bar{T}_S$, and $\bar{T}_W$ are the mean temperatures of coolant flow, stator working medium, stator wall temperature and A_C, A_S are the contact surfaces on the cold and stator hot side, respectively. The coupling condition between the cold and the hot side is provided by the material temperature differential equation:

$$\frac{dT_W}{dt} = \frac{1}{\rho_W \, c_W \, \Delta V_W} \, (\, \dot{Q}_C + \dot{Q}_S \,) \tag{16.123}$$

the heat flow $\dot{Q}_S$ in Eq. (16.123) may assume positive or negative values, whereas $\dot{Q}_C$ is always negative, since heat is rejected. For the case of no cooling $\dot{Q}_C$ is zero. In case of a dynamic temperature equilibrium, where the blade temperature change approaches zero, Eq. (16.123) is reduced to:

$$\dot{Q}_c + \dot{Q}_h = 0 \tag{16.124}$$

To calculate $\dot{Q}_S$ and $\dot{Q}_C$ for inserting into Eq. (16.123), we use the Nusselt number correlation as a result of dimensional analysis:

$$Nu = \frac{\bar{\alpha} c}{k} = f(Re,\ Pr,\ Ti,\ ,Str,\ ,Rs,\ Ar) \tag{16.125}$$

with $\bar{\alpha}$ as the averaged heat transfer coefficient, c the chord length, k the thermal conductivity. Major parameters affecting the compressor or turbine blade heat transfer are Reynold s number Re, Prandtl number Pr, Strouhal number S_{tr}, turbulence intensity Ti, surface roughness R, and acceleration ratio Ar :

$$Re = \frac{V_\infty c}{\nu},\ Pr = \frac{c_p \mu}{k},\ Ti = \frac{\sqrt{v^2}}{V_\infty},\ Str = \frac{f_w c}{V_\infty},\ R = \frac{h_R}{c},\ Ar = \frac{V_2}{V_1} \tag{16.126}$$

The dimensionless parameters in Eq. (16.126) contain a group of flow quantities and geometric parameters that are relevant for heat transfer calculations. Besides the Re- and the Pr number, the turbulence intensity which is the fluctuation velocity divided by the blade mean velocity V_∞ is a major parameter in heat transfer enhancement. Likewise, the Strouhal number that contains the wake passing frequency, the blade chord and the blade mean velocity plays a similar role. Despite tremendous amounts of publications that deal with the heat transfer issues in turbomachinery, no correlation can be found that incorporates the above parameters. Therefore, we resort to simple correlations such as the one given below:

$$Nu = \frac{\bar{\alpha} c}{k} = C_1 Re^m Pr^n \tag{16.127}$$

The coefficient C_1 as well as the exponents m and n in Eq. (16.127) depend upon the type of flow, the surface roughness, and the heat transfer direction. For turbulent flow, empirical correlations by Dittus-Boelter were found to be adequate.

References, Chapter 16

16.1 Lieblein, S., Schwenk, F., Broderick, R.L., Diffusions factor for estimating losses and limiting blade loadings in axial flow compressor blade elements, *NACA RM E53D01* June 1953.

16.2 Lieblein, S., Review of high performance axial flow compressor blade element theory, *NACA RME 53L22* April 1954.

16.3 Lieblein, S., Roudebush, W. H., Theoretical loss relations for low speed two dimensional cascade flow *NACA Technical Note 3662* March 1956.

16.4 Lieblein, S., Analysis of experimental low-speed loss and stall characteristics of two-dimensional compressor blade cascades, NACA RM E57A28 March 1957.

16.5 Lieblein, S., Loss and stall analysis of compressor cascades, *ASME Journal of Basic Engineering*. Sept. 1959.
16.6 *NASA SP-36 NASA Report, 1965*.
16.7 Miller, G.R., Hartmann, M.J., Experimental shock configuration and shock losses in a transonic compressor rotor at design point *NACA RM E58A14b*, June 1958.
16.8 Miller, G.R., Lewis, G.W., Hartman, M.J., Shock losses in transonic compressor blade rows *ASME Journal for Engineering and Power* July 1961, pp. 235-241.
16.9 Schwenk, F.C., Lewis, G.W., Hartmann, M.J., A preliminary analysis of the magnitude of shock losses in transonic compressors *NACA RM #57A30* March 1957.
16.10 Gostelow, J.P., Krabacher, K.W., Smith, L.H., Performance comparisons of the high Mach number compressor rotor blading NASA Washington 1968, NASA CR-1256.
16.11 Gostelow, J.P., Design performance evaluation of four transonic compressor rotors, *ASMEJournal for Engineering and Power*, January 1971.
16.12 Seylor, D.R., Smith, L.H., Single stage experimental evaluation of high Mach number compressor rotor blading, Part I, Design of rotor blading. *NASA CR-54581, GE R66fpd321P*, 1967.
16.13 Seylor, D.R., Gostelow, J.P., Single stage experimental evaluation of high Mach number compressor rotor blading, Part II, Performance of rotor 1B. NASA CR-54582, GE R67fpd236,1967.
16.14 Gostelow, J.P., Krabacher, K.W., Single stage experimental evaluation of high Mach number compressor rotor blading, Part III, Performance of rotor 2E. NASA CR-54583, 1967.
16.15 Krabacher, K.W., Gostelow, J.P., Single stage experimental evaluation of high Mach number compressor rotor blading, Part IV, Performance of Rotor 2D. *NASA CR-54584,* 1967.
16.16 Krabacher, K.W., Gostelow, J.P., Single stage experimental evaluation of high Mach number compressor rotor blading, Part V, Performance of Rotor 2B. *NASA CR-54585*, 1967.
16.17 Monsarrat, N.T., Keenan, M.J., Tramm, P.C., Design report, Single stage evaluation of high Mach number compressor stages, *NASA CR-72562 PWA-3546*, July 1969.
16.18 Koch, C.C., Smith, L.H., Loss sources and magnitudes in axial-flow compressors, ASME *Journal of Engineering and Power,* January 5, Vol. 98, N0. 3, pp. 411-424, July 1976.
16.19 Schobeiri, M.T., Verlustkorrelationen für transsonische Kompressoren, *BBC-Studie*, TN-78/20, 1987.
16.20 König, W.M., Hennecke, D.K., Fottner, L., Improved Blade Profile Loss and Deviation Angle Models for Advanced Transonic Compressor Bladings: Part I-A Model for Subsonic Flow, ASME Paper, No. 94-GT-335.

16.21 Schobeiri, M.T., Verlustkorrelationen für transsonische Kompressoren, *BBC-Studie*, TN-78/20, 1987.
16.22 Schobeiri, M.T., "Advanced Compressors Loss Correlations, Part II: Experimental Verifications," *International Journal of Rotating Machinery*, 1997, Vol. 3, pp. 179-187.
16.23 Levine, Ph., Two-dimensional inlet conditions for a supersonic compressor with curved blades, *Journal of Applied Mechanics*, Vol. 24, No. 2, June 1957.
16.24 Balzer, R.L., A method for predicting compressor cascade total pressure losses when the inletrelative Mach number is greater than unity, *ASME Paper 70-GT-57.*
16.25 Swan, W.C., A practical method of predicting transonic compressor performance, *ASME Journalfor Engineering and Power*, Vol. 83, pp. 322-330, July 1961.
16.26 Lieblein, S., Roudebush, W. H., Theoretical loss relations for low speed two dimensional cascade flow *NACA Technical Note 3662* March 1956.
16.27 Lieblein, S., Schwenk, F., Broderick, R.L., Diffusions factor for estimating losses and limitingblade loadings in axial flow compressor blade elements, *NACA RM E53D01* June 1953.
16.28 Lieblein, S., Loss and stall analysis of compressor cascades, *ASME Journal of Basic Engineering*. Sept. 1959.
16.29 Lieblein, S., Analysis of experimental low-speed loss and stall characteristics of two-dimensional compressor blade cascades, NACA RM E57A28 March 1957.
16.30 Lieblein, S., Analysis of experimental low-speed loss and stall characteristics of two-dimensional compressor blade cascades, NACA RM E57A28 March 1957.
16.31 Smith, L.H., Private communication with the author and the GE-Design Information Memorandum 1954: A Note on The NACA Diffusion Factor, 1995.
16.32 *NASA SP-36 NASA Report 1976*.
16.33 Gostelow, J.P., Krabacher, K.W., Single stage experimental evaluation of high Mach number compressor rotor blading, Part III, Performance of rotor 2E. NASA CR-54583, 1967.
16.34 Gostelow, J.P., Design performance evaluation of four transonic compressor rotors, *ASME Journal for Engineering and Power*, January 1971.
16.35 Seylor, D.R., Smith, L.H., Single stage experimental evaluation of high Mach number compressor rotor blading, Part I, Design of rotor blading. *NASA CR-54581, GE R66fpd321P*, 1967.
16.36 Seylor, D.R., Gostelow, J.P., Single stage experimental evaluation of high Mach number compressor rotor blading, Part II, Performance of rotor 1B. NASA CR-54582, GE R67fpd236,1967.

16.37 Gostelow, J.P., Krabacher, K.W., Smith, L.H., Performance comparisons of the high Mach number compressor rotor blading NASA Washington 1968, NASA CR-1256.

16.38 Krabacher, K.W., Gostelow, J.P., Single stage experimental evaluation of high Mach number compressor rotor blading, Part IV, Performance of rotor 2D. NASA CR-54584, 1967.

16.39 Krabacher, K.W., Gostelow, J.P., Single stage experimental evaluation of high Mach number compressor rotor blading, Part V, Performance of Rotor 2B. *NASA CR-54585,* 1967.

16.40 Monsarrat, N.T., Keenan, M.J., Tramm, P.C., Design report, Single stage evaluation of high Mach number compressor stages, *NASA CR-72562 PWA-3546*, July 1969.

16.41 Monsarrat, N.T., Keenan, M.J., Tramm, P.C., Design report, Single stage evaluation of high Mach number compressor stages, *NASA CR-72562 PWA-3546*, July 1969.

16.42 Sulam, D.H., Keenan, M.J., Flynn, J.T., 1970. Single stage evaluation of highly loaded high Mach number compressor stages. II Data and performance of a multi-circular arc rotor. NASA CR-72694 PWA

16.43 Monsarrat, N.T., Keenan, M.J., Tramm, P.C., Design report, Single stage evaluation of high Mach number compressor stages, *NASA CR-72562 PWA-3546*, July 1969.

16.44 Monsarrat, N.T., Keenan, M.J., Tramm, P.C., Design report, Single stage evaluation of high Mach number compressor stages, *NASA CR-72562 PWA-3546*, July 1969.

16.45 Gostelow, J.P., Krabacher, K.W., Smith, L.H., Performance comparisons of the high Mach number compressor rotor blading NASA Washington 1968, NASA CR-1256.

16.46 Miller, G.R., Hartmann, M.J., Experimental shock configuration and shock losses in a transonic compressor rotor at design point *NACA RM E58A14b*, June 1958.

16.47 Miller, G.R., Lewis, G.W., Hartman, M.J., Shock losses in transonic compressor blade rows *ASME Journal for Engineering and Power* July 1961, pp. 235-241.

16.48 Schwenk, F.C., Lewis, G.W., Hartmann, M.J., A preliminary analysis of the magnitude of shock losses in transonic compressors *NACA RM #57A30* March 1957.

16.49 Schwenk, F.C., Lewis, G.W., Hartmann, M.J., A preliminary analysis of the magnitude of shocklosses in transonic compressors *NACA RM #57A30* March 1957.

16.50 Levine, Ph., Two-dimensional inlet conditions for a supersonic compressor with curved blades,Journal of Applied Mechanics, Vol. 24, No. 2, June 1957.

16.51 Balzer, R.L., A method for predicting compressor cascade total pressure losses when the inlet relative Mach number is greater than unity, *ASME Paper 70-GT-57*.

16.52 Swan, W.C., A practical method of predicting transonic compressor performance, *ASME Journal for Engineering and Power*, Vol. 83, pp. 322-330, July 1961.

16.53 Levine, Ph., Two-dimensional inlet conditions for a supersonic compressor with curved blades, Journal of Applied Mechanics, Vol. 24, No. 2, June 1957.

16.54 Swan, W.C., A practical method of predicting transonic compressor performance, *ASME Journal for Engineering and Power*, Vol. 83, pp. 322-330, July 1961.

16.55 Schwenk, F.C., Lewis, G.W., Hartmann, M.J., A preliminary analysis of the magnitude of shock losses in transonic compressors *NACA RM #57A30* March 1957.

16.56 Levine, Ph., Two-dimensional inlet conditions for a supersonic compressor with curved blades,*Journal of Applied Mechanics*, Vol. 24, No. 2, June 1957.

16.57 Gostelow, J.P., Krabacher, K.W., Smith, L.H., Performance comparisons of the high Mach number compressor rotor blading NASA Washington 1968, NASA CR-1256.

16.58 Krabacher, K.W., Gostelow, J.P., Single stage experimental evaluation of high Mach number compressor rotor blading, Part IV, Performance of rotor 2D. NASA CR-54584, 1967.

16.59 Krabacher, K.W., Gostelow, J.P., Single stage experimental evaluation of high Mach number compressor rotor blading, Part V, Performance of Rotor 2B. *NASA CR-54585,* 1967.

16.60 Grieb, H., Schill, G., Gumucio, R., 1975. A semi-empirical method for the determination of multistage axial compressor efficiency. *ASME-Paper 75-GT-11*.

16.61 Carter, A.D.S., 1948. Three-Dimensional flow theories for axial compressors and turbines, *Proceedings of the Institution of Mechanical Engineers*, Vol. 159, p. 255.

16.62 Hirsch, Ch., 1978. Axial compressor performance prediction, survey of deviation and loss correlations *AGARD PEP Working Group* 12.

16.63 Swan, W.C., A practical method of predicting transonic compressor performance, *ASME Journal for Engineering and Power*, Vol. 83, pp. 322-330, July 1961.

16.64 Schobeiri, M.T., Verlustkorrelationen für transsonische Kompressoren, *BBC-Studie*, TN-78/20, 1987.

16.65 Jansen, W., Moffat, W.C., 1967. The off-design analysis of axial flow compressors ASME, *Journal of Eng for Power*, pp. 453-462.

16.66 Jansen, W., Moffat, W.C., 1967. The off-design analysis of axial flow compressors ASME, *Journal of Eng for Power*, pp. 453-462.

16.67 Davis, W. R., 1971. A computer program for the analysis and design of turbomachinery, *Carleton University Report No. ME/A*.

16.68 Jansen, W., Moffat, W.C., 1967. The off-design analysis of axial flow compressors ASME, *Journal of Eng for Power*, pp. 453-462.

16.69 Davis, W. R., 1971. A computer program for the analysis and design of turbomachinery, *Carleton University Report No. ME/A*.

16.70 Dettmering, W., Grahl, K., 1971. Machzahleinfluß auf Verdichter-charakteristik, ZFW 19.

16.71 Fottner, L., 1979. Answer to questionnaire on compressor loss and deviation angle correlations, AGARD-PEP, 1979. Working Group 12.

17 Turbine Aerodynamic Design and Off-design Performance

As briefly discussed in Chapter 13, within a turbine component, an exchange of mechanical energy (shaft power) with the surroundings takes place. In contrast to compressors, the total energy of the working medium is partially converted into shaft work, thus supplying necessary power to drive a variety of components. In *base load* power generation area the primary function of a turbine unit is to drive generators supplying the electricity. Considering a large steam turbine shown in Fig. 17.1, the power generation is accomplished by a series of multi-stage turbines that consists of a high pressure part (HP), an intermediate pressure part (IP), and a low pressure part (LP). While all three turbine parts are coupled serially driving the generator shaft, the LP-part may consist of two LP-units, each of which is fed by 50% of steam mass flow that exits the IP-turbine. The HP-turbine generally has a blade height to mean diameter ratio of $h/D_m \approx 0.1 - 0.2$ and an aspect ratio of $h/c \approx 1 - 2$. Figure 17.2 shows a Brown Boveri HP-turbine unit with a control stage followed by a multi-stage HP-part. The relatively short blade height allows two-dimensional blade designs with a constant stagger angle from hub to tip.

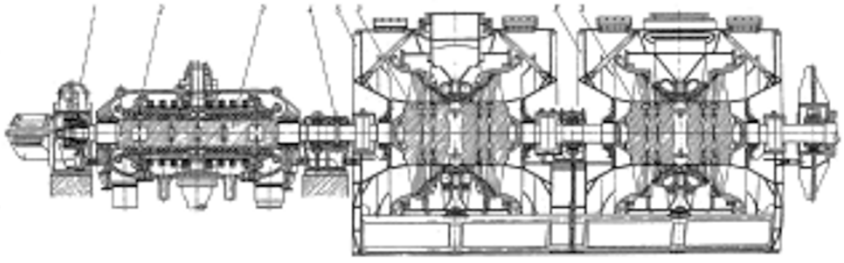

Fig. 17.1: A large Brown Boveri steam turbine with an integrated HP, IP-part and two LP-units. Steam exiting from IP-part is divided into two equal portions to feed the two LP-units

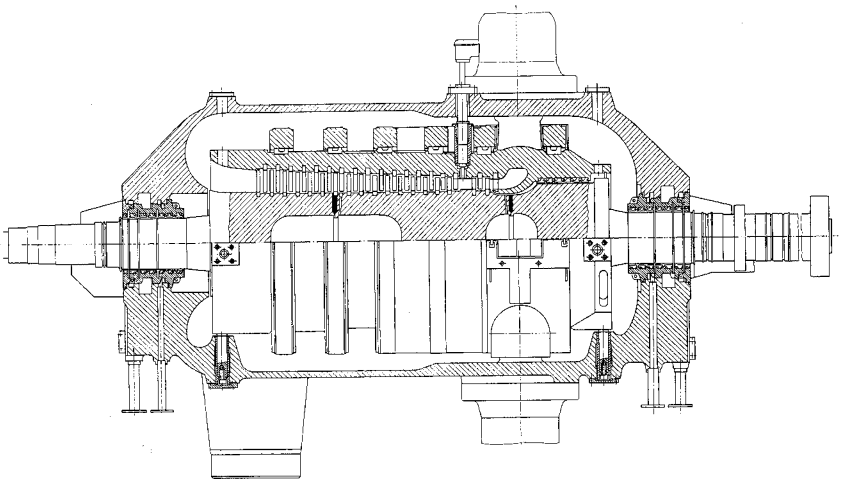

Fig. 17.2: HP- turbine unit of a large steam turbine, Brown Boveri

Figure 17.3 exhibits a three-stage research turbine rotor with cylindrical blades (constant profile shape and stagger angle) from hub to tip. The blades are designed to have a minimum profile loss at the mid-section. The cylindrical configuration causes the flow angle to change from hub to tip resulting in higher profile losses and consequently lower efficiencies. The low aspect ratio also causes relatively high secondary flow losses at the hub and tip sections that originate from the secondary flow, as extensively discussed in Chapter 7. Stacking different profiles from hub to tip improves the efficiency only marginally, but it does not counteract the secondary flow cause and effect. As a result, in the past, most of HP-turbines used a cylindrical blade design, accepting higher losses. In recent years, however, the implementation of computational fluid dynamics (CFD) in the turbine design process has made it possible to design HP-units with efficiencies close to 94% by using three-dimensional (3-D) convex bowed blades (also called compound lean), where the pressure surface is bowed in a convex shape as shown in [1]. Before discussing the effect of 3-D blade design on efficiency and performance of turbine components, we will present the necessary aero-thermodynamic tool for a 1-D turbine design, which is a prerequisite for any 3-D design process. Regarding the turbine component modeling for dynamic simulation similar to the compressor component we discussed in Chapter 16, we present three simulation levels. First, we treat the fundamental aspects of 1-D adiabatic design, followed by a section that deals with generation of global turbine performance characteristics. Three dynamic simulation levels using simple performance characteristics, row-by-row adiabatic, and row-by-row diabatic dynamic performance simulation, concludes the chapter.

Fig. 17.3: The *TPFL*-turbine rotor with cylindrical blades

17.1 Stage-by-Stage and Row-by-Row Adiabatic Design and Off-design Performance

The unifying treatment of the design calculation procedure outlined in Chapter 16 for compressors is now extended to the turbine component. Stage-by-stage and row-by-row methods for calculating the expansion process within a multi-stage turbine component are presented. The performance behavior of a single- or multi-stage turbine component is completely described by the individual stage characteristics in conjunction with the total pressure losses that we extensively discussed in Chapter 7. The meridional view, the blade row configuration, the expansion and the velocity diagram of a typical multi-stage turbine, are shown in Fig. 17.4.Similar to Chapter 16, using the variables in Fig. 17.4(c) and (d), the following dimensionless parameters are defined:

$$\phi = \frac{V_{ax3}}{U_3}\ ,\ \mu = \frac{V_{ax2}}{V_{ax3}}\ ,\ \nu = \frac{U_2}{U_3}\ ,\ r = \frac{\Delta h''}{\Delta h'' + \Delta h'}\ ,$$

$$\lambda = \frac{\Delta h}{U_3^2} = \frac{l_m}{U_3^2} = \frac{U_2\ V_{u2} + U_3\ V_{u3}}{U_3^2}\ ,\ R = \frac{\rho_2}{\rho_3} = \frac{b_3\ D_3}{b_2\ \mu\ D_2} \tag{17.1}$$

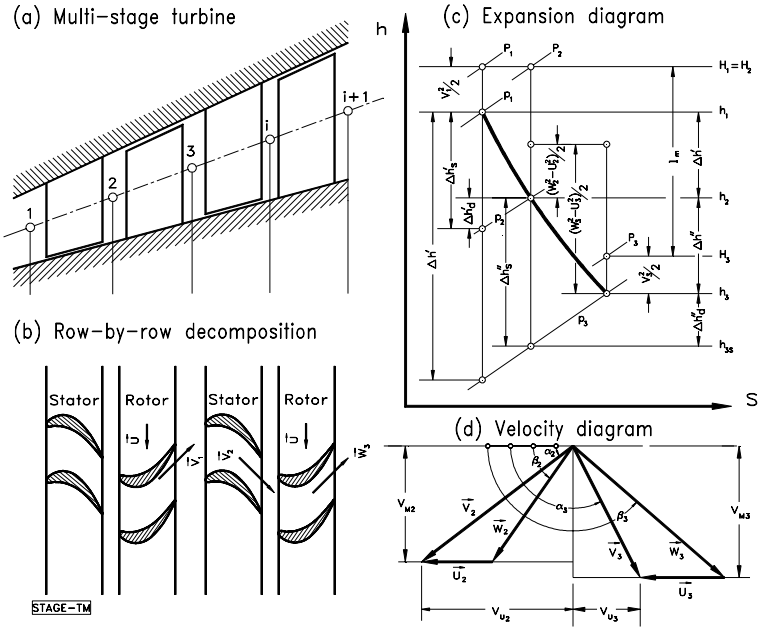

Fig. 17.4: Meridional view, blade row configuration, expansion and velocity diagram of a typical multi-stage turbine

The dimensionless parameters from Eq. (17.1) are used to treat the following stage-by-stage as well as row-by-row design and off-design analysis.

17.1.1 Stage-by-Stage Calculation of Expansion Process

Using the characteristics defined in (17.1) in conjunction with the stage efficiency discussed in Chapter 7, the expansion is accurately calculated from (see also Chapters 5 and 16):

$$
\begin{aligned}
cotg\alpha_2 - cotg\beta_2 &= \frac{\nu}{\mu\phi} \\
cotg\alpha_3 - cotg\beta_3 &= \frac{1}{\phi} \\
\lambda &= \phi(\mu\nu cotg\alpha_2 - cotg\alpha_3) - 1 \\
r &= 1 + \frac{\phi^2}{2\lambda}\left[1 + cotg^2\alpha_3 - \mu^2\left(1 + cotg^2\alpha_2\right)\right]
\end{aligned}
\qquad (17.2)
$$

As we saw in Chapters 5 and 16, the four equations in (17.2) contain nine unknowns.

The following quantities are assumed to be known: (1) the turbine mass flow, (2) the turbine pressure ratio, (3) the type of blades, and (4) their exit metal angles, α_{2m} and β_{3m}, for each individual stage and their configuration in terms of degree of reaction. Further, we may assume the absolute inlet flow angle of the first stage and the exit flow angle of the last stage to be 90°. With these assumptions, all nine stage characteristics are estimated in the first iteration step, which usually does not deliver the required turbine power at the given conditions (pressure ratio, mass flow, inlet or exit enthalpy). The process of iteration is continued until the enthalpy and mass flow convergence has been reached. This stage-by-stage expansion calculation method delivers accurate results, however, it requires some experience in guessing the initial values for unknown characteristics. In the following row-by-row calculation, we will discuss in more detail how it is computationally more efficient and does not require a lot of iterations.

17.1.2 Row-by-Row Adiabatic Expansion

As discussed in Chapter 5, the expansion process within stator and rotor row shown in Fig. 17.5 is summarized as:

$$\begin{aligned}
\Delta h' &= h_1 - h_2 = \frac{1}{2}\left(V_2^2 - V_1^2 \right) \\
\Delta h'_s &= h_1 - h_{2s} = \frac{1}{2}\left(V_{2s}^2 - V_1^2 \right) \\
\Delta h'' &= h_2 - h_3 = \frac{1}{2}\left(W_3^2 - W_2^2 + U_2^2 - U_3^2 \right) \\
\Delta h''_s &= h_2 - h_{3s} = \frac{1}{2}\left(W_{3s}^2 - W_2^2 + U_2^2 - U_3^2 \right)
\end{aligned} \tag{17.3}$$

The quantities in Eqs. (17.3), the decomposition of the turbine stage in its stator and rotor rows, and the expansion diagram are presented in Fig. 17.5. The quantities with superscripts "/ " and "// " in Fig. 17.5, refer to stator and rotor rows, respectively. For the stator row, the expansion diagram shows the details of an adiabatic expansion where the absolute total enthalpy remains constant. The following rotor row with the corresponding expansion diagram exhibits the details of energy balance in a relative frame of reference with constant relative total enthalpy. The expansion diagram for the entire stage exhibits a composite picture of energy balance within the stator and rotor row. We introduce the following efficiency definition for the stator and rotor row:

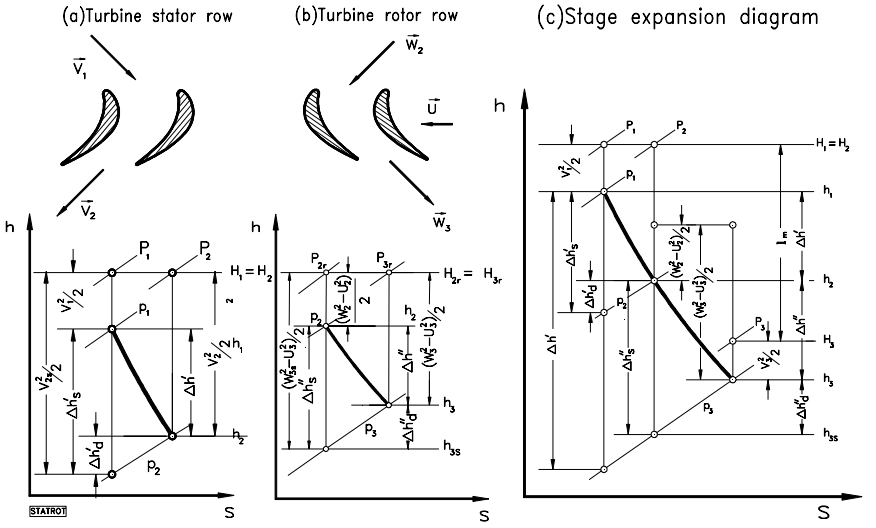

Fig. 17.5: Energy transfer in turbine stator row, turbine rotor row, and turbine stage

$$\eta' = \frac{\Delta h'}{\Delta h_s'} = \frac{V_2^2 - V_1^2}{V_{2s}^2 - V_1^2},$$
$$\eta'' = \frac{\Delta h''}{\Delta h_s''} = \frac{W_3^2 - W_2^2 + U_2^2 - U_3^2}{W_{3s}^2 - W_2^2 + U_2^2 - U_3^2} \tag{17.4}$$

For the sake of completeness, the rotor efficiency definition in Eq. (17.4) includes the difference of circumferential kinetic energies $U_2^2 - U_3^2$ in denominator and numerator. However, this difference may be taken without causing any noticeable error. The choice of efficiency definition varies throughout the literature (see Traupel [2], Vavra [3], NASA [4]). Engine aerodynamicists and researchers frequently prefer to use their own efficiency definition that may serve their design purpose. Regardless how the efficiency is defined, it must be kept consistently throughout the calculation procedure. We chose definition (17.4) which is consistent with the one defined in Chapter 16. Incorporating Eq. (17.4) into Eqs. (17.3), the isentropic enthalpy difference for stator and rotor row, respectively, is expressed by:

$$\Delta h_s^{/} = \frac{1}{2\eta^{/}} \left(V_2^2 - V_1^2 \right)$$
$$\Delta h_s^{//} = \frac{1}{2\eta^{//}} \left(W_{3s}^2 - W_2^2 + U_2^2 - U_3^2 \right) \tag{17.5}$$

Introducing the dimensionless isentropic enthalpy differences by dividing Eqs. (17.5) by the circumferential kinetic energy at the exit of the turbine stage and incorporating the stage parameters Eqs. (17.2), the dimensionless row parameters are developed as follows:

$$\chi^{/} = \frac{1}{2\eta^{/}} \left[\phi \left(\frac{\mu^2}{\sin^2 \alpha_2} - \frac{1}{\sin^2 \beta_3} \right) - 2 \phi \cot \beta_3 - 1 \right] \tag{17.6}$$

$$\chi^{//} = \frac{1}{2\eta^{//}} \left[\phi^2 \left(\frac{\mu^2}{\sin^2 \beta_3} - \frac{1}{\sin^2 \alpha_2} \right) + 2 \mu \nu \phi \cot \alpha_2 - 1 \right] \tag{17.7}$$

Equations (17.6) and (17.7) represent the dimensionless isentropic enthalpy differences for the expansion through stator and rotor row, respectively. As the above equations indicate, the calculation of each row necessitates the knowledge of entire stage parameters which requires few iterations. Similar to the compression process outlined in Chapter 16, to substantially reduce the number of iterations, we subdivide the stage specific polytropic mechanical energy l_{m}, as well as the isentropic mechanical energy $l_{ms,}$ into two virtual contributions $l_m = l_m^{/} + l_m^{//}$ and $l_{ms} = l_{ms}^{/} + l_{ms}^{//}$ that we allocate to stator and rotor row. This step does not imply that the stator row is performing shaft power which would violate the energy balance. It merely provides a smooth transition from stator row to rotor row when calculating the compression and expansion processes. With this re-arrangement, we arrive at the contributions allocated to the stator and rotor rows as:

$$l^{/} = \frac{1}{2} V_2^2 - \frac{1}{2} W_2^2$$
$$l^{//} = \frac{1}{2} \left(W_3^2 - U_3^2 + U_2^2 - V_3^2 \right) \tag{17.8}$$

Similarly we find the isentropic parts:

$$l_s^{/} = \frac{1}{2} V_{2s}^2 - \frac{1}{2} W_2^2$$
$$l_s^{//} = \frac{1}{2} \left(W_{3s}^2 - U_3^2 + U_2^2 - V_3^2 \right) \tag{17.9}$$

As seen, the sum of stator and rotor contributions leads to the stage specific mechanical energy. Using the polytropic specific mechanical energy expressions given in Eqs. (17.8) and dividing them by the circumferential kinetic energy at the exit of the individual row, the dimensionless row polytropic load coefficients for stator and rotor are:

$$\lambda' = \frac{l'}{U_2^2} = \phi' \cot\alpha_2 - \frac{1}{2}$$
$$\lambda'' = \frac{l''}{U_3^2} = -\phi'' \cot\beta_3 - 1 + \frac{v^2}{2} \tag{17.10}$$

with stator and rotor flow coefficient $\phi' = V_{ax2} / U_2$, and $\phi'' = V_{ax3} / U_3$. Combining Eqs. (17.10) with the efficiency definition for the stator and rotor rows, Eq.(17.4) , the following expressions for the efficiency are obtained:

$$\eta' = \frac{V_2^2 - V_1^2}{2l_s' - 2l' + V_2^2 - V_1^2}$$
$$\eta'' = \frac{W_3^2 - W_2^2}{2l_s'' - 2l'' + W_3^2 - W_2^2} \tag{17.11}$$

The isentropic row load coefficient ψ is defined as the dimensionless isentropic specific mechanical energy for the row. Implementing the efficiency expressions from Eqs. (17.11), the isentropic row load coefficients for the stator and rotor rows are obtained:

$$\psi' = \frac{l_s'}{U_2^2} = \lambda' + \frac{\phi'^2}{2}\left(\frac{1}{\sin^2\alpha_2} - \frac{1}{\mu^2\sin^2\alpha_3}\right)\left(\frac{1}{\eta'} - 1\right) \tag{17.12}$$

$$\psi'' = \frac{l_s''}{U_3^2} = \lambda'' + \frac{\phi''^2}{2}\left(\frac{1}{\sin^2\beta_3} - \frac{\mu^2}{\sin^2\beta_2}\right)\left(\frac{1}{\eta''} - 1\right) \tag{17.13}$$

Similar to compressor component treated in Chapter 16, all the information necessary to pursue the expansion process on the h-s diagram is now available to predict the turbine performance behavior at the design point. Likewise, the off-design operation can be predicted accurately providing that a reliable off-design efficiency calculation method exists. Such a method will be presented in the next section.

Given the pressure and temperature at the inlet, the density can be calculated from the equation of state, as well as the enthalpy and entropy of the gas at the inlet. Utilizing the gas tables, the first point on the h-s diagram can be determined easily.

The row flow coefficients ($\phi^{/}$) and ($\phi^{//}$) are calculated using the continuity equation: Given the stator and rotor exit metal angles α_{2m}, β_{3m} as the input data necessary to

$$\phi = \frac{V_{ax}}{U} = \frac{\dot{m}}{\rho A U} = \frac{\dot{m}}{\rho A \omega R} \tag{17.14}$$

describe the geometry, the flow angles α_2, β_3 are calculated using deviation angles outlined in Chapter 11. The remaining flow angles β_2, α_3 are determined by using the flow coefficient from Eq. (17.14):

$$\beta_2 = \tan^{-1}\left(\frac{W_{ax2}}{W_{u2}}\right) = \tan^{-1}\left(\frac{V_{ax2}}{W_{u2}}\right) \tag{17.15}$$

From the velocity diagram of Fig. 17.4, we introduce the relationship:

$$W_{u2} = V_{u2} - U_2 \tag{17.16}$$

Implementing Eq. (17.16) into(17.15) and introducing the stator flow coefficient $\phi^{/}$, we obtain the expression:

$$\beta_2 = \tan^{-1}\left(\frac{\phi^{/}}{\phi^{/}\cot\alpha_2 - 1}\right) \tag{17.17}$$

Similarly for the rotor:

$$\alpha_3 = \tan^{-1}\left(\frac{\phi^{//}}{\phi^{//}\cot\beta_3 + 1}\right) \tag{17.18}$$

Upon the determination of all the angles involved in the velocity diagram, the velocities and their components are fully described. The flow coefficients, $\phi^{/}$ and $\phi^{//}$, and the flow angles α_2, β_2, α_3, β_3 are necessary tools to determine the polytropic and isentropic enthalpy differences between the inlet and exit of the row. The amount of work produced by the flow is fully represented by the load coefficients λ and ψ, as presented in the previous sections. Finally, from the energy balance relationships presented above, the complete expansion process for the turbine stage is determined as follows:

$$
\begin{aligned}
h_2 &= h_1 - l' - \frac{1}{2}\left(W_2^2 - V_1^2 \right) \\
h_{2s} &= h_1 - l_s' - \frac{1}{2}\left(W_2^2 - V_1^2 \right) \\
h_3 &= h_2 - l'' - \frac{1}{2}\left(V_3^2 - W_2^2 \right) \\
h_{3s} &= h_2 - l_s'' - \frac{1}{2}\left(V_3^2 - W_2^2 \right)
\end{aligned}
\tag{17.19}
$$

The above procedure can easily be repeated for all the rows and stages of the turbine under consideration.

17.1.3 Off-Design Efficiency Calculation

Accurate prediction of the turbine cascade off-design efficiency is essential for calculating performance behavior of a turbine stage and component. For multi-stage axial flow turbines, the primary loss coefficient is the major contributor to the overall stage efficiency. Numerous correlations are given in the literature for off-design efficiency calculation procedure, where the off-design primary loss coefficient is related to its design point value (see Kroon and Tobias [5], Kochendorfer and Nettles [6]). In a comprehensive and systematic study, Bammert and Zehner [7] and Zehner [8] investigated the off-design behavior of single- and multi-stage turbines with different turbine blade geometry. Based on the experimental results, Zehner [7] established the following relationship for the off-design primary loss coefficient:

$$
1 - \zeta_p = (1 - \zeta_p^*)\, e^{\left[-a(\Delta\Theta)^b\right]} \tag{17.20}
$$

with

$$
\Delta\Theta = \frac{\theta_i - \theta_i^*}{180 - \theta_i^*} \tag{17.21}
$$

where θ_i, θ_i^* represent the stator/rotor inlet flow angle α_1, β_2 at the off-design point and α_1^*, β_2^* at the design point respectively. The coefficients a, b are functions of the cascade characteristic described by Zehner [7]. Once the off-design primary loss coefficient has been calculated, the row efficiency is calculated by considering the other individual losses such as secondary and clearance losses (see Chapter 7, Schobeiri [9], Zehner [7]):

$$\eta = 1 - \Sigma\zeta_i \tag{17.22}$$

with ζ_i as the individual loss coefficient such as primary, trailing edge, secondary, and shock losses. Equations (17.20) and (17.21) explicitly relate the primary loss @ coefficient of the off-design operation to the design point. A similar relation does not exist for the rest of the losses. This is partially due to the complexity of the secondary flow phenomena. An alternative off-design efficiency correlation presented (, [10]) directly relates the off-design efficiency to the design efficiency as follows:

$$\eta' = \eta^{*\prime}\left(1 - e^{c'}\right), \qquad \eta'' = \eta^{*\prime\prime}\left(1 - e^{c''}\right) \tag{17.23}$$

where, the exponent c is expressed for the stator, and rotor as:

$$c' = A'\left(\frac{\alpha_1}{\alpha_1^*}\right)^{B'}, \qquad c'' = A''\left(\frac{\beta_2}{\beta_2^*}\right)^{B''} \tag{17.24}$$

The coefficients A', A'', B', B'' may, among other things, depend on the Re-number, Ma-number, and blade geometry. For a particular set of turbine blade profiles, N-8000, developed by Brown Boveri & Cie, the following coefficients were found:

$$\begin{aligned} A' &= 0.075\ \alpha_2 - 7.8460, \quad A'' = 0.075\ (180 - \beta_3) - 7.8460 \\ B' &= 0.029\ \alpha_2 + 0.6107, \quad B'' = 0.029\ (180 - \beta_3) + 0.6107 \end{aligned} \tag{17.25}$$

where, the angles are in degrees and the angle directions follow the convention in Fig. 17.4. Equations (17.23), (17.24), and (17.25) satisfactorily relate the off-design efficiency of typical turbine blades to the design point efficiency.

With the procedure described above, it is possible to accurately predict the off-design efficiency of a turbine stage provided that the given off-design mass flow permits a normal turbine operation. However, if the mass flow has been reduced to such an extent that the turbine stage is no longer able to produce mechanical energy, the efficiency has to be redefined in such a way that it reflects the dissipative nature of the energy conversion. To evaluate the degree of dissipation, the following loss coefficients and efficiencies are introduced:

$$\zeta' = \frac{\Delta h_D'}{V_1^2/2}, \quad \zeta' = \frac{\Delta h_D''}{W_2^2/2} \tag{17.26}$$

$$\eta' = 1 - \zeta', \quad \eta'' = 1 - \zeta'' \tag{17.27}$$

with $\Delta h_D^{/} = h_2 - h_{2s}$ and $\Delta h_D^{//} = h_3 - h_{3s}$ from Fig. 17.4c. For the extreme off-design cases, the relationships between the stage parameters based on the normal turbine stage operation as previously described, are no longer valid. In the following section, a method is presented that predicts accurately the off-design behavior of a turbine stage for extreme low mass flows.

17.1.4 Behavior Under Extreme Low Mass Flows

During the shutdown process of a steam turbine or a compressed air storage gas turbine, mass flow and turbine power continuously decrease. By approaching a certain mass flow $\dot{m}_{L=0}$ at which the turbine ceases to produce power, the rear stages of a multi-stage turbine are not able to produce mechanical energy and act as an energy dissipater, Fig 17.6. As a result, the kinetic energy of the rotating shaft dissipates into heat, resulting in excessive temperature and entropy rise.

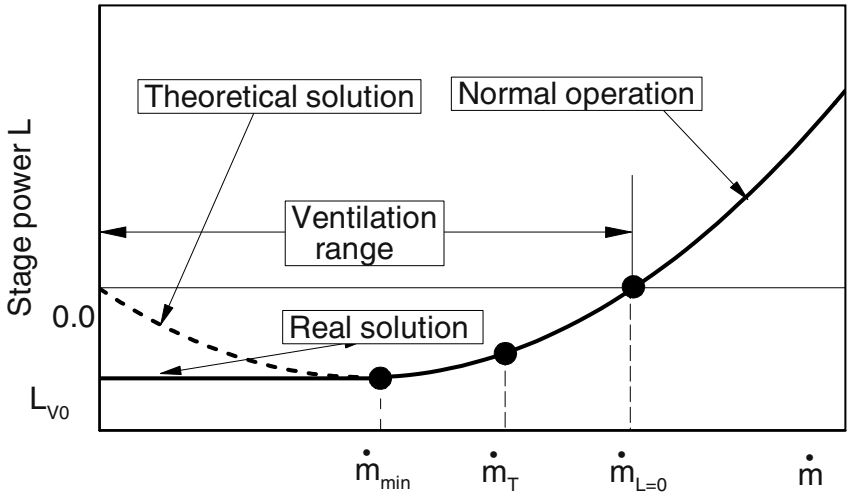

Fig. 17.6: Turbine performance behavior under low mass flow conditions

For $\dot{m} < \dot{m}_{L=0}$ the turbine starts to *ventilate* (wind milling) and is no longer able to remove the heat. In order to prevent the turbine blades and structure from damages caused by excessive temperature development, cooling mass flow must be injected into the flow path to remove the heat. Figure 17.6 shows the detail of the ventilation process. The ventilation process cannot be captured by the method used for predicting the design and normal off-design behavior discussed above. In the following section we present a method discussed in [12] and [13]] that accurately predicts the dissipation process.

Consider a turbine stage operating under normal condition. The stage power determined by a second order polynomial in $\dot{m}$ is:

$$L = \dot{m}\lambda U_3^2 = \dot{m}\left[\phi(\mu\nu\cot\alpha_2 - \cot\beta_3) - 1\right]U_3^2 \tag{17.28}$$

The stage flow coefficient ϕ in Eq. (17.28) is expressed in terms of the stage mass flow rate as follows:

$$\phi = \frac{V_{ax3}}{U_3} = \frac{\dot{m}}{\rho_3\ \pi\ D_{m3}\ h_{b3}\ U_3} = \frac{\dot{m}}{\xi} \tag{17.29}$$

where, ξ is the mass flow parameter defined as:

$$\xi = \rho_3\ \pi\ D_{m3}\ h_{b3}\ U_3 \tag{17.30}$$

with D_{m3}, h_{b3} as the mean radius and the blade height at exit of the stage. Substituting Eqs. (17.29) and (17.30) into (17.28), the power expression is then re-written:

$$L = \frac{\dot{m}^2}{\xi}\ (\ \mu\ \nu\ \cot\ \alpha_2\ -\ \cot\ \beta_3\ )\ U_3^2\ -\ \dot{m}\ U_3^2 \tag{17.31}$$

Equation (17.31) accurately represents the stage power behavior under normal operating conditions. However, for $\dot{m} < \dot{m}_{min}$, it leads to the erroneous theoretical solution shown in Fig. 17.6 dashed line. For ventilation condition, a different expression for the stage power is written that accurately describes the ventilation branch as a second order polynomial:

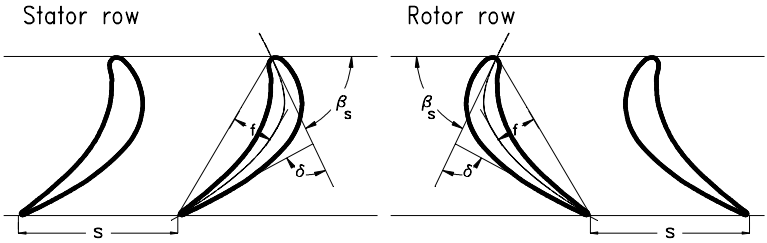

Fig. 17.7: Blade nomenclature for defining the geometry parameter γ

$$L_v = C_1 \dot{m}^2 + C_2 \dot{m} + C_3 \tag{17.32}$$

The constant C_3 is found immediately by setting in Eq. (17.32) $\dot{m} = 0$. This results in $C_3 = L_{vo}$ as seen from Fig. 17.6. For the calculation of the ventilation power at zero mass flow, L_{vo}, Traupel [1] suggests:

$$L_{vo} = C \pi D_{m3} h_{b3} \rho_3 U_3^3 \tag{17.33}$$

where the constant C is obtained from the experiment. Since this constant changes with the blade geometry, it seems appropriate to replace it by a blade geometry functional$f(\gamma)$ with γ as a geometry parameter:

$$L_{vo} = f(\gamma) \xi U^2 \tag{17.34}$$

Zehner [7] proposed for γ the following relationship that accounts for the blade geometry:

$$\gamma = \frac{f}{s}\left(\delta \beta_s\right)^{\frac{1}{2}} \tag{17.35}$$

with s as the blade spacing, δ the total flow deflection, β_s the stagger angle, and f the maximum camber height shown in Fig. 17.7. For the functional $f(\gamma)$we set:

$$f(\gamma) = C_\gamma \gamma^2 \tag{17.36}$$

with $C_\gamma = 0.97121$. To determine the constant C_2, we assume that the maximum power consumption occurs at zero mass flow rate. This assumption leads to the conclusion that $C_2 = 0$.The constant C_1 is calculated from the requirement that L_v must follow the continuous course of L given Eq. (17.31) with the same value, and slope at a common tangent point at $\dot{m}_T$ shown in Fig. 17.6. Equating (17.31) and (17.32) and their respective derivatives at the common tangent point:

$$(L)_{\dot{m}_T} = (L_v)_{\dot{m}_T}, \qquad \left(\frac{\partial L}{\partial \dot{m}}\right)_{\dot{m}_T} = \left(\frac{\partial L_v}{\partial \dot{m}}\right)_{\dot{m}_T} \tag{17.37}$$

As a result, Eqs. (17.37) determine the mass flow at the tangent point $\dot{m}_T$:

$$\dot{m}_T = \frac{\xi}{2\left(\mu \nu \cot \alpha_2 - \cot \beta_3 - \frac{\xi C_1}{\nu U_3^2} \right)} \tag{17.38}$$

and:

$$C_1 = \frac{U_3^2}{\xi''} \left(\mu \nu \cot \alpha_2 - \cot \beta_3 - \frac{\xi U_3^2}{4 L_{vo}} \right) \tag{17.39}$$

Finally, an expression for the stage mechanical power during ventilation is written as:

$$L_v = \frac{\dot{m}^2 U_3^4}{4 L_{vo}} \left(4 f(\gamma) \frac{\nu^3}{\mu} (\mu \nu \cot \alpha_2 - \cot \beta_3) - 1 \right) - L_{vo} \tag{17.40}$$

Equation (17.40) describes the performance behavior of a turbine stage during the ventilation operation. It can be decomposed into portions that are allocated to stator and rotor row, as discussed previously.

17.1.5 Example: Steady Design and Off-Design Behavior of a Multi-Stage Turbine

The row-by-row expansion calculation discussed above provides information relevant for performance and efficiency prediction during design and off-design operation. It also supplies essential information related to reliability aspects of the design that includes thermal and mechanical stress analysis of blade rows. This analysis requires accurate information about the temperature and pressure distributions along the expansion path. Considering these aspects, the method discussed above is applied to a multi-stage turbine, where its design and off-design performance is calculated and the results are compared with the measurement. As an appropriate application example, a seven-stage research turbine is chosen, whose geometry, design, and off-design performance behavior were extensively studied and well documented in [6], [7], and [13]. For this turbine, three different off-design points are calculated and compared with the measurement. The corresponding mass flow and speed ratios are given as $\mu = \dot{m}/\dot{m}_D = 0.13$, 0.38, 0.83 and $\omega/\omega_D = 1$. Figure 17.8 exhibits the dimensionless temperature distribution along the expansion path at different stations with mass flow ratio as the parameter. As shown, temperature increases occur at the rear stages for mass flow ratios less than 0.4, indicating the beginning of a dissipation process associated with entropy and temperature increases. Decreasing the mass flow

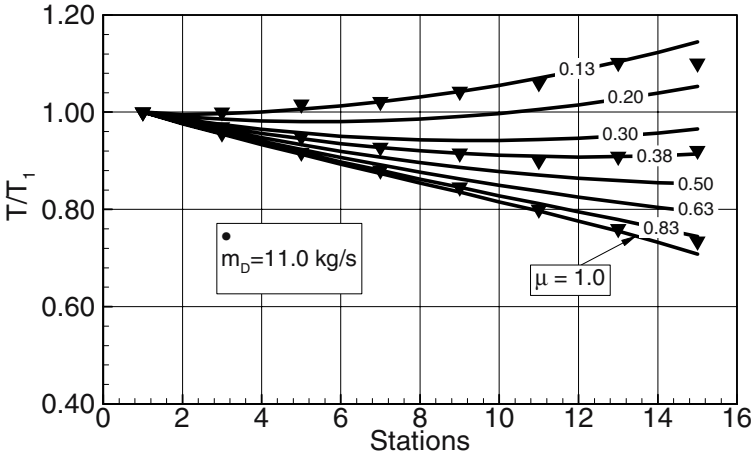

Fig. 17.8: Temperature distribution in a seven stage turbine for design and off-design mass flow rates, experiments denoted by ▼ from [7]

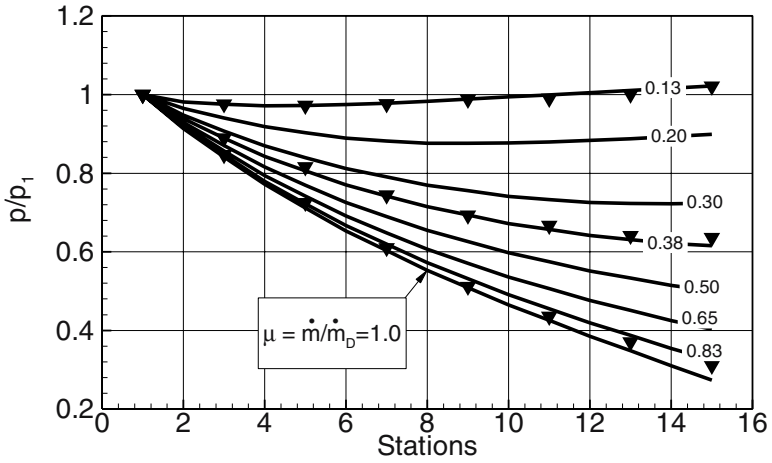

Fig. 17.9: Pressure distribution in a seven stage turbine for design and off-design mass flow rates, experiments denoted by ▼ from [7]

ratio results in strong dissipation with corresponding temperature rise. A similar tendency is displayed by the pressure distribution in Fig. 17.9. As shown, the reduction of the turbine mass flow ratio to 0.13 leads to a considerable distortion of the stage velocity diagram and flow deflection that is associated with dissipation of mechanical energy resulting in pressure increase along the flow path. Figure 17.8 also includes complementary calculations for $\mu = \dot{m}/\dot{m}_D = 0.20, 0.30, 0.50, 1.00$.

17.2 Off-Design Calculation Using Global Turbine Characteristics Method

This method introduced by Stodola [11] and Traupel [1] replaces the turbine component by a nozzle that can be described by a set of algebraic equations. Horlock [12], Pfeil [13], and Schobeiri [14] derived differential equations for predicting the off-deign behavior of multi-stage turbines. These methods require the knowledge of efficiency behavior of the turbine during off-design operation. The method suggested by Stodola [11] exhibits a simple method for calculating the mass flow. However, it does not provide any details relative to the expansion process. The off-design mass flow is determined from the following expression:

$$\dot{m} = \dot{m}^* \frac{P_I}{P_I^*} \left(\frac{T_I^*}{T_I} \right)^{\frac{1}{2}} \left(\frac{1 - \left(\pi \right)^{\frac{n+1}{n}}}{1 - \left(\pi^* \right)^{\frac{n+1}{n}}} \right)^{\frac{1}{2}} \tag{17.41}$$

where π is the turbine pressure ratio defined as $\pi = P_{outlet}/P_{inlet}$, and n as the polytropic exponent given by the expression:

$$n = \frac{\kappa}{\kappa - \eta \left(\kappa - 1 \right)} \tag{17.42}$$

with $\kappa = c_p/c_v$ as the isentropic exponent. Accurate determination of the off-design performance behavior of a multi-stage turbine using the global characteristics method requires accurate calculation of the efficiency. This can be done utilizing the above row-by-row calculation procedure, where the dimensionless velocity parameter ν, as defined below, is varied:

$$\nu = \frac{U}{\sqrt{2\ \Delta h_s}} \tag{17.43}$$

In Eq. (17.43), U is the circumferential velocity and Δh_s is the isentropic enthalpy difference of the turbine component. Once the efficiency versus ν is obtained, the relative efficiency η/η^* can be plotted versus the relative velocity parameter ν/ν^*, where the superscript "*" refers to the design point. Figure 17.10 qualitatively shows the relative efficiency versus relative velocity parameter. The circumferential velocity U in Eq.(17.43) may be calculated using an average mean radius for the entire turbine. The characteristic curve of η/η^* depends on the type of turbine blade geometry and the stage characteristics. Once it is calculated for a particular turbine,

it can be expressed as a polynomial such that:

$$\frac{\eta}{\eta^*} = \sum_{n=1}^{N} a_n \left(\frac{\nu}{\nu^*} \right)^n \tag{17.44}$$

The coefficients a_n are determined by a least square fit or the data calculated from the steady state row-by-row procedure. The turbine exit temperature may then be determined by the expression:

$$T_O = T_I \, \pi^{\left(\frac{\kappa - 1}{\kappa}\eta\right)} \tag{17.45}$$

and finally, the net power production is calculated by:

$$\dot{E} = \dot{m} \, c_p \, \Delta T, \; \dot{E}_{net} = E \, \eta_{mech} \tag{17.46}$$

where ΔT is the temperature difference expressed by $\Delta T = T_I - T_O$, and η_{mech} is the mechanical efficiency, and accounts for bearing friction losses. The mechanical efficiency is a measure of losses due to bearing friction.

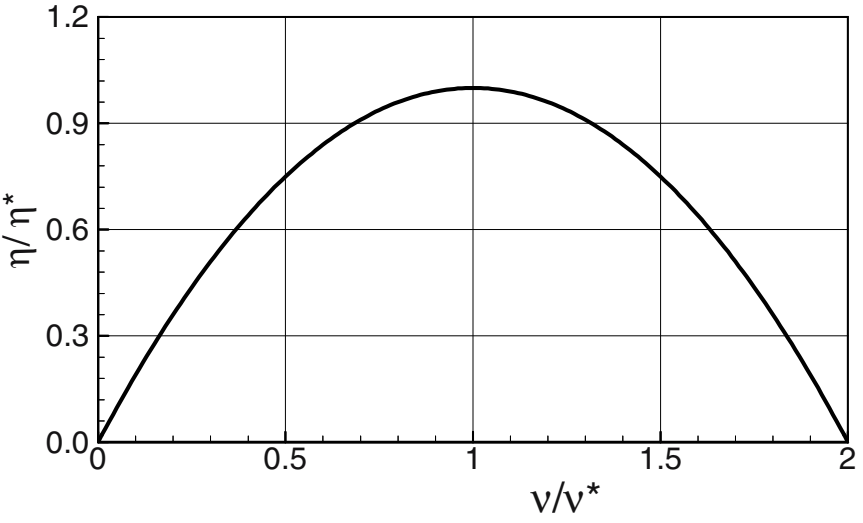

Fig. 17.10: Relative efficiency as a function of relative velocity parameter

17.3 Modeling the Turbine Module for Dynamic Performance Simulation

Three levels of turbine modeling are presented in this section. The first level utilizes the steady performance characteristics discussed in Section 17.2. It exhibits the global performance behavior of a turbine component under dynamic operation conditions. The second level uses the row-by-row adiabatic expansion process and delivers a detailed calculation of the adiabatic expansion process under any dynamic operation condition. In addition to the information provided by the second level model, the third level provides detailed information about the blade temperature under the effect of the different cooling procedures.

17.3.1 Module Level 1: Using Turbine Performance Characteristics

The efficiency and performance characteristic generated in Section 17.2 can be used for a first level turbine simulation. This simulation level obviously does not provide details regarding the aerodynamic events within turbine stages. However, it is capable of globally estimating the thermodynamic state of the turbine component during a dynamic event. In contrast to the compressor module, the global turbine module does not have a performance map that defines surge limits for each individual rotational speed. This is due to the accelerating nature of the flow through the turbine expansion path. Although local flow separation may occur on turbine blade surfaces, particularly on the suction surface of low pressure turbine blades, a total flow separation and reversal under normal operating conditions will never occur. However, strong flow separation may occur at extremely low mass flows far below the normal operating range. The global turbine module is modeled mathematically by a set of algebraic equations. It receives dynamic information from the inlet plenum, performs off-design calculations, and transfers the results to the exit plenum. This arrangement allows a quasi dynamic simulation of the turbine component. The set of algebraic equations (17.41) to (17.46)determine the off-design values of the efficiency, the mass flow rate, $\dot{m}$, the total temperature, T_o, and the power consumption .

Figure 17.11 shows a turbine component using a steady state performance characteristic enclosed within two plena. For a turbine with up to three stages, a single

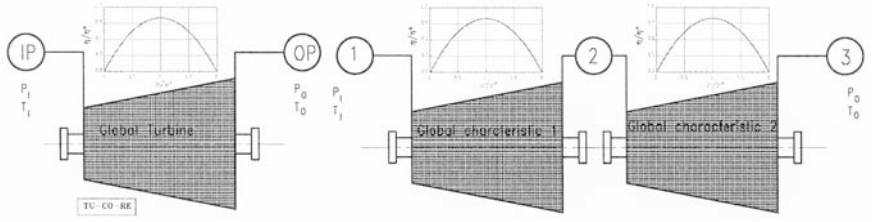

Fig. 17.11: Global simulation of a multi-stage turbine using one turbine characteristic (left) and two characteristics (right)

performance characteristic is sufficient to calculate the global transient behavior of the turbine. However, if the turbine has more than three stages, two or more performance characteristics may be necessary to satisfactorily predict the transient behavior of the turbine. The steady performance characteristic is obviously not able to handle transient events. However, if it is placed between two plena that continuously feed the steady map with unsteady data, it may deliver reasonable dynamic results. The inlet plenum transfers the time dependent pressure and temperature to the global map which calculates the turbine performance and transfers the information to the outlet plenum. For this purpose, the following system of differential and algebraic equations is used: (1) The inlet and outlet plena are described by Eq. (16. 10) and (16.11). For the sake of completeness, these equations are listed below:

$$\frac{\partial T_0}{\partial t} = \frac{1}{\rho V}\left[\sum_{i=1}^{n} \dot{m}_{I_i}\left(\kappa \frac{c_{pI_i}}{c_p} T_{0_{I_i}} - T_0\right) - (\kappa - 1)\sum_{j=1}^{m} \dot{m}_{O_j} T_0\right] \tag{17.47}$$

$$\frac{\partial P}{\partial t} = \frac{\kappa R}{V}\left[\sum_{i=1}^{n} \dot{m}_{I_i} \frac{c_{pI_i}}{c_p} T_{0_{I_i}} - \sum_{j=1}^{m} \dot{m}_{O_j} T_0\right] \tag{17.48}$$

with Eqs.(17.47), (17.48), and the performance characteristic described by algebraic equations (17.41) to (17.46), we are now able to quasi-dynamically model the turbine component.

17.3.2 Module Level 2: Row-by-Row Adiabatic Expansion Calculation

This turbine module provides detailed information about the compressor behavior during dynamic events. Two methods can be used for describing this module. The first method utilizes the time dependent conservation laws for continuity, momentum, and energy Eqs. (14. 26), (14.33), and (14.51) derived in Chapter 14. For adiabatic stage expansion calculation, Eq. (14.51) is reduced to:

$$\begin{aligned}\frac{\partial H}{\partial t} = & -\kappa_k \frac{\dot{m}_k}{\rho_k S_k}\left(\frac{H_{i+1} - H_i}{\Delta x}\right) + \frac{\kappa_k}{\rho_k}\left(\frac{L}{\Delta V}\right) - \\ & - \left(\frac{\kappa - 1}{\rho k}\right)_k \left[\left(\frac{H_k + K_k}{\Delta x}\right)\left(\frac{\dot{m}_{i+1}}{S_{i+1}} - \frac{\dot{m}_i}{S_i}\right) + \frac{\dot{m}_k}{\rho_k S_k^2}\frac{\partial \dot{m}_{i+1}}{\partial t}\right]\end{aligned} \tag{17.49}$$

The stage power L in Eq. (17.49) is directly related to the specific stage mechanical energy $L = \dot{m} l$ with $l = \lambda U_3^2$. Similar to the compressor module discussed in Chapter 16 for row- by-row dynamic calculation of a turbine component, Eq. (17.49)

may be decomposed using the row parameters discussed in Section 17.1. This method allows detailed dynamic calculation of the row properties.

The second method is based on the row-by-row adiabatic calculation procedure outlined in Section 17.1 under utilization of plena Eqs. (17.47) and (17.48) for dynamic coupling. Three alternative coupling configurations for a two-stage turbine are shown in Fig. 17.12. In Configuration (a), each row has an inlet and exit plenum, whereas in (b) each stage is bounded by an exit and inlet plenum. In (c) the entire turbine is placed between an inlet and exit plenum. This configuration provides satisfactory results for gas turbine engines where stage number does not exceed 4. It also can be applied to high pressure steam turbine units, where the volume dynamic is not substantial. However, to accurately account for the volume dynamics of an intermediate or low pressure turbine unit, it is more appropriate to decompose the turbine into several stage groups, where each group may consist of two to three stages that have Configuration (b).

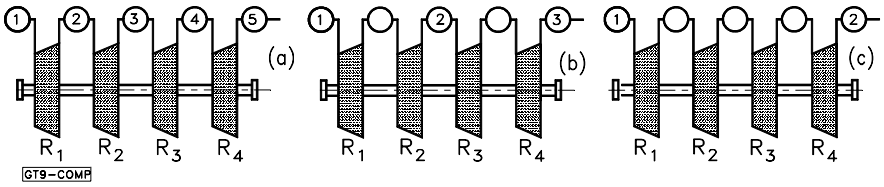

Fig. 17.12: Row-plena configuration, (a) each row is placed between two plane, (b) each stage is placed between two plena, (c) the entire turbine is placed between two plena.

17.3.3 Module Level 3: Row-by-Row Diabatic Expansion

During startup, shutdown, load change, or other transient operation of gas turbine engines, the turbine component experiences adverse temperature changes between the turbine blade material, rotor hub, casing, discs, and the combustion gas. This temperature change causes a heat transfer from the working medium to the blade material and vice versa. In addition, the first three rows of gas turbine engines require cooling. In these cases, the expansion process is no longer adiabatic. Figure 17.13 displays a cooled (diabatic) turbine stage, where heat is removed from the stator and rotor blade material by the stator and rotor cooling mass flows $\dot{m}_{c\,S} = \dot{m}_4$ and $\dot{m}_{c\,R} = \dot{m}_5$. Gas turbine manufacturers may use internal, external, or the combination of internal and external cooling schemes. During the past three decades, numerous papers have been published that discuss different cooling aspects. Since a detail discussion of the turbine cooling issues is beyond the scope of this book, we refer to Han et al. [15], who reviewed the relevant papers and provide a comprehensive

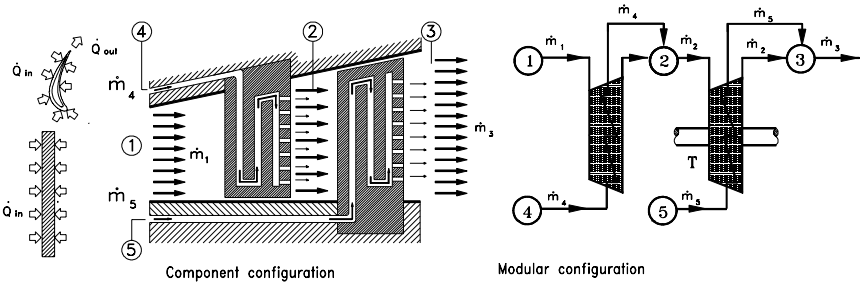

Fig. 17.13: Cooled module component (left) and simulation schematic (right)

summary of the relevant turbine heat transfer results. In conjunction with the modeling, we generically use the major cooling techniques. A high efficiency gas turbine engine with advanced cooling technology requires a total cooling mass flow $\dot{m}_{c\ total} = 3\% - 6\%$ of the compressor air to cool the front turbine rows. This amount is distributed among the rows that require cooling. Air is extracted from different compressor locations and is injected into the stator and rotor blades. The cooling mass flow at the compressor extraction point has a slightly higher pressure than the pressure at the ejection points. The mass flow extraction from the compressor causes a decrease of the engine thermal efficiency. However, the thermal efficiency gained by higher turbine inlet temperature offsets the loss caused by the extraction.

In case of internally cooled blades, the cooling air mass flow $\dot{m}_{c\,S}$ and $\dot{m}_{c\,R}$ passes through different channels that have internal turbulators and pin fins for enhancing the heat transfer as schematically shown in Fig. 17.13. The cooling mass flow $\dot{m}_{c\,S}$ and $\dot{m}_{c\,R}$ may eject at the blade trailing edge or at the blade tip to join the primary mass flow. The trailing edge ejection loss and its optimization were discussed in Chapter 7. As seen, the optimization of the ejection slot geometry minimized the ejection losses.

In case of an external cooling that includes, among others, shower head, full coverage film cooling, and transpiration cooling, the cooling mass flow passes though different blade cooling plena and ejects though a number of holes that are arranged on the blade surface with certain spacings and angles. The purpose of external cooling is to build a thin "cool" buffer layer distributed on the blade surface to prevent hot gas from directly transferring heat to the blade material. Because of discrete spacings of holes, a uniform distribution of cooling air is not possible. This leads to a mixing of the cooling mass flow and the primary hot gas. To circumvent this deficiency, a transpiration cooling technique can be used. The cooling passes through uniformly porous material that builds a uniformly distributed protective cool air shield on the blade surface. Although transpiration cooling is the most efficient cooling technique, it has not reached the state of maturity to be implemented into gas turbines.

For turbine blades without internal or external cooling, heat exchange between the blade material and the primary hot gas occurs during off-design operations. Heat

transfer from hot gas to turbine blade and structure occurs when the turbine component undergoes a transient power increase by adding fuel in the combustion chamber. On the other hand, heat is rejected from blades, when a transient operation triggers throttling of fuel to reduce the turbine power. As shown in an h-s-diagram in Fig. 17.14, the total heat added to the stage is the sum of the heat transferred to the stator and to the rotor $q = q' + q''$. These partial heat contributions may originate from blade cooling, Fig. 17.14(a), or from transient operation of uncooled blades.

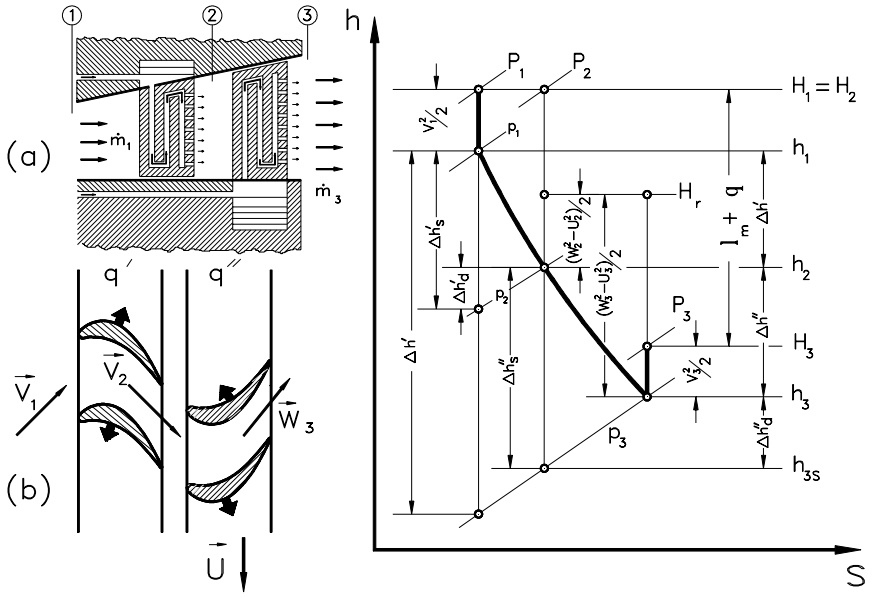

Fig. 17.14: Cooled turbine component with expansion diagram

17.3.3.1 Description of diabatic turbine module, first method: This turbine module provides detailed information about the turbine behavior during dynamic operations and the heat transferred to/from the blade during a transient event. Similar to the adiabatic turbine case discussed in Section 17.3.2, two methods can be used for describing this module. The first method utilizes the time dependent conservation laws for continuity, momentum, and energy, Eqs. (14. 26), (14.33), and (14.51), derived in Chapter 14. For diabatic turbine stage calculation, Eq. (14.51) is re-written:

$$\frac{\partial H}{\partial t} = -\kappa_k \frac{\dot{m}_k}{\rho_k S_k}\left(\frac{H_{i+1} - H_i}{\Delta x}\right) - \left(\frac{\kappa - 1}{\rho k}\right)_k \left[\left(\frac{H_k + K_k}{\Delta x}\right)\left(\frac{\dot{m}_{i+1}}{S_{i+1}} - \frac{\dot{m}_i}{S_i}\right) + \frac{\dot{m}_k}{\rho_k S_k^2}\frac{\partial \dot{m}_{i+1}}{\partial t}\right] + \frac{\kappa_k}{\rho_k}\left(\frac{\Delta \dot{Q} + \Delta L}{\Delta V}\right) \tag{17.50}$$

The stage power ΔL in Eq.(17.50) is directly related to the specific stage mechanical energy $\Delta L \equiv L = \dot{m} l_m$ with $l_m = \lambda U_3^2$. The heat added to the stage is $\Delta \dot{Q} = \dot{m} q$ with q as the specific heat transferred to the stage. For a steady state case with a constant mass flow, Eq.(17.50) immediately yields the conservation of energy $q + l = H_\omega - H_\alpha$. Thus, the equation of energy is rearranged as:

$$\frac{\partial H}{\partial t} = -\kappa_k \frac{\dot{m}_k}{\rho_k}\left(\frac{H_{i+1} - H_i}{\Delta V}\right) - \left(\frac{\kappa - 1}{\rho k}\right)_k \left[\left(\frac{H_k + K_k}{\Delta x}\right)\left(\frac{\dot{m}_{i+1}}{S_{i+1}} - \frac{\dot{m}_i}{S_i}\right) + \frac{\dot{m}_k}{\rho_k S_k^2}\frac{\partial \dot{m}_{i+1}}{\partial t}\right] + \frac{\kappa_k \dot{m}_k}{\rho_k}\left(\frac{q + l}{\Delta V}\right) \tag{17.51}$$

Equation (17.51) together with equations of continuity, momentum, and additional information about the heat transfer, describes the dynamic behavior of the diabatic turbine stage. For a row-by-row analysis it can be decomposed into two equations that describe the individual stator and rotor rows. For stator row, because $l_S = 0$ and $q = q_S$, we find:

$$\frac{\partial c_{p_{i+1}} T_{0_{i+1}}}{\partial t} = -\kappa_k \frac{\dot{m}_k}{\rho_k}\left(\frac{c_{p_{i+1}} T_{0_{i+1}} - c_{p_{i+1}} T_{0_i}}{\Delta V}\right) + \frac{\kappa_k \dot{m}_k}{\rho_k}\left(\frac{q_S}{\Delta V}\right) - \left(\frac{\kappa - 1}{\rho k}\right)_k \left[\left(\frac{c_{p_k} T_{0_k} + K_k}{\Delta x}\right)\left(\frac{\dot{m}_{i+1}}{S_{i+1}} - \frac{\dot{m}_i}{S_i}\right) + \frac{\dot{m}_k}{\rho_k S_k^2}\frac{\partial \dot{m}_{i+1}}{\partial t}\right] \tag{17.52}$$

For the rotor row, because $l_R = l$ and $q = q_R$, we find:

$$\frac{\partial c_{p_{i+1}} T_{0_{i+1}}}{\partial t} = -\kappa_k \frac{\dot{m}_k}{\rho_k}\left(\frac{c_{p_{i+1}} T_{0_{i+1}} - c_{p_i} T_{0_i}}{\Delta V}\right) + \frac{\kappa_k \dot{m}_k}{\rho_k}\left(\frac{q_R + l_m}{\Delta V}\right) - \left(\frac{\kappa - 1}{\rho k}\right)_k \left[\left(\frac{c_{p_k} T_{0_k} + K_k}{\Delta x}\right)\left(\frac{\dot{m}_{i+1}}{S_{i+1}} - \frac{\dot{m}_i}{S_i}\right) + \frac{\dot{m}_k}{\rho_k S_k^2}\frac{\partial \dot{m}_{i+1}}{\partial t}\right] \tag{17.53}$$

with l_m as the stage mechanical energy. To completely describe the diabatic expansion process within stator and rotor rows, heat transfer equations as well as blade material temperature equations must be added to the set of Eqs. (17.52) , (17.53), (14. 26), and (14.33). The terms in the brackets in Equations (17.52) and (17.53) are of second order significance, therefore may be neglected. As a result we obtain for stator:

$$\frac{\partial c_{p_{i+1}} T_{0_{i+1}}}{\partial t} = -\frac{\kappa_k}{\rho_k \Delta V}\left(\dot{m}_k c_{p_{i+1}} T_{0_{i+1}} - \dot{m}_k c_{p_i} T_{0_i} - \Delta \dot{Q}_S\right) - \left(\frac{\kappa - 1}{\rho k}\right)_k \frac{\dot{m}_k}{\rho_k S_k^2}\frac{\partial \dot{m}_{i+1}}{\partial t} \tag{17.54}$$

and for the rotor row,

$$\frac{\partial c_{p_{i+1}} T_{0_{i+1}}}{\partial t} = -\frac{\kappa_k}{\rho_k \Delta V}\left(\dot{m}_k c_{p_{i+1}} T_{0_{i+1}} - \dot{m}_k c_{p_i} T_{0_i} - \Delta L - \Delta \dot{Q}_R\right) - \left(\frac{\kappa - 1}{\rho k}\right)_k \frac{\dot{m}_k}{\rho_k S_k^2}\frac{\partial \dot{m}_{i+1}}{\partial t} \tag{17.55}$$

with ΔV as net volume of the row space occupied by the working medium. The heat added to or rejected from the working medium in Equations (17.54) and (17.55) is transferred to the stator and rotor blade material. The heat transfer aspect is treated in the subsequent section.

17.3.3.2 Description of diabatic turbine module, second method: The second method is an enhanced diabatic calculation procedure that is based on the row-by-row calculation method outlined in Section 17.1. In this case, the thermal energy supplied to the system is included in the governing equations. The new equation set is

combined with the plena Eqs. (17.47) and (17.48) for dynamic coupling. The amount of heat supplied to the stage is expressed in stage mechanical energy balance, Eq.(5.8):

$$1_m + q = \frac{1}{2}\left[\left(V_2^2 - V_3^2\right) + \left(W_3^2 - W_2^2\right) + \left(U_2^2 - U_3^2\right)\right] \tag{17.56}$$

with q as the heat supplied to the stage. Decomposing Eq. (17.56) results in a modified version of Eqs.(17.8) and (17.9). With this decomposition, we arrive at the thermal and mechanical energy contributions allocated to the stator and rotor rows as:

$$\begin{aligned} l' + q' &= \frac{1}{2}\, V_2^2 - \frac{1}{2}\, W_2^2 \\ l'' + q'' &= \frac{1}{2}\,\left(W_3^2 - U_3^2 + U_2^2 - V_3^2 \right) \end{aligned} \tag{17.57}$$

Similarly we find the isentropic parts:

$$\begin{aligned} l_s' + q' &= \frac{1}{2}\left(V_{2s} - W_2^2\right) \\ l_s'' + q'' &= \frac{1}{2}\left(W_{3s}^2 - U_3^2 + U_2^2 - V_3^2 \right) \end{aligned} \tag{17.58}$$

As seen, the sum of stator and rotor contributions leads to the stage specific mechanical energy. Similar to the polytropic specific mechanical energy expressions given in Eqs. (17.8), we divide Eqs. (17.57) and (17.58) by the circumferential kinetic energy at the exit of the individual row. The dimensionless row polytropic load coefficients for stator and rotor with heat transfer are:

$$\begin{aligned} \lambda' &= \frac{l'}{U_2^2} = \phi' \cot\alpha_2 - \frac{1}{2} - \epsilon' \\ \lambda'' &= \frac{l''}{U_3^2} = -\,\phi'' \cot\beta_3 - 1 + \frac{v^2}{2} - \epsilon'' \end{aligned} \tag{17.59}$$

with the dimensionless parameters $\epsilon' = q'/U_2^2$ and $\epsilon'' = q''/U_3^2$. The rotor row parameters in Eq. (17.59) have the same definition as those in Section 17.1.2. For the row-by-row diabatic calculation, the row load coefficients in Eqs. (17.8) must be replaced by (17.59).

17.3.3.3 Heat transfer closure equations: The heat transfer mechanism for cooled and uncooled blades are shown schematically in Fig. 15.9.

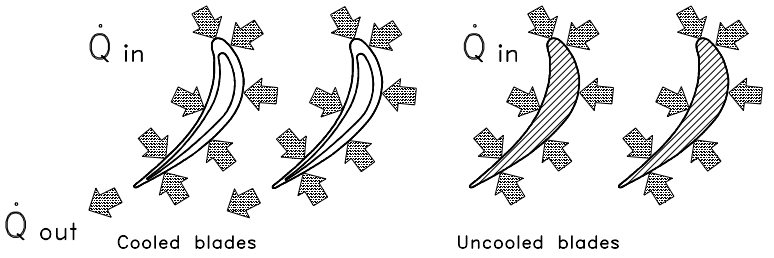

Fig. 17.15: Heat flow is transferred from compressor working medium to compressor blades $\dot{Q}_S$, the amount of $\dot{Q}_C$ is removed by the cooling medium.

Considering cooled turbine blades, the hot gas transfers certain amounts of thermal energy flow or heat flow $\dot{Q}_h$ to the stator ($\dot{Q}_h \equiv \dot{Q}_h^{/}$), and rotor ($\dot{Q}_h \equiv \dot{Q}_h^{//}$). To maintain a desired blade temperature, the cooling mass flow through the blade internal channels has to remove the heat flow $\dot{Q}_C$ from the blade. The transferred thermal energies on hot and cold sides are:

$$\begin{aligned} \dot{Q}_h &= \bar{\alpha}_h A_h \, (\, \bar{T}_h - \bar{T}_W \,) \\ \dot{Q}_C &= \bar{\alpha}_C \, A_C (\, \bar{T}_W - \bar{T}_C) \end{aligned} \tag{17.60}$$

In Eq. (17.60), $\bar{\alpha}_C$, $\bar{\alpha}_h$ are the averaged heat transfer coefficients for internal cooling channels, the row flow path , $\bar{T}_C$, $\bar{T}_h$, and $\bar{T}_W$ are the mean temperatures of coolant flow, row working medium, row wall temperature, and A_C, A_h are the contact surfaces on the cold and hot side, respectively. The coupling condition between the cold and the hot side is provided by the material temperature differential equation:

$$\frac{dT_W}{dt} = \frac{1}{\rho_W \, c_W \, \Delta V_W} \, (\, \dot{Q}_C + \dot{Q}_h \,) \tag{17.61}$$

the heat flow $\dot{Q}_h$ in Eq. (17.61) may assume positive or negative values, whereas $\dot{Q}_C$ is always negative, since heat is rejected. For the case of no cooling, $\dot{Q}_C$ is zero. In case of a dynamic temperature equilibrium where the blade temperature change approaches zero, Eq. (17.61) is reduced to:

$$\dot{Q}_c + \dot{Q}_h = 0 \tag{17.62}$$

To calculate $\dot{Q}_h$ and $\dot{Q}_C$ for inserting into Eq. (17.61), we use the Nusselt number correlation, Eq.(18.25), as discussed in Chapter 16. For blades without cooling, generic Nusselt number correlations from Chapter 7 can be used. For determination of heat transfer coefficients for particular cooling schemes, Han [15] offers a comprehensive source.

References, Chapter 17

17.1 Schobeiri, M.T., M.T. Schobeiri, J.L. Gilarranz, E.S. Johansen, 2000, "Aerodynamic and Performance Studies of a Three-Stage High Pressure Research Tturbine with 3-d-Blades, Design Point and Off-Design Experimental Investigations," ASME-paper: 2000-GT-484.

17.2 Traupel, W., 1977, "Thermische Turbomaschinen," 3. Auflage, Springer-Verlag.

17.3 Vavra, M.H., 1960, "Aero-Thermodynamics and Flow in Turbomachinees," John Wiley & Sons, Inc.

17.4 NASA SP-290, 1975, "Turbine Design and Application," Volume 2

17.5 Kroon, R.P., Tobiasz, H.J., 1971, "Off-Design Performance of Multistage Turbines," Trans. ASME, Jou. Eng. Power 93, pp. 21-27.

17.6 Kochendorfer, F.D., Nettles, J.C., 1948, "An Analytical Method Estimating Turbine Performance," NACA Report 930.

17.7 Bammert, K., Zehner, P., 1980, "Measurement of the Four-Quadrant Characteristics on a Multistage Turbine," Trans. ASME, Journal of Eng. Power, 102, No. 2.

17.8 Zehner, P., 1980, "Vier-Quadranten Charakteristiken mehrstufiger axialer Turbinen," VDI-Forsch. -Ber. VDI-2, Reihe 6, Nr. 75.

17.9 Schobeiri, T., 1990, "Thermo-Fluid Dynamic Design Study of Single and Double Inflow Radial and Single-Stage Axial Steam Turbines for Open-Cycle Ocean Thermal Energy Conversion, Net Power Producing Experiment Facility," ASME Transaction, Journal of Energy Resources, Vol. 112, pp. 41-50.

17.10 Schobeiri, M. T., Abouelkheir, M., 1992, "A Row-by-Row Off-Design Performance Calculation Method for Turbines," *AIAA, Journal of propulsion and Power*, Vol. 8, Number 4, July-August 1992, pp. 823-826

17.11 Stodola, A., 1924, "Dampf- und Gasturbinen," 6. Auflage, Springer-Verlag, Berlin.

17.12 Horlock, J.H., 1973, "Axial Flow Turbines," Robert E. Krieber Publishing Company.

17.13 Pfeil, H., 1975, "Zur Frage des Betriebesverhaltens von Turbinen," VDI-Zeitschrift, *Forschung im Ingenieurwesen,* Bd. 41, Nr. 2, Ppg, 33-36.

17.14 Schobeiri l, M.T, 1987, “Eine einfache Näherungsmethode zur berecchnung des Betriebsverhaltens von Turbinen,” *VDI-Zeitschrift, Forschung im Ingenieurwesen* Bd. 53, Nr. 1, pp-33-36.

17.15 Han Je-Chin, Duta S., Ekkad, S, 2000, “Gas Turbine Heat Transfer Technology,”Tylor and Francis.

18 Gas Turbine Engines, Design and Dynamic Performance

A gas turbine engine is a system that consists of several turbomachinery components and auxiliary subsystems. Air enters the compressor component which is driven by a turbine component and is placed on the same shaft. Air exits the compressor at a higher pressure and enters the combustion chamber, where the chemical energy of the fuel is converted into thermal energy producing combustion gas at a temperature that corresponds to the turbine inlet design temperature. The combustion gas expands in the following turbine component, where its total energy is partially converted into shaft work and exit kinetic energy. For power generation gas turbines, the shaft work is the major portion of the above energy forms. It covers the total work required by the compressor component, the bearing frictions, several auxiliary subsystems, and the generator. In aircraft gas turbines, a major portion of the total energy goes toward generation of high exit kinetic energy that is essential for thrust generation.

Gas turbines are designed for particular applications that determine their design configurations. For power generation purposes, the gas turbine usually has a *single spool*. A spool combines a compressor and a turbine that are connected together via a shaft. Fig. 18.1 exhibits a single-spool power generation gas turbine, where a 14-stage compressor shares the same shaft with a 3-stage turbine.

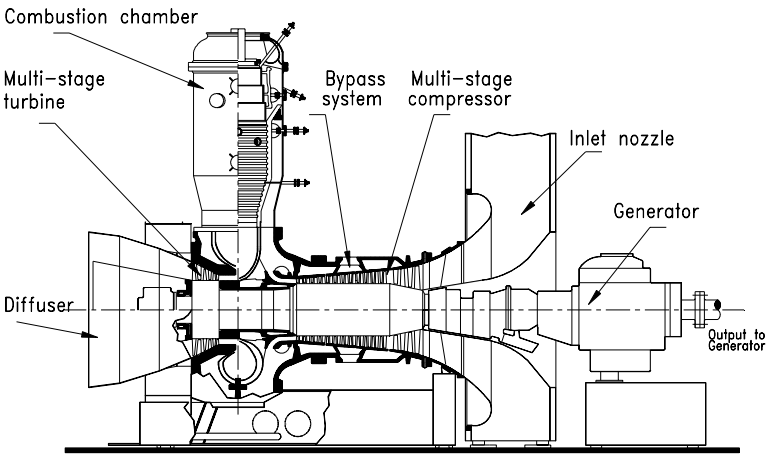

Fig. 18.1: A single- spool power generation gas turbine, BBC-GT9.

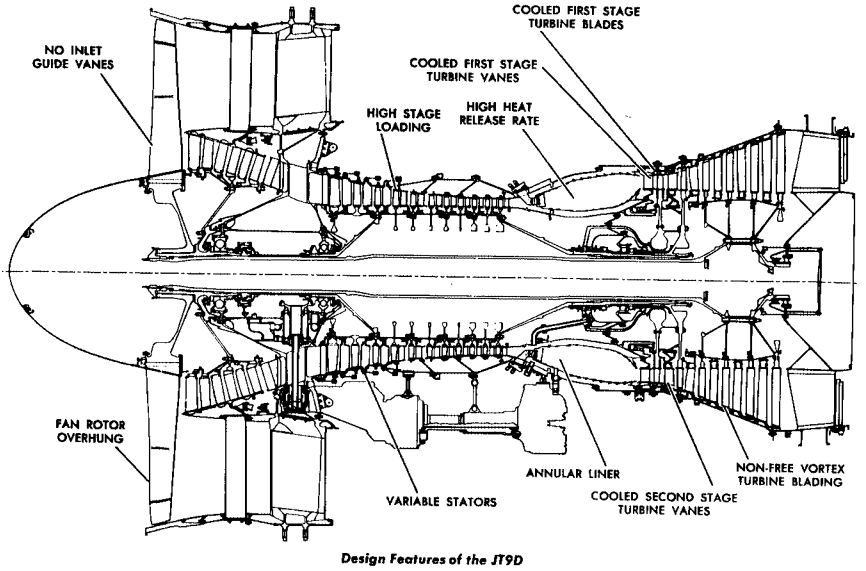

Fig. 18.2: A twin-spool Pratt & Whitney high bypass ratio aircraft engine with multi-stage compressors and turbines

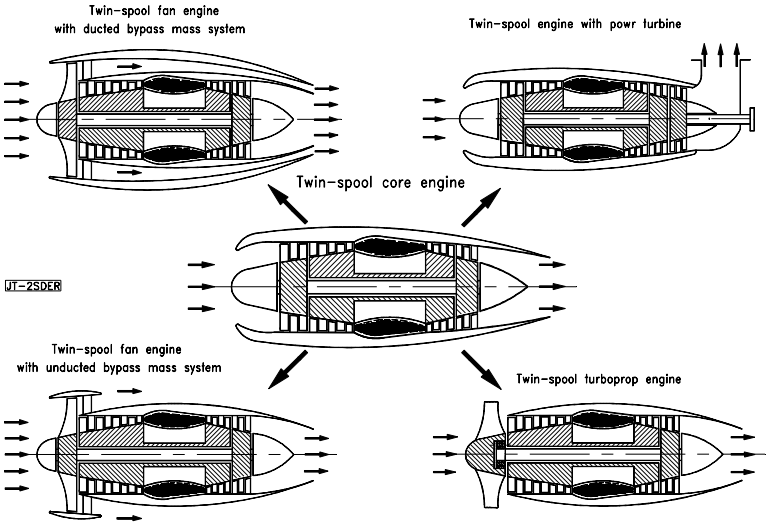

Fig. 18.3: Schematic of a twin-spool core engine with its derivatives

While in power generation gas turbine design the power/weight ratio does not play an important role, the thrust/weight ratio is a primary parameter in designing an aircraft gas turbine. High performance aircraft gas turbine engines generally have twin-spool or multi-spool arrangements. The spools are usually rotating at different angular velocities and are connected with each other aerodynamically via air or combustion gas. Fig. 18.2 exhibits a typical high performance twin spool aircraft gas turbine with a *ducted front fan* as the main thrust generator. Gas turbine engines with power capacities less than 20 MW might have a *split shaft* configuration that consists of a *gas generation spool* and a *power shaft*. While the turbine of the gas generation spool provides the necessary shaft work to drive the compressor, the power shaft produces the net power. In addition to the above design configurations, a variety of engine derivatives can be constructed using a core engine as shown in Fig. 18.3.

18.1 Gas Turbine Processes, Steady Design Operation

Starting with the single-spool power generation gas turbine that consists of a multi-stage compressor, a combustion chamber, and a turbine, the h-s diagram is shown in Fig. 18.4(a).

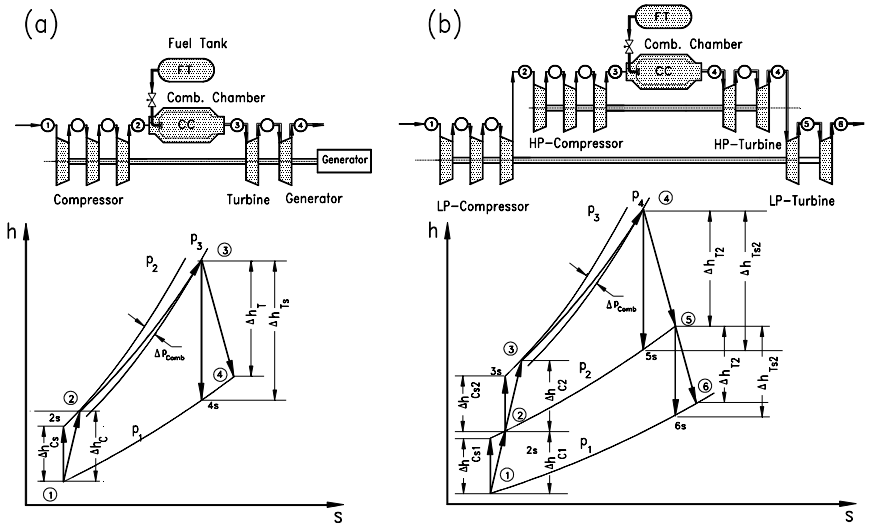

Fig. 18.4: H-s-diagram of a single spool power generation gas turbine (a) and a twin-spool aircraft engine (b).

The compression process from 1 to 2 is accomplished by the compressor with a polytropic efficiency η_{pol} that can be accurately calculated using the row-by-row or stage-by-stage methods discussed in Chapters 16. The combustion process from 2 to 3 is associated with certain total pressure loss coefficient ζ_{comb} thus, it is not

considered isobaric. The expansion process from 3 to 4 causes an entropy increase that is determined by the turbine efficiency. Figure 18.4(b) shows the h-s diagram for a twin spool aircraft engine. In contrast to the single spool engine, the compression process is accomplished by two compressors that are operating at two different angular velocities. Air enters the low pressure compressor (LP-compressor) driven by the LP-turbine and is compressed from 1 to 2. Further compression from 2 to 3 occurs in the high pressure compressor (HP-compressor) driven by the HP-turbine. After addition of fuel in the combustion chamber, fist expansion occurs in the HP-turbine, whose power exactly matches the sum of HP-compressor power and the power required to compensate bearing frictions. Second expansion in LP-turbine matches the power by the LP-compressor, bearing friction, and the auxiliary subsystems. In off-design operation, there is always a dynamic mismatch between the turbine and compressor power that changes the spool rotational speed. This dynamic mismatch is brought to an equilibrium by taking appropriate control measures, as we discuss in the following sections. As mentioned briefly, small gas turbines may have a split shaft configuration as shown in Fig. 18.5. The single spool gas generator unit provides the power turbine with combustion gas that has the required pressure and temperature to produce the power. As seen in Fig. 18.5(a), the specific turbine enthalpy difference is $\Delta h_T \approx \Delta h_C$, leaving the rest enthalpy difference Δh_{PT} for power generation.

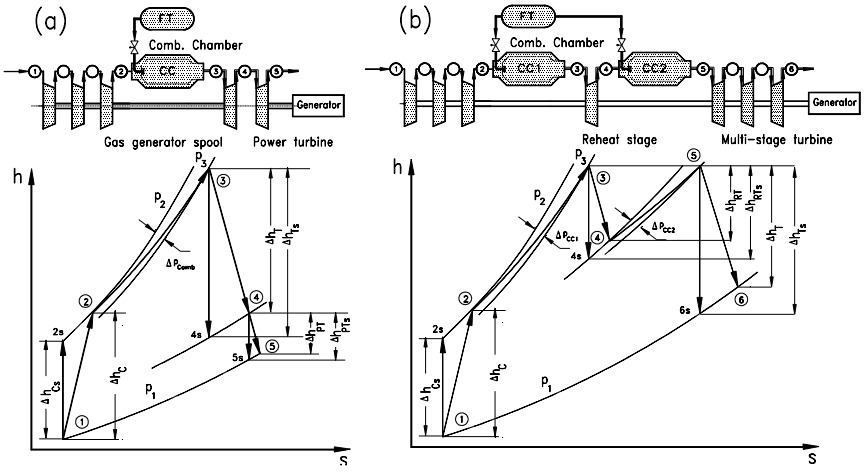

Fig. 18.5: H-s-diagram of a single spool power generation gas turbine with a power shaft (a) and a single spool power generation gas turbine with a reheat stage and two combustion chambers (b).

Figure 18.5(b) shows the h-s diagram of a high efficiency power generation gas turbine. The schematic cross section of this gas turbine is shown in Fig. 18.9. It consists of a multi-stage compressor, *C*, a combustion chamber, *CC1*, providing a

lean combustion gas that expands in a single-stage reheat turbine, *RT*. The exhaust gas from *RT* enters the second combustion chamber, *CC2*, where the remaining fuel is added to insure a stoichiometric combustion. It expands in the multi-stage turbine that produces the major portion of power. As seen in the following sections, the implementation of the reheat process substantially increases the thermal efficiency of gas turbines. The underlying thermodynamic principles of this concept is the reheat process, which has been very well known in steam turbine design for more than a century. However, in gas turbine design, adding a second combustion chamber to a conventionally designed gas turbine seemed to be associated with unforeseeable problems. Based on design experiences with *Compressed Air Energy Storage* (CAES) gas turbines with two combustion chambers, *Brown Boveri* designed and successfully manufactured the first series of power generation gas turbines with a reheat stage and two combustion chambers.

18.1.1 Gas Turbine Process

Accurate prediction of thermal efficiency of a gas turbine engine requires the knowledge of the compressor, combustion chamber, and turbine efficiencies as well as the bearing losses and the losses in auxiliary systems. Furthermore, detailed knowledge of the amount of mass flows with their extraction and injection pressures for cooling the turbine blades and the rotor discs are necessary. In addition, a detailed gas table that accounts for thermodynamic properties of humid air as well as the properties of the combustion gas must be implemented into the calculation procedure. Assuming air and combustion gas as calorically perfect gases results in significant errors. Figure 18.6 exhibits a schematic diagram that shows in detail the extraction of different cooling mass flows and their injection locations.

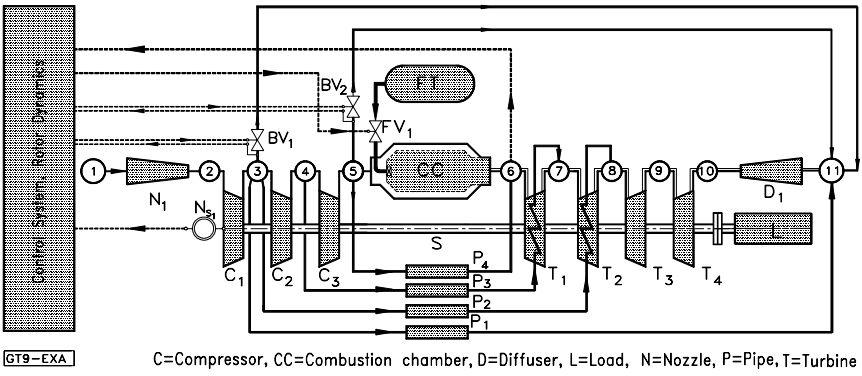

Fig. 18.6: Schematic of a single spool gas turbine illustrating the mass flow extraction from compressor for different cooling purposes.

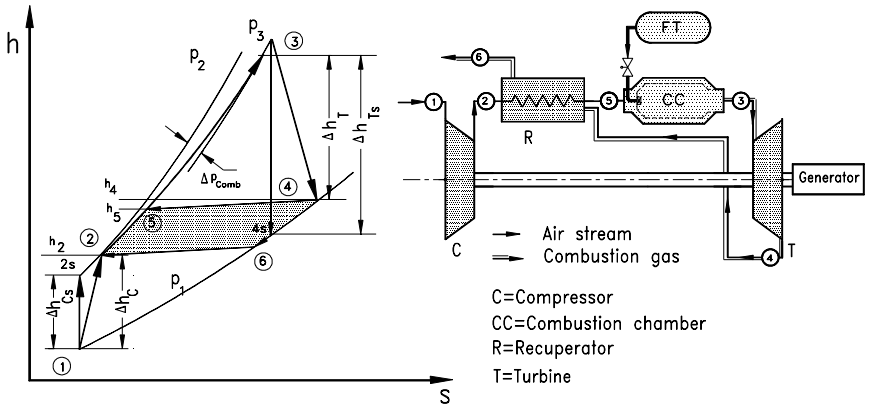

Fig. 18.7: Simple sketch of a gas turbine with recuperator.

Mass flow through P1 extracted from plenum 3 cools the rotor and does not participate in power generation; mass flows through P2 and P3 cool the second and first turbine stages and remain in the system; and finally, mass flow through P4 reduces the combustion chamber exit temperature before it enters the turbine. At stations 6, 7, 8, and 11 humid air is mixed with combustion gas resulting in a local change of water/air and fuel/air ratios, therefore changing the entire thermodynamic properties including the special gas constant *R*. In the absence of the above information, reasonable assumptions relative to component efficiencies can be made to qualitatively determine the thermal efficiency and its tendency with regard to parameter variation. In the following section, a simple thermal efficiency calculation procedure is derived that is appropriate for varying different parameters and qualitatively determining their impacts on thermal efficiency.

The gas turbine with its corresponding process is sketched in Fig. 18.7. It consists of a compressor, a recuperator, a combustion chamber and a turbine. Exhaust gas from the turbine is diverted into the recuperator heating up the compressed air before entering the combustion chamber. The individual processes are compression, expansion, fuel addition and combustion, and heat exchange in recuperator. The compressor and turbine enthalpy differences are calculated from:

$$\begin{aligned} h_2 - h_1 &= \frac{h_{2s} - h_1}{\eta_c} \\ h_3 - h_4 &= \left(h_3 - h_{4s}\right) \eta_T \end{aligned} \tag{18.1}$$

We introduce the following definitions for the recuperator air- and gas-side (*RA, RG)*, as well as combustion chamber (*CC)* pressure loss coefficients:

$$\begin{aligned}
\zeta_{RA} &= \frac{\Delta P_{RA}}{P_2}, \quad \text{with} \quad \Delta P_{RA} = P_2 - P_5 \\
\zeta_{RG} &= \frac{\Delta P_{RG}}{P_1}, \quad \text{with} \quad \Delta P_{RG} = P_4 - P_6 \\
\zeta_{CC} &= \frac{\Delta P_{CC}}{P_2}, \quad \text{with} \quad \Delta P_{CC} = P_5 - P_3
\end{aligned} \tag{18.2}$$

The thermal efficiency is defined as:

$$\eta_{in} = \frac{L_{net}}{\dot{Q}_{in}} = \frac{L_T - L_C}{\dot{Q}_{in}} = \frac{\dot{m}_T l_T - \dot{m}_C l_C}{\dot{Q}_{in}} \tag{18.3}$$

The specific net power is calculated from:

$$\frac{L_{net}}{\dot{m}_1} = \frac{L_T - L_c}{\dot{m}_1} = \frac{\dot{m}_3 l_T - \dot{m}_1 l_C}{\dot{m}_1} = (1+\beta)\, l_T - l_c \tag{18.4}$$

with the fuel air ratio $\beta = \dot{m}_f / \dot{m}_1$. Replacing the specific turbine power l_T by the enthalpy difference from Eq. (18.1), we find:

$$\begin{aligned}
\frac{\dot{m}_3}{\dot{m}_1} l_T &= (1+\beta)\left(h_3 - h_4\right) = \eta_T (1+\beta)\left(h_3 - h_{4s}\right) \\
\frac{\dot{m}_3}{\dot{m}_1} l_T &= \eta_T (1+\beta)\, \bar{c}_{PT}\left(T_3 - T_{4s}\right) \\
\frac{\dot{m}_3}{\dot{m}_1} l_T &= \eta_T (1+\beta)\, \bar{c}_{PT}\, T_3 \left(1 - \frac{T_{4s}}{T_3}\right)
\end{aligned} \tag{18.5}$$

Equation (18.5) expresses the isentropic enthalpy difference in terms of a product of averaged specific heat at constant pressure and the isentropic temperature difference. The specific heat in Eq.(18.5) exhibits an averaged value between the two given temperatures:

$$\bar{c}_{PT} = \frac{h_3 - h_{4s}}{T_3 - T_{4s}} \tag{18.6}$$

The temperature ratio in Eq. (18.5) can be related to the pressure ratio as follows:

$$\frac{T_3}{T_{4s}} = \left(\frac{p_3}{p_4}\right)^{\left(\frac{k-1}{k}\right)_T} = \pi_T^{\left(\frac{k-1}{k}\right)_T} = \pi_T^{m_T}, \quad \text{with } m_T \equiv \left(\frac{k-1}{k}\right)_T \tag{18.7}$$

with Eq. (18.7), Eq. (18.5) becomes:

$$\frac{\dot{m}_3}{\dot{m}_1} l_T = \eta_T (1+\beta)\, \bar{c}_{PT} T_3 \left(1 - \pi_T^{-m_T}\right) \tag{18.8}$$

Because of the pressure losses across the combustion chamber, the turbine and compressor pressure ratios are not the same ($\pi_T \neq \pi c$). Implementing the pressure losses of the combustion chamber and recuperator air side, we find:

$$\pi_T = \frac{p_3}{p_4} = \frac{p_2 - \Delta p_{RA} - \Delta p_{cc}}{p_1 + \Delta p_{RA}} = \frac{p_2}{p_1}\left(\frac{1 - \zeta_{RA} - \zeta_{cc}}{1 + \zeta_{RA}}\right) = \pi_c \frac{1 - \zeta_{RA} - \zeta_{cc}}{1 + \zeta_{RA}} \tag{18.9}$$

We set the fraction on the right hand side of Eq. (18.9):

$$\epsilon = \frac{1 - \zeta_{RA} - \zeta_{cc}}{1 + \zeta_{RA}} \tag{18.10}$$

and arrive at:

$$\pi_T = \epsilon \pi_c, \text{for } \epsilon = 0,\ \zeta_{RA} = \zeta_{CC} = \zeta_{RA} = 0 \quad \text{and for } \epsilon < 0\ \ \zeta_{RA} \neq 0,\ \zeta_{cc} \neq 0 \tag{18.11}$$

For parameter variation, following values may be used: $\zeta_{RA} \cong \zeta_{Rh} = 2 - 8\%$, $\zeta_{cc} \cong 5 - 10\%$. Following exactly the same procedure defined by Eqs. (18.4) through (18.11), we find the compressor specific work as:

$$l_C = \frac{1}{\eta_C} \bar{c}_{Pc} T_1 \left(\pi_C^{m_C} - 1\right), \text{ with } m_C = \left(\frac{k-1}{k}\right)_C \tag{18.12}$$

Inserting Eqs. (18.8) and (18.12) into Eq. (18.4), we arrive at:

$$\eta_{th} = \frac{\eta_T \bar{c}_{PT} T_3 \left[1 - \left(\epsilon \pi_c\right)^{-m_T}\right](1+\beta) - \frac{1}{\eta_c} \bar{c}_{Pc} T_1 \left(\pi_c^{m_c} - 1\right)}{\bar{c}_{Pcc}\left[(1+\beta)\frac{T_3}{T_1} - \frac{T_5}{T_1}\right]} \tag{18.13}$$

The turbine inlet temperature T_3, the environmental temperature $T_{1,}$ and thus their ratio T_3/T_1 is considered as a known parameter. This parameter can also be used for parametric studies. Therefore it is desirable to express the ratio T_5/T_1 in terms of T_3/T_1.We find this ratio by utilizing the recuperator effectiveness $\eta_{R:}$

$$\eta_R = \frac{h_5 - h_2}{h_4 - h_2} \cong \frac{T_5 - T_2}{T_4 - T_2} \tag{18.14}$$

From compressor and turbine energy balance, Eq. (18.1) we find

$$\begin{aligned} T_2 &= T_1 + (T_{2s} - T_1)\frac{1}{\eta_c} = T_1 + T_1\left(\pi_c^{m_c} - 1\right)\frac{1}{\eta_c} \\ T_4 &= T_3 - (T_3 - T_{4s})\eta_T = T_3 - T_3\left[1 - (\epsilon\pi_c)^{-m_T}\right]\eta_T \end{aligned} \tag{18.15}$$

Equation (18.15) in dimensionless form yields:

$$\begin{aligned} \frac{T_2}{T_1} &= 1 + \frac{1}{\eta_c}\left(\pi_c^{m_c} - 1\right) \\ \frac{T_4}{T_1} &= \frac{T_3}{T_1} - \frac{T_3}{T_1}\eta_T\left[1 - (\epsilon\pi_c)^{-m_T}\right] \end{aligned} \tag{18.16}$$

Introducing the temperature ratio $\theta = T_3/T_1$, the temperature ratio T_4/T_1 Eq. (18.16) becomes:

$$\frac{T_4}{T_1} = \Theta\left\{1 - \left[1 - (\epsilon\pi_c)^{-m_T}\right]\eta_T\right\} \tag{18.17}$$

To determine the temperature ratio T_5/T_1, we re-arrange Eq. (18.14)

$$\frac{T_5}{T_1} = \eta_R\left(\frac{T_4}{T_1} - \frac{T_2}{T_1}\right) + \frac{T_2}{T_1} \tag{18.18}$$

Using Eqs. (18.16) and (18.17), Eq. (18.18) is re-arranged as

$$\frac{T_5}{T_1} = \eta_R\left[\theta\left\{1 - \left[1 - (\epsilon\pi_c)^{-m_T}\right]\eta_T\right\} - 1 - \frac{1}{\eta_c}\left(\pi_c^{m_c} - 1\right)\right] + 1 + \frac{1}{\eta_c}\left(\pi_c^{m_c} - 1\right) \tag{18.19}$$

Introduce Eqs. (18.19) and the definition $\theta = T_3/T_1$ into Eq. (18.13), the thermal efficiency equation for a gas turbine with a recuperator is written as:

$$\eta_{th} = \frac{\bar{c}_{PT}\eta_T\theta\left[1-\left(\epsilon\pi_c\right)^{-m_T}\right](1+\beta) - \frac{1}{\eta_c}\bar{c}_{Pc}\left(\pi_c^{m_c}-1\right)}{\bar{c}_{PCC}\left\{\theta\left(1+\beta-\eta_R\right) - \left[1+\frac{1}{\eta_c}\left(\pi_c^{m_c}-1\right)\right]\left[1-\eta_R\right] + \theta\,\eta_R\eta_T\left[1-(\epsilon\pi_c)^{-m_T}\right]\right\}} \tag{18.20}$$

From Eq. (18.20) special cases are obtained. Setting $\eta_R = 0$ gives the thermal efficiency of a gas turbine without recuperator. The ideal case of Brayton cycle is obtained by setting all loss coefficients equal to zero, all efficiencies equal to unity, and $\bar{c}_{PC} = \bar{c}_{PCC} = \bar{c}_{PT} = const.$ Equation (18.20) properly reflects the effects of individual parameters on the thermal efficiency and can be used for preliminary parameter studies. As an example, Fig. (18.8) shows the effect of pressure ratio, the turbine inlet temperature, and the component efficiency on thermal efficiency for two different cases. As Fig. 18.8 shows, for each turbine inlet temperature, there is one optimum pressure ratio. For temperature ratios up to $\theta = 3.5$ pronounced efficiency maxima are visible within a limited π-range. Approaching higher inlet temperature, however, this range widens significantly.

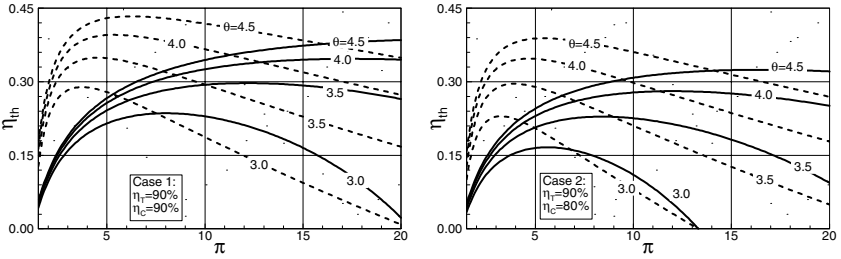

Fig. 18.8: Thermal efficiency as function of pressure ratio with turbine inlet temperature ratio as parameter for (a) gas turbine with recuperator, dashed curves and (b) without recuperator, solid curves. $\eta_R = 0.75$, $\zeta_{CC} = 0.05$, $\zeta_{RA} = \zeta_{RG} = 0.03$, for Case 1 and Case 2. In Case 2 the turbine efficiency is lowered from 90% to 80%.

For a gas turbine without recuperator, the thermal (efficiency solid curves in Fig. 18.8) shows that for $\theta = 4.0$, increasing the pressure ratio above 15 does not bring any noticeable efficiency increase. However, it requires the compressor to have one or two more stages. The temperature ratio $\theta = 4.0$ corresponds to a turbine inlet temperature of $T_3 = 1{,}200\,K$ at a compressor inlet temperature of $T_1 = 300.0\,K$.

Figure 18.8, dashed curves indicate that tangibly higher thermal efficiencies at a substantially lower pressure ratio can be achieved by utilizing recuperators. This is particularly advantageous for small gas turbines (so called "micro-turbines") with power ranging from 50 to 200 kW. The required low maximum pressure ratio can easily be achieved by a single-stage centrifugal compressor. Comparing Case1 and Case 2 in Fig. 18.8 shows that thermal efficiency reduces if low efficiency components are applied.

18.1.2 Improvement of Gas Turbine Thermal Efficiency

The above parameter study indicates that for a conventional gas turbine with a near-optimum pressure ratio with or without the recuperator, the turbine inlet temperature is the parameter that determines the level of thermal efficiency. For small size gas turbines recuperator is an inherent component of the gas turbine. For large power generation gas turbines, however, it is not a practical option. Using a recuperator in a large gas turbine requires significantly lower pressure ratio that results in a large volume recuperator and turbine. As a result in order to improve the thermal efficiency of conventional gas turbines, increasing the turbine inlet temperature seems to be the only option left. Considering this fact, in the last three decades, gas turbine manufacturer have been concentrating their efforts to introduce more sophisticated cooling technologies that is essential for increasing the turbine inlet temperature of conventional gas turbines.

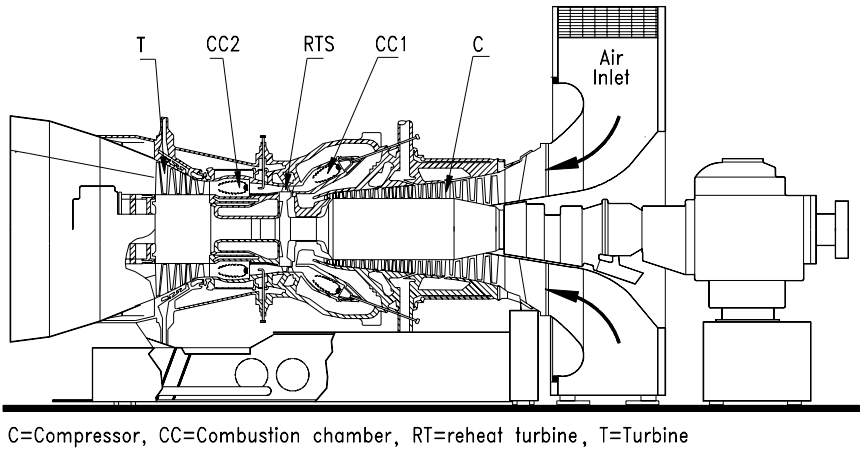

Fig. 18.9: A schematic cross section of GT-24 gas turbine engine with a single stage reheat turbine and a second combustion chamber

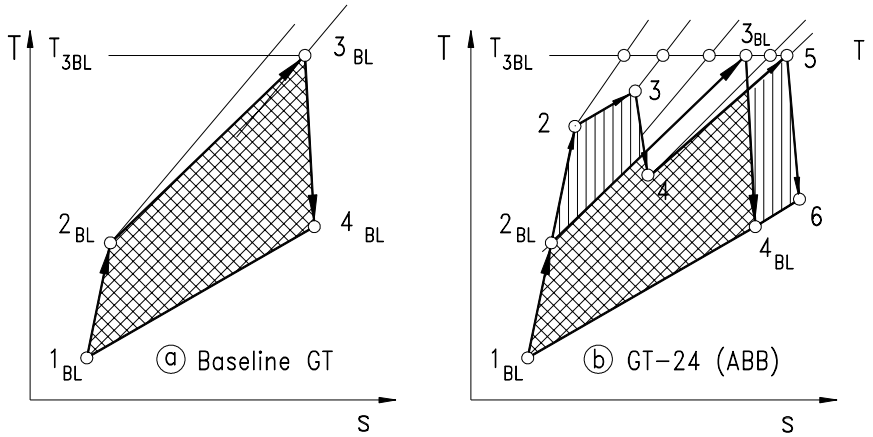

Fig. 18.10: Comparison of a conventional baseline gas turbine process (a) with the GT-24 process (b) from [1].

To substantially improve the thermal efficiency without a significant increase in turbine inlet temperature, a well known reheat principle as a classical method for thermal efficiency augmentation is applied. Although this standard efficiency improvement method is routinely applied in steam turbine power generation, it did not find its way into the aircraft and the power generation gas turbine design. The reason was the inherent problem of integrating a second combustion chamber into a conventionally designed gas turbine engine. This issue raised a number of unforeseeable design integrity and operational reliability concerns. ABB (formerly Brown Boveri & Cie) was the first to develop a gas turbine engine with one reheat stage turbine followed by a second combustion chamber and a multi-stage turbine, Fig. 18.9.

A comparative study by Schobeiri [1] emulates, among others, two conceptually different power generation gas turbine designs utilizing components, whose detailed aerodynamic performance characteristics were known. The first one is a conventional gas turbine, whereas the second one has a reheat turbine stage and a second combustion chamber resembling GT-24 [2]. Starting from a given environmental condition (pressure, temperature) and a consolidated turbine inlet temperature T_{3BL} = 1200 °C for both engines, Fig 18.10a, the thermal efficiency is determined by the compressor pressure ratio and the compressor and turbine polytropic efficiencies η_c, η_T and is plotted in Figure 18.11a.As curve 1 shows, for the given pressure ratio, which is not identical with the optimum pressure ratio, an efficiency of η_{th} = 35% is calculated. Substantial efficiency improvement is achieved by introducing a single-stage reheat principal as applied to GT-24. Details of the process are sketched in Fig. 18.10b with the baseline process as the reference process. The vertically cross-hatched area in Fig. 18.10b translates into the efficiency improvement, which in the case of GT-24 resulted in efficiency improvement of 5.5% above the baseline efficiency. A detailed dynamic engine simulation of the GT-24 gas turbine engine

with GETRAN© [3] verified a thermal efficiency of η_{th} = 40.5% plotted in Fig. 18.11a, curve 2. This tremendous efficiency improvement was achieved despite the facts that (a) the compressor pressure ratio is much higher than the optimal one for baseline engine and (b) the introduction of a second combustion chamber inherently causes additional total pressure losses. Further calculation showed that introducing a third combustion chamber would result only in a marginal improvement of 1 to 1.5% thermal efficiency, which does not justify the necessary R&D efforts to integrate a third combustion chamber. The specific work comparison is plotted in Fig. 18.11(b), which shows a significant increase in specific work .

Additional efficiency improvement requires a major technology change. As Schobeiri [2] showed, major improvement can be achieved by using the UHEGT-technology (ultra high efficiency gas turbine technology). This technology eliminates the combustion chambers altogether and places the combustion process inside the stator and rotor blade passages (see section 18.6).

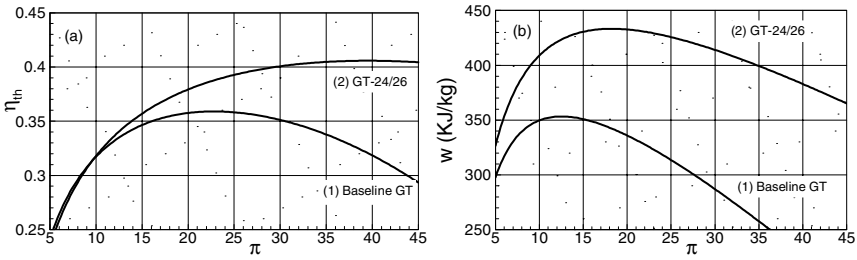

Fig. 18.11: Comparison of efficiency and specific work between a conventional baseline gas turbine and GT-24, (a) efficiency, (b) specific work.

18.2 Non-Linear Gas Turbine Dynamic Simulation

The continuous improvement of efficiency and performance of aircraft and power generation gas turbine systems during the past decades has led to engine designs that are subject to extreme load conditions. Despite the enormous progress in the development of materials, at the design point, the engine components operate near their aerodynamic, thermal, and mechanical stress limits. Under these circumstances, any adverse dynamic operation causes excessive aerodynamic, thermal, and subsequent mechanical stresses that may affect the engine safety and reliability, and, thus, the operability of the engine if adequate precautionary actions are not taken.

Considering these facts, an accurate prediction of the above stresses and their cause is critical at the early stages of design and development of the engine and its components. This section focuses on simulation of dynamic behavior of gas turbine engines and their components. The simulation spectrum encompasses single- and multi-spool gas turbine engines, turbofan engines, and power generation gas turbine engines. The simulation concept is based on a generic modularly structured system

configurations. In the last six chapters, the gas turbine components were represented by individual modules described mathematically by systems of differential equations. Based on these and other necessary modules, a generic concept is presented that provides the reader with necessary tools for developing computer codes for simulation of arbitrary engine and plant configurations ranging from single-spool thrust generation to multi-spool thrust/power generation engines under adverse dynamic operating conditions. It can easily be extended to rocket engines, combined cycles, co-generation cycles and steam power plants. A multi-level system simulation treats different degrees of complexity ranging from global adiabatic simulation to detailed diabatic one. The dynamic behavior of the subject engine is calculated by solving a number of systems of partial differential equations which describe the unsteady behavior of the individual components. Accurate prediction of the dynamic behavior of the engine and the identification of critical parameters by the method enables the engine designer to take appropriate steps using sophisticated control systems. The method may also be used to proof the design concept of the new generation of high performance engines. The modular structure of the concept enables the user to independently develop new components and integrate them into the simulation code. As representative examples, four different case studies are presented that deal with dynamic simulation of a compressed air energy storage gas turbine, different transient cases with single- and multi-spool thrust and power generation engines were simulated. The transient cases range from operating with a prescribed fuel schedule, to extreme load changes and generator shut down.

18.2.1 State of Dynamic Simulation, Background

Dynamic behavior of aircraft gas turbine engines was investigated earlier by several researchers using the component performance map representation for simulating engines. Seldner et al. [4] and Koenig and Fishbach [5] utilized overall component performance maps in their simulation program GENENG, which performs purely steady-state computations. In order to account for system dynamics, Seller and Daniele [6] extended the above code by introducing simplified dynamic equations. In a report about a hybrid simulation of single- and twin-spool turbofan engines, Szuch [7] described the representation of engine components by overall performance maps. To estimate gas turbine starting characteristics, Agrawal and Yunis [8] generated a set of steady component characteristics, where the turbine and compressor components are represented by overall steady performance maps. The engine representation by performance maps, as briefly addressed above and comprehensively discussed by Schobeiri [3], exhibits a useful tool for approximating engine behavior within the operation range defined by the component maps. However, the detailed information that is crucial for engine development and design cannot be provided at this simulation level. Furthermore, the above representation is not viable for providing the control system designer with the necessary input parameters, such as those describing the aero-thermodynamic and structural conditions of the compressor

and turbine blade rows. Consequently, the response of the real system to the intervention of the controller cannot be verified. These and other parameters are required inputs to the controller for triggering precautionary actions such as active surge control, achieved by adjusting variable compressor stator blades.

In order to address the above issues, Schobeiri [9], [10], [11], [12], [13], [14] developed the modularly structured computer code COTRAN for simulating the nonlinear dynamic behavior of single-shaft power generation gas turbine engines. To account for the heat exchange between the material and the working fluid during a transient event, diabatic processes are employed in COTRAN for combustion chamber and recuperator components. The dynamic expansion process through the turbine component is accomplished by a row-by-row calculation using the stage characteristics. COTRAN reflects real engine configurations and components, and is routinely used at the early stages of design and development of new gas turbine engines. Dynamic simulations of different single-shaft engines performed with COTRAN were reported by Schobeiri and Haselbacher [15]. Although COTRAN represents an advanced, nonlinear dynamic code, its simulation capability is limited to single-shaft power generation gas turbine engines and, thus, cannot be used for simulating multi-spool aircraft engines. Considering this circumstance, Schobeiri and his co-workers [3], [16], [17] developed a new computational method with the corresponding, generic, modularly structured computer code GETRAN for simulating the nonlinear dynamic behavior of single- and multi-spool high pressure core engines, turbofan engines, and power generation gas turbine engines. The code is capable of simulating aircraft engines having up to five spools with variable geometry, with or without additional power generation shafts.

18.3 Engine Components, Modular Concept, Module Identification

A schematic component arrangement and modeling of a twin-spool core engine is shown in Fig.18.12. The corresponding modules are implemented into the engine modular configuration schematic Fig.18.13. Figures 18.14 and 18.15 display the lists of components with their corresponding modular representations and symbols that are described by the method presented in Chapters 14 through 19. They exhibit the basic components essential for generically configuring any possible aero- and power generation gas turbine engines. These modules are connected with each other with a plenum, which is a coupling component between two or more successive components. As briefly explained in Chapters 14, the primary function of the plenum is to couple the dynamic information of entering and exiting components such as mass flow, total pressure, total temperature, fuel/air ratio, and water/air ratio. After entering the plenum a mixing process takes place, where the aforementioned quantities reach their equilibrium values. These values are the same for all outlet components .

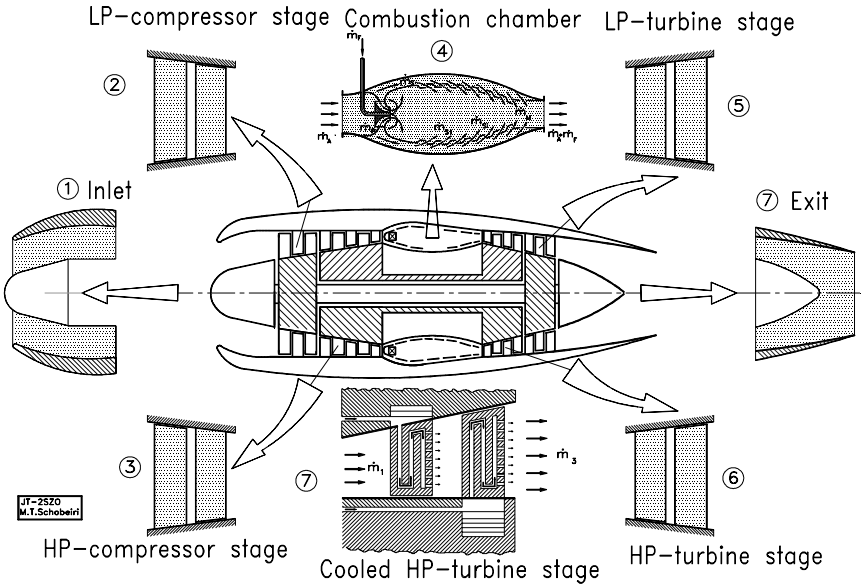

Fig. 18.12: Schematic of a twin spool core engine, component decomposition

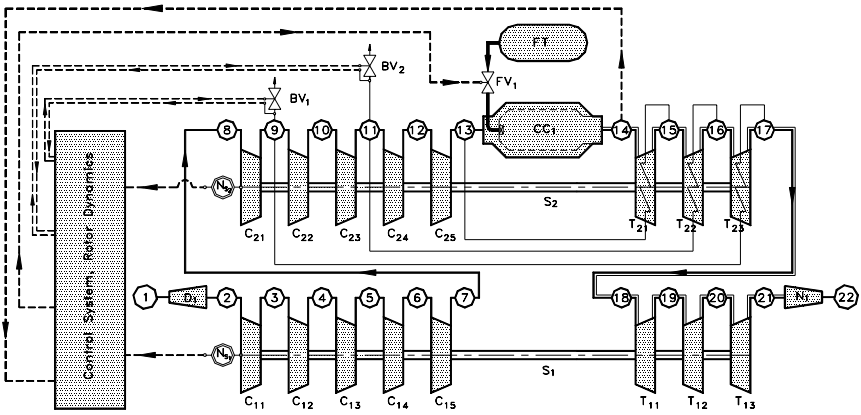

Fig. 18.13: Modular configuration of engine exhibited in Fig.18.12

A survey of power and thrust generation gas turbine engines has led to the practical conclusion that any arbitrary aircraft or power generation gas turbine engine and its derivatives, regardless of configuration, i.e., number of spools and components, can be generically simulated by arranging the components according to

the engine configuration of interest. The present nonlinear dynamic method is based on this generic, modularly structured concept that simulates the transient behavior of existing and new engines and their derivatives. The modules are identified by their names, shaft number, and inlet and outlet plena. This information is vital for automatically generating the system of differential equations representing individual modules. Modules are then combined into a complete system which corresponds to the engine configuration. Each module is physically described by the conservation laws of thermo-fluid mechanics which result in a system of nonlinear, partial differential or algebraic equations. Since an engine consists of a number of components, its modular arrangement leads to a system containing a number of sets of equations. The above concept can be systematically applied to any aircraft or power generation gas turbine engine.

The general application of the modular concept is illustrated in Figs. 18.12 and 18.13. The twin-spool engine shown in Fig. 18.12 exemplifies the modular extension of the single-spool base engine. It consists of two spools with the shaft S_1 and S_2, on which the low and high pressure components such as compressors and turbines are assembled. The two shafts are coupled by the working media air and combustion gas. They rotate with different speeds which are transferred to the control system by the sensors N_{s1} and N_{s2}. Air enters the inlet diffuser D_1, which is connected with the multi-stage compressor assembled on S_1, and is decomposed in several compressor stages C_{1i}. The first index, 1, refers to the spool number and the second index, i, marks the number of the compressor stage. After compression in the S_1 compressor stage group, the air enters the second compressor (HP- compressor) assembled on the S_2 shaft that consists of stages C_{21}-C_{25}. In the combustion chamber (CC_1) high temperature combustion gas is produced by adding the fuel from the tank FT. The gas expands in the high pressure turbine that consists of stages T_{21} - T_{23}. By exiting from the last stage of HP-turbine, the combustion gas enters the low pressure turbine consisting of stages T_{11} - T_{13} and is expanded through the exit nozzle. Two bypass valves, BV_1 and BV_2, are connected with the compressor stator blades for surge prevention. The fuel valve, FV_1, is placed between the fuel tank, FT, and the combustion chamber, CC_1. The pipes, P_i, serve for cooling air transport from the compressor to cooled turbines. The compressor stage pressures, the turbine inlet temperature, and the rotor speed are the input signals to the control system, which controls the valve cross sections and the fuel mass flow.

Gas turbine Generic Components, Modules, and Symbols

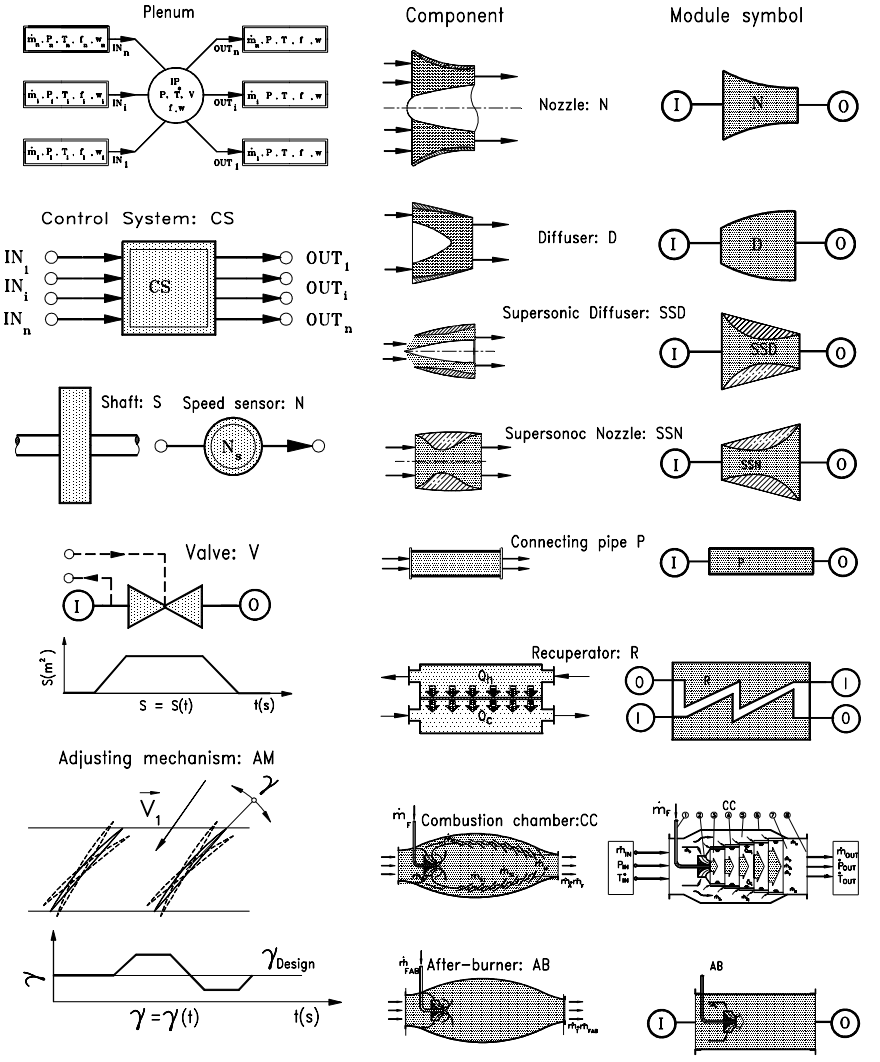

Fig. 18.14: Components, modules, and their symbols: Plenum, Control system CS, Shaft S, with moment of inertia I and the rotational velocity ω, Speed sensor N, Valve with an arbitrary ramp for closing and opening the cross section S, Adjusting mechanism AM for stator blade adjustment, Subsonic nozzle N, Subsonic diffuser D, Supersonic Diffuser SSD, Supersonic nozzle SSN, Recuperator R, Combustion Chamber CC, and Afterburner AB.

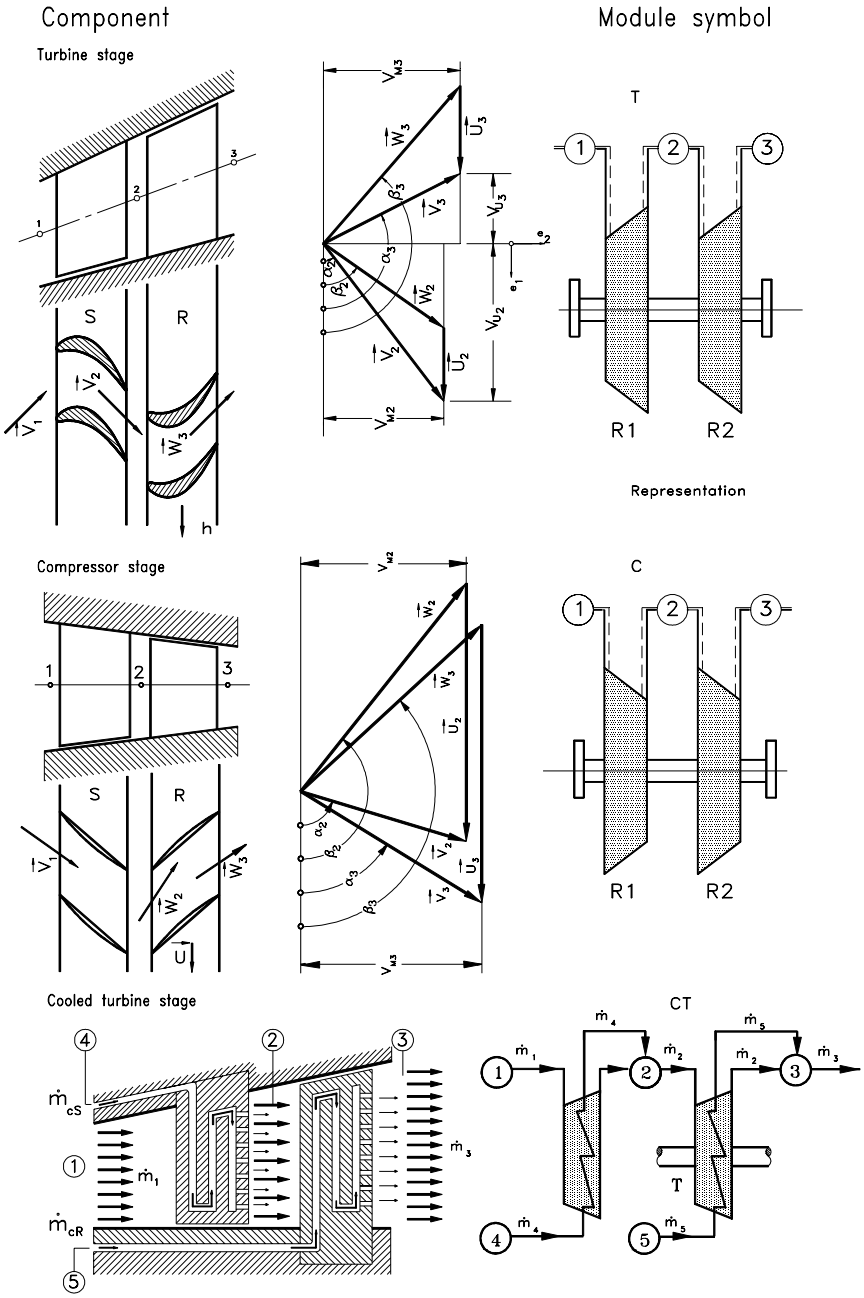

Fig. 18.15: Adiabatic turbine stage with the module T, Adiabatic compressor stage with the module C, Cooled turbine stage with the module CT.

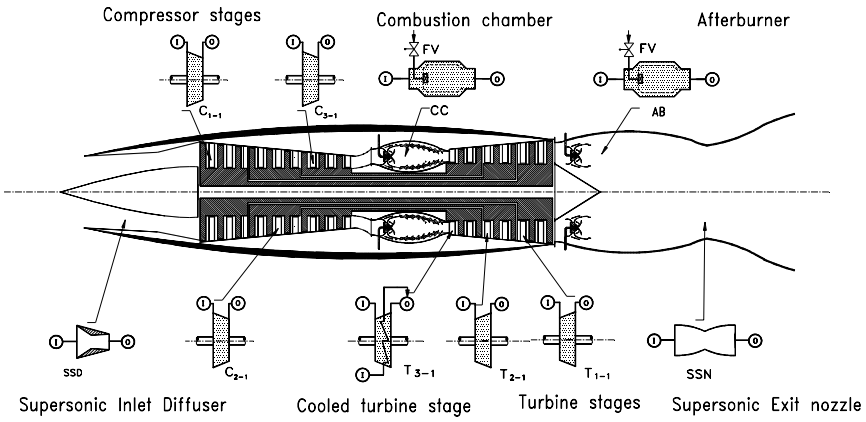

Fig. 18.16: Schematic of a 3-spool high performance core engine, component decomposition.

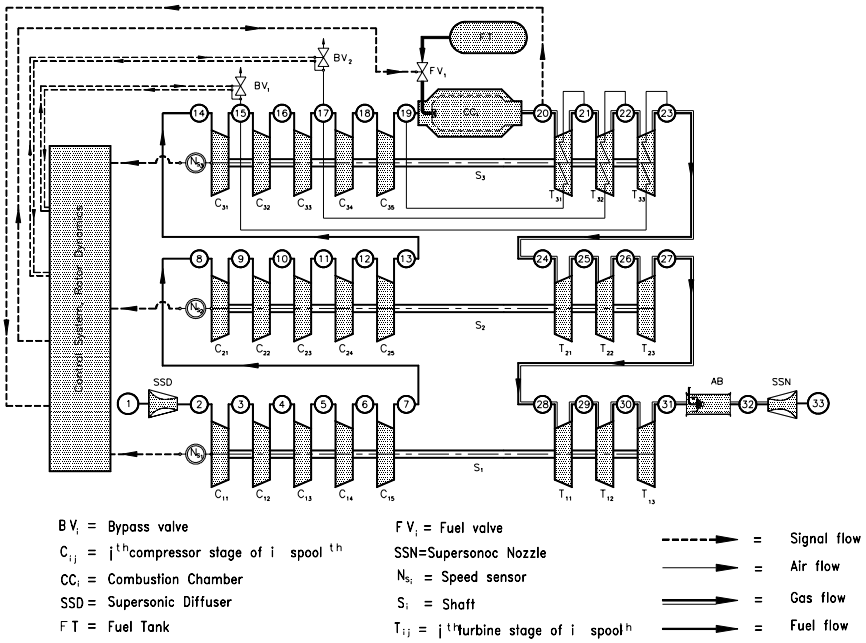

Fig. 18.17: Modular configuration of the 3-spool engine shown in Fig. 18.15. The three compressors and turbines are connected aerodynamically. The plena addressing, the spool number, and the component number uniquely identify the set of differential equations that describe the module.

Figure 18.16 shows a more complex example of a three-spool supersonic engine with its modular decomposition. Figure 18.17 exhibits a systematic modular configuration of Fig. 18.16 that is represented by a large system of differential and algebraic equations.

18.4 Levels of Gas Turbine Engine Simulations, Cross Coupling

Accuracy of gas turbine dynamic simulation is determined by the level of component modeling. It increases by increasing the level of simulation complexity. Four levels of simulation are introduced:

Zeroth simulation level: Is applied to simple cases such as those in [4] through [7], utilizing a fixed system configuration with steady state component characteristics that are described by algebraic equations, simplified differential equations, and lookup tables and maps. Furthermore, there is no dynamic coupling between the components. Since this simulation level does not account for engine dynamics, it will not be discussed further.

First simulation level: This level uses component global performance map only for turbines and compressors. The maps are generated using the row-by-row adiabatic calculation method detailed in Chapters 18 and 19. The other components such as recuperators, coolers, combustion chambers, pipes, nozzles, and diffusers are simulated according to methods discussed in Chapters 14 through 17. Primary air, secondary combustion gas, and metal temperature of the combustion chamber are calculated. All modules are coupled with plena insuring a dynamic information transfer to all modules involved. Modules are described by algebraic and differential equations.

Second simulation level: This level utilizes adiabatic row-by-row or stage-by-stage calculation for compressor and turbine modules. For combustion chamber, primary air, secondary combustion gas, and metal temperature are calculated. Dynamic calculations are performed throughout the simulation, where the modules are coupled by plena. Each module is described by differential and algebraic equations.

Third simulation level: This level uses diabatic row-by-row calculation for compressor and turbine modules. This level delivers a very detailed diabatic information about the compressor and turbine component dynamic behavior. It utilizes cooled turbine and compressor stages and simultaneously calculates the blade temperatures. For combustion chamber, primary air, secondary combustion gas, and metal temperature are calculated. Dynamic calculations are performed throughout the simulation, whereas the modules are coupled by plena. Each module is described by differential and algebraic equations. The details of information delivered by this level and degree of complexity is demonstrated by the following example. The first two stages of a four-stage turbine component of high performance gas turbine engine must

be cooled. For the first four turbine rows we use the diabatic expansion process that requires three differential equations for describing the primary flow, three differential equations for describing the cooling flow, and one differential equation for describing the blade temperature. This leads from two cooled turbine stages to 28 differential equations.

The generic structure allows to cross-couple level 1 to 3. For example, we wish to simulate a gas turbine engine with a global compressor performance map, but need to obtain detailed information about turbine blade temperature, which is necessary to calculate the relative expansion between the blades and the casing, then we may use the diabatic calculation method. In this case, we cross-couple the first and third level simulation.

18.5 Non-Linear Dynamic Simulation Case Studies

Three different case studies dealing with three completely different gas turbine systems are presented. Table 18.1 shows the matrix of the cases where the engine types and transient-type simulations are listed. These studies demonstrate the capability of the generic structured method we discussed in Chapters 15 through 18 to dynamically simulate complex systems with high accuracy.

Table 18.1: Simulation Cade Studies

TESTS	GAS TURBINE TYPE	TRANSIENT TYPE
CASE 1	CAES: Compressed air energy storage power generation gas turbine engine, zero-spool, single shaft, two turbines, two combustion chambers	Engine cold startup, generator and turbine shut down.
CASE 2	Single-spool, single-shaft, power generation gas turbine engine, BBC-GT9.	Adverse load changes.
CASE 3	Three-Spool, four-shaft, thrust and power generation core engine	Operation with fuel schedule.

The case studies presented in this chapter are related to the real world engine simulation and are intended to provide the reader with an insight into the non-linear engine dynamic simulation. The selected cases ranging from zero-spool, single shaft power generation to three-spool four shaft thrust and power generation gas turbine engines provide detailed information about the engine behavior during design and off-

design dynamic operation. For each engine configuration the simulation provides aero-thermodynamic details of each individual component and its interaction with the other system components. Since the presentation of the complete simulation results of the three cases listed in Table 1 would exceed the frame of this chapter, only a few selected plots will be displayed and discussed for each case.

18.5.1 Case Study 1: Compressed Air Energy Storage Gas Turbine

The subject of this case study is a zero-spool, single-shaft compressed air energy storage (CAES) gas turbine[18], which is utilized to efficiently cover the peak electric energy demand during the day. Continuous increase of fuel costs has motivated the power generation industry to invest in technologies that result in fuel saving. Successful introduction of combined cycle gas turbines (CCGT) has drastically improved the thermal efficiency of steam power plants that is equivalent to a significant fuel saving. Further saving is achieved by using the excess electrical energy available during the period of low electric energy demand (6-8 hours during the night) to compress air into a large storage. During the peak demand, the compressed air is injected into the combustion chambers and is mixed with the fuel. After the ignition process is completed, the high pressure, high temperature gas expands in the turbine generating electric energy for about 2 to 4 hours. In contrast to a CCGT, the period of operation of a CAES plant is restricted to a few hours per day resulting in a daily startup followed by a shutdown procedure. This relatively high frequency of startups and shutdowns may cause structural damages resulting in reduced life time if the startup and shutdown procedures are not performed properly. The condition for a safe startup procedure is outlined in this study that helps the engine and control system designer to integrate into their design procedure. The CAES gas turbine system, Fig. 18.18, with the simulation schematic shown in Fig. 18.19 features a large volume plenum (8) for storing the compressed air, a high-pressure combustion chamber (HPCC), a high-pressure turbine (HPT), a low-pressure combustion chamber (LPCC), a low-pressure turbine (LPT2), a cold-air pre-heater with a low pressure and high pressure side (LPP and HPP-side) and a generator (G). During the steady-state turbine operation, cold air from the air-storage facility, plenum 8, passes through the shutdown valve (V_1) to the inlet plenum (1), where it is divided into combustion and cooling-air flows. The addition of fuel in HPCC causes the combustion air to be heated up to the combustion chamber's exit temperature. Immediately upstream of HPT, the combustor mass flow mixed with a portion of the cooling-air flow, which has already been preheated in HPP. As a result, the gas temperature of the turbine mass flow lies below the combustion chamber's exit temperature. After expansion in HPT, the combustion chamber (LPCC) mass flow is mixed in LPT inlet plenum (4) with the rest of the preheated cooling-air flow and the sealing-air flow. After expansion in LPT, the gas gives off some of its heat in LPP before leaving the gas turbine system.

Figure 18.19 shows how the various components are interconnected. Plenum 8, the air storage facility, is connected via two identical pipes (P6) to two shutdown valves (V_1). During steady-state operation, the blow-off valve (V_2) remains closed,

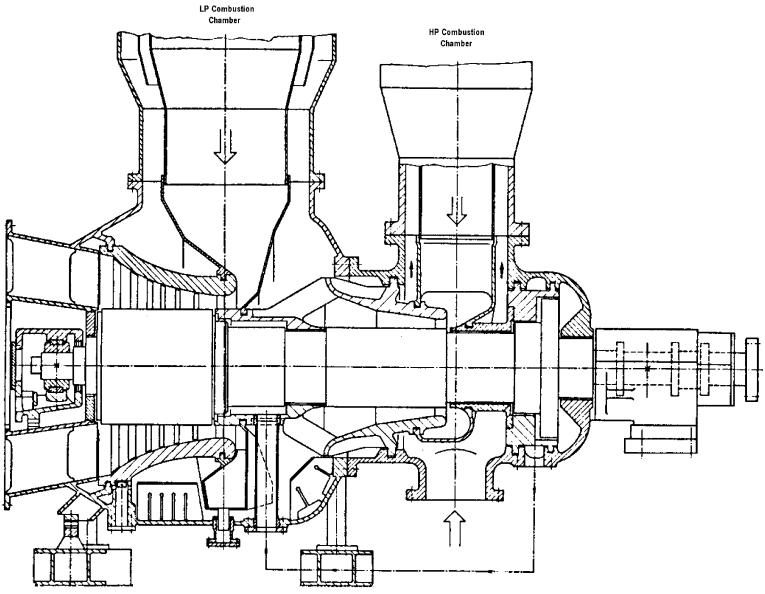

Fig. 18.18: BBC- CAES-Huntorf gas turbine engine [18]

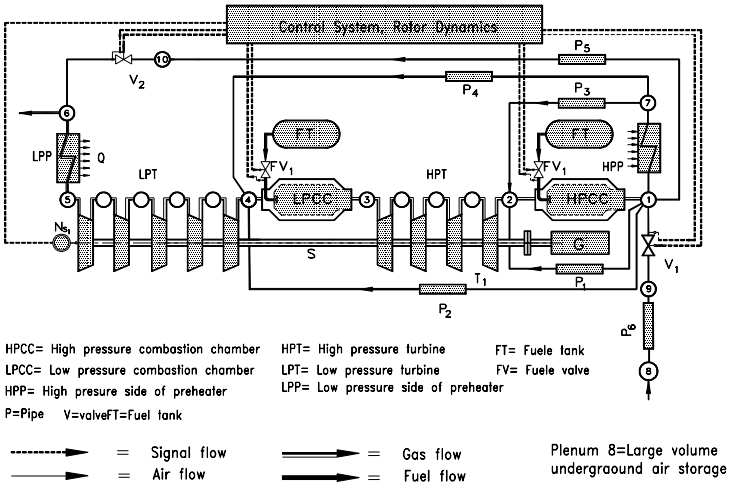

Fig. 18.19: Simulation schematic of the CAES shown in Fig. 18.19.

being opened in the event of a disturbance likely to cause rapid shutdown. In such an event, the valve blows off some of the gas, thereby limiting the maximum rotor speed. For the sake of clarity, the pre-heater (P) has been separated into its air and gas sides, designated HPP and LPP, respectively.

18.5.1.1 Simulation of emergency shutdown: Starting from a steady operating point, a generator trip with rapid shutdown was simulated assuming a failure of the control system. This circumstance necessitates an intervention by the hydraulic emergency system. This incident simulates an extreme transient process within some of the components, as explained briefly. After the generator trip, the rotor is strongly accelerated because of full turbine power acting on it, Fig. 18.20(a).

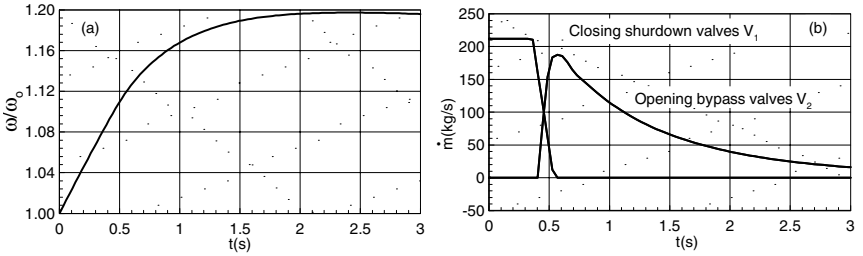

Fig. 18.20: Relative angular velocity (a) and mass flows (b) as function of time. The Inlet-shutdown valves V_1 remain open until the trip speed at t= 0.35 s has been reached. The same procedure is true for opening the blow-off valves V_2. Closing the shutdown valves follow the ramp shown in Fig. 18.20(b).

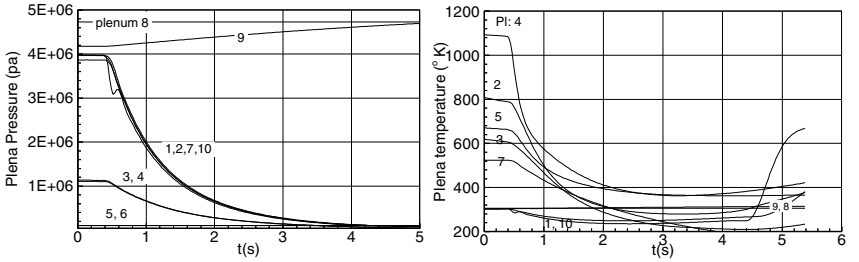

Fig. 18.21:Plena pressure and temperature as functions of time. Shutdown process causes rapid depressurization in high pressure plena1, 2, 7, and 10.

The hydraulic emergency system intervenes only when the speed corresponding to the hydraulic emergency overspeed trip is reached. This intervention involves closing the fuel valves, FV_1 and FV_2, and air valves, V_1, after which the system no longer receives any energy from outside, Fig. 18.20(b). It also involves opening the bypass/blow-off valve V_2 that allows the high pressure air contained in both large volume combustion chambers as well as in the HP-side of pre-heater to discharge. The closing process of the inlet and shutdown valves and the opening of the bypass

valves are shown in Fig. 18.20(b). This process results in a steady drop in plena pressures and temperatures. As Fig. 18.21 shows, the pressure drop in the high-pressure section is initially steeper than in the low-pressure section. This means that the enthalpy difference of the high-pressure turbine is reduced more rapidly than that of the low-pressure turbine. Immediately after the blow-off valve is opened, an abrupt pressure drop takes place in plenum 10, which is connected to plenum 1 via pipe P5. Thereafter, dynamic pressure equalization takes place between the two plena. This drop in pressure and temperature causes a corresponding drop in the shaft power and the mass flow throughout the engine.

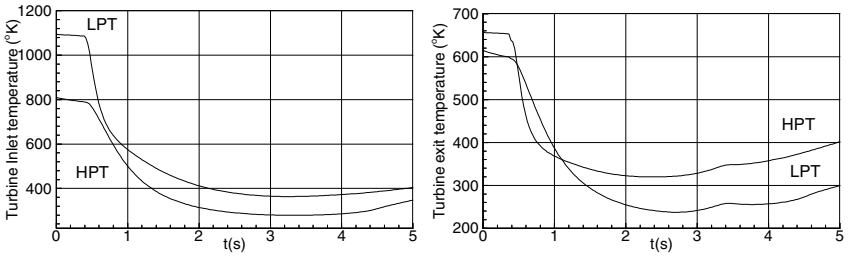

Fig. 18.22: Turbine inlet and exit temperature as functions of time. Note changes of the exit temperature at t=3.4 s

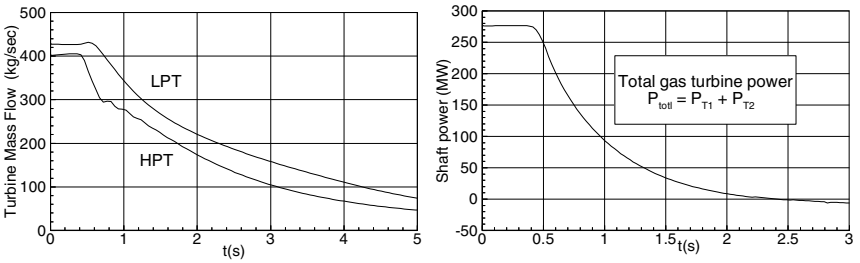

Fig. 18.23: Turbine mass flow and shaft power as function of time

Figure 18.22 shows the resulting drop in turbine inlet and exit temperature. The continuous decrease in turbine mass flow causes a strong dissipation of shaft power resulting in the excessive increase of turbine exit temperature. In order to avoid thermal damages to blades, a small stream of cold air is injected into the turbine flow path that causes a reduction in temperature gradient. This is shown in Fig. 18.22 for the exit temperature at t = 3.4 s.

Dynamic behavior of the rotor speed is generally determined by the turbine power acting on the rotor. How the rotor behaves in response to a generator trip depends, in particular, on how long the full turbine power is available, a process monitored by the control and safety monitoring system. When the control system functions normally, trip is signaled without delay to the shutdown valve. Failure of

the control system causes the hydraulic emergency system to intervene. The intervention begins only when the speed corresponding to the hydraulic emergency overspeed trip is reached. During this process, and also the subsequent valve dead time, the rotor receives the full turbine power. The closing phase is characterized by a steady reduction in energy input from outside, which finally becomes zero. The total energy of the gases still contained in the system is converted by the two turbines into mechanical energy, causing the rotor speed to increase steadily, Fig. 18.20. When the instantaneous turbine power is just capable of balancing the friction and ventilation losses, the rotor speed reaches its maximum, after which it begins to decrease. Reducing the turbine mass flow, Fig. 18.23 (left), below the minimum value discussed in Chapter 19, causes the shaft power to dissipate completely as heat resulting in negative values as Fig. 18.23 (right) shows. From this point on, the rotational speed starts to decrease. The figure depicts the mass flow through both turbines as representatives for the entire engine as well as the total shaft power.

18.5.1.2 Simulation of a cold startup: Since the CAES-gas turbines undergo frequent startups, shutdowns, and load changes, special attention must be paid to cold start procedure. An appropriate cold start procedure reduces the risks of development of excessive transient thermal stresses in various components that reduce the life time of the components and the system. A possible cold-startup simulation is presented below.

Simulation of Ignition Process: Starting from a cold engine structure, an air storage temperature of $T_8 = 300\ ^{o}$ K, and an initial non-zero rotor speed, the air inlet valves are slowly opened that after two seconds reach a mass flow of approximately 30% of the design point mass flow, Fig. 18.24. This mass flow is kept constant for about 20 seconds, followed by an opening ramp that reaches the design point mass flow after 60 seconds. From this point on, the inlet valve cross section remains fully

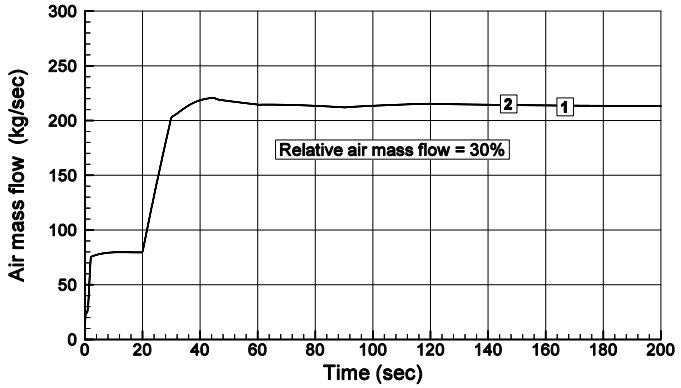

Fig. 18.24: Air mass flow through two identical inlet valves

open resulting in a constant mass flow. Fuel injection into the high pressure combustion chamber HPCC and its ignition starts at t = 30 s and is completed by t = 90 s following the ramp shown in Fig. 18.25. Fuel injection and the ignition of the LPCC occurred with a time lag of 60 seconds, relative to the HPCC ignition. After completing the ignition process at t = 90 s, the LPCC fuel valve starts opening and completes the opening process at t = 150 sec.

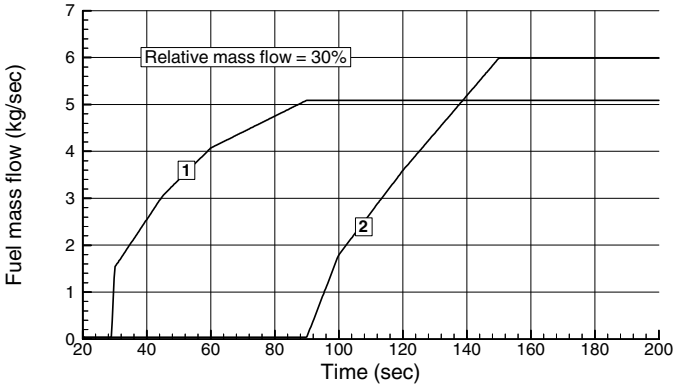

Fig. 18.25: Fuel mass flow schedule through valves FV_1 and FV_2

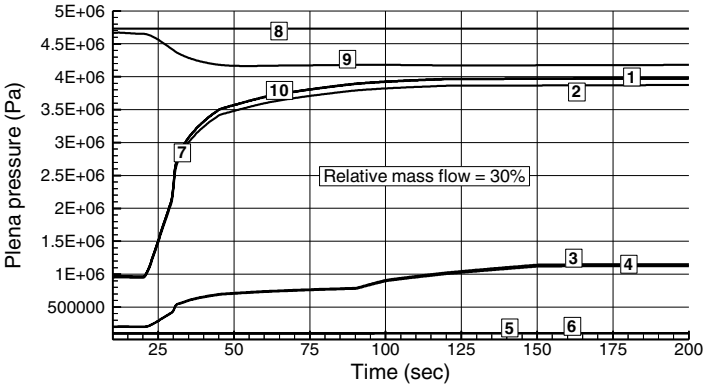

Fig. 18.26: Plena pressure as function of time

Plena Pressure, Temperature: Plena pressures and temperatures are exhibited in Figs. 21.26 and 21.27. Low temperatures are encountered in plena 3, 4, and 5 only during the first 30 seconds prior to igniting the HPCC. After the ignition of HPCC,

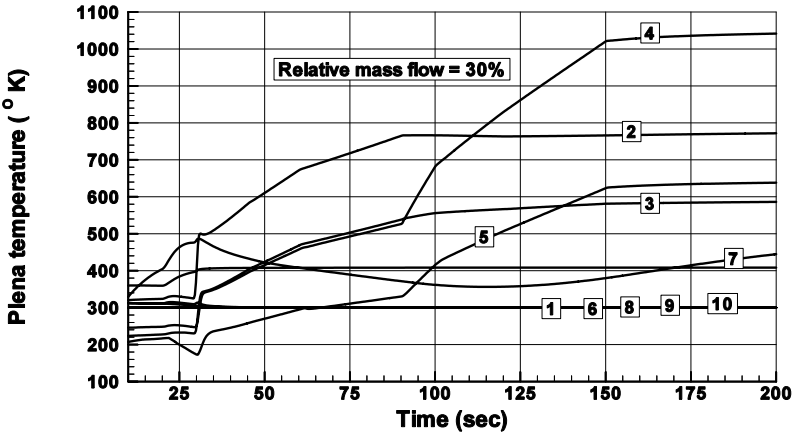

Fig. 18.27: Plena temperature as a function of time.

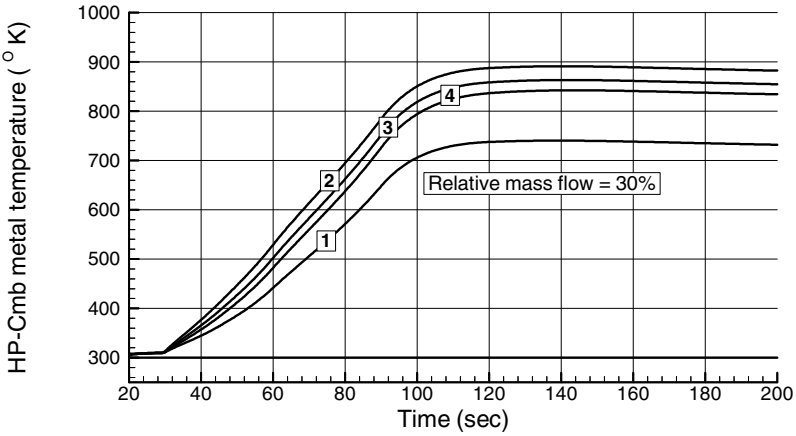

Fig. 18.28: HP-combustion chamber metal temperature as a function of time

the temperature level increases in all plena and finally after 150 seconds of operation pressure and temperature equilibrium is found in all plena.

Combustion Chamber Metal Temperature: The combustion chamber metal temperatures are shown in Fig. 18.28 and 18.29. The segments enclosing the primary combustion zone are numbered in flow direction from 1 to 4.

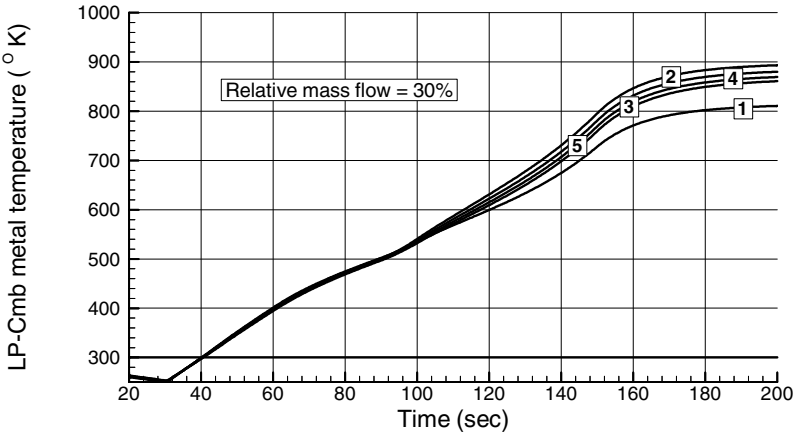

Fig. 18.29:LP-combustion chamber metal temperature as a function of time

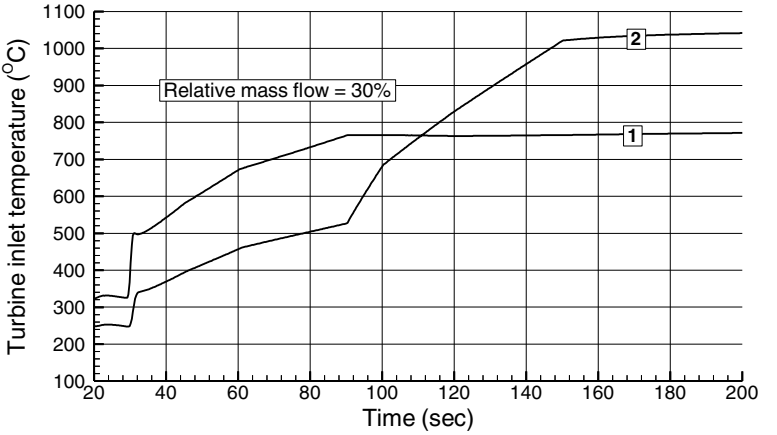

Fig. 18.30:HP- and LP- turbine inlet temperature 1, and 2 as a function of time

All segments of the HPCC have the start temperature of T = 300 °K that corresponds to the air storage temperature. After t = 30 seconds fuel is added causing the combustion gas temperature to rise. Heat is transferred from gas to combustion chamber structure causing the segments temperature to continuously increase to their equilibrium level. The combustion process and heat transfer was described in details in Chapter 15. Similar behavior is found for LPCC.

Turbine Inlet and Exit Temperatures: The inlet temperature transients for HP- and LP-turbines reflect the fuel flow schedule indicating a moderate temperature gradient for both turbines. Igniting the HP-combustion chamber increases the HP-turbine inlet temperature as shown in Fig. 18.30. Hot gas expands in the HP-turbine, where its total energy is partially converted into shaft work. During the first 90 seconds the low pressure combustion chamber LPCC has no fuel injection which is reflected in LP-turbine inlet temperature, curve 2. Sudden change in temperature gradient in Fig. 18.30 occurs at t = 90 seconds, where fuel is injected into in LPCC

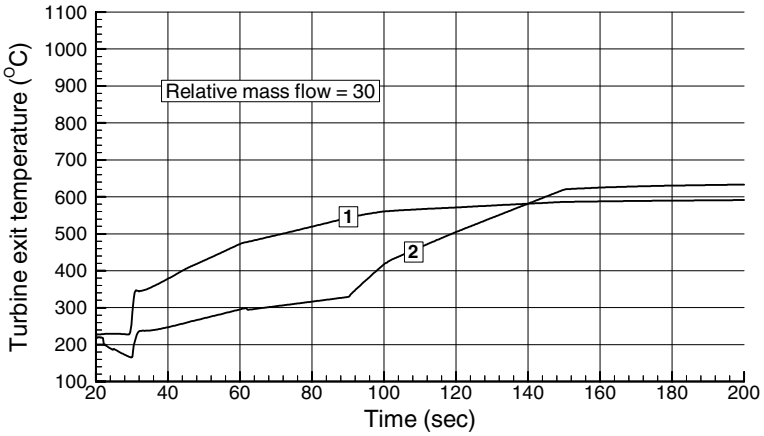

Fig. 18.31: Turbine exit temperature as a function of time

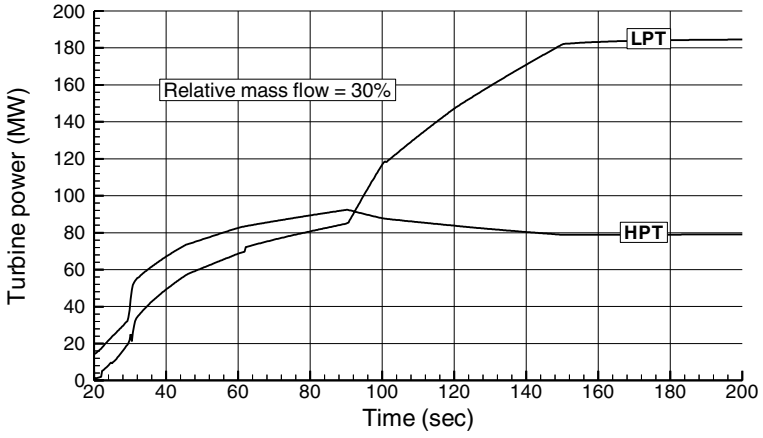

Fig. 18.32: HP- and LP-turbine power functions of time

according to the schedule in Fig. 18.25. The LP-turbine inlet temperature increases and reaches an equilibrium at t = 150 seconds. The turbine exit temperature, Fig. 18.31, shows similar tendencies.

Turbine Power and Rotational Speed Opening the inlet shutdown valves introduces external energy to the system causing HP-turbine to produce power which accelerates the shaft rotational speed before fuel is injected, Fig. 18.32. After reaching the synchronous frequency, the generator is electrically coupled with the grid. From this point on, the gas turbine frequency is rigidly locked as shown in Fig. 18.33.

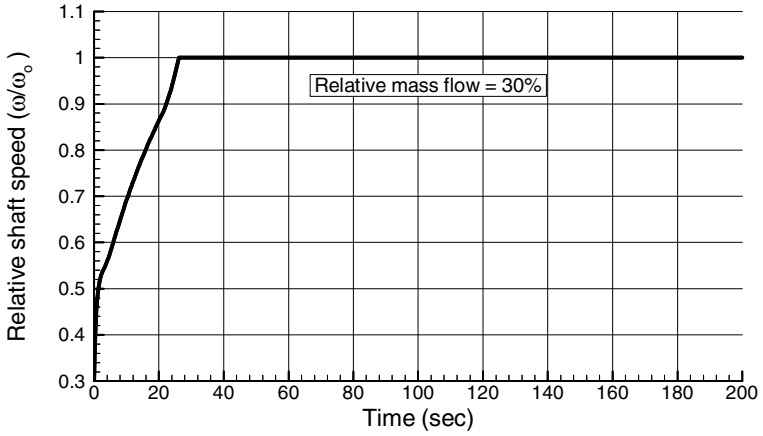

Fig. 18.33: Relative shaft speed as a function of time

18.5.2 Case Study 2: Power Generation Gas Turbine Engine

The subject of this case study is the dynamic simulation of a BBC-GT9 gas turbine which is a single-spool single shaft power generation gas turbine engine. It is utilized as a stand-alone power generator or in conjunction with combined cycle power generation. The engine shown in Fig. 18.34 consists mainly of three compressor stage groups, a combustion chamber, a turbine, a control system, and a generator. The simulation schematic of this engine is presented in Fig. 18.35. The rotor speed and turbine inlet temperature are the input parameters for the controller, its output parameters are the fuel mass flow (fuel valve opening), and the mass flows of the bypass valves (bypass valve opening). The dynamic behavior of BBC-GT9 was experimentally determined for transient tests with extreme changes in its load. Its transient data was accurately documented by Schobeiri [3]. Starting from a given network load schedule, the dynamic behavior of the gas turbine is predicted and the results are presented.

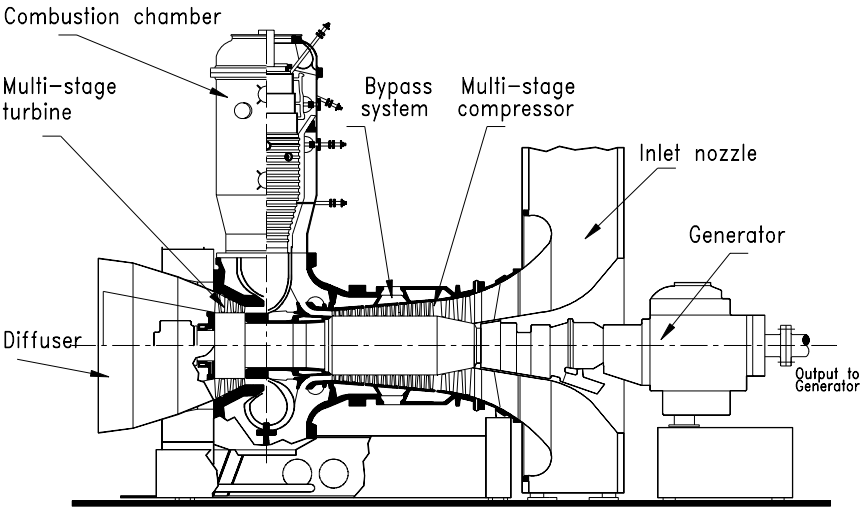

Fig. 18.34: A single spool power generation gas turbine, BBC-GT9

The engine under consideration consists mainly of three compressor stage groups, a combustion chamber, a turbine, a control system, and a generator. The simulation schematic of this engine is similar to that of Fig. 18.36. For dynamic simulation, the first, second and third stage groups are simulated in row-by-row fashion. A similar row-by-row calculation procedure is applied to the turbine component. The rotor speed and the turbine inlet temperature are the input parameters for the controller, its output parameters are the fuel mass flow (fuel valve opening), and the mass flows of the bypass valves (bypass valve opening).

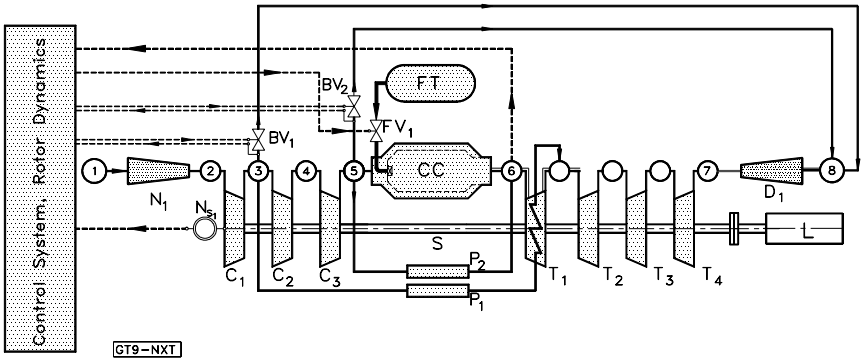

Fig. 18.35: Simulation schematic of BBC-GT9 shown in Fig. 18.34.

Simulation of an adverse dynamic operation: Starting from steady state, in accordance with the load schedule indicated in Fig. 18.36 (left), curve 1, after one second, a generator loss of load is simulated that lasts for six seconds. The rotor at first reacts with a corresponding increase in rotational speed, Fig. 18.36 (right), which results in a rapid closing of the fuel valve, Fig. 18.40 (right). The rotational speed is then brought to an idling point and held approximately constant. The process of control intervention lasts until a constant idling speed is attained. After that, there is an addition of load in sudden increases, such that the gas turbine is supplying approximately 25% of its rated load, Fig. 18.36. The rotor first reacts to this addition of load with a sharp decrease in rotational speed, as exhibited in Fig. 18.36, causing a quick opening of the fuel valve, Fig. 18.40. After completion of the transient process, the steady off-design state is reached.

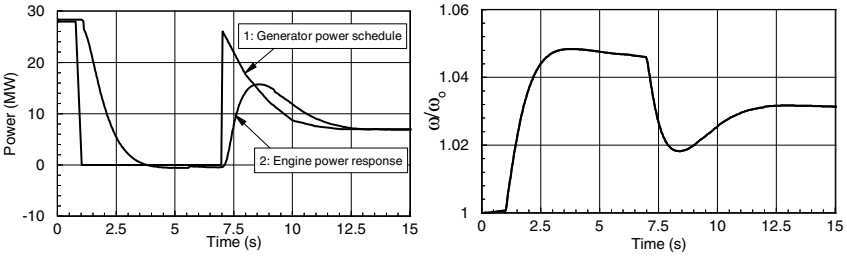

Fig. 18.36: Left, generator load schedule curve 1, sequence of events: Steady operation from 0 to 1 second, sudden loss of load, idle operation, sudden addition of load, continuous decrease of load to 25%. Curve 2: engine power response. Right, relative shaft speed as a function of time.

Plena Pressure and Temperature Transients: The above adverse dynamic operation has triggered temporal changes of flow quantities within individual components. Figure 18.37 shows how the plena pressure and temperature change with time.

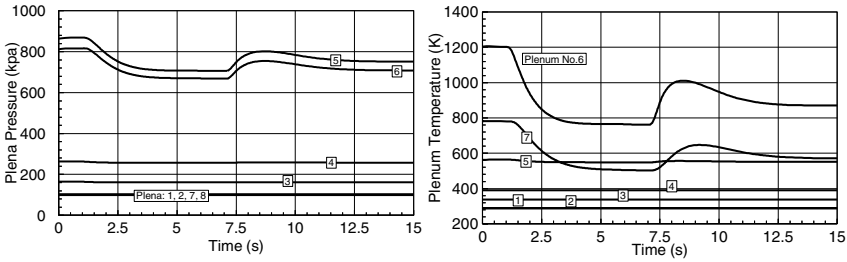

Fig. 18.37: Plena pressure and temperature as functions of time. Individual plena are labeled

Decrease of turbine power and increase of the shaft speed, Fig. 18.36, has caused the HP-compressor exit pressure in plenum 5 to decrease. Temperature at combustion chamber exit, plenum 6, and turbine exit, plenum 7, follow the course of fuel injection shown in Fig. 18.40(right). The plena temperature upstream of the combustion chamber are not affected.

Compressor and combustion chamber Mass Flow Transients: Figure 18.38 exhibits the mass flow transients through LP-, IP-, and HP-compressors. While IP- and HP-stage groups have the same mass flow, the LP-part has a greater mass flow. The difference of 1 kg/s is due to the cooling mass flow extraction. As briefly mentioned, the increase in shaft speed and the simultaneous decrease in compressor power consumption leading to compressor pressure drop has caused an increase in

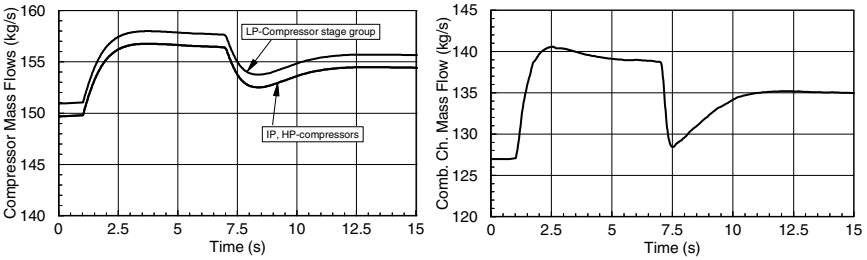

Fig. 18.38: Compressor and combustion chamber mass flows as functions of time.

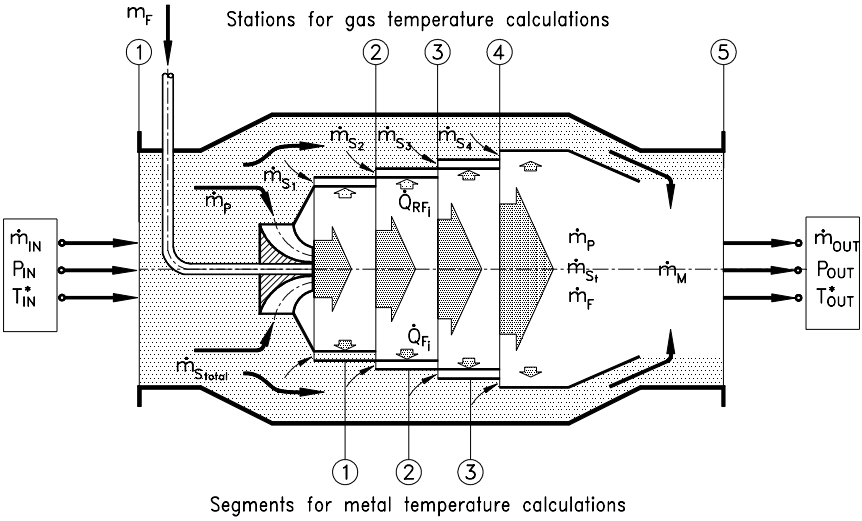

Fig. 18.39:Combustion chamber module, stations and segments, $\dot{m}_P$ = primary air, $\dot{m}_{Stot}$= total secondary air, $\dot{m}_{Si}$= individual secondary air.

compressor mass flow during the process of loss of load that lasts up to t = 6 sec. The sudden load addition reduces the compressor mass flow. The combustion chamber mass flow shows a similar course with a substantial difference. A substantial portion of compressor mass flow is extracted for combustion chamber exit temperature mixing cooling.

Combustion Chamber Gas and Metal Temperature Transients: The combustion chamber component used in this simulation has three segments that separate the primary combustion zone from the secondary cooling air zone. Its module is shown in Fig. 18.39. Figure 18.40 exhibits the combustion chamber gas and metal temperatures as functions of time. Compressed air enters the combustion chamber at station 1, Figs. 18. 39, and 18.40. Fuel is added and the segment cooling occurs according to the procedure described in Chapter 17. The secondary mass flow portions $\dot{m}_{Si}$serve as cooling jets and are mixed with the combustion gas, thus reducing the gas temperature. Before exiting, the combustion gas is mixed with the mixing air stream $\dot{m}_M$, further reducing the temperature. Figure 18.40 (right) shows the mean segment temperatures. In accordance with the measurements on this gas turbine, the flame length extends from station 1 to 3, which makes the segment number 2 the hottest one. We assumed that all secondary cooling channels are open.

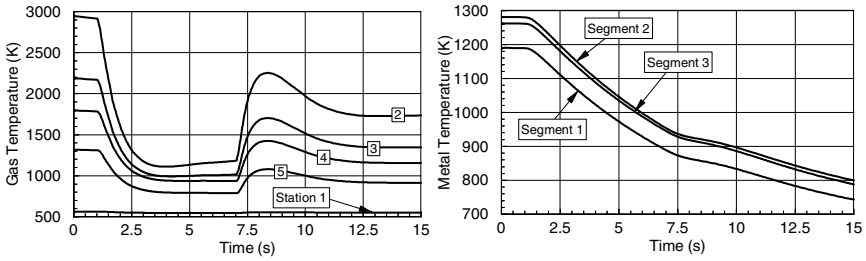

Fig. 18.40: Combustion chamber gas and metal temperature at different positions as functions of time.

Turbine and Fuel Mass Flow Transients: Figure 18.41 (left) exhibits the turbine mass flow transient, which is dictated by the compressor dynamic operation. Difference between the turbine and the compressor mass flow is the injected fuel mass flow. The particular course of fuel mass flow shown in Fig. 18.41 (right) is due to the intervention of the control system. An increase in rotational speed causes the controller to close the fuel valve. Subsequent addition of generator load results in a steep drop of rotational speed which causes an opening of the fuel valve.

18.5.3 Case Study 3: Simulation of a Multi-Spool Gas Turbine Engine

The subject of this study is the non-linear dynamic simulation of a gas turbine engine with a higher degree of complexity than the previous cases. For this purpose a three-spool thrust generating gas turbine engine is designed that incorporates advanced components. The three-spool four shaft high performance gas turbine engine consists of a low pressure spool that incorporates the LP-compressor and turbine connected via shaft S_1. The intermediate pressure spool integrates the IP-compressor and turbine connected via shaft S_2. The high pressure spool carries the HP-compressor and HP-turbine on shaft S_3. To increase the level of engine complexity, a fourth shaft, S_4, with

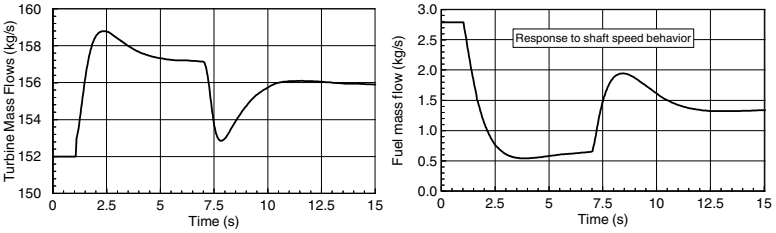

Fig. 18.41: Turbine and fuel mass flow as functions of time. The fuel mass flow is controlled by the shaft rotational speed.

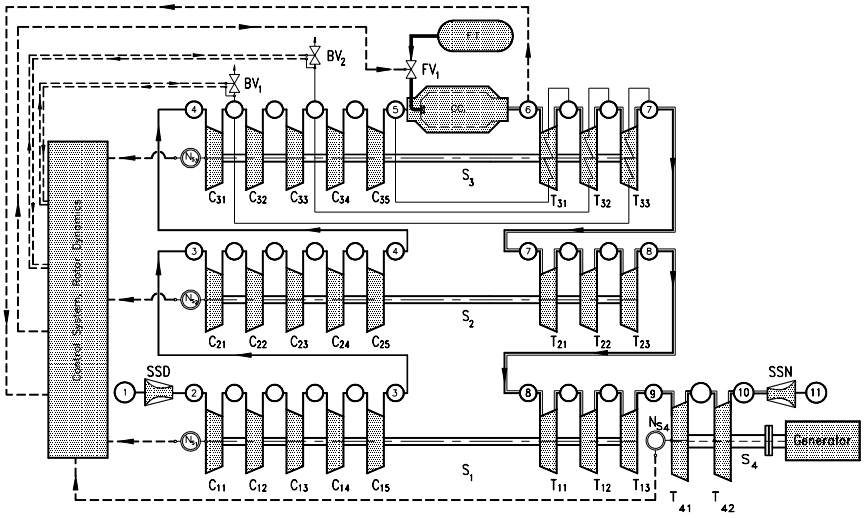

Fig. 18.42:Simulation schematic of three-spool four shaft high performance gas turbine engine. Spool 1 incorporates LP-compressor and LP-turbine connected via shaft S_1; Spool 2 incorporates IP-compressor and IP-turbine connected via shaft S_2; Spool 3 incorporates HP-compressor and HP-turbine connected via shaft S_3.

the power generating turbine, T_4, was attached to the exit of the three-spool gas generating unit as shown in Fig. 18.42. The transient operation is controlled by a given fuel schedule. The component nomenclature for this configuration is the same as for the previous cases. The simulation schematics shown in Fig. 18.42 represents the modular configuration of the gas turbine.

Fuel Schedule, Rotor Response: The dynamic behavior of the above engine is simulated for an adverse acceleration-deceleration procedure. The transient operation is controlled by an open loop fuel schedule shown in Fig. 18.43 (left). The three- spools and the fourth shaft run independently at different rotational speed, Fig. 18.43 (right).

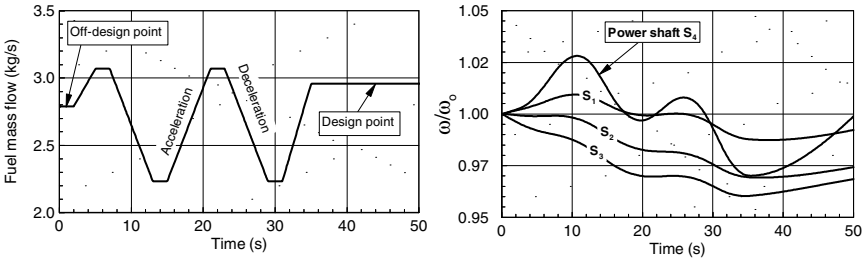

Fig. 18.43: Fuel schedule (left) starts with an off-design mass flow followed by a cyclic acceleration-deceleration procedure. Rotational speed of the three spools and the power shaft.(right).

The fuel schedule generated fully arbitrarily simulates an acceleration-deceleration procedure with emphasis on deceleration. We start with the steady-state operation and reduce the fuel mass flow to $\dot{m}_F = 2.8\,kg/s$ for about two seconds. During this short period of time, the engine operates in a dynamic state which is followed by a cyclic acceleration-deceleration event with the ramps given in Fig. 18.43. The dynamic operation triggers a sequence of transient events within individual components that are discussed in the following sections.

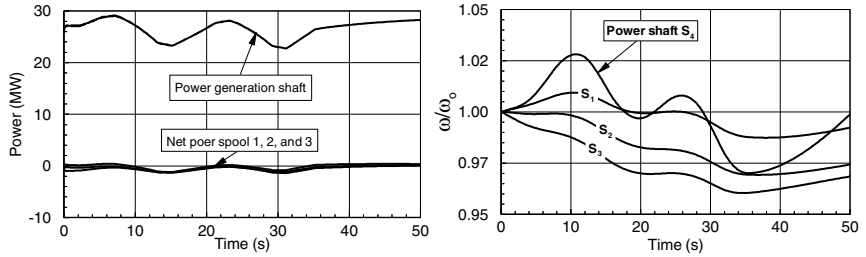

Fig. 18.44: Net power acting on the three spools causing a dynamic mismatch; power generated by the fourth shaft (left). Relative rotor speed of three spools and the fourth shaft.

Rotor Speed Behavior: The transient behavior of the three spools as well as the power shaft is determined by the net power acting on the corresponding rotor. For each individual spool, the cyclic acceleration-deceleration event has caused a dynamic mismatch between the required compressor power consumption and the turbine power generation as shown in Fig. 18.44. While LP- and IP-spools 2 and 3 decelerate under the influence of negative net power, the HP-spool 3 reacts faster to the acceleration. Since the fuel schedule places special weight upon deceleration, the rotational speeds of all three spools have a decelerating tendency as shown in Fig. 18.44.

Pressure and Temperature Transients within Plena: The change in fuel mass flow triggers a chain of transient events within the plena as shown in Fig. 18.45.

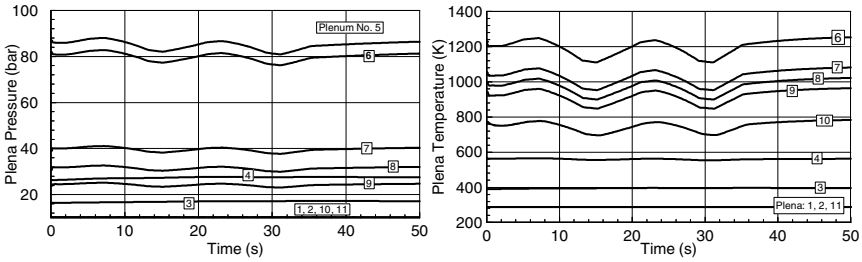

Fig. 18.45: Plena pressure (left) and temperature (right) as functions of time.

Plena pressure 5 and 6 which corresponds to the exit pressure of the HP-compressor and the combustion chamber, are strongly affected by the cyclic fuel change, whereas the other plena that correspond to the inlet and exit plena of the remaining components experiences moderate changes. The plena temperature distributions downstream of the combustion chamber shown in Fig. 18.45 (right) reflect the course of the fuel schedule.

Combustion Chamber Gas and Metal Temperature Transients: Figure 18.46 exhibits the combustion chamber gas and metal temperatures as functions of time. The combustion chamber component used in this simulation has three segments that separate the primary combustion zone from the secondary cooling air zone. Its module is shown in Fig. 18.41. Compressed air enters the combustion chamber at station 1, Figs. 18. 46 (left). Fuel is added and the segment's cooling occurs according to the procedure described in Chapter 17. The secondary mass flow portions $\dot{m}_{Si}$ serve as cooling jets and are mixed with the combustion gas, thus reducing the gas temperature. Before exiting, the combustion gas is mixed with the mixing air stream $\dot{m}_M$ further reducing the temperature. Figure 18.46 (right) shows the mean segment temperatures. The flame length extends from station 1 to 3, which makes the segment number 2 the hottest one. As seen, the gas temperature at station 2 follows the sharp changes in the fuel schedule. By convecting downstream, these sharp changes are

smoothed out. Wall temperatures shown in Fig. 18.46 (right) exhibit similar tendencies.

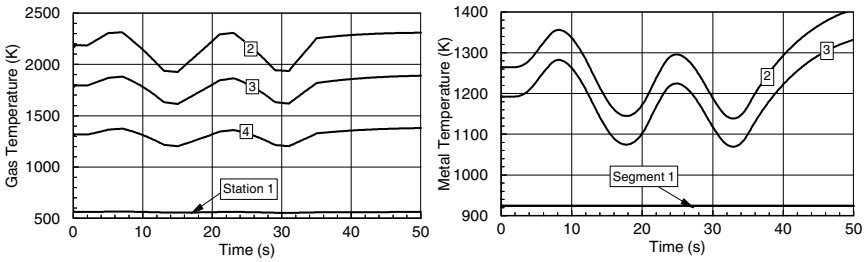

Fig. 18.46: Combustion chamber gas and metal temperature as functions of time.

Compressor and Turbine Mass Flow Transients: Figure 18.47 (left) exhibits the compressor mass flow transients, which are dictated by the compressor dynamic operation. The difference in compressor mass flow is due to the mass flow extraction for cooling purposes. Turbine mass flows are illustrated in Fig. 18.47 (right). Except for a minor time lag, they show identical distributions. The difference in turbine and compressor mass flow is due to the addition of fuel.

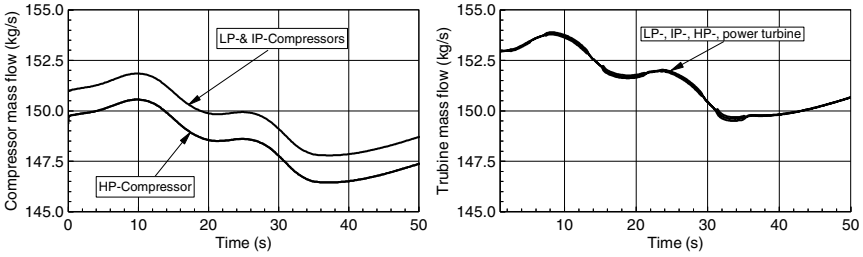

Fig. 18.47: Compressor and turbine mass flow as functions of time.

18.6 A Byproduct of Dynamic Simulation: Detailed Efficiency Calculation

One of the interesting aspects of a dynamic simulation is the capability to dynamically calculate the gas turbine thermal efficiency during steady state and dynamic operations. Such calculations are performed to compare the thermal efficiencies of four gas turbines with different design methodologies. The calculations are performed with the nonlinear dynamic code GETRAN. The first gas turbine dynamically simulated for efficiency calculation is a conventional single-shaft, single-combustion chamber power generation gas turbine. The second one is the ABB, GT 24/26. The third is an ultra-high efficiency gas turbine (UHEGT) with a pre-combustor, a reheat turbine stage and an integrated stator internal combustion as illustrated in Fig. 18.48. For the fourth gas turbine, the combustion process is placed entirely within the stator rows, thus eliminating the combustion chambers all together, Fig. 18.49. The dynamic efficiency calculation results are presented in Fig. 18.50. To

accurately determine the thermal efficiency and specific work of the gas turbines, calculations are performed with **GETRAN**© and the results are presented in Fig. 18.50. To compare the degree of efficiency improvement, the thermal efficiency and specific work of a baseline GT, GT-24, and the three UHEGT gas turbines are included in the figures.

For a UHEGT with three-stator combustion, denoted by the curve UHEGT-0C3S, a thermal efficiency above 45% is calculated. This exhibits an increase of at least 5% above the gas turbine engine GT-24, which is close to 40.5% as Fig. 18.5 (left) shows. Increasing the number of stator internal combustion to 4, curve labeled with UHEGT-0C4S, raises the efficiency above 48%. This is an enormous increase compared to any existing gas turbine engine. In the course of this calculation, the UHEGT technology is applied to a gas turbine engine with a pre-combustion chamber, such as the first one in GT-24, Fig.18.48. Using this combustion chamber with two-stator combustion, the curve labeled with UHEGT-1C2S shows an efficiency of 44%. This is particularly interesting for upgrading the existing gas turbines with UHEGT technology. Figure 18.48 (right) reveals the specific work comparison for the gas turbines discussed above. Compared to GT-24, UHEGT technology has about 20% higher specific work, making these engines very suitable for aircraft, stand-alone, as well as for combined cycle power generation applications. It is interesting to note that this efficiency increase can be established at a compressor pressure ratio of $\Pi_{UHEGT} \approx 35 - 40$, which can be achieved easily by existing compressor design technology with high polytropic efficiency. In performing the GETRAN© calculation, compressor and turbine efficiencies are calculated on a row-by-row basis. This automatically accounts for an increase of secondary flow losses

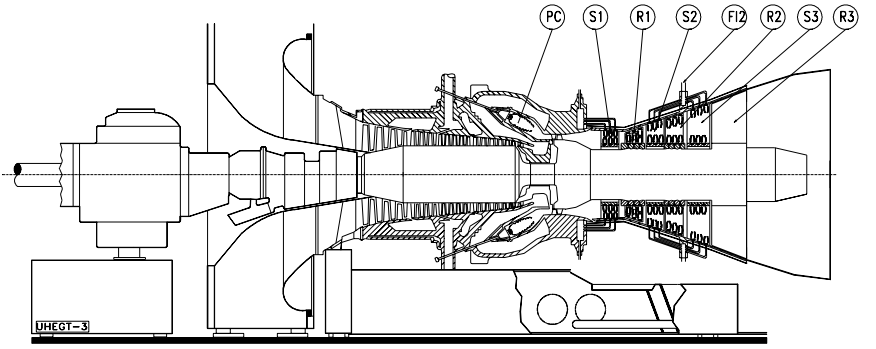

Fig. 18.48: A derivative of the Ultra-High Efficiency Gas Turbine Engine with a multi-stage compressor, a conventional combustion chamber PC, a single-stage reheat turbine RT, a three-stage turbine with an integrated stator internal combustion, B1, B2: compressor bypass blow-off, Fl1, Fl2: Fuel lines to stator. The combustion process takes place inside the pre-combustor and stator flow path, [1]

based on aspect ratio decrease. Thus, in a compressor case, efficiency decrease with pressure ratio increase is inherently accounted for.

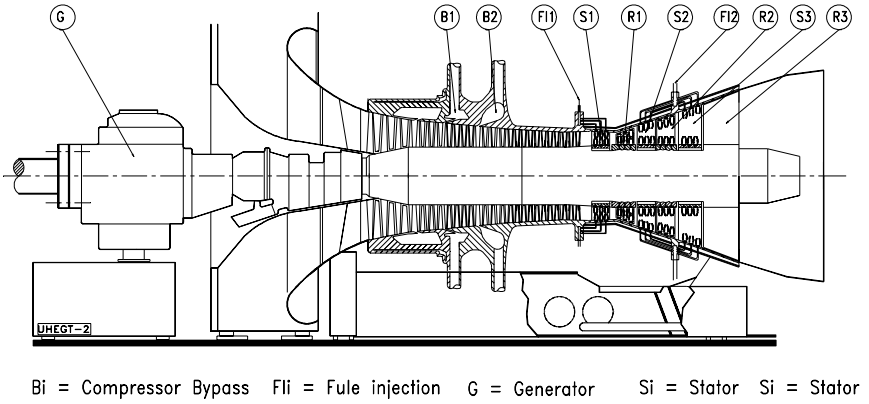

Fig. 18.49: An Ultra-High Efficiency Gas Turbine Engine with a multi-stage compressor, and a three-stage turbine with an integrated stator internal combustion, B1, B2: compressor bypass blow-off, Fl1, Fl2: Fuel lines to stator. The combustion process takes place inside the stator flow path, Schobeiri [1]

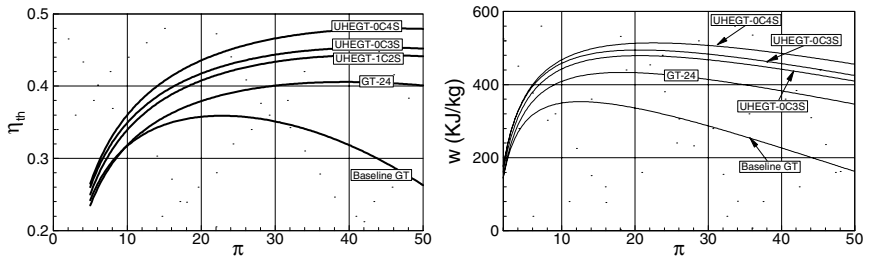

Fig. 18.50: Thermal efficiency (left) and specific work (right) as a function of compressor pressure ratio for the reference baseline gas turbine engine, ABB-GT-24 with two-combustion chamber, the **UHEGT-1C2S** with one conventional combustion chamber and two **UHEGT**-stator combustion, **UHEGT-03S** with three-stator combustion, and **UHEGT-0C4S** with four-stator combustion. Turbine inlet temperature = 1,200^{0}C, calculation with GETRAN [3]

18.7 Summary Part 3, Further Development

This chapter concludes Part 3 of the book that started with Chapter 14. The last six chapters dealt with providing the basic non-linear dynamic equations essential for describing the aero-thermodynamic process within individual turbomachinery components from a generic point of view. The four-dimensional time-space equations were simplified and modules were developed based on two-dimensional time-space coordinates. These modules were used to configure simulation schematics of complex gas turbine engines. Four levels of gas turbine engine simulations with cross coupling were presented. Three representative case studies were presented that aimed at better understanding the concept and the necessity for non-linear dynamic simulation.

Improvement of Thermal Efficiency: To introduce the reader to the problematic of gas turbine operation and process, Chapter 18 started with a brief presentation of a simple method for calculating the thermal efficiency of gas turbines, also a few methods for improving the gas turbine process and thermal efficiency were discussed. The parameter study using Eq. (18.20) illustrated the impact of the turbine inlet temperature (TIT) on thermal efficiency. More accurate results are obtained using the dynamic method applied to the corresponding simulation schematics that may incorporate many components and subsystems that are relevant for gas turbine operation. Considering the current advanced state-of-the-art turbine cooling technology and the technologies utilized to protect the blades from excessive thermal stresses by using thermal barrier coatings, there is not much room left for increasing the TIT. Likewise, the development of turbine and compressor components has reached a high level of polytropic efficiency (above 94%) that additional marginal improvement would not significantly improve the thermal efficiency. However, substantially higher thermal efficiencies at a consolidated TIT level can be obtained by taking advantage of the basic thermodynamic principles as demonstrated by the performance evaluation of GT-24/26. Further efficiency improvement can be achieved by utilizing the UHEGT concept for future generation of gas turbine engines. This concept is based on sound thermodynamic principles and offers a substantial improvement, however it requires substantial R&D efforts.

Necessity for Dynamic Simulation: The case studies showed the capability of a generic modularly structured simulation tool based on equations presented beginning in Chapter 14 through 18. From today's computational point of view, simulating a complex gas turbine power plant or an aircraft engine consisting of various components and subsystems that are described by a large number of systems of differential and algebraic equations, does not exhibit any computational obstacle. It is well known that problems with new gas turbine types arise during dynamic operation. Many of these problems can be eliminated in the early stage of design and development by dynamically simulating possible adverse scenarios that may lead to component and system failures.

Modeling Enhancement: As explained, the modular concept is based on a two-dimensional time space approximation. The models described in Part 3 can be extended to fully four-dimensional time space models. Using the unsteady Navier-Stokes equations requires considerable computational effort and time as we briefly discussed. A time dependent version of the streamline curvature method may deliver sufficiently accurate results for evaluating a dynamic simulation.

References, Chapter 18

18.1 Schobeiri, M.T. 1999, "The Ultra-High Efficiency Gas Turbine Engine with Stator Internal Combustion, UHEGT, U.S. Patent Pending, 1389-TEES-99.

18.2 Schobeiri, M. T., Attia, S., 1996, "Advances in Nonlinear Dynamic Engine Simulation Technology," ASME 96-GT-392, presented at the International Gas Turbine and Aero-Engine Congress and Exposition, Birmingham, UK- June 10- 13, 1996.

18.3 Schobeiri, M. T., Abouelkheir, M., Lippke, C., 1994, "GETRAN: A Generic, Modularly Structured Computer Code for Simulation of Dynamic Behavior of Aero-and Power Generation Gas Turbine Engines," an honor paper, ASME Transactions, *Journal of Gas Turbine and Power*, Vol. 1, pp. 483-494.

18.4 Koenig R.W., Fishbach L.H., 1972, " GENENG- A Program for Calculating Design and Off-Design Performance for Turbojet and Turbofan Engines," NASA TN D-6552.

18.5 Seldner K., Mihailowe J.R., Blaha R.J., 1972, "Generalized Simulation Technique for Turbojet Engine System Analysis," NASA TN D-6610.

18.6 Seller J., Daniele C.J., 1975, "DYGEN- A Program for Calculating Steady-State and Transient Performance of Turbojet and Turbofan Engines," NASA TND-7901.

18.7 Szuch J.R., 1974, "HYDES- A Generalized Hybrid Computer Program for Studying Turbojet or Turbofan Engine Dynamics," NASA TM X-3014.

18.8 Agrawal R.K., Yunis M., 1982, " A Generalized Mathematical Model to Estimate Gas Turbine Starting Characteristics," *Journal of Eng. Power, Vol. 104, pp. 194-201.*

18.9 Schobeiri M.T., 1985 "Aero-Thermodynamics of Unsteady Flows in Gas Turbine Systems." Brown Boveri Company, Gas Turbine Division Baden Switzerland, BBC-TCG-51.

18.10 Schobeiri T., 1985 "COTRAN, the Computer Code for Simulation of Unsteady Behavior of Gas Turbines." Brown Boveri Company, Gas Turbine Division Baden Switzerland, BBC-TCG-53

18.11 Schobeiri, T., 1985 "Digital Computer Simulation of the Dynamic Response of Gas Turbines", *VDI- Annual Journal of Turbomachinery*, pp. 381-400, 1985.

18.12 Schobeiri T., 1986: "A General Computational Method for Simulation and Prediction of Transient Behavior of Gas Turbines." ASME-86-GT-180.

18.13 Schobeiri T., 1987, "Digital Computer Simulation of the Dynamic Operating Behavior of Gas Turbines." *Journal Brown Boveri Review 3-87.*

18.14 Schobeiri T., 1987, "Digital Computer Simulation of the Dynamic Operating Behavior of Gas Turbines." *Journal Brown Boveri Review 3-87.*

18.15 Schobeiri, H. Haselbacher, H, 1985c, "Transient Analysis of Gas Turbine Power Plants Using the Huntorf Compressed Air Storage Plant as an Example." ASME-85-GT-197.

18.16 Schobeiri, M. T., Attia, M, Lippke, C., 1994, "Nonlinear Dynamic Simulation of Single and Multi-spool Core Engines, Part I: Theoretical Method," *AIAA, Journal of Propulsion and Power,* Volume 10, Number 6, pp. 855-862, 1994.

18.17 Schobeiri, M. T., Attia, M, Lippke, C., 1994, "Nonlinear Dynamic Simulation of Single and Multi-spool Core Engines, Part II: Modeling and Simulation Cases," *AIAA Journal of Propulsion and Power*, Volume 10, Number 6, pp. 863-867, 1994.

18.18 Schobeiri, M. T., 1982, "Dynamisches Verhalten der Luftspeichergasturbine Huntorf bei einem Lastabwurf mit Schnellabschaltung," Brown Boveri, Technical Report, TA-58.

A Vector and Tensor Analysis with Applications to Turbomachinery Fluid Mechanics

A. 1 Tensors in Three-Dimensional Euclidean Space

In this section, we briefly introduce tensors, their significance to turbomachinery fluid dynamics an and their analysis. The tensor analysis is a powerful tool that enables the reader to study and to understand more effectively the fundamentals of fluid mechanics. Once the basics of tensor analysis are understood, the reader will be able to derive all conservation laws of fluid mechanics without memorizing any single equation. In this section, we focus on the tensor analytical application rather than mathematical details and proofs that are not primarily relevant to engineering students. To avoid unnecessary repetition, we present the definition of tensors from a unified point of view and use exclusively the three-dimensional Euclidean space, with N = 3 as the number of dimensions. The material presented in this chapter has drawn from classical tensor and vector analysis texts, among others those mentioned in References. It is tailored to specific needs of turbomachinery fluid mechanics and is considered to be helpful for readers with limited knowledge of tensor analysis.

The quantities encountered in fluid dynamics are *tensors.* A physical quantity which has a *definite magnitude* but not a *definite direction* exhibits a *zeroth-order tensor*, which is a special category of tensors. In a N-dimensional Euclidean space, a zeroth-order tensor has $N^0 = 1$ component, which is basically its magnitude. In physical sciences, this category of tensors is well known as a *scalar* quantity, which has a definite magnitude but not a definite direction. Examples are: mass m, volume v, thermal energy Q (heat), mechanical energy W (work) and the entire thermodynamic properties such as density ρ, temperature T , enthalpy h, entropy s , etc.

In contrast to the zeroth-order tensor, a *first-order* tensor encompasses physical quantities with a *definite magnitude* with $N^1 (N^1 = 3^1 = 3)$ components and a *definite direction* that can be decomposed in $N^1 = 3$ directions. This special category of tensors is known as *vector*. Distance $\boldsymbol{X}$, velocity $\boldsymbol{V}$, acceleration $\boldsymbol{A}$, force $\boldsymbol{F}$ and moment of momentum $\boldsymbol{M}$ are few examples. A vector quantity is *invariant* with respect to a given category of coordinate systems. Changing the coordinate system by applying certain transformation rules, the vector components undergo certain changes resulting in a new set of components that are related, in a definite way, to the old ones. As we will see later, the order of the above tensors can be reduced if they are multiplied with each other in a *scalar* manner. The mechanical energy $W = \boldsymbol{F}.\boldsymbol{X}$ is a representative example, that shows how a tensor order can be reduced. The reduction of order of tensors is called *contraction.*

A *second order tensor* is a quantity, which has N^2 definite components and N^2 definite directions (in three-dimensional Euclidean space: $N^2 = 9$). General stress tensor $\boldsymbol{\Pi}$, normal stress tensor $\boldsymbol{\Sigma}$, shear stress tensor $\boldsymbol{T}$, deformations tensor $\boldsymbol{D}$ and rotation tensor $\boldsymbol{\Omega}$ are few examples. Unlike the zeroth and first order tensors (scalars and vectors), the second and higher order tensors cannot be directly geometrically interpreted. However, they can easily be interpreted by looking at their pertinent force components, as seen later in section A.5.4

A.1.1 Index Notation

In a three-dimensional Euclidean space, any arbitrary first order tensor or vector can be decomposed into 3 components. In a Cartesian coordinate system shown in Fig. A1, the *base vectors* in x_1, x_2, x_3 directions $\boldsymbol{e}_1$, $\boldsymbol{e}_2$, $\boldsymbol{e}_3$ are perpendicular to each other and have the magnitude of unity, therefore, they are called *orthonormal unit vectors*. Furthermore, these base vectors are not dependent upon the coordinates, therefore, their derivatives with respect to any coordinates are identically zero. In contrast, in a general curvilinear coordinate system (discussed in Appendix A) the base vectors do not have the magnitude of unity. They depend on the curvilinear coordinates, thus, their derivatives with respect to the coordinates do not vanish.

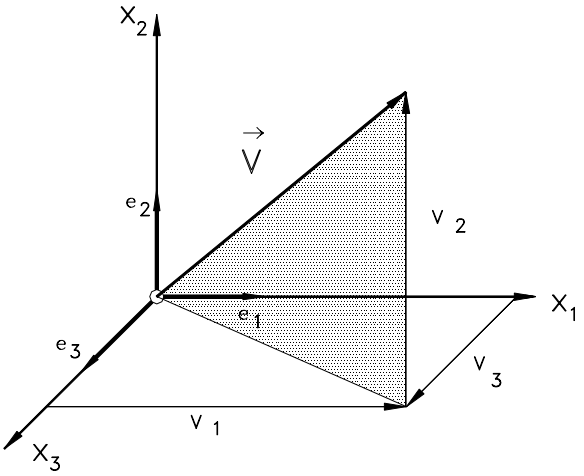

Fig. A.1: vector decomposition in a Cartesian coordinate system.

As an example, vector $\boldsymbol{A}$ with its components A_1, A_2 and A_3 in a Cartesian coordinate system shown in Fig. A1 is written as:

$$\boldsymbol{A} = e_1 A_1 + e_2 A_2 + e_3 A_3 = \sum_{i=1}^{N=3} e_i A_i \tag{A.1}$$

According to Einstein's summation convention, it can be written as:

$$\boldsymbol{A} = e_i A_i \tag{A.2}$$

The above form is called the *index notation.* Whenever the same index (in the above equation *i*) appears twice the summation is carried out from 1 to N (N = 3 for Eucldean space).

A.2 Vector Operations: Scalar, Vector and Tensor products

A.2.1 Scalar product

Scalar or dot product of two vectors results in a scalar quantity $\boldsymbol{A}\cdot\boldsymbol{B}=C$. We apply the Einstein's summation convention defined in Eq. (A.2) to the above vectors:

$$(e_i A_i) \cdot (e_j B_j) = C$$

we rearrange the unit vectors and the components separately:

$$(e_i \cdot e_j)\, A_i B_j = C$$

In Cartesian coordinate system, the scalar product of two unit vectors is called *Kronecker delta*, which is:

$$\delta_{ij} = e_i \cdot e_j = 1, \quad for\ i = j\ ,\ \delta_{ij} = e_i \cdot e_j = 0, \quad for\ i \neq j \tag{A.3}$$

with δ_{ij} as Kronecker delta. Using the Kronecker delta, we get:

$$(e_i \cdot e_j) A_i B_j = \delta_{ij} A_i B_j$$

The non-zero components are found only for $i = j$, *or* $\delta_{ij} = 1$, which means in the above equation the index j must be replaced by I resulting in:

$$\boldsymbol{A}\cdot\boldsymbol{B} = A_i B_i = A_1 B_1 + A_2 B_2 + A_3 B_3 = C$$

A.2.2 Vector or cross product

The vector product of two vectors is a vector that is perpendicular to the plane described by those two vectors. Example:

$$\boldsymbol{F}\times\boldsymbol{R} = \boldsymbol{M} \ \ or\ \ \boldsymbol{A}\times\boldsymbol{B} = \boldsymbol{C}$$

We apply the index notation to:

$$\boldsymbol{A}\times\boldsymbol{B} = (e_i A_i)\times(e_j B_j) = \varepsilon_{ijk} e_k A_i B_j$$

with ε_{ijk} as permutation symbol with the following definition illustrated in Fig. A2:

$\varepsilon_{ijk} = 0$ for I = j, j = k or I = k: (122)
$\varepsilon_{ijk} = 1$ for cyclic permutation: (123)

$\varepsilon_{ijk} = -1$ for anticyclic permutation: (132)

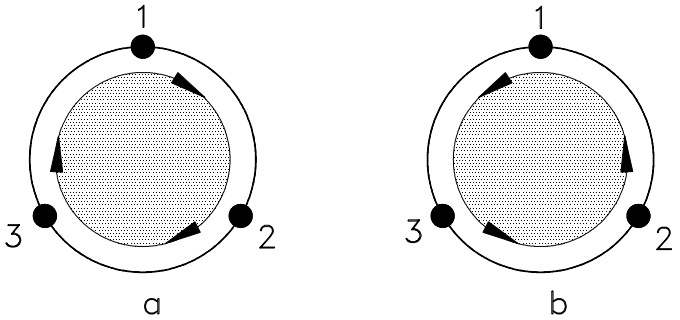

Fig. A2 Permutation symbol, (a) positive , (b) negative permutation.

Using the above definition, the vector product is given by:

$$\boldsymbol{C} = e_k C_k = \varepsilon_{ijk} e_k A_i B_j \tag{A.4}$$

A.2.3 Tensor product

The tensor product is a product of tow or more vectors, where the unit vectors are not subject to scalar or vector operation. Consider the following *tensor operation*:

$$\Phi = \boldsymbol{AB} = (e_i A_i)\ (e_j B_j) = e_i e_j A_i B_j \tag{A.5}$$

The result of this purely mathematical operation is a second order tensor with nine components:

$$\begin{aligned}\Phi = {} & e_1(e_1 A_1 B_1 + e_2 A_1 B_2 + e_3 A_1 B_3) + \\ & e_2(e_1 A_2 B_1 + e_2 A_2 B_2 + e_3 A_2 B_3) + \\ & e_3(e_1 A_3 B_1 + e_2 A_3 B_2 + e_3 A_3 B_3)\end{aligned} \tag{A.6}$$

The operation with any tensor such as the above second order one acquires a physical meaning if it is multiplied with a vector (or another tensor) in scalar manner. Consider the scalar product of the vector $\boldsymbol{C}$ and the second order tensor $\boldsymbol{\Phi}$. The result of this operation is a *first order tensor* or a vector. The following example should clarify this:

$$\boldsymbol{D} = \boldsymbol{C}\cdot\ \Phi = \boldsymbol{C}\cdot\ (\boldsymbol{A}\,\boldsymbol{B}) = e_k C_k \cdot (e_i\, e_j)\, A_i\, B_j \tag{A.7}$$

Rearranging the unit vectors and the components separately:

$$\boldsymbol{D} = \boldsymbol{C}\cdot\ \Phi = \boldsymbol{C}\cdot\ (\boldsymbol{A}\,\boldsymbol{B}) = e_k \cdot (e_i\, e_j)\, C_k A_i\, B_j$$

It should be pointed out that in the above equation, the unit vector $\boldsymbol{e}_k$ must be multiplied with the closest unit vector namely $\boldsymbol{e}_i$

$$\boldsymbol{D} = \boldsymbol{C}\cdot\ \Phi = \boldsymbol{C}\cdot\ (\boldsymbol{AB}) = \delta_{ki}(e_j)C_k A_i B_j = e_j C_i A_i B_j \tag{A.8}$$

The result of this tensor operation is a vector with the same direction as vector *B*. Different results are obtained if the positions of terms in a dot product of a vector with a tensor are reversed as shown in the following operation:

$$\boldsymbol{E} = \Phi\cdot\ C = (\boldsymbol{A}\ \boldsymbol{B})\cdot\ \boldsymbol{C} = e_i A_i B_j \delta_{jk} C_j = e_i A_i B_j C_j \tag{A.9}$$

The result of this operation is a vector in direction of *A*; thus $\boldsymbol{E} = \Phi\cdot\boldsymbol{C} \neq \boldsymbol{C}\cdot\Phi = \boldsymbol{D}$.

A.3 Contraction of Tensors

As shown above, the scalar product of a second order tensor with a first order one is a first order tensor or a vector. This operation is called contraction. The *trace of a second order tensor* is a tensor of zeroth order, which is a result of a contraction and is a scalar quantity.

$$Tr(\Phi) = e_i \cdot e_j \Phi_{ij} = \delta_{ij}\Phi_{ij} = \Phi_{ii} = \Phi_{11} + \Phi_{22} + \Phi_{33} \tag{A.10}$$

As can be shown easily, the trace of a second order tensor is the sum of the diagonal element of the *matrix* Φ_{ij}. If the tensor $\boldsymbol{\Phi}$ itself is the result of a contraction of two second order tensors $\boldsymbol{\Pi}$ and $\boldsymbol{D}$:

$$\boldsymbol{\Phi} = \boldsymbol{\Pi}\cdot\boldsymbol{D} = e_i e_j \Pi_{ij} \cdot e_k e_l D_{kl} = e_i e_l \delta_{jk} \Pi_{ij} D_{kl} = e_i e_l \Pi_{ik} D_{kl} \tag{A.11}$$

then the $Tr(\boldsymbol{\Phi})$ is:

$$Tr(\boldsymbol{\Phi}) = e_i \cdot e_l \Pi_{ik} D_{kl} = \delta_{il} \Pi_{ik} D_{kl} = \Pi_{lk} = \Phi_{ii} D_{kl} \tag{A.12}$$

A.4 Differential Operators in Fluid Mechanics

In fluid mechanics, the particles of the working medium undergo a time dependent or unsteady motion. The flow quantities such as the velocity and the thermodynamic properties of the working substance such as pressure, temperature and density are generally functions of space and time :

$$\boldsymbol{V} = \boldsymbol{V}(\boldsymbol{x}\ t),\quad p = p(\boldsymbol{x},\ t),\quad T = T(\boldsymbol{x},\ t),\quad \rho = \rho(\boldsymbol{x},\ t),\quad Q = Q(\boldsymbol{x},\ t)$$

A.4.1 Substantial derivatives

During the flow, these quantities generally change with respect to time and space. The *temporal* and *spatial change* of the above quantities is described most appropriately by the *substantial* or *material derivative*. Generally, the substantial derivative of a flow quantity Q, which may be a scalar, a vector or a tensor valued function, is given by:

$$DQ = \frac{\partial Q}{\partial t} dt + dQ \tag{A.13}$$

The operator D represents the *substantial or material* change of the quantity Q, the first term on the right hand side of Eq. (A.13) represents the *local change* or *temporal change* of the quantity Q with respect to a fixed vector position $\boldsymbol{x}$. The operator d symbolizes the *spatial or convective change* of the same quantity with respect to a fixed instant of time. The convective change of Q may be expressed as:

$$dQ = \frac{\partial Q}{\partial x_1} dx_1 + \frac{\partial Q}{\partial x_2} dx_2 + \frac{\partial Q}{\partial x_3} dx_3$$

A simple rearrangement of the above equation results in:

$$dQ = (e_1 dx_1 + e_2 dx_2 + e_3 dx_3) \cdot \left(e_1 \frac{\partial}{\partial x_1} + e_2 \frac{\partial}{\partial x_2} + e_3 \frac{\partial}{\partial x_3} \right) Q \tag{A.14}$$

A.4.2 Differential operator ∇

The expression in the second parenthesis is the *spatial differential operator* ∇(*nabla, del*) which has a vector character. In Cartesian coordinate system the operator nabla ∇ is defined as:

$$\nabla = \left(e_1 \frac{\partial}{\partial x_1} + e_2 \frac{\partial}{\partial x_2} + e_3 \frac{\partial}{\partial x_3} \right) = e_i \frac{\partial}{\partial x_i} \tag{A.15}$$

Using the above differential operator, the change of the quantity Q is written as:

$$dQ = (d\boldsymbol{x}) \cdot \nabla Q \tag{A.16}$$

If Q is a scalar quantity, ∇Q is the *gradient* of the scalar field. It is a vector or *first order tensor*. Equation (A.16) indicates that the spatial change of the quantity Q assumes a maximum if the vector ∇Q (*gradient* of Q) is parallel to the vector $d\boldsymbol{x}$. Is the vector ∇Q perpendicular to the vector $d\boldsymbol{x}$, their product will be zero. This is only possible, if the spatial change $d\boldsymbol{x}$ occurs on a surface with $Q = const.$ Consequently, the quantity Q does not experience any changes. The physical interpretation of this

statement is found in Fig. A.3. The scalar field is represented by the point function temperature that changes from the surfaces T to the surface $T + dT$. In Fig. A.3, the gradient of the temperature field is shown as ∇T, which is perpendicular to the surface $T = const.$ at point P. The temperature probe located at P moves on the surface $T = const.$ to the point M, thus measuring no changes in temperature ($\alpha = \pi/2$, $\cos\alpha = 0$). However, the same probe experiences a certain change in temperature by moving to the point Q, which is characterized by a higher temperature $T + dT$ ($0 < \alpha < \pi/2$). The change dT can immediately be measured, if the probe is moved parallel to the vector ∇T. In this case the displacement dN (see Fig. A.3) is the shortest ($\alpha = 0$, $\cos\alpha = 1$). Performing the similar operation for a vector quantity yields:

$$d\boldsymbol{V} = d\boldsymbol{x} \cdot (\nabla \boldsymbol{V}) \tag{A.17}$$

with $\nabla \boldsymbol{V}$ as the gradient of the point vector field which is a second order tensor. To perform the differential operation, first the ∇ operator is applied to the vector V, resulting in a second order tensor. This tensor is then multiplied with the vector $d\boldsymbol{x}$ in a scalar manner. The result is a first order tensor or vector.

$$D\boldsymbol{V} = \frac{\partial \boldsymbol{V}}{\partial t} dt + d\boldsymbol{V} \tag{A.18}$$

where the spatial change of the velocity is expressed as :

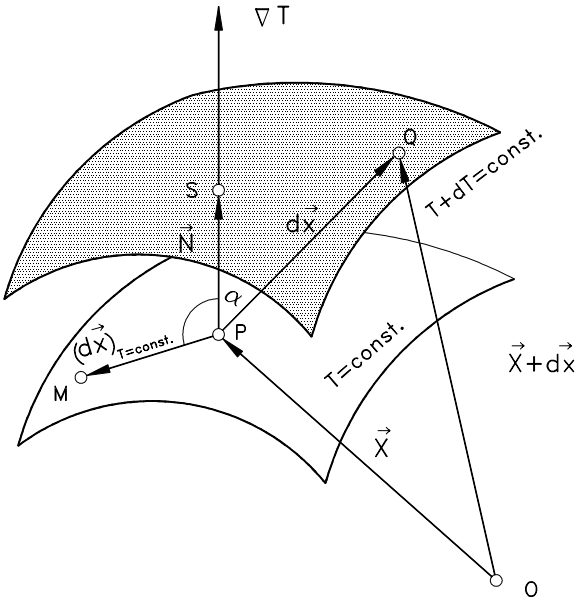

Fig. A.3: Physical explanation of the gradient of scalar field.

$$d\boldsymbol{V} = \frac{\partial \boldsymbol{V}}{\partial x_1} dx_1 + \frac{\partial \boldsymbol{V}}{\partial x_2} dx_2 + \frac{\partial \boldsymbol{V}}{\partial x_3} dx_3 \tag{A.19}$$

Rearrangement of Eq. (A.19) leads to :

$$d\boldsymbol{V} = \left(e_1 dx_1 + e_2 dx_2 + e_3 dx_3\right) \cdot \left(e_1 \frac{\partial}{\partial x_1} + e_2 \frac{\partial}{\partial x_2} + e_3 \frac{\partial}{\partial x_3} \right) \boldsymbol{V} \tag{A.20}$$

From this operation, it follows that spatial change of the velocity component can be expressed as the scalar product of the vector d**x** and the second order tensor $\nabla \boldsymbol{V}$, which represents the spatial gradient of the velocity vector. Equation (A.20) can be written as:

$$d\boldsymbol{V} = d\boldsymbol{x} \cdot \nabla \boldsymbol{V} \tag{A.21}$$

Dividing Eq. (A.21) by *dt* yields the *convective* part of the acceleration vector:

$$\frac{d\boldsymbol{V}}{dt} = \left(\frac{d\boldsymbol{x}}{dt} \right) \cdot (\nabla \boldsymbol{V}) = \boldsymbol{V} \cdot \nabla \boldsymbol{V}$$

The substantial acceleration is then:

$$\frac{D\boldsymbol{V}}{dt} \equiv \frac{D\boldsymbol{V}}{Dt} = \frac{\partial \boldsymbol{V}}{\partial t} + \boldsymbol{V} \cdot \nabla \boldsymbol{V} \tag{A.22}$$

The differential *dt* may symbolically be replaced by *Dt* indicating the material character of the derivatives. Applying the index notation to velocity vector and Nabla operator, performing the vector operation , and using the Kronecker delta, the index notation of the *material acceleration* $\boldsymbol{A}$ is:

$$\boldsymbol{A} = e_i A_i = e_i \frac{\partial V_i}{\partial t} + e_i V_j \frac{\partial V_i}{\partial x_j} \tag{A.23}$$

Equation (A.23) is valid only for Cartesian coordinate system, where the unit vectors do not depend upon the coordinates and are constant. Thus, their derivatives with respect to the coordinates disappear identically. To arrive at Eq. (A.23) with a unified index *I*, we renamed the indices. To decompose the above acceleration vector into three components, we cancel the unit vector from both side in Eq. (A.23) and get:

$$A_i = \frac{\partial V_i}{\partial t} + V_j \frac{\partial V_i}{\partial x_j} \tag{A.24}$$

To find the components in x_i -direction, the index *I* assumes subsequently the values from 1 to 3, while the summation convention is applied to the free index *j*. As a result

we obtain the three components:

$$A_1 = \frac{\partial V_1}{\partial t} + V_1\frac{\partial V_1}{\partial x_1} + V_2\frac{\partial V_1}{\partial x_2} + V_3\frac{\partial V_1}{\partial x_3}$$
$$A_2 = \frac{\partial V_2}{\partial t} + V_1\frac{\partial V_2}{\partial x_1} + V_2\frac{\partial V_2}{\partial x_2} + V_3\frac{\partial V_2}{\partial x_3} \qquad \text{(A.25)}$$
$$A_3 = \frac{\partial V_3}{\partial t} + V_1\frac{\partial V_3}{\partial x_1} + V_2\frac{\partial V_3}{\partial x_2} + V_3\frac{\partial V_3}{\partial x_3}$$

A5 Operator ∇ Applied to Different Functions

This section summarizes the applications of nabla operator to different functions. As mentioned previously, the spatial differential operator ∇ has a vector character. If it acts on a scalar function, such as temperature, pressure, enthalpy etc., the result is a vector and is called the *gradient* of the corresponding scalar field, such as gradient of temperature, pressure, etc. (see also previous discussion of the physical interpretation of ∇Q). If, on the other hand, ∇ acts on a vector, three different cases are distinguished.

A5.1 Scalar Product of ∇ and V

This operation is called the *divergence of the vector* $\boldsymbol{V}$. The result is a zeroth-order tensor or a scalar quantity. Using the index notation, the divergence of $\boldsymbol{V}$ is written as:

$$\nabla \cdot \boldsymbol{V} = (e_i\frac{\partial}{\partial x_i}).(e_i V_j) = \delta_{ij}\frac{\partial}{\partial x_i}V_j = \frac{\partial V_i}{\partial x_i} \qquad \text{(A.26)}$$

The physical interpretation of this purely mathematical operation is shown in Fig. A.4. The mass flow balance for a steady incompressible flow through an infinitesimal volume $dv = dx_1dx_2dx_3$ is shown in Fig. A4.

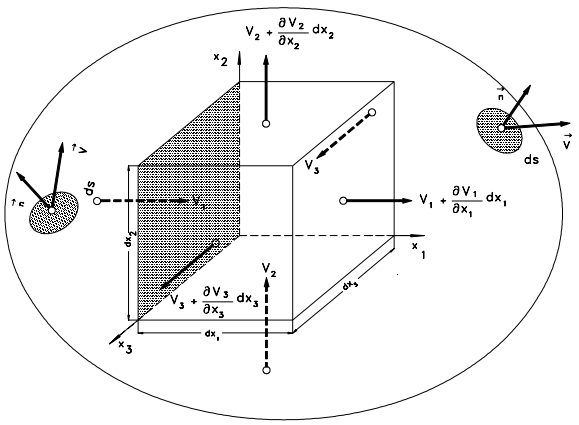

Fig. A.4: Physical interpretation of $\nabla.\boldsymbol{V}$

We first establish the entering and exiting mass flows through the cube side areas perpendicular to x_1- direction given by $dA_1 = dx_2 dx_3$:

$$\dot{m}_{x_1\,en} = \rho(dx_2 dx_3)V_1$$

$$\dot{m}_{x_1\,ex} = \rho(dx_2 dx_3)\left(V_1 + \frac{\partial \boldsymbol{V_1}}{\partial x_1}dx_1\right)$$

Repeating the same procedure for the cube side areas perpendicular to x_2 and x_3 directions given by $dA_2 = dx_3 dx_1$ and $dA_3 = dx_1 dx_2$ and subtracting the entering mass flows from the exiting ones, we obtain the net mass net flow balances through the infinitesimal differential volume as:

$$\rho(dx_1 dx_2 dx_3)\left(\frac{\partial V_1}{\partial x_1} + \frac{\partial V_2}{\partial x_2} + \frac{\partial V_3}{\partial x_3}\right) = \rho dv\,(\nabla\cdot\boldsymbol{V}) = 0 \qquad \text{(A.27)}$$

to the vector ∇T. In this case the displacement dN (see Fig. A.3) is the shortest ($\alpha = 0$, $\cos\alpha = 1$). Performing the similar operation for a vector quantity yields:

$$d\boldsymbol{V} = d\boldsymbol{x}\cdot(\nabla\boldsymbol{V}) \qquad \text{(A.28)}$$

with $\nabla\boldsymbol{V}$ as the gradient of the point vector field which is a second order tensor. To perform the differential operation, first the ∇ operator is applied to the vector V, resulting in a second order tensor. This tensor is then multiplied with the vector $d\boldsymbol{x}$ in a scalar manner. The result is a first order tensor or vector.
where the spatial change of the velocity is expressed as :

$$D\boldsymbol{V} = \frac{\partial \boldsymbol{V}}{\partial t}dt + d\boldsymbol{V} \qquad \text{(A.29)}$$

with the convective change

$$d\boldsymbol{V} = \frac{\partial \boldsymbol{V}}{\partial x_1}dx_1 + \frac{\partial \boldsymbol{V}}{\partial x_2}dx_2 + \frac{\partial \boldsymbol{V}}{\partial x_3}dx_3 \qquad \text{(A.30)}$$

A5.2 Vector product of ∇ and V

This operation is called the *rotation or curl* of the velocity vector $\boldsymbol{V}$. Its result is a first-order tensor or a vector quantity. Using the index notation, the curl of $\boldsymbol{V}$ is written as:

$$\nabla\times\boldsymbol{V} = (e_i\frac{\partial}{\partial x_i})\times(e_i V_j) = \epsilon_{ijk}\,e_k\frac{\partial V_j}{\partial x_i} \equiv \boldsymbol{\omega} \qquad \text{(A.31)}$$

The curl of the velocity vector is known as *vorticity,* $\boldsymbol{\omega} = \nabla x \boldsymbol{V}$. As we will see later, the vorticity plays a crucial role in fluid mechanics. It is a characteristic of a *rotational* flow. For viscous flows encountered in engineering applications, the curl $\boldsymbol{\omega} = \nabla x \boldsymbol{V}$ is always different from zero. To simplify the flow situation and to solve the equation of motion, as we will discuss later, the vorticity vector $\boldsymbol{\omega} = \nabla x \boldsymbol{V}$, can under certain conditions, be set equal to zero. This spacial case is called *the irrotational flow*.

A5.3 Tensor Product of ∇ and V

This operation is called the *gradient* of the velocity vector $\boldsymbol{V}$. Its result is a second tensor. Using the index notation, the gradient of the vector $\boldsymbol{V}$ is written as:

$$\nabla \boldsymbol{V} = (e_i \frac{\partial}{\partial x_i})(e_i V_j) = e_i e_j \frac{\partial V_j}{\partial x_i} \tag{A.32}$$

Equation (A.32) is a second order tensor with nine components and describes the deformation and the rotation kinematics of the fluid particle. As we saw previously, the scalar multiplication of this tensor with the velocity vector, $\boldsymbol{V}.(\nabla \boldsymbol{V})$ resulted in the convective part of the acceleration vector, Eq. (A.22). In addition to the applications we discussed , ∇ can be applied to a product of two or more vectors by using the Leibnitz's chain rule of differentiation:

$$\nabla(\boldsymbol{U} \cdot \boldsymbol{V}) = \boldsymbol{U} \cdot \nabla \boldsymbol{V} + \boldsymbol{V} \cdot \nabla \boldsymbol{U} + \boldsymbol{U} \times (\nabla \times \boldsymbol{V}) + \boldsymbol{V} \times (\nabla \times \boldsymbol{U})$$

For $\boldsymbol{U} = \boldsymbol{V}$, Eq. (A.30) becomes $\nabla(\boldsymbol{V} \cdot \boldsymbol{V}) = 2\boldsymbol{V} \cdot \nabla \boldsymbol{V} + 2\boldsymbol{V} \times (\nabla \times \boldsymbol{V})$ or

$$\boldsymbol{V} \cdot \nabla \boldsymbol{V} = \frac{1}{2} \nabla(\boldsymbol{V} \cdot \boldsymbol{V}) - \boldsymbol{V} \times (\nabla \times \boldsymbol{V}) = \frac{1}{2} \nabla(\boldsymbol{V}^2) - \boldsymbol{V} \times (\nabla \times \boldsymbol{V}) \tag{A.33}$$

Equation (A.33) is used to express the convective part of the acceleration in terms of the gradient of kinetic energy of the flow.

A5.4 Scalar Product of ∇ and a Second Order Tensor

Consider a fluid element with sides dx_1, dx_2, dx_3 parallel to the axis of a Cartesian coordinate system, Fig.A.5. The fluid element is under a general three-dimensional stress condition. The force vectors acting on the surfaces, which are perpendicular to the coordinates x_1, x_2, and x_3 are denoted by $\boldsymbol{F}_1$, $\boldsymbol{F}_2$, and $\boldsymbol{F}_3$,. The opposite surfaces are subject to forces that have experienced infinitesimal changes $\boldsymbol{F}_1 + d\boldsymbol{F}_1$, $\boldsymbol{F}_2 + d\boldsymbol{F}_2$, and $\boldsymbol{F}_3 + d\boldsymbol{F}_3$. Each of these force vectors is decomposed into three components F_{ij} according to the coordinate system defined in Fig. A.5. The first index i refers to the axis, to which the fluid element surface is perpendicular, whereas the second index j indicates the direction of the force component.

We divide the individual components of the above force vectors by their corresponding area of the fluid element side. The results of these divisions exhibit the components of a second order stress tensor represented by $\boldsymbol{\Pi}$ as shown in Fig. A6. As an example, we take the force component F_{11} and divide it by the corresponding area $dx_2 dx_3$ results in:

$$\frac{F_{11}}{dx_2 dx_3} = \pi_{11}$$

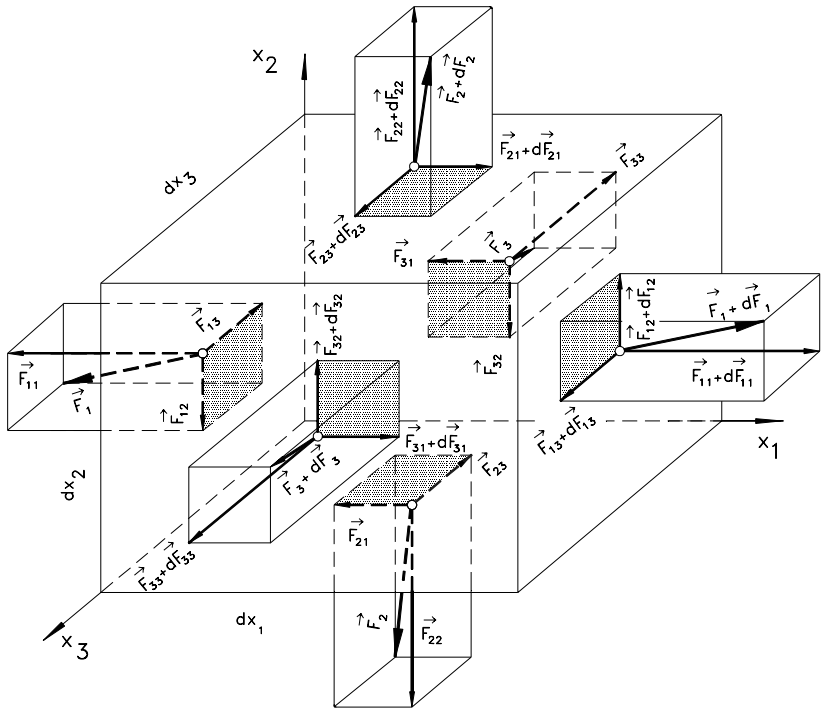

Fig. A.5: Fluid element under a general three-dimensional stress condition

Correspondingly, we divide the force component on the opposite surface $F_{11} + dF_{11}$ by the same area $dx_2 dx_3$ and obtain:

$$\frac{F_{11} + dF_{11}}{dx_2 dx_3} = \pi_{11} + \frac{\partial \pi_{11}}{\partial x_1} dx_1$$

In a similar way we find the remaining stress components, which are shown in Fig. A6.

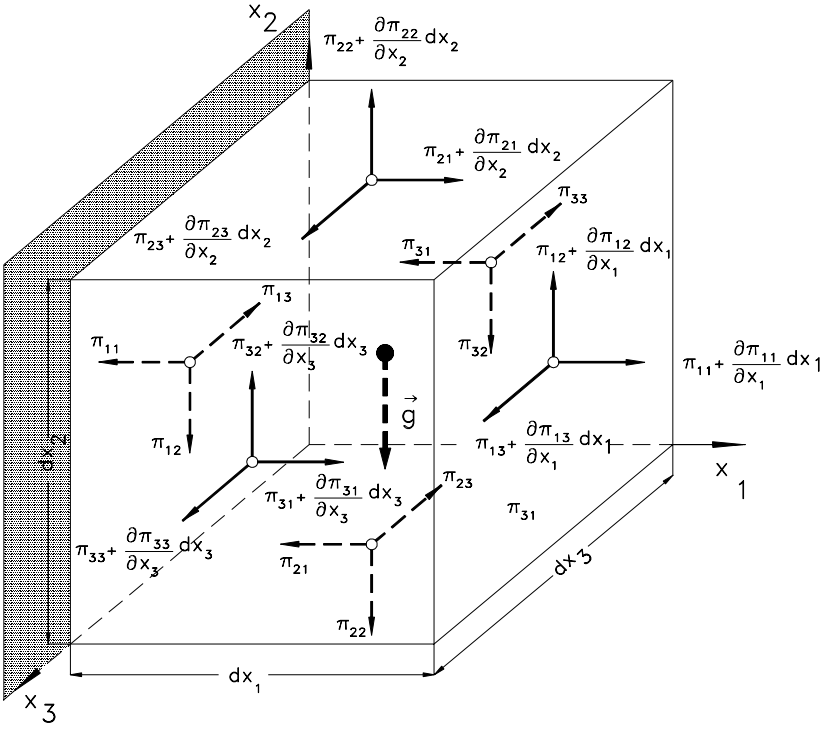

Fig. A.6: General stress condition

The tensor $\boldsymbol{\Pi} = e_i e_j \pi_{ij}$ has the components π_{ij} as the result of forces that are acting on surfaces. Similar to the force components, the first index *i* refers to the axis, to which the fluid element surface is perpendicular, whereas the second index *j* indicates the direction of the stress component.

Considering the stress situation in Fig.A.6, we are now interested in finding the resultant force acting on the infinitesimal fluid particle that occupies the volume element $dV = dx_1 dx_2 dx_3$. For this purpose, we look at the two opposite surfaces that are perpendicular to the axis x_1 as shown in Fig. A.7. As this figure shows, we are dealing with 3 stress components on each surface, from which one on each side is the *normal stress* component such as π_{11} and $\pi_{11} + \frac{\partial \pi_{11}}{\partial x_1} dx_1$. The remaining components are the shear stress components such as π_{12} and $\pi_{12} + \frac{\partial \pi_{12}}{\partial x_1} dx_1$.

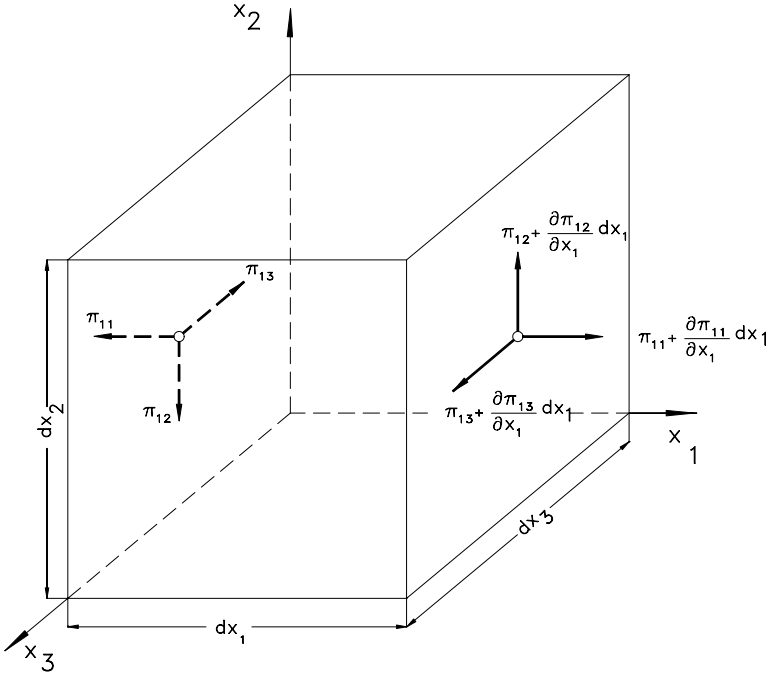

Fig. A.7: General stress condition

According to Fig. A7 the force balance in x_1-directions is

$$e_1\left(\pi_{11} + \frac{\partial \pi_{11}}{\partial x_1}dx_1 - \pi_{11}\right)dx_2dx_3 = e_1\frac{\partial \pi_{11}}{\partial x_1}dx_1dx_2dx_3$$

in x_1-direction, we find

$$e_2\left(\pi_{12} + \frac{\partial \pi_{12}}{\partial x_1}dx_1 - \pi_{12}\right)dx_2dx_3 = e_2\frac{\partial \pi_{12}}{\partial x_1}dx_1dx_2dx_3$$

similarly, in x_2, we obtain

$$e_3\left(\pi_{12} + \frac{\partial \pi_{13}}{\partial x_1}dx_1 - \pi_{13}\right)dx_2dx_3 = e_3\frac{\partial \pi_{13}}{\partial x_1}dx_1dx_2dx_3$$

Thus, the resultant force acting on these two opposite sides is:

$$d\boldsymbol{F}_1 = \left(e_1\frac{\partial \pi_{11}}{\partial x_1} + e_2\frac{\partial \pi_{12}}{\partial x_1} + e_3\frac{\partial \pi_{13}}{\partial x_1}\right)dx_1dx_2dx_3$$

In a similar way, we find the forces acting on the other four surfaces. The total resulting forces acting on the entire surface of the element are obtained by adding the nine components. Defining the volume element $dv = dx_1 dx_2 dx_3$, we divide the results by dv and obtain the resulting force vector that is acting on the volume element.

$$\begin{aligned}\frac{d\boldsymbol{F}}{dv} &= e_1\left[\frac{\partial \pi_{11}}{\partial x_1} + \frac{\partial \pi_{21}}{\partial x_2} + \frac{\partial \pi_{31}}{\partial x_3}\right] + \\ &+ e_2\left[\frac{\partial \pi_{12}}{\partial x_1} + \frac{\partial \pi_{22}}{\partial x_2} + \frac{\partial \pi_{32}}{\partial x_3}\right] + \\ &+ e_3\left[\frac{\partial \pi_{13}}{\partial x_1} + \frac{\partial \pi_{23}}{\partial x_2} + \frac{\partial \pi_{33}}{\partial x_3}\right]\end{aligned} \tag{A.34}$$

Since the stress tensor $\boldsymbol{\Pi}$ is written as:

$$\boldsymbol{\Pi} = e_i e_j \pi_{ij}$$

it can be easily shown that:

$$d\boldsymbol{F} = \nabla \cdot \boldsymbol{\Pi}\, dv \tag{A.35}$$

The expression $\nabla.\boldsymbol{\Pi}$ is a scalar differentiation of the second order stress tensor and is called the divergence of the tensor field $\boldsymbol{\Pi}$. We conclude that the force acting on the surface of a fluid element is the divergence of its stress tensor. The stress tensor is usually divided into its normal and shear stress parts. For an incompressible it can be written as

$$\boldsymbol{\Pi} = -\boldsymbol{I}p + \boldsymbol{T} \tag{A.36}$$

with $\boldsymbol{I}$p as normal and $\boldsymbol{T}$ as the shear stress tensor. with The normal stress tensor is a product of unit tensor $\boldsymbol{I} = e_i e_j \delta_{ij}$ and the pressure p. Inserting Eq. A- (36) into (35) leads to

$$d\boldsymbol{F} = \nabla \cdot \boldsymbol{\Pi}\, dv = (-\nabla p + \nabla \cdot \boldsymbol{T})\, dv \tag{A.37}$$

References, Appendix A

A.1. Aris, R.: Vector, Tensors and the Basic Equations of Fluid Mechanics, englewood Clifs, New Jersey, Prentice-Hall. Inc, 1962.

A.2. Brand, L.: Vector and TesnorAnalysis, John Wiley and sons, New Yuork, 1947.

A.3. Klingbeil, E.: Tensorrechnung für Ingenieure, Mannheim: Bibliographisches Institut, 1966.

A.4. Lagally, M.:Vorlesung über Vektorrechnung, dritte Auflage, Akademische Verlagsgeselschaft, Leipzig, 1944.
A.5. Vavra, M.H, 1960, “Aero-Thermodynamics and Flow in Turbomachines,” John Wiley & Sons, Inc.

B Tensor Operations in Orthogonal Curvilinear Coordinate Systems

B.1 Change of Coordinate System

The vector and tensor operations we have discussed in the foregoing chapters were performed solely in rectangular coordinate system. It should be pointed out that we were dealing with quantities such as velocity, acceleration, and pressure gradient that are independent of any coordinate system within a certain frame of reference. In this connection it is necessary to distinguish between coordinate system and frame of reference. The following example should clarify this distinction. In an absolute frame of reference, the flow velocity vector may be described by the rectangular Cartesian coordinate x_i:

$$\boldsymbol{V} = \boldsymbol{V}(x_1,\ x_2,\ x_3) = \boldsymbol{V}(\boldsymbol{X}) \tag{B.1}$$

It may also be described by a cylindrical coordinate system, which is a non-Cartesian coordinate system:

$$\boldsymbol{V} = \boldsymbol{V}(x,\ r,\ \theta) \tag{B.2}$$

or generally by any other non-cartesian or curvilinear coordinate ξ_i that describes the flow channel geometry:

$$\boldsymbol{V} = \boldsymbol{V}(\xi_1,\ \xi_2,\ \xi_3) \tag{B.3}$$

By changing the coordinate system, the flow velocity vector will not change. It remains invariant under any transformation of coordinates. This is true for any other quantities such as acceleration, force, pressure or temperature gradient. The concept of invariance, however, is generally no longer valid if we change the frame of reference. For example, if the flow particles leave the absolute frame of reference and enter the relative frame of reference its velocity will experience a change. In this Chapter, we will pursue the concept of quantity invariance and discuss the fundamentals that are needed for coordinate transformation.

B.2 Co- and Contravariant Base Vectors, Metric Coefficients

As we saw in previous chapter, a vector quantity is described in Cartesian coordinate system x by its$_i$ components:

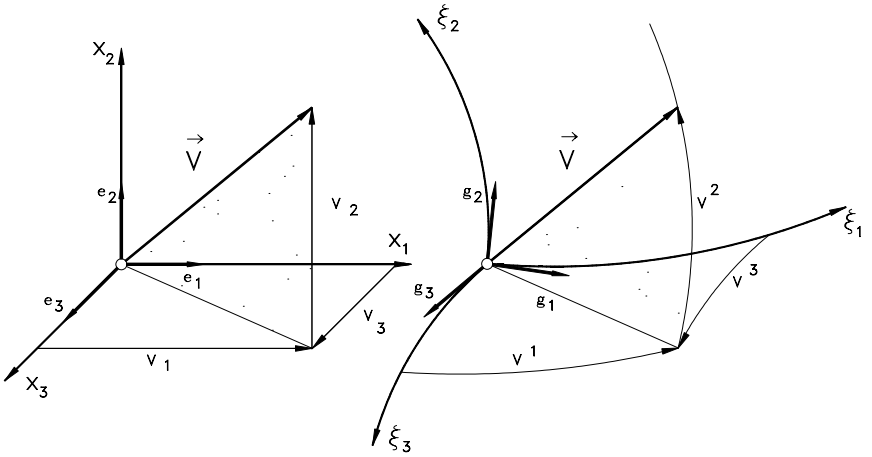

Fig. B.1: Base vectors in a Cartesian (left) and in a generalized orthogonal curvilinear coordinate system (right)

$$\boldsymbol{V} = \boldsymbol{e}_i V_i = \boldsymbol{e}_1 V_1 + \boldsymbol{e}_2 V_2 + \boldsymbol{e}_3 V_3 \tag{B.4}$$

with e_i as orthogonal unit vectors (Fig. B.1 left). The same vector transformed into the curvilinear coordinate system ξ_k (Fig. B.1 right) is represented by:

$$\boldsymbol{V} = \boldsymbol{g}_k V^k = \boldsymbol{g}_1 V^1 + \boldsymbol{g}_2 V^2 + \boldsymbol{g}_3 V^3 \tag{B.5}$$

where $\mathbf{g}_k$ are the base vectors and $\mathbf{V}^k$ the components of $\mathbf{V}$ with respect to the base $\mathbf{g}_k$ in a curvilinear coordinate system. For curvilinear coordinate system, we place the indices diagonally for summing convenience. Unlike the Cartesian base vectors $\mathbf{e}_i$, that are orthonormal vectors (of unit length and mutually orthogonal), the base vectors $\mathbf{g}_k$ do not have unit lengths. The base vectors $\mathbf{g}_k$ represent the rate of change of the position vector $\mathbf{x}$ with respect to the curvilinear coordinates ξ_i.

$$\boldsymbol{g}_k = \frac{\partial \boldsymbol{x}}{\partial \xi_k} = \frac{\partial (\boldsymbol{e}_i x_i)}{\partial \xi_k} \tag{B.6}$$

Since in a Cartesian coordinate system the unit vectors $\mathbf{e}_i$, are not functions of the coordinates x_i, Eq. (B.6) can be written as:

$$\boldsymbol{g}_k = \boldsymbol{e}_i \frac{\partial x_i}{\partial \xi_k} \tag{B.7}$$

Similarly, the reciprocal base vector $\mathbf{g}^k$ defined as:

$$\boldsymbol{g}^j = \boldsymbol{e}_m \frac{\partial \xi_j}{\partial x_m} \tag{B.8}$$

These base vectors are interrelated by:

$$\boldsymbol{g}_k \cdot \boldsymbol{g}^j = \boldsymbol{e}_i \cdot \boldsymbol{e}_m \frac{\partial x_i}{\partial \xi_k} \frac{\partial \xi_j}{\partial x_m} = \delta_{im} \frac{\partial x_i}{\partial \xi_k} \frac{\partial \xi_j}{\partial x_m} = \frac{\partial \xi_j}{\partial \xi_k} = \delta_k^{\ j} \tag{B.9}$$

where $\mathbf{g}_k$ and $\mathbf{g}^j$ are referred to as the covariant and contravariant base vectors, respectively. The new Kronecker delta $\delta_k^{\ j}$ from Eq. (B.9) has the values:

$$\boldsymbol{g}_k \cdot \boldsymbol{g}^j = \delta_k^j, \quad \delta_k^j = 1 \text{ for } k = j, \quad \delta_k^j = 0 \text{ for } k \neq j$$

The vector **V** explained in contravariant base is:

$$\boldsymbol{V} = \boldsymbol{g}^k V_k = \boldsymbol{g}^1 V_1 + \boldsymbol{g}^2 V_2 + \boldsymbol{g}^3 V_3 \tag{B.10}$$

Similarly, the components V_k and V^k are called the covariant and contravariant components respectively. The scalar product of covariant respectively contravariant base vectors results in the covariant and covariant metric coefficients:

$$g_{ij} = \boldsymbol{g}_i \cdot \boldsymbol{g}_j, \quad g^{ij} = \boldsymbol{g}^i \cdot \boldsymbol{g}^j \tag{B.11}$$

The mixed metric coefficient is defined as

$$g_i^{\ j} = \boldsymbol{g}_i \cdot \boldsymbol{g}^j \tag{B.12}$$

The covariant base vectors can be expressed in terms of the contravariant base vectors. First we assume that:

$$\begin{aligned} \boldsymbol{g}^1 &= A^{11}\boldsymbol{g}_1 + A^{12}\boldsymbol{g}_2 + A^{13}\boldsymbol{g}_3 \\ \boldsymbol{g}^2 &= A^{21}\boldsymbol{g}_1 + A^{22}\boldsymbol{g}_2 + A^{23}\boldsymbol{g}_3 \\ \boldsymbol{g}^3 &= A^{31}\boldsymbol{g}_1 + A^{32}\boldsymbol{g}_2 + A^{33}\boldsymbol{g}_3 \end{aligned} \tag{B.13}$$

Generally the contravariant base vector can be written

$$\boldsymbol{g}^i = A^{ij}\boldsymbol{g}_j \tag{B.14}$$

To find a direct relation between the base vectors, first coefficient matrix A^{ij} must be determined. To do so, we multiply Eq. (B.14) with $\mathbf{g}^k$ scalarly:

$$\boldsymbol{g}^i \cdot \boldsymbol{g}^k = A^{ij}\boldsymbol{g}_j \cdot \boldsymbol{g}^k \tag{B.15}$$

This leads to $g^{ik} = A^{ij}\delta_j^k$. The right hand side is different from zero only if j = k. That means:

$$g^{ik} = A^{ik} \tag{B.16}$$

Introducing Eq. (B.16) into (B.14) results in a relation that expresses the contravariant base vectors in terms of covariant base vectors:

$$\boldsymbol{g}^i = g^{ij}\boldsymbol{g}_j \tag{B.17}$$

The covariant base vector can also be expressed in terms of contravariant base vectors in a similar way:

$$\boldsymbol{g}_k = g_{kl}\boldsymbol{g}^l \tag{B.18}$$

Multiply Eq. (B.l8) with (B.17) establishes a relationship between the covariant and contravariant metric coefficients:

$$\boldsymbol{g}^i \cdot \boldsymbol{g}_k = g^{ij} g_{kl} \boldsymbol{g}_j \cdot \boldsymbol{g}^l, \quad \text{and} \quad \delta^i_k = g^{ij} g_{kl} \delta^l_j \tag{B.19}$$

Applying the Kronecker delta on the right hand side results in:

$$g^{ij} g_{kj} = \delta^i_k \tag{B.20}$$

B.3 Physical Components of a Vector

As mentioned previously, the base vectors $\mathbf{g}_i$ or $\mathbf{g}^j$ are not unit vectors. Consequently the co- and contravariant components vector components V_j or V^1 do not reflect the physical components of vector **V**. To obtain the physical components, first the corresponding unit vectors must be found. They can be obtained from:

$$\boldsymbol{g}^*_i = \frac{\boldsymbol{g}_i}{|\boldsymbol{g}_i|} = \frac{\boldsymbol{g}^i}{\sqrt{\boldsymbol{g}_i \cdot \boldsymbol{g}_i}} = \frac{\boldsymbol{g}_i}{\sqrt{g_{(ii)}}} \tag{B.21}$$

Similarly, the contravariant unit vectors are:

$$\boldsymbol{g}^{*i} = \frac{\boldsymbol{g}^i}{|\boldsymbol{g}^i|} = \frac{\boldsymbol{g}^i}{\sqrt{\boldsymbol{g}^i \cdot \boldsymbol{g}^i}} = \frac{\boldsymbol{g}^i}{\sqrt{g^{(ii)}}} \tag{B.22}$$

where $\mathbf{g}^*_i$, represents the unit base vector, $|\mathbf{g}_i|$ the absolute value of the base vector. The index inside the parenthesis does not imply a summing. The vector can now be expressed in terms of its unit base vectors and the corresponding components:

$$\boldsymbol{V} = \boldsymbol{g}_i V^i = \boldsymbol{g}^*_i V^{*i} = \frac{\boldsymbol{g}_i}{\sqrt{g_{(ii)}}} V^{*i} \tag{B.23}$$

Thus the covariant and contravariant physical components can be easily obtained from:

$$V^*_i = \sqrt{g^{(ii)}} V_i, \quad V^{*i} = \sqrt{g_{(ii)}} V^i \tag{B.24}$$

B.4 Derivatives of the Base Vectors, Christoffel Symbols

In a curvilinear coordinate system, the base vectors are generally functions of the coordinates itself. This fact must be considered while differentiating the base vectors. Consider the derivative:

$$\boldsymbol{g}_{i,j} = \frac{\partial \boldsymbol{g}_i}{\partial \xi j} = \frac{\partial}{\partial \xi j}\left(e_k \frac{\partial x_k}{\partial \xi_i}\right) = e_k \frac{\partial^2 x_k}{\partial \xi_j \partial \xi_i} \tag{B.25}$$

Similar to Eq. (B.7), the unit vector $\mathbf{e}_k$ can be written:

$$\boldsymbol{e}_k = \boldsymbol{g}_n \frac{\partial \xi_n}{\partial x_k} \tag{B.26}$$

Introducing Eq. (B.26) into (B.25) yields:

$$\boldsymbol{g}_{i,j} = \frac{\partial^2 x_k}{\partial \xi_j \partial \xi_i} \frac{\partial \xi_n}{\partial x_k} \boldsymbol{g}_n \equiv \Gamma_{ij}^n \boldsymbol{g}_n \tag{B.27}$$

with $\Gamma_{ij}^{\ n}$ as the Christoffel symbol second kind with the definition:

$$\Gamma_{ij}^n = \frac{\partial^2 x_k}{\partial \xi_j \partial \xi_i} \frac{\partial \xi_n}{\partial x_k} \tag{B.28}$$

The derivative of contravariant base vector is:

$$\boldsymbol{g}_{,i}^j \equiv \frac{\partial \boldsymbol{g}^j}{\partial \xi_i} = -\Gamma_{ik}^j \boldsymbol{g}^k \tag{B.29}$$

The Christoffel symbols are then obtained by expanding Eq. (B .28):

$$\Gamma_{ml}^k = \Gamma_{lm}^k = \frac{1}{2} g^{(kk)} \left(g_{mk,l} + g_{kl,m} - g_{lm,k}\right) \tag{B.30}$$

Note that the repeated indices in a parenthesis such as $g^{(kk)}$ does not subject to the summation.

B.5 Spatial Derivatives in Curvilinear Coordinate System

The differential operator ∇, Nabla, is in curvilinear coordinate system defined as:

$$\nabla = g^i \frac{\partial}{\partial \xi_i} \tag{B.31}$$

B.5.1 Application of ∇ to Tensor Functions

In this chapter, the operator ∇ will be applied to different arguments such as zeroth, first and second order tensors. If the argument is a zeroth order tensor which is a

scalar quantity such as pressure or temperature, the results of the operation is the gradient of the scalar field which is a vector quantity:

$$\nabla p = \boldsymbol{g}^i \frac{\partial p}{\partial \xi_i} = \boldsymbol{g}^i p_{,i} \tag{B.32}$$

If the argument is a first order tensor such as velocity vector, the order of the resulting tensor depends on the operation character between the operator ∇ and the argument. For scalar differentiation it follows:

$$\nabla \cdot \boldsymbol{V} = \boldsymbol{g}^i \cdot \left[\frac{\partial \left(\boldsymbol{g}_j V^j \right)}{\partial \xi_i} \right] \tag{B.33}$$

Applying the chain rule and using the Christoffel symbol, the result of the operation is the divergence of the vector quantity and is a zeroth order tensor or a scalar. It should be noticed that a scalar operation leads to a contraction of the order of tensor on which the operator is acting.

$$\nabla \cdot \boldsymbol{V} = V^i_{,i} + V^J \Gamma^i_{ij} \tag{B.34}$$

If there is no operation sign between the differential operator and the first order tensor such as velocity, the result of such an operation is the gradient of tensor field which is a second order tensor:

$$\nabla \boldsymbol{V} = \boldsymbol{g}^i \boldsymbol{g}_j \left(V^j_{,i} + V^k \Gamma^j_{ik} \right) \tag{B.35}$$

If the operator is a second order tensor, such as stress tensor or deformation tensor, the scalar operation results in a first order tensor which is a vector:

$$\nabla \cdot T = \boldsymbol{g}^m \cdot \frac{\partial T}{\partial \xi_m} = \boldsymbol{g}^m \cdot \left(\boldsymbol{g}_k \boldsymbol{g}_l \right) \left(T^{kl}_{,m} + T^{nl} \Gamma^k_{nm} + T^{kn} \Gamma^l_{nm} \right) \tag{B.36}$$

The right hand side is reduced to:

$$\nabla \cdot T = \boldsymbol{g}_j \left(T^{mj}_{,m} + T^{nj} \Gamma^m_{nm} + T^{mn} \Gamma^j_{mn} \right) \tag{B.37}$$

By calculating the shear forces using the Navier-Stokes equation, the second derivative, the Laplace operator Δ, is needed:

$$\Delta = \nabla \cdot \nabla = \nabla^2 \tag{B.38}$$

Applied to the velocity vector yields:

$$\nabla^2 \boldsymbol{V} = \boldsymbol{g}_m \left[V_{,ik}^{m} + V_{,i}^{n} \Gamma_{nk}^{m} + V_{,k}^{n} \Gamma_{ni}^{m} - V_{,j}^{m} \Gamma_{ik}^{j} \right] g^{ik} + \boldsymbol{g}_m \left[V^p \left(\Gamma_{pi}^{n} \Gamma_{nk}^{m} - \Gamma_{ik}^{j} \Gamma_{pj}^{m} + \Gamma_{pi,k}^{m} \right) \right] g^{ik} \tag{B.39}$$

B.6 Application Example 1: Inviscid Flow Motion

As the first application example, the equation of motion for an inviscid flow is transferred into a cylindrical coordinate system, where it should be decomposed in its three components r, θ, z. The coordinate invariant version of the equation is written as:

$$\boldsymbol{V} \cdot \nabla \boldsymbol{V} = -\frac{1}{\rho} \nabla p \tag{B.40}$$

The transformation and decomposition procedure is shown in the following steps.

B.6.1 Equation of Motion in Curvilinear Coordinate Systems

The second order tensor on the left hand side can be obtained using Eq. (B.35):

$$\nabla \boldsymbol{V} = \boldsymbol{g}^i \boldsymbol{g}_j \left(V_{,i}^{j} + V^k \Gamma_{ik}^{j} \right) \tag{B.41}$$

The scalar multiplication with the velocity vector **V** leads to:

$$\boldsymbol{V} \cdot \nabla \boldsymbol{V} = \boldsymbol{g}_m \boldsymbol{V}^m \cdot \boldsymbol{g}^i \boldsymbol{g}_j \left(V_{,i}^{j} + V^k \Gamma_{ik}^{j} \right) \tag{B.42}$$

Introducing the mixed Kronecker delta:

$$\boldsymbol{V} \cdot \nabla \boldsymbol{V} = \delta_m^i \boldsymbol{g}_j V^m \left(V_{,i}^{j} + V^k \Gamma_{ik}^{j} \right) \tag{B.43}$$

For an orthogonal curvilinear coordinate system the mixed Kronecker delta is:

$$\begin{aligned} \delta_m^i &= 1 \quad \text{for} \quad i = m \\ \delta_m^i &= 0 \quad \text{for} \quad i \neq m \end{aligned} \tag{B.44}$$

Taking this into account, Eq. (B.43) yields:

$$\boldsymbol{V} \cdot \nabla \boldsymbol{V} = \boldsymbol{g}_j \boldsymbol{V}^i \left(V_{,i}^{j} + V^k \Gamma_{ik}^{j} \right) \tag{B.45}$$

Rearranging the indices

$$\boldsymbol{V} \cdot \nabla \boldsymbol{V} = \boldsymbol{g}_i \left(V^j V_{,j}^{i} + V^j V^k \Gamma_{kj}^{i} \right) \tag{B.46}$$

The pressure gradient on the right hand side of Eq. (B.40) is calculated form Eq. (B.32):

$$\nabla p = \boldsymbol{g}^i \frac{\partial p}{\partial \xi_i} = \boldsymbol{g}^i p_{,i} \tag{B.47}$$

Replacing the contravariant base vector with the covariant one using Eq. (B.47) leads to:

$$\nabla p = \boldsymbol{g}^i \frac{\partial p}{\partial \xi_i} = \boldsymbol{g}_i g^{ji} p_{,j} \tag{B.48}$$

Incorporating Eqs. (B.46) and B- (48) into Eq. (B.40) yields:

$$\boldsymbol{g}_i \left(V^j V^i_{,j} + V^j V^k \Gamma^i_{kj} \right) = -\frac{1}{\rho} \boldsymbol{g}_i g^{ji} p_{,j} \tag{B.49}$$

In i-direction, the equation of motion is:

$$V^j V^i_{,j} + V^j V^k \Gamma^i_{kj} = -\frac{1}{\rho} g^{ji} p,j \tag{B.50}$$

B.6.2 Special Case: Cylindrical Coordinate System

To transfer Eq. (B.40) in any arbitrary curvilinear coordinate system, first the coordinate system must be specified. The cylinder coordinate system is related to the Cartesian coordinate system is given by:

$$x_1 = r\cos\Theta\,,\; x_2 = r\sin\Theta,\; x_3 = z \tag{B.51}$$

The curvilinear coordinate system is represented by:

$$\xi_1 = r,\; \xi_2 = \Theta,\; \xi_3 = z \tag{B.52}$$

B.6.3 Base Vectors, Metric Coefficients

The base vectors are calculated from Eq. (B.7).

$$\boldsymbol{g}_k = \boldsymbol{e}_i \frac{\partial x_i}{\partial \xi_k} \tag{B.53}$$

Equation (B.53) decomposed in its components yields:

$$\begin{aligned}
\boldsymbol{g}_1 &= \boldsymbol{e}_1 \frac{\partial x_1}{\partial \xi_1} + e_2 \frac{\partial x_2}{\partial \xi_1} + e_3 \frac{\partial x_3}{\partial \xi_1} \\
\boldsymbol{g}_2 &= e_1 \frac{\partial x_1}{\partial \xi_2} + e_2 \frac{\partial x_2}{\partial \xi_2} + e_3 \frac{\partial x_3}{\partial \xi_2} \\
\boldsymbol{g}_3 &= e_1 \frac{\partial x_1}{\partial \xi_3} + e_2 \frac{\partial x_2}{\partial \xi_3} + e_3 \frac{\partial x_3}{\partial \xi_3}
\end{aligned} \tag{B.54}$$

The differentiation of the Cartesian coordinates yields:

$$\begin{aligned}
\boldsymbol{g}_1 &= e_1 \cos\theta + e_2 \sin\theta \\
\boldsymbol{g}_2 &= -e_1 r \sin\theta + e_2 r \cos\theta \\
\boldsymbol{g}_3 &= e_3
\end{aligned} \tag{B.55}$$

The co- and contravariant metric coefficients are:

$$\left(g_{ij}\right) = \begin{pmatrix} 1 & 0 & 0 \\ 0 & r^2 & 0 \\ 0 & 0 & 1 \end{pmatrix}, \quad \left(g^{ij}\right) = \begin{pmatrix} 1 & 0 & 0 \\ 0 & 1/r^2 & 0 \\ 0 & 0 & 1 \end{pmatrix} \tag{B.56}$$

The contravariant base vectors are obtained from:

$$\begin{aligned}
\boldsymbol{g}^i &= g^{ij} \boldsymbol{g}_j \\
\boldsymbol{g}^1 &= g^{11} \boldsymbol{g}_1 + g^{12} \boldsymbol{g}_2 + g^{13} \boldsymbol{g}_3 \\
\boldsymbol{g}^2 &= g^{21} \boldsymbol{g}_1 + g^{22} \boldsymbol{g}_2 + g^{23} \boldsymbol{g}_3 \\
\boldsymbol{g}^3 &= g^{31} \boldsymbol{g}_1 + g^{32} \boldsymbol{g}_2 + g^{33} \boldsymbol{g}_3
\end{aligned} \tag{B.57}$$

B.6.4 Christoffel Symbols

The Christoffel symbols are calculated from Eq. (B.30)

$$\Gamma^k_{ml} = \Gamma^k_{lm} = \frac{1}{2} g^{(kk)} \left(g_{mk,l} + g_{kl,m} - g_{lm,k} \right) \tag{B.58}$$

To follow the calculation procedure, one zero- element and one non-zero element are calculated:

$$\Gamma_{11}^{1} = \frac{1}{2} g^{11} \left(\frac{\partial g_{11}}{\partial \xi_1} + \frac{\partial g_{11}}{\partial \xi_1} - \frac{\partial g_{11}}{\partial \xi_1} \right) = 0$$
$$\Gamma_{22}^{1} = \frac{1}{2} g^{11} \left(\frac{\partial g_{21}}{\partial \xi_2} + \frac{\partial g_{12}}{\partial \xi_2} - \frac{\partial g_{22}}{\partial \xi_2} \right) = -r \tag{B.59}$$

All other elements are calculated similarly. They are shown in the following matrices:

$$\left(\Gamma_{lm}^{1}\right) = \begin{pmatrix} 0 & 0 & 0 \\ 0 & -r & 0 \\ 0 & 0 & 0 \end{pmatrix}, \quad \left(\Gamma_{lm}^{2}\right) = \begin{pmatrix} 0 & 1/r & 0 \\ 1/r & 0 & 0 \\ 0 & 0 & 0 \end{pmatrix}, \quad \left(\Gamma_{lm}^{3}\right) = \begin{pmatrix} 0 & 0 & 0 \\ 0 & 0 & 0 \\ 0 & 0 & 0 \end{pmatrix} \tag{B.60}$$

Introducing the non-zero Christoffel symbols into Eq. (B.50), the components in g_1, g_2, and g_3 directions are:

$$V^1 V_{,1}^{1} + V^2 V_{,2}^{1} + V^3 V_{,3}^{1} + \Gamma_{22}^{1} V^2 V^2 = -\frac{1}{\rho} g^{11} p_{,1} \tag{B.61}$$

$$V^1 V_{,1}^{2} + V^2 V_{,2}^{2} + V^3 V_{,3}^{2} + 2\Gamma_{21}^{2} V^2 V^1 = -\frac{1}{\rho} g^{22} p_{,2} \tag{B.62}$$

$$V^1 V_{,1}^{3} + V^2 V_{,2}^{3} + V^3 V_{,3}^{3} = -\frac{1}{\rho} g^{33} p_{,3} \tag{B.63}$$

B.6.5 Introduction of Physical Components

The physical components can be calculated from Eqs. (B.21) and (B.24):

$$V_i^* = \sqrt{g^{(ii)}}\, V_i, \; V^{*i} = \sqrt{g_{(ii)}}\, V^i$$
$$V^{*1} = \sqrt{g_{(11)}}\, V_1, \; V^{*2} = \sqrt{g_{(22)}}\, V^2; \; V^{*3} = \sqrt{g_{33}}\, V^3 \tag{B.64}$$
$$V^{*1} = \sqrt{1}\, V^1; V^{*2} = \sqrt{r^2}\, V^2; \; V^{*3} = \sqrt{1}\, V^3$$

The V^i -components expressed in terms of V^{*i} are:

$$V^1 = V^{*1} \; ; \; V^2 = \frac{1}{r} V^{*2} \; ; \; V^3 = V^{*3} \tag{B.65}$$

Introducing Eqs.(B.65) into (B.61), (B.62), and (B.63) results in:

$$V^{*1}V^{*1}_{,1} + \frac{V^{*2}}{r}V^{*1}_{,2} + V^{*3}V^{*1}_{,3} + \Gamma^1_{22}\frac{V^{*2}V^{*2}}{r^2} = -\frac{1}{\rho}g^{11}p_{,1} \tag{B.66}$$

$$V^{*1}\frac{V^{*2}_{,1}}{r} - V^{*1}\frac{V^{*2}}{r^2} + \frac{V^{*2}}{r^2}V^{*2}_{,2} + V^{*3}\frac{V^{*2}_{,3}}{r} + \frac{2}{r}\Gamma^2_{21}V^{*2}V^{*1} = -\frac{1}{\rho}g^{22}p_{,2} \tag{B.67}$$

$$V^{*1}V^{*3}_{,1} + \frac{V^{*2}}{r}V^{*3}_{,2} + V^{*3}V^{*3}_{,3} = -\frac{1}{\rho}g^{33}p_{,2} \tag{B.68}$$

According to the definition:

$$\xi_1 = r;\ \xi_2 = \Theta;\ \xi_3 = z \tag{B.69}$$

the physical components of the velocity vectors are:

$$V^{*1} = V_r;\ V^{*2} = V_\Theta;\ V^{*3} = V_z \tag{B.70}$$

and insert these relations into Eqs. (B.66) to (B.68), the resulting components in r, Θ, and z directions are:

$$\begin{aligned}
&V_r\frac{\partial V_r}{\partial r} + \frac{V_\Theta}{r}\frac{\partial V_r}{\partial \Theta} + V_z\frac{\partial V_r}{\partial z} - \frac{V_\Theta^2}{r} = -\frac{1}{\rho}\frac{\partial p}{\partial r}\\
&V_r\frac{\partial V_\Theta}{\partial r} + \frac{V_\Theta}{r}\frac{\partial V_\Theta}{\partial \Theta} + V_z\frac{\partial V_\Theta}{\partial z} + \frac{V_rV_\Theta}{r} = -\frac{1}{\rho}\frac{\partial p}{r\partial \Theta}\\
&V_r\frac{\partial V_z}{\partial r} + \frac{V_\Theta}{r}\frac{\partial V_z}{\partial \Theta} + V_z\frac{\partial V_z}{\partial z} = -\frac{1}{\rho}\frac{\partial p}{\partial z}
\end{aligned} \tag{B.71}$$

B.7. Application Example 2: Viscous Flow Motion

As the second application example, the Navier-Stokes equation of motion for a viscous incompressible flow is transferred into a cylindrical coordinate system, where it is decomposed in its three components r, θ, z. The coordinate invariant version of the equation is written as:

$$\boldsymbol{V}\cdot\nabla\boldsymbol{V} = -\frac{1}{\rho}\nabla p + \nu\nabla^2\boldsymbol{V} \tag{B.72}$$

The second term on the right hand side of Eq. (B.72) exhibits the shear stress force. It was treated in section B.5, Eq. (B.39) and is the only term that has been added to the equation of motion for inviscid flow, Eq. (B.40).

B.7.1 Equation of Motion in Curvilinear Coordinate Systems

The transformation and decomposition procedure is similar to the example in section B. 6. Therefore, a step by step derivation is not necessary.

$$\begin{aligned} \boldsymbol{g}_i\left(V^j V^i_{,j} + V^j V^k \Gamma^i_{kj}\right) &= -\frac{1}{\rho}\boldsymbol{g}_i g^{ji} p_{,j} + \nu \boldsymbol{g}_m \Big[V^m_{,ik} + \\ & V^n_{,i}\Gamma^m_{nk} + V^n_{,k}\Gamma^m_{ni} - V^m_{,j}\Gamma^j_{ik} + \\ & V^p\left(\Gamma^n_{pi}\Gamma^m_{nk} - \Gamma^j_{ik}\Gamma^m_{pj} + \Gamma^m_{pi,k}\right)\Big] g^{ik} \end{aligned} \tag{B.73}$$

B.7.2 Special Case: Cylindrical Coordinate System

Using the Christoffel symbols from section B.6.4 and the physical components from B.6.5, and inserting the corresponding relations these relations into Eqs. (B.73), the resulting components in r, Θ, and z directions are:

$$\begin{aligned} V_r\frac{\partial V_r}{\partial r} + \frac{V_\Theta}{r}\frac{\partial V_r}{\partial \theta} + V_z\frac{\partial V_r}{\partial z} - \frac{V_\Theta^2}{r} &= -\frac{1}{\rho}\frac{\partial p}{\partial r} + \\ \nu\left(\frac{\partial^2 V_r}{\partial r^2} + \frac{1}{r^2}\frac{\partial^2 V_r}{\partial \Theta^2} + \frac{\partial^2 V_r}{\partial z^2} - 2\frac{\partial V_\Theta}{r^2\partial\Theta} + \frac{\partial V_r}{r\partial r} - \frac{V_r}{r^2}\right) & \end{aligned} \tag{B.74}$$

$$\begin{aligned} V_r\frac{\partial V_\Theta}{\partial r} + \frac{V_\Theta}{r}\frac{\partial V_\Theta}{\partial \Theta} + V_z\frac{\partial V_\Theta}{\partial z} + \frac{V_r V_\Theta}{r} &= -\frac{1}{\rho}\frac{\partial p}{r\partial\Theta} \\ + \nu\left(\frac{\partial^2 V_\Theta}{\partial r^2} + \frac{1}{r^2}\frac{\partial^2 V_\Theta}{\partial \Theta^2} + \frac{\partial^2 V_\Theta}{\partial z^2} + \frac{2}{r^2}\frac{\partial V_r}{r^2\partial\Theta} + \frac{1}{r}\frac{\partial V_\Theta}{\partial r} - \frac{V_\Theta}{r^2}\right) & \end{aligned} \tag{B.75}$$

$$\begin{aligned} V_r\frac{\partial V_z}{\partial r} + \frac{V_\Theta}{r}\frac{\partial V_z}{\partial z} + V_z\frac{\partial V_z}{\partial z} &= -\frac{1}{\rho}\frac{\partial p}{\partial z} \\ + \nu\left[\frac{\partial^2 V_z}{\partial r^2} + \frac{\partial^2 V_z}{r^2\partial\Theta^2} + \frac{\partial^2 V_z}{\partial z^2} + \frac{1}{r}\frac{\partial V_z}{\partial r}\right] & \end{aligned}$$

$$d\boldsymbol{F} = \nabla\cdot\boldsymbol{\Pi}\, dv = (-\nabla p + \nabla\cdot\boldsymbol{T})\, dv \tag{A.37}$$

References, Appendix B

B.1 Aris, R.: Vector, Tensors and the Basic Equations of Fluid Mechanics, englewood Clifs, New Jersey, Prentice-Hall. Inc, 1962.
B.2 Brand, L.: Vector and TesnorAnalysis, John Wiley and sons, New Yuork, 1947.
B.3 Klingbeil, E.: Tensorrechnung für Ingenieure, Mannheim: Bibliographisches Institut, 1966.
B.4 Lagally, M.:Vorlesung über Vektorrechnung, dritte Auflage, Akademische Verlagsgeselschaft, Leipzig, 1944.
B.5 Vavra, M.H, 1960, “Aero-Thermodynamics and Flow in Turbomachines,” John Wiley &S ons, Inc.

Index